PHYS VIEW

VOLUME 100 NUMBER 4

1958

PHYSICAL REVIEW

A Journal of Experimental and Theoretical Physics established by E. L. Nichols in 1893

Published by the American Institute of Physics for the

AMERICAN PHYSICAL SOCIETY

Officers

President

R. T. Birge
University of California
Berkeley, California

Vice-President

S. P. Wilgard
Princeton University
Princeton, New Jersey

Secretary

E. U. Condon
Bell Telephone Laboratories
Office:
Columbia University
New York 27, New York

Treasurer

G. B. Pegram
Columbia University
New York 27, New York

Local Secretary
for the Pacific Coast

William A. Nierenberg
University of California
Berkeley, California

Managing Editor

S. A. Goudsmit
Brookhaven National Laboratory
Upton, Long Island
New York

BOARD OF EDITORS

Editor

S. A. Goudsmit

Associate Editors

1950-1952

W. A. Fowler
Kenneth Greisen
Charles Kittel
R. E. Marshak
W. K. H. Panofsky
V. F. Weisskopf

1951-1953

E. M. Purcell
J. C. Slater

Manuscripts for publication should be submitted to S. A. Goudsmit, Brookhaven National Laboratory, Upton, Long Island, New York. Detailed authors' instructions are contained in each issue of the publication on the first page which, if honored, should result in the most rapid publication. Proofs will be sent with galley proofs.

Proof and all correspondence concerning changes in the proofs should be addressed to the Production Manager, American Institute of Physics, 57 East 55 Street, New York 22, New York.

Subscription Rates

United States and Canada .....
Elsewhere .....

Publication Schedule

Yearly book number and other publication dates as available:

Prior to 1949: [illegible]

Thereafter:

Single copies: $1.00 each, [illegible];
$1.50 each, July, 1941 – December, 1941;
$2.00 each, January, 1942 – December, 1944;
$3.00 each, thereafter.

General rates, 1951: Price $4.00

1951 [illegible] Foreign Handling $0.50 (Members); $1.00 (Non-Members); Canada Handling $0.25 (Members); $0.50 (Non-Members); Foreign [illegible]

Subscriptions, renewals, and changes of address should be addressed to the American Institute of Physics, 57 East 55 Street, New York 22, New York.

Changes of address for the case of members of the American Physical Society should be addressed to the Treasurer's Office. In case of other subscribers to the American Institute of Physics.

[illegible]

The Physical Review is published semi-monthly at Prince and Lemon Streets, Lancaster, Pennsylvania.

Entered as second-class matter March 6, 1917, at the Post Office at Lancaster, Pennsylvania, under the Act of March 3, 1879. Acceptance for mailing at special rate of postage provided for in paragraph [illegible] of the act of [illegible] authorized [illegible]

THE
PHYSICAL REVIEW

A journal of experimental and theoretical physics established by E. L. Nichols in 1893

SECOND SERIES, VOL. 100, NO. 4 NOVEMBER 15, 1955

Interatomic Correlations in Liquid He^4

LOUIS GOLDSTEIN
University of California, Los Alamos Scientific Laboratory, Los Alamos, New Mexico
(Received March 21, 1955)

The direct correlation functions, of generally short-range character over most of the liquid temperature interval, have been obtained with the liquid He^4 x-ray scattering data of Reekie, using the 701 IBM Electronic Calculator. The geometrical simplicity of these functions when compared with the indirect correlation functions, of more intuitive physical significance, is automatically demonstrated. They closely satisfy two types of integral test relations, and this fact proves their over-all correct character and the internal consistency of the numerical analysis.

The previously obtained indirect correlation functions will be used here in studying the interference properties of the liquid in slow-neutron scattering processes, in the limiting static approximation. At temperatures not too close to the critical region, the static interference integrals are always negative as a result of the preponderant destructive interference effects arising from the local density defects from the mean density, outweighing the local density excesses. At short and moderate neutron wavelengths, where the use of the static interference integrals is better justified, the total slow-neutron scattering cross sections in liquid He^4, and in liquids in general, always increase with increasing temperature. The static interference integrals will be shown to provide an additional integral test on the indirect correlation functions. The latter were found to satisfy this test relation with good accuracy.

Part of this paper is devoted to a numerical evaluation of mean kinetic energies per liquid He^4 atom as a function of the temperature. The existence of a large zero-point kinetic energy of the liquid as compared with the kinetic energy of thermal origin is demonstrated. Furthermore, the previously given qualitative proof of the kinetic energy origin of the lambda transition could be made semiquantitative. Finally, root-mean-square forces acting on a liquid atom are evaluated, this physical quantity of elementary character having become, in principle at least, accessible through the experimental investigation of slow-neutron scattering properties of liquids.

1. INTRODUCTION

IN a recent work, Reekie and the writer[1] have given an extensive analysis of the liquid helium indirect correlations described by the space- and temperature-dependent functions $g(r,T)$. The latter define the local positive or negative deviations of the atomic concentration from its mean value $n(T)$ in a liquid in thermodynamic equilibrium. The indirect correlations result from the ever present concentration fluctuations of the liquid under isothermal conditions. For physical processes of short duration in comparison with the finite time needed by the liquid to establish the local concentration deviations from the mean, the functions $g(r,T)$ may be considered to express a permanent or static feature of the atomic distribution in a liquid viewed from an origin atom, all surface effects being neglected. The functions $g(r,T)$ enter into the static two-atom or pair distribution functions $n(r,T)$, which define the probability per unit volume of finding an atom at some specified distance r from the origin atom. These functions are isotropic.

In addition to the indirect correlation functions $g(r,T)$, one also defines a direct correlation function $f(r,T)$ which is indicative, so to speak, of the first-neighbor correlations. The functions f and g are connected by an unique relation given by Ornstein and Zernike,[2] who were also the first to introduce the concepts of these two types of spatial correlation functions in statistical systems. We shall henceforth refer to f and g as interaction and correlation functions, and shall, occasionally, abbreviate them as i.f. and c.f., respectively. While the c.f.'s have a more intuitive physical interpretation, the i.f.'s are generally of shorter range, above all in the region of the critical temperature. The i.f.'s are expected to be analytically more regular than the c.f.'s at all temperatures. This property may thus make them preferable to handle in the critical region where the c.f.'s become of very long-range character.

Using the liquid helium x-ray scattering structure

[1] L. Goldstein and J. Reekie, Phys. Rev. **98**, 857 (1955). This paper will be referred to in the text by S.D.

[2] L. S. Ornstein and F. Zernike, Proc. Acad. Sci. Amsterdam **17**, 793 (1914).

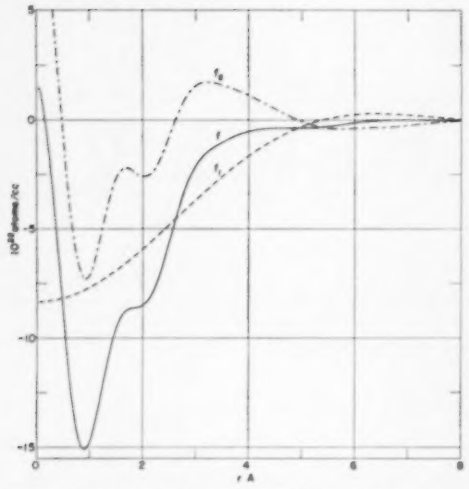

FIG. 1. Partial, $f_1(r,2.06°K)$, $f_2(r,2.06°K)$, and total interaction functions $f(r,2.06°K)$, (atoms/cc), *vs* the interatomic separation r, (A).

factors of Reekie,[3] we have here obtained, over a wide temperature interval and distance range, the functions $f(r,T)$. The expected moderate-ranged character of these functions, over most of the temperature interval, is hereby fully confirmed. Their geometrical simplicity, when compared with the $g(r,T)$ functions, is also demonstrated. To our knowledge, these $f(r,T)$ functions have not been derived for other liquids, in spite of the extensive x-ray scattering data available for some of them.

As in our work on the c.f.'s, the i.f.'s here obtained have been submitted to two types of integral checks. In one of these, their space integrals have been calculated. The latter are completely determined by some of the macroscopic properties of the liquid, and the calculations verify with good accuracy the predicted values. In the second type of integral check, they reproduced closely their generating functions, i.e., the x-ray scattering structure factors. These studies prove the over-all correctness of the numerical analysis. They also tend to support the likely possibility that the $f(r,T)$ functions here derived are fair approximations, over most of their range, to their presently unknown rigorous form.

A major part of the present work is devoted to the investigation of the static indirect interference integrals appearing in the total slow-neutron scattering cross sections in liquids. While these involve the c.f.'s or $g(r,T)$ functions of liquid helium, the results derived should have general significance and be valid, qualitatively, in all monatomic liquids. In these numerical calculations, only the so-called generalized indirect interference integrals can be obtained. These integrals depend not only on the liquid temperature and the de Broglie wavelength of the neutrons, but also on the upper limit of the radial integration through which they are defined. These limits determine the radii of spheres centered at the origin atom, the atoms of which contributed to the static interference term of the scattered intensity of the waves. The temperature effect on the interference integral will be shown to correspond to the competition of the constructive interference effects of the local positive density deviations from the mean, and the destructive interference effects arising from the local negative deviations from the mean density. The characteristic temperature T_c or T_0 defined previously[1,4] will be shown to divide approximately the liquid temperature interval, for not too short wavelengths, in such a way that for $T<T_0$ the interference term is completely destructive, while for $T_0 \leqslant T \leqslant T_c$, T_c being the critical temperature, it becomes positive. This forecasts, in the static approximation, the large increase in the total slow-neutron scattering cross section at medium or longer wavelengths, at the approach of the critical temperature, i.e., the occurrence of the slow-neutron critical opalescence effect.[5]

The static interference integral tends to lose its validity with increasing neutron wavelength, because of the increasingly important liquid relaxation type of time effects.[6] Stated in other terms, the static interference integral, which depends only on the momentum change on scattering by the assumed rigid atomic distribution, becomes, for slower neutrons, an increasingly worse approximation to the actual interference term which is associated with a nonrigid distribution and which depends also on the relatively large energy change of the slower neutrons on scattering. Should one consider the long-wavelength static interference integrals as only crude approximations, even of quite limited physical significance, their study and comparison with the direct interference integrals, defined by the x-ray scattering structure factors, may be looked upon as providing a new integral test for the $g(r,T)$ functions. In view of the latter fact that they are involved in the evaluation of various elementary physical properties of liquids, such an additional test of these functions is of evident importance.

As a further application of the mean potential energies per liquid He^4 atom obtained in S.D., we have evaluated, using the empirically determined latent heat values, the mean kinetic energies at various liquid temperatures. The results of these calculations may be said to be of twofold interest. On the one hand, they provide a proof for the large zero-point kinetic energy of the liquid He^4 atoms over the whole temperature range investigated. On the other hand, a semiquantitative sharpening of the

[3] C. F. A. Beaumont and J. Reekie, Proc. Roy. Soc. (London) **A228**, 363 (1955); J. Reekie and T. S. Hutchison, Phys. Rev. **92**, 827 (1953).

[4] L. Goldstein, Phys. Rev. **84**, 466 (1951).

[5] L. Goldstein, Bull. Am. Phys. Soc. **25**, 38 (1950); Phys. Rev. **83**, 289 (1951).

[6] L. Van Hove, Phys. Rev. **95**, 249 (1954).

proof given in S.D. of the kinetic energy origin of the lambda transition has been achieved.

The paper ends with an evaluation of the root mean square forces per liquid He^4 atom, using the pair distribution functions derived in S.D. This elementary physical quantity is, in principle at least, experimentally accessible in liquids through their slow-neutron scattering properties, as shown recently by Placzek.[7]

2. THE DIRECT CORRELATION OR INTERACTION FUNCTION IN LIQUID He^4

The interaction function $f(r,T)$ may be defined either in terms of the indirect correlation function $g(r,T)$, or with the help of the scattering intensity structure factor for radiation. With the latter, one finds[4]

$$f(r,T)=(1/2\pi^2 r)\int_0^\infty [1-F_L^{-2}(\Delta k,T)] \times(\sin r\Delta k)(\Delta k)d(\Delta k). \quad (2.1)$$

Here, Δk or $2|\mathbf{k}|\sin\theta$, or $(4\pi\sin\theta/\lambda)$, is the momentum change on scattering into the direction forming the angle 2θ with the direction of incidence of the radiation, and $F_L^2(\Delta k,T)$ is the scattering intensity structure factor, per atom, of the monatomic system. It is seen that

$$\lim_{r\to 0} f(r,T)=(1/2\pi^2) \times\int_0^\infty [1-F_L^{-2}(\Delta k,T)](\Delta k)^2 d(\Delta k), \quad (2.2)$$

showing that the finite limit $f(0,T)$ at the origin is fully determined by structure factor. In contrast, however, with the c.f.'s, there is no elementary physical significance attached to $f(0,T)$. The behavior of $f(r,T)$ at small separations results at once from (2.1). Expanding there $(\sin r\Delta k)/(r\Delta k)$, and keeping the first two terms, one finds

$$\lim_{r\ \text{small}} f(r,T)=f(0,T)-(r^2/12\pi^2) \times\int_0^\infty [1-F_L^{-2}(\Delta k,T)](\Delta k)^4 d(\Delta k), \quad (2.3)$$

showing the parabolic character of $f(r,T)$ at small r.

The structure factors are available in such a form[1] as to suggest the decomposition of the Fourier integral (2.1) into two integrals, namely,

$$f(r,T)=f_1(r,T)+f_2(r,T) =(1/2\pi^2 r)\left[\int_0^1 [1-F_L^{-2}(\Delta k,T)] \times(\sin r\Delta k)(\Delta k)d(\Delta k)+\int_1^{\Delta K}\cdots\right], \quad (2.4)$$

[7] G. Placzek, Phys. Rev. **86**, 377 (1952); see also G. C. Wick, Phys. Rev. **94**, 1228 (1954).

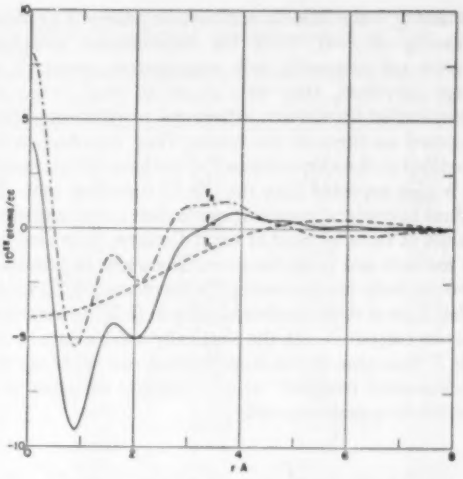

FIG. 2. Partial, $f_1(r,4.20°K)$, $f_2(r,4.20°K)$ and total interaction functions $f(r,4.20°K)$, (atoms/cc), *vs* the interatomic separation r, (A).

where the integrand of the second integral is identical with the integrand of the first, and where ΔK is the limiting value of Δk beyond which the experimental structure factor reduces approximately to unity, i.e., the integrand vanishes. As in the analysis of the c.f.'s given in S.D., the functions f_1 and f_2 have been obtained by numerical integration in intervals of 0.025 A^{-1} in Δk. These functions have been obtained at every 0.05 A in r, from vanishing r out to 20 A. The numerical integrations have been performed on the "701" IBM Electronic Calculator.

We give in Figs. 1 and 2, the functions $f_1(r,T)$, $f_2(r,T)$, and their resultant, the actual interaction function $f(r,T)$, at 2.06°K and 4.20°K liquid temperatures, respectively. The graphs extend only to 8 A separation. At larger separations, these functions are only very small fractions of their values at closer separations, at 2 A, for instance. These functions, as representative of the low- and high-temperature functions, exhibit both qualitative and quantitative differences. At low temperatures, the $f(r,T)$'s have a deep and sharp minimum. At the higher temperatures, the principal minimum is less deep and less sharp. At larger separations, the low temperature i.f.'s remain negative, becoming quite small though; at the higher temperatures, they become positive at medium separations. It will be observed that the component functions f_1 and f_2 remain, numerically, relatively close at most distances r. This result is similar to the one obtained with the $g(r,T)$ functions[1] and underlines the importance of the small Δk-value structure factors in the determination of the $f(r,T)$ functions. The relatively short-range character of the $f(r,T)$ functions is apparent on the graphs.

It should be remembered here that, in contrast with the c.f.'s, which have to satisfy a physical condition at

vanishing r, the i.f.'s do not have as precise a physical meaning at $r \to 0$. Since the experimental structure factors are necessarily only approximate, above all at large Δk-values, they were found to lead[1] to $g(r,T)$ functions which did not satisfy the physical condition imposed on them at the origin. They thus had to be modified at close separations. On the basis of this result, it is also expected that the $f(r,T)$ functions here obtained be cruder approximations to their actual unknown values at the origin and at small distances than they are at medium and large distances. There are, in principle, two methods for improving the functions $f(r,T)$ somewhat. One of these consists in using in (2.1) the structure factors computed with the physically correct form of the $g(r,T)$ functions. In the other method, one might use the fundamental relation[2,4] with its integral extended over the whole space, essentially,

$$f(r,T)=g(r,T)-\int g(|r-r'|,T)f(r',T)dv(r'), \quad (2.5)$$

and obtain with it the first iterated $f^{(1)}(r,T)$ by replacing in the folding integral $f(r,T)$ by its zero-order approximation, and so on. Neither of these methods of improving the interaction functions has been made use of here, and, hence, only their zero-order approximation has been derived here.

At large separations the functions $f(r,T)$, while becoming very small, are oscillatory. At 2.06°K, and $8\text{ A} \leqslant r \leqslant 20\text{ A}$, one finds the following zeros: 9.60, 14.70, 15.05, 15.65, and 17.70 A. The zeros in the range 8–20 A, at 4.2°K, are 11.05, 14.50, 14.95, 15.55, and 18.50 A. The absence of oscillations at medium separations assures the analytical simplicity of these functions when compared to the c.f.'s. At larger separations also, the number of zeros of the i.f.'s is less than that of the c.f.'s. Their analytical simplicity notwithstanding, the i.f.'s cannot be used alone in the all-important pair distribution functions, as the fundamental relation (2.5) excludes the simple substitution of $g(r,T)$ in the pair distribution functions by $f(r,T)$.

TABLE I. The space integrals $F(20\text{ A},T)$ of the interaction functions at various temperatures.

T °K	$-F(20\text{ A},T)$ calc.	$-F(T)$ exp.
1.25	19.6	20.3
1.50	15.8	15.7
1.75	13.1	13.3
2.06	11.1	11.2
2.25	9.03	9.20
2.50	7.55	7.62
2.75	6.08	6.14
3.01	4.99	5.02
3.25	4.15	4.02
3.50	3.09	3.12
3.75	2.33	2.30
3.97	1.68	1.69
4.20	1.17	1.18

As in the investigation of the c.f.'s in S.D., it was important to submit the i.f.'s obtained here to the important integral checks available for these functions. In spite of their probable crude character at small separations, it will be seen that they satisfy with good accuracy these integral tests. One of these concerns their space integral which is defined by a general statistical thermodynamic relation[2,4]:

$$\int_0^\infty f(r,T)4\pi r^2 dr = F(T) = 1-[\langle \Delta N^2\rangle_{\text{Av}}/N]^{-1}. \quad (2.6)$$

Here,

$$\langle \Delta N^2\rangle_{\text{Av}}/N = n(T)kT\chi_T \quad (2.7)$$

is the isothermal mean square fluctuation of the number of atoms, N, per atom, $n(T)$ stands for the mean atomic concentration and χ_T is the isothermal compressibility of the liquid at the temperature T. The generating function of the interaction functions is essentially, by Eq. (2.1),

$$\Phi(\Delta k,T)=1-F_L^{-2}(\Delta k,T). \quad (2.8)$$

With the rigorous formula[4]

$$\lim_{\Delta k\to 0} F_L^{-2}(\Delta k,T)=[n(T)kT\chi_T]^{-1}, \quad (2.9)$$

one obtains

$$F(T)=\lim_{\Delta k\to 0}\Phi(\Delta k,T), \quad (2.10)$$

in some analogy with the corresponding relation valid for the space integral $G(T)$ of the c.f.'s discussed in S.D.[1,4] The functions $F(T)$ and $G(T)$ of liquid He^4 have both been graphed previously.[4] These functions are complementary to each other, to some extent, as far as their qualitative behavior is concerned. They are both negative at low temperatures, defined by the characteristic temperature[1,4] T_0 or T_i, or at $T<T_0$. They vanish at T_0 and become positive at the high temperatures $T_0 \leqslant T \leqslant T_c$. In normal liquids, $F(T)$ decreases with decreasing temperature down to the normal melting point T_m, or

$$F(T_m) \leqslant F(T) \leqslant F(T_0)=0. \quad (2.11)$$

In liquid He^4 a unique situation is realized, because when it is in equilibrium with its vapor, this liquid phase seems to extend, according to all evidence available at the present time, down to absolute zero. As a result, $F(T)$ tends to larger and larger negative values as the temperature tends toward very small values. Both $F(T)$ and $G(T)$ are monotonically increasing functions of the temperature. In liquid He^4, their complementary aspect is clearly expressed by the relations

$$\lim_{T\to 0}F(T)\to -\infty\,; \quad \lim_{T\to T_c}F(T)=1, \quad (2.12)$$

and

$$\lim_{T\to 0}G(T)\to -1\,; \quad \lim_{T\to T_c}G(T)\to \infty\,. \quad (2.13)$$

Their common zero is at T_0. The preceding relations indicate that the functions $f(r,T)$ may be expected to be more regular then the $g(r,T)$'s in the interval $T_0 \leqslant T \leqslant T_c$. In certain applications of these functions, the use of the $f(r,T)$'s, when alone, might become necessary in preference to the $g(r,T)$ functions.

Since the $f(r,T)$ functions are only available in tabular form over a necessarily finite separation range r, the complete space integrals $F(T)$ cannot be obtained with them. One has to calculate the generalized integrals

$$F(r,T)=\int_0^r 4\pi r^2 f(r,T)dr. \tag{2.14}$$

These have been computed at the various liquid temperatures over most of the r range over which the $f(r,T)$'s are available. We give in Table I, the values of $F(20\text{ A},T)$ together with their experimental values or $\{1-[n(T)kT\chi_T]^{-1}\}$. A glance at the table shows that the $f(r,T)$ functions satisfy rather well their space integral test. Clearly, since this is an integral test, it is not justified to infer from it the locally correct character of the functional behavior of the $f(r,T)$'s. On the other hand, these results lend some support to the likelihood that the $f(r,T)$ functions represent, at the present time, the best approximations to the unknown rigorous interaction functions. Clearly, if the space integral checks do not allow for any rigorous justification of the locally correct character of the derived i.f.'s, neither do they allow the drawing of the opposite conclusion. It seems to us that the results of Table I justify at least the not unreasonable conjecture on the fair degree of approximation to the unknown rigorous interaction functions achieved locally, by the results of the present analysis. As mentioned above, the functions derived here are probably worse at close separations.

A second type of integral test applied to the $f(r,T)$ functions consisted in the inversion of the Fourier integrals (2.1), or the calculation of $[1-\Phi(\Delta k,T)]$ or $F_L^{-2}(\Delta k,T)$, Eq. (2.8). Here, again, the generalized integrals

$$\Phi(r,\Delta k,T)=4\pi\int_0^r f(r,T)[\sin r\Delta k/r\Delta k]r^2dr, \tag{2.15}$$

had to be computed. These were obtained at intervals of 0.25 A^{-1} in Δk, from 0.25 to 6.0 A^{-1}, at the two liquid temperatures of 2.06 and 4.20°K. The calculated reciprocal structure factors are given by $[1-\Phi(20\text{ A},\Delta k,T)]$, they are denoted by $F_L^{-2}(\Delta k,T,20\text{ A})$, 20 A being the upper limit of the integrals (2.15). Table II gives the experimental and calculated reciprocal structure factors. The former result from those used in S.D. It will be observed that the interaction functions $f(r,T)$ reproduce fairly well the experimental structure factors, demonstrating the internal consistency and good accuracy of the numerical calculations.

TABLE II. Experimental $F_{L,\,exp}^{-2}(\Delta k,T)$ and calculated $F_L^{-2}(\Delta k,T,20\text{ A})$ reciprocal structure factors at 2.06 and 4.20°K.

Δk, A^{-1}	$F_{L,exp}^{-2}$ (Δk,2.06°K)	F_L^{-2} (Δk,2.06,20 A)	$F_{L,exp}^{-2}$ (Δk,4.20°K)	F_L^{-2} (Δk,4.20,20 A)
0.25	11.4	11.4	2.62	2.62
0.50	8.62	8.59	3.33	3.32
0.75	5.81	5.81	3.77	3.78
1.00	3.92	3.94	3.19	3.18
1.25	2.61	2.62	2.23	2.24
1.50	1.74	1.75	1.50	1.50
1.75	1.10	1.06	0.980	0.975
2.00	0.758	0.770	0.781	0.780
2.25	0.787	0.785	0.813	0.813
2.50	0.885	0.879	0.917	0.924
2.75	0.962	0.962	0.990	0.993
3.00	1.00	1.00	1.03	1.03
3.25	1.02	1.02	1.04	1.04
3.50	1.02	1.02	1.03	1.03
3.75	1.00	0.998	1.01	1.01
4.00	0.962	0.957	0.990	0.999
4.25	0.917	0.920	0.952	0.957
4.50	0.901	0.901	0.935	0.934
4.75	0.909	0.907	0.926	0.926
5.00	0.926	0.922	0.926	0.927
5.25	0.943	0.943	0.935	0.930
5.50	0.962	0.966	0.943	0.946
5.75	0.980	0.984	0.980	0.980
6.00	1.000	0.995	1.01	1.01

Some additional properties of the interaction functions will be given in the next section.

3. INTERFERENCE PROPERTIES OF STATIC ATOMIC DISTRIBUTIONS IN LIQUID He⁴

Neglecting all effects arising from the relative motion of the atoms of the scattering medium and the incident neutrons, as well as all specific atomic binding effects, the total slow-neutron scattering cross section per liquid atom, in units of the isolated stationary free-atom total scattering cross section σ_f, may be written as[7]

$$\begin{aligned}\sigma_L(k,T)/\sigma_f &= 1+[(1+\mu^{-1})^2/4\pi]\\ &\quad\times\int_0^{\pi/2}[F_L^2(\Delta k,T)-1]2\pi\sin(2\theta)d(2\theta)\\ &=1+(1+\mu^{-1})^2 I_d(k,T).\end{aligned} \tag{3.1}$$

I_d, the static direct interference integral written in terms of the correlation function $g(r,T)$, becomes the indirect static interference integral, or

$$\begin{aligned}I(k,T)&=\int_0^\infty(\sin kr/kr)^2 g(r,T)4\pi r^2dr\\ &=I(\lambda,T).\end{aligned} \tag{3.2}$$

Here μ is the mass of the spinless scattering atom in units of the neutron mass. For not too light atoms, $\mu\gg1$, the bound-atom total scattering cross section σ_∞ or $\sigma_f(1+\mu^{-1})^2\sim\sigma_f$, and (3.1) reduces to the form con-

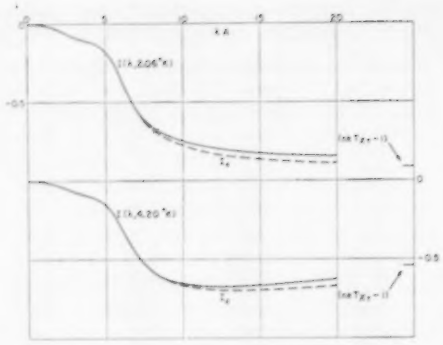

FIG. 3. The direct and indirect interference integrals, $I_d(\lambda,T)$ and $I(\lambda,T)$ as a function of the wavelength λ(A), at 2.06 and 4.20°K.

sidered by us previously.[4] The transformation leading from $I_d(k,T)$, defined in terms of the structure factor F_L^2, to $I(k,T)$ is elementary, requiring simply the expression of the static structure factor[4] $F_L^2(\Delta k,T)$ in terms of the static correlation function $g(r,T)$.

With the exception of neutrons of relatively short wavelength, to be defined more closely below, the interference term in (3.1) is an important element of the total scattering cross section. With the analysis of the liquid He^4 x-ray scattering data of Reekie[3] performed in S.D., we are now in a position to study the interference term in detail. The results which will thus be obtained are, however, of interest not only for liquid He^4 but for any monatomic liquid, as well as for polyatomic liquids, insofar as their intermolecular interference properties are concerned.

The physical assumptions underlying the interference term in (3.1) correspond to neglecting the energy change of the neutron in the scattering as well as to the frozen or static character of the local concentration deviations from the mean concentration. These assumptions are evidently the better justified, the faster are the incident neutrons. With decreasing neutron velocities, the static interference term becomes an increasingly cruder approximation to the actual interference term. Nevertheless, an investigation of the interference integrals is still of great interest for several reasons. One of these stems from the fact that the very long wavelength asymptotic limit of the static interference integral is given by the space integral $G(T)$. If the correct asymptotic behavior is obtained, then an additional integral check has also been achieved on the correlation functions $g(r,T)$. The physical justification of the evaluation of the integrals $I(\lambda,T)$ at medium wavelengths λ will be considered below.

Since terms arising from the neutron-atom relative motion effect cannot but increase the total scattering cross section, (3.1) represents its lower limit, as long as small specific binding effects are neglected.

At sufficiently short wavelengths, replacing $\sin^2 kr$ by its mean value of $\frac{1}{2}$, one obtains with (3.2),

$$\lim_{\lambda \text{ small}} I(\lambda,T)=\lambda^2 r_G^{(-2)}(T)/8\pi^2, \tag{3.3}$$

where

$$r_G^{(-2)}(T)=\int_0^\infty r^{-2}g(r,T)4\pi r^2 dr \tag{3.4}$$

is the second negative moment of the correlation function. The interference integral vanishes parabolically with neutron wavelength.

We have discussed on various occasions[1,4] the positive even moments of the correlation function. With the known details of $g(r,T)$, it may be expected that $r_G^{(-2)}(T)$ be negative over most of the temperature range, both in liquid He^4 and in normal liquids. However, the possibility that $r_G^{(-2)}(T)$ vanishes at some temperature T_{-2} such that $T_0<T_{-2}<T_e$, and becomes positive in the range (T_e-T_{-2}), cannot be ruled out. There might thus be a small though finite and accessible temperature interval (T_e-T_{-2}), where $I(\lambda,T)$ would be positive at short wavelengths, leading thus to a total scattering cross section per liquid atom larger than the isolated free-atom cross section. Such an effect, if observed, would be a manifestation of the longer-wavelength critical neutron opalescence phenomenon discussed by us some time ago.[5] Using the previously obtained[1] $g(r,T)$ functions, we have calculated the second negative moments $r_G^{(-2)}(T)$ at a series of liquid temperatures. These are given in Table III. They all correspond to the integrals (3.4) extended to the upper limit of 20 A. These integrals converge rapidly so that their limiting values are already achieved at about 10 A. The slight jump in the values of these moments between 2.75 and 3.01°K is associated with the approximate character of the correlation functions in passing from the low-temperature region, $T\leq 2.75$°K, to the high-temperature region, $T\geq 3.01$°K, as discussed in S.D., where the preceding division of the explored temperature interval is fully defined.

Replacing (3.3) in (3.1), one obtains

$$\lim_{\lambda\to 0}\sigma_L(\lambda,T)/\sigma_f=1+[(1+\mu^{-1})^2/8\pi^2]\lambda^2 r_G^{(-2)}(T), \tag{3.5}$$

the asymptotic short-wavelength total scattering cross section. It is, of course, of evident interest to compare the asymptotic cross-section formula with the rigorous one, Eq. (3.1), where the interference term is computed exactly. This comparison, whose details need not be given here, shows that the asymptotic formula is quite acceptable out to λ equal to about 4 A at all the liquid temperatures here investigated, or at $1.25\leq T\leq 4.20$°K. It should be noted that for heavier liquids, where μ^{-1} becomes small, the asymptotic formula may become valid out to somewhat longer wavelengths.

We give in Fig. 3 two indirect interference integrals as a function of the wavelength at the two representative temperatures of 2.06 and 4.20°K. The interference

integral vanishes, of course, in the limit of vanishing wavelength. It decreases from this limit slowly at first, in the range of about $\lambda \lesssim 2$ A, and at an increasing rate for somewhat larger λ. The slight wiggles at short wavelengths can be traced essentially to the approximate angular shape of the $g(r,T)$ functions, at small separations, which was discussed in detail in S.D. It will be seen that in the range $5 \lesssim \lambda \lesssim 9$ A there is a rather rapid drop in the value of the integral, reminiscent of the Bragg edge anomaly. It is connected, of course, to the main peak of the structure factor curves, which were given in S.D. The characteristic rapid drop of $I(\lambda,T)$ will be seen to be sharper at the low rather than at the higher temperature as might have been expected. Beyond the sharp drop, the interference integrals flatten out and reach their asymptotic long wavelength range. We will return below to the discussion of this range of large λ.

We give in the same Fig. 3, the direct interference integrals I_d, beyond about 4 A. These two integrals coincide to about 8–9 A, and deviate slightly from each other at longer wavelengths.

From Eq. (3.1), the direct interference integral is, changing the integration variable,

$$I_d(k,T) = (1/2k^2)\int_0^{2k} [F_L^2(\Delta k,T)-1](\Delta k)d(\Delta k). \quad (3.6)$$

Identifying this with $I(k,T)$, Eq. (3.2), and going over to the limit $\lambda \to 0$ or $k \to \infty$, one obtains the theorem

$$r_G^{(-2)}(T) = \int_0^{2k\to\infty} [F_L^2(\Delta k,T)-1](\Delta k)d(\Delta k), \quad (3.7)$$

which is an expression of the second negative moment of the correlation function $g(r,T)$ in terms of its generating function which is $F_L^2(\Delta k,T)$. A more direct proof of (3.7) can be obtained at once by replacing in the definition (3.4) the c.f., or $g(r,T)$ by its expression in terms of the Δk Fourier integral of the structure factor,[4,1] and integrating over r. Also, the definition of the second negative moment of the interaction function

$$r_F^{(-2)}(T) = \int_0^\infty r^{-2} f(r,T) 4\pi r^2 dr, \quad (3.8)$$

with Eq. (2.1), yields in this way the rigorous relation

$$r_F^{(-2)}(T) = \int_0^\infty [1-F_L^{-2}(\Delta k,T)](\Delta k)d(\Delta k). \quad (3.9)$$

The knowledge of the second negative moment $r_G^{(-2)}(T)$, Eq. (3.7), directly through the structure factor is, in principle, a great advantage for the use of the asymptotic short wavelength limit (3.5) of the interference integral. Actually, the problem is more complicated. The complication arises from the empirical character of the structure factor, the precision of which decreases with increasing Δk values. With the physical condition[1,4] imposed upon the $g(r,T)$ functions at small separations r, and above all at $r \to 0$, one, indirectly, modifies the empirical structure factors at large Δk values. Hence, the second negative moments obtained with carefully derived correlation functions should be, under these conditions, more satisfactory than those calculated directly with the uncorrected structure factors using (3.7). If the experimental structure factors had been obtained with precision over a large Δk interval, one might have expected to verify with them the correct limit of $g(r,T)$ as $r \to 0$, and also to derive with them the fairly well approximated second negative moments $r_G^{(-2)}(T)$ or $r_F^{(-2)}(T)$. At the present time, the indirectly obtained moments given in Table III are more accurate than those which result from the theorems expressed by (3.7) or (3.9).

TABLE III. Second negative moments $r_G^{(-2)}(20\text{ A},T)$ of the correlation functions $g(r,T)$ at various temperatures.

T°K	$-r_G^{(-2)}(20\text{ A},T)$ A^{-2}
1.25	0.633
1.50	0.633
1.75	0.633
2.06	0.634
2.25	0.634
2.50	0.629
2.75	0.620
3.01	0.625
3.25	0.613
3.50	0.597
3.75	0.577
3.97	0.559
4.20	0.539

In comparing now the direct interference integral $I_d(k,T)$, Eq. (3.6) and the indirect interference integral $I(k,T)$, Eq. (3.2), the former is, evidently, to be preferred to the latter, with the exception of the region of the short wavelengths or large k values, as we have just shown. Since $I_d(k,T)$ is preferable, with the above exception, to $I(k,T)$, the question arises as to the usefulness of the latter. It is, however, easy to see that the studies of $I(k,T)$ lead to two different types of results concerning the correlation function. One of these concerns an additional integral check on $g(r,T)$ as expressed by (3.2). In Fig. 3 we have a graphical illustration, at two liquid temperatures, of the over-all correct character of the c.f.'s. It will be seen that at the longer wavelengths, the largest deviations between I_d and I amount to at most five percent. Below 4 A, I_d becomes unreliable as discussed above. In view of the multiple uses[1] of the $g(r,T)$'s in the evaluation of various properties of the liquid, such an additional check on the correlation function is of evident interest. It will be noted that the indirect interference integrals tend to approximate (but to be somewhat greater than) the more correct direct interference integrals at the longer wavelengths.

Another type of result included in the indirect inter-

ference integrals consists in their yielding the extension of the spatial regions, around the origin atom, which contribute effectively to the scattering process through their concentration deviations from the mean. In the numerical calculations here performed, one indeed obtains the generalized interference integrals

$$I(\lambda,T,r)=\int_0^r\left[\frac{\sin(2\pi r/\lambda)}{2\pi r/\lambda}\right]^2 4\pi r^2 g(r,T)dr, \quad (3.10)$$

as a function of the variable upper limit r. The very form of the indirect interference integrals proves that their destructive character, over the whole temperature range here investigated, results predominantly from the existence of the hole in the atomic distribution around any atom within the liquid, which atom was chosen arbitrarily to be at the origin of the coordinate system. Of course, the positive concentration deviations from the mean, or the hills in the atomic distribution, tend at larger separations to minimize, through their constructive interference effects, the large destructive effects arising from the density defects at close separations. At a given temperature, the shorter the wavelength the smaller is the spatial region, around the origin atom, the atoms of which take an active part in the scattering process. This region is seen to increase in size with increasing wavelengths. In the limit of λ very large, or k very small, one has from (3.10),

$$\lim_{\lambda \text{ large}} I(\lambda,T,r)=G(r,T), \quad (3.11)$$

which was shown to oscillate[1] out to quite large separations r. Clearly, the preceding spatial properties of the indirect interference integral do not appear in their direct evaluation through $I_d(k,T)$.

We should like to discuss briefly the behavior of the interference integrals in the asymptotic long-wavelength or small wave-vector region. Remembering the parabolic approach[1,4] of $F_L^2(\Delta k,T)$ in Δk toward its limit $F_L^2(0,T)$ or $n(T)kT\chi_T$, (3.6) leads to

$$\lim_{k\to 0} I_d(k,T)\cong[F_L^2(0,T)-1](1/2k^2)\int_0^{2k}(\Delta k)d(\Delta k)$$
$$=n(T)kT\chi_T-1, \quad (3.12)$$

showing that $I_d(k,T)$ has the same limit at vanishing k as $[F_L^2(\Delta k\to 0,T)-1]$. The same result obtains, of course, with (3.2), since

$$\lim_{k\to 0} I(k,T)=\int_0^\infty 4\pi r^2 g(r,T)$$
$$=G(T)$$
$$=n(T)kT\chi_T-1. \quad (3.13)$$

In order to obtain now the more detailed behavior of the interference integrals at small k, one has but to expand $(\sin x/x)^2$ in $I(k,T)$, Eq. (3.2), and keep the first two terms. This yields

$$\lim_{k \text{ small}} I(k,T)=G(T)-\tfrac{1}{3}k^2 r_G^{(2)}(T)$$
$$=n(T)kT\chi_T-1-\frac{4\pi^2}{3}(r_G^{(2)}(T)/\lambda^2), \quad (3.14)$$

where the first equation, expressing the parabolic approach of $I(k,T)$ in k toward its limit $I(0,T)$, is quite similar to the parabolic approach of the difference $F_L^2(\Delta k,T)-1$ in Δk toward its limit $[F_L^2(0,T)-1]$ or $[n(T)kT\chi_T-1]$, according to

$$\lim_{\Delta k \text{ small}} [F_L^2(\Delta k,T)-1]=G(T)-\tfrac{1}{6}(\Delta k)^2 r_G^{(2)}(T). \quad (3.15)$$

Since, as shown in S.D., at $T\leqslant T_2$, $r_G^{(2)}(T)<0$, and at $T\geqslant T_2$, $r_G^{(2)}(T)>0$, it will be seen that as a function of λ, for instance, $I(\lambda,T)$ approaches its limit from above at $T\leqslant T_2$, while the approach is from below at $T\geqslant T_2$. But since $I(\lambda,T)$ vanishes parabolically from below at $\lambda\to 0$, and since it approaches its very long wavelength limit $\lambda\to\infty$ from below also, it must have at least one minimum in the wavelength interval, at $T\geqslant T_2$. This is exhibited clearly in Fig. 3. The characteristic temperature T_2 was shown[1] to be in the range 2.25–2.50°K.

A special discussion of the interference integral is now needed in the vicinity of the critical temperature. Because of the anomalous behavior of the correlation function, it is indicated here to use the expression of the structure factor in terms of the interaction function whose behavior is normal at the approach of the critical temperature. One has here[4]

$$\lim_{T\to T_c,\ \Delta k \text{ small}} F_L^2(\Delta k,T)-1\sim\lim F_L^2(\Delta k,T)$$
$$=n(T)kT\chi_T[1+\tfrac{1}{6}n(T)kT\chi_T(\Delta k)^2 r_F^{(2)}(T)]^{-1}. \quad (3.16)$$

Replacing (3.16) in (3.1) or (3.6) and integrating, one finds

$$\lim_{T\to T_c,\ k \text{ small}} I_d(k,T)$$
$$=(\tfrac{3}{2}k^2 r_F^{(2)}(T))^{-1}\ln[1+\tfrac{3}{2}n(T)kT\chi_T k^2 r_F^{(2)}(T)]. \quad (3.17)$$

However, the full use of the preceding result[5] to obtain the k or λ behavior of $I_d(k,T)$ could be misleading. This is so because (3.16) is valid only under the assumption that the $(\Delta k)^2$ term in its denominator is large in comparison with the next term, which is proportional to $(\Delta k)^4$, in an alternating infinite series.[4] The $(\Delta k)^2$ term is assumed to be large compared to the sum of the terms of order higher or equal to the fourth in (Δk). Hence, (3.17) is actually valid only up to terms in k^2, or one has to

[5] This was also obtained in reference 6 in an entirely different way.

expand (3.17) and write

$$\lim_{T\to T_c,\ k \text{ small}} I_d(k,T)$$
$$= n(T)kT\chi_T[1-\tfrac{1}{2}n(T)kT\chi_T k^2 r_F^{(2)}(T)]$$
$$= n(T)kT\chi_T - \tfrac{1}{2}k^2 r_G^{(2)}(T), \qquad (3.18)$$

which is identical to what one obtains directly with (3.15), provided one uses the rigorous relation,

$$r_G^{(2)}(T) = r_F^{(2)}(T)n(T)kT\chi_T, \qquad (3.19)$$

between the second positive moments[4,9] of the correlation and interaction functions. In the limit, $k\to[1/r_G^{(2)}(T)]^{\frac{1}{2}}\to 0$, (3.18) reduces to $n(T)kT\chi_T$, which may be called the optical or radiation limit. Hence, as far as the static interference integral is concerned, its approach toward the limit $k\to 0$ is strictly parabolic at all temperatures. At the approach of the critical temperature the slope dI/dk at $k\to 0$ becomes very large because $r_G^{(2)}(T)\to\infty$ at $T\to T_c$. To the approximation of the static interference integral, the critical opalescence of very slow neutrons[5] is expressed essentially by the first term on the righthand side of Eq. (3.18) or the isothermal mean square fluctuation per atom of the total number of atoms of the system, that is, $\langle\Delta N^2\rangle_{kT}/N$.

We have to discuss finally the limitations on the validity of the static interference integral at decreasing wave numbers k or increasing wavelengths λ of the slow neutrons. As far as the collective portion of the slow-neutron scattering process is concerned, the assumption of the frozen or static atomic concentration deviations from the mean $n(T)$, defined by $g(r,T)$, is equivalent to neglecting completely the energy exchange between the neutron and the collection of the scattering atoms forming the scattering system. For short collective interaction times of the neutron and the liquid τ, which might be estimated to be of the order of l/v, l being some length over which $g(r,T)$ is appreciable, the use of a frozen or static correlation function is equivalent to assuming the existence of a group of rigidly connected atoms. Hence, in the collective part of the scattering process, the energy transferred to this massive system is indeed negligible. With decreasing neutron velocities, τ increases and when it becomes of the same order of magnitude or larger than some characteristic time of the liquid which is a measure for the time needed for the concentration deviations to be built up or to disappear, the apparent "rigidity" of the interatomic correlations loses its significance. As a result, the energy change of the neutrons in the collision becomes more and more significant and affects now the collective or interference part of the scattering cross section. The effect of the energy change of the neutrons on the interference integral may be expected to decrease the numerical value of the static interference integral. At liquid temperatures such that $T\lesssim T_0$, the static interference integral is likely to be negative, at not too short neutron wavelengths, and will tend to underestimate the collective part of the total scattering cross section. At $T>T_0$, at the same neutron wavelengths, the opposite situation might be expected to prevail. At any rate, slower and slower neutron scattering processes, in liquids for instance, involve relaxation type of time effects in their formal description, as first pointed out by Van Hove.[6] A method of evaluating the generalized dynamic or time dependent correlation function $g(r,T,t)$ has also been given. However, a correct evaluation of the characteristic liquid times, which are expected to be temperature dependent, presents a problem as yet unsolved. Hence to find, for a given liquid at a given temperature, that critical neutron velocity below which the static approximation to the interference integral starts to lose its validity, is itself a problem whose correct solution is closely tied to the liquid characteristic relaxation time problem. The length l mentioned above may be taken approximately to be the square root of the second positive moment $[r_G^{(2)}(T)]^{\frac{1}{2}}$ of the static correlation function, at least at those liquid temperatures where this quantity is reasonably well defined. We have seen that this is not the case in the vicinity of the characteristic temperature T_2. In a temperature interval containing T_2, the approximate definition of the length l is to be completed possibly with the help of some other moments of $g(r,T)$, such as $r_G^{(-2)}(T)$ or $r_G^{(4)}(T)$, for instance.

A particularly interesting situation arises at the approach of the critical temperature. Here, the order of magnitude of the momentum change of the neutron on scattering arising from the collective effect of the liquid atoms is defined essentially by the characteristic structural length $[r_G^{(2)}(T)]^{\frac{1}{2}}$, through $\hbar[r_G^{(2)}(T)]^{-\frac{1}{2}}$ or, in virtue of (3.19), by $\hbar[r_F^{(2)}(T)n(T)kT\chi_T]^{-\frac{1}{2}}$, which quantity is small and tends to vanish as $T\to T_c$. As a result the neutron energy change on scattering is considerably reduced, which circumstance reestablishes the validity of the static approximation to the interference integrals at all wavelengths. However, this situation is claimed[6] to be valid only in an extremely small temperature interval near the critical temperature. Hence the static interference integral coincides with the dynamic one at short and medium wavelengths, it deviates from the latter at longer wavelengths, at all temperatures, with the exception of the point-like interval near T_c, where the two expressions are always identical. This result suggests that the static interference integral might be at least a crude approximation to the dynamic one at those wavelengths and temperatures where the latter is the only one which is physically justified.

4. AVERAGE KINETIC ENERGIES AND ROOT MEAN SQUARE FORCES PER ATOM IN LIQUID He⁴

We should like now to further exploit the results obtained in S.D. on the approximate evaluations of the

[9] L. S. Ornstein and F. Zernike, Physik. Z. 19, 134 (1918). The relation between the even positive moments $r_G^{(2n)}$ and $r_F^{(2n)}$ is given in reference 4.

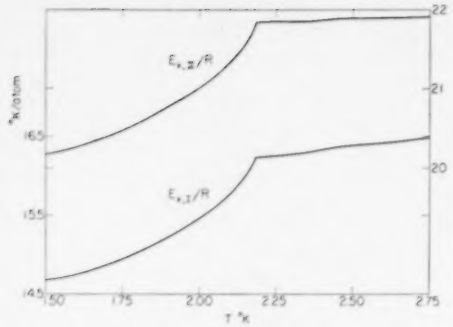

FIG. 4. Mean kinetic energies $E_{k,\mathrm{I}}(T)/R$ and $E_{k,\mathrm{II}}(T)/R$, (°K/atom), as a function of the liquid temperature (°K).

average potential energies per atom at the various liquid temperatures. With the rather well founded expression of the total energy per atom,

$$E(T)=E_k(T)+\Phi(T), \tag{4.1}$$

where $\Phi(T)$ is the ensemble average of the potential energy per atom, exchange energy included, based on the pair approximation, it becomes possible to compute the mean kinetic energies $E_k(T)$. Here, the liquid energies $E(T)$, or the binding energies taken with the negative sign, are available experimentally, omitting the small pressure-liquid volume product, through

$$E(T)=-L(T)+\epsilon(T), \tag{4.2}$$

where $L(T)$ is the latent heat per atom and $\epsilon(T)$ the total enthalpy, per atom, of the saturated vapor in equilibrium with the liquid at the temperature T. Keeping only the second virial coefficient in the thermal equation of state of the He^4 vapor, a procedure largely justified by Keller[10] at least below about 4°K, one obtains therefrom the vapor volume $V(T)$, with

$$pV=RT[1+(B(T)/V)], \tag{4.3}$$

which volume is then introduced into the enthalpy equation

$$\epsilon(T)=kT[5/2-(T/V)(dB/dT)+(B/V)]. \tag{4.4}$$

In (4.3) and (4.4) the second virial coefficients measured recently by Keller[10] in this Laboratory, as well as the empirical function $B(T)$ and its extrapolation[11] below 2°K have been used. In contrast with the vapor energies per atom $\epsilon(T)$, the latent heats at $T\leqslant 2.50$°K are of questionable accuracy, above all around the lambda point. In this low-temperature range the calculated latent heats[12] have been made use of. These calculated latent heats seem to reproduce well the experimental ones.[13] Above 2.75°K, more accurate latent heats became available recently.[14] The energies $\Phi(T)$ depend on the analytical approximation of the mutual potential energy of a pair of isolated stationary He^4 atoms as well as on the pair distribution functions $n(r,T)$ derived in S.D. In the vicinity of the lambda point, both the latent heats and the energies $\Phi(T)$ correspond to interpolated values. The kinetic energies thus calculated are quite approximate and carry automatically the uncertainties in the energies $\Phi(T)$ and $L(T)$. We give in Fig. 4 these average kinetic energies in the interval 1.50–2.75°K. The energies $E_{k,\mathrm{I}}(T)$ and $E_{k,\mathrm{II}}(T)$ are associated with the two approximations to the mean potential energies $\Phi_{\mathrm{I}}(T)$ and $\Phi_{\mathrm{II}}(T)$ which were discussed in detail in S.D.

It will be observed that these approximate kinetic energies per atom of the saturated liquid exhibit the expected angular point at the normal lambda temperature. This provides a quantitative sharpening of the qualitative proof given previously,[1] for the kinetic energy origin of the lambda transition in liquid He^4. The crude lambda discontinuities of both kinetic heat capacities $(dE_{k,\mathrm{I}}/dT)$ and $(dE_{k,\mathrm{II}}/dT)$ amount to about $5.5-6.0R$. It seems reasonable to expect that while the kinetic energies themselves, for a given potential energy set $\Phi(T)$, are quite approximate, their temperature derivatives be cruder approximations to the correct kinetic heat capacities. It turns out that the two types (I) and (II), of kinetic heat capacities are quite close to each other below the lambda point; their differences above T_λ are larger, as was to be expected from the previously[1] calculated potential heat capacities at these temperatures.

The very large values of both approximate kinetic energies $[E_{k,\mathrm{I}}(T)/R]$ and $[E_{k,\mathrm{II}}(T)/R]$ in comparison with the liquid temperatures T prove that they are essentially zero-point kinetic energies. Only a relatively small fraction of these kinetic energies appears to be of thermal excitation origin, in agreement with the values of the small empirical thermal energies $\int^T c(T)dT$, evaluated with the total heat capacity $c(T)$. Although only semiquantitative and indirect, the kinetic energies here obtained provide an interesting demonstration of the existence of a large zero-point kinetic energy at all the liquid temperatures investigated $1.25\leqslant T\leqslant 4.20$°K. Improved values of pair distribution functions, a decision on the best pair potential energy approximation as well as better latent heat values should lead, of course, to a unique and closer approximation of liquid He^4 kinetic energies.

The estimated zero-point kinetic energies per atom, resulting from extrapolating the kinetic energy curves toward low temperatures, are about 13 and 18°K, associated, respectively, with the potential energies $\Phi_{\mathrm{I}}(T)$ and $\Phi_{\mathrm{II}}(T)$.

In analogy with the calculation of the mean potential energies per atom in terms of the pair distribution functions $n(r,T)$, it appears interesting to evaluate the

[10] W. E. Keller, Phys. Rev. **90**, 1 (1955).
[11] Kilpatrick, Keller, and Hammel, Phys. Rev. **97**, 9 (1955).
[12] J. Kistemaker, Physica **12**, 281 (1946).
[13] W. H. Keesom, *Helium* (Elsevier Publishing Company, Amsterdam, 1942), pp. 229–232.
[14] R. Berman and J. Poulter, Phil. Mag. [7], **43**, 1047 (1952).

mean forces per atom. This will be done here through the calculation of the mean square force, yielding the root mean square force.[15] Beside being of intrinsic interest, this quantity is of some importance in a direct analysis of slow-neutron scattering processes in liquids in general, and in liquid He^4 in particular.

Let $f(r)$ be the force acting on an atom of a pair of isolated stationary atoms separated by the distance r. Assuming that this force originates in the pair potential energy $\varphi(r)$, of purely central character, we have, by definition,

$$f(r) = -\text{grad}\varphi(r) = -d\varphi/dr. \tag{4.5}$$

The differential mean square force in the liquid due to the distribution existing at a distance r from the origin atom is, omitting the cross term depending on the unknown three-atom distribution function $n(r,r',T)$,

$$dF^2(r,T) = 4\pi r^2 f^2(r) n(r,T) dr, \tag{4.6}$$

and the total mean square force, in the pair representation approximation, is

$$F^2(T) = 4\pi \int f^2(r) n(r,T) r^2 dr, \tag{4.7}$$

the integral being extended over the whole volume of the system. Since the pair distribution functions $n(r,T)$ include exchange effects, the mean square forces $F^2(T)$ also include these effects. With the $n(r,T)$ functions available in tabular form, out to the extreme separation of $r = 20$ A, only the generalized square force integrals $F^2(r,T)$ can be obtained. These are functions of the upper limit r in the integrals (4.7). Using the two analytical approximations to the pair potential energies $\varphi_I(r)$ and $\varphi_{II}(r)$, defined previously,[1] we have obtained the mean square forces $F^2(20\text{ A},T)$ at a series of liquid temperatures. The effective ranges of the square forces $f_I^2(r)$ and $f_{II}^2(r)$ being moderate, the integrals (4.7) converge very rapidly, indicating that these mean square forces are determined, for all practical purposes, by the details of their fields extending over separations of the first neighbor atoms, at most. We give in Table IV, the root mean square forces $[F_I^2(20\text{ A},T)]^{\frac{1}{2}}$ and $[F_{II}^2(20\text{ A},T)]^{\frac{1}{2}}$. These two series of root mean square forces differ from each other as expected from the shapes of the potential energy functions $\varphi_I(r)$ and $\varphi_{II}(r)$. The former, being higher than the latter, gives rise to steeper gradients than the latter. The origin of the slight jumps in the values of these forces in passing from the low, $T \lesssim 2.75$°K, to the high temperature group, $T \gtrsim 3.01$°K, has been discussed in S.D., and was already referred to above. Over the temperature range 1.25–4.20°K, the forces $(F_I^2)^{\frac{1}{2}}$ and $(F_{II}^2)^{\frac{1}{2}}$ first increase up to the lambda point, and then decrease beyond it with increasing temperatures, if the jump at 2.75–3.01°K is disregarded as it should be. The forces $(F_I^2)^{\frac{1}{2}}$ are close to about 110 cal/mole×A, and the $(F_{II}^2)^{\frac{1}{2}}$ forces are grouped around 80 cal/mole×A.

TABLE IV. Root mean square forces in liquid He^4 at various temperatures.[a]

T °K	$(F_I^2(20\text{ A},T))^{\frac{1}{2}}$ cal/mole×A	$(F_{II}^2(20\text{ A},T))^{\frac{1}{2}}$ cal/mole×A
1.25	115.0	83.3
1.50	115.2	83.6
1.75	115.2	83.6
2.06	117.3	85.1
2.25	117.3	85.1
2.50	115.5	83.8
2.75	113.4	82.3
3.01	125.4	89.8
3.25	122.2	87.6
3.50	118.8	85.2
3.75	115.0	82.5
3.97	111.0	79.5
4.20	105.3	75.6

[a] These are evidently approximate because of the omission of the cross term $\int f(r) f(r') n(r,r',T) dr(r) dr(r')$ in Eq. (4.7). Lack of information on $n(r,r',T)$ prevents one from estimating the value of the cross term, at the present time.

The problem of the closeness of either series of forces to the actual root mean square forces is of course similar to the corresponding problem of the potential energies $\Phi_I(T)$ and $\Phi_{II}(T)$. At the present time, no well-justified decision is available on the degree of fitness of the original analytical approximations to the pair potential energies of two isolated He^4 atoms, $\varphi_I(r)$ and $\varphi_{II}(r)$. There appear to be indications,[11] as far as the helium vapor second virial coefficient is concerned, that $\varphi_{II}(r)$ tends to overestimate, in absolute value, the pair potential energy. The problem of the degree of approximation achieved on the pair forces, $[-\text{grad}\varphi_I(r)]$ and $[-\text{grad}\varphi_{II}(r)]$, was not raised so far, because the intervention of the forces, in the rather fragmentary status of the theory of liquids, seemed to be remote. However, as first shown by Placzek,[7] the investigation of slow neutron scattering phenomena in liquids may put the force problem to the fore, adding thus a new elementary physical quantity to be probed in liquids.

In concluding, I should like to thank Mr. Max Goldstein for his kind cooperation in coordinating the various numerical calculations. Thanks are due to Mr. P. E. Harper for his work on the "701" IBM Electronic Calculator, to Miss M. L. Johnson and Mrs. J. E. Powers for the many hand calculations, to Mrs. A. M. Snowden and Mrs. L. E. Moss for the preparation of the graphs.

[15] These calculations originated in the discussions with Dr. H. S. Sommers, Jr., of the Los Alamos slow-neutron scattering data in liquid He^4. See Sommers, Dash, and Goldstein, Phys. Rev. 97, 855 (1955).

Wave Mechanical Treatment of the Fermi Gas

WILHELM MACKE
Instituto de Física Teórica, São Paulo, Brazil
(Received July 21, 1954)

A wave mechanical treatment of a Fermi gas is described using a generalized Ritz method, which gives in a zero approximation the well-known energy terms of Thomas-Fermi, Weizäcker, and Gombás, and which can be refined to any desired degree.

FOR the treatment of a Fermi gas, there exist two methods of importance, both of which neglect the correlation between the particles; the exact one of Hartree-Fock[1] and the statistical model of Thomas-Fermi.[2] In the region of approximation methods, only little has been done because of the difficulty of finding approximate single-particle wave functions which satisfy the condition of orthogonality.

This paper is intended to remove the deficiency by presenting a general approximation method, which in zero approximation gives the statistical model of Thomas and Fermi from a new, wave mechanical standpoint and makes understandable the discrepancy between the good results of this model and the rough assumptions under which it was developed. On the other hand, it is shown explicitly in what directions the statistical model can be refined.

The approximation here used represents the particle wave function $\psi_n(\mathbf{x})$ by a known orthogonal system of functions $\varphi_n(y_k)$, where y_k represents a transformation of the space,

$$y_k = y_k(\mathbf{x}), \quad k=1, 2, 3, \tag{1}$$

which is arbitrary, except for two conditions; to form a set of orthogonal coordinates in the $\mathbf{x}$-space and to transform the whole space into a box of unit length. Then, as trial wave functions ψ_n, there are used

$$\psi_n(\mathbf{x}) = (\sigma/N)^{\frac{1}{2}}\varphi_n(y_k), \tag{2}$$

where the quantity σ/N is defined as the functional determinant $|\partial y_k/\partial x_\lambda|$, and where the $\varphi_n(y_k)$ represent the set of normalized eigenfunctions of the unit box. These functions ψ_n are orthogonal and normalized for all possible transformations (1) and the total energy can be represented as a functional of the y_k only.

For any arbitrary definition (2) of a function $\sigma(\mathbf{x})$ and the related functions φ_n, the kinetic part of the total energy transforms into

$$E_{\text{kin}} = \int d\mathbf{x} \frac{\hbar^2}{2m}\left\{\frac{\sigma}{N}\sum\left|\frac{\partial\varphi_n}{\partial\mathbf{x}}\right|^2 + \left(\frac{\partial\sqrt{\rho}}{\partial\mathbf{x}}\right)^2 - \sigma\left(\frac{\partial(\rho/\sigma)^{\frac{1}{2}}}{\partial\mathbf{x}}\right)^2\right\}, \tag{3}$$

as an easy calculation shows. Under the special assumptions made with the definition of (2), the first two terms of (3) represent the statistical energy terms derived by Fermi[2] and Weizsäcker.[3] Regarding the density of particles,

$$\rho = \sigma\cdot\frac{1}{N}\sum|\varphi_n|^2 \tag{4}$$

one sees that ρ goes over into σ in the limit, for N very large, The sum in (4) contains only the fluctuations of the density, arising from the occupation of special states, whereas σ is a slowly varying function.

The treatment of the first term of (3) under the assumptions made for $\varphi_n(y)$, gives the well-known Fermi energy, for the ground state,

$$E_F = \int d\mathbf{x} k_F \sigma^{5/2}, \quad k_F = \frac{\hbar^2}{2m}\cdot\frac{3}{5}\left(\frac{3}{8\pi}\right)^{\frac{1}{3}}, \tag{5}$$

if one replaces the sum over the states by an integral. In the limit for increasing N, the ρ appearing in the other terms of the kinetic and potential energy, can be replaced by σ. This shows, that in this limit the energy is no longer a function of the transformation (1) itself, but only of its functional determinant σ/N. The calculation of σ is now made in the usual way by variation of the energy with respect to σ and gives the Thomas-Fermi equation in its most developed form.

The physical meaning of the approximation (2) is easy to understand. All wave functions appear as depending on the three arbitrary functions y_k only. They all have the same general form $(\sigma/N)^{\frac{1}{2}}$, whereas φ_n describes only a fluctuation part with a different number of nodes, which makes all the different functions orthogonal to each other. Under variation of the energy, the ψ_n no longer have the possibility of building their own individual form. There is only one general form for all the wave functions together, which is so varied as to make the energy a minimum. The underlying physical idea of the trial functions (2) consists therefore in the assumption of an equal distribution for all particles, if one disregards the special fluctuations of each particle. Such an assumption is best fulfilled when the Fermi gas contains many particles and when there is a strong, potential, which localizes the different particle states in nearly the same way.

[1] D. R. Hartree, Proc. Cambridge Phil. Soc. **24**, 89 (1928); V. Fock, Z. Physik **61**, 126 (1930); **62**, 795 (1930).
[2] L. H. Thomas, Proc. Cambridge Phil. Soc. **23**, 542 (1927); E. Fermi, Z. Physik **48**, 73 (1928).
[3] C. F. v. Weizäcker, Z. Physik **96**, 431 (1934).

This treatment of the Fermi gas shows that the statistical model can be derived from much better assumptions than the former ones (classical limit and free particles in the interior of the atom). The good results of this theory with respect to many general properties of the atom can now be understood on the basis of this more general wave mechanical treatment. The further advantage of this method is that it can be improved in many directions. First, if the potential V has a spherical symmetry, one can treat the angular part of the wave functions exactly, using the approximation method only for the radial part of ψ_n. Secondly, one can easily find the corrections which appear when N is not large, these corrections of the type discussed by Gombás.[4]

Further, one can repeat after a first and rough calculation of σ the calculation of E_F in (5), by using the summation instead of the integration as is required in (3). A general discussion reveals the shell-structure of the Fermi gas. A density σ of the type $e^{-\alpha r}$, a monotonically decreasing function of r, gives the well-known magic numbers of the atomic shells. On the other hand, a density which is nearly constant and then drops within a small region gives rise to the magic numbers of the nucleus, as far as the kinetic energy contributes to it. (It needs the well-known, further assumption of a strong spin orbit coupling.) Finally, one can regard these calculations as a zero and first approximation for σ and φ_n. The higher approximations then can be calculated by an iteration of the treatment, starting with the solutions of zero order. By these higher approximations the hypothesis of equal distribution of the particles has been overcome and one can go on to calculate the energy as well as the ψ_n up to any desired degree of accuracy. A paper in which the new theory is outlined in more detail, will appear soon,[5] and further work on its applications is in preparation.

[4] P. Gombás, Acta Phys. Acad. Sci. Hung. III, 105, 127 (1953).

[5] W. Macke, Ann. Physik (to be published).

PHYSICAL REVIEW VOLUME 100, NUMBER 4 NOVEMBER 15, 1955

Improved Value of the Velocity of Light Derived from a Band Spectrum Method*

D. H. Rank, H. E. Bennett, and J. M. Bennett
Department of Physics, The Pennsylvania State University, University Park, Pennsylvania

(Received August 1, 1955)

The previously reported value of the velocity of light as obtained from B'' of the 002 band of HCN has been improved as a result of an absolute interferometric wavelength determination of the band origin. The new value, 299 791.9±2.2 km/sec, is in good agreement with that obtained from all other modern methods.

THE recent determination of the velocity of light by Rank, Shearer, and Wiggins[1] by means of the band spectrum method was subject to a small error occasioned by the inaccuracy of knowledge of the absolute value of the wavelength of the band origin. The experiment of Rank *et al.* was performed by using the $P(1)$ line of the 002 band of HCN as the calibration standard for the interferometer. This procedure had been adopted so that in the event of improved knowledge of the absolute wavelength of the band origin it would be possible to correct the velocity of light without a complete remeasurement of the band.

We have succeeded in measuring absolute wavelengths in vacuo in the 1 to 1.5μ region by means of the Fabry-Perot interferometer. The measurements have been made using the Hg^{198} green line as the standard for calibration of the interferometer. Mercury-198 lines at λ10 140 A, λ13 570 A, and λ15 295 A were measured with the interferometer. The line at λ10 140 A, $6s7s\ ^1S_0 \rightarrow 6s6p\ ^1P_1^0$ arises from energy levels which have been measured in the photographic region of the spectrum. Our direct measurements of this line agree with the value calculated from the Combination Principle within 0.003 cm^{-1}. We believe that our determinations at 1.5μ have comparable accuracy.

We have measured six absorption lines of the 002 band of HCN by essentially the same interferometric technique employed on the Hg^{198} lines. A full description of the interferometric techniques employed in these wavelength measurements will appear elsewhere.

The HCN lines which we have measured absolutely arise from low-J levels, which allow us to calculate the absolute frequency of the band origin using the molecular constants previously determined.[1] We obtain a value of $\nu_0 = 6519.6148 \pm 0.003$ cm^{-1} for the 002 band of HCN. The result of our new absolute calibration is to give slightly different values to B' and B'' than previously quoted. We obtain $B' = 1.45706_3$ cm^{-1} and $B'' = 1.47822_8$ cm^{-1}. The new value of B'' yields a value for c, the velocity of light, of 299 791.9±2.2 km/sec. The decrease in the probable error over that quoted previously[1] is due solely to lessened uncertainty in the absolute calibration of the interferometer.

* This research was assisted by support from the Office of Naval Research.

[1] Rank, Shearer, and Wiggins, Phys. Rev. 94, 575 (1954).

Atomic Distribution in Liquid Helium by Neutron Diffraction

D. G. Hurst and D. G. Henshaw
Division of Physics, Atomic Energy of Canada Limited, Chalk River, Ontario, Canada
(Received July 18, 1955)

The angular distribution of 1.04 A neutrons scattered by liquid helium has been measured for a series of temperatures between 1.6°K and 5.04°K over the angular range 3° to 70°. The scattering patterns are characterized by one principal maximum at an angle of 19.6±0.5° over a large range in liquid density. No marked change in the scattering pattern accompanies the λ transition. It is shown that for large-angle scattering the liquid behaves like a system of free helium atoms. Scattering intensities normalized to the differential cross section for a free helium atom have been transformed to give the radial distribution functions at 5.04°K, 4.24°K, and in the region of 2°K. The first maximum in the density is at 3.5_0 A for the lowest temperature and at 3.6_8 A for the highest. The density change is not accounted for by the shift of the maximum, and a decrease in the number of neighbors is postulated. The mean radial positions assigned to the first and second neighbors using the analysis of this paper agrees with a close-packed configuration of symmetrical particles, but the average number of first neighbors appears to be less than a complete close-packed arrangement, in keeping with the random arrangement expected for a liquid.

INTRODUCTION

INFORMATION about the atomic arrangement in a liquid can be obtained from x-ray or slow neutron diffraction patterns. Because the details of the mechanism of the transition from He I to He II are unexplained, such information is especially interesting in the case of liquid helium. Early studies[1,2] with 1.54 A x-rays showed a peak in the scattering at an angle of 28°. Recent work[3,4] has confirmed the position of the peak and gives further details of the pattern. No difference was reported due to the transition. The x-ray scattering at small angles has also been studied,[5] and has been shown to be in agreement with the theoretically predicted scattering at zero angle. Egelstaff[6] has measured the scattering of long-wavelength (>4 A) neutrons by liquid helium in an unsuccessful search for extra scattering[7] expected to result from Bose-Einstein condensation in the He II region. In this connection Goldstein *et al.*[8] measured the transmission of long-wavelength neutrons through the liquid and found no evidence for the expected effect.

Neutrons have certain advantages over x-rays for the study of liquids because scattered intensities do not depend upon the atomic structure factor and Compton scattering is absent. On the other hand, both neutron and x-ray coherent intensities are reduced by the Debye-Waller factor, which allows for the displacement of the atoms from their equilibrium positions. The zero-point motion in liquid helium is so large that the decrease due to the Debye-Waller factor is even more rapid with increasing angle than that due to the atomic structure factor. As a result, the advantage of neutrons is not so great with helium as with other liquids.

At large angles the total neutron scattering is expected to be largely inelastic diffuse scattering, with an average energy loss about the same as the recoil energy of a free helium atom for the same angular deflection of the neutron. To confirm this energy loss the transmission of scattered neutrons through a filter containing gadolinium, an element whose cross section varies rapidly with energy, was measured at two angles. The measured energy loss agreed with the predictions.

Preliminary measurements[9] of the scattering of 1.08-A neutrons showed a peak characteristic of liquid patterns. This work has been resumed and the present paper reports results and analysis of measurements of the angular distribution of 1.04 A neutrons scattered by liquid helium at several temperatures between 1.65°K and 5.04°K. The atomic arrangement was deduced by the usual Fourier integral transformation of the scattered intensity, which gives the average atomic density as a function of distance from an atom. Our results indicate an atomic shell at a distance which, depending on the temperature, varies between 3.7_0 and 3.9_4 A. X-ray measurements[3] have been interpreted as showing atomic shells at distances of 3.15 A, 4.24 A, and 5.40 A. The present results are not consistent with this complicated picture, but suggests a simple structure in keeping with the symmetry of the atoms of inert gases.

APPARATUS

The angular distribution of the scattered neutrons was measured on one of the Chalk River neutron spectrometers,[10] with the NaCl monochromating crystal set to diffract neutrons of wavelength 1.04 A.

The cryostat, which was mounted on the table of the

[1] W. H. Keesom and K. W. Taconis, Physica **5**, 270 (1938).
[2] J. Reekie, Proc. Cambridge Phil. Soc. **36**, 236 (1940).
[3] J. Reekie and T. S. Hutchison, Phys. Rev. **92**, 827 (1953); Hutchison, Beaumont, and Reekie, Proc. Phys. Soc. (London) **A66**, 409 (1953); C. F. A. Beaumont and J. Reekie, Proc. Roy. Soc. (London) **A228**, 363 (1955).
[4] Gordon, Shaw and Daunt, Phys. Rev. **96**, 1444 (1954).
[5] A. G. Tweet, Phys. Rev. **93**, 15 (1954).
[6] P. A. Egelstaff and H. London, Proceedings of the Kjeller Conference, Jener Publication No. 7 (1953).
[7] Goldstein, Sweeney, and Goldstein, Phys. Rev. **77**, 319 (1950).
[8] Goldstein, Sommers, and Dash, Phys. Rev. **91**, 490 (1953); Sommers, Dash, and Goldstein, Phys. Rev. **97**, 855 (1955).
[9] D. G. Henshaw and D. G. Hurst, Phys. Rev. **91**, 1222 (1953).
[10] Henshaw, Hurst, and Pope, Phys. Rev. **92**, 1229 (1953).

spectrometer, is shown in Fig. 1. It is of all-metal construction and consists of a scattering chamber surrounded by four jackets containing liquid nitrogen[11] arranged in three concentric sets, the assembly being contained in an outer vacuum jacket. The jackets are hung from the top plates by 0.010-in. wall stainless steel tubing. For additional thermal protection, the central liquid nitrogen jacket and the "liquid helium" jacket were maintained at the temperature of solid nitrogen by pumping. This arrangement allowed scattering measurements to be made for periods up to 24 hours with a single filling of the cryostat.

The lower portion of the scattering chamber is thermally protected by radiation shields attached to the liquid nitrogen jackets. Three sets of spacers maintain the scattering chamber axial in the cryostat. For a height of 2 inches at the level of the neutron beam the scattering chamber, radiation shields, and outer vacuum jacket are thin walled (0.010 in., 0.0005 in., and 0.015 in., respectively) in order to reduce the background scattering. In addition the outer vacuum wall is of reduced diameter. Cadmium walls attached to the bottom of the scattering chamber define the scattering volume and reduce the intensity of multiply scattered neutrons reaching the counter. Windows in the lower section of the outer vacuum jacket allowed a pin (not shown) at the center of the base of the scattering chamber to be placed on the axis of the spectrometer. Adjustments were made using the aligning screws.

The helium was liquefied in a Collins Liquefier[12] and transported to the cryostat in a liquid helium storage and transport vessel.[13,14] Liquid helium was transferred from the storage flask to the cryostat through all-metal transfer siphons, the progress of filling being followed with carbon resistors.[15] Rate of transfer to the cryostat was controlled by varying the pressure applied to the helium in the storage vessel. Under normal operation this pressure was about 6 psi.

Before a filling, the scattering chamber was precooled with liquid nitrogen and was then evacuated to ensure that no impurities were present. The possibility that some particles of solidified air were carried over into the scattering chamber by the liquid helium was considered small because, owing to the low density of liquid helium, all medium- and large-sized impurities would sink to the bottom of the storage vessel. In addition, a 200-mesh screen attached to the bottom of the siphon in the cryostat would have stopped any large particles which may have been transferred through the siphon.

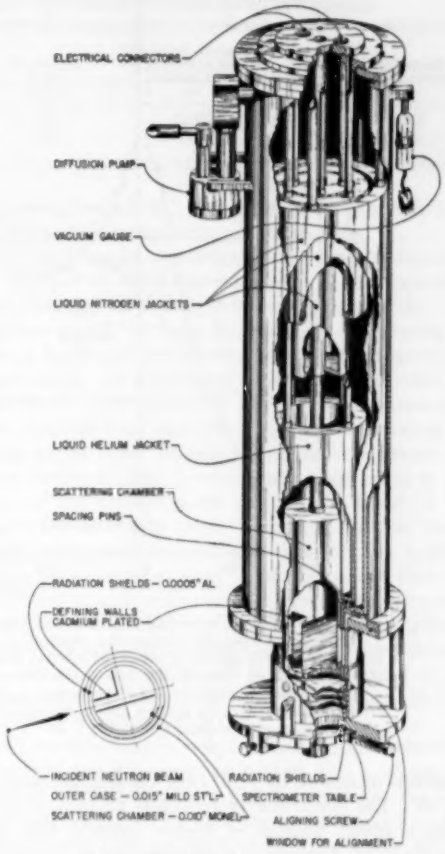

FIG. 1. The liquid helium cryostat.

We think that no significant part of the scattering pattern is to be attributed to impurities.

The temperature of the liquid helium was measured, controlled, and recorded by means of its vapor pressure. The 1949 Cambridge Temperature Scale was used to convert pressures to temperatures. Pressures in the range 0–800 mm were measured with a Heise Bourdon Gauge[16] stated to have an error less than 0.75 mm. For greater pressures a laboratory type pressure gauge was used. This was checked and found to be within $\pm\frac{1}{4}$ psi. A Foxboro Controller Recorder[17] coupled to a restrictor valve was used to control the pressure. This controller had two ranges, 760 mm and 100 mm full scale, allowing the temperature to be controlled to ± 0.04°K in the higher range and ± 0.02°K in the lower range. No corrections have been made for the small loss in pressure due to pumping and the thermomolecular pressure difference.

Measurements were made at a series of fixed angular

[11] In practice, liquid nitrogen was used in the jacket labeled "liquid helium jacket."
[12] Arthur D. Little Inc., Cambridge, Massachusetts.
[13] Superior Air Products Company, Newark, New Jersey.
[14] In the arrangement used earlier,[9] the liquefier was mounted beside the cryostat and the liquid was transferred directly from the liquefier to the cryostat.
[15] J. R. Clement and E. H. Quinnel, Rev. Sci. Instr. **23**, 213 (1952).
[16] Heise Bourdon Tube Company, Inc., Newtown, Connecticut.
[17] The Foxboro Company, Foxboro, Massachusetts.

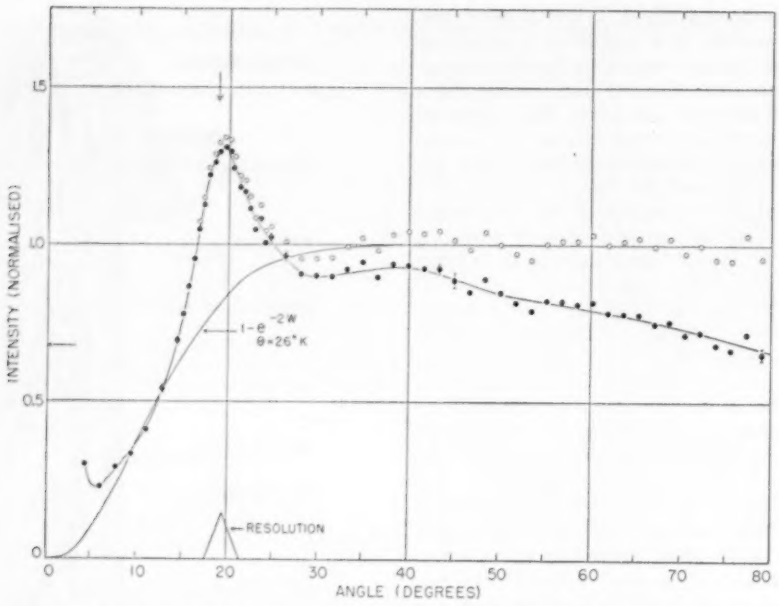

FIG. 2. Scattering of 1.04 A neutrons by liquid helium at 4.24°K. The full circles are the experimental results corrected for background, resolution, and the variation of effective volume with angle. The vertical arrow shows the predicted position of an x-ray peak based on published results for 1.54 A x-rays. The arrow on the ordinate scale shows the calculated zero angle scattering. The open circles were obtained by dividing the full circle values by the differential cross section of a free helium atom and normalizing to unity at large angles. Standard deviations based solely on the total number of counts are shown for several points.

positions separated by 1.70° over the angular range 3° to 70°. The spectrometer remained at each position until a preset number of counts (usually 800) had accumulated. The results were expressed as counts per monitor count. In the vicinity of the peak, where greater resolution was required, the spectrometer was moved in steps of 0.57°. (As the average counting rate was of the order of 40 counts per minute, one complete curve required 15 hours operation of the spectrometer.) Because the liquid helium lasted 10 hours at 1.5°K and 24 hours at 4.2°K, in general more than one filling of liquid helium was necessary to complete a curve. Several traverses were made at each temperature in order to accumulate enough counts for acceptable statistics.

The background was measured with the liquid helium scattering chamber evacuated and at the temperature of liquid nitrogen. Except at angles below 10°, the background was essentially constant at 4 counts per minute. Below 10°, the background rose continuously and became very large for angles of 3° and less. No peaks were observed in the background pattern. The excess above 4 counts per minute was corrected for the transmission through the liquid helium.

The incident beam of neutrons was analyzed by means of a calcite crystal in transmission. Rocking curves were taken in the parallel and antiparallel positions. The wavelength was calculated from the calcite d spacing and the angle between the positions of the peak in the parallel and the antiparallel position. The mean wavelength was 1.04 A with a spread of ± 0.03 A as given by the width of the antiparallel rocking curve.

The zero of the spectrometer was taken as the mid position between the peaks of the parallel and antiparallel rocking curves, and was checked by determining the setting of the spectrometer arm for maximum intensity in the forward direction. These two methods gave agreement to better than 0.1°. A further check of the spectrometer zero and neutron wavelength was made by measuring the scattering pattern of nickel powder contained in a cylindrical cassette 1 cm in diameter. The measured positions of the peaks agreed with the values calculated from the neutron wavelength, the spectrometer zero and the nickel d spacing. The position of the (200) line of potassium bromide corresponds closely to the position of the liquid helium peak. The full width at half-maximum of this line was measured as 2°. This was taken as the resolution of the instrument and used in the correction for resolution which was applied in the region of the peak.

MEASUREMENTS

The transmission of the neutrons through the 5-in. diameter liquid helium specimen was measured with the helium at 4.24°K. The result was 0.84, corresponding to a cross section per helium atom of 0.73 barn, in agreement with the published value of 0.74±0.04 barn.[8]

The average changes in energy of the neutrons scattered through 19.6° and 60.0° were determined from measurements of the transmission through a gadolinium filter.[18] The transmission of the filter was calculated as a function of energy by use of the measured transmission for the incident neutrons and the variation with energy of the gadolinium cross section.[19] The experimentally determined energy losses are shown in Table I. Because of the small atomic weight of helium, relatively large energy losses accompany neutron scattering by free helium atoms. As seen from Table I, the measured energy loss at 60° for liquid helium agrees within the experimental error with the loss for free helium atoms.

The results of measurements of the angular dependence of scattering at a temperature of 4.24°K are shown in Fig. 2. The full circles are the experimental points corrected for effective scattering volume, background counting rate and instrumental resolution. No corrections have been made for multiple scattering as these were calculated and found to be unimportant. Standard deviations based solely on the total number of counts are shown for several points; all the points lying between two points so marked have the same statistical deviations. The position of the peak is 19.6±0.5°. The vertical arrow marks the position (18.8°) predicted for the peak due to 1.04-A x-rays, based on an observed peak at 28°[1,2] with 1.54 A x-rays, according to the formula $[\sin(\frac{1}{2}\varphi)]/\lambda = \text{constant}$.[20] The arrow on the ordinate scale marks the zero-angle scattering calculated from the isothermal compressibility,[5] and the first point shows the onset of the scattering expected at angles smaller than included in these observations.

If the liquid is represented by the simple Debye model[21] of a system of independent oscillators, the diffuse scattering would have the form $1-e^{-2W}$, where W is a function of temperature and of a characteristic temperature Θ. The curve $1-e^{-2W}$ calculated for $\Theta = 26$°K is plotted on Fig. 2.

The quantity e^{-2W} is roughly the fraction of scattering power available for coherent scattering. It will be seen that this theory predicts essentially no coherent scattering beyond 35°, and suggests that there is considerable diffuse scattering under the peak.

Table I. Energy change on scattering.

Scattering angle degrees	Calculated energy loss for scattering by free helium atom ev	Energy loss corresponding to measured transmission ev
19.6	0.002	0.003±0.002
60.0	0.017	0.016±0.003

At large angles the neutron scattering is expected to decrease in much the same way as the scattering from free helium atoms; it is only necessary that the neutron energy be large compared to the spacing of energy levels and that coherent effects be unimportant. Accordingly, the experimental points were divided by the differential cross section of a free helium atom and the quotients were normalized to make the average at large angles equal to unity. The result is shown by open circles on Fig. 2, where each open circle is the ratio of the scattering per atom in the liquid to the scattering by a free atom. The scatter of the circles about unity over the last two-thirds of the angular range gives strong support to the hypothesis that the scattering at large angles may be treated as if the atoms were free. Further support is given by the completely diffuse character of the large angle scattering predicted by the formula $1-e^{-2W}$ and by the agreement of the measured energy loss at 60° with the calculated loss for scattering from free atoms.

All the experimental results have been put in the form described and are shown plotted in Fig. 3, where the scale of angles is the same for all curves but the zero of ordinates differs for each curve, as marked on the lefthand side. The curves have similar shape, differing in detail; in particular, the height of the peak changes with density although the position remains at 19.6 ±0.5°. Comparison of the 2.25°K and 1.95°K curves, which bracket the λ point, show small differences only. In all cases there is a valley just beyond the peak and evidence for a small rise above unity further out. These may be smooth variations in diffuse scattering corresponding to the peaks in the diffuse scattering which acompany Debye-Scherrer lines from powdered crystals.[22]

The increase with temperature of the scattering in the region of 10° and lower is to be expected on the basis of the known small-angle scattering of x-rays.[5]

An important feature of the patterns is the constant angular position of the peak for a large change in density. In order to understand its significance, some relationship between the scattering pattern and the structure of the liquid must be accepted. The usual assumption is that the transformation commonly used for x-rays may be applied to neutron scattering. The atomic density $\rho(r)$ at a distance r from an average

[18] This filter contained 7.5 mg/cm² of Gd_2O_3 and was kindly loaned to us by B. N. Brockhouse.

[19] *Neutron Cross Sections*, Atomic Energy Commission Report AECU-2040 (Technical Information Division, Department of Commerce, Washington, D. C., 1952).

[20] φ is the scattering angle. For precise comparison the position of the x-ray peak should be taken from a curve corrected for atomic structure factor. This would increase the angle slightly.

[21] R. W. James, *The Optical Principles of the Diffraction of X-rays* (G. Bell & Sons Ltd., London, 1948), Chaps. I and V.

[22] B. E. Warren, Acta Cryst. 6, 803 (1953).

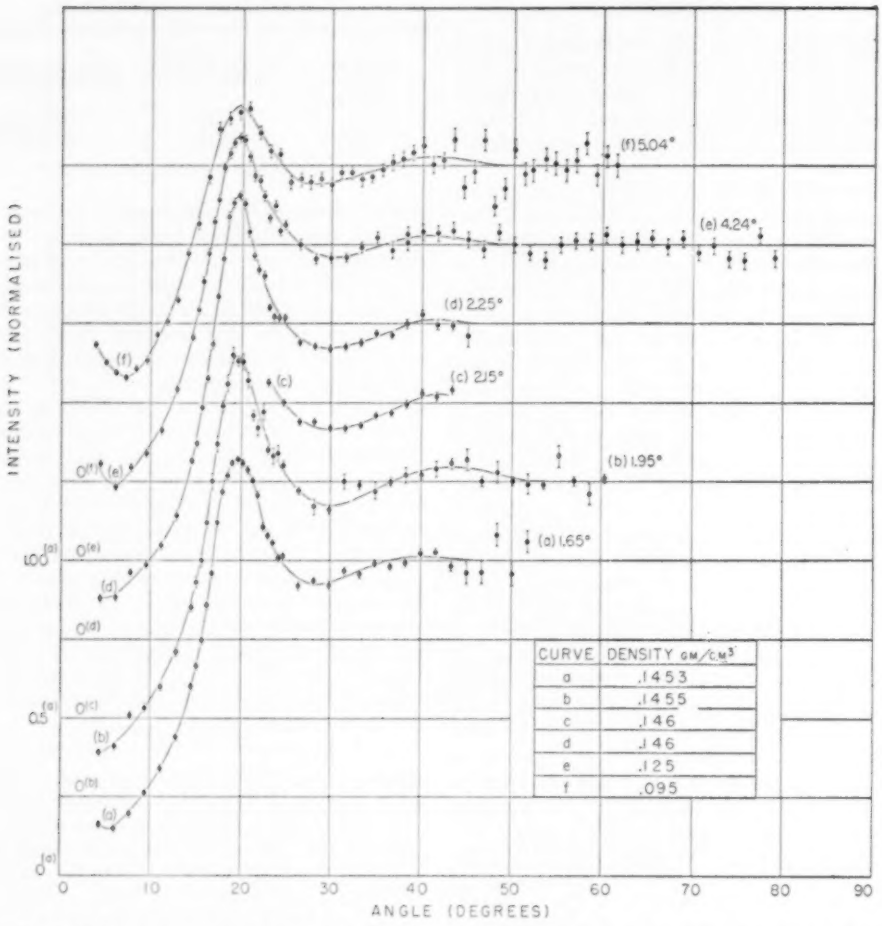

FIG. 3. The experimental results expressed as the ratio of the scattering per atom in the liquid to the scattering by a free helium atom. Standard deviations are shown for each point. The curves are shifted vertically, the zero for each curve being marked.

atom is given by

$$4\pi r^2[\rho(r)-\rho_0]=\frac{2r}{\pi}\int_0^\infty si(s)\sin rs\,ds, \qquad (1)$$

where ρ_0 = mean atomic density of the liquid, $s=(4\pi/\lambda)\times\sin(\varphi/2)$, λ = wavelength, φ = angle of scattering, $i(s)=[I(s)-I_\infty]/I_\infty$, $I(s)$ = intensity of scattering for a value s of the variable, and I_∞ = value of $I(s)$ as $s\to\infty$.

In applying this formula to neutron scattering, some latitude exists in the choice of $I(s)$ appropriate to a set of experimental results and in the treatment outside the experimental range of s. The formula was derived on the assumption that $I(s)$ is the coherent scattering. For reasons similar to those discussed for oxygen, nitrogen, and argon,[10] the measured scattering will be treated as coherent for the purpose of the transformation. Because the measured intensity decreases steadily at large angles, $I(s)$ cannot be identified with the measured intensity on account of the difficulty of choosing I_∞. To the extent that the decrease is due to the scattering being like the scattering from free atoms, the measured intensity is not a function of s but rather of φ, and I_∞ has no meaning. (Putting $I_\infty=0$ is not possible because $i(s)$ would then be positive and the relation $-2\pi^2\rho_0=\int_0^\infty s^2 i(s)ds$, which ensures $\rho(r)\to 0$ as $r\to 0$, could not be satisfied.) The normalized ratio of measured scattering to the differential cross section of a free atom, (open circles in Fig. 2), is a very suitable function for $I(s)$. The role of the free atom cross section in this treatment has something in common with the use of the atomic form factor in deriving $I(s)$ for x-ray scat-

tering.[23] Accordingly, we have used the values plotted on Fig. 3 for $I(s)$. The transforms were computed on Ferut (Ferranti Electronic Computer at the University of Toronto).[24]

In preparing the experimental results for transformation, the normalized intensities for each temperature were plotted as a function of s and a smooth curve was drawn through the experimental points. At small angles the curves were extrapolated to the calculated zero angle scattering. For each temperature two extrapolations to zero angle from the smallest experimental angle were used: a linear extrapolation and a smooth curve with horizontal tangent at zero. The difference between the resulting transforms is small, and those corresponding to the horizontal tangent are used in what follows. The transforms as calculated give $4\pi r^2[\rho(r)-\rho_0]$, and from these $r\rho(r)/\rho_0$ has been calculated and is plotted in Fig. 4 for three cases: 5.04°K, 4.24°K, and the average of the $i(s)$ curves for the four lowest temperatures.

Although the form of the measured scattering is typical of liquid scattering, the peak is relatively small and correspondingly the peaks in the transform are not pronounced. On this account it is difficult to analyze the $4\pi r^2\rho(r)$ into separate peaks, as is commonly done.[22] The density fluctuations are brought into more prominence in the graphs of Fig. 4 where $r\rho(r)/\rho_0$ is plotted against r. Each curve shows low density for small values of r; a higher than average density for r between 3 A and 4.5 A with a peak near 3.8 A; and some evidence for a slight ordering further out. The fluctuations between $r=0$ and $r\approx 2$ A are certainly spurious, arising from statistical errors and the finite range of s. They may influence slightly the apparent position of the maximum. A maximum occurs between 3.7_0 and 3.9_4 A for all three cases, although the liquid density increases by a factor 1.54 between 5.04°K and the lambda point. The deduction can be made immediately that, to the accuracy with which Fig. 4 represents the structure, there is no marked change in arrangement of the helium atoms as the temperature falls from 5.04°K to <2.25°K. Graphs of the functions $\rho(r)$ have maxima at 3.50, 3.50, and 3.68 A for bulk densities 0.146, 0.125, and 0.095 gram/cc respectively. If density changes were due solely to a uniform dilation the radii would be in the ratios $(0.146)^{-\frac{1}{3}}:(0.125)^{-\frac{1}{3}}:(0.095)^{-\frac{1}{3}}=1:1.05:1.15$, whereas they are in the ratios $3.50:3.50:3.68=1:1:1.05$. Clearly, only a small part of the density change can be ascribed to dilation. A possible model to explain the remaining density change is the existence of unoccupied atomic sites in an array with separations which are little, if at all, temperature dependent. Increased density would then be largely due to increased occupation of these sites, i.e., the filling of "holes."

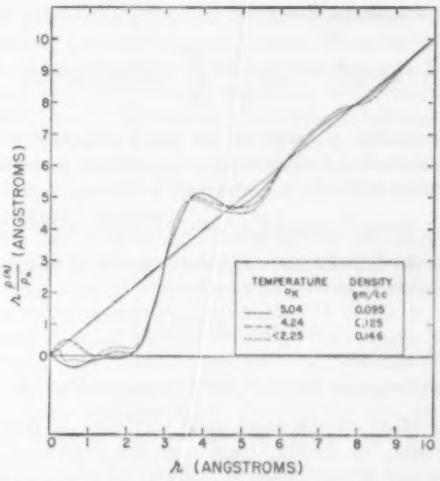

FIG. 4. The results of transforming the measured scattering to radial density distribution. The quantity plotted is $r\rho(r)/\rho_0$, where ρ_0 is the mean atomic density, i.e., $\rho(r)_{\overset{}{r}\to\rho_0}$ as $r\to\infty$. The abscissa r is the radial distance from an atom. Three cases are given. (The dotted line represents the average over the temperature range 1.65°K to 2.25°K.) The straight line is r, the value which $r\rho(r)/\rho_0$ would have if the atomic distribution were uniform.

The curves of Fig. 4 show none of the fine structure reported by Reekie and Hutchison[3] in their transforms of x-ray measurements.

Use of the average of the four low-temperature curves, 1.65°K to 2.25°K, in the transform ignores their differences. The 1.65°K curve differs most, having a lower peak and being slightly broader. The change which would be caused in the transform by use of the 1.65°K curve instead of the average curve has been calculated. The effect is small and, as might be expected, gives a slightly smaller density fluctuation than the average. Conversely, use of the 2.25°K curve slightly sharpens the transform. Although both effects are in the directions to be expected from density changes, they depend on differences which may be experimental errors.

DISCUSSION

The results of transforming the measured scattering to radial density distribution depend on the treatment given the data before transformation. The curves of Fig. 4 are based on the normalized experimental intensities, i.e., the ratio of scattering per atom of the liquid to scattering by a free atom. Two possible modifications will be considered.

The pattern may be broken up into the sum of the main pattern, $I_1(s)$, and small-angle scattering, $\Delta I(s)$, by writing

$$I(s)=I_1(s)+\Delta I(s). \qquad (2)$$

[23] N. S. Gingrich, Revs. Modern Phys. **15**, 90 (1943).

[24] The earlier statement[10] that the calculation was based on Simpson's Rule is incorrect. The program uses Filon's rule for the integration; see L. N. G. Filon, Proc. Roy. Soc. Edinburgh **49**, 38 (1928–1929).

The transforms then give

$$\rho(r)-\rho_0=\rho_1(r)-\rho_{1,0}+\frac{1}{2\pi^2 r}\int_0^\infty s(\Delta I/I_e)\sin rs\,ds, \quad (3)$$

where $\rho_1(r)$, $\rho_{1,0}$ refer to the liquid structure which would produce $I_1(s)$ as a scattering pattern. A plausible form for $\Delta I(s)/I_e$ is $A\exp(-\beta^2 s^2)$. Then

$$\rho(r)-\rho_0=\rho_1(r)-\rho_{1,0}+[A/(2\beta\sqrt{\pi})^3]\exp(-r^2/4\beta^2). \quad (4)$$

If in the structure $\rho(r)$ and the structure $\rho_1(r)$ we require zero density as $r\to 0$, we must write

$$\rho_0=\rho_{1,0}-A/(2\beta\sqrt{\pi})^3;$$

then

$$\rho(r)=\rho_1(r)-[A/(2\beta\sqrt{\pi})^3][1-\exp(-r^2/4\beta^2)]. \quad (5)$$

The effect of the small-angle scattering is thus to decrease the density below $\rho_1(r)$, the density of the structure corresponding to $I_1(s)$, by an amount which is zero at $r=0$ and which changes in the region $r\approx 2\beta$ to a maximum decrease of $A/(2\beta\sqrt{\pi})^3$, showing the connection between the small-angle scattering and grouping of atoms into clumps of average radius 2β.

The density decrease is so sensitive to the value of β that accurate measurements would be necessary before trustworthy results could be obtained. However, a rough size 2β may be obtained from the measurements at 5.04°K and is about 5 A. The corresponding density decrease is roughly 10^{-3} atoms/A^3, a 5% decrease. Although the small-angle scattering does not materially influence the density obtained from the transforms, it does suggest that at the higher temperature there is a tendency for the helium atoms to occur in clumps about 10 A across, corresponding to density fluctuations arising from the finite compressibility.

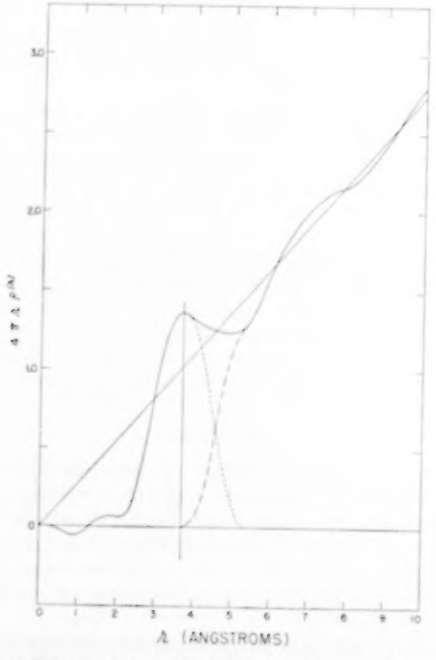

FIG. 5. The quantities $4\pi r\rho(r)$ (full line) and $4\pi r\rho_0$ (straight line) for the low-temperature case, where $\rho(r)$, ρ_0 are in atoms per A^3. The dotted and broken lines represent a possible analysis into shells of neighbors.

The second possible modification would be an attempt to take account of the diffuse scattering. Instead of using the values of $I(s)$ in Fig. 3, the formulas of the Debye theory can be taken as applicable. The diffuse scattering is $1-e^{-2W}$, leaving $I(s)-(1-e^{-2W})$ as the coherent scattering. According to the theory this includes a factor e^{-2W}, which reduces the coherent scattering in the same way as the atomic structure factor which occurs in x-ray scattering. To treat it in the same way as the atomic structure factor, the quantity which would be used in the Fourier integral is

$$I_2(s)=\frac{I(s)-(1-e^{-2W})}{e^{-2W}}=e^{2W}[I(s)-1]+1. \quad (6)$$

Thus

$$i(s)=e^{-2W}i_2(s).$$

The corresponding transforms are

$$T(r)=\frac{2r}{\pi}\int_0^\infty si(s)\sin rs\,ds$$

$$=\frac{2r}{\pi}\int_0^\infty se^{-2W}i_2(s)\sin rs\,ds, \quad (7)$$

$$T_2(r)=\frac{2r}{\pi}\int_0^\infty si_2(s)\sin rs\,ds. \quad (8)$$

A suitable form for $2W$ is $2W=\alpha^2 s^2$. (The same form occurs in the Debye model for solids, where

$$\alpha_D^2=(3\hbar^2/mk\Theta)[\tfrac{1}{4}+\varphi(x)/x],$$

which is the usual Debye formula derived for harmonic binding of atoms. At a temperature of 4°K, $\alpha_D=0.64$ A, in which Θ has been taken as 26°K. Correspondingly, at 2°K, $\alpha_D=0.61$ A; and at 0°K, $\alpha_D=0.59$.) For $2W=\alpha^2 s^2$, the connection between $T(r)$ and $T_2(r)$ is readily found to be[25]

$$\frac{T(r)}{r}=4\pi r[\rho(r)-\rho_0]=\int_{-\infty}^{\infty}\frac{T_2(u)}{u}\frac{\exp[-(r-u)^2/4\alpha^2]}{2\alpha\sqrt{\pi}}du$$

$$=\int_{-\infty}^{\infty}4\pi u[\rho'(u)-\rho_0']\frac{\exp[-(r-u)^2/4\alpha^2]}{2\alpha\sqrt{\pi}}du. \quad (9)$$

This means that the quantity $4\pi r[\rho(r)-\rho_0]$ obtained from $i(s)$ is equal to the quantity $4\pi r[\rho'(r)-\rho_0']$,

[25] J. Waser and V. Schomaker, Revs. Modern Phys. **25**, 671 (1953).

which would be obtained from $i_2(s)$, averaged over the "resolution function" $\exp[-(r-u)^2/4\alpha^2]/2\alpha\sqrt{\pi}$.

The use of e^{-2W} in $i_2(s)$ is, in principle, equivalent to getting rid of the smearing due to atomic motion including zero-point motion. Thus, in a solid, $\rho'(r)$ has the property that

$$\int_{\text{over one shell of atoms}} 4\pi r^2\rho'(r)dr = N_q,$$

where N_q = number of atoms in the qth shell, i.e., $\rho'(r)$ has characteristics similar to a delta function. If we denote by a_q the radius of the qth shell, then

$$4\pi r\rho(r) = \frac{1}{2\alpha\sqrt{\pi}} \sum_q \frac{N_q}{a_q} \exp\left[-\left(\frac{r-a_q}{2\alpha}\right)^2\right]. \quad (10)$$

If the shells do not overlap, a_q corresponds to the maximum in $r\rho(r)$. Consequently, the radius of this maximum will be quoted as the radius of the shell. It follows from (10) that

$$\begin{aligned} N_1 &= a_1[4\pi a_1\rho(a_1)]2\alpha\sqrt{\pi}, \\ N_2 &= a_2[4\pi a_2\rho(a_2)]2\alpha\sqrt{\pi}, \\ N_3 &= \cdots. \end{aligned} \quad (11)$$

In a liquid, the lack of long-range order restricts the application of these formulas to the first few shells.

If the values of $4\pi r\rho(r)$ of Fig. 5 for $2 \leqslant r \leqslant 3.7_0$ A are about 3.7_0 A, we obtain the dotted line. The resulting peak may be ascribed to the first neighbors. Subtracting this peak from $4\pi r\rho(r)$ gives the broken line, which suggests, by its similarity to the shape of the curve between 2 and 3.7 A, a peak with maximum at 5.24 A. Applying formula (11) gives $N_1=8.4$, $N_2=11.0$ for $a_1=3.70$ A, $a_2=5.25$ A respectively. The width of the two peaks are roughly equal and lead to $2\alpha=0.94$ A or $\alpha=0.47$ A, to be compared with $\alpha_D=0.61$ A as calculated on the Debye theory.

An alternative method commonly used for calculating the number of neighbors in liquids is to integrate $4\pi r^2\rho(r)$. The absence of distinct peaks in the helium curve precludes simple analysis into groups, but integration out to the radius of the first maximum in $4\pi r\rho(r)$ gives half the number of first neighbors if the peak is symmetrical in $4\pi r^2\rho(r)$. Alternatively, if the peak is symmetrical in $4\pi r\rho(r)$, a correction can be derived to yield the number of first neighbors from the integral. In Table II the number of neighbors found by these methods is tabulated for the three temperatures. It is of interest to compare these results with the number of neighbors in an incompletely filled close-packed arrangement (cubic or hexagonal) having the experimentally determined spacing. At 4.24°K the mean atomic density is 1.84×10^{-2} atoms/A^3 and a cube of side $3.72\sqrt{2}$ A (the unit cell edge of the close packed cubic structure with nearest neighbor distance 3.72 A) contains 2.74 atoms. In a complete close-packed structure this cube contains 4 atoms. Thus, instead of the 12 first neighbors of the complete structure there would be $12(2.74/4)=8.2$ neighbors, to be compared with 8.1 and 7.3 of Table II. The corresponding number for 5.04°K is 7.4 and for <2.25°K is 9.45. Precise agreement is not to be expected because the analysis of diffraction results assumes that there is always an atom at the origin.

For the ratio of second-neighbor to first-neighbor radii, (a_2/a_1), the method gives values 1.47, 1.41, 1.42, agreeing closely with $\sqrt{2}=1.414$, the ratio for close packing of spheres.[26] The number of atoms in the second shell, as deduced from Eq. (11), ranges from 10 to 12. This is considerably more than the number in a close-packed arrangement, but the second shell is not clearly distinguishable, showing that the use of delta functions may not be valid beyond the first shell in liquid helium and that the analysis which yields the second peak should be treated with reserve. If, however, the experimental results and the analysis into peaks are taken at their face value, the average atomic arrangement at the low temperature has 8 neighbors at a mean distance of 3.7 A and 11 neighbors at a mean distance of 5.25 A from an atom. Diffraction measurements on liquid helium have been interpreted[1,3] in terms of completely filled lattices. In general, liquid elements appear not to form such arrangements,[10,32] although they approach this condition at the freezing point. Our interpretation implies that liquid helium under its saturated vapor pressure does not form a complete array. Under high pressure it may be expected to approximate a filled structure.

The change of density from 0.095 g/cm^3 at 5.04°K to 0.146 g/cm^3 at 2.25°K is not accounted for by the measured shift of the density maximum from 3.68 to 3.50 A or by the changing number of neighbors separately, but is probably due to a combination of these two effects. This appears to be a general behavior of liquids, unlike the behavior of solids where the fractional change in lattice spacing per degree is equal to the linear expansion coefficient. Between the low temperature (<2.25°K) and the high temperature (5.04°K), there is a broadening of the first density peak by about 20% and the number of atoms inside the first maximum decreases from 3.7 to 2.9. As seen in Fig. 4, the ratio

TABLE II. First neighbors by two methods.

Temperature °K	Distance angstroms	Number by integration	Corrected to symmetry in $4\pi r\rho(r)$	Number by Eq. (11)
5.04	3.94	$5_{.8}$	$7_{.9}$	$7_{.4}$
4.24	3.72	$7_{.0}$	$8_{.1}$	$7_{.3}$
<2.25	3.70	$7_{.4}$	$8_{.6}$	$8_{.4}$

[26] In a close packed arrangement the first and second shells contain 12 and 6 atoms respectively and the relative radii are as $1:\sqrt{2}$.

$\rho(r)/\rho_0$ is not very dependent on ρ_0, and in fact the differences could arise from the spurious fluctuations evident near $r=0$. $\rho(r)/\rho_0$ would be independent of temperature if the decrease of ρ_0 with rising temperature were caused entirely by the production of empty sites in an established configuration. This is not quite the case and to some extent the structure expands.

The small mass and low binding energy of helium have a marked influence on its structure as compared with other liquids. The interatomic potential has a minimum at about 3 A,[27] well inside the distance 3.8 ± 0.1 A reported here for the first shell of neighbors in the liquid. This is in contrast to argon where the interatomic potential has a minimum at 3.7 A and the first shell of neighbors occurs at 3.8 ± 0.1 A. The relatively large zero-point energy of helium causes the atom to stay far up in the potential well, producing a maximum density at a radius much beyond that of the potential minimum on account of the anharmonicity of the potential. In argon, the energy levels are so close to the minimum of potential that the atom is not appreciably displaced. Thus, unlike normal liquids, helium has its structural dimensions determined very largely by the properties of the zero-point motion, and not directly by the position of the minimum of the interatomic potential.

If a Morse function is fitted to the minimum of the interatomic potential of helium, one parameter remains. This can be used to produce a bound state of the molecule. For reasonable values of the parameter, the bound states lie close to the top of the potential well. The wave mechanical density of such a bound state matches reasonably well the shape of the density found experimentally out to 3.8 A. Although in the liquid the potential near 3.7 A and beyond differs greatly from the potential of an isolated pair of atoms, the difference is probably much less inside 3.7 A and the calculations give some support to the experimentally determined shape.

When the atoms combine to form a liquid we know that bound states occur, but, on account of the large zero-point energy of liquid helium, there may be sensitiveness to details of the potential and nonlocalized states may be produced small changes in the potential. It is interesting to speculate that the small changes which take place in the radial distribution function as the temperature falls to the lambda point may be sufficient to affect the potential in a critical manner, producing nonlocalized "running levels," and may thus be associated with superfluidity.

[27] Kirkpatrick, Keller, and Hammel, Phys. Rev. 97, 9 (1955).

The experimental width at e^{-1} at the height of the density peak obtained by folding about the first maximum varies from 1.9 to 2.3 A, depending on temperature. This value is considerably greater than 1.2 A, approximately the width of the peaks fitted by Reekie and Hutchison[3] to their transform.

CONCLUSION

It has been seen that the scattering distribution and the corresponding atomic density distribution show little change, if any, on crossing the lambda point temperature. The constancy and form of the atomic distribution show a close similarity to those for other simple liquid elements. Applying the usual interpretation for such liquids, the results indicate that at low temperatures the average atom in liquid helium has approximately 8 first neighbors at a mean distance of 3.7 A and perhaps 11 neighbors at a distance of 5.25 A (the assignment of atoms to the second peak is somewhat arbitrary). Although the derived density distribution could presumably be fitted by complete lattice arrangements, which would involve fine structure below our experimental resolution, the results suggest no reason or guide for this elaboration. The observed width of the diffraction peak would require that the order in lattice type structures is not rigidly preserved beyond a range of a few atomic spacings.

On the present interpretation, the isothermal compressibility of the liquid and its thermal expansion are explained largely by a change in the number of neighbors at an approximately fixed interatomic spacing. This spacing would be expected to depend on pressure in much the same way as the spacing in the solid. At the freezing pressure the liquid is expected to be nearly close-packed, consistent with the structure of the solid[28] in which the first neighbor distance is 3.61 A, in good agreement with the presently proposed single peak at 3.7 A. As a possible explanation for the lambda transition it is suggested that, as the temperature is lowered to the lambda point, a critical stage is reached in the atomic distribution which causes some states to lose their localized character and give rise to "running levels."

ACKNOWLEDGMENTS

Thanks are due to Mr. W. McAlpin for mechanical design of the cryostat, to Mr. J. Freeborn for technical assistance, to Miss Iris Hay for calculations, and to the Computation Center, University of Toronto, for the calculations of the Fourier transforms on FERUT.

[28] W. H. Keesom, *Helium* (Elsevier Publishing Company, Amsterdam, 1942).

Motion of Nuclei in Liquid Helium

W. V. HOUSTON AND H. E. RORSCHACH
The Rice Institute, Houston, Texas

(Received August 11, 1955)

It is suggested that nuclear motions in a solid or a liquid at very low temperatures should be treated along the lines usually used for electrons, and the method is applied to liquid helium. Treating the nuclei as independent particles gives indications of the observed behavior of both the specific heat and the paramagnetic susceptibility of He^3. Further consideration of the internuclear interactions brings the results closer to the observed values. Application to He^4 gives also a qualitative understanding of the observed phenomena.

THE usual treatment of the motion of atomic nuclei in a solid is based on the approximation by means of normal vibrations suggested by Born and von Kármán and by Debye. It gives a good qualitative understanding of the low-temperature specific heats of crystals and, in many cases, can be made satisfactorily quantitative. It does not, however, permit the nuclear spins to be taken into account; apparently, no way has yet been devised to determine the effect of the Pauli exclusion principle on the normal vibrations. For some problems, particularly the investigation of low-temperature behavior, it may be of importance to introduce the quantum mechanical treatment from the beginning.

As a different approach, one can apply to the nuclear motions a treatment similar to that ordinarily applied to electrons. The problem is simpler in one respect, since all atoms are one-nucleus atoms. On the other hand, the greater masses and charges tend to make the kinetic energy less important, relative to the potential energy, than is the case with electrons.

One limiting case in such a treatment would be the use of localized wave functions giving the motion of each nucleus about its position of equilibrium. Following the Heitler-London scheme for molecules, one would start out by considering the nuclei as completely independent of one another. In the lowest approximation, this would lead to the Einstein formula for specific heat, which is not especially good, and to a simple Curie law for nuclear paramagnetic susceptibility. However, Slater[1] has emphasized the inadequacy of this kind of a treatment for electrons and the same objections will hold for nuclei. Whenever the wave functions of adjacent nuclei overlap sufficiently to indicate significant interaction, the lack of orthogonality makes the analysis almost impossible, if not divergent. Furthermore, to symmetrize such functions properly would lead to complications such as appear in the Ising[2] problem in three dimensions.

Another limiting treatment corresponds to the free-electron case or to the Bloch treatment of electrons. It may seem difficult at first to picture each nucleus as moving through the crystal in a periodic potential field, but the difficulty is only quantitatively a little greater than in the case of electrons. The use of this method leads to bands of energy levels to be occupied by individual nuclei, and the application of the Pauli principle follows the usual lines. However, because of the differences in charge and mass between nuclei and electrons, the dangers inherent in the energy-band treatment of electrons are even greater for nuclei, and the results obtained without consideration of configuration interaction can be very misleading.

APPLICATION TO HELIUM-3

The application of the above point of view to hydrogen is not the simplest because hydrogen is generally regarded as a molecular solid. The application to solid He would be most appropriate but the data available on the solid are limited. Nevertheless, as emphasized by Frenkel and Landau,[3] the liquid is certainly much more similar to the solid than to the gas; and instead of the usual attempt to treat the liquid as an imperfect gas, let us treat it as essentially like a solid and give principal attention to the nuclei.

The magnetic susceptibility[4] of He^3 and the specific heats[5] of both He^3 and He^4 have been measured to very low temperatures. In the limiting case of completely independent nuclei, (the zero-order approximation in the Heitler-London method), the paramagnetic susceptibility would be inversely proportional to the temperature down to very low temperatures, 10^{-7}°K, at which the magnetic interaction between the nuclei would come into play.[6] The specific heat would be given by the Einstein expression,

$$C=3R(h\nu_0/kT)^2e^{h\nu_0/kT}/(e^{h\nu_0/kT}-1)^2,$$

where the characteristic frequency ν_0 is determined by the compressibility and the density to be 3.3×10^{11} sec^{-1} for He^3. The low-temperature specific heat given by this expression is far below that observed.

The other limiting case, in which the nuclei are treated as free independent particles, gives a value for

[1] J. C. Slater, Revs. Modern Phys. **25**, 199 (1953), also various other recent publications by Slater.
[2] G. F. Newell and E. W. Montroll, Revs. Modern Phys. **25**, 159 (1953).
[3] See F. London, *Superfluids* (John Wiley & Sons, Inc., New York, 1954), pp. 88–110, for references and a general discussion.
[4] Fairbank, Ard, and Walters, Phys. Rev. **95**, 566 (1954).
[5] Reference 3, p. 110; T. R. Roberts and S. G. Sydoriak, Phys. Rev. **98**, 1672 (1955).
[6] I. Pomeranchuk, J. Exptl. Theoret. Physics (U.S.S.R.) **20**, 919 (1950).

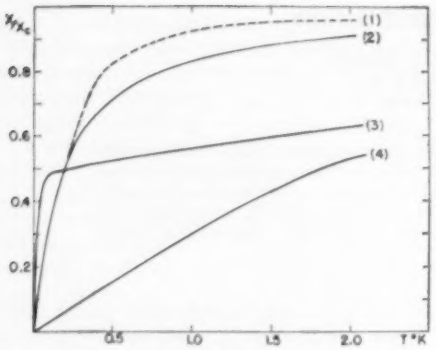

FIG. 1. Calculated and observed values of the ratio of the paramagnetic susceptibility χ to the classical value $\chi_c=\mu^2H/kT$. (1) Observed values. (4) Values for a Fermi-Dirac gas of free particles with the mass of He^3 atoms. (3) Calculated for independent particles with the energy level distribution given by Eqs. (1) and (1a). (2) Equation (15) with $T_0=0.2°K$.

the entropy in fair agreement with the observations, but predicts a departure from the classical susceptibility at temperatures far higher than those observed. Clearly, something between these two extremes is necessary.

Let us then consider the nuclei as moving in a periodic potential field composed of minima corresponding to classical oscillators of the above frequency and separated by about 4 A, the distance between the nuclear rest positions. For He^3, the maximum depth corresponds to 54×10^{-16} erg below the intersection of two adjacent paraboloids. The lowest quantum-mechanical state of an isolated oscillator would be 33×10^{-16} erg above this minimum. The first-excited state would then be at a height corresponding to the top of the barrier between the atoms. With this picture there should be only one narrow band of low-lying nuclear levels, and the next levels should approximate the continuum of levels for free particles.

An estimate of the width of this low band can be made by using the harmonic oscillator functions and computing the effect of the adjacent potential minima. Assuming a close-packed structure with 12 nearest neighbors suggests a band width of roughly 5×10^{-17} erg, which corresponds to a temperature of some 0.36°K. Such a width clearly shows that the nuclei are not independent, and that departures from the classical susceptibility should appear at temperatures much above that suggested by the magnetic interaction.

As a basis for a rough calculation let us assume a band of energy levels whose density is given by

$$g(E)=(NE_0/\pi)\sin(\pi E/E_0),\quad 0<E<E_0,\qquad(1)$$

where E_0 is taken equal to $0.2k$ and N is the number of nuclei in the crystal. Then for E above the value E_0 let

$$g(E)=(V/2\pi^2)(2M/\hbar^2)^{\frac{3}{2}}(E-E_0)^{\frac{1}{2}}.\qquad(1a)$$

This assumption conforms roughly to the model described above, although there could be a much larger gap between the two bands.

With this distribution of states, and treating the nuclei as independent particles, it is possible to compute the magnetic susceptibility and the specific heat or the entropy. The results are shown in Figs. 1 and 2.

The ratio of the susceptibility to the classical value shows some of the observed characteristics. It rises rapidly from zero and then more slowly as the temperature is increased above 0.2°K. The entropy also shows, in an extreme form, some of the observed characteristics in that it rises rapidly at low temperatures and at higher temperatures behaves more or less like that of a normal gas.

However, these two computations also indicate clearly the principal difficulty with the energy band theory, which has been so often emphasized by Slater.[1] All possible ways of filling the low-lying band of energy levels give rise to many states which correspond to two or more nuclei on each of a number of atoms. These states must, of course, be considered, but their energies are much higher than the values given by the simple band energies of the individual particles. All combinations of N particles in the $2N$ low states lead to $(2N)!/(N!)^2$ states of the whole system, instead of only the 2^N states when all ionic states are excluded. It is the inclusion of so many ionic states with paired spins that leads to the paramagnetic susceptibility being too small. If only the states in the low-lying band are considered, the ratio of the susceptibility to the classical value approaches $\frac{1}{2}$ instead of 1 at high temperatures. But when the levels of the upper continuum are included in addition, the ratio finally approaches 1 at temperatures above the degeneracy temperature of the free nuclei.

The entropy shows the same effect. Far too many states are included at low temperatures, so the calculated value rises rapidly from zero to almost twice the observed value. When only the isolated lower band is considered, the entropy approaches $2Nk\log2$ instead of $Nk\log2$, at low temperatures.

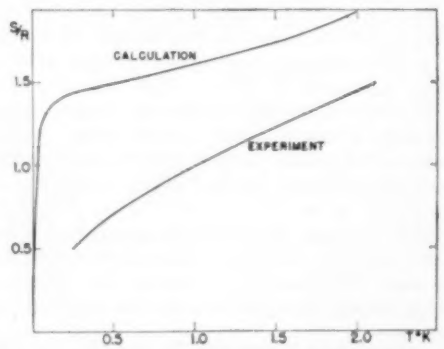

FIG. 2. Calculated values of the entropy of He^3 based on a model of independent particles with the energy level distribution of Eqs. (1) and (1a).

At very low temperatures one should not include the states representing more than one nucleus in an atom. The electrostatic interaction energy of such states is greater than the gap between the low-lying band and the continuum. Excitation to such a state requires as much or more energy than the excitation of nuclei to the upper continuum. Hence, we may estimate the magnetic behavior at low temperatures by considering only the 2^N states, consistent with the Pauli principle, obtained by putting only one nucleus in each Bloch state.

Let n_+ and n_- be the number of nuclei with positive and negative spins respectively. Then $n_++n_-=N$, and $n_+-n_-=m$. For each value of the magnetic quantum number m there are $N!/n_+!n_-!=N!/[\frac{1}{2}(N+m)]![\frac{1}{2}(N-m)]!$ states. When only the band energies of the individual particles are considered, all 2^N have the same energy; but when the interactions between the nuclei are considered, the energies are spread out into a band. For a first estimate of the distribution of energies we may find the sum, or the mean, of the energies corresponding to each m.

Consider the particle states i and j. The number of states of the whole system in which i and j are occupied by + or − spins is given in the following table:

i	j	Number of states
+	+	$(N-2)!/[\frac{1}{2}(N+m-4)]![\frac{1}{2}(N-m)]!$
+	−	$(N-2)!/[\frac{1}{2}(N+m-2)]![\frac{1}{2}(N-m-2)]!$
−	+	$(N-2)!/[\frac{1}{2}(N+m-2)]![\frac{1}{2}(N-m-2)]!$
−	−	$(N-2)!/[\frac{1}{2}(N+m)]![\frac{1}{2}(N-m-4)]!$

The direct interaction integral

$$J_{ij}=\int d\tau_1\int d\tau_2|u_i(1)|^2H(1,2)|u_j(2)|^2, \quad (2)$$

will occur in all of these cases, or $N!/[\frac{1}{2}(N+m)]!\times[\frac{1}{2}(N-m)]!$ times. The exchange integral,

$$K_{ij}=\int d\tau_1\int d\tau_2 u_i^*(1)u_j^*(2)H(1,2)u_i(2)u_j(1), \quad (3)$$

will occur only in those cases in which both i and j have the same spin. The sum of these terms gives the sum of the energies of all of the states considered with the quantum number m:

$$\sum E=\frac{N!}{[\frac{1}{2}(N+m)]![\frac{1}{2}(N-m)]!}\left\{\sum_i E_i+\sum_{i<j}J_{ij}-\frac{N(N-2)+m^2}{2N(N-1)}\sum_{i<j}K_{ij}\right\}, \quad (4)$$

and the mean energy is

$$\bar{E}_m=\sum_i E_i+\sum_{i<j}J_{ij}-\frac{N(N-2)+m^2}{2N(N-1)}\sum_{i<j}K_{ij}, \quad (5)$$

where the E_i are the band energies.

Equation (5) shows that the mean energy depends on m^2, but to see more clearly the significance of the integrals it is desirable to transform to Wannier functions.[7] Although these functions are not simple solutions of the Schrödinger equation in one potential minimum, they are nevertheless concentrated about a single minimum and fall off rapidly with the distance from it.

$$J_{kk'}=\frac{1}{N^2}\sum_{R_1R_2R_3R_4}e^{ik(R_1-R_2)}e^{ik'(R_3-R_4)}\times\int a^*(r_1-R_2)a(r_1-R_1)H(1,2)\times a^*(r_2-R_3)a(r_2-R_4)d\tau_1d\tau_2. \quad (6)$$

The sum over k' gives zero unless $R_3=R_4$, and in that case it gives N. Hence,

$$\sum_{kk'}J_{kk'}=\sum_{R_1,R_2}\int a^*(r_1-R_1)a(r_1-R_1)\times H(1,2)a^*(r_2-R_2)a(r_2-R_2)d\tau_1d\tau_2=NC_{00}+N\sum_{l\neq0}C_{0l}. \quad (7)$$

where

$$C_{0l}=\int|a(r_1-R_0)|^2H(1,2)|a(r_2-R_l)|^2d\tau_1d\tau_2.$$

Similarly

$$\sum_{kk'}K_{kk'}=NC_{00}+N\sum_{l\neq0}E_{0l}, \quad (8)$$

where

$$E_{0l}=\int a^*(r_1-R_0)a(r_1-R_l)H(1,2)\times a^*(r_2-R_l)a(r_2-R_0)d\tau_1d\tau_2.$$

These sums in Eqs. (7) and (8) differ from those in Eqs. (4) and (5) in that they include the terms with $k=k'$. Since

$$\sum_k J_{kk}=\sum_k K_{kk}=C_{00}+\sum_{l\neq0}C_{0l}+\sum_{l\neq0}E_{0l}, \quad (9)$$

$$\sum_{i<j}J_{ij}=\frac{N-1}{2}C_{00}+\frac{N-1}{2}\sum_{l\neq0}C_{0l}-\tfrac{1}{2}\sum_{l\neq0}E_{0l}, \quad (10)$$

and

$$\sum_{i<j}K_{ij}=\frac{N-1}{2}C_{00}+\frac{N-1}{2}\sum_{l\neq0}E_{0l}-\tfrac{1}{2}\sum_{l\neq0}C_{0l}. \quad (11)$$

The mean energy of the states with a given value of m is

$$E(m)=\sum E_i+\frac{N}{4}\left\{C_{00}+\frac{2N-3}{N-1}\sum_{l\neq0}C_{0l}-\sum_{l\neq0}E_{0l}\right\}-\frac{m^2}{4N}\left\{C_{00}+\sum_{l\neq0}E_{0l}-\frac{1}{N-1}\sum_{l\neq0}C_{0l}\right\}=E_0-m^2A. \quad (12)$$

[7] Gregory H. Wannier, Phys. Rev. 52, 191 (1937).

The dominant term in A would appear to be C_{00}, which is positive. Hence this calculation leads to the usual result in suggesting that the state of lowest energy is the one of maximum magnetic moment. Clearly, such is not the case, and the discrepancy can be understood as due to two causes. In the first place, although we have used the right number of states, we have not used the right ones. The 2^N states in which each Bloch function is used just once are not the states from which can be formed the 2^N states representing each nucleus in a different atom. Evidence for this fact is the appearance of C_{00} in Eq. (12). In the second place, the states with a given value of m will be spread out into a band which will include some states of energy less than the energy for $m=N$.

To make a rough estimate of the susceptibility in this situation, let us assume that for each m the states are distributed uniformly about the mean over the range $2(N^2-m^2)\alpha A$, where α is a dimensionless constant. For paramagnetism $\alpha>1$ and for ferromagnetism $\alpha<1$. The partition function is

$$Z=\sum_{m=-N}^{m=N}\left\{\frac{N!}{[\frac{1}{2}(N+m)]![\frac{1}{2}(N-m)]!}\right\}\times\exp\left(-\frac{E_0-Am^2+m\mu H}{kT}\right)\times\int_{-(N^2-m^2)\alpha A}^{(N^2-m^2)\alpha A}\frac{e^{-x/kT}dx}{2(N^2-m^2)\alpha A}, \quad (13)$$

where the sum is over even values of m. In the limit $\mu H/kT\to 0$,

$$Z=\frac{2N\mu}{kT}\exp\left(\frac{N^2\alpha A-E_0}{kT}\right)\int_0^1\exp(-\beta^2x^2)dx=\frac{2N\mu\sqrt{\pi}}{kT\beta}\exp\left(\frac{N^2\alpha A-E_0}{kT}\right), \quad (14)$$

with $x=m/N$, and $\beta^2=\frac{1}{2}N[1+NA(\alpha-1)/kT]\gg 1$. The Stirling approximation has been used for the factorials, and the sum replaced by an integral which can be carried to infinity since β is large.

In a similar fashion $\partial Z/\partial H$ can be evaluated, and it follows that

$$\frac{\chi}{\chi_c}=\frac{kT}{kT+NA(\alpha-1)}=\frac{T}{T+T_0}. \quad (15)$$

The temperature T_0 cannot be evaluated directly from the model because of the *ad hoc* nature of the assumption made in introducing α. However, a value around 0.2°K is not unreasonable and Fig. 1 shows the curve with this value of T_0.

APPLICATION TO HELIUM-4

In applying these conceptions of nuclear motion to He^4, there is no magnetic susceptibility to act as a guide. There are, however, the properties of the superfluid, which seem to be consistent with our picture.

Again we may try an independent-particle treatment of the nuclear motion. The potential wells will be approximately the same as in He^3, although the heavier mass will make the energy levels a little lower. To see what results could be obtained in this way, calculations were made with a density of independent-particle levels given by

$$g(E)=\frac{N}{E_0}\left(1-\cos\frac{2\pi E}{E_0}\right) \quad \text{for} \quad 0<E<E_0, \quad (16)$$

$$g(E)=\frac{V}{2\pi^2}\left(\frac{2M}{\hbar^2}\right)^{\frac{3}{2}}(E-E_0)^{\frac{1}{2}} \quad \text{for} \quad E>E_0. \quad (16a)$$

With the Bose-Einstein statistics, and with E_0 equal to 3.85k, a numerical computation gives the specific heat as shown in Fig. 3. The computed curve shows some of

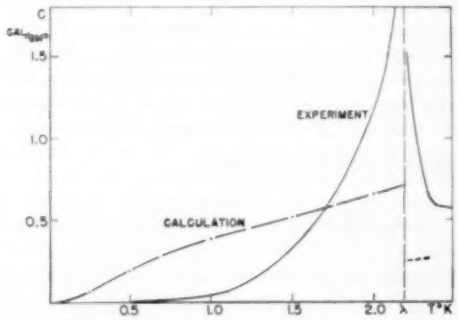

FIG. 3. Calculated values of the specific heat of He^4 treated as a gas of independent particles with the energy level distribution of Eqs. (16) and (16a).

the features of the observed values. In particular, it shows a discontinuity at a critical temperature. However, it also points directly to the same deficiencies as appear in the case of He^3.

The independent-particle calculation shows much too high a specific heat at low temperatures, due to the assumed presence of too many low-lying states of the system. In the above discussion of He^3 it was pointed out that instead of $(2N)!/(N!)^2$ states there are only 2^N whose energy is low enough to affect the low-temperature behavior. In He^4, instead of the $(2N)!/2(N!)^2$ states considered in the independent-particle model there is only a single ground state. This ground state is the appropriate symmetrical linear combination of all the possible ways of occupying the low-lying band. This single ground state represents the superfluid. The

motion of the superfluid then is represented by adiabatic changes in this ground state under the influence of changing boundary conditions.

The significant difference between He^3 and He^4 stands out at this point. In He^4 there is a single ground state, while in He^3 there are 2^N states very close together just above the lowest one. Hence superfluidity is not to be expected in He^3, except possibly at extremely low temperatures and extremely low velocities.

In He^4, excitation above the ground state can take two forms. There is first the excitation associated with a redistribution of the nuclei among the individual particle states of the low-lying band. Such excitation will involve significant amounts of energy, since it will lead to the equivalent of ionic states. The other form involves excitation of one or more nuclei to the band of excited particle levels. The energy involved in such an excitation may well correspond to as much as the 8°K assumed by London in his model of He^4.

This point of view as to the nature of He^4 appears to embody some of the aspects of the treatments of both Landau and London-Tisza.[3] The liquid is treated as a whole and attention is given to the states of excitation of the whole system. On the other hand, the treatment is based on individual particle states separated by an energy gap. The symmetry properties of the wave functions must be taken into account, and the difference between He^3 and He^4 is correlated to the ways in which these individual-particle states can be occupied.

Further calculations are now in progress to clarify the energy relations among these various kinds of excited states.

PHYSICAL REVIEW VOLUME 100, NUMBER 4 NOVEMBER 15, 1955

Hypothesis for the Origin of the Magnetic Fields and Angular Rotations of Stars and Planets

WINSTON H. BOSTICK
University of California Radiation Laboratory, Livermore, California
(Received June 22, 1955)

From theoretical considerations it is to be expected that gravitational contraction of ionized material across a magnetic field will produce an enhancement of the magnetic field and a rotational angular momentum of the mass. This process may be associated with the magnetic fields and rotations of galaxies, stars, and planets, and may possibly play a role in expanding universe.

IF it can be assumed that originally a general, weak magnetic field occupied space in which matter was originally diffusely distributed in an ionized state, the action of gravitational force would be such as first to draw the material together *along* the lines of magnetic force to produce the disklike or lenticular-shaped structures resembling our galaxy (the axis of the disk being parallel to the magnetic field). The contraction of the material under gravitational forces *across* the magnetic lines of force is a process slower by ν_e^2/ω_e^2, where ν_e and ω_e are respectively the collison and gyrofrequencies for electrons. As this latter process occurs, one would expect that the total magnetic flux enclosed by the matter would remain the same. This conservation of flux is accomplished by an adiabatic compression of the enclosed magnetic field; the field is enhanced by currents induced in the contracting ionized matter.

This quiescent, collision-permitted process of gravitational contraction across the magnetic field occurs as long as the e-folding time constant, τ, for Kruskal-Schwarzschild[1] instability is long compared with the times involved. The value of τ is given by $(\lambda/2\pi g)^{\frac{1}{2}}$, where λ is the wavelength of a perturbation (λ must be much greater than the gyro-radius of positive ions) and g is the gravitational acceleration. During the initial stages of the contractional process, g will presumably be so small and λ so large that instabilities have no opportunity to develop. However, eventually the concentration of matter and magnetic field will reduce the minimum value of λ and increase g to the point where instabilities will develop, and the matter may be expected to jet inward at various locations, producing enhanced inward motion and fluctuations in ion density. (The fluctuations in ion density produced by this general type of instability have been observed in the laboratory.[2,3]) These local regions of higher ion density can now become local centers for gravitational attraction across the magnetic field. Local enhancement of magnetic fields may be expected to occur around these local centers, and further instabilities will eventually permit the matter to contract into stars and planets in the various localities. Each star and planet then presumably has trapped within it its own dipole magnetic field which is the concentration of flux which was swept up over a large area.

For such a dipole field the relaxation time τ (L/R

[1] M. Kruskal and M. Schwarzschild, Proc. Roy. Soc. (London) **A223**, 348–360 (1954).

[2] W. H. Bostick and M. A. Levine, Phys. Rev. **97**, 13 (1955).
[3] W. H. Bostick and M. A. Levine, Phys. Rev. **87**, 671 (1950).

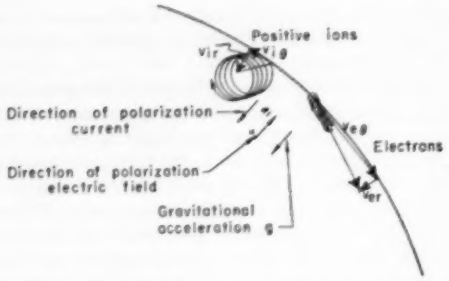

FIG. 1. Drift velocity relationships and polarization involved in the gravitational contraction of ionized matter across a magnetic field. H up out of plane of paper.

time-constant, where L is inductance in henries and R is resistance in ohms) is given[4] approximately by $\tau=4\pi^2/10^9\pi\rho$ sec, where r is the radius of the celestial body in cm and ρ is the resistivity in ohm cm. For the sun, ρ is low enough and r high enough to give a value of τ which is long enough for practically all the originally concentrated field to be present. For the earth $r\cong7\times10^8$ cm, and if the value of ρ taken is that for iron ($\cong10\times10^{-6}$ ohm cm), then $\tau\cong2\times10^6$ years, which is about 500 times shorter than the age of the earth. However, if the resistivity under conditions of temperature and pressure encountered in the interior of the earth is substantially less than that of solid iron, the value of τ will be larger. Furthermore, it is quite possible that the earth, during a large fraction of its history, possessed a highly conducting extensive atmosphere, which would effectively increase r and reduce ρ during this period, and hence increase the value of τ. The possibility that even the earth's magnetic field is the residue of a primeval field generated by the contractional enhancement of a general, weak field should, therefore, in spite of Schuster's[4] statement to the contrary, be seriously considered, especially if it can be assumed that some generating process exists which continues to supply enough energy to this field to take care of the relaxation losses.

It can even be reasoned that the rotations of the earth and the sun and astronomical bodies in general have been induced by the gravitational contraction across the magnetic field. The diagram of Fig. 1 illustrates the process whereby the field-enhancing currents are carried primarily by the θ-drift velocity of the electrons, $v_{e\theta}=-(\omega_e/\nu_e)v_r$, but the θ momentum is carried primarily by the positive ions[2] whose θ velocity is $v_{i\theta}=(\omega_i/\nu_i)v_r$. Ambipolar conditions prescribe that the steady-state radial velocities of electrons and positive ions are equal, i.e., $v_{er}=v_{ir}\equiv v_r$. In the approximation that $\omega_e/\nu_e\gg\omega_i/\nu_i$, we can write that $v_r=gm_i\nu_e/m_e\omega_e^2$, where g is the effective inward gravitational acceleration at the point in question, and m_i and m_e refer to the masses of positive ion and electron, respectively. This general rotation may be expected to be imparted to the galaxy as a whole and individual rotations will be imparted to the various stars and planets as they are formed. In general the rotations and magnetic fields should line up. The torque for the production of this angular momentum is produced by the inward polarization current, carried by the positive ions, crossed with the magnetic field (see Fig. 1). The magnetic field must be assumed to be anchored in conducting matter elsewhere so that angular momentum as a whole can be conserved.

It is noteworthy that the alignment of magnetic field and rotation outlined in Fig. 1 is consistent with that found in the sun, and the alignment and sign agree with those for the earth.

A more detailed analysis of the gravitational contraction across a magnetic field is being prepared.

It should be kept in mind that this contractional process represents a conversion of gravitational potential energy to magnetic energy and to kinetic energy of rotation of the mass. In the later phases of contraction into stars where instabilities and recombination may be expected to play a large role, the gravitational energy, of course, is converted largely into heat. This conversion of gravitational energy to magnetic energy in the formation of a galaxy produces varying magnetic fields at large distances from that galaxy. These varying magnetic fields will have a repelling effect on any conducting matter at these large distances, and should therefore have a tendency to expand galaxies away from each other. This mechanism of expansion is essentially the operation of Lenz' law in which the model is that of a group of coils (free to move) in which changing currents are being excited. These coils will move away from each other, the ones on the periphery receding with the highest speed. This effect should be assessed numerically on an intergalactic scale to ascertain whether it is strong enough to produce the observed expansion of the universe.

[4] S. Chapman and J. Bartels, *Geomagnetism* (Oxford University Press, London), p. 704.

Coulomb Scattering of Electrons at Very Small Angles*

MICHAEL J. MORAVCSIK
Laboratory of Nuclear Studies, Cornell University, Ithaca, New York

(Received August 10, 1955)

Electrostatic scattering of highly relativistic electrons at very small angles is discussed. The Hartree wave function is used to calculate the screening effects for the smallest angles. The calculations are facilitated by a theorem which states that, in the Born approximation for elastic scattering by any physical central potential, the total cross section in the relativistic limit is independent of energy.

Both the "elastic" (nuclear) and "inelastic" (electronic) contributions to the scattering are investigated. It is found that at very small angles the inelastic differential cross section exceeds by many times the elastic differential cross section. Numerical calculations were carried out for scattering by nitrogen atoms, where the total cross section of the scattering by atomic electrons is 3.6 times the total cross section due to screened nuclear scattering.

SCATTERING due to Coulomb forces has been widely discussed in textbooks and papers.[1] However, relatively little attention has been paid to the scattering at very small angles, where the details of the various cutoffs assume great importance. This paper presents a discussion of the scattering of highly relativistic electrons at very small angles.

The necessity for such a study arose in connection with some calculations of the scattering by the residual gas in the "Mesotron," Cornell University's high-energy strong-focusing electron synchrotron. Details of the application to the "Mesotron" of results obtained in this paper will be published elsewhere.[2] Another field of application of small-angle Coulomb scattering is electron microscopy,[3] although there the energy of the electrons is below 1 Mev and hence the rest-mass contribution to the total energy cannot be neglected.

1. GENERAL REMARKS

The simplest treatment of screened Coulomb scattering, when calculating the total cross section, uses a small angle cutoff, the so-called Thomas-Fermi cutoff given by

$$\vartheta_{\min}\sim\frac{\lambda}{a}=\frac{\hbar/p}{\hbar^2/me^2Z^{\frac{1}{3}}}=\frac{cme^2}{\hbar}\frac{Z^{\frac{1}{3}}}{E}\sim 3.7\times10^{-2}\frac{Z^{\frac{1}{3}}}{E_{\text{Mev}}}\text{ radians},\tag{1.1}$$

where m is the rest mass of the electron. This cut-off angle can be expected to give the order of magnitude of the angle at and below which we will have to be seriously concerned with the details of the screening.

In taking into account screening we have to adopt some model of the atom, such as the Thomas-Fermi statistical picture, or the Hartree model. At very small angles the Thomas-Fermi model provides a poor approximation, since very small scattering angles correspond to large impact parameters and the asymptotic behavior of the Thomas-Fermi charge density is r^{-6} instead of the actual exponential decrease. Thus, we should use the Hartree model for at least the very smallest angles. At somewhat larger angles the two models will closely coincide. For a numerical illustration of the difference between the two models at moderate energies, see reference 3.

Another important point to consider is the relativistic correction to the cross section. In general, if we use the Born approximation (which should be good for high energies, small angles, and light nuclei), the differential cross section for spin $\frac{1}{2}$ particles will be[4]

$$I(\vartheta)=\frac{|f(\vartheta)|^2}{1-\beta^2}[1-\beta^2\sin^2(\vartheta/2)],\tag{1.2}$$

where

$$f(\vartheta)=\frac{m}{2\pi\hbar^2}\int V(r')e^{i\mathbf{q}\cdot\mathbf{r}'}d\tau',\tag{1.3}$$

and $\mathbf{q}$ is essentially the momentum change of the scattered particle

$$\mathbf{q}=(\mathbf{p}-\mathbf{p}')/\hbar.\tag{1.4}$$

The $(1-\beta^2)^{-1}$ arises from the increase of the apparent mass of the incident particle, while the $1-\beta^2\sin^2(\vartheta/2)$ is due to spin factors. We will henceforth omit this latter spin factor, since at 1 Mev or above the contribution to scattering for any kind of screened Coulomb field is negligible at those angles where $1-\beta^2\sin^2(\vartheta/2)$ is appreciably different from 1.

It is to be noted that $f(\vartheta)$ is a function of the momentum change. For pure Rutherford scattering we have

$$f(\vartheta)=\frac{2mZe^2}{\hbar^2q^2}=\frac{mZe^2}{2p^2}\frac{1}{\sin^2(\vartheta/2)}=\frac{mc^2Ze^2}{2E^2\sin^2(\vartheta/2)}\tag{1.5}$$

in the highly relativistic limit, where

$$(E/mc^2)^2=(1-\beta^2)^{-1}.\tag{1.6}$$

* Assisted by the joint program of the Office of Naval Research and the U. S. Atomic Energy Commission.

[1] E.g., J. M. Greenberg and T. H. Berlin, Rev. Sci. Instr. **22**, 293 (1951).

[2] M. J. Moravcsik and J. M. Sellen, Jr., Rev. Sci. Instr. (to be published).

[3] E. g., F. Lenz, Z. Naturforsch. **9a**, 185 (1954).

[4] N. F. Mott and H. S. W. Massey, *Theory of Atomic Collisions* (Clarendon Press, Oxford, 1949), second edition, pp. 120, 188–190, 240.

Thus we get

$$I(\vartheta)=\frac{|f(\vartheta)|^2}{1-\beta^2}=\frac{Z^2e^4}{4E^2\sin^4(\vartheta/2)} \tag{1.7}$$

which is, except for a factor of 4, the same as the nonrelativistic Rutherford formula expressed in terms of the kinetic energy. This simple conversion from nonrelativistic to relativistic cross section is, however, a special feature of the unscreened Coulomb field. In general, the ratio of the nonrelativistic and highly-relativistic differential cross sections can be expected to depend on angle and energy.

Still, the situation is not as complicated as it may appear at first sight. The simplification is brought about by a very useful theorem which is valid for elastic scattering by any physical central potential in the Born approximation. It is only necessary that the spin factor $[1-\beta^2\sin^2(\vartheta/2)]$ can be omitted, which is true for most physical potentials to a high degree of accuracy. Under these conditions the total cross section in the highly relativistic limit is independent of energy.

The proof is trivial. The total cross section in the highly relativistic limit is

$$\sigma_t=2\pi\int_0^\pi |f(\vartheta)|^2\sin\vartheta d\vartheta\frac{1}{1-\beta^2}$$

$$=\frac{2\pi}{1-\beta^2}\left(\frac{h}{p}\right)^2\int_0^\infty |f(q)|^2qdq, \tag{1.8}$$

where

$$q=(2p/\hbar)\sin(\vartheta/2). \tag{1.9}$$

But

$$\left(\frac{h}{p}\right)^2\frac{1}{1-\beta^2}=\left(\frac{h}{mv}\right)^2\approx\left(\frac{h}{mc}\right)^2=\lambda_c^2, \tag{1.10}$$

where λ_c is the Compton wavelength of the scattered particle. Thus we have

$$\sigma_t=2\pi\lambda_c^2\int_0^\infty |f(q)|^2dqq, \tag{1.11}$$

which is independent of energy.

This result provides physical insight as well as aid in calculation. While the total cross section remains constant as we increase the energy, more and more of the scattering will take place at very small angles. This is so because the total cross section from a given q_0 to $q=\infty$ is also independent of energy, while the ϑ_0 corresponding to $q_0\sim E\vartheta_0$ will decrease as we increase the energy, indicating a larger fraction of the scattering at very small angles. In addition, (1.11) also shows that the differential cross section will be given by the same curve for all highly relativistic energies, except for a change of scale on both axes. This considerably simplifies the practical calculations.

To keep the total cross section constant, the differential cross section at any given very small angle must increase with energy at least until the energy is so high that most of the scattering takes place inside that angle. In particular, the differential cross section at zero angle will increase monotonically with energy. In fact, at zero angle,

$$f(\vartheta)=\frac{m}{2\pi\hbar^2}\int V(r)d\tau$$

is independent of the energy and thus the $(1-\beta^2)^{-1}$ factor in $I(\vartheta)$ gives us an E^2 dependence. This dependence in turn agrees with the result discussed above, that the angle within which a given fraction of the scattering takes place varies as E^{-1}.

So far we have discussed some general features of scattering from a screened Coulomb field. We will now turn to the more specific discussion of the scattering of electrons by atoms.

2. ELASTIC SCATTERING

Electrons are scattered by both the atomic nuclei and the atomic electrons. These two contributions are called elastic and inelastic respectively. We will accept this nomenclature, although it is worth pointing out that calling the scattering by the electrons "inelastic scattering" is slightly misleading. As we will see, the inelastic nature of the scattering by electrons is important only at very small angles. At larger angles the scattering by electrons can be treated as a simple elastic Coulomb scattering (which takes into account the screening of other charges present), even if, as far as the whole atom is concerned, the scattering process, strictly speaking, is still inelastic.

The elastic scattering deviates at small angles from the Rutherford formula only because of the shielding

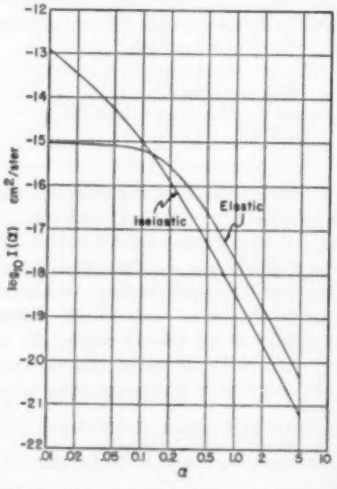

FIG. 1. Differential cross section for "elastic" and "inelastic" Coulomb scattering of highly relativistic electrons by nitrogen atoms. α is defined by (2.1).

effect of the atomic electrons. In accord with the remark in Sec. 1, the Hartree model should be used to calculate this deviation, at least at the smallest angles. Such calculations of $|f(q)|^2$ as a function of q are tabulated for various atoms in reference 4. It should be remarked that the relationship between q and $V^{\frac{1}{2}}\sin(\vartheta/2)$ as given there is valid only for nonrelativistic electrons.

It is convenient to use instead of q the parameter

$$\alpha \equiv \frac{10^{-8}}{4\pi} q = \frac{\sin(\vartheta/2)}{\lambda} \times 10^{-8} = 40.3(E_{\text{Mev}} + \tfrac{1}{2})\vartheta_{\text{rad}}, \quad (2.1)$$

where the last equality holds for the relativistic case. The table in reference 4 just referred to gives $|f(\alpha)|^2$ for $0.1 \leqslant \alpha \leqslant 1.1$. For larger values of α the function $|f(\alpha)|^2$ is tabulated in the same reference using the Thomas-Fermi model.

Because of the application of these results to scattering in air, the actual numerical calculations were carried out for nitrogen. There, around $\alpha = 1.1$, the two models give identical results and thus it is justified to use the Thomas-Fermi model at larger values of α. Beyond $\alpha = 5$ the Rutherford cross section can be used. The justification is again the agreement of the Rutherford cross section and the Thomas-Fermi result for $\alpha \gtrsim 5$.

For values less than $\alpha = 0.1$ the function $|f(\alpha)|^2$ is not tabulated. We can however calculate it from the Hartree model without much trouble. For this purpose we expand $f(q)$ in a power series in q:

$$f(q) = \int V(r) e^{iq\cdot r} d\tau$$

$$= \int e^{iq\cdot r}\left(-\frac{Ze^2}{r} + e^2 \int \frac{\rho(r')}{|r - r'|} dr'\right) d\tau$$

$$= \frac{4\pi}{q^2}\left(-Ze^2 + e^2 \int \rho(r') e^{iq\cdot r'} d\tau'\right). \quad (2.2)$$

But

$$\int \rho(r) e^{iq\cdot r} d\tau = 4\pi \int \rho(r) r^2 dr - \frac{q^2}{6} 4\pi \int \rho(r) r^4 dr$$

$$+ \frac{q^4}{120} 4\pi \int \rho(r) r^6 dr - \cdots = Z - B\frac{q^2}{6} + C\frac{q^4}{120} - \cdots, \quad (2.3)$$

because the odd powers of q drop out in the angular integration. B and C can be evaluated using the Hartree wave function.[5] One gets for nitrogen

$$B = 15.6 a_0^2, \quad C = 122 a_0^4. \quad (2.4)$$

We can then evaluate $f(q)$ at $q = 0$, where only the q^2 term will contribute. Furthermore, we can estimate the ratio of the q^2 and q^4 terms at $\alpha = 0.1$. For nitrogen this ratio is 0.18, which means that to quite a good approximation we can consider the differential cross section constant for $\alpha \leqslant 0.1$. Thus the differential cross section has been determined for all angles.

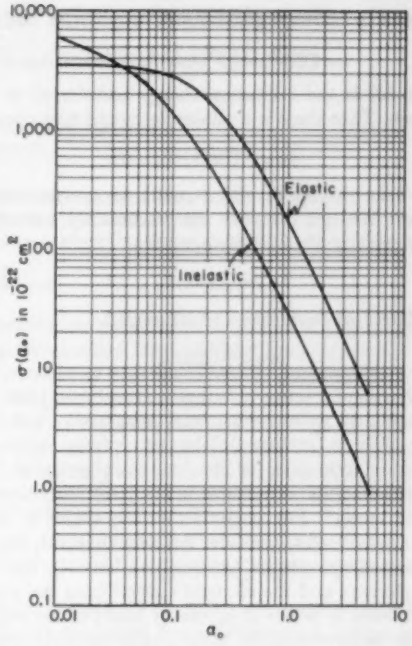

FIG. 2. $\sigma(\alpha_0)$, the total cross section from $\alpha = \alpha_0$ to $\alpha = \infty$ for "elastic" and "inelastic" Coulomb scattering of highly relativistic electrons by nitrogen atoms. α is defined by (2.1).

For nitrogen, the total cross section turns out to be 3.43×10^{-19} cm^2. In comparison, the pure Rutherford formula with the Thomas-Fermi cut-off angle gives 2.51×10^{-19} cm^2.

The differential cross section, $I(\alpha)$, calculated for nitrogen is shown in Fig. 1. $\sigma(\alpha_0)$, the total cross section for scattering from α_0 to $\alpha = \infty$, is shown in Fig. 2.

3. INELASTIC SCATTERING

If the Rutherford formula held precisely (as it does for larger angles), then the inelastic contribution would be only $1/Z$ times the nuclear scattering. This is so because the cross section due to the nucleus is Z^2 times as large as the cross section due to one of the Z electrons. Therefore we can include electronic effects into the Rutherford formula by writing $Z(Z+1)$ instead of Z^2.

The deviation of the electronic contribution from the Rutherford formula at small angles is determined not only by screening effects but also by the inelastic nature of the collision. While in the case of the nuclear contribution any amount of momentum transfer was permissible, for the scattering by atomic electrons the

[5] Brown, Bartlett, and Dunn, Phys. Rev. 44, 296 (1933).

relationship between q and ϑ will be

$$q=(2\pi/\lambda)[\vartheta^2+(\Delta E/E)^2]^{\frac{1}{2}}, \tag{3.1}$$

where ΔE is the excitation energy transferred to the electron. Thus there is a minimum momentum transfer

$$q_{\min}=(2\pi/\lambda)(\Delta E/E). \tag{3.2}$$

To take this effect into account we can proceed as follows: We can preserve the relationship between q and ϑ used in the elastic kinematics,

$$q\sim(2\pi/\lambda)\vartheta, \tag{3.3}$$

and define an equivalent cut-off angle,[6]

$$\vartheta_{\min}=(\Delta E/E). \tag{3.4}$$

For most purposes it is not necessary to treat the excitation of each atomic level separately, but it is permissible to replace ΔE by an average excitation energy, of the order of the ionization potential.[3] Of course, ionization is included in the term "excitation of atomic levels." For larger scattering angles it is no longer permitted to consider ΔE as a constant, but we get instead momentum conservation between the incident electron and the electron ejected from the atom,[6] which leads to rather large energy losses of the former. But, as we have seen, for larger angles the scattering by electrons is only a small fraction of the elastic contribution anyway.

For a given value of the momentum transfer, the scattering of electrons may be written[4] as the Rutherford scattering,

$$I_R(\vartheta)=4e^4Z/E^2\vartheta^4, \tag{3.5}$$

multiplied by a scattering factor S which represents the screening effects. This S is only a function of q and hence the differential cross section again depends only on q. This suggests using again the theorem concerning the total cross section stated in Sec. 1. Now the lower limit of the integral over q will not be zero because of the cutoff, but it will still be a constant, independent of E and ϑ, namely

$$q_{\min}=(2\pi/\lambda)(\Delta E/E)=\Delta E/\hbar c. \tag{3.6}$$

Thus the theorem will still hold and the calculations will be simplified in the same way as they were in the nuclear case.

The function $S(\alpha)$ has been tabulated[4] using the Born approximation with the Thomas-Fermi model. For values of α larger than those indicated in the table we can use the Rutherford formula, since there S is very nearly 1.

[6] H. A. Bethe, *Handbuch der Physik* (Verlag Julius Springer, Berlin, 1933), Vol. 24, Part 1, Chap. 3, pp. 491–506.

For values of α less than those given in the table we can use the Hartree wave function to calculate S. We have[3]

$$S=1-Z^{-1}\sum_{i=1}^{Z}f_i^2, \tag{3.7}$$

where

$$f_i=\int_0^\infty \rho_i(r)4\pi r^2\frac{\sin qr}{qr}dr\sim$$

$$1-\frac{q^2}{6}\int^\infty \rho_i(r)r^2 4\pi r^2 dr\equiv 1-\frac{q^2}{6}R_i. \tag{3.8}$$

So that

$$S=1-Z^{-1}\sum_{i=1}^{Z}\left(1-\frac{q^2}{3}R_i\right)=\frac{q^2}{3Z}\int r^2\rho(r)4\pi r^2 dr. \tag{3.9}$$

This integral is the same as the quantity B in (2.4). It is to be noted that this rather remarkable relationship between elastic and inelastic scattering holds only for very small values of q.

$S(q)$ is therefore a quadratic function of q near the origin. The S calculated in this way joins smoothly the values given in the table referred to before.

With the help of this S, the differential cross section can be calculated as a function of α. It is shown for nitrogen in Fig. 1. It is to be noted that at very small values of α the inelastic cross section considerably exceeds the elastic one. From $I(\alpha)$ one can immediately obtain $I(\vartheta)$ for any given E. The angle at which the inelastic contribution overtakes the elastic cross section will be inversely proportional to the energy. At 10 Mev the two differential cross sections become equal at 3×10^{-4} radian or at 1 minute of arc.

Just as in the case of the elastic scattering, we can also calculate $\sigma(\alpha_0)$, the total cross section for scattering from α_0 to $\alpha=\infty$. It is given for nitrogen in Fig. 2.

The total cross section for the inelastic contribution will, of course, depend on the value chosen for ΔE, which is an average value and hence is not available without some calculations. However, because of the quadratic dependence of S on α near the origin, the total cross section will depend on ΔE only logarithmically and hence an approximate estimate of ΔE will suffice. The value of ΔE used in the calculations for nitrogen was 80 ev. With this value, the total cross section of the scattering by electrons is 1.26×10^{-18} cm^2, about 3.6 times the elastic contribution.

ACKNOWLEDGMENTS

The author would like to thank Professor H. A. Bethe for his patient guidance throughout this work.

Mean-Value Calculations for Spatial Multiple Scattering*

JEAN SNOVER GOLDBERG† AND HARTLAND S. SNYDER, *Brookhaven National Laboratory, Upton, New York*

AND

WILLIAM T. SCOTT, *Smith College, Northampton, Massachusetts*

(Received June 20, 1955)

Calculation of five types of mean values for the spatial (three-dimensional) multiple-scattering theory of Molière and Snyder-Scott is reported: arithmetic mean, half-width, $1/e$ width, median, and a "Gaussian" width fitted to the zero-angle scattering intensity. The results are expressed in terms of simple interpolation formulas accurate to one percent.

IN a previous paper,[1] six mean-value expressions for the Snyder-Scott-Molière projected multiple-scattering distribution were calculated and shown to obey a convenient linear relationship with the logarithm of the mean number of scatterings. In the present note, similar work is reported for the three-dimensional case based on Molière's development.[2]

Molière gives the following expansion for the distribution function of the true spatial angle Θ:

$$f(\Theta)\Theta d\Theta=[2\exp(-\theta^2)+f^{(1)}(\theta)/B+f^{(2)}(\theta)/B^2]\theta d\theta. \quad (1)$$

The dimensionless angle θ is

$$\theta=\Theta/\chi_\gamma(B\Omega)^{\frac{1}{2}}, \quad (2)$$

where B is an expansion parameter chosen by Molière to make the above expansion possible. B is related to the mean number of scatterings, Ω, as

$$1.167e^B/B=\Omega. \quad (3)$$

The angular unit χ_γ, as in the two-dimensional case, is

$$\chi_\gamma=0.257Z^{\frac{1}{2}}(1+3.33\gamma^2)^{\frac{1}{2}}/pc \text{ degrees}, \quad (4)$$

and the mean number of scatterings, Ω, is given by the relation

$$\chi_\gamma\Omega^{\frac{1}{2}}=[515\sigma Z'^2\langle Z^2\rangle_{Av}/A\beta^2c^2\beta^2]^{\frac{1}{2}} \text{ degrees}, \quad (5)$$

where Z' and Z are, respectively, the atomic numbers of the scattered particle and the scattering nucleus, βc is the velocity of the scattered particle, $\gamma=ZZ'/137\beta$, pc is the momentum of the scattered particle measured in Mev, σ is the track length measured in grams/cm^2 of scatterer, and A is the atomic weight of the scatterer.

Molière tabulates the functions $f^{(1)}(\theta)$ and $f^{(2)}(\theta)$ to make evaluation of Eq. (1) possible.[2,3] Values for the two-dimensional scattering distribution so calculated from Molière's tables compared very favorably with the Snyder-Scott tables for a range of Ω from 100 to 84 000, as reported in reference 1. Values of the three-dimensional distribution from Molière's expansion and from an extension of the Snyder-Scott approach have also been computed, and compare favorably. For the latter, the following expansion for the distribution function, in $\log\Omega$, was made about $\Omega=\Omega_0=3000$ (the logarithm of which is centrally located in the range of Ω's considered):

$$f(\theta,\Omega)=2\pi B(\Omega_0/\Omega)\{P_0(\theta(B\Omega_0)^{\frac{1}{2}},\Omega_0)-\ln(\Omega/\Omega_0)P_1(\theta(B\Omega_0)^{\frac{1}{2}},\Omega_0)+[\ln(\Omega/\Omega_0)]^2P_2(\theta(B\Omega_0)^{\frac{1}{2}},\Omega_0)\}, \quad (6)$$

where the coefficients P_n, which are functions of $\theta(B\Omega_0)^{\frac{1}{2}}$ and Ω, are computed from intermediate values which arose in preparing the distribution tables for projected scattering.

The agreement between the two calculations of spatial scattering distribution at $\theta=0$ is better than 0.4% except for extreme values of Ω; at $\Omega=100$, the dis-

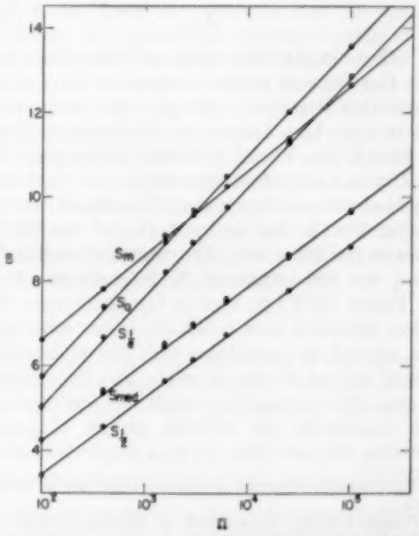

FIG. 1. Graphs of the interpolation formulas (7–11). Each S represents the product of B with the square of the appropriate mean angle (see text). The points represent direct calculations to which the lines are fitted. (Two sets for S_{med} arise from calculations based on both one-half and $1/e$ widths.)

* Research performed at Brookhaven National Laboratory under the auspices of the U. S. Atomic Energy Commission.

† Present address: Radiation Laboratory, University of California, Livermore, California.

[1] W. T. Scott, Phys. Rev. 85, 245 (1951).

[2] G. Molière, Z. Naturforsch. 3a, 78 (1948).

[3] More accurate and extensive tables of these quantities are given by H. A. Bethe, Phys. Rev. 89, 1256 (1953). Their use would not change in any significant way the results in the present paper, which were computed from Molière's tables.

crepancy is two percent; at $\Omega = 102\,400$ the discrepancy is 0.6%. Graphical comparison shows that the two curves are identical within the accuracy of Molière's tabulated values.

The mean values calculated are the following: arithmetic mean, $\theta_m = \langle\theta\rangle_{\text{Av}}$; half-width angle, $\theta_{\frac{1}{2}}$, given by $f(\theta_{\frac{1}{2}}) = f(0)/2$; $1/e$ width angle, $\theta_{1/e}$, given by $f(\theta_{1/e}) = f(0)/e$; median angle, θ_{med}; and θ_0, the $1/e$ width of a normalized Gaussian fitted to the value $f(0)$, namely, $\theta_0 = [2/f(0)]^{\frac{1}{2}}$. $\theta_{\frac{1}{2}}$ and $\theta_{1/e}$ were derived by interpolating $\log f(\theta)$ against θ^2. Unnormalized Gaussians fitted to $f(0)$ and, respectively, $\theta_{\frac{1}{2}}$ and $\theta_{1/e}$, were used to calculate θ_{med}, giving two results that agreed to one percent. The mean of the two is given here as θ_{med}.

For each of these mean values, the product (designated by S) of its square with the value of B varies almost linearly with $\log\Omega$, so that a straight line fitted at seven points by a least-square relative-error calculation is adequate for interpolation for experimental comparisons.

We find for the S's:

$$S_m = B\theta_m^2 = 2.601 + 2.002\log_{10}\Omega, \tag{7}$$

$$S_{\frac{1}{2}} = B\theta_{\frac{1}{2}}^2 = -0.146 + 1.799\log_{10}\Omega, \tag{8}$$

$$S_{1/e} = B\theta_{1/e}^2 = -0.170 + 2.601\log_{10}\Omega, \tag{9}$$

$$S_{\text{med}} = B\theta_{\text{med}}^2 = 0.675 + 1.801\log_{10}\Omega, \tag{10}$$

$$S_0 = B\theta_0^2 = 2B/f(0) = 0.529 + 2.614\log_{10}\Omega. \tag{11}$$

Figure 1 shows these lines and the points to which they are fitted. The fit is everywhere within one percent.

PHYSICAL REVIEW VOLUME 100, NUMBER 4 NOVEMBER 15, 1955

Relaxation Times in Magnetic Resonance*

DAVID PINES† AND CHARLES P. SLICHTER
Department of Physics, University of Illinois, Urbana, Illinois

(Received July 21, 1955)

Line-widths and relaxation times in magnetic resonance are discussed via a random walk model which is derived by a simple argument. Using the result, various topics in nuclear resonance and in conduction-electron spin resonance are discussed. The physical basis for the effect of motion in narrowing resonance lines is clearly evident, and a simple picture presented of the electron relaxation processes analyzed by Overhauser.

I.

THE subjects of line-widths and spin-lattice relaxation times in magnetic resonance have received considerable attention in the past few years. Various aspects have been treated by Bloembergen, Purcell, and Pound,[1] Van Vleck,[2] Anderson,[3] Overhauser,[4] Kubo and Tomita,[5] and others. One of the most fundamental aspects of this problem is that of motional narrowing, i.e., the effect of the bodily motion of the absorbing center on the line width. The concept of motional narrowing was first introduced by Bloembergen, Purcell, and Pound (BPP) to explain the narrowness of the nuclear resonance lines in liquids. It has subsequently been applied in connection with the phenomena of internal nuclear motion in solids, and the conduction electron spin resonance in metals and semiconductors.

In considering the physical picture of motional narrowing we have been led to a simple derivation of the narrowed line width, which includes as a special case the usual static expression. Our derivation is based on the picture of spin dephasing as a random walk process; we find

$$1/T_2 = (\delta\omega)^2\tau_c, \tag{1}$$

where $\hbar\delta\omega$ is the interaction energy, and τ_c the correlation time for the dephasing mechanism under consideration. For short correlation times[6] this expression also yields the spin-lattice relaxation time. In this paper we derive Eq. (1), apply it to several examples in nuclear resonance and discuss in some detail the spin-lattice relaxation time for conduction electrons in the alkali metals.[6] Although our derivation is not rigorous and although we do not obtain results not accessible to previous theories, the simplicity of our considerations enables one to gain physical insight and to obtain results quickly which display the main features of interest.

II.

Line widths may be characterized in several ways; by a width in magnetic field or frequency, or, alternatively, by a time conventionally called T_2,[7] which is the

* This research supported in part by the Office of Naval Research.

† Present address: Department of Physics, Princeton University, Princeton, New Jersey.

[1] Bloembergen, Purcell, and Pound, Phys. Rev. **73**, 679 (1948).
[2] J. H. Van Vleck, Phys. Rev. **74**, 1168 (1948).
[3] P. W. Anderson, J. Phys. Soc. Japan **9**, 316 (1954).
[4] A. W. Overhauser, Phys. Rev. **89**, 689 (1953).
[5] R. Kubo and K. Tomita, J. Phys. Soc. Japan **9**, 888 (1954).

[6] An elegant and more rigorous treatment of line widths along these lines may be found in the paper by Anderson, reference 3.
[7] F. Bloch, Phys. Rev. **70**, 460 (1946).

inverse of the width in frequency. Classically the time T_2 represents the time for a group of spins initially precessing in phase to dephase as a result of their slightly different precession frequencies. There are a variety of definitions of T_2 which appear in the literature, differing from one another by factors of order unity. Because of the approximate nature of our method, the precise definition of T_2 need not concern us here. However, it will be seen that our approach leads us to a T_2 which is closely related to that appearing in the Bloch equations.[7]

Our model for line-broadening is based on the assumption that dephasing takes place by a random walk process.[8] In Appendix I we derive a differential equation for the (classical) distribution of spins in angle on the random walk model and show that the solution leads to the familiar Bloch equations. Here we wish to give a simple derivation of our basic expression.

Let us consider a given spin in interaction with its environment. This interaction will produce a change, $\delta\omega$, in the spin precessional frequency. This change may be positive or negative; we assume that it maintains its sign for a time which we call τ_c. τ_c is thus the correlation time for the interaction under consideration. During this time an *extra* phase angle, $\delta\phi=\pm\delta\omega\tau_c$, is accumulated by the spin in addition to its angular displacement due to the uniform precession. After n such intervals in a time, t, the mean square angular deviation due to this process will be

$$\langle\Delta\phi^2\rangle_{Av}=n\delta\phi^2. \tag{2}$$

Since $n=t/\tau_c$, we have

$$\langle\Delta\phi^2\rangle_{Av}=t\tau_c(\delta\omega)^2. \tag{3}$$

In this time t, a group of spins initially in phase will thus have accumulated phase differences characterized by $\langle\Delta\phi^2\rangle_{Av}$; the time t for which $\langle\Delta\phi^2\rangle_{Av}\sim 1$ may then be defined as T_2. Thus we obtain our basic expression for line width,

$$1/T_2=(\delta\omega)^2\tau_c. \tag{4}$$

Equation (4) expresses in simple form the results of the noise theory of BPP. Our model for the dephasing is a random walk in which the "step length" is constant, corresponding to a fixed interaction of strength $\delta\omega$ acting for a fixed time, τ_c. In practice there will be a distribution in step lengths, corresponding to a more or less continuous strength and duration of interaction of the spin with its environoment. Equation (4) will still apply, but appropriate averages must be introduced for $\delta\omega$ and τ_c. The quantities $(\delta\omega)^2$ and τ_c may be averaged independently unless the choice of τ_c depends on $\delta\omega$, in which case we must average the entire expression (4). A number of examples involving such joint averaging will be discussed.

Equation (4) has been derived on the basis of classical considerations. However, it applies in quantum-theoretical problems provided we understand by $\delta\omega$ the interaction energy, ΔE, divided by $\hbar$.[9]

There are several general applications of Eq. (4) in resonance problems. One concerns the situation in which the dephasing interaction is present for only a certain fraction, α, of the time intervals τ_c. Such a case arises, for example, in line widths due to added impurities in liquids. We then find

$$1/T_2=(\delta\omega)^2\alpha\tau_c. \tag{5}$$

Another case of interest is that of very long correlation times, in which case Eq. (4) yields the familiar expression for the rigid lattice line width. For if the interaction maintains its sign and effectiveness for the entire time T_2, then τ_c is by definition T_2, and we have

$$1/T_2=\delta\omega. \tag{6}$$

This suggests an alternative physical picture for the basic expression, (4), in which the presence of a correlation time (i.e., a time-dependent environment) introduces a certain ineffectiveness in the maximum dephasing interaction $\delta\omega$. The measure of this ineffectiveness is just $\tau_c\delta\omega$.

When the correlation time is very short compared with the inverse of the Larmor frequency, ω_0, with which the spin precesses, then $T_2=T_1$, the spin-lattice relaxation time, and we may use the basic expression, (4), to calculate T_1. The physical basis for putting $T_1=T_2$ under these circumstances may be seen by transforming to a coordinate system rotating at the Larmor frequency. In such a coordinate system the static external field is zero. If the correlation time is short compared with the Larmor period, the effective interaction is unchanged by this transformation. The surroundings appear isotropic to the nucleus, and the rate of decay of magnetization will be the same in all directions. Hence the "transverse" time T_2 equals the "longitudinal" time T_1. The equality of T_2 and T_1 under these circumstances was recognized by BPP and proven explicitly by Block and Wangsness.[10]

III.

We now turn to several applications of the expression (4) in nuclear magnetic resonance. Our examples are chosen to elucidate the phenomenon of motional narrowing.

A. Relative Narrowing for Two Nuclear Species

We wish to compare the line widths of two different nuclear species, A and B, occurring in the same sample,

[8] Forms of line broadening that result from inhomogeneous magnetic fields and similar causes are not contained in our theory, since although they introduce a distribution of precession frequencies, they do not introduce any random dephasing of spins of a particular precession frequency. That is to say, the spins maintain phase memory even though they get out of step with one another. The existence of phase memory of this type is clearly demonstrated by the spin-echo experiments of Hahn.

[9] That $\delta\omega=\Delta E/\hbar$ follows because the phase character of the precession is carried by the complex time factors in the wave function.

[10] R. K. Wangsness and F. Bloch, Phys. Rev. 89, 728 (1953).

under the assumption that species B occurs in relatively low abundance. We assume that the line width is due to magnetic dipolar interactions among the nuclei. Since species A is dominant we may think of it as producing a local field, $H_{\rm loc}$, at either A or B, and we would naively expect a line width $H_{\rm loc}$, which is the same for both species. This result is indeed correct for the rigid lattice.[11] In the case of motional narrowing, however, we note that $\delta\omega_A=\gamma_A H_{\rm loc}$ and $\delta\omega_B=\gamma_B H_{\rm loc}$, where γ_A and γ_B are the nuclear gyromagnetic ratios. In terms of T_2, the line width ΔH is given by $\Delta H=1/\gamma T_2$, so that the ratio of the two line widths is

$$\Delta H_B/\Delta H_A=\gamma_A T_A/\gamma_B T_B=\gamma_B/\gamma_A, \tag{7}$$

where we make use of Eq. (4). We see that contrary to our naive expectation, the two line widths are no longer the same. The reason is clearly that the step length differs between the two species since they possess different γ's.

B. Diffusion—Narrowed Lines

The bodily motion of a diffusing nucleus will narrow the rigid lattice line width. Let us consider pure translational diffusion as found, for instance, in the alkali metals,[12] and further restrict our attention to dipolar interactions between different nculei. $\delta\omega$ is given by the dipole-dipole expression,

$$\delta\omega\sim\gamma^2[I(I+1)]^{\frac{1}{2}}\hbar/r^3,$$

where I is the nuclear spin, r is the internuclear distance, and we neglect angular factors. Since the correlation time is that time for which the interaction varies appreciably, it is effectively the time for the nuclei to diffuse a distance relative to one another comparable to r. If D is the coefficient for self-diffusion, we have[1] $\tau_c\sim r^2/12D$. We notice that both the interaction strength and the correlation time depend upon r, so that we must sum the contributions, $(\delta\omega)^2\tau_c$, over all r. We then find

$$\frac{1}{T_2}=\frac{\gamma^4 I(I+1)\hbar^2 N}{12D}\int_a^\infty\frac{4\pi r^2 dr}{r^4}, \tag{8}$$

where N is the number of nuclei per unit volume, and a is the distance between nearest neighbors. Thus

$$1/T_2=\gamma^4 I(I+1)N\hbar^2/Da, \tag{9}$$

in good agreement with the corresponding expression derived from the BPP theory.[1]

C. Nuclear Spin—Conduction-Electron Hyperfine Interaction

Let us think of the atoms of the metal as initially widely separated, so that there is a hyperfine interaction of nucleus and electron appropriate to one electron per atom. When the atoms are assembled to form the metal, the electrons no longer remain localized, but we may picture them as jumping from atom to atom, giving a motionally narrowed line.

While on a given atom, the electron interacts with the nucleus with energy ΔE given by the expression appropriate for s-states:

$$\Delta E=(8\pi/3)\gamma_e\gamma_n\hbar^2|\psi(0)|^2\mathbf{I}\cdot\mathbf{S}N, \tag{10}$$

where $|\psi(0)|^2$ is the square of the conduction electron wave function at the nucleus normalized per unit volume and N the number of atoms per unit volume. There are two features of interest in this interaction. First because of the exclusion principle only the electrons lying within a region κT of the Fermi surface are free to take part in this interaction. Thus we should apply our expression (5) for the calculation of T_2, where α is $\kappa T/E_F$. Second, the correlation time is determined by the jump rate of an electron from atom to atom. The jump rate may be found conveniently by considering a wave packet of Bloch waves constructed to localize an electron on one atom. Such a packet requires the entire range of electron momenta and will therefore spread significantly in a time $\hbar/E_f$. We therefore chose $\tau_c=\hbar/E_f$. Since $\tau_c\omega_0\ll 1$ we will have $T_1=T_2$, giving

$$\frac{1}{T_1}=\frac{64\pi^2}{9}\frac{\gamma_e^2\gamma_n^2\hbar^3}{E_F}|\psi(0)|_F^4\frac{\kappa T}{E_F}N^2, \tag{11}$$

where $|\psi(0)|_F^2$ represents the average of $|\psi(0)|^2$ at the Fermi surface. This expression agrees with results previously derived.[13–15]

IV.

We now turn to the conduction-electron spin resonance in the alkali metals. Because the correlation time for all processes of interest is very short with respect to ω_0^{-1}, we may apply our basic expression to the direct calculation of the spin-lattice relaxation time for the electron. Overhauser[4] has calculated the effect of a variety of relaxation mechanisms for this process. We consider a number of these from our point of view: electron-nuclear hyperfine interaction, the electron spin-longitudinal phonon interaction, the spin-orbit interaction with impurities, and the spin-spin and spin-current interaction between the electrons.

A. Electron-Nuclear Hyperfine Interaction

The interaction energy and correlation time for this mechanism will be identical with those deduced in Sec. III C, since the same interaction is involved. However because we now focus our attention on the electron,

[11] We are neglecting a slight difference due to the resonant coupling of identical nuclei. See for example Van Vleck, reference 2.
[12] R. E. Norberg and C. P. Slichter, Phys. Rev. **83**, 1074 (1951); D. F. Holcomb and R. E. Norberg, Phys. Rev. **98**, 1074 (1955).
[13] W. Heitler and E. Teller, Proc. Roy. Soc. (London) **A155**, 637 (1936).
[14] N. Bloembergen, Physica **15**, 588 (1949).
[15] J. Korringa, Physica **16**, 601 (1950).

the factor $\kappa T/E_F$ does not apply and we acquire a factor $I(I+1)$ since the nuclear moment is squared. We obtain

$$\frac{1}{T_1}=\frac{64\pi^2}{9}\frac{\gamma_e^2\gamma_n^2\hbar^3}{E_F}|\psi(0)|_F^4N^2I(I+1). \tag{12}$$

This relaxation time, which agrees with that calculated by Overhauser, is far too long to explain the experimentally observed times.

B. Electron Spin-Longitudinal Phonon Interaction

The spin-orbit interaction of the electron with the nuclear electric field is modulated by the nuclear motion, giving rise to an effective electron spin-longitudinal phonon interaction. We may calculate this in two ways. We first use a plane-wave approach similar to that adopted by Overhauser, in which we neglect the modulation of the electron wave function by the periodic field of the lattice. The potential acting on an electron due to the ionic motion may be written as

$$\sum_k q_k v_k e^{i\mathbf{k}\cdot\mathbf{x}},$$

where v_k represents the field due to the ions, as compensated by the other electrons and q_k is the phonon amplitude. In the plane wave approximation this may be calculated rather accurately by making a Fermi-Thomas approximation[4,16]; v_k turns out to be the Fourier component of a screened electron-ion interaction and is given by

$$v_k=-\frac{4\pi Ne^2i}{k\sqrt{\rho}}\frac{k^2}{k^2+6\pi Ne^2/E_F}\sim-\frac{2}{3}\frac{ikE_F}{\sqrt{\rho}}, \tag{13}$$

in the long-wavelength approximation. Here N is the number of electrons/cc and ρ is the metallic density. The interaction which is capable of flipping the electron spin is the spin-orbit interaction of the electron with the phonon electric field, and is

$$\Delta E\sim\gamma_e\hbar\mathbf{S}\cdot(\mathbf{E}_k\times\mathbf{p})/2mc, \tag{14}$$

for an electron of momentum $\mathbf{p}$ interacting with a longitudinal phonon of wave vector $\mathbf{k}$ and electric field $\mathbf{E}_k$. E_k is given by

$$E_k=-kv_kq_k/e, \tag{15}$$

and we may write

$$\Delta E\sim\gamma_e\hbar p_0k^2E_Fq_k/(3emc\sqrt{\rho}) \tag{16}$$

since we are only considering electrons at the top of the Fermi distribution. For these electrons the correlation time is just the time for the electron to travel a phonon wavelength,

$$\tau_c\sim\lambda/v_0\sim2\pi/kv_0.$$

Since the correlation time and interaction are related, we must sum over $(\delta\omega)^2\tau_c$ jointly over the spectrum of phonon wavelengths, k. If we use an averaged value for the sound-wave amplitude,

$$\langle q_k^2\rangle_{\text{Av}}=\kappa T/2\omega^2=\kappa T/2k^2s^2, \tag{17}$$

where s is the sound velocity, we obtain for our summation

$$\frac{1}{T_1}\sim\frac{\pi^3}{128}\frac{N^2\hbar^5\kappa TK_{\max}^4}{\rho s^2m^5c^4k_0}. \tag{18}$$

$K_{\max}$ is the maximum phonon wave vector. This relaxation time is 4/3 as long as that obtained by Overhauser. As shown by him, it leads to a relaxation time considerably longer than that observed experimentally.

Actually this represents something of an underestimate of the effectiveness of this relaxation mechanism. For the electronic wave function is rather far from being a plane wave in the region close to the nucleus where the spin-orbit interaction is strongest. We may consider what is effectively the opposite limit by introducing the spin-orbit splitting constant ξ to characterize the strength of the interaction. Thus the spin-orbit Hamiltonian in the absence of ionic motion is taken as

$$\mathcal{H}=\frac{-\hbar}{4m^2c^2}(\boldsymbol{\sigma}\times\mathbf{p})\cdot\nabla V(R)\sim\xi\boldsymbol{\sigma}\cdot\mathbf{l}, \tag{19}$$

and our assumption is equivalent to taking the metallic wave functions as atomic in the region near the nucleus. We may easily calculate the spin flip induced by the nuclear motion using perturbation theory and we obtain for the interaction energy associated with the kth phonon,

$$\Delta E\sim kq_k\xi. \tag{20}$$

This represents an overestimate of this term, since in the regions close to the nucleus the electrons probably respond more nearly adiabatically to the nuclear motion.[17] The correlation time is again $2\pi/kv_0$, and we find

$$\frac{1}{T_1}\sim\frac{\xi^2mK_{\max}{}^3\kappa T}{4\pi\hbar^3k_0\rho s^2}\sim\pi\left(\frac{\xi}{E_F}\right)^2\frac{\kappa T}{\hbar}. \tag{21}$$

For lithium, this leads to a T_1 which is roughly comparable with that obtained in the plane-wave approximation.[18] On the other hand, for sodium we find T_1 according to (21) is $\sim2\times10^{-6}$ sec at room temperature. This is very much shorter than the value calculated in the plane wave approximation and is of the right order of magnitude to explain the experimental results.[19] However because we have probably considerably over-

[16] See J. Bardeen and D. Pines, Phys. Rev. **99**, 1140 (1955), for a discussion of the validity of this approximation.

[17] This fact has been noted independently at Y. Yafet (private communication).

[18] It was this approximate agreement of these two different methods of estimating T_1 which led Overhauser to conclude that the plane wave approximation would be adequate for the alkali metals.

[19] G. Feher and A. F. Kip, Phys. Rev. **98**, 337 (1955); T. R. Carver, thesis, University of Illinois, 1954 (unpublished); Holcomb, Carver, and Slichter (to be published).

estimated ΔE, not too much reliance should be placed on this order of magnitude agreement. Elliott[20] has proposed an alternative mechanism based on the small admixture of opposite spin wave function introduced in the wave function of an electron of given spin by the spin-orbit interaction. This gives rise to a spin flip when the electron is scattered by the phonon field, and may account for the observed line width in sodium. More accurate calculations are needed to distinguish between Elliott's and Overhauser's mechanisms based on the spin-orbit interaction.

C. Electron-Impurity Spin-Orbit Interaction

Neither of the foregoing mechanisms can explain the observed relaxation time for lithium, which is temperature independent and of the order of 10^{-7} sec. This independence of temperature naturally suggests an impurity mechanism. The experiments in fact indicate an impurity effect.[19] We here estimate one such mechanism; our estimate is again something of an overestimate, for we assume that the wave function of the metallic electron rather resembles that of the atomic impurity in the region near the impurity. In this case the interaction energy is $\Delta E \sim \xi_I$, where ξ_I is the hyperfine splitting for the impurity. The correlation time is $\sim a/v_0$, where a is the size of a unit cell in the lattice, and we must take as our basic expression (5), where α is the fraction if impurities, f, in the metal. We then obtain

$$\frac{1}{T_1} \sim \frac{\xi_I^2}{\hbar^2} \frac{a}{v_0} f. \tag{22}$$

If we consider sodium impurities in lithium we find $T_1 \sim 10^{-9}/f$ using the observed value of the atomic splitting. Thus a concentration of 1% sodium in lithium could give rise to relaxation times of the order of those experimentally observed. Smaller fractions of heavier impurities would be equally effective. Although we have doubtless overestimated ΔE considerable, it is not implausible that spin flip by an impurity atom is responsible for the spin-lattice relaxation in lithium.

D. Electron-Electron Spin-Spin and Spin-Current Interaction

These mechanisms are not as effective as those discussed in Secs. B and C in producing spin-lattice relaxation, but they are interesting to consider because they illustrate a very complicated case for which our simple expression (5) leads us to the correct form for the relaxation time, even though we considerably underestimate its magnitude. The spin-spin interaction between two electrons may be written

$$\mathcal{H}_{ss} = (\gamma_e^2 \hbar^2/r^3)[\mathbf{S}_1 \cdot \mathbf{S}_2 r^2 - 3(\mathbf{S}_1 \cdot \mathbf{r})(\mathbf{S}_2 \cdot \mathbf{r})], \tag{23}$$

whereas the spin-current interaction is given by

$$\mathcal{H}_{sc} = (\gamma_e e\hbar/mcr^3)(\mathbf{r} \times \mathbf{p}_2 \cdot \mathbf{S}_1 + \mathbf{r} \times \mathbf{p}_1 \cdot \mathbf{S}_2). \tag{24}$$

H_{ss} leads to both single spin-flip and double spin-flip processes, whereas H_{sc} leads to only single spin-flip processes. As pointed out by Overhauser, single-flip and double-flip processes must be calculated separately since interference effects are possible between the two terms in the former case. However we are interested only in the general form of the relaxation time, so we consider only the double spin flip associated with H_{ss} and the single flip due to H_{sc}. We furthermore neglect all exchange effects, an approximation which is principally responsible for our underestimate of the interaction energy. We then obtain:

$$\Delta E)_{ss} \sim 2\gamma_e^2 \hbar^2/r^3, \quad \Delta E)_{sc} \sim (\gamma_e e\hbar/mcr^2) p_0. \tag{25}$$

The correlation time τ_c is the same for both mechanisms and is given by $\sim r/v_0$, the interelectronic distance divided by the electronic velocity. We must thus jointly sum over $(\Delta E)^2 \tau_c$. Furthermore we must apply our expression (1) since only a fraction α of the electrons are available to flip spins due to the Pauli principle. We obtain

$$1/T_1)_{ss} \sim 4\gamma_e^4 \hbar^2 2\pi N\alpha/R_{\min}^2 \sim 8\pi\gamma_e^4 \hbar^2 N k_0^3 \alpha, \tag{26}$$

where $R_{\min}$ is the minimum value of r to which the above concepts apply, and is of the order of the electron de Broglie wavelength, k_0^{-1} or the lattice constant.

The role of the exclusion principle in limiting the effectiveness of the electron interactions is somewhat complicated, and a detailed calculation, such as that by Overhauser, is usually desirable to clarify matters. However we may obtain some insight into its operation on the basis of the following rather rough arguments. First of all, only a fraction $\kappa T/E_F$ of the other electrons are available to make collisions with the electron under consideration. Secondly, we may expect that the Pauli principle will limit the number of final momentum states available provided the momentum transfer in the collisions of importance is such as to make possible electron transitions to occupied states within the Fermi sea. For spin-spin interactions this is the case, since as we see in Eq. (26), the important contributions to line broadening come from close collisions, of impact parameter $R_{\min}$, and hence involve large momentum transfers. Thus for the spin-spin interactions we find $\alpha = (\kappa T/E_F)^2$. On the other hand, as will be seen in Eq. (28) below, for the spin-current interaction the important contributions to the line width come from distant collisions involving small momentum transfers. These momentum transfers are in fact sufficiently small that the exclusion principle will here not be needed to limit the final momentum states, so that for this mechanism $\alpha = \kappa T/E_F$.[21]

[20] R. J. Elliott, Phys. Rev. **96**, 266 (1954).

[21] A similar situation applies in the coupling of electron spins to longitudinal phonons. The exclusion principle does not limit the final momentum states available because the important collisions involve only a small momentum transfer to the electrons.

For the spin-spin interaction, with double spin-flips, we thus obtain

$$1/T_1)_{ss}=8\pi\gamma_e^4\hbar^2Nk_0^2(\kappa T)^2/E_F^2. \tag{27}$$

This result has the same dependence on the metallic constants as Overhauser's result; it corresponds to a time which is longer than this by about a factor of ten, due to our neglect of exchange effects.

For the spin current interaction, we find

$$\frac{1}{T_1}\Big)_{sc}=\frac{4\pi N\gamma_e^2e^2v_0}{c^2}\ln\left(\frac{R_{\max}}{R_{\min}}\right), \tag{28}$$

where $R_{\max}$ and $R_{\min}$ are the maximum and minimum distances over which this interaction will be effective. $R_{\min}$ is, as before, k_0^{-1}. $R_{\max}$ must, however, be taken with some care. Because of electron-electron interaction, the magnetic interactions in a dense electron case are screened out in a distance $\sim c/\omega_p=c(m/4\pi ne)^{\frac{1}{2}}$.[22]

This maximum parameter will apply unless energy conservation limits the minimum momentum transfer (and hence the maximum impact parameter) in such a way as to provide a cutoff which is smaller than c/ω_p. According to Overhauser, the minimum momentum transfer is $\sim m\beta H/p_0$, and so the ratio of the two impact parameters is $R_{\max}^{\text{cons}}/R_{\max}^{sc}\sim p_0\omega_p\hbar/mc\beta H\sim E_F/150\beta H$ for sodium. We see that for all practical magnetic fields, the screening value of c/ω_p will come into play first. We have gone into this in such detail because Overhauser used energy conservation to obtain $R_{\max}$, and in so doing has overestimated the effectiveness of this mechanism somewhat. The correction is only in the logarithm, as we see, so that Overhauser's relaxation time is probably in error by only a factor of ~ 3. As in the previous case, our expression for T_1,

$$\frac{1}{T_1}\Big)_{sc}\sim\frac{4\pi Ne^2\gamma_e^2v_0}{c^2}\ln\left(\frac{ck_0}{\omega_p}\right), \tag{29}$$

has the correct dependence on metallic density and the like, but underestimates the effectiveness of this mechanism by a factor of order 10.

V. CONCLUSIONS

The examples we have given show the general utility of our simplified approach in giving physical insight into complex problems. Often the answers agree quite well with the results of more precise theories. One must always bear in mind the limitations of the model, based as it is on the assumption that the dephasing processes of an individual spin are random. We have already pointed out that line broadening due to magnetic field inhomogeneities does not involve random dephasing. One of the most striking examples of the limitations of the random walk theory is the line breadths of electron spin resonance in metal samples whose thickness is large compared to the skin depth. One is tempted to say that electrons diffusing in and out of the alternating field see a randomly modulated alternating signal with consequent line broadening. However, as the detailed theory of Dyson[23] shows, electrons may diffuse out of the alternating fields at a time t_0, and then back in again at a time t_1. The alternating fields they see on re-entry at t_1 have well-defined phase relations with respect to those at the earlier time t_0. The result of this residual coherence is that the electron resonance has a narrow peak at the center comparable in width to the natural width (as observed in samples whose particles are small compared to the skin depth), but that there are also broad wings present. Much of the intensity of the line is moved into the wings, but the central portion remains narrow. A similar effect is used by Ramsey to obtain high resolution in molecular beam experiments.[24] The subtle coherent effects in this example are easily overlooked, illustrating clearly the care that must be exercised in applying the concept of randomness.

ACKNOWLEDGMENTS

Many of the simple pictures presented in this paper have grown from conversations with our colleagues. It is a pleasure to acknowledge in particular the stimulating discussions with Dr. John Bardeen, Dr. Myer Bloom, Dr. Thomas Carver, Dr. Donald Holcomb, and Dr. Richard Norberg.

APPENDIX I. RANDOM WALK ON A SPHERE

We wish to treat the problem of spin relaxation classically for the case of very short correlation time using the random walk description. We will show that the assumption of short correlation time then leads to equality between the transverse relaxation time T_2 and the longitudinal time T_1, but that the transverse magnetization decays to zero whereas the longitudinal decays to the value $\mu^2/3\kappa T$, the classical Langevin value, where μ is the spin magnetic moment. The decay is exponential as with the Bloch equations, and the decay time is given essentially by our Eq. (1).

We shall describe the distribution of spins in angle by a time-dependent function $f(\Omega,t)$, where $f(\Omega)d\Omega$ is the probability that a spin lies in the solid angle $d\Omega$ about the angle θ,ϕ and is normalized so that $\int_{4\pi}fd\Omega=1$. We introduce axes x, y, z, the last lying along the static magnetic field H_0. We wish to compute the average spin magnetizations μ_x, μ_y, and μ_z as a function of time. These averages are

$$\langle\mu_z\rangle_{\text{Av}}=\int\mu_zfd\Omega, \quad \text{etc.} \tag{30}$$

[22] D. Bohm and D. Pines, Phys. Rev. **82**, 625 (1951).

[23] F. J. Dyson, Phys. Rev. **98**, 349 (1955).

[24] N. F. Ramsey, Phys. Rev. **76**, 996 (1949).

with $\mu_x=\mu\sin\theta\cos\phi$, $\mu_y=\mu\sin\theta\sin\phi$, and $\mu_z=\mu\cos\theta$. We begin by determining the differential equation for f, and then obtain a suitable solution. The presence of the external field causes all the spins to precess at the same rate, so that it will rotate the entire distribution function at the Larmor frequency. This effect is easily removed from the problem by transforming to a reference frame rotating at the Larmor frequency. We do, however, take account of the fact that changes in θ represent a change of magnetic energy of a spin in the magnetic field and require, therefore, a change in energy of the "lattice" which is the thermal reservoir.

We find the differential equation for f by a slight generalization of the model of Debye[23] for dielectric relaxation. Debye treats dielectric relaxation as a random walk problem; however, he is concerned with a problem in which there is no gyroscopic action, and his motion is the turning of a sphere in a viscous medium. We take account of the precession by our transformation above, and replace his viscous model with a condition of detailed balance on the ratio $W(\Omega,\Omega')/W(\Omega',\Omega)$. Here $W(\Omega,\Omega')d\Omega$ is the probability that in a specified time δt a spin originally at angle Ω' is scattered into the solid angle $d\Omega$ about Ω. The quantity δt is chosen long compared to τ_c, but short enough that $W(\Omega,\Omega')$ is negligible if Ω and Ω' differ in orientation by more than a few degrees. The requirement of detailed balance is that at equilibrium $W(\Omega,\Omega')f(\Omega')=W(\Omega',\Omega)f(\Omega)$ or $W(\Omega,\Omega')/W(\Omega',\Omega)=\exp[(\cos\theta-\cos\theta')\mu H_0/\kappa T]$. That $W(\Omega,\Omega')\neq W(\Omega',\Omega)$ results from the fact that the "lattice" must gain or lose energy when $\theta'\neq\theta$. Therefore transitions will be weighted by the "lattice" distribution in energy.

The equation for f expressing conservation of probability of spins may be written down by considering a particular angle Ω and is

$$\delta t\frac{\partial f}{\partial t}=\int_{4\pi}[f(\Omega')W(\Omega,\Omega')-f(\Omega)W(\Omega',\Omega)]d\Omega'. \quad (31)$$

We then proceed, as does Debye, to expand $f(\Omega')$ in terms of $\theta'-\theta$, $\phi'-\phi$, and likewise to expand $W(\Omega,\Omega')/W(\Omega',\Omega)$.

Because of the short correlation time, we assume that $W(\Omega,\Omega')$ depends only on the angle between the Ω and Ω' directions except for an anisotropy of order $(\cos\theta-\cos\theta')\mu H/\kappa T$. Through straightforward manipulations involving relations from spherical trigonometry and following the lines of Debye in calculating his quantity Δ_2 (we have included his Δ_1 in Δ_2 by the detailed-balance condition) we arrive at the differential equation

$$\frac{\partial f}{\partial t}=\frac{1}{\tau}\left[\frac{1}{\sin\theta}\frac{\partial}{\partial\theta}\sin\theta\frac{\partial f}{\partial\theta}+\frac{1}{\sin^2\theta}\frac{\partial^2 f}{\partial\phi^2}\right.$$
$$\left.\times\frac{\mu H}{\kappa T}\left(2\cos\theta f+\sin\theta\frac{\partial f}{\partial\theta}\right)\right], \quad (32)$$

where $1/\tau=\alpha^2/4\delta t$ and α^2 is the mean angular jump in time δt.

We seek a solution of the form $f=\sum_{l,m}g_{lm}(t)Y_{lm}(\theta,\phi)$, where the Y_{lm} are spherical harmonics. The averages μ_x, etc., will require only knowledge of $g_{1m}(t)$, $m=\pm1,0$ since the components μ_x, μ_y, and μ_z are essentially spherical harmonics of $l=1$. On substituting (33) into (32), we obtain:

$$\frac{dg_{1m}}{dt}+\frac{2}{\tau}g_{1m}=-\frac{1}{\tau}\frac{\mu H}{\kappa T}\sum_{rs}g_{rs}\int Y_{1m}^*$$
$$\times\left(2\cos\theta Y_{rs}+\sin\theta\frac{\partial}{\partial\theta}Y_{rs}\right)d\Omega. \quad (34)$$

Furthermore $g_{00}=1/4\pi$ from the normalization conditions, and all other g_{lm}'s will be of order $\mu H/\kappa T$ since the distribution never corresponds to large percentage magnetization in any direction. Therefore we may neglect all g_{rs} except g_{00} and so find

$$g_{1m}=A_m e^{-2t/\tau}+\frac{\mu H}{\kappa T}\frac{1}{(12\pi)^{\frac{1}{2}}}\delta_{m0}, \quad (35)$$

where A_m is a constant dependent on m which is adjusted to fit the magnetization at $t=0$. We then find that

$$\langle\mu_x(t)\rangle_{\text{av}}=\langle\mu_x(0)\rangle_{\text{av}}e^{-2t/\tau},$$
$$\langle\mu_y(t)\rangle_{\text{av}}=\langle\mu_y(0)\rangle_{\text{av}}e^{-2t/\tau}, \quad (36)$$
$$\langle\mu_z(t)\rangle_{\text{av}}=\frac{\mu^2H}{3\kappa T}+\left(\langle\mu_z(0)\rangle_{\text{av}}-\frac{\mu^2H}{3\kappa T}\right)e^{-2t/\tau}.$$

Our results are the same as the solution of the Bloch equations for $T_1=T_2=\tau/2=2\delta t/\langle\alpha^2\rangle_{\text{av}}$. We note that μ_x and μ_y decay to zero, but μ_z decays to the classical Langevin value. Calculation of the decay time may be done by estimating the mean square angular displacement α^2 in time δt and using $1/T_2=\langle\alpha^2\rangle_{\text{av}}/2\delta t$. This is, apart from a factor of 2, the result expressed in Eq. (1).

[23] P. Debye, *Polar Molecules* (Dover Publications, New York, 1945).

Second Virial Coefficients of He^3-He^4 Mixtures between 2 and 4°K*

WILLIAM E. KELLER
Los Alamos Scientific Laboratory, University of California, Los Alamos, New Mexico
(Received May 9, 1955)

P-V isotherms of a gaseous mixture containing 54.75 atomic percent He^3, 45.25% He^4 have been measured at 2.146 and 3.944°K. The values of the second virial coefficients, B_{mix}, obtained from these isotherms are, respectively, −144.5 and −70.0 cc/mole, as compared with −144.9 and −72.8 cc/mole computed from the experimentally determined second virial coefficients of the pure components and the theoretical solution nonideality parameter. It is shown that the solutions are very nearly ideal and that in the temperature range 2 to 4°K reliable values of B_{mix} can be obtained for all compositions.

RECENTLY we have reported[1,2] the measurements on the equation of state of pure He^3 and He^4 gas below 4°K. To complete this program of work on the He isotopes, we have investigated the *P-V-T* properties of a mixture of He^3 and He^4 in the same temperature region. Calculations[3] of the second virial coefficient of the mixture, B_{mix}, using the Lennard-Jones potential have indicated that except at very low temperatures the solution of the two gases is nearly ideal. No hope was entertained of quantitatively verifying this conclusion by experiment since the calculated departure from ideality is much smaller than the most favorable estimate of errors in the measurements.

For a qualitative check on the computations, it was considered sufficient to work with one mixture only, one having a composition of nearly equal parts of the two isotopes. It is expected for such a mixture that any effects of solution nonideality would be maximized. All the experiments, therefore, were performed on a mixture containing 54.75 atomic percent He^3, 45.25% He^4. During the course of the work the constancy of the isotopic ratio was monitored with the aid of a mass spectrometer; no significant variation was observed.

Several modifications were made upon the apparatus[1] used for measurements on the pure gases: the vacuum jacket around the cell was removed as well as the vapor pressure thermometer; also a solder joint in the cell itself was reworked. Temperatures were measured from bath pressures; corrections for bath height were made only above the λ point. Above 2.18°K the temperature ascribed to the sample gas on the basis of the bath pressure may be in error by several millidegrees. This error is reproducible, however, and affects neither the precision with which the isotherm can be determined, nor the accuracy of the virial coefficients; but the value obtained for RT does not bear any significant relationship to the nominal value of T of the isotherm. On the other hand, for the region slightly below the λ point, temperatures derived from the bath pressure have been found reliable.[2]

It was necessary to establish that the modifications had produced no significant difference in the cell volume. The volume was not recalibrated directly but was checked by the value of RT obtained for an isotherm of the mixture at 2.1520°K on the 1948 scale. It can be easily shown that a certain percentage error in the volume determination produces the same percentage error in both the temperature and the second virial coefficient (using the inverse-volume virial expansion terminated after the linear term). From the results of Isotherm I (Table II) we see that the value of T is too high by 0.0041°K, or 0.2%, if we accept the values of $T_{48}-T$ given by Erickson and Roberts.[4] This discrepancy is only slightly larger than the limits observed for the pure gases, so we may conclude that the corresponding error in B due to a volume change of the cell is not appreciable.

All other parts of the apparatus as well as experimental procedures and methods of analyzing the data duplicated those employed in the experiments on the pure gases.

TABLE I. Experimental data for the isotherms of a mixture containing 54.75% He^3 and 45.25% He^4.

Exp. No.	P, mm Hg	$(N/V)\times10^4$ mole/cc	$T_{bath(48)}$°K	$(PV/N)_{exp}$ cc-mm/mole	δ
		$T_{48}=2.1520$°K			
I-2-1	33.811	2.6251	2.1522	128 789	28
I-2-2	16.958	1.2895	2.1545	131 355	10
I-4-1	39.349	3.0893	2.1447	127 825	−38
I-5-1	41.769	3.2692	2.1558	127 526	11
I-5-2	21.444	1.6363	2.1576	130 702	28
I-5-3	12.477	0.9458	2.1503	132 027	18
I-6-1	38.293	2.9953	2.1488	128 044	−1
I-6-2	26.999	2.0825	2.1494	129 810	−1
I-6-3	14.708	1.1182	2.1505	131 623	−53
		$T_{48}=3.9500$°K			
II-1-2	180.15	7.7445	3.9496	232 640	−9
II-2-1	259.55	11.4543	3.9553	226 265	−1
II-2-2	114.77	4.8250	3.9519	237 748	77
II-3-1	309.59	13.9399	3.9525	221 933	−56
II-3-2	151.81	6.4602	3.9511	234 925	67
II-3-3	82.10	3.4216	3.9467	240 153	67
II-4-1	318.61	14.3851	3.9534	221 274	51
II-4-2	224.00	9.7684	3.9535	229 093	−74
II-4-3	35.180	1.4448	3.9521	243 367	−121

* Work done under the auspices of the U. S. Atomic Energy Commission.

[1] W. E. Keller, Phys. Rev. **97**, 1 (1955).
[2] W. E. Keller, Phys. Rev. **98**, 1571 (1955).
[3] Kilpatrick, Keller, Hammel, and Metropolis, Phys. Rev. **94**, 1103 (1954).
[4] R. A. Erickson and L. D. Roberts, Phys. Rev. **93**, 957 (1954).

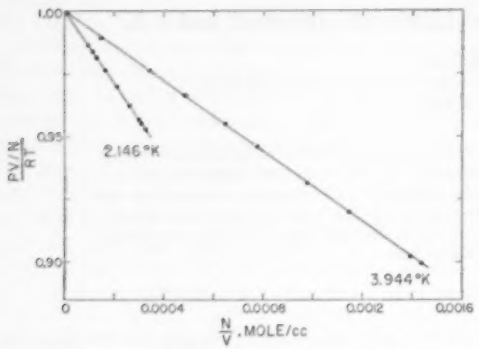

FIG. 1. Plot of $(PV/N)/RT$ vs N/V for two isotherms of a mixture containing 54.75% He^3 and 45.25% He^4. Values of RT were obtained from the analyses of the data.

RESULTS

In Table I are collected the experimental data for two isotherms of the mixture. The symbolism in this table parallels that used in the corresponding tables of references 1 and 2. The data are plotted in Fig. 1 relative to the value of RT computed by using the relation:

$$PV/N=RT(1+B_{\text{mix}}N/V). \tag{1}$$

Information derived from the analyses of the measurements is summarized in Table II. We present only the results of the two-constant analyses; but as can be seen from the values of Q, the third virial coefficients for the temperatures and densities measured are not significant.

Two isotherms at a relatively wide temperature interval were considered to be adequate for the purpose of qualitatively checking the calculations of B_{mix}. No new information would be gained by determining isotherms at intermediate temperatures, especially in view of the high precision attained for isotherms I and II. Of the several methods of comparing the calculated and experimental second virial coefficients we choose the following:

We first recapitulate the definitions given in reference 3.

$$B_{\text{mix}}=N_3^2B_{33}+2N_3N_4B_{34}+N_4^2B_{44}, \tag{2}$$

where N_3 and N_4 are the mole fractions of He^3 and He^4, respectively, B_{33} and B_{44} are the second virial coefficients of the pure components, and B_{34} is the cross coefficient. If the solution is ideal, $B_{34}=\frac{1}{2}(B_{33}+B_{44})$, and Eq. (2) becomes

$$B_{\text{mix}}=N_3B_{33}+N_4B_{44}. \tag{3}$$

We may then further rewrite Eq. (2) for the general case,

$$B_{\text{mix}}=N_3B_{33}+N_4B_{44}+2N_3N_4\Delta, \tag{4}$$

with

$$\Delta=B_{34}-\tfrac{1}{2}(B_{33}+B_{44}). \tag{5}$$

We now substitute in Eq. (4) values of Δ obtained from Table I, reference 3 and values of B_{44} and B_{33} obtained from the interpolation formulas, Eqs. (1) and (2) of reference 2. For $T=2.1461°K$, $\Delta=-1.73$ cc/mole, $B_{44}=-173.20$ cc/mole, and $B_{33}=-119.87$ cc/mole; for $T=3.9442°K$, the corresponding quantities are -0.98, -83.73, and -62.93 cc/mole. The resulting values of B_{mix}(calc) are given on line 6 of Table II. It is seen that the experimental and calculated values are

TABLE II. Summary of data derived from isotherms of a mixture containing 54.75% He^3 and 45.25% He^4.

Isotherm T in °K	I 2.1520	II 3.9500
$A=RT$, cc-mm/mole	133 840	245 973
T °K	2.1461	3.9442
B_{mix}, cc/mole	−144.5	−70.0
Prob. error of a measured point, %	0.015	0.021
$Q=E_3/E_2$	0.928	0.959
B_{mix}(calc), cc/mole	−144.9	−72.8

in favorable agreement. For the sake of consistency, in the above calculations we have chosen to take the values of B_{33} and B_{44} from the empirical data rather than from either of the two recent sets of theoretical results.[3,5] This is especially valid since all of the measurements were obtained with essentially the same apparatus.

Concerning the second virial coefficients of mixtures of He_3 and He^4 between 2 and 4°K, we come to the following conclusions: (1) the solutions of He^3 and He^4 gas are nearly ideal; and (2) B_{mix} for *all* concentrations is well represented by Eq. (4), taking B's for the pure components from the interpolation formulas of reference 2 and using the small corrections for solution nonideality as given in Table I of reference 3.

[5] Kilpatrick, Keller, and Hammel, Phys. Rev. **97**, 9 (1955).

Quantum Theory of Fluctuations*

HANS EKSTEIN AND NORMAN ROSTOKER
Armour Research Foundation of Illinois Institute of Technology, Chicago, Illinois

(Received August 4, 1955)

An operator is constructed for the spectral density of a fluctuating dynamical variable. The formulation is based on an analysis of method of measurement. An essential feature of the operator is the replacement of classical dynamical variables by time-dependent Heisenberg operators. The expectation value of the spectral density includes fluctuations of statistical origin, as well as fluctuations of quantum mechanical origin. It can be computed for any physical system when the initial state has been specified. Two applications are given: Nyquist's law is rigorously deduced for a physical system that is similar to the one discussed by Callen and Welton, and the shot effect is calculated for free uncorrelated electrons. A quantum correction is obtained whose origin lies in the wavelike character of the electron.

I. INTRODUCTION

FLUCTUATION phenomena are common and important features of all branches of the physical sciences. Since the origin of most fluctuations is of a statistical nature, it is perhaps not surprising that classical methods dominate the literature on the subject. Callen and Welton[1] (C-W) have given a quantum mechanical theory of thermal (Nyquist) noise. More recently, Weber has made some additional applications of their method.[2] The C-W method did not give a well-defined procedure for calculating what is usually measured, namely the spectral density. Instead, the total fluctuation was obtained in the form of an integral. The integrand was conjectured to be the spectral density.

According to the usual theory of measurement in quantum mechanics, the procedure for predicting the results of a measurement is to formulate an operator corresponding to the quantity measured and then to calculate the expectation value of the operator with respect to the state of the system.

The measurements usually considered in quantum mechanics involve observations at a definite time, given a complete or partial knowledge of the state of the system at a previous time. It was pointed out recently by Schrödinger[3] that the vast majority of measurements actually performed in the laboratory have an entirely different character. Measurements of the spectral power density of fluctuations, for example, do not fall into the usual pattern because the observation takes place over a very long time. While operators corresponding to such measurements have not been previously used, to our knowledge,[4] it is possible to construct them by consistent application of the accepted postulates of the theory of measurement in quantum mechanics, as will be shown presently. Thus it is not necessary, at least for the present purpose, to "recast the conceptual scheme of quantum mechanics."[3]

II. DEFINITION OF THE SPECTRAL DENSITY OPERATOR

We shall give a definition of the operator in question for two definite measurements which are only slightly idealized versions of actual observations (Fig. 1).

We assume that the fluctuating variable $A(t)$ produces by some means an electric voltage proportional to it which we will also designate by $A(t)$. The voltage is fed into a band-pass filter which transmits only the frequency components between $\nu_0-\Delta\nu/2$ and $\nu_0+\Delta\nu/2$, so that only the part $\delta A(t)$ is transmitted. This signal heats a thermocouple whose temperature variations are determined by the time integral of $[\delta A(t)]^2$. We now distinguish two cases:

(1) The thermocouple is connected to a ballistic galvanometer which indicates the magnitude

$$\int_{-\infty}^{+\infty}[\delta A(t)]^2 dt.$$

This arrangement is meaningful only if $A(t)$ is constant outside a finite time interval, or, more generally, if the

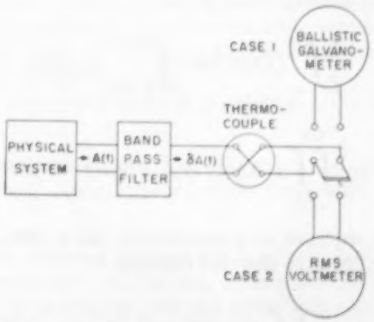

FIG. 1. Experimental arrangement for measurement of spectral density.

* Supported, in part, by the Bureau of Ordnance, Department of the Navy. A brief summary of this work has previously been reported at the 1954 Chicago Meeting of the American Physical Society. [H. Ekstein and N. Rostoker, Phys. Rev. **98**, 222(A) (1955).]

[1] H. B. Callen and T. A. Welton, Phys. Rev. **83**, 34 (1951).

[2] J. Weber, Phys. Rev. **96**, 556 (1954); **94**, 214 (1954); **90**, 977 (1953).

[3] E. Schrödinger, Nuovo cimento **1**, 5 (1955).

[4] We disregard the discussion of measurements in relativistic field theory where the time interval of the measurements is assumed to be very small, and is ultimately shrunk to zero. See, for example, W. Heitler, *The Quantum Theory of Radiation* (Clarendon Press, Oxford, 1954).

integrand decreases rapidly enough so that the integral exists. In other words, the fluctuation begins and terminates.

If the Fourier transform of $A(t)$ is

$$A(\nu)=\int_{-\infty}^{+\infty} A(t)\exp(-2\pi i\nu t)dt, \tag{1}$$

then the part of the signal transmitted through the filter is

$$\delta A(t)=\int_{\nu_0-\Delta\nu/2}^{\nu_0+\Delta\nu/2} 2\,\mathrm{Re}[A(\nu)\exp(2\pi i\nu t)]d\nu, \tag{2}$$

and the ballistic galvanometer reading is

$$\int_{-\infty}^{\infty}[\delta A(t)]^2dt=\int_{\nu_0-\Delta\nu/2}^{\nu_0+\Delta\nu/2} G_s(\nu)d\nu, \tag{3}$$

where

$$G_s(\nu)=2|A(\nu)|^2$$

$$=2\int_{-\infty}^{+\infty}\int_{-\infty}^{+\infty} A(t)A(t')\exp[-2\pi i\nu(t-t')]dtdt'. \tag{4}$$

(2) The fluctuation does not decrease for $t\to\pm\infty$. In this case, the measurement consists in observing the time-average of the thermal emf produced by the thermocouple, if the physical system is connected to the measuring device between the times $-T/2$ and $+T/2$.

One may assume a sequence of measurements with increasing T, in which the observed value tends to a limit. In this case, the voltage flowing through the filter is given by

$$\delta A(t)=\int_{\nu_0-\Delta\nu/2}^{\nu_0+\Delta\nu/2} 2\,\mathrm{Re}[A_T(\nu)\exp(2\pi i\nu t)]d\nu, \tag{2a}$$

with

$$A_T(\nu)=\int_{-T/2}^{T/2} A(t)\exp(-2\pi i\nu t)dt, \tag{1a}$$

and the deflection of the meter is determined by the average value of $[\delta A(t)]^2$:

$$\frac{1}{T}\int_{-\infty}^{+\infty}[\delta A(t)]^2dt=\int_{\nu_0-\Delta\nu/2}^{\nu_0+\Delta\nu/2} G_T(\nu)d\nu, \tag{3a}$$

where

$$G_T(\nu)=\frac{2}{T}\int_{-T/2}^{T/2}\int A(t)A(t')\exp[-2\pi i\nu(t-t')]dtdt'. \tag{4a}$$

If the sequence of measurements has a limit, as assumed, then the observed quantity is

$$G(\nu)=\lim_{T\to\infty}\frac{2}{T}\int_{-T/2}^{T/2}\int A(t)A(t')\exp[-2\pi i\nu(t-t')]dtdt'. \tag{5}$$

We have now given a classical definition of the observed quantities in the two cases. The accepted procedure for the construction of the corresponding quantum mechanical operators[5] consists in replacing the classical variable A by the corresponding operator and to "Hermitize" the resultant expression. The only peculiarity of the present case consists in the fact that these operators must obviously be Heisenberg operators. The resultant operators for the spectral density in the two cases are

$$G_s(\nu)=\int_{-\infty}^{+\infty}\int_{-\infty}^{+\infty}[A(t)A(t')+A(t')A(t)]\times\exp[-2\pi i\nu(t-t')]dtdt' \tag{6}$$

for case 1, and

$$G(\nu)=\lim_{T\to\infty}\frac{1}{T}\int_{-T/2}^{+T/2}\int[A(t)A(t')+A(t')A(t)]\times\exp[-2\pi i\nu(t-t')]dtdt' \tag{7}$$

for case 2.

The expectation value

$$\langle G(\nu)\rangle=(\psi_0,G(\nu)\psi_0) \tag{8}$$

can be computed if the initial state ψ_0 is specified. If, however, the initial state is not precisely known, then all information concerning it can be expressed by the density matrix ρ, and the expectation value of $G(\nu)$ or $G_s(\nu)$ is[6]

$$\langle G(\nu)\rangle=\mathrm{Tr}(G(\nu)\rho). \tag{9}$$

We can now express precisely what the term "fluctuating variable" means. A variable A is fluctuating with respect to an initial state ψ_0, if the expectation value of $G(\nu)$ or of $G_s(\nu)$ exists.

It is sometimes more convenient to consider the correlation function, which has the classical expression

$$F(\tau)=\lim_{T\to\infty}\frac{1}{T}\int_{-T/2}^{T/2} A(t)A(t+\tau)dt. \tag{10}$$

The same procedure leads to the operator

$$F(\tau)=\lim_{T\to\infty}\frac{1}{2T}\int_{-T/2}^{T/2}[A(t)A(t+\tau)+A(t+\tau)A(t)]dt. \tag{11}$$

Since only time or frequency integrations are involved, the Wiener-Khintchine theorem applies to $G(\nu)$ and $F(\tau)$. That is, the operators $G(\nu)$ and $F(\tau)$ are Fourier transforms, as are $\langle G(\nu)\rangle$ and $\langle F(\tau)\rangle$.

While we have defined an operator for the correlation function $F(\tau)$, it must be admitted that it is not directly

[5] E.g., H. A. Kramers, *Grundlagen der Quantentheorie* (Akademische Verlagsgesellschaft, Leipzig, 1938).

[6] J. von Neumann, *Mathematische Grundlagen der Quantenmechanik* (Dover Publications, New York, 1943).

derived from an analysis of a precise experiment. According to the experimental procedure chosen, other operators may be appropriate.

III. NYQUIST NOISE

As an application, we shall calculate the spectral density of current fluctuations for the physical system considered by Callen and Welton.[1] The system is characterized by boundary conditions (such as reflecting walls) that lead to zero current for every eigenstate. A detailed specification of the Hamiltonian is not required. The initial state is not completely known. Instead it is known that, at $t=0$, the system is in thermodynamic equilibrium at temperature T. This fact is expressed by the density matrix which in energy representation has the form

$$\rho_{ns;\,ns}=\exp(-E_n/kT)/[\textstyle\sum_{ns}\exp(-E_n/kT)], \quad (12)$$

while all nondiagonal elements vanish. The eigenvalues E_n may be degenerate, as provided for in the notation which includes a degeneracy parameter s. From Eq. (9) the expectation value of the spectral density operator is

$$\langle G(\nu)\rangle=\textstyle\sum_{ns}\rho_{ns;\,ns}G_{ns;\,ns}. \quad (13)$$

The Schrödinger operator for the x component of the electric current, averaged over the system's volume, is

$$\dot{Q}=(i/\hbar)(HQ-QH), \quad (14)$$

where $Q=\sum_n e_n x_n/L$, e_n is the charge of the nth particle, x_n is its x-coordinate, and L is the length of the system in the x direction. The Heisenberg operator for the current is $\dot{Q}(t)=\exp(iHt/\hbar)\dot{Q}\exp(-iHt/\hbar)$. The matrix element $G_{ns;\,ns}$ of the operator $G(\nu)$ [Eq. (7) with $A=\dot{Q}$] in the energy representation is

$$G_{ns;\,ns}=\lim_{T\to\infty}\frac{2}{T}\int_{-T/2}^{T/2}\int\{\sum_{n's'}\omega_{nn'}{}^2|Q_{n's';\,ns}|^2 \times\cos[\omega_{nn'}(t-t')]\exp[-i\omega(t-t')]\}dtdt',$$

where $\hbar\omega_{nn'}=E_n-E_{n'}$, $\omega=2\pi\nu$, and $Q_{n's';\,ns}$ is the matrix element of the operator Q in Eq. (14). After carrying out the time integrations and recognizing that

$$\lim_{T\to\infty}\frac{2\sin^2[(\omega_{nn'}\pm\omega)T/2]}{\pi(\omega_{nn'}\pm\omega)^2T}=\delta(\omega_{nn'}\pm\omega),$$

we obtain

$$G_{ns;\,ns}=2\pi\sum_{n's'}\omega_{nn'}{}^2|Q_{n's';\,ns}|^2 \times[\delta(\omega_{nn'}+\omega)+\delta(\omega_{nn'}-\omega)]. \quad (15)$$

Substituting Eq. (15) into Eq. (13), one obtains a final expression for $\langle G(\nu)\rangle$. When the eigenvalues E_n are discrete, $\langle G(\nu)\rangle$ is singular if the frequency ν is equal to the jump frequency of a spontaneous transition. In the case of quasi-continuous eigenvalues, the summation over n' in Eq. (15) can be replaced by an integration, so that the matrix elements $G_{ns;\,ns}$ are nonsingular.

A more explicit expression for $\langle G(\nu)\rangle$ requires detailed knowledge of the eigenstates. Instead of continuing in this direction, we consider other measurements for which the expectation value involves the same matrix elements. For example, the rate at which the system absorbs energy when subjected to a uniform sinusoidal electric field involves the matrix elements of Q, since the perturbation term is $V(t)Q$, where $V(t)=V_0\sin\omega t$ is the voltage applied across the length of the system in the x-direction. We assume the system to be initially in an eigenstate ϕ_{ns} and calculate the state at time t,

$$\psi=\sum_{n's'}C_{n's'}(t)\phi_{n's'}\exp\left[-\frac{iE_{n'}}{\hbar}t\right]. \quad (16)$$

According to first-order time-dependent perturbation theory,

$$|C_{n's'}|^2=\frac{V_0{}^2}{\hbar^2}|Q_{n's';\,ns}|^2 \times\left\{\frac{\sin^2[(\omega_{nn'}+\omega)t/2]}{(\omega_{nn'}+\omega)^2}+\frac{\sin^2[(\omega_{nn'}-\omega)t/2]}{(\omega_{nn'}-\omega)^2} +\frac{1}{2}\frac{1+\cos2\omega t-\cos(\omega_{nn'}+\omega)t-\cos(\omega_{nn'}-\omega)t}{(\omega_{nn'}-\omega)(\omega_{nn'}+\omega)}\right\}. \quad (17)$$

The transition probability $w(t)=(1/t)\sum_{n's'}|C_{n's'}(t)|^2$ has a useful form in the limit of large t. That is,

$$w=\lim_{t\to\infty}w(t)=\frac{\pi V_0{}^2}{2\hbar^2}\sum_{n's'}|Q_{n's';\,ns}|^2 \times[\delta(\omega_{nn'}+\omega)+\delta(\omega_{nn'}-\omega)]. \quad (18)$$

The limit $t\to\infty$ would appear to have dubious validity in a calculation involving first-order perturbation theory. Some comfort may be derived from the thought that the perturbation term may be made vanishingly small, and from the fact that the procedure leads to physically significant results.

If the system is initially in the state ϕ_{ns}, the power absorbed is[7]

$$\frac{\pi V_0{}^2}{2\hbar}\omega\sum_{n's'}|Q_{n's';\,ns}|^2[\delta(\omega_{nn'}+\omega)-\delta(\omega_{nn'}-\omega)].$$

The power absorbed if the system is initially in a state of thermodynamic equilibrium, at temperature T, is obtained by averaging over the eigenstates weighted

[7] In the transition for which $\omega_{nn'}=\omega$, the system loses energy $\hbar\omega$; for $\omega_{nn'}=-\omega$ the system gains energy $\hbar\omega$.

according to the Boltzmann factor. That is,

$$P=\frac{\pi V_0^2}{2\hbar}\omega\sum_{ns;n's'}\rho_{ns;ns}|Q_{n's';ns}|^2\times[\delta(\omega_{nn'}+\omega)-\delta(\omega_{nn'}-\omega)]. \quad (19)$$

The power absorbed can be expressed in terms of the experimentally determined complex impedance $Z=R+iX$. That is,

$$P=\tfrac{1}{2}V_0^2R/|Z|^2. \quad (20)$$

It is now clear that the expressions for $R/|Z|^2$ and $\langle G(\nu)\rangle$ are related. We consider the ratio:

$$\frac{\langle G(\nu)\rangle}{R/|Z|^2}=\frac{2\hbar}{\omega}\frac{\sum_{ns;n's'}[\exp(-E_n/kT)]\omega_{nn'}^2|Q_{n's';ns}|^2[\delta(\omega_{nn'}+\omega)+\delta(\omega_{nn'}-\omega)]}{\sum_{ns;n's'}[\exp(-E_n/kT)]|Q_{n's';ns}|^2[\delta(\omega_{nn'}+\omega)-\delta(\omega_{nn'}-\omega)]}.$$

The only terms which contribute to the sums are those for which $\omega_{nn'}=\pm\omega$, or $E_n=E_{n'}\pm\hbar\omega$. For example, consider E_1 and E_2 such that $E_1=E_2+\hbar\omega$. The contribution to the numerator is

$$[\exp(-E_1/kT)]\omega_{12}^2|Q_{21}|^2\delta(\omega_{12}-\omega)+[\exp(-E_2/kT)]\omega_{21}^2|Q_{12}|^2\delta(\omega_{21}+\omega)=[\exp(-E_1/kT)]\omega^2|Q_{21}|^2\delta(\omega_{12}-\omega)\times[1+\exp(-\hbar\omega/kT)].$$

Similarly the contribution to the denominator is

$$\exp[-E_1/kT]|Q_{21}|^2\delta(\omega_{12}-\omega)[1-\exp(-\hbar\omega/kT)].$$

Except for different factors, the sums in the numerator and denominator are identical. Thus

$$\frac{\langle G(\nu)\rangle}{R/|Z|^2}=2\hbar\omega[1+\exp(-\hbar\omega/kT)]/[1-\exp(-\hbar\omega/kT)],$$

or

$$\langle G(\nu)\rangle=\frac{4R}{|Z|^2}\left[\frac{h\nu}{2}+\frac{h\nu}{\exp(h\nu/kT)-1}\right]. \quad (21)$$

Equation (21) is Nyquist's law in the form obtained with quantum statistics.[1]

The calculation establishes a rigorous relationship between the exact result for $\langle G(\nu)\rangle$ and the approximate (first-order perturbation theory) result for $R/|Z|^2$. Since Nyquist's law is established experimentally, we may consider that the present calculations plus the experimental data establish the validity of the technique for calculating $R/|Z|^2$, although the latter calculation has not been actually carried out.

Equation (21) was derived by Callen and Welton. The present method differs from their derivation in several respects. The spectral density is computed directly, whereas in the C-W paper the total fluctuation was calculated and the deduction of the spectral density was not rigorous. Secondly, the C-W calculation was limited to cases where the energy levels of the physical system are quasi-continuous. This restriction has been removed, providing it is understood that the quantity $R/|Z|^2$ is evaluated for a vanishingly small perturbation. We have considered a degenerate physical system instead of a nondegenerate one as in the C-W paper. The computed values of $\langle G(\nu)\rangle$ and P will certainly be altered by degeneracy, but in the same way so that the Nyquist theorem is unaltered.

IV. SHOT EFFECT

When a series of charged particles arrives at a detector, current fluctuations are observed due to the discreteness of the charges. The current consists of a series of pulses at uncorrelated times if the electrons are independent, as is usually supposed. Any one pulse has a white spectral density and the effect of many electrons can be obtained by simple addition if the electrons are independent. Quantum corrections should be expected, due to the Pauli principle which introduces correlation of electrons, and due to the wave-like character of the electron. We shall treat only the latter correction in the present paper. For simplicity, we consider only one electron. In the usual calculation of shot effect, one determines the spectral density, such that

$$\int_0^\infty G(\nu)d\nu=\lim_{T\to\infty}\frac{1}{T}\int_{-T/2}^{T/2}J_x^2(t)dt,$$

where J_x is the current. For only one electron, $G(\nu)$ would vanish. In order to obtain finite results, we use the definition of $G_s(\nu)$ for case 1, [Eqs. (4) and (6)]. The classical expression for $G(\nu)$ for many electrons is $G(\nu)=2eJ_x$. For one electron, we obtain the finite result $G_s(\nu)=2e^2$. For N independent electrons, $G_s(\nu)=2e^2N$, and $G(\nu)=\lim_{T\to\infty}[G_s(\nu)/T]=2eJ_x$ since $J_x=\lim_{T\to\infty}(eN/T)$.

1. Classical Calculation

We consider fluctuations in the current arriving at a detector located in the region $-x_0/2\leq x\leq x_0/2$. An electron is observed only if it is in the detector region so that the current from a single electron may be defined as

$$J_x=-\frac{ep_x}{mx_0}f(x,x_0), \quad (22)$$

where p_x is the x-component of the momentum of the electron, $-e$, m are, respectively, charge and mass of the electron, and $f(x,x_0)$ is a function which has the

property that

$$f(x,x_0)=1 \quad \text{for} \quad -x_0/2\leq x\leq x_0/2$$
$$=0 \quad \text{if } x \text{ is outside this interval.}$$

An explicit form for $f(x,x_0)$ can be given in terms of the Dirichlet integral. That is

$$f(x,x_0)=\frac{1}{\pi}\int_{-\infty}^{\infty}\frac{\sin(\rho x_0/2)}{\rho}\exp(i\rho x)d\rho. \tag{23}$$

The definition of J_x can be idealized for a detector of infinitesimal extension in the x-direction by taking the limit as $x_0\to 0$. In this case Eq. (22) takes the simpler form

$$J_x=(-e/m)p_x\delta(x), \tag{24}$$

where

$$\delta(x)=\frac{1}{2\pi}\int_{-\infty}^{\infty}\exp(i\rho x)d\rho.$$

We assume that no force acts on the electron, so that $p_x=\text{const}$ and $x(t)=x(0)+(p_x t/m)$. Substituting

$$J_x(t)=\frac{-ep_x}{2\pi m}\int_{-\infty}^{\infty}\exp\left\{i\rho\left[x(0)+\frac{p_x}{m}t\right]\right\}d\rho$$

into Eq. (4), the classical expression for $G_x(\nu)$, and carrying out the indicated integrations, one obtains

$$G_x(\nu)=2e^2. \tag{25}$$

We shall compare this result with that obtained by quantum-mechanical treatment.

2. Quantum-Mechanical Calculation

The Heisenberg operator corresponding to $G_x(\nu)$ is, by Eq. (6),

$$G_x(\nu)=\int_{-\infty}^{\infty}\int[J_x(t)J_x(t')+J_x(t')J_x(t)]\times\exp[-i\omega(t-t')]dtdt', \tag{26}$$

where now $J_x(t)$ is the Heisenberg time-dependent operator which is constructed from the classical expression for the dynamical variable given by Eq. (24). That is,[5]

$$J_x(t)=-(e/2m)\exp(iHt/\hbar)\times[p_x\delta(x)+\delta(x)p_x]\exp(-iHt/\hbar), \tag{27}$$

where p_x is the Schrödinger operator for the x component of momentum. We consider a single free electron, for which $H=(1/2m)(p_x^2+p_y^2+p_z^2)$. The expectation value of the spectral density is

$$\langle G_x(\nu)\rangle=\int\psi_0^*G_x(\nu)\psi_0 d\tau. \tag{28}$$

The wave function ψ_0 at $t=0$ is assumed to be a wave packet of the form

$$\psi_0=\frac{1}{(2\pi)^{\frac{1}{2}}}\int_{-\infty}^{\infty}c(\mathbf{k})\exp(i\mathbf{k}\cdot\mathbf{r})d^3k. \tag{29}$$

The integrations are carried out in the order t, t', τ. Making use of the relations

$$H\exp(i\mathbf{k}\cdot\mathbf{r})=E(\mathbf{k})\exp(i\mathbf{k}\cdot\mathbf{r}),$$
$$E(\mathbf{k})=(\hbar^2/2m)(k_x^2+k_y^2+k_z^2),$$

we obtain for a typical t integration:

$$\int_{-\infty}^{\infty}\exp\left\{\frac{i}{\hbar}[E(\mathbf{k})-E(\mathbf{k}')+\hbar\omega]t\right\}dt=2\pi\hbar\delta[E(\mathbf{k})-E(\mathbf{k}')+\hbar\omega].$$

The resultant expression for $\langle G_x(\nu)\rangle$ is

$$\langle G_x(\nu)\rangle=(2\pi\hbar)^2\int\int\int d^3k d^3k' d^3k'' c^*(\mathbf{k}')c(\mathbf{k})(J_x)_{\mathbf{k}',\mathbf{k}''}\times(J_x)_{\mathbf{k}'',\mathbf{k}}\delta[E(\mathbf{k})-E(\mathbf{k}')]\{\delta[E(\mathbf{k})-E(\mathbf{k}'')-\hbar\omega]+\delta[E(\mathbf{k})-E(\mathbf{k}'')+\hbar\omega]\}. \tag{30}$$

The form of this expression is similar to the usual result from perturbation theory for an electron that makes elastic transitions from $\mathbf{k}$ to $\mathbf{k}'$ through an intermediate state $\mathbf{k}''$, whose energy differs from the initial state by $\pm\hbar\omega$. The matrix elements $(J_x)_{\mathbf{k},\mathbf{k}'}$ have the specific form

$$(J_x)_{\mathbf{k},\mathbf{k}'}=\int\phi_{\mathbf{k}}^*J_x\phi_{\mathbf{k}'}d\tau,$$

where

$$\phi_{\mathbf{k}}=(2\pi)^{-\frac{1}{2}}\exp(i\mathbf{k}\cdot\mathbf{r}),$$

and

$$J_x=(-e/2m)[p_x\delta(x)+\delta(x)p_x]$$

is the Schrödinger current operator. After carrying out the indicated integrations, $(J_x)_{\mathbf{k},\mathbf{k}'}$ takes the form

$$(J_x)_{\mathbf{k},\mathbf{k}'}=(-e\hbar/4\pi m)(k_x+k_x')\times\delta(k_y-k_y')\delta(k_z-k_z'). \tag{31}$$

Further reduction of Eq. (30) is accomplished by carrying out first the integrations with respect to k_y, k_y'; k_z, k_z' and finally the integrations with respect to k_x, k_x', making use of relations such as[5]

$$\delta\left[\frac{\hbar^2}{2m}(k_x^2-k_x''^2)\pm\hbar\omega\right]=\frac{m}{\hbar^2a^{\mp}}[\delta(k_x-a^{\mp})+\delta(k_x+a^{\mp})],$$

where

$$a^{\pm}=\{k_x''^2\pm(2m\omega/\hbar)\}^{\frac{1}{2}}.$$

[5] P. A. M. Dirac, *Quantum Mechanics* (Clarendon Press, Oxford, 1935).

The final expression for the expectation value of the spectral density is

$$\langle G_s(\nu)\rangle=\frac{e^2}{2}\int_{-\infty}^{\infty}\int dk_y dk_z\left\{\int_a^{\infty}\frac{k_x dk_x}{(k_x^2-\alpha^2)^{\frac{1}{2}}}\right.$$

$$\times\left[\left[|c(k_x)|^2+|c(-k_x)|^2\right]\left(2-\frac{\alpha^2}{k_x^2}\right)\right.$$

$$\left.-\left[c^*(-k_x)c(k_x)+c^*(k_x)c(-k_x)\right]\frac{\alpha^2}{k_x^2}\right]$$

$$+\int_0^{\infty}\frac{k_x dk_x}{(k_x^2+\alpha^2)^{\frac{1}{2}}}\left[\left[|c(k_x)|^2+|c(-k_x)|^2\right]\left(2+\frac{\alpha^2}{k_x^2}\right)\right.$$

$$\left.\left.+\left[c^*(-k_x)c(k_x)+c^*(k_x)c(-k_x)\right]\frac{\alpha^2}{k_x^2}\right]\right\}. \quad (32)$$

We have written α^2 for $2m\omega/\hbar$ and omitted the designation of the functional dependence of c on k_y and k_z in this expression.

The specific form of the spectral density depends on the form of the wave packet as prescribed by $c(k_x,k_y,k_z)$. The expression given by Eq. (32) for $\langle G_s(\nu)\rangle$ is not particularly simple, and in order to appreciate its implications, it is necessary to consider a specific case. We shall consider the limiting case of an electron with a definite momentum and therefore assume that $|c(\mathbf{k})|^2=\delta(\mathbf{k}-\mathbf{k}^0)$. Introducing the circular frequency ω_0 that corresponds to the electron's energy of motion in the x direction, the result of carrying out the integrations indicated in Eq. (32) may be expressed as follows:

$$\langle G_s(\nu)\rangle=\frac{e^2}{2}\left\{\frac{2-(\omega/\omega_0)}{[1-(\omega/\omega_0)]^{\frac{1}{2}}}+\frac{2+(\omega/\omega_0)}{[1+(\omega/\omega_0)]^{\frac{1}{2}}}\right\}\quad(\text{for }\omega<\omega_0)$$

$$=\frac{e^2}{2}\frac{2+(\omega/\omega_0)}{[1+(\omega/\omega_0)]^{\frac{1}{2}}}\quad(\text{for }\omega>\omega_0). \quad (33)$$

$\omega_0=E(k_x^0)/\hbar$, where $E(k_x^0)=\hbar^2(k_x^0)^2/2m$. In the classical limit when $\hbar\to 0$, $\omega_0\to\infty$ and $\langle G_s(\nu)\rangle=2e^2$ which is the same as the result in Eq. (25) obtained by classical mechanics. For finite ω_0, a singularity appears at $\omega=\omega_0$, which is similar to what one might expect for the spectral density of the electromagnetic field of a photon. The result expressed by Eq. (33) can, therefore, be interpreted in the following way. The electron exhibits a compromise between "wave-like" and "particle-like" behavior. At low frequencies, $\omega\ll\omega_0$, the behavior is "particle-like" and the classical result obtains. At frequencies of the order of ω_0 the behavior is "wave-like," exhibiting a resonance such as would be expected for a photon of circular frequency ω_0.

3. Shot Effect for a Finite Detector

The current operator for this case is

$$J_s=(-e/2m)[p_x f(x,x_0)+f(x,x_0)p_x], \quad (34)$$

where

$$f(x,x_0)=\frac{1}{\pi x_0}\int_{-\infty}^{\infty}\frac{\sin(\rho x_0/2)}{\rho}\exp(i\rho x)d\rho,$$

and x_0 is the width of the detector region.

The calculation follows the same pattern as the previous case. If we define

$$\gamma^2\equiv 1+\frac{\omega}{\omega_0},\quad \beta^2\equiv 1-\frac{\omega}{\omega_0},$$

then the result for an electron with definite momentum is

$$\langle G_s(\nu)\rangle=\frac{e^2}{4\gamma}\left\{\left(\frac{1+\gamma}{1-\gamma}\right)^2\frac{\sin^2[(1-\gamma)\omega_0\tau]}{(\omega_0\tau)^2}\right.$$

$$\left.+\left(\frac{1-\gamma}{1+\gamma}\right)^2\frac{\sin^2[(1+\gamma)\omega_0\tau]}{(\omega_0\tau)^2}\right\}$$

$$+\frac{e^2}{4\beta}\left\{\left(\frac{1+\beta}{1-\beta}\right)^2\frac{\sin^2[(1-\beta)\omega_0\tau]}{(\omega_0\tau)^2}\right.$$

$$\left.+\left(\frac{1-\beta}{1+\beta}\right)^2\frac{\sin^2[(1+\beta)\omega_0\tau]}{(\omega_0\tau)^2}\right\} \quad (35)$$

for $\omega<\omega_0$, and

$$\langle G_s(\nu)\rangle=\frac{e^2}{4\gamma}\left\{\left(\frac{1+\gamma}{1-\gamma}\right)^2\frac{\sin^2[(1-\gamma)\omega_0\tau]}{(\omega_0\tau)^2}\right.$$

$$\left.+\left(\frac{1-\gamma}{1+\gamma}\right)^2\frac{\sin^2[(1+\gamma)\omega_0\tau]}{(\omega_0\tau)^2}\right\}$$

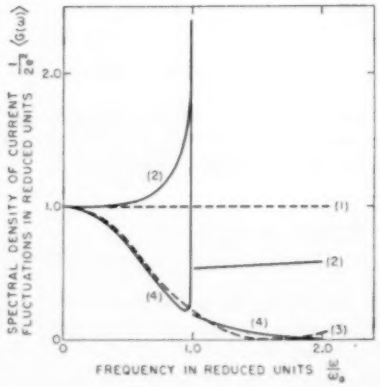

FIG. 2. Quantum corrections for the shot effect. (1) Classical: zero-width detector. (2) Quantum theory: zero-width detector. (3) Classical: finite detector, $\omega_0\tau=4$. (4) Quantum theory: finite detector, $\omega_0\tau=4$.

for $\omega > \omega_0$. In Eq. (35), ω_0 has the same meaning as before and $\tau = x_0 k_z^0 / 2\omega_0$ is the transit time. We now consider a number of limiting cases in order to appreciate the significance of Eq. (35). When $x_0 \to 0$, and, therefore, $\tau \to 0$, Eq. (35) reduces to the previous result of Eq. (33). In the classical limit $\hbar \to 0$ and $\omega_0 \to \infty$ in which case, Eq. (35) has the limit

$$\langle G_s(\nu) \rangle = 2e^2 \sin^2(\tfrac{1}{2}\omega\tau)/(\tfrac{1}{2}\omega\tau)^2. \quad (36)$$

Equation (36) is the familiar classical result for this case.

In the case of $x_0 = 0$, the previous result of Eq. (33) for the spectral density was singular at $\omega = \omega_0$. The present result for finite x_0 also has this property. Also, for $x_0 = 0$, $\lim_{\nu \to \infty} \langle G_s(\nu) \rangle = \infty$. In the case of finite x_0, $\lim_{\nu \to \infty} \langle G_s(\nu) \rangle = 0$. In Fig. 2, some numerical calculations of the spectral density for various cases are shown.

PHYSICAL REVIEW VOLUME 100, NUMBER 4 NOVEMBER 15, 1955

Transmission of Positrons and Electrons*†

H. H. SELIGER
National Bureau of Standards, Washington, D. C.

(Received June 22, 1955)

The transmissions of monoenergetic beams of positrons and electrons with energies up to 960 kev have been measured in aluminum, brass, silver, tin, lead, and gold. The absorber forms the window of a 2π counter whose counting efficiency is better than 99% down to a few hundred electron volts. Particles from a radioactive source, focused into a beam by a 90-degree magnetic analyzer impinge perpendicularly on the absorber window of the 2π counter. The total transmission is therefore measured independently of forward angle of emergence or of partial energy loss. Positrons are found to be transmitted to a greater extent than electrons except at low energies in aluminum. These results are correlated with previous backscattering experiments and are in qualitative agreement with theoretical calculations of Rohrlich and Carlson. The shapes of the transmission curves are compared semiquantitatively with predictions of the Spencer theory of electron penetration.

I. INTRODUCTION

THE author has previously reported an excess of electron backscattering over positron backscattering.[1-3] The question naturally arises as to whether, in view of their excess backscattering, electrons are transmitted to a lesser degree than positrons. As will be shown in this paper, a lower transmission of electrons is usually, but not always, observed.

The problem of the penetration of positrons and electrons in thick foils has not been calculated at the present time. Bothe[4] has made estimates of the backscattering of electrons using nonrelativistic single-scattering cross sections. Miller[5] used Bothe's results, substituting the relativistic cross sections obtained by Bartlett and Watson[6] and Massey[7] for electrons and positrons, respectively, to show that an excess of electron backscattering over positron backscattering is to be expected. Rohrlich and Carlson[8] have published the results of theoretical calculations of range and stopping power of positrons and electrons, providing a qualitative interpretation of the experimental results to be reported here.

Recently, a theory of electron penetration in infinite media has been developed by Spencer.[9] This theory does not quite apply to the present experiments because

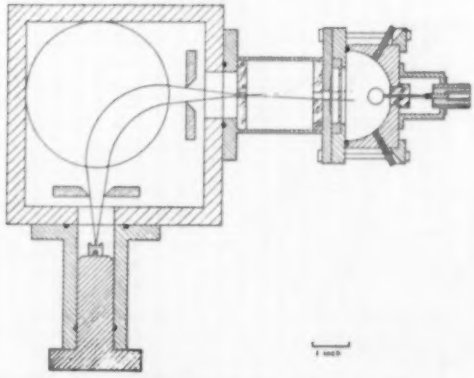

FIG. 1. Scale drawing of transmission geometry. The Lucite lining is not shown.

* This work was reported at the Washington, D. C., meeting of the American Physical Society in May, 1954 [H. H. Seliger, Phys. Rev. **95**, 610(A) (1954)].

† This paper is a portion of a thesis submitted in partial fulfillment of the requirements for the degree of Doctor of Philosophy at the University of Maryland.

[1] H. H. Seliger, Phys. Rev. **78**, 491 (1950).

[2] H. H. Seliger, Phys. Rev. **85**, 724 (1952).

[3] H. H. Seliger, Phys. Rev. **88**, 408 (1952); National Bureau of Standards Circular 527, March, 1954 (unpublished).

[4] W. Bothe, Ann. Physik **6**, 44 (1948).

[5] W. Miller, Phys. Rev. **82**, 452 (1951).

[6] J. H. Bartlett and T. A. Watson, Phys. Rev. **56**, 612 (1939); Proc. Am. Acad. Arts Sci. **74**, 53 (1940).

[7] H. S. W. Massey, Proc. Roy. Soc. (London) **A181**, 14 (1942).

[8] F. Rohrlich and B. C. Carlson, Phys. Rev. **93**, 38 (1954).

[9] L. V. Spencer, Phys. Rev. **98**, 1597 (1955).

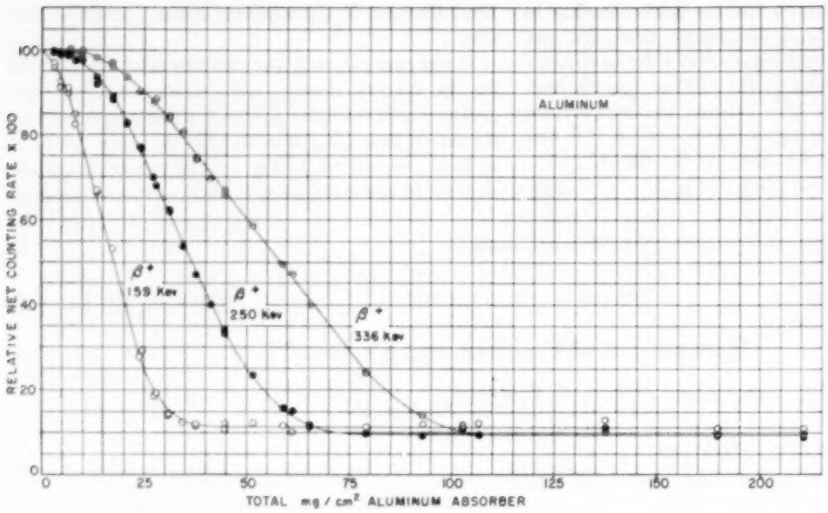

FIG. 2. Curves showing $N(x)/N(0)$ for positrons in aluminum.

it disregards the effect of transitions between the foil material and the surrounding gas. Nevertheless, it provides a frame for a semiquantitative analysis of the experimental data.

II. EXPERIMENTAL PROCEDURE

The purpose of the present experiments was to compare the transmissions of monoenergetic collimated beams of positrons and electrons. The only suitable long-lived positron emitter available was Na^{22}; this fact limited the range of electron energies used in the initial measurements. At energies lower than 150 kev, the attenuation was rapid, especially for higher-Z absorbers, and accuracy was therefore difficult to obtain. Data were therefore taken initially between 159 kev and 360 kev for both positrons and electrons. Subsequently, transmission measurements were made at 960 kev using 9-hour Ga^{66} and long-lived $Ce^{144}-Pr^{144}$ as sources of positrons and electrons, respectively.

In view of the large backscattering differences previously observed, a momentum resolution of 5 percent was assumed to be adequate to demonstrate any transmission differences. A 90-degree magnetic analyzer was designed, based on improvements suggested by

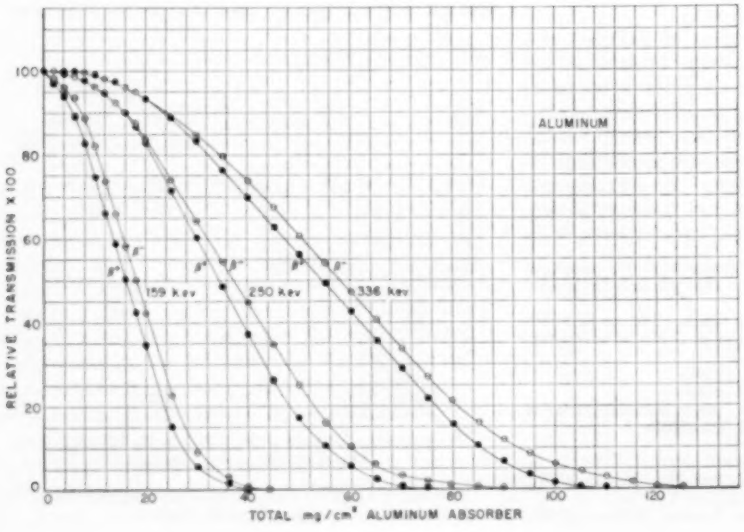

FIG. 3. Relative transmissions of positrons and electrons in aluminum.

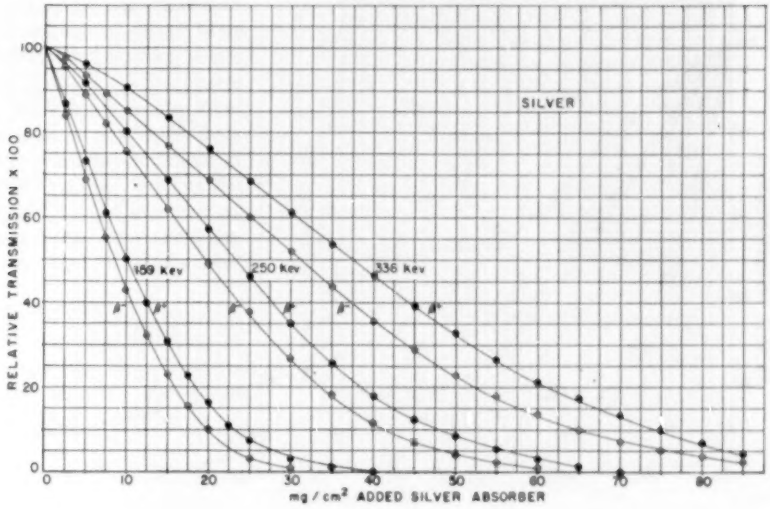

FIG. 4. Relative transmissions of positrons and electrons in silver.

Kerwin[10] and Hintenberger.[11] Second-order focusing conditions in the median plane were obtained with circular pole faces of only 10 centimeters diameter. All inside surfaces of the analyzer chamber were lined with $\frac{3}{16}$-in. Lucite to minimize scattering. The analyzer beam was collimated into a cone of half-angle 2 degrees whose central axis impinged perpendicularly on the face of an absorber which formed the window of a 2π absolute beta counter. All particles emerging from the opposite face of the absorber were detected regardless of energy loss down to an energy of a few hundred electron volts. The techniques of absolute beta counting which made the experiments feasible have been described previously.[12,13]

Figure 1 is a top-view scale drawing of the experimental arrangement showing source, pole faces, particle trajectories, collimating holes, and the 2π counter in position.

The absorbers were introduced into the beam by means of a sliding window assembly. The 2π counter

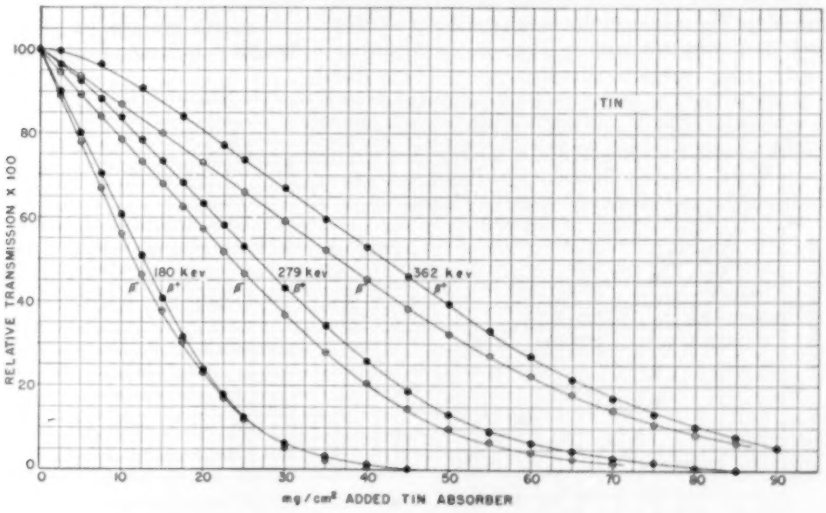

FIG. 5. Relative transmissions of positrons and electrons in tin.

[10] L. Kerwin, Rev. Sci. Instr. **20**, 36, 381 (1949).
[11] H. Hintenberger, Rev. Sci. Instr. **20**, 748 (1949).
[12] H. H. Seliger and L. Cavallo, J. Research Natl. Bur. Standards **47**, 41 (1951).
[13] W. B. Mann and H. H. Seliger, J. Research Natl. Bur. Standards **50**, 197 (1953).

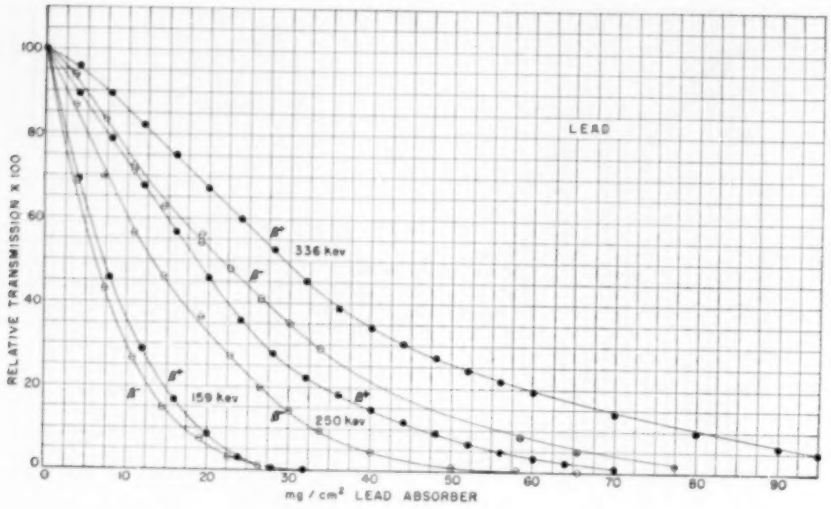

FIG. 6. Relative transmissions of positrons and electrons in lead.

was clamped on the outside of this assembly so that an absorber, placed in the path of the beam by sliding the window into position, formed the window of the 2π counter. The uniformity of the beam was verified by measuring the counting rate along the horizontal diameter of the exit hole, using a lead diaphragm with a 0.028-inch central hole.

The magnet constant-current control circuit was basically a voltage regulator. The current was read directly from a $\frac{1}{2}$ percent 0–300 milliampere meter.

The magnetic fields for both positrons and electrons were calibrated with a synchronous-motor rotating-coil assembly. The output of the rotating coil was rectified and then measured with a Type K potentiometer. In the course of the experiments, the magnet coil currents were varied from 52 milliamperes to 152 milliamperes. All currents were obtained from zero in a positive direction. The momentum calibration was obtained from the $H\rho = 3367$ gauss-cm conversion line of Ba^{137}.

The exit port of the spectrometer was sealed by a 1.8-mg/cm² aluminum foil. A pressure of the order of 0.1 micron was maintained for all measurements.

Thin films of aluminum and thicker films of brass and gold were available. For silver, tin, and lead, it was necessary to prepare thin films of the order of 1 mg/cm² by vacuum evaporation. The techniques used are thought to warrant a brief description.

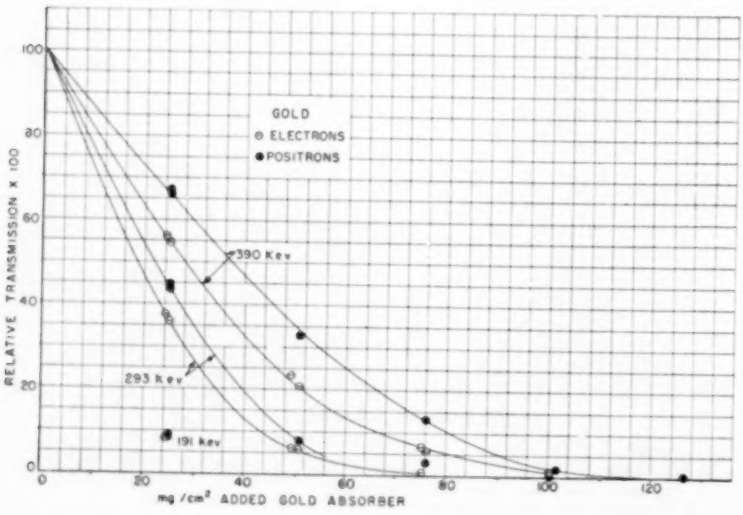

FIG. 7. Relative transmissions of positrons and electrons in gold.

The direct evaporation of the metal films onto thin (5–10 micrograms per square centimeter) plastic films was not too successful because of the formation of pin holes, owing to minute dust particles on the plastic film during drying causing weak spots in the film. Uniform lead films could be floated off onto water from the surfaces of clean microscope slides on which sodium chloride had previously been vacuum evaporated. These films could then be picked up and mounted on aluminum-disk absorber mounts. The above technique was possible because the thin lead films remained ductile.

The silver films were brittle and did not respond to the sodium chloride technique. The water, in lifting up part of the film, cracked and split the film. However, if silver is evaporated directly onto the grease-free surface of blued spring steel, films of the order of

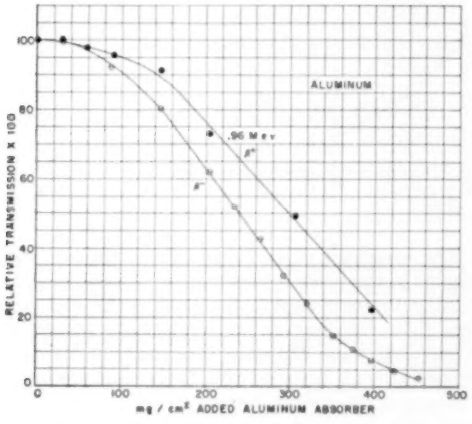

FIG. 8. Relative transmissions of 960-kev positrons and electrons in aluminum.

1 in.×1 in. can be peeled off the surface of the steel by gentle flexing under water.

In the case of tin, it appeared that some lead was always present. Owing to the lower melting point of lead relative to tin, the thin tin films probably had a much higher percentage of lead than the original tin foil used as the evaporating source.

Cs^{137} and Ce^{144}–Pr^{144} were used as sources of electrons and Na^{22} and Ga^{66} were used as sources of positrons. The sources were prepared by evaporation in air directly onto a cupped source mount. Activities of the order of 1–2 millicuries were necessary. All nuclides, with the exception of Ga^{66}, were obtained from the Oak Ridge National Laboratory. The Ga^{66} was prepared by a $Cu^{63}(\alpha,n)Ga^{66}$ reaction in the cyclotron of the Carnegie Institute of Washington. The chemical separation of gallium was made with ethyl ether.

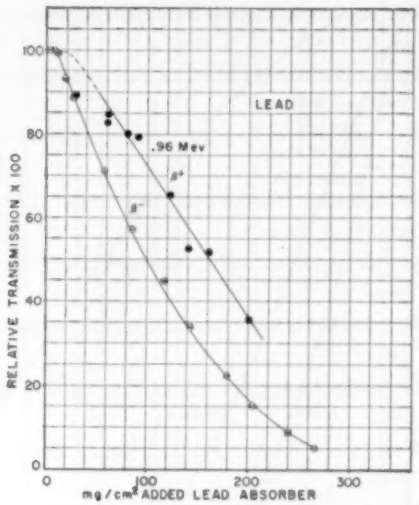

FIG. 9. Relative transmissions of 960-kev positrons and electrons in lead.

III. MEASUREMENTS AND RESULTS

The transmissions of positrons and electrons were measured for discrete energies ranging from 159 kev to 960 kev. The sequence of measurement was as follows:

1. The absorber was placed in position in front of the 2π counter and a number of readings of counting rate were taken for zero magnetic field ($I=0$). Owing to the low transmission of the analyzer and the use of Lucite to minimize scattering, the net counting rate in the 2π counter for $I=0$ was the same as for fields sufficiently high to deflect all particles past the exit hole ($I=\infty$). These readings at $I=0$ constituted the background for the particular absorber used. This point is important, for an absorber in front of the 2π counter in the presence of gamma rays acts as a radiator. The background, as expected, increased slightly with thickness of absorber and with Z.

2. The magnetic field was increased from zero to the

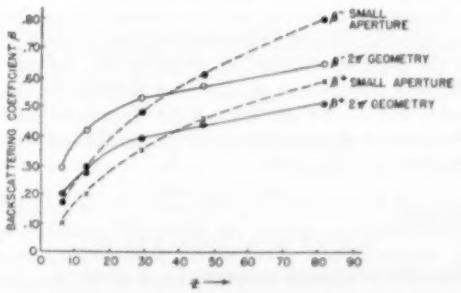

FIG. 10. Backscattering coefficients for positrons and electrons as functions of Z, measured with 2π geometry (solid curves) and with low geometry (dashed curves).

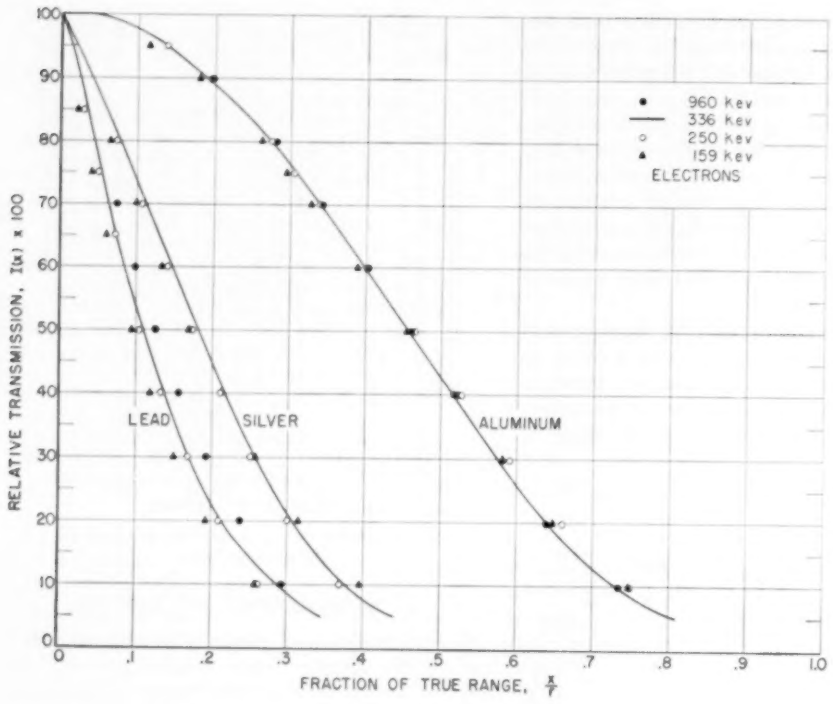

FIG. 11. Transmissions of electrons in aluminum, silver, and lead as functions of the fractional true range.

appropriate value and readings of counting rate were obtained.

The magnetic field was then increased for the next energy under consideration and a like set of readings was obtained.

3. Steps 1 and 2 were repeated for absorbers of different Z varying in thickness from 1 mg/cm² to 500 milligrams per square centimeter, depending on the beam energy.

The relative transmission of electrons is defined by

$$T_{\beta^-}=N(x)/N(0), \tag{1}$$

where $N(x)$ is the net observed counting rate for given absorber of thickness x and $N(0)$ is the net observed counting rate at "zero added absorber."

Equation (1) is not entirely correct for positrons because of annihilation radiation from positrons stopped in the absorber window. If $N'(x)$ is the number of positrons transmitted per unit time through the thickness x and $\epsilon_{\gamma a}$ the efficiency of the 2π counter for the detection of annihilation radiation originating at the absorber and defined by

$$\epsilon_{\gamma a}=N(\infty)/N(0), \tag{2}$$

we have

$$N(x)=N'(x)+[N(0)-N'(x)]\epsilon_{\gamma a}. \tag{3}$$

Thus, the relative transmission T_{β^+} is given by

$$T_{\beta^+}=\frac{N'(x)}{N(0)}=\frac{N(x)-N(\infty)}{N(0)-N(\infty)}=\frac{[N(x)/N(0)]-\epsilon_{\gamma a}}{1-\epsilon_{\gamma}}. \tag{4}$$

The magnitude of $\epsilon_{\gamma a}$ in the case of positron transmission in aluminum is shown in Fig. 2 where the ratios $N(x)/N(0)$ are plotted as functions of absorber thickness. The flat portions at ordinate 10 percent are $N(\infty)/N(0)=\epsilon_{\gamma a}$. The same data corrected for $\epsilon_{\gamma a}$ are shown in Fig. 3, together with T_{β^-} for electrons having the same initial energy. Similar transmission curves for silver, tin, lead, and gold are shown in Figs. 4, 5, 6, and 7, respectively.

Brass was used to observe the transmission trend in the intermediate region of atomic number. For thicknesses of 22.0 mg/cm² and 43.8 mg/cm², positron transmission exceeded electron transmission at all energies.

Transmission curves were also measured in aluminum and in lead at 960 kev and are shown in Figs. 8 and 9, respectively. In this case Ga^{66} was the positron source and $Ce^{144}-Pr^{144}$ was the electron source.

IV. DISCUSSION

In the absence of knowledge of any differences in positron-electron stopping-power, one assumes that electrons, being backscattered to a greater degree than positrons, are transmitted to a lesser degree. Any reversal of this trend should be explained on the basis of stopping-power differences. Thus, the results of Fig. 3 for aluminum imply a larger stopping power for positrons than for electrons.

The excess of electron backscattering over positron backscattering observed in the previous experiments

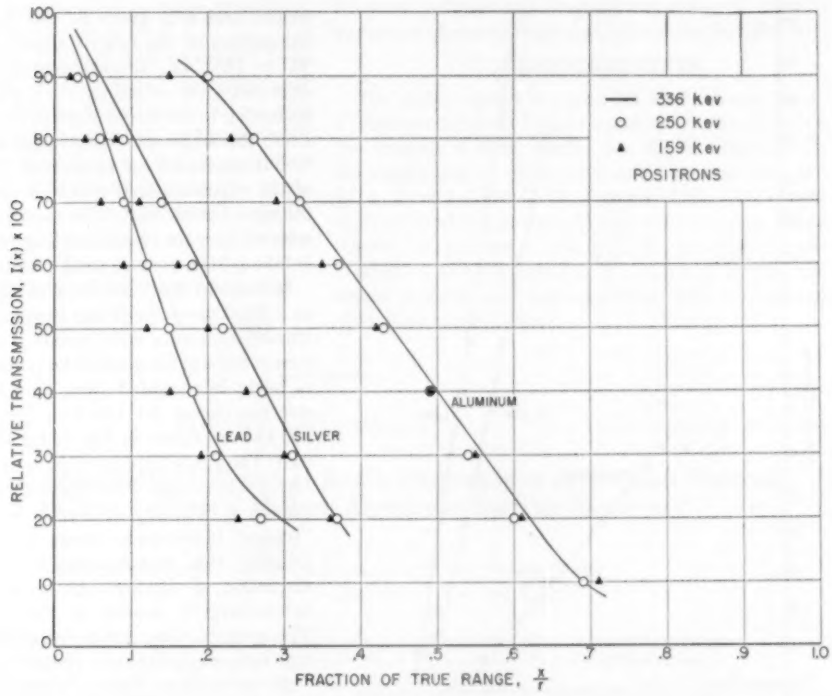

FIG. 12. Transmissions of positrons in aluminum, silver, and lead as functions of the fractional true range.

was explained on the basis of the cumulative effect in multiple scattering of the larger electron single-scattering cross sections. The experimental ratio of electron backscattering to positron backscattering, β^-/β^+, of 1.3 is in qualitative agreement with Miller's calculations. However, on the basis of scattering alone, β^-/β^+ should approach unity at low Z. That such is not the case is evident from the solid curves of Fig. 10, where β^-/β^+ for aluminum is even greater than for lead. This would attribute the large excess of electron backscattering at low Z to a greater stopping of positrons rather than to an excess scattering of electrons.

From the transmission data in aluminum given in Figs. 3 and 8, it follows that a cross over in transmission between positrons and electrons occurs between 336 kev and 960 kev. In all other cases studied the transmission of electrons was lower than that of positrons.

Rohrlich and Carlson[8] have calculated positron-electron differences in energy loss and in multiple scattering in aluminum, tin, and lead, using the correct elastic and inelastic scattering cross sections. They find that, below 350-kev, positrons lose energy at a faster rate than electrons. This, coupled with the fact that at low Z the scattering of electrons is only very slightly greater than that of positrons, implies that at low energy and for low Z it is possible for a greater stopping power for positrons to overshadow a small excess scattering of electrons. At higher Z, the excess scattering (proportional to Z^2) overcomes any energy-loss differences. For energies above 345 kev, the stopping power for positrons becomes *smaller* than for electrons and works *with* the excess scattering of electrons to make positron transmission greater than electron transmission.

The multiple-scattering effect can be evaluated in terms of $\langle\cos\theta\rangle_{Av}$, the average obliquity of the electron trajectories at a path length s after entrance into the medium. This is given by

$$\langle\cos\theta\rangle_{Av}=\exp\left[-2\pi N\int_0^s ds'\int_{-1}^{1}\sigma(\theta,s')\times(1-\cos\theta)d(\cos\theta)\right]. \quad (5)$$

A distance of penetration z_d at which the particles have lost their initial orientation can be defined by the condition $\langle\cos\theta\rangle_{Av}=1/e$, that is,

$$2\pi N\int_0^{z_d} ds'\int_{-1}^{1}\sigma(\theta,s')(1-\cos\theta)d(\cos\theta)=1. \quad (6)$$

Rohrlich and Carlson use z_d as an index of the ability to penetrate. The larger the value of z_d, the farther the particles penetrate before being turned around and diffused. For an initial energy of 358 kev, $z_d^+/z_d^-=1.04$ for aluminum and $z_d^+/z_d^-=1.35$ for lead. The present experimental results also show the increase of the ratio of positron transmission to electron transmission with

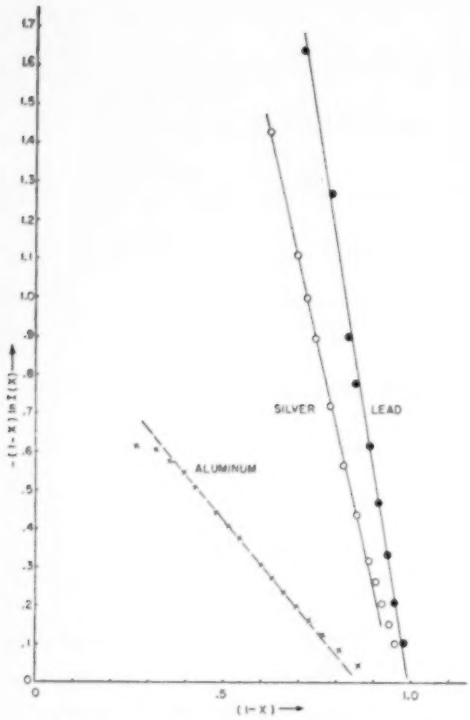

FIG. 13. The function $(1-x)\ln I(x)$ plotted against $(1-x)$ for aluminum, silver, and lead.

increasing atomic number. The fact that at 100 kev Rohrlich and Carlson find $z_d^+/z_d^-=1.01$ in aluminum while the experimental results show a greater electron transmission casts some doubt on the usefulness of z_d as an index of the transmission.

There are some further points that can be made regarding the shapes of the transmission curves. These concern (a) the effect of single scattering on the initial slope of the transmission curve, (b) the constancy of the shape of the transmission curves as functions of x/r_0 = absorber thickness/true range, and (c) the comparison of the transmission curves at deep penetrations with the predictions of the Spencer theory for infinite media.

The Rutherford single-scattering cross section modified for screening, inelastic collisions, and relativistic effects is given as

$$2\pi\sigma[r(T),\theta]=\tfrac{1}{4}(Z+1)\left(N_A\phi_0\frac{Z}{A}\right)\times\left[\frac{T+1}{T(T+2)}\right]^2(1+2\eta-\cos\theta)^{-2}, \quad (6)$$

where N_A is Avogadro's number, A is the atomic weight and η is given by the formula of Molière.[14] Integration of the single-scattering cross section from 90° to 180°, i.e., single scattering out of the forward direction, gives an estimate of the contribution of single scattering to the initial slope of the transmission curve. From this single-scattering initial slope, a thickness for 0.99 transmission can be derived. Table I is a summary of the experimentally observed transmissions at these calculated thicknesses. The departures from 0.99 transmission show the extent to which the multiple scattering is taking hold, even at small penetration thicknesses.

In order to study the shape of the transmission curves as a function of the initial energy of the electrons, the transmission data were replotted with absorber thickness in units of fractional true range x/r_0, the true range r_0 being interpolated from data in reference 9. The electron curves for 159 kev, 250 kev, 336 kev, and 960 kev are shown in Fig. 11 for aluminum, silver, and lead. The shape appears to be nearly a constant for the 150–350 kev range. The constancy of shape with energy implies a balancing of energy loss and scattering or "scaling" in this energy range. It was just this "scaling" property that was *assumed* in order to simplify the discussion of the previous backscattering results for heteroenergetic sources of electrons and positrons.[15] The corresponding curves for positrons, using positron true ranges calculated by Nelms,[16] are shown in Fig. 12.

In the Spencer theory, which neglects range straggling, the flux of electrons at deep penetrations has the form

$$I(x)=C(1-x)^{-\xi}e^{-A/(1-x)}, \quad (7)$$

where A is a function of source energy and scattering material, ξ is a constant, [equal to $\frac{3}{2}$] and x is the fraction of the true range traversed. In Fig. 13, the quantity $(1-x)\ln I(x)$ is plotted as a function of $(1-x)$ for electrons in aluminum, silver, and lead. Because of the "scaling" property, only one energy needed to be considered for each absorbing material. The curves can be approximated by straight lines over a large portion of their range, in qualitative agreement with the Spencer theory with $\xi=0$. The deviation at small absorber thicknesses in aluminum is due to the fact that the theory is an asymptotic one and the tail at large ab-

TABLE I. Experimentally observed transmissions at thicknesses calculated for 0.99 transmission based on single scattering.

	Aluminum		Silver		Lead	
Electron energy (kev)	Calc thickness for 0.99 trans. mg/cm²	Observed transmission	Calc thickness for 0.99 trans. mg/cm²	Observed transmission	Calc thickness for 0.99 trans. mg/cm²	Observed transmission
159	3.2	0.98	0.98	0.94	0.62	0.93
250	7.1	0.98	2.2	0.96	1.4	0.94
336	11.8	0.98	3.6	0.96	2.3	0.96

[14] G. Molière, Z. Naturforsch. **2a**, 133 (1947).
[15] C. H. Blanchard and U. Fano, Phys. Rev. **82**, 767 (1951).
[16] A. T. Nelms (private communication).

sorber thicknesses is probably due to range straggling, which has been neglected in the theory.

The present data are in qualitative agreement with the results of Bascova and Dzhelepov,[17] who measured a higher positron to electron transmission in lead and with the measurements of Chang, Cook, and Primakoff[18] on positron-electron transmission through a 10.16-mg/cm² platinum end-window G-M counter. The latter workers made measurements in aluminum only at 10.83 mg/cm² and no significant transmission difference between positrons and electrons was observed. Thicker aluminum absorbers might have shown up the difference.

[17] K. A. Bascova and B. S. Dzhelepov, Doklady Akad. Nauk. (S.S.S.R.) **77**, 1001 (1951).
[18] Chang, Cook, and Primakoff, Phys. Rev. **90**, 544 (1953).

V. ACKNOWLEDGMENTS

The author wishes to thank Dr. U. Fano and Dr. L. V. Spencer for their helpful suggestions and advice on the analysis of these results, Dr. R. W. Hayward for his suggestions on the experimental arrangement, Dr. M. A. Tuve and Dr. G. M. Temmer of the Department of Terrestrial Magnetism, Carnegie Institute of Washington, for the use of the D.T.M. cyclotron for the production of Ga^{66}, and Dr. W. B. Mann for his continued interest and encouragement both during and after these experiments.

PHYSICAL REVIEW VOLUME 100, NUMBER 4 NOVEMBER 15, 1955

Interaction of Electromagnetic Waves of Radio-Frequency in Isothermal Plasmas: Collision Cross Section of Helium Atoms and Ions for Electrons*

J. M. ANDERSON AND L. GOLDSTEIN
Department of Electrical Engineering, University of Illinois, Urbana, Illinois
(Received April 12, 1955; revised manuscript received June 2, 1955)

The elements of the theory of interaction of radio-frequency electromagnetic waves in gaseous discharge plasmas are reviewed. The applicability of this phenomenon of wave interaction to the measurement of quantities involved in fundamental processes in such plasmas is considered.

A measurement of the "effective" electron-atom collision frequency in helium, found to be 3.12×10^8/sec/mmHg for room temperature electrons (~300°K), gives a value for the probability of collision for momentum transfer, P_m, of the helium atom equal to 24.0 cm²/cm² at 0°C and 1 mm Hg.

An experimental determination of the "effective" electron-ion collision frequency (for singly charged ions) has also been determined which closely agrees with earlier theoretical predictions. The ratio of the effective cross sections, associated with electron collisions, of ions and helium atoms in the room temperature isothermal plasma is $\sim3.0\times10^8$ at an ion density of 10^{11}/cm³.

INTRODUCTION

IT has been known for some time[1] that when two low- or medium-frequency radio waves traverse a common region of the ionosphere, and one of the waves is of sufficient strength, an interaction between the two electromagnetic waves is observed. When the stronger wave is amplitude modulated, there is a measurable transfer of modulation from the stronger wave to the carrier of the weaker. Bailey and Martyn[2] proposed a theory for this phenomenon of "ionospheric cross-modulation."

According to this theory, absorption of the interfering waves increases the mean energy of the electrons in the appropriate region of the ionosphere. This increased mean energy of the electrons leads to a change in the collision frequency of the electrons. As the absorption of an electromagnetic wave in a region of the ionosphere is determined, in part, by the collision frequency of the electrons in that region, the absorption of the "wanted" wave is modified by the presence of the absorbed "disturbing" wave. Bailey[3] later extended this theory by considering the effect of the earth's magnetic field. According to this more complete theory, an enhancement of transfered modulation at radio-frequencies corresponding to the gyrofrequency of the electrons was predicted which has since been observed experimentally.[4,5]

We have recently[6] described experiments of interaction between microwaves, which are simultaneously propagated in gaseous discharge plasmas. These controllable laboratory experiments offer a method of more general exploration of the fundamental processes involved in these phenomena. The purpose of this paper is then twofold: First to describe the experimental techniques relative to the method, and second, to

* This work was supported by Air Force Cambridge Research Center.
[1] B. D. H. Tellegen, Nature **131**, 840 (1933).
[2] V. A. Bailey and D. F. Martyn, Phil. Mag. **18**, 369 (1934).
[3] V. A. Bailey, Phil. Mag. **23**, 774 (1937).
[4] M. Cutolo, Nature **166**, 98 (1950).
[5] Bailey, Smith, Landecker, Higgs, and Hibberd, Nature **169**, 911 (1952).
[6] Goldstein, Anderson, and Clark, Phys. Rev. **90**, 151 (1953); and **90**, 486 (1953).

report experimental results obtained in the study of collisional processes in helium.

THEORY

As has been mentioned, the processes of interaction involve absorption of radio-frequency energy in the propagating medium. Consequently, in describing wave interaction phenomena in gaseous discharge plasmas, let us consider the mechanism of energy absorption. If the medium is isotropic and the electric field has a time dependence $\sim E_0' e^{i\omega t}$, then the total rate at which power is dissipated is

$$P_L = \int_V \frac{|E_0'|^2}{2} \sigma_r dV, \tag{1}$$

where σ_r is the real part of the complex conductivity, σ. For the case of a medium containing free electrons in a gas of heavier molecules and ions, experience and theory have shown that there is little error introduced by using a functional form of σ, as

$$\sigma = \sigma_{\text{real}} + i\sigma_{\text{imag}} = \frac{n_e e^2}{m}\left[\frac{\nu - i\omega}{\omega^2 + \nu^2}\right], \tag{2}$$

where n_e is the electron number density, e and m are the electronic charge and mass, respectively, and ν is the "effective" electron collision frequency with other heavier constituents of the gas.

The more exact expression for conductivity in an ionized gas is given by Margenau[7] and Ginsburg[8] for the case of a Maxwellian distribution of electron velocities as

$$\sigma = \frac{8}{3\sqrt{\pi}} \frac{e^2 n_e}{m}\left[\int_0^\infty \frac{\nu(u) u^4 \exp(-u^2) du}{\omega^2 + \nu^2(u)} - i\omega \int_0^\infty \frac{u^4 \exp(-u^2) du}{\omega^2 + \nu^2(u)}\right], \tag{3}$$

where $u = (m/2kT_e)^{\frac{1}{2}} v$, v is the electron velocity, k is Boltzmann's constant, and T_e is the "temperature" of the electron gas. If expressions (2) and (3) are equated under the condition that $\nu^2 \ll \omega^2$, a value of "effective" electron collision frequency to employ in Eq. (2) is obtained as

$$\nu \cong \frac{8}{3\sqrt{\pi}} \int_0^\infty \nu(u) u^4 \exp(-u^2) du. \tag{4}$$

For the low frequency and direct current case, $\omega^2 \ll \nu^2$, the equating of (2) and (3) demands the defining of the effective electron collision frequency as

$$\frac{1}{\nu} \cong \frac{8}{3\sqrt{\pi}} \int_0^\infty \frac{u^4 \exp(-u^2) du}{\nu(u)}. \tag{5}$$

We then have, for the high-frequency case ($\nu^2 \ll \omega^2$),

$$P_L = \frac{|E_0'|^2}{2} \frac{e^2 n_e}{m} \frac{\nu}{\omega^2} \tag{6}$$

per unit volume. In this volume, however, there are n_e electrons on the average and therefore the energy per unit time supplied to each electron is

$$P_1 = \frac{1}{2} \frac{e^2}{m} \frac{\nu}{\omega^2} |E_0'|^2. \tag{7}$$

While energy is gained by the electrons from the impressed electric field, they lose energy through collisions with the heavier gas molecules and ions. In general, it may be said that the mean fractional energy, λ, lost by an electron upon collision with a molecule is[9]

$$\lambda = G\left(1 - \frac{Q_m}{Q_e}\right), \tag{8}$$

where Q_m and Q_e are the mean agitational energies of the molecules and electrons, respectively, and G is a factor of proportionality. When a collision is elastic G is independent of the velocity of the electron and is then $\sim 2m/M$, where M is the mass of the molecule. For the sake of illustration, G for helium is $\sim 2.7 \times 10^{-4}$. For the isothermal electrical discharge plasma, equipartition of energy requires that $Q_e = Q_m$. While a Maxwellian distribution of velocities is assured for the molecules and ions, it can be assumed with some degree of confidence in what follows that the electrons in these experiments possess also, at all times, this same distribution of velocities.[10] If for any reason a change from this distribution is accomplished momentarily, it will be assumed that the return to the Maxwellian distribution takes place in a time interval much shorter than the smallest average interval of time to be observed in our experiment, namely, $\sim$0.05 microsecond. The maintenance of a Maxwellian distribution of electron velocities is accountable primarily to the electron-electron interaction at the electron densities used in our experiments.

A balance of power for the average electron, in the case where electron-ion interaction is negligible, may now be written

$$dQ_e/dt + G\nu(Q_e - Q_m) = P_1, \tag{9}$$

where G and ν pertain to electron-molecule collisions.

[7] H. Margenau, Phys. Rev. **69**, 508 (1946).
[8] V. L. Ginsburg, J. Phys. (U.S.S.R.) **8**, 253 (1944).
[9] Sir John Townsend, *Electrons in Gases* (Hutchinson's Publications, London, 1947), Chap. III.
[10] J. H. Cahn, Phys. Rev. **75**, 838 (1949).

An explicit solution in time cannot be given for this equation until a relationship giving the dependence of ν upon Q_e is known (either obtained from experiment or postulated). G may also possess dependence upon Q_e. To proceed, it will be assumed initially that the probability of collision of electrons with the molecules is independent of velocity. In helium and for electrons with energies below ~ 2 ev, this is a good approximation.[11] The "effective" collision frequency, with the aid of (4), becomes

$$\nu_m = (4/3) q_m N_m \bar{v}, \tag{10}$$

where q_m is the effective cross-sectional area of the molecule, N_m is the molecular density, and $\bar{v} = (8kT_e/\pi m)^{\frac{1}{2}}$, which is the arithmetic mean velocity of the electrons. One neglects, in general, the motion of the molecules. The cross-sectional area, q_m, is related to the probability of collision for momentum transfer, P_m, by $q_m N_m = P_m p_0$, where p_0 is the pressure normalized to 1 mm Hg pressure and 0°C.

From (7), (9), and (10) the time variation of ν may be obtained when a constant electric field, E, is suddenly applied to the plasma (the subscript m pertaining to molecules is temporarily dropped):

$$\nu(t) = \nu' \left[\left(\frac{\nu' + \nu_0}{\nu' - \nu_0} \right) e^{G\nu' t} - 1 \right] \Big/ \left[\left(\frac{\nu' + \nu_0}{\nu' - \nu_0} \right) e^{G\nu' t} + 1 \right], \tag{11}$$

where ν_0 is the initial undisturbed value of ν, and ν' is the final steady state value of ν, after the field has been applied for a time sufficient to reach steady-state conditions;

$$\nu' = \left\{ \nu_0^2 + \left[\frac{16 q_m N_m}{3(3\pi)^{\frac{1}{2}}} \right] \frac{e^2}{Gm\omega^2} |E_0'|^2 \right\}^{\frac{1}{2}}. \tag{12}$$

ν' obtains when the rate at which energy lost by the collisional contact of electrons with molecules equals the rate at which energy is received from the field. The increase or "rise" of ν to approach ν' requires a lapse of time, but no simple time constant may be associated. If the field is suddenly removed, we have for the "fall" of ν, back to the value ν_0,

$$\nu(t) = \nu_0 \left[\left(\frac{\nu' + \nu_0}{\nu' - \nu_0} \right) e^{G\nu_0 t} + 1 \right] \Big/ \left[\left(\frac{\nu' + \nu_0}{\nu' - \nu_0} \right) e^{G\nu_0 t} - 1 \right]. \tag{13}$$

Again no simple time constant applies. However, if the difference $(\nu' - \nu_0)$ is made quite small, for example, by reducing the amplitude of E', Eq. (13) approaches

$$(\nu - \nu_0)/(\nu' - \nu_0) \sim e^{-G\nu_0 t}. \tag{14}$$

The same can be shown for the "rise" of ν. The condition $\nu'/\nu_0 \sim 1$ is quite important experimentally, since direct measurement of the relaxation time constant $\tau = 1/G\nu$ yields the collision frequency ν, if G is known, or *vice versa*. The theory of wave interaction applicable to the ionosphere may be expressed in a convenient approximate form (under the condition $\nu'/\nu_0 \sim 1$) since, to date, the amplitude of field strength applied to the ionosphere is necessarily small, even with the most powerful radio transmitters.

From the foregoing, it is seen that an electric field of sufficient amplitude can alter the electron collision frequency in an ionized medium and therefore modify its complex conductivity. If a second wave of low amplitude and appropriate frequency propagates in this "disturbed" region, the dissipative loss suffered by this wave is proportional to the altered conductivity caused by the first "disturbing" wave. Therefore, if the disturbing wave is amplitude modulated at a rate sufficiently low to allow the electron temperature to follow the field variation, some degree of amplitude modulation is impressed on the second wave. The second wave (sometimes referred to in ionospheric research as the "wanted wave") acts, then, much as a probe to determine the extent of alteration of the medium properties. Experimentally, the phenomenon of wave interaction provides a useful research tool, especially to determine the relaxation of the medium properties in the wake of the disturbing wave. It should be remarked that the disturbing wave also suffers a form of self-distortion or self-modulation.

The method of wave interaction leads by appropriate measurements to a determination of

(a) the product of $G\nu$ in the isothermal or nonisothermal plasma;

(b) the variation of the effective collision frequency as a function of electron mean energy and hence indirectly to the probability of electron collision for momentum transfer with molecules or ions. This method complements the swarm method of Townsend and the beam method of Ramsauer, in that extremely low electron energies may be considered (~ 0.005 ev). Preliminary cross-section measurements[12] in gases possessing the "Ramsauer effect" have been reported by us and more complete work will be reported at a later date;

(c) the variation of the electron density in the essentially isothermal plasma, as a result of the controlled temperature rise of the electrons in the presence of the disturbing field. The conductivity, Eq. (2), depends upon n_e as well as ν. By proper choice of conditions, changes in either ν or n_e may be emphasized;

(d) the effect of application of a magnetic field to the plasma (magneto-ionic effects, "gyro-interaction");

(e) the electron temperature dependence of the

[11] L. Gould and S. C. Brown, Phys. Rev. **95**, 897 (1954); C. Ramsauer and R. Kollath, Ann. Physik **395**, 536 (1929).

[12] L. Goldstein and J. M. Anderson, "Interaction of Microwaves in Gaseous Discharge Plasmas and the Ramsauer Effect," reported in the published record of the Fourteenth Annual Conference on Physical Electronics, Massachusetts Institute of Technology, March, 1954.

electron-molecule attachment process in electronegative gases;

(f) the interaction of free electrons with positive or negative ions of the plasma, and indirectly to a study of the positive ion-electron recombination process.[12]

The above listed measurements may be complemented and summarized by stating that microwave cross-modulation techniques permit the study of phenomena which are associated with the controlled variation of electron density and effective electron collision frequency brought about by a disturbing field, without the objectionable transients associated with direct measurements on the high amplitude field. It further permits the study of relaxation effects of the plasma in the wake of a disturbing field.

EXPERIMENTAL SETUP

Low-amplitude guided microwaves in the X-band ($\sim$9000 Mc/sec) play the role, for our experiment, of the "disturbing" and "wanted" waves and are propagated in the isothermal plasma which obtains in the afterglow of a pulsed dc discharge. Gases which have been used are the rare gases and molecular gases such as hydrogen and nitrogen. The discharge plasma is contained in a 152-cm long, $a'=1.85$-cm inside diameter, thin-wall Pyrex, cylindrical discharge tube, located coaxially in a square brass wave guide with inside dimensions of $a=2.07$ cm on a side. The discharge is formed by application of a high-voltage dc two-microsecond-duration pulse to a hot cathode and anode external to the wave guide, at a repetition frequency of 25 pulses per second. This gives an afterglow period of $\sim$40 000 microseconds. At appropriate delayed times in this afterglow, with respect to the discharge pulse, the microwave signals are propagated. For our immediate purposes, the disturbing wave is a 1- to 100-microsecond duration square pulse (0.05-microsecond rise time) of microwave energy at a frequency of 8600 Mc/sec. The wanted wave, lower in power level by, at least, $\sim$20 db, is a continuous wave at 9400 Mc/sec. Both microwaves are derived from Varian type X-13 klystrons having maximum output powers of $\sim\frac{1}{2}$ watt. For the above-mentioned frequencies the square wave guide limits propagation of the waves to the lowest mode, the TE_{10}, both waves being propagated in the same polarization. Measurement may be made on both transmitted and reflected signals, yielding total loss and phase shift introduced by the plasma with respect to no plasma (air guide) condition. Of particular importance is the appearance of the crystal-detected envelope of the transmitted wanted wave in the presence of, and in the wake of, the disturbing wave. By appropriate filters the direct pickup of the disturbing wave is effectively eliminated. It is assumed here that, for the short time intervals of application of the disturbing wave pulse, only the electron collision frequency changes, and the density changes due to normal diffusion and elevated temperatures are negligible. Wide-band amplifiers and a Tektronix 514 AD oscilloscope serve to display the detected envelope. A crystal-controlled timing generator supplies the 25-cps basic repetition frequency and also timing markers of high time-interval accuracy. Various other delay pulse generators for synchronizing are necessary but will not be described here. An abbreviated diagram of the experimental setup is shown in Fig. 1.

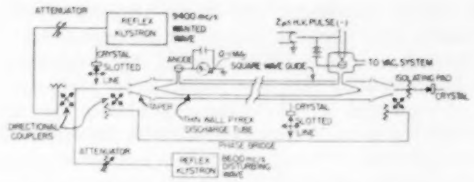

FIG. 1. Abbreviated schematic of experimental apparatus.

The spectroscopically pure gases used in the experiment are obtained from 1-liter bulbs supplied by Linde Air Products. Sufficient attention is given to maintenance of the impurity level in the gas to a negligible amount for the type of experiment reported here.

THEORY OF THE EXPERIMENT: MICROWAVE DETERMINATION OF ELECTRON DENSITY AND ELECTRON COLLISION FREQUENCY

The electron density and electron collision frequency for the case where the electron density uniformly fills the entire cross section of the wave guide can be calculated exactly[14] by a measurement of the total insertion loss and relative phase shift caused by the plasma in the wave guide. Here the wave equation describing propagation separates to give "modes" which are independent. For the case of the inhomogeneously filled guide, the modes are generally dependent (many modes are excited when an attempt is made to propagate a single mode) and a complete solution becomes extremely difficult to obtain and to use practically. Therefore, an approximate approach is employed. This amounts to assuming that the fundamental mode propagated in the air-filled wave guide is little disturbed in its propagation through the plasma except perhaps for a change only in the relative magnitude of the electric field strength, and in the guide wavelength. This dictates that the electric field distribution in the plasma is sinusoidal (TE_{10} mode) from wall to wall of the wave guide, a situation only approximately true for reasonably low electron densities (for our case, less than $\sim 5\times 10^{11}$ electrons/cc). The electron density calculated by phase shift measurements represents an average of the actual density, known to exist in an inhomogeneous manner. It is then necessary to assume, or measure by other techniques, the exact density distribution function. When such is done the peak elec-

[12] Goldstein, Anderson, and Clark, Phys. Rev. **90**, 486 (1953).

[14] Goldstein, Lampert, and Geiger, Elec. Commun., **243**, September, 1952.

tron density, neglecting dissipative loss, may be calculated in terms of the measurable guide wavelengths with and without the plasma present, by equating imaginary parts of the general expression,

$$\iint \sigma |E'|^2 dxdy \Big/ \iint |E'|^2 dxdy = \frac{1}{i\omega\mu_0}\left[\gamma^2+\left(\frac{2\pi}{\lambda_{g0}}\right)^2\right], \quad (15)$$

where E' is the field strength in the plasma-filled portion of wave guide, μ_0 is the permeability of free space, $\gamma=\alpha+j\beta_g$ is the measurable propagation constant in the plasma-filled portion of guide, consisting of an attenuation constant, α, and a phase constant $\beta_g = 2\pi/\lambda_g$, λ_g is the plasma-filled guide wavelength, and λ_{g0} is the air-filled guide wavelength. The transverse coordinates of the wave guide are x and y and propagation is in the z-direction along the guide. Here the electron density is contained in the imaginary part of the conductivity, σ_i. For the specific purpose of this paper, that is, afterglows established in helium, we will assume that the electron density decay in the afterglow is principally due to ambipolar diffusion which dictates that the density distribution is described by the zero-order Bessel function form for our cylindrical discharge tube. This Bessel function may be closely approximated in the interest of simplified calculations by a cosine distribution:

$$n_e = n_0 \cos(\pi x/a') \cos(\pi y/a'), \quad (16)$$

where n_0 is the peak density along the axis of the discharge tube, a' is the internal diameter of the tube, y is in the direction of height of the wave guide, x is in the direction of breadth of the guide, and the origin of coordinates is taken at the central axis of the guide. At important points of relatively high field, namely in the center of the guide, this approximation of distribution is quite good.

The total loss under the above assumptions may be found for the case of electron-molecule collision frequency by the volume integral

$$P_{L_m} = 4\int_0^{a'/2}\int_0^{a'/2}\int_0^{s}\frac{(E_0')^2}{2}\sigma_{r_{\max}{}^m} \times \cos^2\frac{\pi x}{a}\cos\frac{\pi x}{a'}\cos\frac{\pi y}{a'}e^{-2\alpha z}dxdydz, \quad (17)$$

where the field dependence along the propagation direction, z, is $E'\sim e^{-\alpha z}$ and $\sigma_{r_{\max}{}^m}$ is the maximum value of σ_r along the center of the discharge tube due to electron-molecule collisions.

For the case of effective electron collision frequency with charged particles of the plasma, in particular, with ions, ν_i,[15] most theoretical calculations may be reduced to the functional form

$$\nu_i = A\frac{n_i}{T_e^{\frac{3}{2}}}\ln\left[\frac{B}{n_i^{\frac{1}{2}}}T_e\left(\frac{2T_eT_i}{T_e+T_i}\right)^{\frac{1}{2}}\right], \quad (18)$$

where the Debye shielding radius,

$$\lambda_D = \left[\frac{k}{4\pi e^2 n_i}\frac{T_eT_i}{T_e+T_i}\right]^{\frac{1}{2}},$$

is taken as the maximum impact parameter in the evaluation of the otherwise divergent integrals. Only singly ionized ions are considered. Here T_i is the ion temperature, n_i is the ion number density per cc, and A and B are constants. For the plasma of our experiment $n_i=n_e$. The influence of limited variations of n_i in the logarithmic term of Eq. (18) on the variation of ν_i is negligible and ν_i may therefore be simplified, for $T_e=T_i=T_g=$constant, to

$$\nu_i \cong Cn_i, \quad (19)$$

where C is a constant. The effective electron-ion collision frequency then varies with position in the cross section of the wave guide due to the inhomogeneity of electron density. The total power loss due to electron-ion collisions is

$$P_{L_i} = 4\int_0^{a'/2}\int_0^{a'/2}\int_0^{s}\frac{(E_0')^2}{2}\sigma_{r_{\max}{}^i} \times \cos^2\frac{\pi x}{a'}\cos^2\frac{\pi y}{a'}\cos^2\frac{\pi x}{a}e^{-2\alpha z}dxdydz, \quad (20)$$

where

$$\sigma_{r_{\max}{}^i} = \frac{n_0e^2}{m\omega^2}\nu_{i\max} = \frac{n_0^2e^2}{m\omega^2}C.$$

Finally the integration of (17) and (20) for our experimental condition, $a'/a=1.85/2.07$, gives

$$P_{L_m}+P_{L_i} = (E_0')^2\frac{a^2}{\pi^2}\frac{1}{2\alpha}(1-e^{-2\alpha s}) \times [1.14\sigma_{r_{\max}{}^m}+0.765\sigma_{r_{\max}{}^i}]. \quad (21)$$

But, from the definition of insertion loss, and waveguide relations for power transmission, we have,

$$P_L = P_{\text{incident}}(1-e^{-2\alpha s}) = (E_0')^2\frac{a^2}{4}\frac{1}{\omega\mu_0}\left(\frac{2\pi}{\lambda_g}\right)(1-e^{-2\alpha s}). \quad (22)$$

Equating the two independent expressions for power

[15] ν_i is defined from a momentum transfer viewpoint. Electron-electron collisions are neglected since they do not contribute directly to electrical conductivity. Such collisions, however, may intervene in heat transfer considerations.

loss, Eq. (21) and Eq. (22), yields

$$\alpha=\frac{2\omega\mu_0}{\pi^2}\left(\frac{\lambda_g}{2\pi}\right)\frac{e^2n_0}{m\omega^2}[1.14\nu_{m_{max}}+0.765\nu_{i_{max}}], \quad (23)$$

where α and λ_g are measurables.

Returning now to the relation for the rate of energy loss and gain for the average electron, Eq. (9) may be written to include both electron-molecule and electron-ion collisions as

$$\frac{dQ_e}{dt}=\frac{3}{2}k\frac{dT_e}{dt}=\frac{1}{2}\frac{e^2}{m\omega^2}(E')^2(\nu_i+\nu_m)$$
$$-G_m\nu_m(Q_e-Q_m)-G_i\nu_i(Q_e-Q_i), \quad (24)$$

where G_i has the significance for electron-ion collisions defined by (8), and $G_m=2m/M$. The ionic mean energy, Q_i, is assumed $=Q_m=Q_0$ at all times. Immediately after the disturbing field is applied and sufficient time has not elapsed to permit appreciable alteration of the electron temperature, the difference (Q_e-Q_0) is of the order of zero. Therefore, the initial rate of change of the electron temperature is due directly to the prevailing (isothermal) total electron collision frequency and the square of the applied electric field,

$$\left.\frac{dT_e}{dt}\right|_{t=0}=\frac{e^2}{3km\omega^2}(E')^2(\nu_i+\nu_m). \quad (25)$$

Considering now the electron temperature dependence of the electron-molecule and electron-ion effective collision frequencies, the rate of change of collisions frequency as a function of time may be obtained by differentiation,

$$\frac{d\nu_m}{dt}=\tfrac{7}{3}q_mN_m\left(\frac{8k}{\pi m}\right)^{\frac{1}{2}}T_e^{-\frac{1}{2}}\frac{dT_e}{dt}, \quad (26)$$

$$\frac{d\nu_i}{dt}=-\frac{3}{2}\frac{An_i}{T_e^{5/2}}$$
$$\times\left\{\ln\left[\frac{BT_e}{n_i^{\frac{1}{2}}}\left(\frac{2T_eT_i}{T_e+T_i}\right)^{\frac{1}{2}}\right]-\frac{1}{3}\frac{T_e}{T_e+T_i}\right\}\frac{dT_e}{dt}. \quad (27)$$

Here q_m is considered constant with electron velocity. It will be noted that the rate of change of ν_i with T_e is negative and the rate of change of ν_m with T_e is positive. The rate of change of power loss in the plasma at the instant the disturbing field is applied is proportional to the rate at which the electron collision frequency is changing, provided the electron density remains essentially constant. Therefore, the following interesting possibility presents itself: At the instant the disturbing field is applied the experimental conditions may be adjusted until the initial rate of change of microwave energy loss in the plasma is zero. The zero rate of change of loss obtains for different conditions at different points in the wave-guide cross section, even though rapid heat transfer may occur in the electron gas.[16] However, when integration is performed over the cross section, a total rate of change of loss is obtained and set equal to zero. The attainment of this condition is observed by the adjustment of the rate of change of cross modulation to the wanted wave equal to zero at the time of introduction of the disturbing wave.

The effect of cross modulation in helium is shown by photographs of the oscilloscope presentation on Figs. 2(a) and 2(b). Here the detected incident-disturbing wave pulse of microwave energy at 8600 Mc/sec is shown as traces 1*b* of both Figs. 2(a) and 2(b), and is increasing in amplitude with downward deflection of the oscilloscope trace. The upper sine wave traces of each photo are 100-kc/sec timing waves. The disturbing 8600-Mc/sec pulse is therefore seen to be present for a time interval ~20 microseconds. The 9400-Mc/sec continuous wanted wave, transmitted through the plasma and crystal detected, is shown as traces 2*a* and 2*b* of both photos. Trace 2*a* is the transmitted wanted wave without the presence of the disturbing wave pulse and trace 2*b* shows the alteration of the transmitted wanted wave with simultaneous transmission of the higher

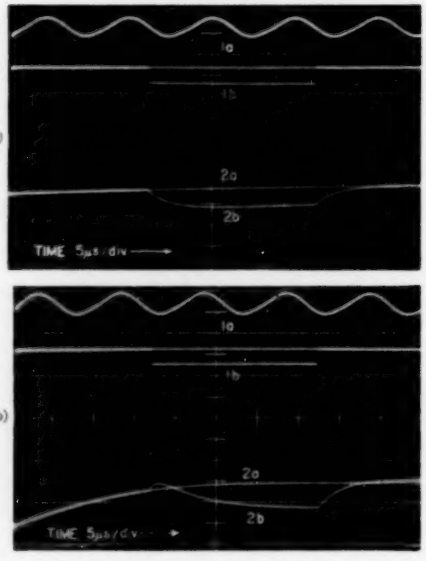

FIG. 2. Effect of wave interaction in the decaying plasma established in helium; (a) Influence of electron-molecule elastic collisions (pressure 4.36 mm Hg); (b) Influence of mixed electron-molecule and electron-ion elastic collisions (pressure 1.67 mm Hg). See text for description.

[16] Based on the calculations of L. Spitzer and R. Härm [Phys. Rev. **89**, 977 (1953)], heat transfer from electrons in the center of the wave guide outward takes place at a rate slower than the time element involved in these experiments. The correction due to this effect, which has been computed, is within the experimental error.

power level disturbing wave pulse. The amplitude of the transmitted wanted wave is increasing with upward deflection of the oscilloscope trace. It will be noted in Fig. 2(a), where the gas pressure is relatively high (4.36 mm Hg) and the influence of electron-ion collisions is negligible, that the effect upon the transmitted wanted wave in the presence of the disturbing wave is to *increase* attenuation. The time constant associated with the relaxation of the electron temperature to the isothermal plasma temperature in the wake of the disturbing wave pulse was measured from a considerably enlarged photo to be ~ 2.6 microseconds which implies an electron collision frequency with helium atoms $\sim 1.4\times 10^6$ sec^{-1} at 4.36 mm Hg. In Fig. 2(b), at a lower gas pressure (1.67 mm Hg), the attenuation of the wanted wave is seen to *decrease* momentarily with introduction of the disturbing wave pulse. As the electron temperature increases in the presence of the disturbing wave pulse the wanted wave is seen to be attenuated in a manner similar to Fig. 2(a). As the electron temperature returns to the gas temperature the transmitted wanted wave is seen to pass again through a region of decreased attenuation [extreme right of Fig. 2(b)]. The decreased attenuation upon introduction of the disturbing wave is presumed due to a decrease in the magnitude of electron-ion collision frequency with increasing electron temperature as indicated by Eq. (18).

Consistent with the conditions given above

$$\left.\frac{dP_L}{dt}\right|_{t=0} = 0 = 4\int_0^{a'/2}\int_0^{a'/2}\int_0^{z}\frac{(E_0')^2}{2} \times\cos^2\frac{\pi x}{a}\left(\left.\frac{d\nu_i}{dt}\right|_{t=0}+\left.\frac{d\nu_m}{dt}\right|_{t=0}\right)\frac{e^2 n_0}{m\omega^2} \times\cos\frac{\pi x}{a'}\cos\frac{\pi y}{a'}e^{-2\alpha z}dxdydz. \quad (28)$$

By using (26), (27), and (28) and integrating,[17] a working expression is obtained:

$$0.533\nu_m^2 - 0.770\nu_m n_0 C' T_e^{-\frac{1}{2}} - 0.915 C'^2 T_e^{-3} n_0^2 = 0, \quad (29)$$

where $C' = A[\ln(BT_e^{\frac{1}{2}}/n_i^{\frac{1}{2}}) - \frac{5}{2}]$, evaluated at time $t=0$, when $T_e = T_i$. Note that the attainment of this condition is independent of the magnitude of the field strength, E', and frequency, ω, of the disturbing wave or wanted wave employed, and therefore independent of position *along* the discharge tube. The set of two equations, (23) and (29) suffice to calculate the two unknown constants A and B, if ν_m is known and n_0 is obtained from Eq. (15). The value of ν_m for helium may be found by use of Eqs. (23) and (15) at sufficiently high gas pressures or low ion densities to make electron-ion collisions negligible. The value of ν_m may also be obtained from time-constant measurements, Eq. (14), with cross-modulation techniques, again at higher gas pressure or low ion densities. The value of G to use for helium is the classical value $= 2m/M$.[18]

[17] Here a' is replaced by a in the x-integration for ease of handling. This is not likely to introduce more than a few percent error.

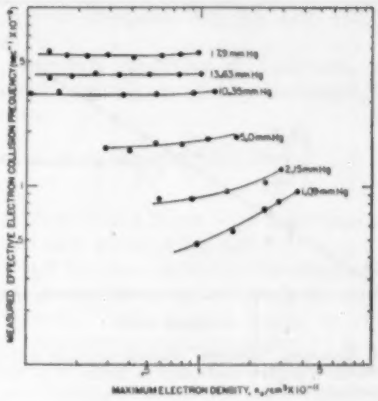
MEASURED EFFECTIVE ELECTRON COLLISION FREQUENCY (sec⁻¹) X 10⁻⁶
1.29 mm Hg
1.67 mm Hg
2.35 mm Hg
3.0 mm Hg
2.75 mm Hg
4.39 mm Hg
MAXIMUM ELECTRON DENSITY, n₀/cm³ X 10⁻¹¹

FIG. 3. Measured "effective" electron collision frequency in the afterglow established in helium as a function of gas pressure and maximum electron density.

EXPERIMENTAL RESULTS

It is necessary, at first, to establish the value of the "effective" collision frequency for electrons with helium atoms, ν_m, in the isothermal plasma at room temperature (300°K). Measurements were therefore made of relative phase shift and relative loss suffered by the microwave during propagation through the plasma. The variables were the gas pressure and the time of measurement in the afterglow delayed from the time of establishment of the plasma. Initially the electron density and electron collision frequency were calculated from Eqs. (23) and (15) with no regard for electron-ion collisions ($\nu_i/\nu_m \ll 1$). The results of these measurements are given in Fig. 3. It will be noted that at high gas pressures the measured collision frequency is independent of the density of electrons (and/or positive ions) but dependent upon gas pressure. The values of ν_m as a function of gas pressure obtained from Fig. 3 are plotted as the crossed circles on Fig. 4. A linear dependence upon gas pressure is obtained as would be expected. A further check upon the value of ν_m may be obtained from measurements of the time constant $\tau = 1/G\nu_m$, associated with the relaxation of the disturbed plasma, in the vicinity of $T_e = 300$°K. The results of such measurements give the values of ν_m indicated by the small circles on Fig. 4. It may thus be concluded for our later purposes that the value of the

[18] This is consistent with the work of Cravath [A. M. Cravath, Phys. Rev. **36**, 248 (1930)] who concludes $G = (4/3)(2m/M) = 2.66m/M$, since the factor 4/3 is included in the definition of ν used here, Eq. (10), while the ν employed by Cravath is void of the 4/3 factor.

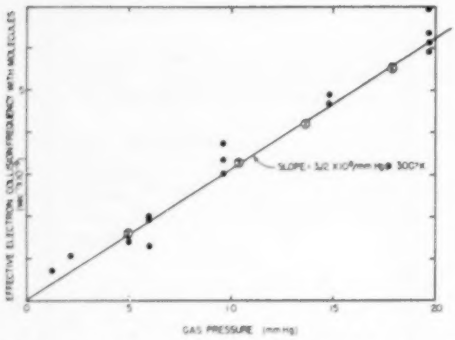

FIG. 4. Measured "effective" electron-molecule collision frequency in the afterglow established in helium as a function of gas pressure.

effective collision frequency with helium atoms is $\nu_m = 3.12 \times 10^8$/sec/mm Hg at 300°K. Reference to Eq. (10) and the text immediately following, indicates that the above value of ν implies a value of the collision probability for momentum transfers: $P_m = 24.0$ cm²/cm³ at 0°C and 1 mm Hg.

Returning to Fig. 3, it will further be noted that the values of measured ν indicate a strong dependence upon the electron density and/or positive ion density for the lower gas pressures where experimental conditions still insure an isothermal state of the plasma. In view of the strong density dependence of the collision frequency, it appears reasonable to postulate that this "anomaly" is due to the presence of electron-ion collisions, ν_i, and by utilizing Eq. (23) the value of ν_i may be separated from ν_m. The resultant electron-ion collisions as a function of electron density are plotted as crosses on Fig. 5. A pattern may be noted to these crossed points, which indicates an almost linear dependence upon electron density ($n_e = n_i$). If ν_i is to follow the form given by Eq. (18), it will be quite difficult to assign a value to the constant B under the logarithm since large changes in B influence only slightly the slope of ν_i *vs* n_0. However, by utilization of experimental results under the conditions of Eqs. (28) and (29) the constant C' and hence ν_i multiplied by the factor

$$\frac{\ln(BT_e^{\frac{1}{2}}/n_i^{\frac{1}{2}}) - \frac{5}{6}}{\ln(BT_e^{\frac{1}{2}}/n_i^{\frac{1}{2}})}$$

may be found. These results, namely, $C'n_e/T^{\frac{1}{2}}$, are plotted as the small circles on Fig. 5. From the average of crosses and the average of circles of Fig. 5 at a given density, the constants A and B may be calculated. More specifically, at $n_0 = 1.5 \times 10^{11}$ elec/cc,

$$\nu_i = Cn_0 = 4.0 \times 10^8, \quad C'n_0 T_e^{-\frac{1}{2}} = 3.1 \times 10^8,$$

yielding $A = 3.6$ and $B = 3.7 \times 10^8$.

Finally, with these experimental values, ν_i may be written

$$\nu_i = 3.6 \frac{n_i}{T_e^{\frac{1}{2}}} \ln\left\{\frac{3.7 \times 10^8}{n_i^{\frac{1}{2}}} T_e \left(\frac{2T_eT_i}{T_e + T_i}\right)^{\frac{1}{2}}\right\}, \quad (30)$$

where n_i is the ion density/cc, and T_e and T_i are electron and ion temperatures, respectively. In the theoretical determination of the electron-ion collision frequency, the influence of the dielectric constant of the plasma, which alters the Coulomb attraction forces, has been judged negligible for our experimental conditions.

Before concluding the experimental results, it should be noted that an attempt was made to obtain a value of the factor G defined in a manner similar to that of Eq. (8), but for energy exchange in electron-ion collisions. It was not possible to give an immediate answer, but an observation of the nature of the cross modulation to the wanted wave indicated the G factor to be considerably smaller than that associated with electron-molecule collisions. The relaxation of the elevated temperature of the electron gas to the temperature of the gas appears always to be a function of the product of the prevailing ν_m and $G \sim 2m/M$, and to bear little relation to the prevailing ν_i.

CONCLUSIONS

A value for the "effective" electron-molecule collision frequency in helium for the isothermal room temperature (~300°K) plasma has been found equal to 3.12×10^8/mm Hg. From the definition of effective collision frequency adopted for these experiments, Eqs. (4) and (10), a value of probability of collision for momentum transfer, P_m, for electrons having energies ~0.04 ev may be calculated equal to 24.0 cm²/cm³. It is assumed that P_m is reasonably constant over the range of electron energies involved in this experiment. It is doubtful that this value of P_m differs by more than a few percent from the value of probability of collision, P_c, obtained

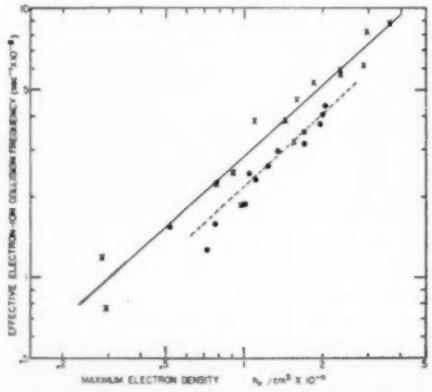

FIG. 5. Experimentally determined "effective" electron-ion collision frequency (solid line and/or crosses) as a function of maximum electron density.

in monoenergetic beam type experiments, since slow electrons (<1 ev) are, with good approximation, scattered isotropically. However, this value of $P_m=24.0$ is in some disagreement with a value recently found by Gould and Brown,[19] namely, $P_m=18.3$. It is curious to note that the ratio of these two different values of P_m is almost the factor 4/3. The value, $P_m=24.0$, is, however, in excellent agreement with the slightly extended results of Ramsauer and Kollath,[20] which were made with monoenergetic electron beams at energies down to <0.2 ev. The effective cross-sectional area of the helium atom for electrons with energies ~0.04 ev may be found by Eq. (10) to be $q_m=6.8\times10^{-16}$ cm². If this experimentally found q_m is expressed in units of πa_0^2 (where $a_0=0.53\times10^{-8}$ cm is the radius of the first Bohr orbit of the hydrogen atom), we obtain $q_m=7.7(\pi a_0^2)$. This is in good agreement (~12% discrepancy) with the recent theoretical work of Moiseiwitsch[21] which predicts for the total cross section, a value of $q=8.6(\pi a_0^2)$ for helium atoms and electrons with energies ~0.04 ev. In the light of the above, however, the total cross section is not likely to differ significantly from the momentum transfer cross section.

The magnitude of effective collision frequency of electrons with ions in the isothermal plasma at room temperature (~300°K) has also been found. This experimentally determined electron-ion collision frequency was stated in Eq. (30) and is plotted *vs* electron density as the solid line of Fig. 5. In a manner similar to the definition of effective electron-molecule collision frequency, an *effective cross-sectional area* for collision of electrons with ions may be defined by

$$\nu_i=(4/3)q_i n_i\bar{v}. \tag{31}$$

Such a procedure is not strictly correct but allows a comparison with the electron-molecule cross section. At $n_i=1\times10^{11}$ elec/cc the effective cross-sectional area for electron-ion collisions is $q_i\sim2.0\times10^{-10}$ cm² in the isothermal plasma at 300°K. The ratio of effective cross sections for electron-ion and electron-molecule collision then is $\sim3.0\times10^{+3}$, under the above stated conditions. This points up the importance of electron-ion collisions, even in plasmas with low degrees of ionization.

It is interesting to compare the experimental results for electron-ion collisions, as stated in Eq. (30) with those theoretical works applicable to our experimental conditions. The best and almost exact correspondence is with the work of Ginsburg[8] which has been recently restated more correctly by Vilenski.[22] From Ginsburg's work (for the case where $T_i=T_e$), we obtain

$$\nu_i=3.59\frac{n_i}{T_e^{\frac{3}{2}}}\ln\left[3.32\times10^{\frac{3}{2}}\frac{T_e^{\frac{3}{2}}}{n_i^{\frac{1}{2}}}\right], \tag{32}$$

which is to be compared with Eq. (30) with T_e set equal to T_i.

The theoretical prediction of Burkhardt, Elwert, and Unsöld,[23] recently restated by Burkhardt,[24] gives, for our case,

$$\nu_i=2.25\frac{n_i}{T_e^{\frac{3}{2}}}\ln\left[8.4\times10^{\frac{3}{2}}\frac{T_e^{\frac{3}{2}}}{n_i^{\frac{1}{2}}}\right], \tag{33}$$

which appears to be a factor ~0.8 lower than the experimental value given by Eq. (30).

Other high-frequency effective electron-ion collision frequency predictions have been made by Westfold[25] and Majumdar,[26] both of which appear to be higher than our experimental value by a factor ~1.3.

A recent exhaustive work of Spitzer and Härm[27] for the dc conductivity of completely ionized gases cannot be strictly compared to our experiment, since the validity of the approximate relation, Eq. (2), which reduces to

$$\nu=n_e e^2/m\sigma \quad \text{for} \quad \omega\to0, \tag{34}$$

cannot be assured for the high-frequency case. For the case of electron-molecule collisions and probability of collision independent of electron velocity, it can be shown that an error of ~13% enters by use of Eq. (34) when going from dc collision frequency to high-frequency collision frequency. However, this can be corrected by redefining the effective collision frequency properly for use in Eq. (34) ,as

$$\nu_m=\tfrac{3}{8}\pi q_m N_m\bar{v} \tag{35}$$

from Eq. (5). This equation is valid only for a Maxwellian distribution of electron velocities which for the dc case implies small values of the electric field. The procedure of correction for the case of electron-ion collision frequency is not clear and will not be attempted. However, use of Eq. (34) and the results of Spitzer and Härm give a value of dc effective electron collision frequency which is a factor ~0.6 lower than Eq. (30).

A dc value of electron-ion collision frequency given by Gvosdover[28] is a factor ~0.75 lower than Eq. (30).

Some agreement between measurements of dc conductivity due to positive-ion scattering and theory has been obtained in the past, and are summarized by Rompe and Steinbeck.[29]

It is interesting to note that a recent experimental work for dc conductivity due to mixed electron-molecule and electron-ion collision by Lin, Resler, and Kantrowitz[30] gives a close correlation with the theory of

[19] L. Gould and S. C. Brown, reference 11.
[20] C. Ramsauer and R. Kollath, reference 11.
[21] B. L. Moiseiwitsch, Proc. Roy. Soc. (London) **A219**, 102 (1953).
[22] I. M. Vilenski, J. Exptl. Theoret. Phys. (U.S.S.R.) **22**, 544 (1952).
[23] Burkhardt, Elwert, and Unsöld, Z. Astrophys. **25**, 310 (1948).
[24] G. Burkhardt, Ann. Physik **5**, 373 (1950).
[25] K. C. Westfold, Phil. Mag. **44**, 712 (1953).
[26] R. C. Majumdar, Z. Physik, **107**, 599 (1937).
[27] L. Spitzer and R. Härm, Phys. Rev. **89**, 977 (1953).
[28] S. D. Gvosdover, Physik Z. Sowjetunion **12**, 164 (1937).
[29] R. Rompe and M. Steinbeck, "The Plasma State of Gases," in *Ergebnisse der Exakten Naturwissenschaften* (Verlag Julius Springer, Berlin, 1939), Vol. 18.
[30] Lin, Resler, and Kantrowitz, J. Appl. Phys. **26**, 95 (1955).

Spitzer and Härm. This work was performed in high temperature isothermal plasmas in argon (~10 000 to 15 000°K) and for high degrees of ionization (>0.1%), while in our experiment the degree of ionization is ~0.001% and the temperature ~300°K.

ACKNOWLEDGMENTS

We wish to acknowledge Mr. R. C. Hwa for reading the manuscript and for discussion of these problems.

APPENDIX. EXPERIMENTAL DETERMINATION OF THE PHASE AND ATTENUATION CONSTANTS

The data to be described were obtained in the following manner:

(a) The phase constant, $\beta_g = 2\pi/\lambda_g$, associated with propagation in the plasma-filled square wave guide is determined in comparison with the phase constant, $\beta_{g0} = 2\pi/\lambda_{g0}$, associated with propagation in the air-filled square wave guide by the measured shift in voltage standing wave pattern. This shift is measured, as mentioned in the text, on a slotted line in standard X-band wave guide (RG 52/u).

(b) Attenuation in the plasma is measured on a precision wave-guide attenuator (in db) and compared to that in the air-filled guide by maintaining constant output on a crystal detector which is located on the far side of the plasma from the microwave source.

For the geometry of this experiment, and the assumption regarding the electron density distribution, Eq. (16), there results

$$\left(\frac{n_0 e^2}{\epsilon_0 m\omega^2}\right)\frac{1}{2.16} = \left(\frac{\lambda_0}{2\pi}\right)^2\left[\alpha^2 + \left(\frac{2\pi}{\lambda_{g0}}\right)^2 - \left(\frac{2\pi}{\lambda_g}\right)^2\right] \quad (37)$$

and

$$\left(\frac{n_0 e^2}{\epsilon_0 m\omega^2}\right)\frac{4}{\pi^2\omega}(1.14\nu_m + 0.765\nu_{i\max}) = \left(\frac{\lambda_0}{2\pi}\right)^2\left[2\alpha\left(\frac{2\pi}{\lambda_g}\right)\right], \quad (38)$$

where the various symbols are those defined in the text.

The value of λ_{g0} to use in (37) must be determined experimentally in the presence of the glass discharge tube. At 8600 Mc/sec it was found that the presence of the glass altered the "air guide" wavelength in the square guide from 6.49 cm to 5.64 cm.

As typical data we take the following: *Data* (1): gas pressure—17.9 mm Hg, attenuation—4.3 db, and phase shift—3.97 cm shift of slotted line; *Data* (2): gas pressure—2.15 mm Hg, attenuation—3.2 db, and phase shift—14.53 cm shift of slotted line. The data relative to phase shifts were obtained by the alternative scheme mentioned in the text.

For data (1), λ_g becomes 5.81 cm and from Eq. (37), neglecting α, $n_0 = 4.2\times10^{10}$ elec/cc. Similarily, for data (2), $n_0 = 1.45\times10^{11}$ elec/cc.

The change in guide wavelength brought about by the plasma medium implies an increased value of electric field in the wave guide (in particular, in the glass discharge tube) under our assumptions. The measured value of attenuation in decibels must be corrected for this effect, the increased power loss being proportional to the ratio λ_g/λ_{g0}. For data (1), 4.3 db corrects to 4.17 db, and for data (2), 3.2 db corrects to 2.75 db. The value of α is readily obtained from the definition

$$\text{No. of db (measured and corrected)} = 20\log_{10}e^{\alpha z}. \quad (39)$$

Under the experimental conditions of data (1), $\nu_m \gg \nu_i$, and Eq. (38) gives $\nu_m = 5.5\times10^9$/sec. Normalized to 1 mm Hg, $\nu_m = 3.1\times10^8$/mm Hg, at 300°K, the assumed temperature of the isothermal plasma. Now for the gas pressure of data (2), $\nu_m = 6.7\times10^8$ and from Eq. (38), $\nu_i = 3.95\times10^8$ corresponding to $n_0 = 1.45\times10^{11}$ elec/cc.

In these experiments the field intensity of the probing microwave signal (here 8600 Mc/sec) did not exceed ~1/10 volt/cm.

Minority Carrier Extraction in Germanium*†

RALPH BRAY
Physics Department, Purdue University, Lafayette, Indiana
(Received June 20, 1955)

The concentration of minority carriers in a sample can be effectively decreased below its equilibrium value by an extraction process in which, (a) the minority carriers in the sample are swept out by an electric field in a time ≪lifetime, while (b) the minority carrier flow into the sample at the entry contact, is suppressed. Procedures are discussed for making contacts satsifying condition (b). Such contacts have low resistance, and give photovoltages of opposite polarity to that of injecting contacts. With increasing field during extraction, there is a saturation increase of sample resistance, corresponding to approximately complete minority carrier depletion. Saturation extraction suppresses the intrinsic decrease in resistivity for a range of some 50°C for a group of *p*-type samples with resistivities of 7 to 40 ohm-cm at 300°K. Limitations on the range of effectiveness of extraction are imposed by failure of conditions (a) and (b) to hold at higher temperatures and/or deeper in the intrinsic range. Transport and transient effects associated with extraction can be used, as with injection, for measurement of minority carrier mobility and lifetime. Extraction is further useful for controlling collector contact properties, and for determining the composition of reverse current of point contact rectifiers, in terms of hole and electron components.

I. INTRODUCTION

THE concentration of free minority carriers in germanium may be made to deviate from equilibrium value by various means. Since, in the absence of trapping, there is an equivalent deviation in free majority carrier concentration due to requirements of neutrality, one can speak of deviations in hole-electron pair concentration. As is well known, the concentration of hole-electron pairs can be increased above the equilibrium value by optical excitation within the fundamental absorption band, or by injection of minority carriers at a *p-n* junction or a metal contact. It is also possible by several procedures to decrease the concentration of hole-electron pairs below the equilibrium value. We shall use the term "extraction" to represent whatever process produces such carrier depletion. We refer only to depletion occurring over a region without appreciable space charge. Complete depletion corresponds to extraction of all hole-electron pairs, leaving behind only the majority carriers of extrinsic origin. The change in conductivity due to extraction increases very rapidly as the sample approaches intrinsic behavior. Extraction may be an effective and useful auxiliary to injection for modulating bulk and contact properties.

Three types of extraction may be distinguished:

(1) Extraction, which utilizes the Suhl[1] effect, has been described in great detail by Welker.[2] Electrons and holes in germanium are deflected in crossed electric and magnetic fields to a surface of high recombination velocity. If they recombine there more rapidly than they can be generated in the bulk or at the other surfaces, the concentration of hole-electron pairs in the sample is reduced.

(2) Extraction from the vicinity of *reverse-biased rectifying contacts* has been reported by Banbury[3] for the case of point contacts on lead sulphide and germanium and by Angello and Ebert[4] for *p-n* junctions in germanium. According to rectifier theory,[5,6] the reverse current may consist in whole or in part of a diffusion of thermally generated minority carriers to the junction. This would lead to depletion of minority carriers over a distance of the order of a diffusion length from the junction, when reverse voltage is applied. A general statement of the condition for depletion at reverse-biased junctions has been given by van Roosbroeck.[7]

(3) In the method of extraction[8,9] to be discussed in this paper,‡ special contacts on *n*- or *p*-type germanium are prepared which severely limit the current of minority carriers entering the sample, while imposing no barrier to majority carriers. Consequently, when an electric field is established in the sample, the minority

* Work supported by a Signal Corps contract.

† Preliminary accounts of this work were presented at the American Institute of Electrical Engineers and the Institute of Radio Engineers, Semiconductor Devices Research Conference, Minneapolis, Minnesota, June, 1954, and the Chicago meeting of the American Physical Society, November, 1954. [Phys. Rev. **98**, 229 (1955).]

[1] H. Suhl and W. Shockley, Phys. Rev. **76**, 180 (1949).

[2] H. Welker, Z. Naturforsch. **6(a)**, 184 (1951); also, E. Weisshaar and H. Welker, Z. Naturforsch. **8(a)** 681 (1953).

[3] P. C. Banbury, Proc. Phys. Soc. (London) **B66**, 50 (1953). The term "extraction" was first used by Banbury to apply to this process.

[4] S. J. Angello and T. E. Ebert, Phys. Rev. **96**, 221 (1954). They called the effect "egression."

[5] W. J. Bardeen and W. H. Brattain, Phys. Rev. **75**, 1208 (1949).

[6] W. Shockley, *Electrons and Holes in Semiconductors* (D. Van Nostrand Company, Inc., New York, 1950), Chap. 4.

[7] W. van Roosbroeck, Phys. Rev. **91**, 282 (1953).

[8] All future references to "extraction" in this paper will be to type (3), except where specifically noted. Subsequent to the initiation of this work, it was brought to my attention by I. M. Ross that extraction by this mechanism had been observed in the course of experiments with unipolar transistors by G. Dacey and I. M. Ross, Proc. Inst. Radio Engrs. **41**, 970 (1953).

[9] Gibson has reported extraction in near-intrinsic *n*-type germanium, to which specially doped contacts were grown. A. G. Gibson, Physica **20**, 1058 (1954); also, Arthur, Bardsley, Brown, and Gibson, Proc. Phys. Soc. (London) **B68**, 43 (1955).

‡ *Note added in proof.*—Recently, it has been suggested that extraction of this type be called *carrier exclusion* [G. G. E. Low, Proc. Phys. Soc. (London) **B68**, 310 (1955)].

carriers which are normally present in the interior can be swept out of the sample at the exit contact without being replenished at the entry contact. If the sweepout rate is greater than the rate at which minority carriers are thermally regenerated in the sample, then appreciable depletion of minority carrier concentration can be achieved throughout the sample. This is in contrast to extraction of type (2) above, where depletion originates and is localized at the minority carrier exit contact. Almost complete depletion was obtained with electric fields well under 50 volts/cm on samples one to two cm in length, and with minority carrier lifetime of the order of 100 μsec. Increase of resistance by as much as a factor of about 13, corresponding to extraction of about 90% of *all* the carriers, was observed at 65°C for a sample having a resistivity of 32 ohm-cm at room temperature.

II. THEORY

The nature of the contact to the semiconductor determines whether there occurs the well-known injection, or the extraction, of minority carriers when forward[10] voltage is applied.

Extraction will occur if the net minority carrier current entering the sample, I_{nc}, is *less* than the instantaneous minority carrier current established in the interior when the voltage is applied. The latter is given by

$$I_{n0}=n_0 e\mu_n E, \tag{1}$$

where n_0 is the equilibrium minority carrier concentration in the sample, μ_n is the corresponding mobility, and E is the electric field in the interior. Since fewer minority carriers are entering the sample than are being swept away from the entry contact, a deficit in concentration is established at the edge of this contact, and swept into the interior. For ideal extraction, the entering minority carrier current is completely suppressed: i.e., $I_{nc}=0$. The contact may be characterized by the parameter γ_c, the ratio of minority carrier current to total current at the contact. The significant quantity for a contact is actually $\gamma_c-\gamma_0$, where γ_0 is a constant representing the same ratio in the interior, and defined for equilibrium carrier concentrations; i.e.,

$$\gamma_0=n_0 b/(p_0+n_0 b), \tag{2}$$

where n_0 and p_0 are the interior, equilibrium, minority and majority carrier concentrations,[11] respectively, and b is the ratio of minority to majority carrier mobility, μ_n/μ_p. Thus, the condition $(\gamma_c-\gamma_0)>0$ corresponds to injection, and $(\gamma_c-\gamma_0)<0$ to extraction.

The condition for extraction may be realized in general at any boundary in a sample between regions of low and high concentration of minority carriers. At such a boundary, the minority carrier current into the region of high concentration is limited, and extensive depletion can occur in the latter region. Such a boundary cannot hinder the flow of majority carriers, and consequently the boundary resistance must be small.

A specific example will now be considered for the case of a metal contact on p-type germanium. The boundary condition here is established at the surface of the sample. The conditions for injection and extraction are compared, as illustrated in Fig. 1.

The equilibrium potential energy diagrams show the conduction and valence bands bending down at the contact for the case of injection, and bending in the reverse direction for extraction. The direction of the barrier at the surface depends on the germanium surface treatment and the interaction between this surface and the metal. At the injection contact, the minority carrier concentration, n_c, is greater than n_0; if forward voltage is applied, part of its appears across the barrier in the semiconductor, thereby decreasing it and permitting propagation of excess electrons into the interior.

In contrast, at the extraction contact, there is a surface layer which is strongly p-type, producing a boundary where $n_c \ll n_0$. When forward voltage is applied, it appears predominantly across the bulk, and a deficit in concentration is swept into the interior, as illustrated.

The condition for extraction can also be satisfied at a junction, formed inside a crystal, by low- and high-resistivity material of the same type. Not only can extensive depletion occur in the latter region, but localized depletion of type (2) can simultaneously occur on the edge of the low-resistivity side.

Methods of producing contacts for extraction will be discussed in the next section.

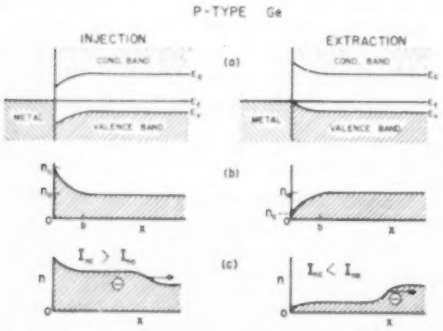

FIG. 1. The schematic diagram compares conditions for injection and extraction at a metal contact on p-type Ge. (a) Equilibrium potential energy diagrams comparing direction of the barrier at the contact. (b) The equilibrium electron concentration along the sample. (c) The propagation of an excess or a deficit concentration of electrons from the negative contact into the interior by a large sweeping field.

[10] The term "forward voltage" is used here to represent that polarity of the applied voltage at the contact, for which minority carriers flow into the semiconductor.

[11] The notation here is that usually taken for p-type material, but since we have not specifically identified the minority carrier, the equations, as defined in the text, are valid for either n- or p-type Ge.

Extraction of minority carriers was studied experimentally mainly in terms of the transient and steady state changes produced in sample conductance as a function of voltage and temperature. An expression for the change in conductance G, in terms of parameters of the sample is derived below for the linear, one-dimensional case. The sample is taken to be in the form of a bar of length L, and rectangular cross section A. Low-resistance, area contacts are made at the ends of the sample.

The solution is obtained in the approximation that the continuity equations are linear, which is valid[12] under the condition $n_0 \ll p_0$. Then, if a pulse of constant voltage, V, is applied to the sample, the electric field, E, being uniform and constant during extraction, is given by V/L. The change of conductance, ΔG, is independent of the spatial distribution of the deficit in carrier concentration in the sample. For simplicity, diffusion is neglected.

When the pulse is applied to the sample, at $t=0$, a minority carrier current,

$$I_{nc}=n_b e\mu_n E \tag{3}$$

is introduced in the sample at the edge of the forward-biased contact, at $x=b$. Elsewhere in the sample the minority current is still I_{n0}. A change in minority carrier concentration, Δn, is quickly established at $x=b$, such that,

$$\Delta n/n_0=(n_b-n_0)/n_0=(I_{nc}-I_{n0})/I_{n0}. \tag{4}$$

If $\Delta G/G_0 \ll 1$, then

$$\Delta n/n_0=(\gamma_c-\gamma_0)/\gamma_0. \tag{4a}$$

Here, Δn represents either an increase or decrease in concentration, depending on whether $(\gamma_c-\gamma_0)>0$ or $(\gamma_c-\gamma_0)<0$.

In either case, Δn is swept into the interior with constant velocity, $v=\mu_n E$. As it proceeds, the magnitude of Δn decays exponentially in time, with the decay constant given by τ, the minority carrier lifetime in the sample. The decay is due to excess recombination or thermal generation, depending on whether $\Delta n>0$ or $\Delta n<0$.

The steady-state condition is attained when the perturbation reaches the end of the sample after a time, $t_s=L/v$, which may be called the transit time. The total change in the number of minority carriers in the sample, ΔN, is obtained by integrating the deficit over the whole sample. For $t<t_s$, we get

$$\Delta N=Av\tau\Delta n[1-\exp(-t/\tau)]. \tag{5}$$

The change of conductance is

$$\Delta G=e\Delta N(b+1)\mu_p L^{-2}. \tag{6}$$

[12] The conditions for linearity have been thoroughly discussed by van Roosbroeck (reference 7).

On combining Eqs. (4), (5), and (6), we have the expression for the transient change of conductance,

$$\frac{\Delta G}{G_0}=(\gamma_c-\gamma_0)\frac{b+1}{b}\frac{v\tau}{L}[1-\exp(-t/\tau)]. \tag{7}$$

The dependence of $\Delta G/G_0$ on E in the steady state, $\geq t_s$, is given by

$$\frac{\Delta G}{G_0}=(\gamma_c-\gamma_0)\frac{b+1}{b}\frac{\mu_n E\tau}{L}[1-\exp(-L/\mu_n E\tau)]. \tag{8}$$

Of the several parameters of the sample, γ_0, may be calculated from the conductivity, and τ and μ_n may be measured independently. However, γ_c is an unknown, determined by the height and structure of the barrier, and it may be voltage dependent. Its general form will be deduced from the experimental dependence of $\Delta G/G_0$ on E. For ideal extraction, $\gamma_c \to 0$ and then, as $L/\mu E\tau \to 0$,

$$\frac{\Delta G}{G_0} \to \left(\frac{\Delta G}{G_0}\right)_{\max}=-\frac{b+1}{b}\gamma_0=-\frac{n_0(b+1)}{p_0+n_0 b}, \tag{9}$$

which is the maximum change due to extraction.

III. THE CONTACT

A. Methods of Formation

Early experiments on near-intrinsic p- and n-type germanium to which low-resistance contacts had been soldered, revealed unpredictable injecting or extracting behavior of the contacts. These observations led to the study of extraction, and of techniques for obtaining reproducible behavior as regards injection or extraction with low-resistance contacts.

Most of the contact experiments were made with relatively high-resistivity samples (20–40 ohm-cm) at room temperature. The greatest reproducibility in results was obtained when contacts were made to surfaces which had been strongly etched with, e.g., CP_4.

The results obtained with various types of contacts are summarized in Table I, where the contacts are

TABLE I. Behavior of different contacts on n- and p-type Ge, with respect to the production of injection (I) or extraction (E).

	Type of contact[a]	n-type Ge	p-type Ge
I	Silver paint	I	E
	Rhodium plate	I	E
	Point contacts of tungsten or phosphor bronze	I	E,I
II	Indium solder (L.T.)[b]	I	E
	Indium solder (H.T.)[c]	I	E
	Tin solder (L.T.)	I	E
	Tin solder (H.T.)	E	I

[a] Except as indicated, all contacts were large area contacts.
[b] (L.T.) represents "low temperature," for contacts soldered very close to the melting point of the particular solder.
[c] (H.T.) represents a "high-temperature" treatment of contacts initially formed at L.T. This treatment consisted of heating on a hot plate at 300°C for one or more minutes in air.

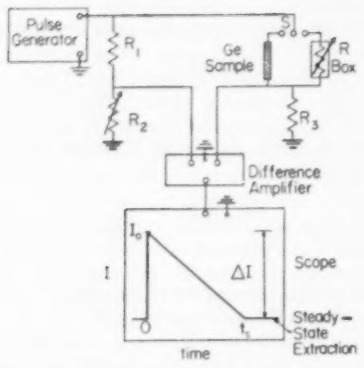

FIG. 2. Arrangement of pulse bridge circuit for observing change of current with time during extraction. The resistance of the sample is measured at any time by switching S from sample to standard-resistance box. Change of current for linear case is illustrated. The abrupt transition to steady-state current gives the transit time, t_0, for minority carriers.

divided into two classes. Those of class II are soldered, while those of class I are mechanically applied or electroplated. In the latter case the properties of the contact depend on the barrier already present at the free surface of the germanium and its possible modification by the presence of the metal contact. The silver-paint and rhodium-plated contacts invariably gave injection (and rectification) on n-type Ge, in accordance with the concept of a p-type surface inversion layer on n-type Ge. These contacts usually gave extraction on p-type samples.[13] This suggests the presence of a strong p-type layer also on the surface of p-type Ge. Pressure contacts with tungsten or phosphor-bronze whiskers gave results consistent with the above on n-type Ge, but gave erratic effects on p-type Ge. In the latter case, both injection and extraction contacts were obtainable. These were not stable and could be converted one into the other with slight physical disturbances.

The most reproducible behavior was obtained with contacts made by soldering pure tin or indium at slightly above their melting points to well-etched surfaces. With such low temperature, "L. T.," soldered contacts, extraction was invariably obtained on p-type and injection on n-type Ge. Area contacts of this type usually showed negligible contact resistance. Heat treating such contacts at about 300°C in air for about one minute converted the tin contacts so that they gave injection on p-type, and extraction on n-type. No conversion was obtained for indium contacts. Conversion upon heating was, however, also obtained with several commercial solder mixtures containing tin, including a tin and indium mixture. The early unpredictability of behavior of soldered contacts is therefore traceable mainly to the dependence on the temperature of soldering. Such heat-treated contacts are designated "H. T."

It seems likely that when conversion is observed with H.T. contacts, it is due to doping of the contact region with donors, producing n-type layers on both p- and n-type Ge.

No attempt was made to definitely identify the donor, although it seems to be associated with the presence of tin.[14] Neither has the cause of the p-type behavior of the L.T. contacts been determined. In this case, appreciable influx of acceptors is not expected in the few seconds the contacts are heated at $T<200$°C. Surface effects are likely to be predominant here.

Deliberate doping to make contact regions which are of the same type as the bulk, but more extrinsic, is a recognized technique for suppressing excess minority carrier injection. Such junctions are usually made at appreciably higher temperatures ($T>400$°C) than those reported here, and may also be expected to give extraction. Gibson *et al.*[9] obtained extraction with junctions made by growing a long, heavily-doped n-type section onto one end of a near-intrinsic n-type crystal.

B. Contact Photovoltage

The sign of the photovoltage generated at a contact should depend on the direction of bending of the energy bands at the contact. As Fig. 1 illustrates, the bending of the bands at the contact on the semiconductor side is expected to be in opposite directions for injection and extraction. It is expected, then, that the sign of the open-circuit photovoltage would have opposite polarity for these two types of contacts. Photovoltaic polarity tests were made on extracting and injecting contacts, using silver paint and soldered contacts. Under illumination, the metal contact became negative for injection and positive for extraction contacts on p-type Ge. As expected, just the reverse effects were found for contacts on n-type Ge. The photovoltages were all very small compared to those obtained on high-resistance contacts and had to be observed under strong illumination with white light.

IV. BULK CONDUCTANCE EXPERIMENTS

In this section, the measurements of the changes in bulk conductance during extraction of minority carriers are described. The dependence of transient and steady-state changes on voltage and temperature was explored for samples of various resitivities.

[13] Complications were observed with silver paint contacts. There was appreciable contact resistance, of order of 20% of the total sample resistance. Furthermore, when fields ~50 volts/cm were applied, sudden conversion from extraction to very strong injection could be observed. With successive applications of voltage, conversion occurred at lower voltages.

[14] W. C. Dunlap, Jr., has commented (personal communication) that attempts at the General Electric Research Laboratories to grow germanium crystals with tin as an impurity, have failed to show any acceptor or donor activity on the part of the tin.

A. Method

All the experiments described below were performed with p-type germanium. The samples were bars, one to two cm long, with rectangular cross sections, about 2 mm on a side; extracting end contacts were made by soldering with indium by the low-temperature procedure. The resistance of the whole sample was measured in the bridge-type circuit illustrated in Fig. 2. Pulse technique was necessary not only to observe transient effects, but also to minimize heating effects in steady-state measurements at high voltages.

The pulse generator was a low-impedance source giving pulses up to 100 volts across the sample, with pulse lengths variable between 0.1 μsec and 1000 μsec. The detector in the bridge is a Tektronix difference amplifier whose output is observed on an oscilloscope. Either the total sample current can be displayed from the voltage drop across the small resistor, R_3, or the amplified change in current during extraction can be observed by adjusting R_2.

The steady-state resistance was measured by substituting a variable standard-resistance box for the sample. This procedure makes the measurement independent of any discrepancies in the gain of the difference amplifiers, and of the calibration of the resistances in the arms of the bridge.

B. Approach to Steady-State Extraction

The approach to steady state under extraction conditions is followed by observing the change of current with time for constant voltage applied across the sample. This change reflects the decrease in conductance as the deficit in carrier concentration moves through the sample. The rate of decay of current with time is described by Eq. (7). In general, this decay is nonlinear, and terminates at $t=t_s$, when the deficit concentration reaches the end of the sample. However, if $t_s \ll \tau$, there is a linear decay with sharp termination. This is illustrated in Figs. 3(a) and 3(b) by oscillographs of the change in current vs time. From the measurement of t_s, the minority-carrier drift mobility is readily determined, and found to give good agreement with standard values.[15]

The above discussion and Eq. (7) are valid as long as $n_0 \ll p_0$. When n_0 becomes appreciable, as the temperature rises, or if the sample is strongly illuminated, the current decay greatly increases in amplitude, becomes strongly nonlinear, and t_s increases appreciably. All these features are illustrated in Fig. 3(c) for the same sample as used for 3(a) and 3(b), but strongly illuminated. The lower trace in Fig. 3(c) shows the dark current on the same scale.

Essentially similar effects have been observed and explained[7,16] in terms of the decrease in the velocity of transport of a given concentration of minority carriers as $n_0 \to p_0$. This transport velocity may become much smaller than the carrier drift velocity. This phenomenon is very important for extraction, since it imposes a limitation on its practicability as a sample approaches deeper into the intrinsic range.

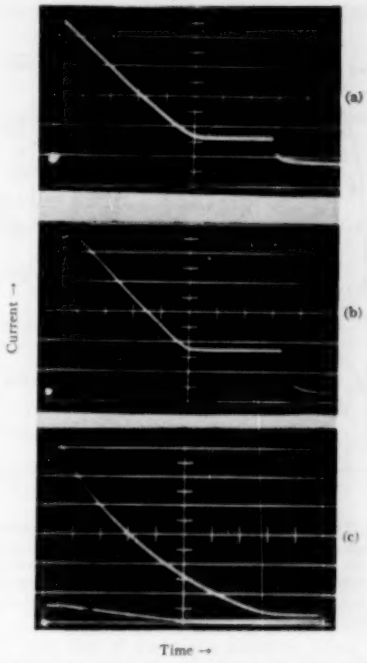

FIG. 3. Current decay characteristics during extraction in p-type Ge sample, $\rho=23$ ohm-cm, $L=1.38$ cm, $T=297°$K; curves (a) and (b) correspond to sample in the dark, curve (c) in strong illumination. (a) Somewhat nonlinear: $V=14.7$ volts, $t_s=35$ μsec, $\mu_n=3700$ cm^2/volt sec. (b) Linear: $V=51$ volts, $t_s=10$ μsec, $\mu_n=3700$ cm^2/volt sec. (c) Strongly nonlinear: $V=51$ volts, $t_s\approx 16$ μsec; compare with smaller trace representing dark characteristic on same scale.

This limitation becomes evident from examination of the general expression for the transport velocity[17] of the minority-carrier concentration,

$$v(I,n)=\frac{I\mu_n}{e\mu_p(p_0-n_0)[1+(b+1)n_0/(p_0-n_0)]^2}, \quad (7)$$

where I is the total current density. Not only is the transport velocity, v, low at the beginning of a constant-voltage pulse if $n_0 \to p_0$, but v becomes still smaller as I decreases during the extraction pulse. This means the carriers are being swept out with progressively smaller sweep field due to conductivity modulation. This essentially accounts for the nonlinearity of the decay.

[15] Similar observations, but with weakly injecting contacts, have been reported by A. Many, Proc. Phys. Soc. (London) **B67**, 9 (1954), and for extracting contacts by J. B. Arthur *et al.* (reference 9).

[16] M. B. Prince, Phys. Rev. **91**, 271 (1953). This paper also contains previous relevant references.

[17] See reference 6, p. 329.

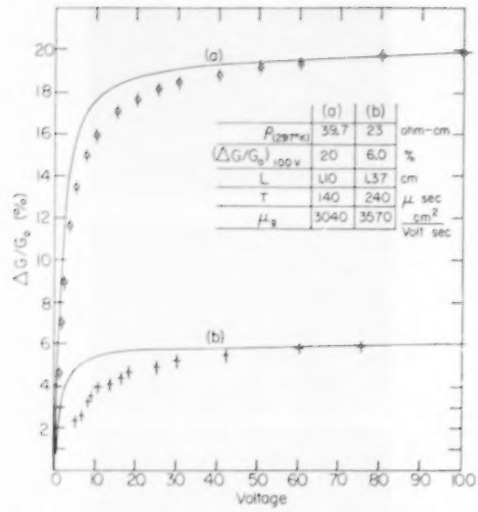

FIG. 4. The relative change of conductance upon extraction vs the voltage applied across p-type Ge samples. Experimental data is given by circles and crosses. Solid curves are calculated from Eq. (8) using the data given in the chart, and assuming γ_e is voltage independent. Deviation between calculated curve and experiment is ascribed to voltage dependence of γ_e.

When the transit time in such circumstances becomes so large that $t_s > \tau$, then the sweepout of minority carriers during extraction becomes ineffective. This has been observed for samples deep in the intrinsic range.

C. Steady-State Extraction—Voltage Dependence

The experimental dependence of the steady-state change of conductance upon sample voltage is shown in Fig. 4, for two p-type samples, having resistivities of 39.7 and 23 ohm-cm, respectively, at 297°K. Other relevant data for the sample are tabulated on the figure. The plotted data is to be compared with the solid curves, which represent $\Delta G/G_0$ calculated according to Eq. (5). In the calculation, τ was obtained from an independent measurement,[18] and E was set equal to V/L. Instead of the carrier drift mobility, $\mu_n \simeq 3800$ cm²/volt sec, the pulse drift mobility,[19] μ_g, was calculated and used. This serves as a partial correction for the fact that n_0 is appreciable in these samples. For the term $(\gamma_e - \gamma_0)(b+1)/b$, where γ_e is the unknown, the experimental value of $\Delta G/G_0$ at 100 volts (where $L/\mu_n E\tau \ll 1$) was used. The solid curves were drawn as if the value of γ_e so obtained, was independent of voltage. The calculated curves show a more rapid rise and saturation with voltage than is shown by the experimental data. Most of this discrepancy is attributed to a dependence on voltage for γ_e; the form of this dependence is readily obtained. Thus for the 23 ohm-cm sample, γ_e turns out to be appreciably greater than zero at low voltage (for $V \sim 5$ volts, $\gamma_e \sim \gamma_0/2$) but decreases with increasing voltage,[20] and either saturates or becomes very small as V becomes greater than 50 volts. For the other sample, the discrepancy is smaller, implying γ_e at low voltage is already small and close to its saturation value. The fact that Eq. (5) is a poorer approximation in this case, where n_0 is much larger, is partially responsible for the discrepancy. In the next section it is shown for several samples, that for temperature below 340°K, $\gamma_e \sim 0$, at least for $V \sim 100$ volts.

It is clearly desirable for efficient extraction, that $\Delta G/G_0$ rise and saturate rapidly with increasing voltage. The efficiency of extraction thus depends on how large the lifetime is, and on how rapidly γ_e decreases and approaches zero. The latter is determined by the structure of the particular contact barrier. For example, if the barrier is thin, and if I_{es} is the thermal emission current of minority carriers across the contact into the semiconductor, then, with bulk diffusion current neglected, it is easily shown that

$$\gamma_e/\gamma_0 = I_{es}/(I_{es} + n_0 e \mu_n E). \tag{8}$$

Here, γ_e will decrease with increasing field. The smaller I_{es}, the smaller is the field at which extraction becomes effective.

D. Dependence of Extraction on Resistivity and Temperature

Temperature-dependence curves of normal resistivity, ρ_0, and resistivity after extraction, ρ_e, are shown in Fig. 5 for four samples which have ρ_0 between 7.0 and 37.9 ohm-cm at 300°K. Measurements of ρ_e were made at pulse voltages of about 100 volts to provide saturation extraction where possible. While ρ_0 goes through a maximum and begins to decrease approximately exponentially with temperature as the sample enters the intrinsic range, ρ_e continues to increase along the low-temperature, extrinsic-range curve. Only at higher temperatures, between 340° and 360°K for these particular samples, does ρ_e reach a maximum, and then it decreases rapidly. Ratios of ρ_e/ρ_0 as high as 13 were achieved. This corresponds to extraction of about 8 out of every 9 carriers in the sample.

To determine how close extraction comes to removing all hole-electron pairs of intrinsic origin, the data of Fig. 5 were compared with calculations of the change in conductivity corresponding to complete depletion. The calculations were based on Eq. (9); the parameters n_0, p_0, and b were obtained from the normal sample resistivity, and the most recent empirical data of Morin and Maita[21] for the magnitude and temperature de-

[18] The method used is that described in Sec. IV E.

[19] The values of μ_g (given on Fig. 4) are obtained from $\mu_n/[1+(\Delta G/G_0)_{max}]$. The correction is small when $n_0 \ll p_0$. The larger the correction, the less valid is Eq. (5). Thus, Eq. (5) is a better approximation for the 23 ohm-cm sample than for the 39.7 ohm-cm sample.

[20] A. Many has measured γ_e for weakly *injecting* contacts, and found it to increase with voltage (reference 15).

[21] E. J. Morin and J. P. Maita, Phys. Rev. **94**, 1525 (1954).

pendence of the n_0p_0 product and of mobility. The solid curves in Fig. 6 represent the calculated values of $\Delta\sigma/\sigma_0$ at various temperatures between 300° and 340°K for samples with normal resistivities between 7 and 40 ohm-cm at 300°K. It can be seen that the measured values fit well to the curves, indicating that depletion is almost complete in this temperature range. Thus, under the various conditions of this experiment, it may be concluded that $\gamma_e \to 0$ at high voltage.

Extraction suppresses the intrinsic rise in minority carrier density for a range of some 50°K. There are several factors limiting the range over which extraction is effective. The difficulty with transport of minority carriers as the sample becomes more intrinsic, as $n_0 \to p_0$, was discussed in Sec. IV B. Another important factor is the structure of the extraction contact itself. It may be expected that the emission current at the entry contact, I_{es}, will increase with temperature, thereby increasing γ_e, and making extraction less effective. For the samples investigated here, the peak in ρ_s occurred at temperatures where the transit time was still appreciably less than the lifetime. The bending over of ρ_s as temperature increases must then be due to the contacts. However, at somewhat higher temperatures, it is observed that the transit time does become very large, thereby invoking the transport limitation, causing ρ_s to drop even more rapidly.

E. Recovery after Extraction

After the extracting voltage pulse is over, there is recovery to equilibrium concentrations by thermal generation of hole-electron pairs in the sample. If a small constant measuring current passes through the sample, the decay in sample voltage (proportional to resistance) during recovery may be observed on an oscilloscope. From this decay, the minority carrier lifetime is readily determined. The technique is the same as has already been described for measuring lifetime from recovery after injection.[22] By making injecting contact on one end of a sample, and extracting contact on the other end, it was possible to compare decay curves on the same sample after injection and after extraction. For both cases the same value of lifetime was measured, whether for etched or ground surfaces. These measurements were made only at room temperature, where $n_0 \ll p_0$.

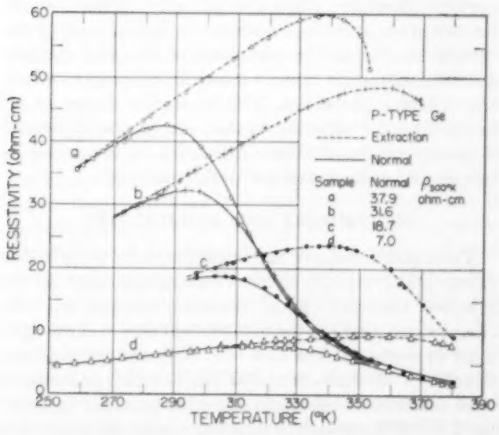

FIG. 5. Resistivity of p-type Ge samples as a function of temperature. The solid lines are for the normal resistivity measured at very small voltage or at beginning of an extraction pulse. They show the usual transition from extrinsic to intrinsic behavior. The broken lines represent the resistivity corresponding to extraction for pulse voltage of 100 volts. These show the extension of the extrinsic region and delay of intrinsic region for a temperature interval of about 50°C.

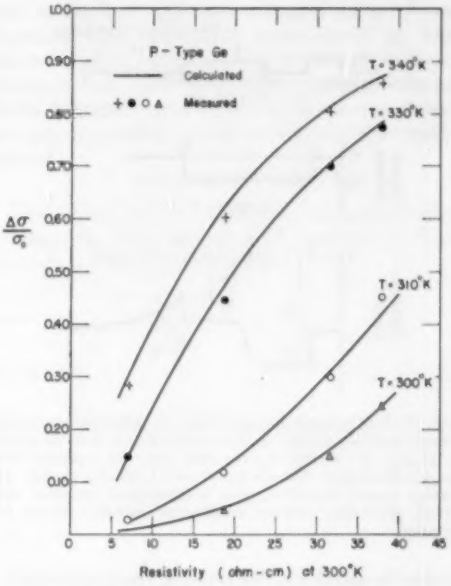

FIG. 6. The relative change in conductivity at saturation extraction, as a function of the resistivity at 300°K. Solid lines are calculated using data of Morin and Maita for p-type Ge. The measured points are taken from the curves of Fig. 5. The agreement indicates that for the particular samples and extracting contacts, there is obtained almost complete depletion of thermally generated hole-electron pairs.

V. COLLECTOR CURRENT MODULATION

As a counterpart to the effect of excess minority carrier injection, the depletion of minority carriers in the vicinity of a collector contact by some external extraction mechanism may be expected to, and does,[23] decrease the collector conductance. A collector contact may therefore be used as a probe to detect the extraction of minority carriers from a sample. In turn, ex-

[22] Navon, Bray, and Fan, Proc. Inst. Radio Engrs. 40, 1342 (1952).

[23] Such an effect, produced by different extraction procedures, has been reported by Shockley (reference 6, p. 66), and Angello and Ebert (reference 4).

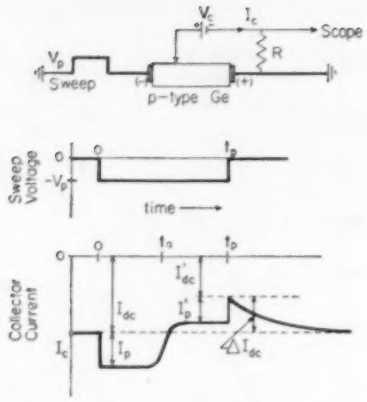

FIG. 7. Arrangement for studying the collector conductance modulation during extraction of minority carriers from the sample. The change of collector current with time for constant sweep voltage is illustrated. There is a decrease of collector current upon minority carrier depletion, and a subsequent recovery when thermal generation restores equilibrium minority-carrier concentration.

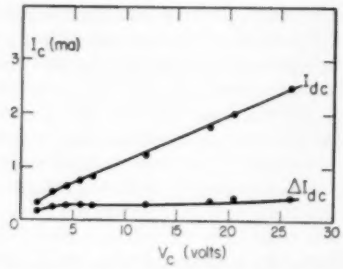

FIG. 8. Collector current as a function of reverse bias on a collector point contact (phosphor-bronze on p-type germanium). I_{dc} is the normal collector current. ΔI_{dc} is the change of collector current at the given bias, due to minority carrier depletion. Minority carriers in bulk are responsible for only part of total reverse collector current.

traction is useful for determining the composition of reverse current in a collector. To the extent that the collector conductance is sensitive to minority carrier depletion, extraction can be used to modulate the collector conductance.

The arrangement used for investigating the influence of extraction of minority carriers from a sample on a collector contact is shown in Fig. 7. Extraction contacts are soldered to the ends of a Ge sample. A pulsed electric field controls the degree of minority carrier extraction from the sample. The collector is a metal point-contact rectifier; the collector current, I_c, is observed on the oscilloscope.

For a constant voltage pulse of duration t_p, the time dependence of collector current is shown in Fig. 7. For $t<0$, there is a collector current, I_{dc}, corresponding to a given dc collector bias, V_c. At $t\geq 0$, there is an additional collector current I_p, due to added biasing effect by the pulse voltage. At time, t_a, the deficit in minority carrier concentration arrives at the collector; I_c decreases to I_c'. It stays constant again until time, t_p, when the pulse voltage drops to zero; I_p' drops to zero, leaving I_{dc}'. This is the collector current at the given dc bias, for the condition of depleted minority-carrier concentration in the sample. I_{dc}' then recovers to its steady-state value, I_{dc}.

The composition of the reverse current for the collector is deduced from the I_c curve. The change in reverse current at a given dc bias, due to extraction of minority carriers from the sample, is represented by ΔI_{dc}. It may therefore be associated with that part of the reverse current due to diffusion of thermally generated minority carriers from the bulk to the contact. It was observed that even for complete depletion, ΔI_{dc} was appreciably less than I_{dc}. For collectors made with tungsten and phosphor-bronze whiskers on 20–40 ohm-cm, p- and n-type samples having lifetimes of several hundred microseconds, $\Delta I_{dc}/I_{dc}$ was rarely more than 0.5, and usually less, at room temperature, and in the dark.

This ratio can depend on the collector reverse bias, as is illustrated in Fig. 8 by curves of I_{dc} and ΔI_{dc}, *vs* V_c, for a phosphor-bronze contact to p-type Ge. The characteristics were taken at room temperature in the dark. In this case, I_{dc} increases almost linearly with reverse bias, while ΔI_{dc} is nearly constant. It is to be expected, however, that behavior of this kind may vary considerably with surface treatment and the forming of the rectifier contact.

It may be concluded that, under the conditions described above, most of the collector reverse current is composed of majority carrier and/or surface leakage current. However, when the minority carrier concentration in the sample is made much larger, most of the reverse current can be composed of minority carriers, and then extraction is much more effective in controlling the collector properties. This is readily shown by illuminating the collector so that the reverse resistance is greatly decreased. Upon extraction, it is possible to restore and even exceed the dark resistance.

VI. SUMMARY AND APPLICATIONS

Two conditions have been established for the effective extraction of minority carriers from germanium: (a) the injection efficiency, γ_e, at the entry contact must be close to zero, and (b) the minority carriers in the sample must be swept out in a time $\ll\tau$. With a series of p-type samples (7–40 ohm-cm at 300°K), to which In contacts were soldered, these conditions were generally satisfied for $T\lesssim 370$°K; complete minority carrier depletion was obtained for $T\lesssim 340$°K. The decrease in effectiveness of extraction at higher temperature and/or deeper in the intrinsic range is attributed to increase in γ_e with temperature, and the decrease in the transport velocity of the minority carrier concentration as $n_0\rightarrow p_0$. Within its range of effectiveness, extraction is a useful supple-

ment to injection for modulating bulk and contact properties. Transient and transport effects associated with extraction can be used for measuring minority carrier drift mobility and lifetime. A special feature of extraction is its usefulness in extending the temperature range of operation of diodes and transistors. This may be accomplished with an auxiliary, extraction electrode and sweep field, or more simply, if less efficiently, by utilizing a base contact which satisfies the condition for extraction. In the latter case, when reverse current at the collector is high enough to permit appreciable field in the base region, considerable minority carrier depletion, and consequent enhancement of reverse resistance of the collector can be observed. Thus an extraction base contact, not only suppresses undesirable excess minority-carrier injection, but it also depresses the minority-carrier current which would normally be present.

ACKNOWLEDGMENTS

The author wishes to express his appreciation to Professor K. Lark-Horovitz and Professor H. Y. Fan for their interest and discussions.

PHYSICAL REVIEW VOLUME 100, NUMBER 4 NOVEMBER 15, 1955

Effect of Shape Anisotropy on the Coercive Force of Elongated Single-Magnetic-Domain Iron Particles

T. O. Paine, L. I. Mendelsohn, and F. E. Luborsky
Measurements Laboratory, General Electric Company, Lynn, Massachusetts

(Received April 19, 1955)

Elongated single-magnetic-domain iron particles, 150 angstrom units in diameter, have been prepared with properties that definitely confirm the existence of a shape anisotropy effect on coercive force. This conclusion is based upon four observations: (1) Torque curve analysis shows the predominating anisotropy effect to be uniaxial. (2) With increasing particle elongation, the temperature coefficient of coercive force departs from the temperature coefficient of crystal anisotropy and approaches the temperature coefficient of saturation induction. (3) Coercive forces greater than 2000 oersteds for iron have been measured. (4) A direct correlation is observed between particle coercive force and elongation.

I. INTRODUCTION

A BETTER understanding of the basic factors which determine the properties of high-coercive-force magnetic materials is emerging from studies of submicroscopic ferromagnetic particles, too small to contain magnetic domain boundaries. These "single-domain particles" cannot change their magnetization in response to an externally applied field by the relatively easy process of domain boundary movement, in the manner of soft magnetic materials, but respond to a field by the more difficult process of rotating their magnetization vectors. The magnetic anisotropy effects, opposing domain rotation, thus determine the coercive force of these particles.[1] Although the sources of magnetic anisotropy are not completely understood, four effects have been suggested: magnetocrystalline anisotropy,[2] strain anisotropy,[3,4] shape anisotropy,[4] and surface anisotropy.[5] The existence of these proposed anisotropy effects has not been experimentally confirmed, with the exception of crystal anisotropy, which was conclusively demonstrated in an investigation of the coercive force of fine particles of manganese-bismuth by Guillaud.[2] Crystal anisotropy has also been studied in iron by Néel[6] and in barium-iron oxide and related compounds by Went *et al.*[7]

It is now eight years since Stoner and Wohlfarth,[4] Néel,[5] and Guillaud[3] first suggested that the shape anisotropy of an elongated single-domain particle of iron should be more than ten times as great as its crystal anisotropy. Although the existence of shape anisotropy has not been confirmed experimentally during this time, Weil,[9,10] Galt,[11] and Meiklejohn[12] have attributed discrepancies between observed and calculated coercive force values to a possible shape-anisotropy effect arising from statistical fluctuations in particle dimensions, and Nesbitt[13,14] and Kronenberg[15] have established the presence of an elongated precipitate

[1] C. Kittel, Phys. Rev. **70**, 965 (1946); see also Revs. Modern Phys. **21**, 541 (1949).
[2] C. Guillaud, thesis, Strasbourg, 1943 (unpublished).
[3] C. Guillaud, J. phys. radium **8**, 347 (1947).
[4] E. Stoner and E. Wohlfarth, Trans. Roy. Soc. (London) **A240**, 599 (1948).
[5] L. Néel, Compt. rend. **237**, 23 (1953).
[6] L. Néel, Compt. rend. **224**, 1488 (1947).
[7] Went, Rathenau, Gorter, and van Oosterhout, Phillips Tech. Rev. **13**, 194 (1952).
[8] L. Néel, Compt. rend. **224**, 1550 (1947).
[9] L. Weil and S. Marfoure, J. phys. et radium **8**, 358 (1947).
[10] L. Weil, International Powder Metallurgy Day, Graz, July, 1948, No. 17 (unpublished).
[11] J. Galt, Phys. Rev. **77**, 845 (1950).
[12] W. Meiklejohn, Revs. Modern Phys. **25**, 302 (1953).
[13] Nesbitt, Williams, and Bozorth, J. Appl. Phys. **25**, 1014 (1954).
[14] E. Nesbitt and P. Heindenreich, Elec. Eng. **71**, No. 6, 530 (1952).
[15] K. J. Kronenberg, Z. Metallkunde **45**, 440 (1954).

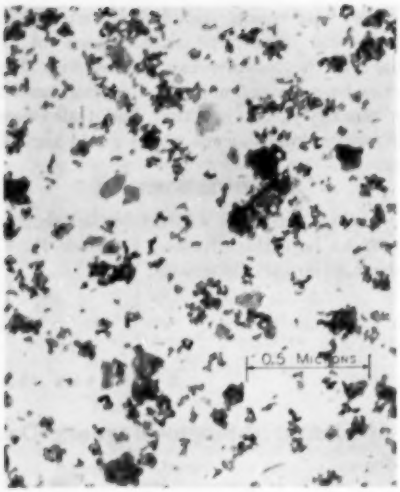

FIG. 1. Fine particle iron *A*. Median elongation 1.3; coercive force 1090 oersteds.

possessing shape anisotropy in the permanent-magnet alloy Alnico V.

It is the purpose of this paper to report on recent work at this laboratory which has resulted in the production of substantially elongated single-domain iron particles of high coercive force with properties that definitely confirm the existence of the shape-anisotropy effect.

II. DESCRIPTION OF THE PARTICLES

The preparation and observation of elongated iron particles with diameters between 100 and 1000 angstrom units present experimental difficulties which have prevented previous confirmation of the shape anisotropy effect. The particles described in this paper were produced by electrodepositing iron into a molten metal cathode. This venerable technique was employed by Herschel[16] over a century ago, and has since been used by Nagaoka,[17] Antik,[18] Dean,[19] Pawlek,[20] Mayer,[21] and Meiklejohn[12] to produce single-domain iron particles. By modifying this process in certain essential details, it was discovered that substantially elongated iron particles could be produced.

Figures 1 through 4 are electron micrographs of these particles at 50 000× magnification made by dispersing the particles on a thin film for direct observation with a high resolution electron microscope.[22] This technique successfully achieved resolutions down to 20 angstrom units, and permitted a direct measurement of particle size and shape. The diameter and length of each of the

FIG. 3. Fine particle iron *C*. Median elongation 3.0; coercive force 1600 oersteds.

FIG. 2. Fine particle iron *B*. Median elongation 2.7; coercive force 1360 oersteds.

several hundred particles that could be resolved in a 100 000× electron micrograph were measured to the nearest quarter of a millimeter (corresponding to 25 angstrom units actual size), and distribution curves prepared for each sample. Typical curves are shown in Fig. 5. The diameter distribution was essentially Gaussian, with a standard deviation on the order of 35 angstrom units for most samples. The length-to-

[16] J. Herschel, Trans. Roy. Soc. (London) **114**, 183 (1824).
[17] H. Nagaoka, Ann. Physik. (3) **59**, 66 (1896).
[18] I. Antik and T. Kubyschkina, Wiss. Ber. Univ. Mosk. **11**, 143 (1934).
[19] R. Dean and C. Davis, U. S. Patent 2,239,144 April 22, 1941.
[20] F. Pawlek, Z. Metallkunde **42**, 451 (1950).
[21] A. Mayer and E. Vogt, Z. Naturforsch. **7a**, 334 (1952).
[22] M. Schuster and E. Fullam, Ind. Eng. Chem., Anal. Ed. **18**, 653 (1946). The authors are deeply indebted to E. F. Fullam of E. F. Fullam, Inc., for his beautifully detailed electron micrographs which have contributed so greatly to this work.

diameter ratio of the particles showed a logarithmic rather than a linear Gaussian distribution.

Figure 1 shows the almost spherical particles of sample *A*. The authors have prepared similar particles by the low-temperature decomposition of iron salts as described by Honda[22] and others.[24–28] Particles from sample *B* with twice this elongation, but characterized by an irregular, roughened surface, are shown in Fig. 2. Even greater elongations with a somewhat different structure are shown in Figs. 3, 4, and 6. These views of samples *C*, *D*, and *E* reveal the presence of dendritic branches on many of the particles. Samples *A* through *D* have mean particle diameters between 140 and 150 angstrom units; sample *E* has a larger mean particle diameter of 175 angstrom units. These diameters refer to the main body of the particles without any correction for the dendritic branches.

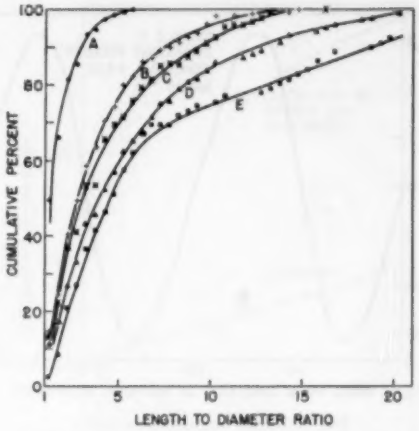

FIG. 5. Distribution of particle elongations for samples *A*, *B*, *C*, *D*, and *E*.

FIG. 4. Fine particle iron *D*. Median elongation 4.0; coercive force 1600 oersteds

It is interesting to note that the median length-to-diameter ratio of the particles in sample *E* is 4.6 and that 25% of this sample consists of particles with an elongation ratio greater than 10, with a few as high as 40. Stereoscopic electron micrographs have shown that the dispersion technique used causes most of the particles to lie flat on the film, minimizing distortion due to third-dimension alignment.

III. MAGNETIC MEASUREMENTS

To determine the intrinsic coercive force of each sample, the particles were dispersed in a liquid to a packing density below 5%, and then frozen in liquid nitrogen. The sample was then magnetized, and the reverse field required to reduce its intrinsic induction to zero determined at −197°C. Zero induction was detected by a sensitive galvanometer connected to a search coil fixed in the demagnetizing field. Coercive force values given are reproducible to 2%, with an overall accuracy well within 5%. More precise magnetic permeameter measurements of the complete hysteresis loops were made on bars prepared by dispersing the particles in a lead-tin-bismuth low-melting alloy. The intrinsic coercive force measurements were confirmed by the permeameter, which is accurate to within 2%. The particles dispersed in the low-melting alloy were

FIG. 6. Fine particle iron *E*. Median elongation 4.6; coercive force 1850 oersteds.

[22] K. Honda, Nippon Kinzoku Gakkai-Shi No. 1, 3 and 19 (1937).
[24] British Patent 590,392, April 7, 1942.
[25] F. Bertaut, Compt. rend. **229**, 417 (1949).
[26] F. Lihl, Acta Phys. Austriaca **4**, 360 (1951).
[27] B. Kopelman, Elec. Eng. **71**, No. 5, 447 (1952).
[28] Stewart, Conard, and Libsch, J. Metals **7**, 152 (1955).

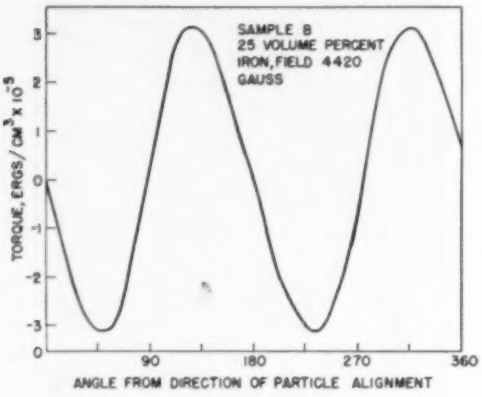

FIG. 7. Torque magnetometer curve.

suitable for precise measurements over the temperature range from −197°C to +25°C, which allowed the temperature coefficients of induction and coercive force to be established.

To provide further information on the nature of the anisotropy responsible for the observed magnetic properties, samples were prepared suitable for torque magnetometer studies. These one-inch diameter disks, 24 mils thick, contained 25% iron by volume, and were directionalized by applying a 5000 gauss field along the diameter during the solidification of the low-melting alloy matrix. The measurements were made by R. D. Robinson using the recording torque magnetometer at the General Electric Research Laboratory.

DISCUSSION

The electron micrographs clearly reveal the elongation of the particles, and the magnetic properties observed are all consistent with the concept of single-domain particles of iron with a high coercive force derived from shape anisotropy. Each of the observed magnetic properties will be considered in turn.

A. Torque Magnetometer Curves

The typical torque magnetometer curve shown in Fig. 7 indicates that the magnetic anisotropy of the sample is uniaxial rather than cubic. If any crystalline anisotropy is present, it was either not aligned by the directionalizing field, or was too small to be detected. No torque was measurable on the round particle samples. Electron microscope work to be published elsewhere reveals that the long axis of each particle is aligned by the directionalizing field. This, in conjunction with the observed uniaxial anisotropy, eliminates crystal anisotropy as the predominating effect.

B. Temperature Coefficient of Coercive Force

The coercive force due to crystal anisotropy should be proportional to K/I_s, while that due to shape anisotropy is predicted to be proportional to I_s, where K is the crystal-anisotropy constant, and I_s the saturation induction.[1] By comparing the observed temperature coefficient of coercive force for the elongated iron particles with the temperature coefficients of K/I_s and I_s measured for bulk iron, it is possible to discriminate between crystal- and shape-anisotropy effects.

The measurements reported in Table I show a clear correlation between particle elongation and temperature coefficient of coercive force. Round particles have the expected large temperature coefficient of coercive force proportional to the temperature coefficient of K/I_s, but with increasing particle elongation the temperature coefficient of coercive force is observed to approach the smaller temperature coefficient of I_s. These results demonstrate that crystal anisotropy determines the coercive force of the round iron particles produced by the low-temperature reduction of iron salts, but with increasing particle elongation shape anisotropy becomes the predominating effect.

C. High Coercive Force

To a first approximation the predicted coercive force of a round single-domain particle due to crystal anisotropy is:

$$H_{ci}=2K/I_s \quad \text{for favorable orientation;} \qquad (1)$$

$$H_{ci}=0.64K/I_s \quad \text{for random orientation;} \qquad (2)$$

where K is the cubic crystal anisotropy constant (4.2×10^5 ergs/cm³ for iron) and I_s is the saturation magnetization (1700 gauss for iron). This predicts a coercive force of 490 oersteds for favorably-oriented iron particles, and 160 oersteds for random orientation.[1] In view of the approximate nature of these calculations, it is not surprising that the experimentally-observed values for round iron particles have run as high as 1000 oersteds.[10–12,21] In addition, discrepancies may arise from the difficulty of producing ideal crystals, free of strains or elongation.

A length-to-diameter ratio as low as 1.3 might account for the reported coercive force of iron particles, according to the calculations by Stoner and Wohlfarth.[4] They proposed that the coercive force of a randomly-oriented elongated particle should be

$$H_{ci}=0.479(N_d-N_l)I_s, \qquad (3)$$

TABLE I. Correlation between median particle elongation and temperature coefficient of coercive force.

	−200°C to +25°C temperature coefficient %/°C
Predicted for crystal anisotropy (K/I_s)	97×10^{-4}
Round iron from formate reduction	85×10^{-4}
Sample *A*, elongation ratio 1.3	58×10^{-4}
Sample *B*, elongation ratio 2.7	28×10^{-4}
Predicted for shape anisotropy (I_s)	7×10^{-4}

where N_d and N_l represent the demagnetizing factors of the particle along the diameter and length, respectively. For particles with a length-to-diameter ratio of 1.3, a coercive force of 1000 oersteds is predicted. This increases to 4800 oersteds for particles with an elongation of 10.

The coercive force values as high as 2100 oersteds observed in the course of this work are much greater than crystal anisotropy could reasonably explain, and are strong evidence for the existence of the shape-anisotropy effect.

D. Correlation between Particle Elongation and Coercive Force

Table II summarizes the results of the elongation and coercive-force measurements. Figure 8 compares these results with Stoner and Wohlfarth's predictions for single-domain prolate ellipsoids. It is assumed that the intrinsic coercive force of a sample made up of single-domain particles represents the condition of zero induction caused by the reversal of 50% of the particles, and that the coercive force of the sample will therefore be related to the median elongation.

There are a number of reasons why the observed coercive forces might be substantially less than predicted. The irregularities and dendritic branches of the actual particles are far from the ideal prolate ellipsoids assumed by Stoner and Wohlfarth. The particle diameters are less than optimum, so the smaller particles may lose coercive force by the thermal reversal mechanism described by Néel,[29] Bertaut,[25] and Meiklejohn.[12] The inevitable agglomeration of these magnetic particles will certainly decrease the coercive force of the samples[1]; infinite dilution was assumed in the calculations. Any omission of small round particles in the counting would make the median elongation appear to be higher than actual. The coercive force of a sample containing a variety of particle shapes and diameters is not well understood, and may be less than the median.[30] It has been suggested by Bean and Jacobs that the uniform rotation of the magnetization vector assumed by Stoner and Wohlfarth may not take place, and instead these particles may reverse their magnetization by an easier nonuniform process.[31] Finally, the contribution of crystal anisotropy is not known, and may act to increase or decrease the coercive force of the particles depending upon the crystallographic orientation of the particle axis. Any of these factors may account for the discrepancies between the predicted and observed results. The measurements do not provide quantitative confirmation of Stoner and Wohlfarth's predictions, but the observed relation between elongation and coercive force confirms the existence of a shape anisotropy effect.

TABLE II. Measured properties of single-domain iron particles.

Sample	Mean diameter, angstroms	Median length-to-diameter ratio	Coercive force, oersteds
A	145	1.3	1090
B	150	2.7	1360
C[a]	140	3.0	1600
D[a]	140	4.0	1600
E[a]	175	4.6	1850

[a] Particles with dendritic structure.

[29] L. Néel, Compt. rend. **228**, 664 (1949).
[30] E. Wohlfarth, Research **7**, No. 3, S18, March, 1954.

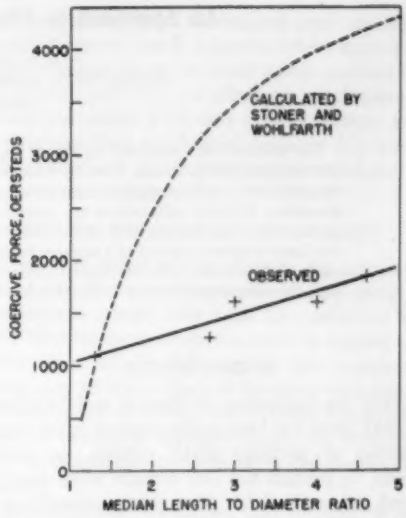

FIG. 8. Relation between median elongation and coercive force.

V. CONCLUSIONS

The uniaxial anisotropy indicated by torque magnetometer curves, the agreement between the temperature coefficients of coercive force and induction, the coercive force values of 2100 oersteds observed for pure iron, and the direct correlation between particle elongation and coercive force, all confirm the existence of a shape anisotropy effect on the coercive force of single magnetic domain particles.

ACKNOWLEDGMENTS

The authors are deeply indebted to I. F. Kinnard, whose encouragement and support made this work possible. The invaluable contributions of J. H. Hollomon, J. C. Fisher, W. H. Meiklejohn, and A. H. Geisler of the General Electric Research Laboratory, and Miss P. G. Gormley of this laboratory, are gratefully acknowledged.

[31] C. Bean and I. Jacobs (to be published).

An Approach to Elongated Fine-Particle Magnets

I. S. JACOBS AND C. P. BEAN
General Electric Research Laboratory, Schenectady, New York
(Received June 21, 1955)

The coercive force predicted by theory for single-domain particles with shape anisotropy frequently far exceeds the observed value. From an examination of the results of Paine, Mendelsohn, and Luborsky on elongated iron particles, several approximate models are suggested which may exist in certain experimental situations. Detailed calculations are presented for a "chain-of-spheres" model remagnetizing by several mechanisms. Comparison with experiment on certain single-domain particles of known elongation favors the chain-of-spheres model as a suitable description of their magnetic behavior. A successful calculation is made of the coercive force of material prepared by several earlier workers. A comparison of the new models with the older ones indicates a direction for experimental advance.

INTRODUCTION

SINCE the suggestion of Frenkel and Dorfman[1] in 1930, there has been active interest in the magnetic properties of particles small enough, on energetic grounds, to contain but one domain when there is no applied magnetic field. The theory describing such single-domain particles has been enlarged by Guillaud,[2] Néel,[3] Kittel,[4] Stoner and Wohlfarth,[5] and Kondorskii.[6] Thorough expositions of this field may be found in the survey by Kittel[7] and in the work of Stoner and Wohlfarth,[5] with much experimental work appearing in the reports of recent conferences on magnetism.[8,9]

The coercive force of a single-domain particle is generally expected to have a high value, since the magnetization changes occur, as a limiting case, through the usually high field process of rotation of the total magnetic moment of the particle. This rotation process is controlled by the effective anisotropy of the particle, for which a number of sources are usually considered.[7] The present paper is concerned with the coercive force of fine particles, resulting from anisotropy of particle shape. If the particle has the shape of a prolate spheroid whose major axis coincides with the field direction, its intrinsic coercive force is given by $H_c=(N_t-N_0)I_s$, where I_s is the saturation magnetization, and N_0, N_t are the demagnetizing factors of the spheroid along the major and minor axes, respectively. Stoner and Wohlfarth have presented a very detailed treatment of this process, including the averaging for random orientation of particle axes. This mechanism is probably operative in certain heterogeneous alloys[5,10,11] and it probably contributes to the coercive force of some fine particles produced by reduction or electrodeposition of ferromagnetic materials.[5,12–15]

The realization of the predicted magnetic properties for elongated single-domain particles has been hindered by experimental difficulties. On the theoretical side, there exists the possibility of finding a mechanism for magnetization reversal with lower energy than the Stoner and Wohlfarth mechanism of simultaneous parallel rotation of all the atomic moments.[16,17] In a current paper,[18] Paine, Mendelsohn, and Luborsky demonstrate the predominance of a shape-anisotropy effect on the coercive force of elongated single-domain particles of iron produced during electrodeposition. Dilute suspensions of this material have coercive forces as high as 2000 oe. Observations in an electron microscope reveal the anisotropy of shape of these particles and an average particle diameter of 150 A. Such electron micrographs enable the preparation of particle elongation distribution curves for each sample. This information makes possible a comparison of fine-particle theory with single-domain particles of known elongation. An ideal situation of this kind has seldom, if ever, been realized in fine-particle work.

It is instructive to make a rough comparison of the elongated fine-particle iron described by Paine *et al.* with the predictions of the Stoner-Wohlfarth analysis. Theoretically, two situations are of interest, that of perfect alignment and that of complete randomness in the orientation of the elongated particles. Experimentally, this material is capable of a partial alignment with some resulting directionality in magnetic properties. For the present we neglect crystal anisotropy and use the median elongation to characterize the assembly. For dilute suspensions with a median elongation of 3 to 1 (Samples *B* and *C* of reference 18), a representative

[1] J. Frenkel and J. Dorfman, Nature **126**, 274 (1930).
[2] C. Guillaud, Revs. Modern Phys. **25**, 308 (1953).
[3] L. Néel, Compt. rend. **224**, 1488, 1550 (1947).
[4] C. Kittel, Phys. Rev. **70**, 965 (1946).
[5] E. C. Stoner and E. P. Wohlfarth, Trans. Roy. Soc. (London) **A240**, 599 (1948).
[6] E. Kondorskii, Doklady Akad. Nauk. S.S.S.R. **70**, 215 (1950).
[7] C. Kittel, Revs. Modern Phys. **21**, 541 (1949).
[8] Revs. Modern Phys. **25**, 1–351 (1953).
[9] J. phys. radium **12**, 151–508 (1951).
[10] L. Néel, Compt. rend. **225**, 109 (1947); Appl. Sci. Research **B4**, 13 (1954).
[11] Nesbitt, Williams, and Bozorth, J. Appl. Phys. **25**, 1014 (1954); E. A. Nesbitt and R. D. Heidenreich, J. Appl. Phys. **23**, 366 (1952).
[12] L. Weil, J. phys. radium **12**, 437 (1951).
[13] J. K. Galt, Phys. Rev. **77**, 845 (1950).
[14] A. Mayer and E. Vogt, Z. Naturforsch. **7a**, 334 (1952).
[15] W. H. Meiklejohn, Revs. Modern Phys. **25**, 302 (1953).
[16] L. J. Dijkstra, *Thermodynamics in Physical Metallurgy* (American Society for Metals, Cleveland, 1950), p. 271.
[17] C. P. Bean (unpublished).
[18] Paine, Mendelsohn, and Luborsky, this issue [Phys. Rev. **100**, 1055 (1955)].

coercive force when in the random arrangement is about 1500 oe (measured at −196°C). Alignment may raise this to 1700 or 1800 oe in the parallel direction by about 1200 to 1400 oe in the transverse direction. The Stoner-Wohlfarth calculations predict about 3500 oe for the random-state coercive force and 7200 oe by 0 oe for the aligned state. This discrepancy warrants further attention. In what follows, there will be described a simple model with several variations which is capable of accounting for a number of experimental observations made on this elongated fine-particle iron.

"CHAIN-OF-SPHERES" MODEL

An alternative model of an elongated particle is a chain of single-domain spheres, rather than the prolate ellipsoid employed by Stoner and Wohlfarth. In this idealized model the spheres are sometimes assumed to have only point contact, or even to be slightly separated so as to be magnetically isolated. We shall refer to this model as a "chain of spheres."

This sort of model has been envisaged in the past,[19,20] and suggestions have been made for obtaining the chain experimentally. Beischer and Winkel[20] have noted a self-alignment feature in the model and presented some experimental evidence for it. Briefly stated, the self-alignment mechanism is that single-domain spheres have a tendency to line up with their moments along the common axis, due to magnetostatic interactions. To consider the alignment mechanism, we treat each sphere as a dipole of moment μ and diameter a, and examine their interactions. If dipoles μ_i and μ_j, separated by a distance r_{ij}, make angles θ_i and θ_j with the vector joining them, their energy is

$$W=(\mu_i\mu_j/r_{ij}^3)[\cos(\theta_i-\theta_j)-3\cos\theta_i\cos\theta_j]. \quad (1)$$

Adding terms of this type, it is easy to show that two spheres in contact are most stable with their moments aligned along the line of centers. Similarly, for three spheres the aligned configuration is more stable than any other, including those which offer a sort of flux closure. This situation changes when we allow four spheres to come together. Now, the flux closure configuration of a square array, moments at 45° to connecting lines, is more stable than the aligned configuration. The self-alignment mechanism need not fail at this point, however, for if a fourth sphere approaches a straight chain of three, its most stable position is at the chain end, provided we admit no mechanism for deforming the chain. With this growth feature, aided by some unspecified welding of spheres, this scheme may be added to those previously considered for making connective chains.

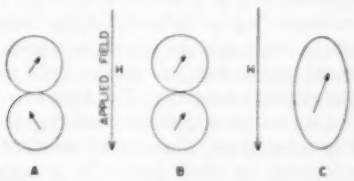

FIG. 1. Magnetization reversal of aligned chain or particle. Chain-of-spheres model: *A*—symmetric fanning mechanism; *B*—parallel rotation mechanism. Prolate spheroid model: *C*—parallel rotation mechanism.

COERCIVE FORCE OF ALIGNED CHAINS

The principal object of this paper is the calculation of the coercive force of dilute suspensions, using the chain-of-spheres model. We shall be concerned first with the coercive force when the chain is aligned with the field. This will be followed by the appropriate averaging over all orientations of the chain with respect to the field, so as to obtain the coercive force for an assembly of randomly oriented chains. At that point we may compare the predictions of the model with experiment.

For the calculation, we assume that the spheres have no crystal anisotropy. The shape anisotropy of the chains will follow from the arrangement of the dipolar spheres as they interact with each other and with the external field. There are two reversal mechanisms which will be considered for the chain of spheres. (See Fig. 1.) The simpler one is that of simultaneous parallel rotation of each of the dipole moments in the chain. (This will be designated as mechanism *B*.) This mechanism is identical to that employed by Stoner and Wohlfarth, with the exception that the specific value for the coercive force of a chain proves to be lower than that for an ellipsoid of the same axial ratio. The averaging procedure is identical, yielding the same numerical factor (0.479) relating the coercive force of the randomly oriented assembly to that of the perfectly aligned (noninteracting) assembly. The second mechanism is that in which the moments fan out in a plane, alternating in the sense of their rotation from one sphere to the next, proceeding along the chain. We assume here that there is no exchange-energy interaction where adjacent spheres are closest. In other words, the "wall" area is confined to the "point" of contact, or the spheres are slightly separated. It is easy to show that fanning in a plane is favored over any other arrangement of fanning with respect to the chain axis. A special case of this observation is that the mechanism of fanning in a plane yields a lower magnetostatic energy during magnetization reversal than does the simultaneous parallel-rotation mechanism. It is instructive, however, to include the calculations for the higher-energy process, as it may occur if the wall energy contribution becomes significant. It is important to note that a simplifying assumption is made in the calculations for the fanning mechanism, i.e., the magnitude of the angle of fanning is constant along the length of the chain. This assumption of symmetric fanning is rigorously correct for the two-sphere chain and for the infinitely long chain whose

[19] U. S. Materials Advisory Board, Panel on Permanent Magnet Materials, Report MMAB–34–M, 1953 (unpublished).
[20] D. Beischer and A. Winkel, Naturwiss. **25**, 420 (1937).

ends meet. Separate calculations of the coercive force, made without the above restriction, for aligned chains of finite and semi-infinite length show the existence of an end effect. This leads to lower coercive forces than those predicted by symmetric fanning. Exact solutions are readily obtained for aligned chains of six or less spheres. For the semi-infinite chain a close approximation is obtained by starting with a trial solution suggested by a soluble model involving only nearest neighbor interactions. When considering the reversal by fanning of unaligned chains, the symmetric-fanning model is more tractable. Consequently this mechanism will be retained for detailed investigation. It will be shown that the errors originating in its use are small when the chains are not long. (We shall designate the symmetric-fanning process as A and the nonsymmetric-fanning process as A'.)

To calculate the coercive force for a chain aligned with the field, we consider the total energy of the chain at some point during the reversal, being the sum of the interdipole magnetostatic energy and the field energy with the field directed opposite to the initial direction of magnetization of the chain. This energy is minimized with respect to its angle parameter to obtain an expression for the equilibrium field for a given angle. The coercive force is obtained from this expression by inspection. In the case of parallel rotation, $\theta_i=\theta_j=\theta$ for all i, j in the chain of n. The total energy is then

$$W_n=(\mu^2/a^3)nK_n(1-3\cos^2\theta)+n\mu H\cos\theta, \quad (2)$$

where

$$K_n=\sum_{j=1}^{n}(n-j)/nj^3. \quad (3)$$

Proceeding as described, the coercive force for parallel rotation, B, is

$$H_{c,n}=(\mu/a^3)6K_n. \quad (4)$$

In similar fashion, for the symmetric fanning mechanism where $\theta=\theta_1=-\theta_2=\theta_3=-\theta_4=\cdots$, we write for the total energy:

$$W_n=(\mu^2/a^3)nL_n(\cos2\theta-3\cos^2\theta)+(\mu^2/a^3)nM_n(1-3\cos^2\theta)+n\mu H\cos\theta, \quad (5)$$

where

$$L_n=\sum_{j=1}^{\frac{1}{2}(n-1)<j\leq\frac{1}{2}(n+1)}[n-(2j-1)]/n(2j-1)^3, \quad (6)$$

$$M_n=\sum_{j=1}^{\frac{1}{2}(n-2)<j\leq\frac{1}{2}n}(n-2j)/n(2j)^3, \quad (7)$$

$$L_n+M_n=K_n. \quad (8)$$

Thus we obtain for the coercive force in the fanning mechanism, A,

$$H_{c,n}=(\mu/a^3)(6K_n-4L_n). \quad (9)$$

Noting that $\mu/a^3=\pi I_s/6$ which is about 900 oe for iron, we may tabulate the coercive forces for chains (or elongated particles) of various lengths (or axial ratios). This is done in Table I, and includes the results for the nonsymmetric fanning mechanism, A', along with the coercive forces for prolate spheroids, C, calculated as indicated previously.

TABLE I. Comparison of coercive force of chains or particles of iron aligned with magnetic field. (A) Chain of n, symmetric fanning mechanism Eq. (9). (A') Chain of n, nonsymmetric fanning mechanism. (B) Chain of n, parallel rotation mechanism, Eq. (4). (C) Prolate spheroid of axial ratio n, parallel rotation mechanism.

n Chain length or axial ratio	H_c in oersteds A	A'	B	C
1	0	0	0	0
2	900	900	2700	5160
3	1420	1400	3820	7260
4	1690	1590	4430	8340
5	1870	1680	4810	8980
6	2020	1720	5070	9400
7	2090	···	5260	9650
8	2160	···	5390	9860
9	2220	···	5530	10 000
10	2270	···	5630	10 100
11	2310	···	5700	10 200
12	2340	···	5760	10 300
∞	2700	1750	6470	10 800

Several points are of interest in connection with the data of Table I. As implied above, the fanning mechanisms (A,A') have lower coercive forces than the other mechanisms. For experiments with elongated particles, it is particularly significant that the maximum coercive forces by fanning are considerably lower than the corresponding maximum attainable with parallel rotation of the magnetic moments in an ellipsoid (C). The lower coercive forces of the various chain models compare attractively with existing experimental results.

MAGNETIZATION OF RANDOMLY ORIENTED CHAINS

We have now to obtain the hysteresis loop for an assembly of randomly oriented chains of spheres, when the magnetization reversal mechanism of a chain aligned with the field is the symmetric-fanning process, A. For mechanism A', we shall use an approximation based on A, while B is similar to C, previously described.[5] The composite loop is synthesized from the family of loops corresponding to different angles between the field and the chain axis. As this angle approaches 90°, the reversal mechanism will change over to that of simultaneous parallel rotation. This feature is responsible for an approximate equivalence of the random and aligned coercive forces. There is no universal random loop, adjustable to chain length by a scale factor, because the ratio K_n/L_n, Eq. (9), is a slowly varying function of n. We carry out specific calculations for two cases, a chain of two spheres and an infinitely long chain, and interpolate for chains of intermediate length.

The choice of coordinates facilitates the calculation. Consider that the field, H, is applied along the z-axis,

in the $-z$-direction. Let the chain lie in the xz-plane, its axis making an angle ψ with the z-axis. The sphere moments will be described by their polar angle θ, with respect to the z-axis, and their azimuthal angle ϕ measured in the xy-plane, with respect to the x-axis. During the fanning process, the angle ϕ alternates in sign from one sphere to the next along the chain, but $|\phi|$ is constant in accordance with our assumption for this process, A. In terms of this description, the total energy for a chain of n spheres, comprised of magnetostatic and field energy terms, is given by

$$\begin{aligned} W_t(\theta,\phi,\psi,H) &= W_{ms}(\theta,\phi,\psi)+W_f(\theta,H) \\ &= -3nK_n(\mu^2/a^3)(\sin\psi\sin\theta\cos\phi \\ &\quad +\cos\psi\cos\theta)^2+nL_n(\mu^2/a^3)(\sin^2\theta\cos2\phi \\ &\quad +\cos^2\theta)+nM_n(\mu^2/a^3)+n\mu H\cos\theta, \end{aligned} \tag{10}$$

where K_n, L_n, and M_n are given by Eqs. (3), (6), and (7). To determine the hysteresis loop for a chain making a given angle ψ with the field, we calculate the equilibrium values of θ and ϕ at various values of the field H, i.e., minimize W_t at fixed ψ, H. The loop is then formed by plotting the resolved relative magnetization $I/I_s=\cos\theta$ *versus* H. The equations to be solved simultaneously are

$$(\partial W_t/\partial\phi)_\theta=(\partial W_{ms}/\partial\phi)_\theta=0, \tag{11}$$

$$(\partial W_t/\partial\theta)_\phi=(\partial W_{ms}/\partial\theta)_\phi+dW_f/d\theta=0. \tag{12}$$

From Eq. (11) we obtain a relation between θ and ϕ, which, upon substitution into Eq. (12), yields an equation in θ alone, depending on ψ and H as parameters. We complete the solution for θ graphically, by fixing ψ, plotting $(\partial W_{ms}/\partial\theta)_\phi$ and $-(dW_f/d\theta)$ for a given H, and determining their intersection. A simplification is introduced by using $\sin\theta$ as abscissa, in which case $(dW_f/d\theta)$ is a straight line whose slope is proportional to H.

To describe the features of the reversal, we first examine the roots of Eq. (11), which are

$$\sin\phi=0, \quad \phi=0,\pi \tag{13}$$

and

$$\cos\phi=A(\psi)\cot\theta, \tag{14}$$

where

$$A(\psi)=(3K_n/4L_n)\sin2\psi/[1-(3K_n/2L_n)\sin^2\psi]. \tag{15}$$

The first of these indicates parallel rotation of the moments, leading to the results of Stoner and Wohlfarth. The correct choice for our model is obtained by invoking a necessary condition for a minimum, i.e., $(\partial^2W_t/\partial\phi^2)_\theta>0$. This condition is satisfied as follows:

(*a*) by $\phi=0$, for $0\le\theta<\tan^{-1}A(\psi)$;

(*b*) by $\phi=\cos^{-1}[A(\psi)\cot\theta]$, for $|\tan\theta|\ge A(\psi)$;

(*c*) by $\phi=\pi$, for $\cot^{-1}(-1/A(\psi))<\theta\le\pi$.

The reversal mechanism is some sort of fanning in range (*b*), but this range becomes smaller as ψ increases until $\psi\ge\psi_0=\sin^{-1}(2L_n/3K_n)^{\frac{1}{2}}$ for which there is no longer a solution to Eq. (14). The angle ψ_0 varies from 54.8° for $n=2$ to 49.8° for $n=\infty$. For $\psi\ge\psi_0$, the complete reversal is by the parallel-rotation mechanism. The polar angle $\theta=\tan^{-1}A(\psi)$, marking the transition from parallel-rotation reversal to fanning reversal, increases with increasing ψ until $\psi=\psi_0$, at which point $\theta(\psi_0)=\pi/2$. Other features of the reversal appear in the graphical solution. For $\psi<\psi_0$, as H increases, there is a gradual change in $\cos\theta$, followed by a discontinuous change just at the angle θ marking the transition from parallel to fanning reversal. The only stable solutions occur in ranges (*a*) and (*c*), while range (*b*) is needed to permit the discontinuous reversals at fields lower than would occur with the parallel rotation mechanism alone. These fields mark the coercive forces for the loops in question. For $\psi\ge\psi_0$, discontinuous changes occur at $H>H_c$, as described by Stoner and Wohlfarth.

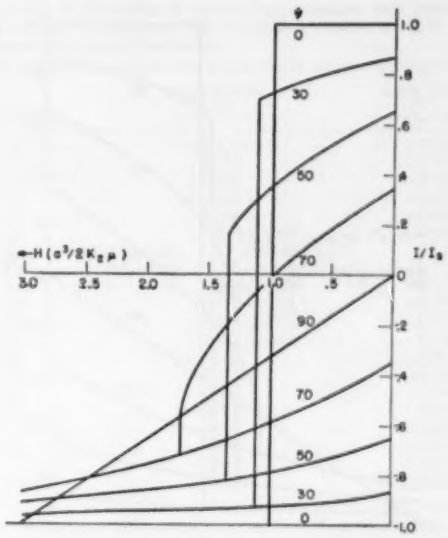

FIG. 2. Hysteresis loops for two-sphere chains oriented at various angles ψ to field. (Fanning mechanism.)

The results, in the form of graphs of representative hysteresis loops, are shown in Figs. 2 and 3 for $n=2$ and $n=\infty$, respectively. In Fig. 4, showing H_c *versus* ψ for mechanisms A and B, it is interesting to note the gradual rise in H_c (fanning) from its value at $\psi=0$, until it meets H_c (parallel rotation) at $\psi=\psi_0$ and then falls rapidly to zero. This comparison demonstrates the large difference between mechanisms A and B in their numerical "averaging" factor relating the aligned coercive force to that for a randomly oriented assembly.

Using data calculated for loops of constant ψ in 10° intervals, we proceed to the synthesis of the loops for an assembly of randomly oriented chains, all having either $n=2$ or $n=\infty$. The mean resolved value of the relative magnetization of the assembly at a particular

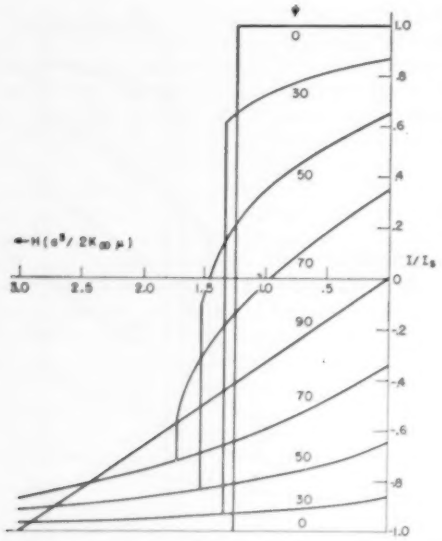

FIG. 3. Hysteresis loops for ∞-sphere chains oriented at various angles ψ to field (symmetric fanning mechanism).

field H is given by

$$\langle (I/I_s)_H \rangle_{\text{av}} = \langle (\cos\theta)_H \rangle_{\text{av}} = \int_0^{\pi/2} (\cos\theta)_H \sin\psi d\psi, \quad (16)$$

where the value of θ may depend on the previous history. In performing the graphical integration, integrand discontinuities lead to uncertainty in some of the points, but the resulting curves are sufficiently accurate for present purposes. The curves for $n=2$ and $n=\infty$ are shown in Figs. 5 and 6, while Table II presents data from which these curves may be reproduced. The most important results are the values of the random coercive force, as follows:

Chain length $n=2$;

$$\bar{H}_c = (1.13 \pm 0.02)(2K_2\mu/a^3) = 1.13 H_c(\psi=0),$$

Chain length $n=\infty$;

$$\bar{H}_c = (1.35 \pm 0.03)(2K_\infty\mu/a^3) = 1.08 H_c(\psi=0).$$

These findings are novel, in that the random coercive force exceeds the aligned coercive force, but, in practice, a number of factors may tend to mask this effect.

Figure 7 presents a comparative summary and evaluation of the results for the field of fine-particle ferromagnetic material having shape anisotropy. Specifically considered are the hysteresis loops for random and aligned assemblies reversing by three mechanisms,

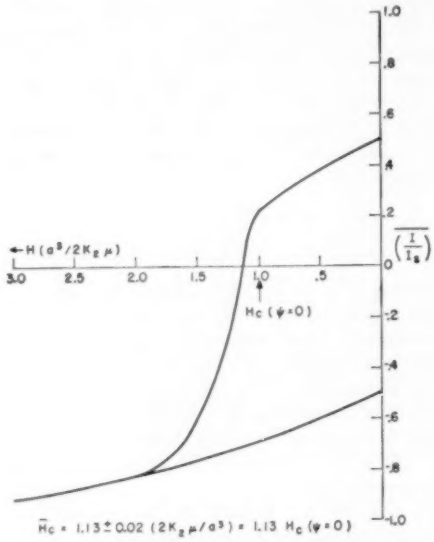

FIG. 5. Hysteresis loop of assembly of randomly oriented two-sphere chains. (Fanning mechanism.)

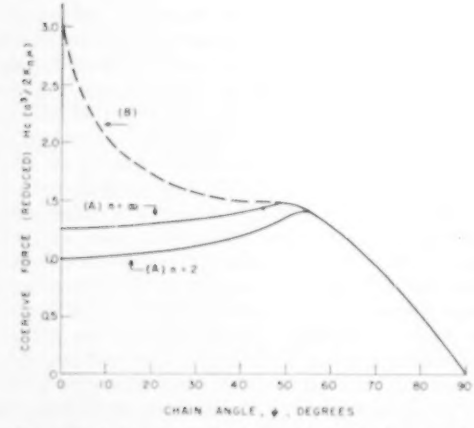

FIG. 4. Variation of coercive force with angle ψ between chain and field. (*A*) Symmetric fanning mechanism; $n=2$, $n=\infty$. (*B*) Parallel-rotation mechanism, all n.

fanning (*A*) and parallel rotation (*B*) for chains of spheres, and parallel rotation (*C*) for prolate spheroids. Curves *A* describe the magnetic behavior when the spheres of the chain appear isolated to the extent of feeling no exchange forces, but are subject to strong magnetostatic interaction. Curves *B* pertain when there is sufficient common boundary between the spheres of the chain to allow a strong exchange interaction which forces the reversal mechanism to be parallel rotation. This interaction raises the random coercive force but slightly, while the aligned coercive force increases by a factor of three over that in *A*. Curves *C* show a twofold increase in both coercive forces over those in *B*, illustrating the improvement in magnetic properties to be obtained when the chain is "filled out" to become a prolate spheroid. From the theoretical

side, there are three idealized models for analysis of actual situations which may be close to one of them, or lie between two of them.

COMPARISON WITH EXPERIMENT

The particle elongation distribution curves presented by Paine, Mendelsohn, and Luborsky[18] enable us to compare the magnetic properties predicted by the various models with their results. For the chain-of-spheres model, only integral elongation ratios are allowed, so unit length is assigned to particles whose ratios lie between 1 and 1.5, length 2 to particles between 1.5 and 2.5, and so on. This information is converted to histograms showing the volume percentage of particles in each group. The existence of universal hysteresis loops for mechanisms B and C facilitates

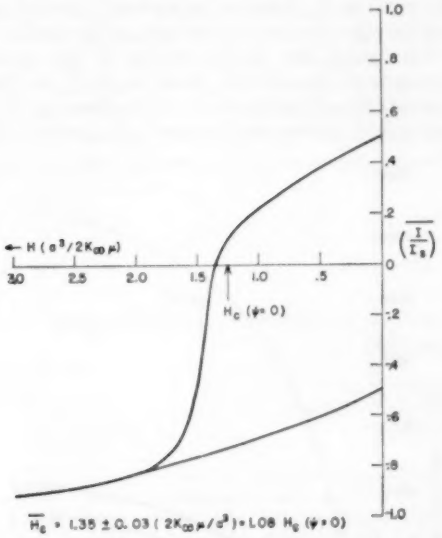

FIG. 6. Hysteresis loop of assembly of randomly oriented ∞-sphere chains (symmetric fanning mechanism).

the application of these data following the procedure recently described by Wohlfarth.[21] His integration is replaced here by a summation. When calculating the random coercive force for the symmetric fanning mechanism (A), the variation with n of the reduced hysteresis loops, Figs. 5 and 6, introduces a little more work. The required interpolation for intermediate values of n is done in a straightforward manner, and the results are relatively insensitive to the exact method employed. For the nonsymmetric fanning mechanism (A'), only an approximate calculation of coercive force can be made, in the absence of a detailed hysteresis loop for a randomly oriented assembly. One simple approximation is to use the loop for a chain of two

[21] E. P. Wohlfarth, Research (London) 7, S1 (1954).

TABLE II. Variation of relative magnetization with field for a randomly oriented assembly of n-sphere chains; $n=2$, $n=\infty$ (symmetric fanning mechanism).

$H a^3/\mu 2K_\infty$	Upper branch (I/I_s) $n=2$, $n=\infty$		Lower branch (I/I_s) $n=2$, $n=\infty$
0.0	+0.500[a]		−0.500[a]
0.2	+0.453		−0.542
0.4	+0.402		−0.582
0.6	+0.349		−0.620
0.8	+0.288		−0.655
1.0	+0.220±0.002		−0.687
1.2	−0.195±0.005	+0.140±0.002	−0.718
1.4	−0.495±0.005	−0.150±0.050	−0.747
1.6	−0.675±0.005		−0.774
1.8	−0.775±0.005		−0.799
2.0	−0.822±0.002		−0.822
2.2	−0.840±0.002		−0.841
2.4	−0.862		−0.864
2.6	−0.884		−0.884
2.8	−0.898		−0.898
3.0	−0.913		−0.913
3.5	−0.938		−0.938
4.0	−0.957		−0.957
5.0	−0.972		−0.972
6.0	−0.981		−0.981

[a] The data listed without error limits were interpolated from Stoner and Wohlfarth (reference 5), Table VI. The graphical solution is accurate to ±0.002 except as noted.

spheres, applying a suitable scaling factor based on the aligned coercive forces of Table I.

Calculations of the coercive force were made with the various models for two rather different dilute samples. The first of these, designated $S-C$ (about the same as sample C of reference 18), is typical of those for which the chain-of-spheres model was devel-

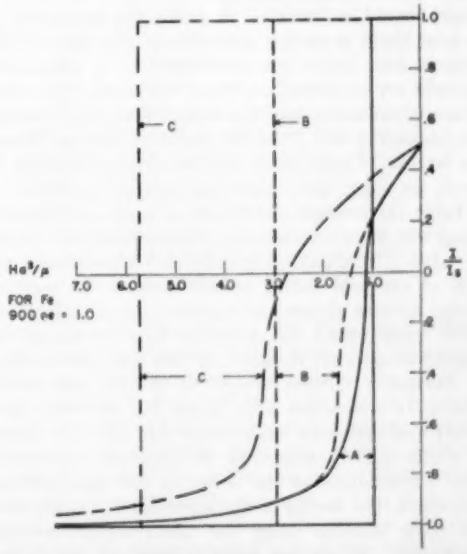

FIG. 7. Comparison of hysteresis loops for assemblies of randomly oriented and aligned two-sphere chains; three reversal mechanisms. A—fanning; B—parallel rotation of sphere moments; C—parallel-moment rotation in spheroid of axial ratio 2:1.

TABLE III. Summary of coercive force calculations. Samples described by Paine *et al.*[a] Mechanisms of reversal: *A*—chain of spheres, symmetric fanning; *B*—chain of spheres, parallel rotation; *C*—prolate spheroids, parallel rotation. Combinations use *C* for elongations <1.5.

Sample	$S-C$		$S-A$	
Observed $H_{c\parallel}=H_{c\perp}$	1500 oe		1100 oe	
Model	H_c Random[b] oe	H_c Aligned oe	H_c Random[a] oe	H_c Aligned oe
A	1590	1690	420	900
B	1750	4430	400	2700
C	3280	8340	1250	5160
$A+C$	1610	1700	970	1420
$B+C$	1750	4430	980	2700

[a] Reference 18.
[b] The error in the calculational procedure is estimated as ±20 oe.

oped. Its particles have a mean diameter of about 150 A, and a median elongation ratio of about 3, with contributions from particles having axial ratios up to 13. The second sample, $S-A$ (about the same as sample *A* of reference 18), was prepared under different conditions and is less suited to the chain-of-spheres model. This sample is similar in its magnetic and particle-shape properties to material investigated by Meiklejohn[13] and by Mayer and Vogt.[14] Its particles have the same mean diameter of 150 A, but they exhibit very little elongation, the median being 1.3 to 1 with the largest about 5 to 1. As this sample has an important fraction of its volume in the range of elongation between 1.0 and 1.5, the arbitrary criterion above, which assigned unit length and zero coercive force to this range, should be modified. A useful approximation is to treat them as prolate spheroids of axial ratio 1.25. This is done below for mechanism *C* in which all particles are considered as Stoner-Wohlfarth spheroids. This approximation may also be combined with reversal mechanisms *A* and *B* for the chains of spheres. When the fraction of material in this low elongation group is small, the use of such a combination is unimportant.

Table III presents the results of such calculations, along with the experimentally observed coercive forces at −196°C, in directions parallel and perpendicular to that of the field during solidification of the matrix. These samples showed no tendency to directionalize while many others did. Coercive force estimates for aligned samples are included, as they will prove useful in discussing samples which do exhibit directional effects. In connection with Table III, we shall note errors and omissions made along the way. The error of about ±20 oe stated for H_c (random) represents only an estimate of the error in the calculational procedure. The results of the approximate calculations for these samples using the nonsymmetric-fanning mechanism, *A'*, are not listed as they fall within the error limits. A significant error from this source does not appear until the median elongation ratio is about five or greater. An important omission is the effect of magnetocrystalline anisotropy. This could add to the calculated coercive force an amount varying from $2K/I_s$ to $-2K/I_s$ depending on the degree of crystalline order along the chain. For iron at −196°C, the higher estimate amounts to about 600 oe.

On the basis of the evidence up to this point, sample $S-C$ seems best described by mechanism *A*, although we cannot reject mechanism *B*. This agreement with the chain-of-spheres model is not surprising inasmuch as this sample exhibits a symmetrically wavy profile along the sides of its elongated particles. (See Figs. 2 and 3 of reference 18.) With regard to sample $S-A$, the agreement with experiment of either of the two combination models is gratifying. The prolate spheroid model *C*, also gives reasonable results for this sample. These estimates for $S-A$ have a more quantitative basis than previous estimates for this type of sample.[3,12,21]

In recent work, Paine and co-workers[22] have investigated the effect, on the coercive forces, of the magnitude of the aligning field during freezing of the matrix. Measurements on a sample similar to $S-C$, in directions parallel and perpendicular to the direction of the freezing field, show a small increase in $H_{c\parallel}$ and a rather

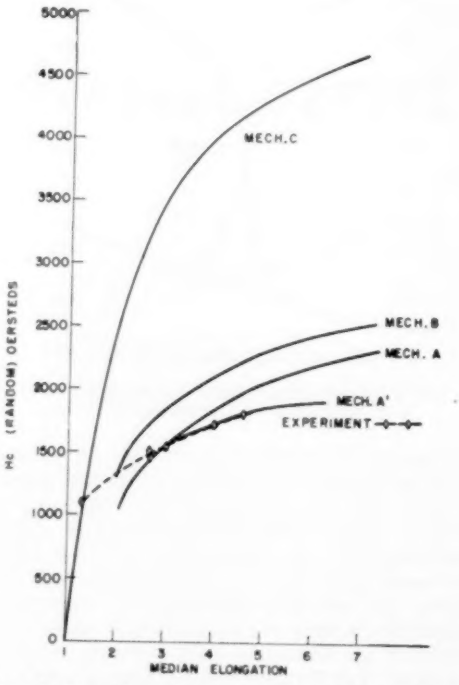

FIG. 8. Comparison of observed and calculated values of random coercive force of fine particle iron as a function of median elongation. Chain-of-spheres model: *A*—symmetric fanning mechanism; *A'*—nonsymmetric-fanning mechanism; *B*—parallel-rotation mechanism. Prolate spheroid model: *C*—parallel-rotation mechanism.

[22] Paine, Mendelsohn, and Luborsky (private communication).

larger decrease in $H_{c\perp}$. The magnitude of the decrease is more than twice that of the increase. This asymmetrical spread resembles the behavior expected from mechanism A. For the completely aligned state, each mechanism predicts $H_{c\perp}\approx 0$, but for mechanism A, $H_{c\parallel}\approx \bar{H}_c$, as compared to the predictions for mechanisms B and C of $H_{c\parallel}\approx 2\bar{H}_c$.

An additional comparison between theory and experiment may be made with the relation between random coercive force and median elongation ratio. Data have been collected[18,22] for samples ranging in median elongation ratio (by frequency) from 1.3 to 4.6, with particle diameters lying between 140 A and 180 A. For the models, we assume that the median elongation adequately characterizes the behavior, and we determine the random coercive force of a sample of uniformly elongated particles (neglecting magnetocrystalline anisotropy). Figure 8 presents the comparison of experiment with mechanisms A, A', B, and C. Mechanism C is ruled out at high elongation, as noted earlier. The failure of models A, A', and B at low elongation is also as expected. The general trend of predictions A, A', and B is in fair agreement with the experimental results at higher elongations. In particular, despite the crudeness of the assumptions, there is apparent support for the fanning mechanism A' in this correlation.

SUMMARY

We have re-examined the predictions of magnetic behavior arising from shape anisotropy in single-domain particles. Several approximate models have been suggested which may exist in certain experimental situations. Detailed calculations have been carried out for a "chain-of-spheres" model. Comparison with recent results on certain elongated iron particles favors the chain-of-spheres model as a suitable description of their magnetic behavior. A successful calculation has been made of the coercive force of material prepared by several earlier workers. A comparison of the new models with the older ones indicates a direction for experimental advance.

ACKNOWLEDGMENTS

It is a pleasure to acknowledge the close cooperation and encouragement of T. O. Paine, L. I. Mendelsohn, and F. E. Luborsky. Thanks are also due to W. H. Meiklejohn and J. C. Fisher for helpful suggestions.

PHYSICAL REVIEW VOLUME 100, NUMBER 4 NOVEMBER 15, 1955

Magnetic and Thermal Properties of $MnCl_2$ at Liquid Helium Temperatures. I. Magnetic Susceptibility*

R. B. MURRAY† AND L. D. ROBERTS
Oak Ridge National Laboratory, Oak Ridge, Tennessee
(Received July 28, 1955)

Measurements of the magnetic susceptibility of polycrystalline and single-crystal samples of anhydrous $MnCl_2$ have been carried out from 1.1° to 4.2°K with an ac mutual-inductance bridge. The susceptibility was found to be essentially independent of an applied magnetic field up to 2400 oersteds throughout this region, and displayed anomalous behavior near 2°K indicating a magnetic ordering transition. In view of the observed susceptibility behavior this transition is interpreted as one of an antiferromagnetic nature, although the susceptibilities of both the single-crystal and polycrystalline samples were found to rise slowly with decreasing temperature below the transition region. This interpretation is supported by preliminary neutron diffraction studies below 2°K. A calculation of the magnetic anisotropy is in reasonable agreement with that observed at 4.2°K.

INTRODUCTION

ANHYDROUS $MnCl_2$ is a member of the series of iron-group anhydrous chlorides. The magnetic and thermal properties of these compounds have been previously investigated at a number of laboratories from liquid hydrogen temperatures to room temperature and above. An extensive study of the magnetic susceptibilities of the members of this group has been carried out by Starr, Bitter, and Kaufmann[1] (SBK); references to earlier work may be found in their paper. This series of compounds is of interest because of the high density of magnetic ions which leads to strong magnetic interactions, and hence to magnetic ordering transitions at relatively high temperatures. Many of these compounds are crystallographically isomorphous, having a hexagonal layer structure, so that their magnetic properties may be compared directly. Magnetic susceptibility measurements have shown well defined maxima in the susceptibilities of several compounds of this series, characteristic of an antiferromagnetic

* Reported at the New York meeting of the American Physical Society, January, 1955.

† Graduate Fellow of the Oak Ridge Institute of Nuclear Studies from the University of Tennessee. This work was included in a thesis submitted in partial fulfillment of the requirements for the degree of Doctor of Philosophy at the University of Tennessee.

[1] Starr, Bitter, and Kaufmann, Phys. Rev. 58, 977 (1940).

transition. The unusual low-temperature magnetic properties of these latter compounds have earned them the name "metamagnetic"; these metamagnetic properties have recently been interpreted by Néel[2] as arising from an antiferromagnetic structure. Measurements of the specific heats of $CrCl_3$, $FeCl_2$, $CoCl_2$, and $NiCl_2$ by Trapeznikowa *et al.* (see reference 1) have revealed sharp λ-type anomalies at temperatures close to the corresponding susceptibility maxima, in the range 20° to 50°K.

$MnCl_2$, however, retains its normal, paramagnetic behavior down to 14°K, the magnetic susceptibility χ following a Curie-Weiss law, $\chi=C/(T+\theta)$, where T is the absolute temperature, C the Curie constant, and θ the Weiss constant. The measured Curie constant is approximately that expected for a free spin moment of 5/2, corresponding to the ${}^6S_{5/2}$ ground state of the Mn^{++} ion. SBK found the Weiss constant to be 3.3°K; earlier workers measured somewhat different values of the Weiss constant, all of which, however, were quite small (see reference 1). The specific heat of $MnCl_2$ was measured from 14° to 130°K by Trapeznikowa and Miljutin[3]; later measurements by Kelley and Moore[4] covered the region between 50° and 300°K. No evidence of a co-operative transition was found between 14° and 300°K.

In view of the absence of a magnetic transition in $MnCl_2$ above 14°K, it is of interest to extend a study of its magnetic and thermal properties to lower temperatures in a search for a transition to a state of magnetic order. The fact that the Weiss constant is found to be several degrees Kelvin suggests that such a transition might occur at liquid helium temperatures. The purpose of the investigation reported here is to determine whether or not such a transition occurs at liquid helium temperatures by a study of the magnetic susceptibility and specific heat, and to gain as much information as possible concerning the nature of the low-temperature magnetic state of $MnCl_2$ from these measurements.

SUSCEPTIBILITY MEASUREMENTS

The magnetic susceptibility of $MnCl_2$ was measured from 1.1° to 4.2°K by using a cryostat and an ac mutual inductance bridge which was constructed and described by Erickson, Roberts, and Dabbs.[5] The susceptibility measured by this technique is the differential magnetic susceptibility, and is determined with an oscillating (500 cycles/sec) measuring field of about two-oersteds strength. Susceptibility measurements were carried out on both a polycrystalline and a single-crystal sample of $MnCl_2$. Sample temperatures were determined from the measured vapor pressure of the liquid helium bath employing the 1948 temperature scale[6] with the corrections to this scale as given by Erickson and Roberts.[7] The measured vapor pressures were corrected for the hydrostatic pressure of the liquid helium above the sample level, and measured pressures were normalized to standard gravity and temperature (20°C). The relative susceptibilities read on the bridge were converted to absolute susceptibilities by a previous bridge calibration,[5] assuming the validity of the Curie-Weiss law for $MnCl_2$ at 77°K.

SAMPLE PREPARATION

The polycrystalline sample of $MnCl_2$ studied was part of the sample used in the specific heat measurements, to be described in the accompanying paper, Part II.[8] The anhydrous material was obtained by the dehydration of reagent grade $MnCl_2 \cdot 4H_2O$ in an atmosphere of dry HCl gas. During the dehydration the temperature was raised to about 400°C over a period of several hours until no more water was given off. The dehydrated powder was then melted in an HCl atmosphere, cooled over a period of about one hour to room temperature, and the fused solid was broken into particles of average size 1 to 4 mm. In order to prevent chemical reactions or contamination, the sample was contained in a platinum boat throughout the dehydration and melting procedures. This coarse powder (0.03690 mole) was then loosely packed in a flat bottomed glass tube which was sealed off in an atmosphere of helium gas at room temperature. This helium gas served as a heat exchange medium to insure thermal equilibrium between the particles of $MnCl_2$ and their surroundings. The polycrystalline specimen occupied a cylindrical volume of radius 5 mm and height 25 mm. The anhydrous material was handled at all times in an inert, dry atmosphere to prevent any exposure to water vapor.

In the preparation of the single-crystal specimen of $MnCl_2$, the anhydrous powder, contained in a cylindrical quartz tube of 2 inch diameter, was melted in a furnace. The quartz tube containing the liquid $MnCl_2$ was then slowly withdrawn, over a period of days, from the furnace, allowing the growth of the single crystal from the liquid state. Susceptibility measurements were carried out on a sphere of $\frac{1}{2}$ inch diameter which was machined from the large single crystal ingot. Precautions were taken to prevent exposure to water vapor in the preparation and handling of the single crystal. The authors are indebted to D. E. Lavalle for all preparations of anhydrous $MnCl_2$ and to J. Schenck for growing the single crystal.

[2] L. Néel, Brussels Conference, September, 1954 (unpublished).
[3] O. Trapeznikowa and G. Miljutin, Physik. Z. Sowjetunion **11**, 55 (1937).
[4] K. K. Kelley and G. E. Moore, J. Am. Chem. Soc. **65**, 1264 (1943).
[5] Erickson, Roberts, and Dabbs, Rev. Sci. Instr. **25**, 1178 (1954).
[6] H. Van Dijk and D. Shoenberg, Nature **164**, 151 (1949).
[7] R. A. Erickson and L. D. Roberts, Phys. Rev. **93**, 957 (1954). These corrections are in accord with the temperature scale revisions adopted at the 1955 Paris Low Temperature Conference.
[8] R. B. Murray, following paper [Phys. Rev. **100**, 1071 (1955)].

SINGLE-CRYSTAL SUSCEPTIBILITIES

The crystal structure of $MnCl_2$ is a hexagonal layer structure of the $CdCl_2$ type.[9] The Mn^{++} ions assume a hexagonal structure in sheets; each sheet of Mn^{++} ions is sandwiched between two sheets of Cl^- ions. The crystalline c-axis is perpendicular to these layers of Mn^{++} and Cl^- ions, while the a- and b-axes are contained in the layers. Susceptibility measurements were performed on the crystalline specimen so as to measure, first, the susceptibility along the c-axis (χ_c). The crystal was then reoriented with respect to the cryostat so that the measuring field was parallel to the crystallographic ab planes; the susceptibility measured in this orientation is denoted χ_{ab}. The orientation of the c-axis of the spherical crystal was determined by neutron diffraction from the (003) and (006) planes (indexed in terms of a hexagonal system). The (006) reflections were found to be sharp and single, indicating an unique c-axis in the spherical specimen studied.

The results of the measurements of χ_c and χ_{ab} are shown in Fig. 1. The ordinate in Fig. 1 represents the reactive component of the susceptibility only, the resistive component being negligibly small and temperature independent.

In order to examine the field dependence of both χ_c and χ_{ab}, external fields from an air-core solenoid up to 2400 oersteds were applied to the sample parallel to the oscillating measuring field. This was done over the entire temperature range for χ_c and at 1.13°K for χ_{ab}. No evidence of field dependence was found.

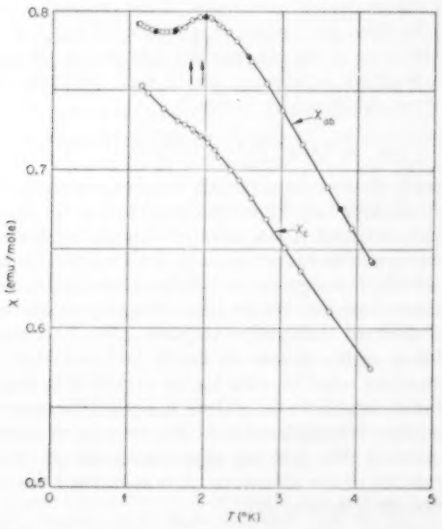

FIG. 1. Magnetic susceptibility of $MnCl_2$ (spherical crystal) as a function of temperature. The arrows locate specific heat maxima (see reference 8). Open and closed circles represent different experiments.

[9] L. Pauling and J. L. Hoard, Z. Krist. **74**, 546 (1930).

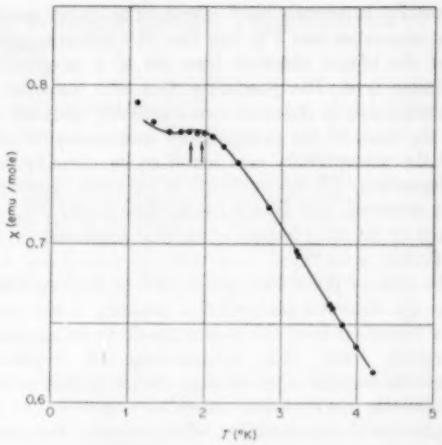

FIG. 2. Magnetic susceptibility of $MnCl_2$ (powder sample) as a function of temperature. The arrows locate specific heat maxima (see reference 8).

These measurements were carried out in collaboration with Dr. R. A. Erickson.

POWDER SUSCEPTIBILITY

The techniques used in measuring the susceptibility of the polycrystalline sample were the same as those applied in the single crystal measurements. The data points, shown in Fig. 2, were obtained from the bridge readings by applying a small, approximate shape correction and normalizing to the powder average (χ_p) of the single-crystal susceptibilities, Fig. 1, at 4.2°K. By virtue of the symmetry of the $MnCl_2$ lattice, χ_p is taken to be

$$\chi_p = \tfrac{2}{3}\chi_{ab} + \tfrac{1}{3}\chi_c.$$

The curve in Fig. 2 is this average; it is seen to be in good agreement with the data points for the polycrystalline sample. This good agreement is taken as evidence that the single-crystal material was not contaminated in the process of crystal growing and machining to a spherical shape. As before, the ordinate of Fig. 2 is the reactive component of the susceptibility only, the resistive component being negligible.

DISCUSSION

The irregular behavior of the susceptibility observed in both the single crystal and polycrystalline samples near 1.9°K, Figs. 1 and 2, suggests either a Schottky-type effect due to electric field splittings, or a cooperative magnetic ordering transition. In that the over-all splitting of the spin multiplet of an S-state ion (Mn^{++}) due to crystalline electric fields[10] may reasonably be expected to be quite small compared with 2°K, we dismiss the possibility that this transition is due

[10] M. H. L. Pryce, Phys. Rev. **80**, 1107 (1950).

primarily to electric field effects. The sharp specific heat anomalies near 2°K (see Part II[8]) indicate, rather, that the effects observed here are of a co-operative ordering type. The possibility that this transition is ferromagnetic in character can reasonably be ruled out on the basis of the susceptibility measurements since (1) the susceptibility was found to be virtually field independent, (2) no evidence of magnetic hysteresis was observed, and (3) the susceptibility near 2°K was found to be small compared to that predicted by the Curie law, $\chi=C/T$.

In view of the above, we are led to the conclusion that the observed susceptibility anomaly is the result of a transition from the paramagnetic to an antiferromagnetic state. This antiferromagnetic transition, however, must be of an unusual nature in that neither the powder susceptibility nor either component of the single-crystal susceptibility demonstrates the usual maximum in the transition region. In particular, the fact that χ_c does not decrease with falling temperature below the Néel point indicates that the antiferromagnetic state is not one in which the spin moments are aligned along the crystalline c-axis. In view of the unusual behavior of the susceptibility below the Néel point, it does not seem possible to derive the magnetic structure from these measurements. In this connection, it is interesting to note a recent calculation by Anderson[11] showing that a falling susceptibility is not a necessary property of certain types of antiferromagnetic order.

It is to be noted, that, although Mn^{++} has the largest spin moment ($S=5/2$) of the isomorphous group $MnCl_2$, $FeCl_2$, $CoCl_2$, and $NiCl_2$, it nevertheless has a Néel temperature which is an order of magnitude lower than that of the others.

In connection with this investigation, a neutron diffraction study of $MnCl_2$ at liquid helium temperatures (1.4°–4.2°K) has been initiated at this laboratory by M. K. Wilkinson and C. G. Shull. Preliminary results demonstrate magnetic superstructure lines which first appear near 1.9°K, confirming the above interpretation of the observed susceptibility anomaly as due to an antiferromagnetic transition near 1.9°K. No evidence of ferromagnetism was found.

MAGNETIC ANISOTROPY

The observed magnetic anisotropy in the single-crystal susceptibilities, Fig. 1, may arise from (1) both long- and short-range order in the spin system, (2) magnetic dipole interactions, and (3) crystalline electric fields. At 4.2°K the entropy has achieved approximately 90% of its saturation value R ln6, so that the cooperative ordering is largely dissipated at that temperature (Part II[8]). Within this assumption, the observed anisotropy should be accounted for mainly in terms of magnetic dipole interactions and crystalline electric field effects. We consider first the effect of magnetic dipole interactions.

Keffer[12] has shown that the contribution to the magnetic anisotropy of a single crystal arising from dipole interactions is given approximately by

$$\chi_{\parallel}-\chi_{\perp}=(\chi_{\parallel}\cdot\chi_{\perp})(\Phi_c-\Phi_a), \qquad (1)$$

where Φ_c and Φ_a are dipole sums taken over the neighbors of a Mn^{++} ion, $\chi_{\parallel}$ is the susceptibility measured parallel to the crystalline summetry axis (χ_c), and $\chi_{\perp}$ that measured perpendicular to the symmetry axis (χ_{ab}). The dipole sums Φ_c and Φ_a, whose values are determined by the crystalline symmetry and lattice parameters, were evaluated numerically in this case by the Oak Ridge digital computer, the ORACLE. The sums were performed over neighbors contained within a sphere, and were evaluated out to 5×10^3 neighbors. The numerical value of these sums converge rapidly as a function of the number of neighbors counted. The results of the calculation give $\Phi_c=-0.163$, $\Phi_a=0.081$. Inserting these values into Eq. (1), along with the values of χ_c and χ_{ab} measured at 4.2°K, we obtain $\chi_c-\chi_{ab}=-0.090$. This is to be compared with the observed anisotropy of -0.068.

We turn next to the contribution from crystalline electric fields. Pryce[10] has shown that the predominant term in the spin Hamiltonian of a Mn^{++} ion, arising from the interaction of the Mn^{++} charge distribution with the tetragonal component of the crystalline field, is of the form DS_z^2, where D is a constant and S_z is the z-component of the spin angular momentum operator. The magnetic anisotropy due to such an interaction has been calculated by Yosida,[13]

$$\chi_{\parallel}-\chi_{\perp}=\chi_p(-D/kT)[0.4S(S+1)-0.3], \qquad (2)$$

where S is the spin quantum number, equal to 5/2. The calculation of the coefficient D in Eq. (2) can be carried out only to an order of magnitude. A rough estimate, similar to that given by Keffer, indicates that, for $MnCl_2$, D is negative and of the order of hundredths of a wave number. We note that exact agreement with the observed anisotropy requires $D\approx-0.06$ cm^{-1}, which is within reason. It should be noted that the precautions taken in orienting the crystal with respect to the cryostat were not elaborate, so that the observed anisotropy is considered to be known only to $\pm20\%$. In view of this, and the approximate nature of the calculation of the anisotropy, it is considered that the agreement is satisfactory.

[11] P. W. Anderson, Phys. Rev. **79**, 705 (1950).

[12] F. Keffer, Phys. Rev. **87**, 608 (1952).

[13] K. Yosida, Progr. Theoret. Phys. (Japan) **6**, 691 (1951).

Magnetic and Thermal Properties of $MnCl_2$ at Liquid Helium Temperatures. II. Specific Heat*

R. B. MURRAY†
Oak Ridge National Laboratory, Oak Ridge, Tennessee
(Received July 28, 1955)

The specific heat of anhydrous $MnCl_2$ has been measured from 1.25° to 4.2°K in a search for the anomaly associated with the magnetic transition observed near 2°K. The measuring techniques are discussed briefly. The results of a series of experiments show two λ-type anomalies, each of magnitude 12 joules/mole-degree, located at 1.81° and 1.96°K. These two maxima are interpreted as arising from a multiple transition from the paramagnetic to an antiferromagnetic state. A plot of magnetic entropy *vs* temperature, obtained by integration of the specific heat data, shows that approximately $\frac{1}{3}$ of the available spin entropy has been achieved at the upper transition point.

INTRODUCTION

MEASUREMENTS of the magnetic susceptibility of $MnCl_2$ at liquid helium temperatures, discussed in the preceding paper (Part I),[1] demonstrated an unusual anomaly near 2°K which was interpreted as arising from a transition to the antiferromagnetic state. This paper reports a study of the specific heat of $MnCl_2$ in the same temperature region in a search for the specific heat anomaly associated with this transition.

EXPERIMENTAL PROCEDURE

Specific heat measurements were carried out by the techniques of low temperature adiabatic calorimetry. Two polycrystalline samples of $MnCl_2$ were studied, samples I (0.2056 mole) and II (0.3078 mole). The preparation of the anhydrous material is described in the preceding paper[1]; sample I was in the form of a coarse powder of average particle size 1 to 4 mm. Large particles were used to decrease the total surface area of $MnCl_2$ powder, so as to minimize adsorption of the helium heat exchange gas sealed into the calorimeter cup. In the preparation of sample II, the dehydrated powder was melted in a cylindrical platinum cup and cooled slowly to form a single, fused mass within this cup. In the preparation and handling of both samples, the anhydrous material was kept in a dry, inert atmosphere at all times to avoid contamination with water vapor. Chemical analysis after the specific heat measurements gave the following results: sample I, 43.22% Mn, 56.35% Cl, 0.46% H_2O; sample II, 43.29% Mn, 56.14% Cl, 0.25% H_2O; theoretical values, 43.65% Mn, 56.35% Cl.

A schematic diagram of the calorimeter with sample I in place is shown in Fig. 1. The chips of $MnCl_2$ were sealed with helium exchange gas (20 cm Hg pressure at room temperature) into a thin-walled brass calorimeter cup. A carbon resistance thermometer *R* (Allen-Bradley, $\frac{1}{2}$-watt size) with its exterior coating ground off was sealed in the cup in direct contact with the $MnCl_2$; thermometer leads were brought out through vacuum tight Kovar seals. A heater coil, *H*, of Constantan wire was bound to and insulated from the exterior wall of the calorimeter cup by a thin layer of Araldite cement. The calorimeter cup was suspended under spring tension from a brass cage by nylon threads *T* as shown. The use of spring tension provides a rigid sample mounting and reduces vibration induced heating of the sample during measurement. Thermometer and heater current leads between the sample and helium bath were of 0.005-inch Constantan wire coated with soft solder so that they were superconducting at liquid helium temperatures. Current and potential leads, joined at the bottom of the vacuum jacket, are taken through the helium bath to standard resistors and a precision potentiometer for all electrical measurements.

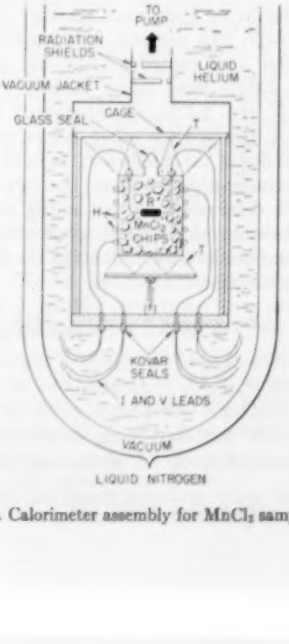

FIG. 1. Calorimeter assembly for $MnCl_2$ sample I.

* Reported at the New York meeting of the American Physical Society, January, 1955 [Bull. Am. Phys. Soc. **30**, No. 1, 41 (1955)].

† Graduate Fellow of the Oak Ridge Institute of Nuclear Studies. This work was included in a thesis submitted in partial fulfillment of the requirements for the degree of Doctor of Philosophy at the University of Tennessee.

[1] R. B. Murray and L. D. Roberts, preceding paper [Phys. Rev. **100**, 1067 (1955)].

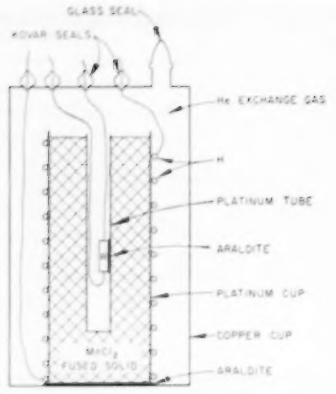

FIG. 2. $MnCl_2$ sample II.

Figure 2 shows the assembly of sample II in which the heater coil H of Constantan was sealed with the $MnCl_2$ and thermometer, R, inside the copper calorimeter cup along with helium exchange gas at a pressure of 20 cm Hg at room temperature. The thermometer was bonded with Araldite to a thin-walled platinum tube imbedded in the sample. The thermometer and heater in this case were different from those used with sample I.

The measuring technique used with both samples was the same. The resistance thermometer in both cases was initially calibrated against the measured vapor pressure of the liquid helium bath, thermal contact between the sample and bath being achieved through helium exchange gas in the vacuum jacket, Fig. 1. Measured vapor pressures were converted to temperatures by the 1948 temperature scale[2] with the corrections to this scale as noted previously.[3] The correction due to the hydrostatic pressure of the helium bath was taken into account, and pressure readings were corrected to standard gravity and temperature. Calibration points were taken initially every 0.2°K between 1.2° and 4.2°K; in subsequent experiments several check points were taken before every run to insure constancy of the calibration. In both the calibration and measurement procedure, the thermometer resistance was determined by measuring the potential across the resistor with a measuring current of 10.000 μa.

The calibration data were fitted by the least-squares method to a function of the form

$$\ln R = A + B \ln T + (C/T) + DT,$$

where R is the measured resistance, T the absolute temperature, and A, B, C, D constants to be determined. Three such functions were used to cover the region 1.2° to 4.2°K, each function being determined over an interval of approximately 1.2° so that any two neighboring functions overlapped several tenths of a degree. Such a procedure permits a very accurate fit of the observed data with a calculated function. In a typical calibration, all data points fell within 0.002° of the calculated curve while a majority of the points were within 0.001°, these deviations being comparable to the uncertainty in the temperature scale. Having determined the four constants for a given temperature interval, the slope of the curve at a particular temperature T_0 is obtained by analytically evaluating $(d/dT)(\ln R)$ at T_0.

During the measurement process the vacuum jacket was evacuated by a high-speed diffusion pump (MCF 300) and the thermometer resistance as a function of time was followed for 7–10 minutes before and after a heating period which was usually 3 minutes. Thermal equilibrium in the sample was achieved in 30 seconds or less after a heating period. The resistance-time curves before and after heating, which were normally straight, almost horizontal lines, were extrapolated to the midpoint of the heating period for the determination of the initial and final resistance, R_i and R_f. The temperature T_0 at which the specific heat was determined was taken to be that corresponding to the average logarithmic resistance during the heating period, $\frac{1}{2} \ln R_i R_f$, and was determined from an accurate plot of the calculated function $\ln R$ *vs* T. The specific heat is then given by

$$C(T_0) = \frac{IV\tau}{\Delta(\ln R)} \left(\frac{d}{dT} (\ln R) \right)_{T_0},$$

where I and V are the heater current and potential, τ is the length of the heating period, and $\Delta(\ln R) = \ln(R_f/R_i)$. Between 1.3° and 2.2°K, where the specific heat is varying rapidly, the temperature change during a heating period was made small (0.030°–0.050°K); at higher temperatures the increments were of the order of 0.075°–0.100°K.

The measured specific heats of samples I and II agreed well throughout the liquid helium region, Fig. 3. Measurements on sample I could not be satisfactorily carried out below 1.5°K as the external heater tends to degas the exterior wall of the calorimeter cup at the lowest temperatures. This effect was avoided in sample II by bonding the heater coil to the sample container *within* the sealed calorimeter cup.

The small contribution to the measured specific heat from the calorimeter cup, heater, etc., was calculated and corrected for. Its maximum contribution to the total specific heat occurs at 4.2°K and amounted there to only 1.4% in the case of sample II.

RESULTS AND DISCUSSION

The results of a series of experiments on both samples I and II are shown in Fig. 3. The measured specific heat can be taken as either C_P or C_V, since their difference is negligible at such low temperatures. The most striking

[2] H. Van Dijk and D. Shoenberg, Nature **164**, 151 (1949).
[3] See reference 7 in Part I.

feature of the specific heat behavior is the appearance of two well-defined λ-type anomalies, located at 1.81° and 1.96°K. It was initially thought that such behavior might arise from the presence of two crystalline lattice phases; such a two-phase system could conceivably be brought about by mechanical deformations in the layer-lattice structure in breaking up sample I into coarse chips before loading the calorimeter cup. The subsequent experiments on sample II, which was subject to no mechanical working after solidification, agreed quite well, however, with the earlier results on sample I. X-ray diffraction studies at room temperature on $MnCl_2$ (carried out by R. D. Ellison of this laboratory) indicated that the crystalline lattice is unaffected by the mechanical working suffered by sample I. The crystalline cell size of sample I agreed with that reported in the crystallography literature.[4] Preliminary results from neutron diffraction studies in progress at this laboratory[1] show that $MnCl_2$ does not undergo a crystallographic phase change between room temperature and 1.4°K. This is supported by the specific heat measurements[5,6] between 14°K and room temperature, which showed no evidence of phase transitions. In view of these facts, and with particular reference to the good agreement between two different samples studied with an entirely different thermometer, heater, and sample assembly, it is concluded that the two specific heat maxima are an inherent property of $MnCl_2$. Throughout the series of measurements, the specific heat was found to be independent of the thermal history of the sample.

An independent study of the specific heat of $MnCl_2$ at liquid helium temperatures has recently been reported by Kostryukov,[7] whose measurements show a single maximum near 1.96°K. The double peak observed in our measurements, however, may have been masked in the work of Kostryukov by the scatter of his data points in the region of the anomaly.

Reference to Figs. 1 and 2 of Part I[1] shows that the temperatures at which the specific heat maxima occur coincide with the region of the susceptibility anomaly. The sharply peaked shape of each maximum is characteristic of a cooperative transition. As discussed previously, the magnetic susceptibility and neutron diffraction studies indicate that a transition from the paramagnetic to an antiferromagnetic state occurs near 1.9°K. The appearance of *two* λ-type specific heat maxima indicates, moreover, that this transition is of a multiple nature, i.e., the peak at 1.96°K arising from the onset of long-range order, the peak at 1.81°K corresponding to a reorientation of the spin system to the low-temperature antiferromagnetic state. In the absence of any observed incipient ferromagnetic behavior, it appears that the state between 1.81° and 1.96°K may be one of antiferromagnetic order also. In such a case, the long-range antiferromagnetic order in this very narrow temperature interval would be only partially developed.

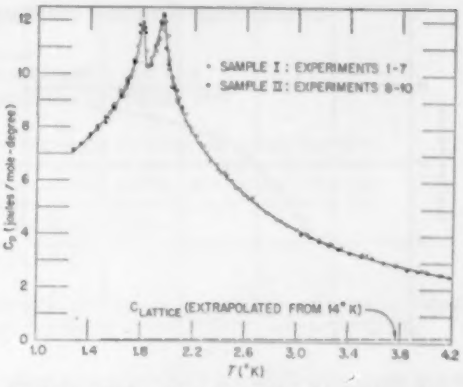

FIG. 3. Specific heat of $MnCl_2$ as a function of temperature.

Multiple transitions involving a magnetic structure change as suggested above have been observed in other materials, e.g., MnBi[8] and MnAs.[9] In these cases, the structure transition is apparently one from ferromagnetism to antiferromagnetism and occurs at a high temperature, i.e., above room temperature. The evidence of a structure transition in $MnCl_2$ is most unusual, however, in view of the extremely low transition temperature (~1.9°K) and the very narrow temperature interval (0.15°K) separating the specific heat maxima. In this case it is difficult to visualize a mechanism which would bring about two transitions at such a low temperature in the absence of any evidence of crystallographic transformations. The suggestion of Smart,[10] that magnetic structure transitions might arise as a result of the temperature dependence of crystalline lattice parameters, would not seem to apply here.

Turning now to the specific heat above 2°K, it is of interest to examine the behavior of the high-temperature specific heat tail for comparison with the prediction of Van Vleck,[11]

$$C_{mag}=b/T^2-d/T^3+\cdots, \qquad (1)$$

at temperatures above the transition point. It is usual to drop terms of order $1/T^3$ and higher, taking only the leading $1/T^2$ term. In order to examine the behavior of the magnetic specific heat alone, it is necessary to subtract from the measured specific heat the contribution arising from lattice vibrations. The lattice specific heat in the liquid helium region can be estimated from the measurements of Trapeznikowa and Miljutin[5] above 14°K. An examination of their data between 14° and

[4] L. Pauling and J. L. Hoard, Z. Krist. **74**, 546 (1930).
[5] O. Trapeznikowa and G. Miljutin, Physik. Z. Sowjetunion **11**, 55 (1937).
[6] K. K. Kelley and G. E. Moore, J. Am. Chem. Soc. **65**, 1264 (1943).
[7] M. O. Kostryukov, Doklady Akad. Nauk S.S.S.R. **96**, 959 (1954).
[8] C. Guillaud, J. phys. radium **12**, 223 (1951).
[9] A. Serres, J. phys. radium **8**, 146 (1947).
[10] J. S. Smart, Phys. Rev. **90**, 55 (1953).
[11] J. H. Van Vleck, J. Chem. Phys. **5**, 320 (1937).

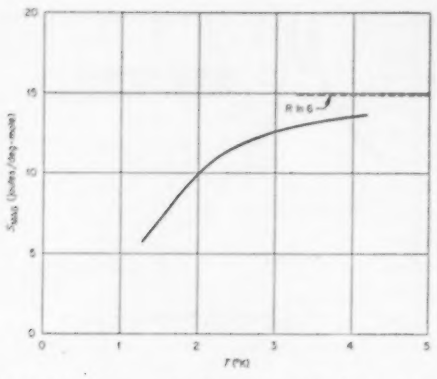

FIG. 4. Spin entropy of $MnCl_2$ as a function of temperature.

25°K shows that the specific heat increases very nearly as T^2 rather than the usual Debye T^3 dependence. A T^2 dependence of the lattice specific heat at low temperatures arises from the two-dimensional character of the $MnCl_2$ layer lattice structure. In the absence of specific heat measurements between 4.2° and 14°K, the assumption was made that the T^2 behavior can be extrapolated to the liquid helium region. This extrapolation is shown in Fig. 3, taking $C=0.0106T^2$ joules/mole-deg as the best fit to the data of Trapeznikowa and Miljutin. This contribution to the total specific heat at liquid helium temperatures is quite small (7.5% at 4.2°K, decreasing rapidly with falling temperature), so that a relatively large error in its determination will have little effect on the evaluation of the magnetic specific heat.

An examination of the magnetic specific heat of $MnCl_2$ above the transition region reveals that between 3.0° and 4.2°K the data cannot be fitted with the usual b/T^2 approximation. The product $C_{mag}T^2$ increases from 36.5 joule-deg/mole at 3.0°K to a value of 40.0 joule-deg/mole at 4.2°K. A good fit to the data points is achieved, however, by including a d/T^3 term. A least squares fit of the data points, corrected for the lattice contribution, gives

$$C_{mag}=48.9/T^2-36.6/T^3 \qquad (2)$$

between 3.0° and 4.2°K.

We may note at this point that the conclusions in the above paragraph are qualitatively unchanged if the lattice specific heat at helium temperatures goes as T^n, $n>2$, since in this case the lattice specific heat would be smaller than that obtained by extrapolating the T^2 law.

It is interesting to note that the specific heat is falling rather slowly with decreasing temperature in the region near 1.4°K, rather than the steep fall-off usually characteristic of magnetic ordering transitions. It would be of interest to extend the measurements to the region below 1°K.

CALCULATION OF THE ENTROPY

In the absence of specific heat data below 1.25°K, it is not possible to evaluate the magnetic entropy as a function of temperature by the relation

$$S(T')=\int_0^{T'}\frac{C_{mag}}{T}dT.$$

Since the Mn^{++} ion is in a ${}^6S_{\frac{5}{2}}$ state, however, the total spin entropy realized at a high temperature must be given by

$$S=R\ln(2S+1)=R\ln 6.$$

With the use of Eq. (2) above 4.2°K, the entropy at 4.2°K is given approximately by

$$S(4.2)=R\ln 6-\int_{4.2}^{\infty}(48.9/T^2-36.6/T^3)dT.$$

Numerical integration of the specific heat data at helium temperatures then results in the entropy curve shown in Fig. 4.

On the basis of this calculation, approximately $\frac{2}{3}$ of the total spin entropy has been achieved in the transition region (~2°K), so that $\frac{1}{3}$ of the entropy remains to be gained above the critical temperature through short-range order in the spin system. It is interesting to note that the entropy behavior of antiferromagnetic $CuCl_2\cdot 2H_2O$ (critical temperature 4.3°K) is quite similar, $\frac{2}{3}$ of the spin entropy being realized at the Néel point.[12]

ACKNOWLEDGMENTS

It is a pleasure for the author to acknowledge the continued interest and valuable advice of Dr. L. D. Roberts throughout this investigation. Dr. R. A. Erickson (now at The Ohio State University) contributed materially to the program in its early stages. Mr. J. B. Capehart provided valuable technical assistance. This work was made possible through the grant of a Graduate Fellowship by the Oak Ridge Institute of Nuclear Studies.

[12] S. A. Friedberg, Physica **18**, 714 (1952).

Electrical Properties of Near-Degenerate Boron-Doped Silicon

R. O. Carlson
General Electric Research Laboratory, Schenectady, New York
(Received June 29, 1955; revised manuscript received July 18, 1955)

Measurements of extrinsic resistivity and Hall effect have been carried out for a group of single crystals of silicon containing a wide range of boron concentration, with particular stress on samples in the near-degenerate range, 10^{18} to 10^{19} boron atoms per cm³. The anomalous Hall mobility effect previously observed by Morin and Maita in silicon was studied in finer detail over the temperature range 25°K to 300°K. For degenerate samples the 300°K Hall mobility is approximately 46 cm²/volt sec.

INTRODUCTION

An extensive study of the electrical properties of single-crystal silicon containing a wide range of boron and arsenic impurities has been made by Morin and Maita,[1] yielding values of the forbidden band gap, the ionization energies of these impurities, the lattice scattering mobility dependence on temperature, and the Hall mobility dependence on impurity concentration. An anomalous low-temperature behavior of the Hall mobility of several of the boron- and arsenic-doped samples suggested that impurity band conduction might be occurring at low temperatures with low-mobility charge carriers. Impurity band conduction has been experimentally observed in germanium[2] at temperatures of less than 10°K. The temperature at which impurity band conduction becomes experimentally observable shifts toward room temperature with increasing impurity concentration. The data reported in this paper were principally taken on samples in the near-degenerate range of silicon with impurity concentrations of 10^{18} to 10^{19} per cm³. Measurements to 25°K were sufficient to observe the Hall mobility anomaly.

METHOD

The single crystals used in this experiment were prepared by the Czochralski technique. A highly concentrated boron-silicon zone melt was used as the doping material[3] and added to the melt in weighed quantities before each crystal was pulled. Samples were cut transverse to the crystal axis with approximate dimensions 2.5×2.0×10 mm. Phosphor bronze springs were used in the sample holder to make contact to rhodium-plated areas on the etched samples. The sample holder was glued to a thin mica sheet held against a copper backing strip, the latter in turn being coupled through a heater strip and stainless steel heat leak to a liquid nitrogen or liquid hydrogen reservoir in a cryostat. The Hall field was provided by a 900-gauss permanent magnet which could be rotated through 360° about the sample. Voltages were measured with a vibrating reed electrometer, and the temperature with a potentiometer and calibrated copper constantan thermocouple.

DATA AND RESULTS

Figures 1 and 2 are plots of the extrinsic resistivity and Hall coefficient as a function of the reciprocal of the Kelvin temperature. Note the rapid change in electrical properties between samples 51*D* and 120*H*. Their impurity concentrations differ by less than a factor of four at room temperature. Hole concentrations shown in Fig. 3 were calculated from the Hall data using the relation $p=1/R_H e$ throughout the concentration range.

Hall mobility, taken as R_H/ρ, is given as a function of temperature in Fig. 4. Curves obtained by Morin and Maita[1] are plotted in the same figure for comparison.[4] For the purer samples, the data in this report give steeper slopes, but lower room temperature mobilities[5]; for sample *RR48A*, $\mu_H \propto T^{-2.9}$. The data reported here were taken at a constant field of 900 gauss; a possible dependence of Hall coefficient, and hence Hall mobility, on magnetic field was not investigated.[6] The positive slopes in the Hall mobility curves for crystal sample 51*D* and Morin and Maita's sample 141 indicate a mobility temperature dependence greater than the $\frac{3}{2}$ power characteristic of ionized-impurity-scattering mobility.[7] Neutral-impurity scattering[8] could not give rise to such a rapid drop in mobility at low temperatures.

The model of impurity-band conduction described by Hung and Gliessman[2] can be characterized as follows. Conduction in a *p*-type semiconductor can take place not only in a valence band but also in an acceptor impurity band. At extremely low impurity concentrations, there is essentially no overlap of impurity-atom wave functions and hence no impurity banding. With increasing concentrations, the larger overlap of wave functions will cause a broadening of the impurity band. For large impurity concentrations, the conductivity in

[1] F. J. Morin and J. P. Maita, Phys. Rev. **96**, 28 (1954); see also G. L. Pearson and J. Bardeen, Phys. Rev. **75**, 865 (1949).
[2] H. Fritzsche and K. Lark-Horowitz, Physica **20**, 834 (1954); C. S. Hung and J. R. Gliessman, Phys. Rev. **96**, 1226 (1954).
[3] F. H. Horn, Phys. Rev. **97**, 1521 (1955).
[4] Net carrier concentrations given by Morin and Maita for their samples are: *M* 127—7.0×10^{14}; *M* 117—2.4×10^{16}; *M* 119—2.0×10^{17}; *M* 141—1×10^{18}; *M* 125—1.5×10^{19}.
[5] P. P. Debye and T. Kohane, Phys. Rev. **94**, 724 (1954).
[6] Willardson, Harman, and Beer, Phys. Rev. **96**, 1512 (1954).
[7] E. Conwell and V. F. Weisskopf, Phys. Rev. **77**, 388 (1950); H. Brooks, Phys. Rev. **83**, 879 (1951); P. P. Debye and E. M. Conwell, Phys. Rev. **93**, 693 (1954).
[8] C. Erginsoy, Phys. Rev. **79**, 1013 (1950).

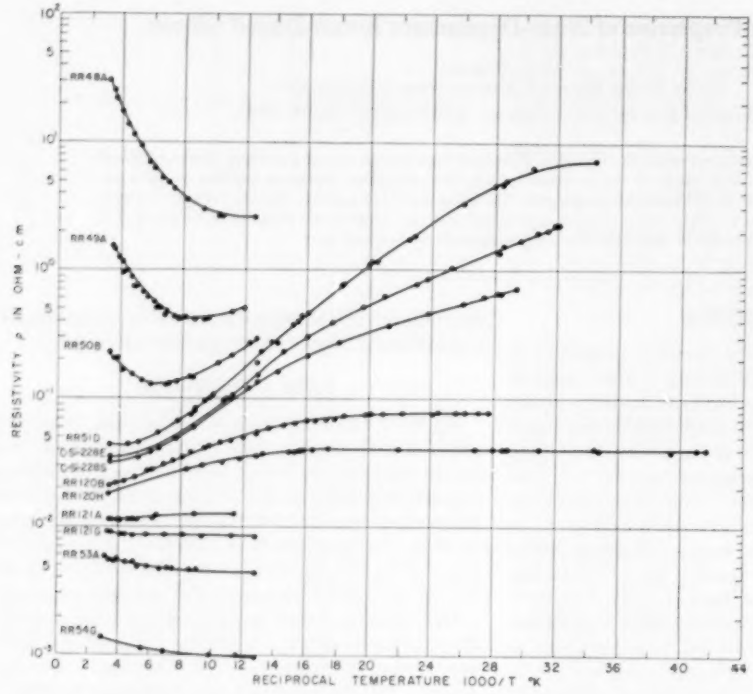

FIG. 1. Extrinsic resistivity of boron-doped silicon samples as a function of reciprocal temperature. The curve for sample *RR51I* almost overlaps that for *C-Si-228E* and is omitted for clarity.

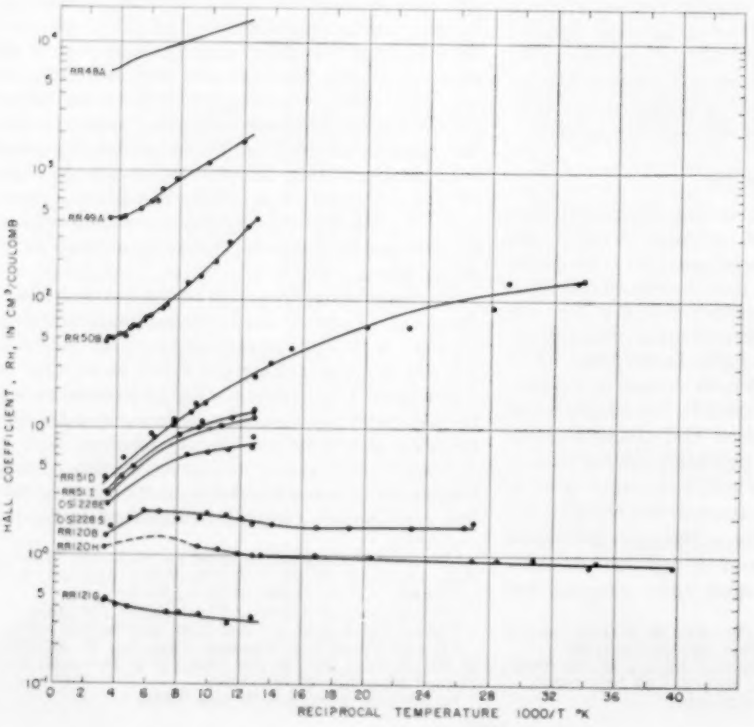

FIG. 2. Hall coefficient of boron-doped silicon samples as a function of reciprocal temperature.

the impurity band can become comparable to that in the valence band at sufficiently low temperatures. When the impurity concentration becomes great enough, the impurity band formed will overlap the valence band and a simple model of two parallel conducting bands will not be valid.

The question of the sign of the charge carrier in the impurity band is not fully settled. In germanium,[2] no change in the sign of the Hall coefficient is observed over the temperature range in which impurity band conduction dominates the conductivity process, leading to the conclusion that in an acceptor impurity band the charge carriers are holes. The present data and that of Morin and Maita[1] for silicon also indicate no change in Hall coefficient. For samples *RR*120*B* and *RR*120*H*, resistivity and Hall coefficient are nearly temperature independent from 70°K to ~30°K, indicating Fermi degeneracy and conduction by holes in the acceptor

TABLE I. Room-temperature data for boron-doped silicon samples

Crystal	Sample[a]	Cryostat data 300°K Resistivity ohm-cm	Hall coefficient cm³/Coulomb	Hall mobility cm²/volt sec	Net hole concentration cm⁻³	Conductivity[b] mobility cm²/volt sec
*RR*55						46
*RR*54	*G*	0.0014				47
*RR*53	*A*	0.0053				46
*RR*52	*A*	0.0092				53
*RR*121	*G*	0.0090	0.44	49	1.4×10^{19}	
	A	0.013	0.55	49	1.1×10^{19}	
*RR*120	*H*	0.018	1.16	65	5.4×10^{18}	
	B	0.020	1.43	72	4.4×10^{18}	
	A	0.020	1.48	74	4.2×10^{18}	
C-Si-228	*S*	0.033	2.57	78	2.4×10^{18}	
	E	0.035	3.12	89	2.0×10^{18}	
*RR*51	*I*	0.037	3.07	82	2.0×10^{18}	
	D	0.043	3.7	86	1.7×10^{18}	
	B	0.049	3.8	78	1.6×10^{18}	101
*RR*50	*B*	0.225	48	213	1.3×10^{17}	202
*RR*49	*A*	1.65	430	260	1.45×10^{16}	288
*RR*48	*A*	26	6000	230	1.0×10^{15}	

[a] Samples marked *A* are taken from transverse cross sections approximately one-third way down the crystal; other samples are from cross sections further down the crystal.
[b] Computed from data of Horn. See references 3 and 10.

impurity bands. The crossover of mobility curves for these samples may perhaps be accounted for by an increase in hole mobility in the impurity band with increasing acceptor concentration. For samples *RR*51*D* and *M*141, the data point to the possibility that the Hall mobility will become zero between 10 to 20°K due to a sign change in Hall coefficient. This possibility is supported by the Seebeck effect data of Geballe and Hull[9] which shows a sign change in the thermoelectric power of sample *M*141 at 19°K. Their data indicate that electrons are the charge carriers in the acceptor impurity band.

The ionization energy for the boron impurity level has been computed for sample *RR*50*B* (impurity concentration ~10^{17} cm^{-3}) from the Hall data with best fit for $E=0.044$ ev and hole mass $=0.8M_0$, in agreement with previous work.[1] Since the slope of the Hall curve for sample *RR*51*D* (impurity concentration ~10^{18} cm^{-3})

[9] T. H. Geballe and G. W. Hull, Phys. Rev. **98**, 940 (1955).

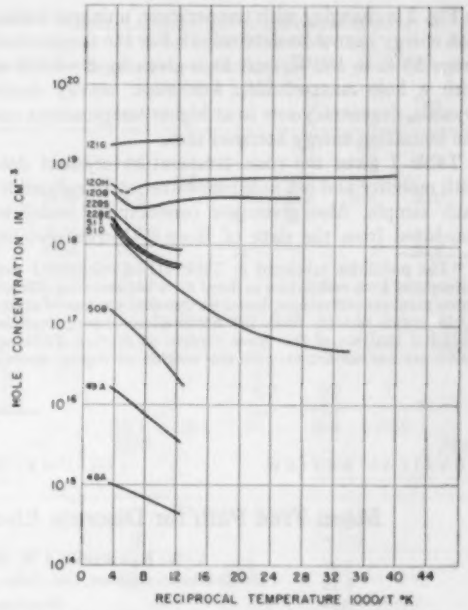

FIG. 3. Charge carrier concentration of boron-doped silicon samples as a function of reciprocal temperature.

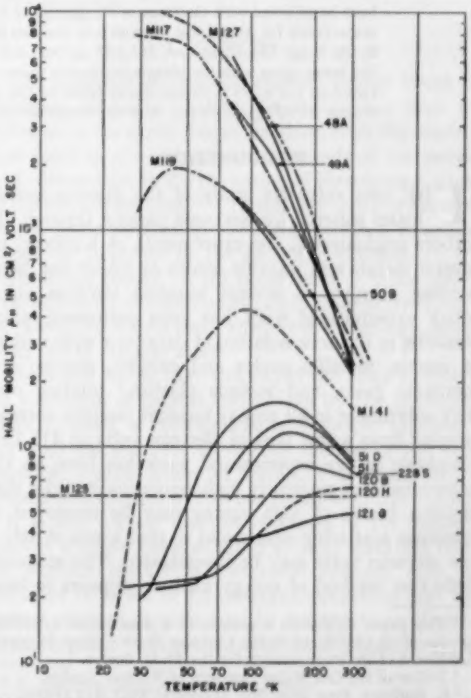

FIG. 4. Hall mobility for boron-doped samples as a function of temperature. Dashed lines refer to samples (composition given in footnote 4) previously measured by Morin and Maita.

in Fig. 2 is changing with temperature, a unique ionization energy cannot be determined. For the temperature range 50°K to 150°K, best fit is given by $E=0.020$ ev with a hole mass $=0.5M_e$. For more heavily doped crystals, degeneracy sets in at higher temperatures and the ionization energy becomes zero.

Table I gives the room-temperature cryostat data with mobility and net hole concentration calculated for each sample. Also given are conductivity mobilities computed from the data of Horn.[10] Carrier mobility appears to be constant in the degenerate range at 46 cm²/volt sec.

ACKNOWLEDGMENTS

I wish to thank the members of the Semiconductors Studies Section at the G. E. Research Laboratory for their guidance and assistance. I am indebted to Dr. F. H. Horn for discussions on the interpretation of his data and to Professor J. Bardeen for his interest in this problem.

[10] The mobilities tabulated in Table III of reference 3 were recomputed from resistivities as listed there but assuming different boron atom concentrations, based on chemical analysis of crystal *RR55* grown directly from the boron-silicon doping material. Chemical analyses of the boron content of crystals *RR54* and *RR55* are not consistent with the weights of doping material used in growing these crystals. The concentrations given by Horn were based on the analysis of crystal *RR54*, but better agreement of net hole concentration computed from Hall effect data and the boron atom concentration is obtained when crystal *RR55* is used as the standard.

PHYSICAL REVIEW VOLUME 100, NUMBER 4 NOVEMBER 15, 1955

Mean Free Path for Discrete Electron Energy Losses in Metallic Foils*

A. W. Blackstock,† R. H. Ritchie, and R. D. Birkhoff
Health Physics Division, Oak Ridge National Laboratory, Oak Ridge, Tennessee

(Received June 6, 1955)

The discrete energy losses observed when a beam of electrons passes through a thin foil have been studied as a function of incident energy. Foils of Al, Mg, and Cu ranging in thickness from 14 to 85 $\mu g/cm^2$ have been bombarded with electrons of energies 25 to 115 kev. Losses appear at multiples of 14.9 ev and 10.7 ev respectively for Al and Mg whereas only one loss is found in Cu at 22.6 ev. Mean free paths for the losses lie in the range 25 ± 10 $\mu g/cm^2$, 165 ± 55 $\mu g/cm^2$, and 90 ± 30 $\mu g/cm^2$ for the three metals. The magnitudes of the losses agree with the plasma oscillation theory of Pines and Bohm for Al and Mg if the number of free electrons per atom is chosen about equal to the valence. In addition the mean free path as a function of energy for Al agrees closely with the theoretical curve.

INTRODUCTION

THE first extensive study of the discrete energy losses suffered by electrons passing through absorbers originated in the experiments of Rudberg[1] on several metals and metallic oxides at rather low bombarding energies of several hundred electron volts. Much experimental work has been performed since, resulting in the accumulation of data on a wide variety of metals, metallic oxides and sulfides, organic and inorganic gases, and various plastics,[2] totaling over fifty substances in all and at incident electron energies ranging from a few tens of electron volts to 115 kev. Emphasis in the experimental work has been on the achievement of extremely high resolution in order that electron beams of high energy may be employed to minimize scattering effects and so that losses of only a few electron volts may be investigated. The magnetic deflection method of energy analysis appears to have been exploited most successfully by Ruthemann[3] in his work on Al_2O_3, Be, Al, and Ag, and by Lang[4] in his investigation of Al, Cu, and Ni. Electrostatic deflection for the determination of electron energy has been used by Reichertz and Farnsworth[5] in the study of the electrons reflected from the (100) face of a copper single crystal and by Lander[6] in his study of Auger peaks in Al and Be wherein he noticed in the energy distribution of his primary beam additional peaks displaced from the incident beam energy by amounts corresponding to the losses reported by Ruthemann.

More recent work has utilized the chromatic aberration present in off-axis rays of certain electrostatic lenses for the separation of the energy components of an electron beam after it has traversed a thin foil, when such components differ only slightly in energy. This technique, originated by Mollenstedt[7] in his work on a dozen or more different materials, has been carried on

* This paper represents a portion of a dissertation submitted by one of us (AWB) to North Carolina State College in partial fulfillment of the requirements for the Ph.D. degree.

† Fellow of the Oak Ridge Institute of Nuclear Studies.

[1] E. Rudberg, Proc. Roy. Soc. (London) **A127**, 111 (1930).

[2] For a review of the literature, see A. W. Blackstock, Ph.D. thesis, North Carolina State College, 1955 (unpublished).

[3] G. Ruthemann, Ann. Physik **2**, 113 (1948).

[4] W. Lang, Optik **3**, 233 (1948).

[5] P. P. Reichertz and H. E. Farnsworth, Phys. Rev. **75**, 1902 (1949).

[6] J. J. Lander, Phys. Rev. **91**, 1382 (1953).

[7] G. Mollenstedt, Optik **5**, 499 (1949).

most completely by Marton and Leder[8] who have investigated not only losses in many metals and nonmetals but also the increase in the energy loss[9] in the oxides and sulfides of the same metals. Additional experimental work using this method has been reported recently by Watanabe.[10,11]

A fourth experimental method first reported in 1954 by Blackstock, Slater, and Birkhoff[12] and described in detail in a recent paper[13] employs a stopping potential method with an electrostatic analyzer for the final energy separation. Such an apparatus was used in the investigation described here. Incidental to this series of experiments, a summary of the losses obtained previously is found in Table I for the metals Al, Mg, and Cu. It will be noted that losses found by some workers are not found by others, a characteristic of most of the substances which have been investigated by more than one group.

In some cases identification of losses has been possible as in the study of collodion[14] in which losses at 298 ev, 400 ev, and 546 ev corresponding to the K-shell ionization energies in carbon, nitrogen, and oxygen, respectively, have been found. Similar experiments[15] utilizing metals and gases ranging in atomic number from 4 to 30 have found similar agreement. Generally, however, the small losses such as those listed in Table I have not been explained. The recent plasma oscillation theory of Pines and Bohm[16–19] has at last offered some possible basis for understanding the losses in conductors.

Two predictions of the theory can readily be tested experimentally; the energy lost to the plasma, and the number of free electrons which must be assumed to account for this loss; the mean free path for the interaction. The latter has not been investigated previously and constitutes the principal purpose of the present paper.

It is interesting to note that the fine structure which has been found on the K edge in x-ray absorption spectra appear to be separated by discrete energy intervals which correspond roughly to those found in the electron experiments. For instance, Cauchois[20] has given absorption curves in Al showing absorption maxima differing from the K edge by amounts corresponding to some of those found by us and others.

TABLE I. Summary of measurements of energy losses in Al, Cu, and Mg.[a]

Energy loss (ev) Al							
(3)	(4)	(7)	(7)	(8)	(11)	This research
		7	9	6.2	6.5	
14.72	14.5	15		13.9	14.8	14.8
		22	18	19.2	23	
29.59	29.4			27.8	29.5	30.0
			36	35.0		
44.34	44.2					44.2
59.34	58.6		54			59.8
73.84	75.2					
	90.4					

Energy loss (ev) Cu							
(1)	(21)	(4)	(7)	(5)	(8)	(11)	This research
3.4	4.2			3.0			
6.9	7.2			6.0	6.9	7	
12.3				12.3	11.3		
		19.1	20.4	20	19.6	19.5	
		22.9[b]					22.6[c]
25.5							
34.5							

Energy loss (ev) Mg		
(8)	(11)	This research
9.7	10.3	10.5
20.3	20.7	21.5
	31.2	31.6
	41.5	

[a] The numbers in parentheses are reference numbers.
[b] Cu on collodion.
[c] Cu on zapon.

THEORY

The existence of multiple discrete energy losses by energetic electrons incident on metals has been attributed to the excitation of electrons from the conduction band to allowed unoccupied bands of the metal[21] and, alternately, to the excitation of plasma oscillations in the free electron sea.[16–19] In the first case it is assumed that a single electron in the metal makes a transition under the influence of the incoming electron. In the Pines-Bohm theory, on the other hand, it is the collective oscillation of a number of nearly free electrons, each one absorbing only a small amount of the energy, which gives rise to discrete losses.

Pines and Bohm have calculated the mean free path for excitation of plasma oscillations by the impinging particle, using a correspondence principle argument. We shall discuss their theory by the use of the conventional optical theory of metals. The results of the present experiments will be compared with this theory.

It is well known that for collisions of the incident particle with electrons situated at large distances from the particle track, the electronic medium may be described in terms of its dielectric properties and the passing charged particle may be treated as an electromagnetic pulse.[22] From dispersion theory, neglecting the

[8] L. Marton and L. B. Leder, Phys. Rev. **94**, 203 (1954).
[9] L. B. Leder and L. Marton, Phys. Rev. **95**, 1345 (1954).
[10] H. Watanabe, Phys. Rev. **95**, 1684 (1954).
[11] H. Watanabe, J. Phys. Soc. Japan **9**, 920, 1035 (1954).
[12] Blackstock, Birkhoff, and Slater, Phys. Rev. **95**, 303 (1954).
[13] Blackstock, Birkhoff, and Slater, Rev. Sci. Instr. **26**, 274 (1955).
[14] G. Ruthemann, Naturwiss. **30**, 145 (1942).
[15] J. Hillier and R. F. Baker, J. Appl. Phys. **15**, 663 (1944).
[16] D. Bohm and D. Pines, Phys. Rev. **82**, 625 (1951).
[17] D. Pines and D. Bohm, Phys. Rev. **85**, 338 (1952).
[18] D. Bohm and D. Pines, Phys. Rev. **92**, 609 (1953).
[19] D. Pines, Phys. Rev. **92**, 626 (1953).
[20] Y. Cauchois, Acta Cryst. **5**, 351 (1952).
[21] E. Rudberg, Phys. Rev. **50**, 138 (1936).
[22] E. Fermi, Phys. Rev. **57**, 485 (1940); O. Halpern and E. Hall, Phys. Rev. **73**, 477 (1948); P. Budini, Nuovo cimento **10**, 236 (1953).

Lorentz correction, the dielectric constant of a metal may be written

$$\epsilon(\omega)=1+\frac{4\pi Ne^2}{m}\sum_i \frac{f_i}{\omega_i^2-ig_i\omega-\omega^2}, \tag{1}$$

where N is the density of atoms in the medium. The effect of free electrons in the medium is represented by a term in the above sum for which the "binding frequency," ω_1, say, is very small. In this case the oscillator strength f_1 is the effective number of electrons per atom in the conduction band. The other terms in the sum represent the contribution from electronic interband transitions with transition frequencies ω_i, oscillator strengths f_i, and damping constants g_i.

Using Maxwell's equations, one may calculate the classical expression for the energy lost per cm, dW/dx, by an impinging electron with velocity V to nearly free electrons belonging to impact parameters $b>b_{\min}$.[22] One finds approximately

$$-\frac{dW}{dx}=\frac{4\pi f_1 Ne^4}{mV^2}\ln\frac{1.123V}{\tilde{\omega}_0 b_{\min}}, \tag{2}$$

where $\tilde{\omega}_0=[\omega_1^2+4\pi f_1 Ne^2/m]^{\frac{1}{2}}$. Now if the binding frequency ω_1^2 of the nearly free electrons is small compared with the "plasma frequency" $\omega_0=[4\pi Nf_1e^2/m]^{\frac{1}{2}}$,

$$-\frac{dW}{dx}=\frac{e^2\omega_0^2}{V^2}\ln\frac{1.123V}{\omega_0 b_{\min}}, \tag{3}$$

which is just the Pines-Bohm formula. In the quantum limit the smallest unit of energy which may be absorbed in plasma oscillations is $\hbar\omega_0$. Pines and Bohm use $b_{\min}\simeq\lambda_D=[v_F^2/3\omega_0^2]^{\frac{1}{2}}$, the Debye length in the plasma. Here v_F is the maximum velocity in the Fermi-Dirac plasma, i.e., $v_F^2=(3h^2/8\pi)^{\frac{2}{3}}(n^{\frac{1}{3}}/m)^2$.

To determine the mean free path λ for loss of a quantum of energy $\hbar\omega_0$ in the thickness dx by the incident electron, one sets

$$-(dW/dx)dx=\hbar\omega_0 dx/\lambda.$$

Then

$$\lambda=\frac{\hbar\omega_0 V^2}{\omega_0^2e^2\ln(1.123V/\omega_0\lambda_0)}. \tag{4}$$

Now, if one assumes that plasma oscillations may be excited only in single-quantum jumps involving absorptions of the energy $\hbar\omega_0$ and that no double or higher order transitions are possible, the probability that an impinging electron shall lose $\hbar\omega_0$ in traversing a thickness dx of the foil is given by dx/λ. Then it may be easily shown that the probability $p_k(x)$ that k quanta are lost in a foil of thickness x is given by the Poisson distribution, i.e.,

$$p_k(x)=\frac{1}{k!}\left(\frac{x}{\lambda}\right)^k e^{-x/\lambda}. \tag{5}$$

It may be noted that optical data on the reflection and absorption of light by metal surfaces may be useful in interpreting discrete loss data. In particular, optical measurement of the transition frequency, i.e., that frequency at which a metal ceases to be a reflector and becomes transparent, furnishes an independent determination of the plasma frequency for that metal. Such measurements are available only for the alkali metals.[23] The optical transition occurs at 2100 A and 3150 A corresponding to quantum energies of 5.9 and 3.9 ev for sodium and potassium, respectively. These values compare well with the electron beam values obtained by Marton and Leder.[3] For sodium on backings of quartz and collodion, the losses of 5.4 and 10.7 ev, and 5.1 and 10.8 ev respectively, may be added and the sum divided by six, the number of quanta assumed to be involved. The result of 5.3 ev compares favorably with the optical data. In addition, the same authors report results on potassium on backings of silicon and collodion. Although the smallest losses occur at 7.8 and 8.0 ev, higher losses are spaced at increments of about half these values, indicating a quantum energy of their order. If all the losses are added and the sum divided by the assumed number of quanta involved, an average of 3.8 ev for the quantum energy is obtained, again comparing well with the corresponding optical value.

Ferrell,[24] using the quantum-mechanical approach of Pines and Bohm, has investigated the angular distribution of electrons after loss of a quantum of energy to plasma oscillation. He finds that the differential cross section for scattering through an angle θ per plasma electron is given by

$$\sigma(\vartheta)d\Omega=\frac{1}{2\pi a_0 n}\frac{\vartheta_E}{\vartheta_E^2+\vartheta^2}d\Omega,$$

if

$$\vartheta\leq p_c/(2mE)^{\frac{1}{2}},$$

where $\vartheta_E=\hbar\omega_0/2E$, a_0= Bohr radius, p_c is the cut-off momentum $\approx\hbar/\lambda_D$, and n is the density of free electrons.

APPARATUS

The electron accelerator and spectrometer have been described in detail in the literature[18] and so will be discussed only briefly. Electrons from a 5*BP*1 cathode-ray gun are accelerated down a conventional accelerating tube typical of those employed in Cockcroft-Walton and Van de Graaff machines. The beam then enters an identical tube which is used as a decelerator and derives its potential from the same source as the accelerator. Electrons are slowed to an energy of 100 ev and then enter an electrostatic analyzer set for this energy. Detection is accomplished with a Faraday cup at one end of the analyzer. The use of the analyzer eliminates defocusing and secondary emission problems en-

[22] R. W. Wood, Phys. Rev. **44**, 353 (1933); R. W. Wood and C. Lukens, Phys. Rev. **51**, 352 (1938).
[24] R. A. Ferrell, Phys. Rev. **99**, 647(A) (1955).

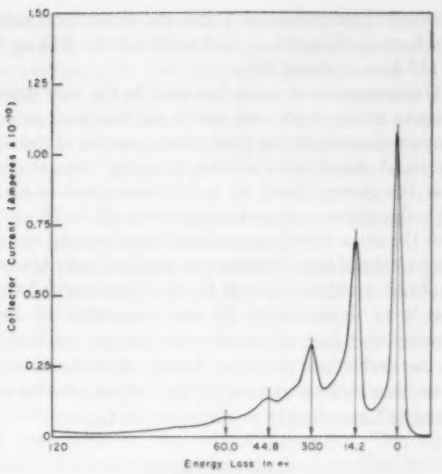

FIG. 1. Energy spectrum of electrons initially at 45 kev after passing through a 15-$\mu g/cm^2$ Al foil. Peak to right represents electrons which lose no energy. Other peaks at ~15-ev intervals represent discrete losses to the conduction electron plasma.

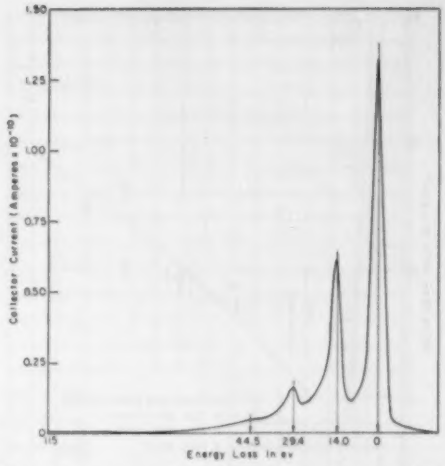

FIG. 2. Same as Fig. 1 except that initial energy is 100 kev.

countered when collection is attempted at zero energy. Energy lost in foils placed between accelerator and decelerator may be restored to the beam by reducing slightly the decelerator voltage or by raising slightly the accelerating voltage with a small biasing potential, thus permitting collection of electrons in the cup. In practice either of these potentials may be scanned by a motor-driven potentiometer with the resulting current distribution being drawn on a Brown recorder driven by an electrometer amplifier. A resolution of 2 volts (an improvement over the value of 2.9 volts given previously[13]) is obtained which is independent of beam energy in the range 15 kev to 115 kev, thus providing an energy resolution of 0.0017% at the highest energy. The beam may be focused by adjusting electron gun potentials and may be moved radially either with the electrostatic deflecting plates of the gun or with the magnetic fields set up to compensate for the earth's field.

RESULTS

All foils were prepared by vacuum evaporation of the various metals onto thin films of Zapon or Formvar which were shown to contribute no energy losses for the film thicknesses and sensitivities of detection used.

The energy spectrum resulting when 45-kev electrons strike an aluminum foil 15 $\mu g/cm^2$ in thickness is shown in Fig. 1. The peak to the right represents electrons which have lost no more than one electron volt energy and will henceforth be called the "no-loss peak." Spectral distribution of incident electrons may be represented by an isosceles triangle 2 electron volts wide at half-height for these and all other data. It is apparent then that the no-loss and all other peaks are somewhat wider than the resolution of the instrument, the exact reason for which is not understood. The next peak indicates a group of electrons which have lost an energy of 14.2 electron volts, presumably to the electron plasma in the metal. Additional maxima are attributable to multiple losses of the same incremental energy.

The ratio of the foil thickness to the mean free path may be obtained by taking the ratio of the area under any one peak to the area under any other peak and applying Eq. (5) in the section under theory. In practice the area under each maximum is compared with the area under each other maximum, thus affording several estimates of x/λ from each spectral distribution. These are then averaged and, if the foil thickness is known, the value of λ may be calculated.

A comparison of Fig. 1 with Fig. 2, a similar distribution but with a bombarding energy of 100 kev, indicates a change in λ with incident energy. As is anticipated, the no-loss peak has increased in area at the expense of the 15-ev peak, indicating an increase of mean free path.

The quantum energy is obtained by adding all the losses, including those in which more than one quantum is involved, and dividing the result by the total number of quanta. For multiple experimental runs over two different Al foils with 174 losses being recorded in all, an average loss of 14.9 ev with a probable error of ± 0.1 ev is found. This average appears to be slightly higher than the average of the single-quantum loss values but the latter is within the experimental error.

Substitution of this average loss in Eq. (2) gives a value of 2.68 for the number of free electrons per atom in aluminum, a number about equal to the normal valence. If in turn this number is substituted into Eq. (4), a theoretical estimate of the mean free path may be calculated for various incident energies. Figure 3 shows the relatively good agreement between theo-

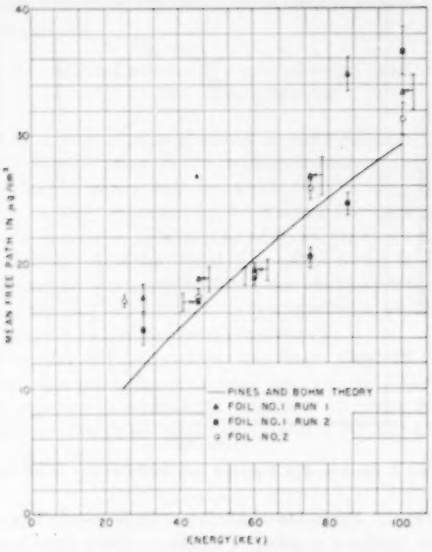

FIG. 3. Mean free path for plasma excitation *versus* kinetic energy of incident electrons.

retical and experimental values of this quantity for several aluminum foils, the foil thickness being determined by weighing on a quartz fiber microbalance. For the purposes of calculation, the ordinary electron mass is used for the effective mass.

Similar experiments were run using Mg and Cu as absorbers, typical spectral distribution being shown in Figs. 4 and 5. Losses were multiples of 10.6 ev for Mg, but only a single loss of average value about 22.6 ev was found in Cu. Calculating the number of free electrons per atom in Mg from this value, one finds a value of 1.90 identifiable with the valence. However, the single loss in Cu leads to a figure of 4.42 for the number of free electrons per atom, which appears to be quite unreasonable.

Calculations of mean free path were difficult in Mg because of the wide disparity in foil thickness estimates between the value obtained from weighing on a quartz fiber torsion balance and the value calculated from the amount of metal which left the filament in the evaporation process by which the foils were made, assuming an isotropic distribution of material leaving the filament. The weighed values were checked by chemical analysis to within about 30%, but use of these values leads to a value of mean free path which is 7.5 times as large as the theoretical value. In addition, the determination of λ from different magnesium foils (165 ± 55 $\mu g/cm^2$) differed by 40% when using these thicknesses. Use of the latter, calculated values of foil thickness leads to better agreement between theoretical and experimental values of λ and also to results which are more consistent for different foils. The difference between these values of λ and the theoretical values, which range from 13 $\mu g/cm^2$ at 40 kev to 27.5 $\mu g/cm^2$ at 115 kev, is about 20%.

Measurements of mean free path in Cu were difficult because of the small area under the loss peak and the absence of multiple-loss peaks characteristic of the other metals. A mean value of 90 ± 30 $\mu g/cm^2$ was obtained over the energy range 45 to 115 kev which compares with theoretical values ranging from 38 to 74 $\mu g/cm^2$ over the same energy range if the experimental value of the number of free electrons per atom is used. Attempts to obtain multiple losses in Cu by increasing foil thickness were unsuccessful. It was impossible to decide whether this lack of success was due to the inability of the decelerator to focus beams of electrons which have been badly scattered by the foil, or whether such multiple losses simply do not occur in Cu.

CONCLUSIONS

It is apparent that the data obtained on Al agree within experimental error with the plasma oscillation theory as regards the number of free electrons per atom, the quantum energy of the oscillation and the mean free path for the excitation of the plasma. Such agreement extends over an energy range from 20 to 100 kev.

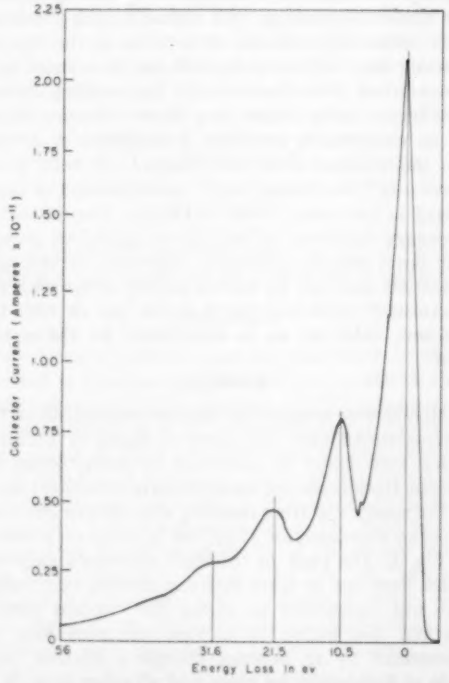

FIG. 4. Energy spectrum of 115-kev electrons after passing through a 69-$\mu g/cm^2$ Mg foil. Conduction electron plasma is seen to absorb energy in increments of ~10.5 ev.

Similarly the data for Mg agree with the theory on the number of free electrons and the plasma energy. The ambiguity in foil thickness determination makes difficult any quantitative assessment of mean free path from the available data. Plainly a more careful preparation and treatment of the Mg foils is necessary before this question may be resolved. Preferably the foils should be evaporated, used, and weighed without ever leaving the vacuum system, thus preventing oxidation and the adsorption of water vapor.

In Cu both the lack of multiple losses and the large number of free electrons needed to account for the large single loss indicate a disagreement with the plasma theory. The large width of the single peak is in contrast to the sharp lines characteristic of the other metals. In a recent paper, Wolff[25] has estimated the effect of the electrons in the 3*d* shell on the plasma frequency and the width of the plasma resonance. The rapid transfer of plasma energy to a single *d* electron has the effect of broadening the width of the resonance in accordance with the uncertainty principle. The ratio of width to plasma energy is of the order of one to two in Cu on the basis of optical absorption data. Thus the width of the lines in Sc through Ni should increase as the 3*d* shell is filled. However, Marton and Leder[8] in their work on Ti, Cr, Mn, Fe, Co, and Ni indicate that "this may not be the case."

A shift in the plasma energy of about 10 electron volts toward higher energy due to the interaction with the 3*d* electrons is also to be anticipated according to Wolff. Subtracting this energy from the observed energy would give a plasma frequency which would in turn lead to a more reasonable value for the number of free electrons per atom.

The 7-ev loss in Al found by some (Table I) but not by us may be explained with reference to the large angular aperture of our instrument (30×10^{-3} rad) as compared with, say, the chromatic lens of Leder and Marton (10^{-3} rad). According to Ferrell,[26] for 30-kev incident electrons the angular distribution of those which have lost 15 ev should be reduced to half the value at $\theta=0$ at an angle of $\theta_E=0.25\times10^{-3}$ rad and should extend out to a cut-off angle $\theta_C=22\times10^{-3}$ rad, whereas the angular range for those losing 7 ev should be more narrow with $\theta_E=0.12\times10^{-3}$ rad and $\theta_C=22\times10^{-3}$ rad as before. That is, an instrument of aperture 10^{-3} rad will see about twice as many electrons which have lost 7 ev as of those which have lost 15 ev, thus making the cross sections for the excitations of the two processes appear to be more nearly comparable.

Experimentally, it is difficult to distinguish between an excitation of the electron plasma as against a loss to a single bound electron because: (a) the amount of energy transferred in the two cases is of the same order of magnitude; (b) the Poisson distribution for multiple losses would be expected to hold in both cases; (c) the stopping power (and mean free path) would be the same. That is, Eq. (3) may be derived from classical Bohr collision theory without reference to the plasma phenomenon; and (d) the angular distributions in both cases will be similar.[26]

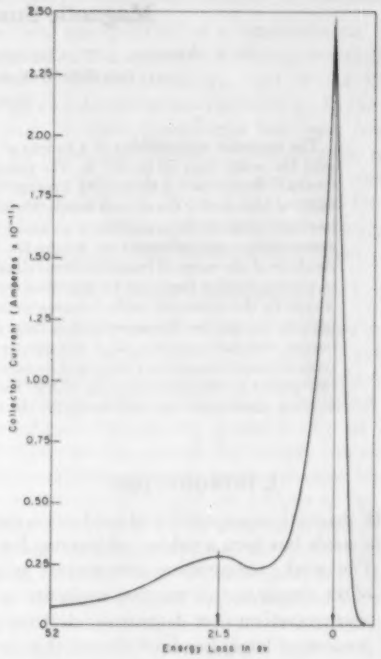

FIG. 5. Same as Fig. 4 except for 115-kev electrons incident on a 66-μg/cm^2 Cu foil. Spectrum is typical of heavy elements in that only a single wide loss peak is observed.

ACKNOWLEDGMENTS

The authors would like to acknowledge the cooperation with Dr. L. Marton, Dr. L. Leder, and others of the Electron Physics Section of the National Bureau of Standards which has existed during the pursuit of this work. We are grateful for the opportunity of seeing the manuscript of the article, "Characteristic Energy Losses of Electrons," by L. Marton, L. B. Leder, and H. Mendlowitz which is to appear soon in the Advances in Electronics. Finally, the authors wish to express their gratitude to Dr. H. H. Hubbell of the Health Physics Division of Oak Ridge National Laboratory for his many helpful suggestions throughout this investigation.

[25] P. A. Wolff, Phys. Rev. **92**, 18 (1953).

[26] Discussion following paper by R. A. Ferrell at the 1955 Washington Meeting of the American Physical Society [R. A. Ferrell, Phys. Rev. **99**, 647(A) (1955)].

Magnetic Susceptibility of Germanium

D. K. Stevens, J. W. Cleland, J. H. Crawford, Jr., and H. C. Schweinler
Oak Ridge National Laboratory, Oak Ridge, Tennessee

(Received August 3, 1955)

The magnetic susceptibility of a variety of Ge specimens has been measured as a function of temperature over the range from 70 to 300°K. The susceptibility of high-purity specimens shows an unexpected temperature dependence: a decreasing diamagnetism with increasing temperature. By subtracting the susceptibility of high-purity Ge at each temperature from that of impure material, the charge carrier susceptibility has been obtained for a number of *n*- and *p*-type specimens. The effective mass of electrons obtained from susceptibility measurements on *n*-type Ge is in agreement with values yielded by cyclotron resonance. Analysis of the range of transition from classical to Fermi-Dirac statistics suggests that the energy surfaces of the conduction band can be described by four rather than eight ellipsoids of revolution in *k*-space. In *p*-type Ge the agreement with cyclotron resonance results is not nearly so good in that a larger hole effective mass is required by the susceptibility data. Measurements have been made on one *n*-type specimen bombarded with fast neutrons. After exposures sufficient to produce essentially intrinsic behavior, there was no trace of the paramagnetic component expected from unpaired spins of trapped electrons. This result has been interpreted as indicating that the energy levels associated with bombardment-produced defects form overlapping, degenerate impurity bands for the exposure in question.

I. INTRODUCTION

THE magnetic susceptibility of conduction electrons in solids has been a subject of interest for many years. The weak, temperature-independent paramagnetism of the simple metals was first explained in terms of the paramagnetism of a degenerate electron gas by Pauli.[1] Somewhat later, Landau[2] showed that, because of quantum effects, free electrons should exhibit an orbital diamagnetism whose magnitude is precisely one-third of their spin paramagnetism. Stoner[3] has given a complete treatment of the combined effects in the case of free electrons. In a solid, Peierls[4] has shown that because of interactions between the conduction electrons and the periodic potential of the crystal, Landau's result holds only when the Bohr magneton is replaced by an effective Bohr magneton which takes account of the interactions in terms of the appropriate effective mass of the charge carriers.[5]

Although much can be learned concerning the band structure of metals from the temperature dependence of their magnetic susceptibility,[6] because their electron gas is essentially completely degenerate, it is virtually impossible to separate experimentally the contribution of the conduction electrons from the total susceptibility in most metals with static magnetic susceptibility measurements. In semiconductors, however, this limitation does not apply. Here statistics governing the behavior of charge carriers range over the domain of classical as well as Fermi-Dirac statistics and the magnetic behavior of a classical gas of quasi-free electrons or holes is well understood.[7] Consequently, it is possible in many semiconductors of interest to examine separately the susceptibility of the charge carriers, a property which, as we shall see, provides a significantly new approach to the study of the electronic structure of semiconductors.

The importance of magnetic susceptibility in electronic structure investigations of semiconductors was first recognized by Busch and Mooser.[8] From a systematic study of the susceptibility of gray or α tin, they were able to determine the forbidden energy gap, the ionization energy of various doping impurities and the effective masses of electrons and holes in this material. The effectiveness of such an approach is brought out even more forcefully when it is remembered that, at the time of their work, α Sn was available only in the form of powder or pressed compacts. Consequently, the more customary approach involving measurements of electrical conductivity and Hall constant were rendered ineffective because of the interparticle resistance in the compacted specimens. This limitation indicates the unique advantage of magnetic susceptibility measurements in that the carrier susceptibility is essentially independent of transport or scattering processes.

Since the outstanding work of Busch and Mooser, this method of study has been applied to two other diamond-lattice semiconductors: InSb and Ge. Analysis of the magnetic behavior of InSb in both the intrinsic and extrinsic ranges[9] yields a forbidden energy gap of 0.262 ev in reasonable agreement with the value obtained from electrical measurements,[10] and an electron effective mass of $\sim 0.028 m_0$.

[1] W. Pauli, Z. Physik **41**, 81 (1927).
[2] L. Landau, Z. Physik **64**, 629 (1930).
[3] E. C. Stoner, Proc. Roy. Soc. (London) **152**, 672 (1935).
[4] R. Peierls, Z. Physik **80**, 763 (1933); **81**, 186 (1933).
[5] H. Frohlich, *Theorie der Metalle* (Verlag Julius Springer, Berlin, 1937), pp. 144–156.
[6] C. J. Kriessman, Revs. Modern Phys. **25**, 122 (1953); C. J. Kriessman and H. B. Callen, Phys. Rev. **94**, 837 (1954).
[7] See for example R. H. Fowler, *Statistical Mechanics* (Cambridge University Press, Cambridge, 1937), Chap. XII.
[8] G. Busch and E. Mooser, Z. physik. Chem. **198**, 23 (1951); Helv. Phys. Acta **26**, 611 (1953).
[9] D. K. Stevens and J. H. Crawford, Phys. Rev. **99**, 487 (1955).
[10] M. Tanenbaum and J. P. Maita, Phys. Rev. **91**, 1009 (1953); R. G. Breckenridge *et al.*, Phys. Rev. **96**, 571 (1954).

The magnetic properties of Ge have been investigated by several workers. The first measurements of Ge specimens of known impurity content were made in 1952 by McGuire[11] over the range from 77 to 300°K. Although his results suffer to some extent from poor sensitivity, they are in qualitative agreement with those reported here. In a preliminary report[12] of the present work, it was shown that the carrier susceptibility χ_c is of sufficient magnitude in both n- and p-type material to make a magnetic investigation worthwhile, and, in addition, an unexplained temperature-dependent diamagnetism which can only be attributed to the lattice atoms was observed in high-purity specimens. A subsequent analysis[13] of the earlier results gives electron effective masses which are consistent with those obtained from cyclotron resonance experiments.[14,15] Moreover, in the case of n-type Ge, the data suggest that the energy surfaces of the conduction band are best represented by four ellipsoids rather than eight which is the expected result if the minima of the E *vs* k curves along the [111] direction lie at the boundary of the first Brillouin zone rather than within it.[16] Recently Busch and Helfer[17] have extended the range of measurement to high temperature and, besides observing the onset of the intrinsic process, have noticed a curious hysteresis in the susceptibility on cycling through temperatures in excess of 650°K. They attribute this effect to the thermal introduction of lattice imperfections. In a subsequent paper van Itterbeek *et al.*[18] report susceptibility measurements in the liquid hydrogen range and have observed the recombination of carriers with their parent donor and acceptor centers.

In this paper we wish to summarize the results of a study of the magnetic behavior of a wide variety of Ge specimens. This investigation was motivated by a long-standing study of the effect of fast-neutron bombardment on the semiconductivity of Ge.[19] It was hoped that a study of the susceptibility of irradiated specimens would be of value in understanding the nature of the bombardment-induced energy levels. Consequently, in addition to results on unirradiated specimens, we include preliminary information obtained on specimens exposed to fast neutrons. The experimental results have been interpreted in the light of recent ideas concerning the band structure of Ge.

[11] T. R. McGuire (unpublished).
[12] D. K. Stevens and J. H. Crawford, Jr., Phys. Rev. **92**, 1065 (1953).
[13] Crawford, Schweinler, and Stevens, Phys. Rev. **99**, 1330 (1955).
[14] Dresselhaus, Kip, and Kittel, Phys. Rev. **92**, 827 (1953); Phys. Rev. **95**, 568 (1954); Phys. Rev. **98**, 368 (1955).
[15] Lax, Zeiger, Dexter, and Rosenblum, Phys. Rev. **93**, 1418 (1954); Dexter, Zeiger, and Lax, Phys. Rev. **95**, 557 (1954); Lax, Zeiger, and Dexter, Physica **20**, 818 (1954).
[16] C. Kittel, Physica **20**, 829 (1954).
[17] G. Busch and N. Helfer, Helv. Phys. Acta **27**, 201 (1954).
[18] van Itterbeek, de Greve, and Duchateau, Appl. Sci. Research **B4**, 300 (1955).
[19] Cleland, Crawford, Lark-Horovitz, Pigg, and Young, Phys. Rev. **83**, 312 (1951); Cleland, Crawford, and Pigg, Phys. Rev. **99**, 1170 (1955).

II. THEORY OF SUSCEPTIBILITY IN GERMANIUM

The total susceptibility of a semiconductor may be represented as the sum of three components: the contribution of lattice atoms χ_A, that of the impurity atoms χ_I, and the carrier susceptibility χ_c. In the general case, each of these components has been treated in detail by Busch and Mooser.[8] Consequently, we shall confine our attention to those points of immediate interest as regards Ge. Our task is to obtain the carrier susceptibility and this requires that there be an accounting for the impurity and lattice contributions.

A. Lattice Susceptibility

The diamagnetism of an assembly of atoms is usually expected to be rather small ($<10^{-6}$ emu/g) and essentially temperature independent.[20] The theory is applicable, however, only to spherical, closed-shell atoms, the resultant diamagnetic susceptibility of a solid being taken as the sum of the atomic contributions. In diamond-lattice structures, the covalent binding is produced by the sp^3 hybridized orbitals of the valence electrons and, because of the directional nature of such bonds, the usual assumptions no longer hold. It is expected, however, that the contribution of the cores can be obtained in good approximation by such an approach. We have computed the susceptibility of the Ge^{4+} ion from the Hartree functions[21] and the customary relation

$$\chi_{\text{ion}} = N z_i e^2 \langle r^2 \rangle_{\text{Av}} / 6mc^2, \qquad (1)$$

where N is the number of ions per gram of Ge, z_i is the number of electrons per ion and $\langle r^2 \rangle_{\text{Av}}$ is the average of the squares of the radii. The value obtained is $\chi_{\text{ion}} = 1.265 \times 10^{-7}$ emu/g. This value would be reduced somewhat if Hartree-Fock functions were used, but these unfortunately are not available. As we shall show, this value is greater than that observed for the total diamagnetism for a pure specimen, the latter including the effect of the valence electrons as well. Moreover, the observed χ_A is appreciably temperature dependent. The reason for this curious behavior is not yet understood. Consequently, we rely entirely on experiment for the value of χ_A.

B. Carrier Susceptibility

The results obtained for the susceptibility of a perfect electron gas, modified appropriately for the periodic potential of the lattice, may be applied directly to conduction electrons.[5] If one neglects higher order terms in the magnetic field, the specific susceptibility for electrons is

$$\chi_c = (\beta^2/3\rho k)\omega_s C M_c^{(N)} T^{\frac{1}{2}} (3 - \langle f_c^2 \rangle_{\text{Av}}) F_{\frac{1}{2}}'(\eta), \qquad (2)$$

where β is the Bohr magneton, ρ is the density of Ge, ω_s is the statistical weight or degeneracy of

[20] See, for example, P. W. Selwood, *Magneto Chemistry* (Interscience Publishers, Inc., New York, 1943), Chap. II.
[21] Hartree, Hartree, and Manning, Phys. Rev. **59**, 306 (1941).

states (exclusive of spin) in the conduction band, $C=[4\pi(2m_0k)^{\frac{3}{2}}]/h^3$, $M_c^{(N)}$ is the effective mass ratio for the density of states expression ($M=m^*/m_0$) and $\langle f_c^2\rangle_{Av}$ is the appropriate value of the square of the reciprocal mass ratio tensor for orbital motion of the electrons in the magnetic field. The function $F_{\frac{1}{2}}'(\eta)$, where $\eta=\zeta/kT$, is the first derivative of the Fermi integral

$$F_{\frac{1}{2}}(\eta)=\int_0^\infty x^{\frac{1}{2}}[1+e^{x-\eta}]^{-1}dx. \tag{3}$$

The values of $F_{\frac{1}{2}}(\eta)$ and, by means of the tabulated functions,[22] $F_{\frac{1}{2}}'(\eta)$ may be obtained from the electron concentration n and the relation

$$n=\omega_c C(M_c^{(N)}T)^{\frac{3}{2}}F_{\frac{1}{2}}(\eta). \tag{4}$$

For sufficiently high temperatures or low carrier concentrations ($\eta<-3$), classical statistics apply. Under these conditions Eq. (2) becomes

$$\chi_c=(\beta^2/3\rho kT)n(3-\langle f_c^2\rangle_{Av}), \tag{5}$$

from which it is evident that the slope of the χ_c *vs* $1/T$ curve is proportional to $(3-\langle f_c^2\rangle_{Av})$. Since n is readily obtained from Hall coefficient measurements, $\langle f_c^2\rangle_{Av}$ may be obtained from Eq. (5) in the classical range. Although we have treated conduction electrons only, analogous expressions apply to holes in the valence band. Since the extrinsic range is the only one of interest here, we shall not treat the carrier susceptibility in the intrinsic range.[23]

The values of effective mass ratios appropriate to the density of states ($M_c^{(N)}$) and orbital motion [$M_c^{(M)}=(\langle f_c^2\rangle_{Av})^{-1}$] depend on the curvature of energy surfaces in **k**-space. Cyclotron resonance experiments[14,15] have firmly established that for the conduction band of Ge the energy surfaces can be represented by ellipsoids of revolution whose major axes lie along the [111] **k** directions. Hence, the energy surfaces are described in terms of two mass parameters, M_t and M_l, which are the transverse and longitudinal effective mass ratios respectively. The values of the effective mass ratios may be obtained conveniently by a transformation of coordinates. In the case of $M_c^{(N)}$ a transformation of the momentum coordinates with respect to each minimum into an isotropic coordinate frame results in the introduction of the factor $\omega_c(M_t^2M_l)^{\frac{1}{3}}$ into the expression for the classical partition function. The quantity ω_c is equal to the number of complete minima[18] and takes a value of eight if the minima lie within the first Brillouin zone or a value of four if they lie at zone boundary. Hence $M_c^{(N)}=(M_t^2M_l)^{\frac{1}{3}}$.

The method of averaging used for $\langle f_c^2\rangle_{Av}$ is somewhat more complex. Here, a similar transformation of momentum coordinates made in the expression for energy in the presence of a magnetic field requires a further transformation of the magnetic field components. When the details of the computation are carried through, the appropriate combination of principal mass ratios turns out to be

$$\langle f_c^2\rangle_{Av}=(2M_t+M_l)/3M_t^2M_l.$$

Using now the reported values for the principal masses[14,15] ($M_t=0.083$ and $M_l=1.4$), we obtain $M_c^{(N)}=0.216$ and $\langle f_c^2\rangle_{Av}=54.1$. If in addition we use $\omega_c=4$, as indicated by an analysis of the temperature dependence of the susceptibility of n-type Ge,[13] Eqs. (2) and (4) may be written

$$\chi_c=4.26\times10^{-9}T^{\frac{1}{2}}F_{\frac{1}{2}}'(\eta), \tag{2a}$$

$$n=2.12\times10^{15}T^{\frac{3}{2}}F_{\frac{1}{2}}(\eta). \tag{4a}$$

The calculations of Kittel *et al.*[14] and Herman[24] indicate that the valence band is composed of three doubly-degenerate, nonspherical bands and is therefore somewhat more complex than the conduction band. The maximum of these bands appears to fall at $\mathbf{k}=0$, two of them coinciding at that point to form the valence band edge. Because of spin-orbit interactions the third band which is nearly spherical lies below the other two by the interaction energy ΔE. In order to evaluate the effective mass parameters of Eq. (2), it is necessary to use the energy expressions for these bands which, to a good approximation for Ge, are given by Kittel *et al.*[14] in terms of three curvature parameters. The value of $M_h^{(N)}$ is obtained directly from the classical partition function, which can be summed rigorously by using the energy expressions. Such a sum for the two upper bands leads directly to the double integral

$$M_{1,2}^{\frac{3}{2}}=\frac{1}{4\pi}\int\int\frac{d\Omega}{\{A\pm[B^2+C^2g(\vartheta,\varphi)]^{\frac{1}{2}}\}^{\frac{3}{2}}}, \tag{6}$$

where the subscripts 1 and 2 and the upper and lower signs in the integral refer to the "light" and "heavy" bands respectively, the curvature parameters are identical to those of Kittel *et al.*[14] except for the factor $(\hbar^2/2m_0)$, and

$$g(\vartheta,\varphi)=\sin^4\vartheta\cos^2\varphi\sin^2\varphi+\sin^2\vartheta\cos^2\vartheta. \tag{7}$$

The lower band (Band 3) gives

$$M_3^{\frac{3}{2}}=A^{-1}. \tag{8}$$

Numerical integration of Eq. (6), using the appropriate values of the curvature parameters, yields $M^{\frac{3}{2}}$ values of 0.0091, 0.199, and 0.0213 for Bands 1, 2, and 3 respectively. Hence

$$M_h^{(N)\frac{3}{2}}=0.208+0.0213e^{-\Delta E/kT}. \tag{9}$$

The orbital effective mass presents additional difficulties, and a rigorous treatment requires an approach for each band similar to that used for electrons. However, it was observed in the integration of Eq. (6) that

[22] J. McDougall and E. C. Stoner, Trans. Roy. Soc. (London) **A237**, 67 (1936).

[23] For a treatment of the intrinsic range see references 8, 9, and 17.

[24] F. Herman, Physica **20**, 801 (1954).

the corrections for lack of sphericity were small even for the most nonspherical band (Band 2). Consequently, we use an approximate approach in which the error is probably not greater than 5%. To a good approximation, even in the magnetic field,

$$M_{1,2}^{-1}=\frac{1}{4\pi}\int\int\{A\pm[B^2+C^2g(\vartheta,\varphi)]^{\frac{1}{2}}\}^{\frac{1}{2}}d\Omega. \quad (10)$$

Integration leads to $M_h^{-\frac{1}{2}}$ values of 4.80, 1.74, and 3.605 for Bands 1, 2, and 3 respectively. Hence

$$\langle f_h^2\rangle_{Av}=M_h^{-\frac{1}{2}}/M_h^{\frac{1}{2}}\cong 31.4+14.1e^{-\Delta E/kT}. \quad (11)$$

Consequently, both $M_h^{(N)}$ and $\langle f_h^2\rangle_{Av}$ are temperature dependent through the Boltzmann factor containing the spin-orbit splitting energy. Optical absorption of holes in Ge suggests[25] that $\Delta E\sim 0.3$ ev. If such is the case, the mass parameters are expected to be essentially temperature independent in the temperature range used here and $M_h^{(N)\frac{1}{2}}=0.208$ and $\langle f_h^2\rangle_{Av}=31.4$. A similar calculation using the slightly different curvature parameters of Lax *et al.*[15] gives almost identical values.

C. Impurity Contribution

In the specimens used here we are interested only in the usual acceptor and donor doping impurities of the third and fifth columns of the periodic system. Since these impurity atoms presumably fit substitutionally into the semiconductor lattice, they may be treated as hydrogen-like systems to an approximation sufficiently good for this purpose. Busch and Mooser[8] have examined this case in detail both for the low-concentration limit in which the impurity atoms may be treated independently and for concentrations sufficiently high that the impurity wave functions overlap and form degenerate impurity bands. Because of their substitutional arrangement, one expects an appreciable contribution only when they are un-ionized. Besides the paramagnetic term associated with the unpaired electron-spin, these authors show that for a large dielectric constant the electron or hole orbit is of such a size that an appreciable diamagnetic term may also exist in the small concentration case. If one uses the numerical constants appropriate for Ge, the low concentration limit gives

$$\chi_I=N_I^0[1.17\times 10^{-28}T^{-1}-3.4\times 10^{-28}], \quad (12)$$

where N_I^0 is the concentration of un-ionized impurities of the type in question. In obtaining the diamagnetic term it is assumed that the effective mass of the bound carrier is equal to the electronic mass and germanium has a dielectric constant of 16.1. In the case of impurity bands, equations analogous to Eq. (2) are obtained which contain the effective mass ratios appropriate to the impurity band. There is no way available at present for evaluating these mass ratios.

In nearly all specimens used here, the ionization energies are so small that the impurities are essentially completely ionized over the entire temperature range (70 to 300°K). Therefore, the impurity contribution discussed above is not of immediate interest. For the irradiated specimens, however, an estimate of the contribution of the trapped carriers is important. In order to do this, a model of the bombardment-introduced defects is necessary and the only one available at present which is to any extent justified is that proposed by James and Lark-Horovitz.[26] This model, which has been tested experimentally,[19] requires that each interstitial and each vacancy be responsible for two localized states in the forbidden band. When these defects are present in equal concentration, there are two vacant states capable of trapping conduction electrons in *n*-type Ge: one which lies below the middle of the forbidden band and is therefore capable of acting as an acceptor in *p*-type Ge, and another much more shallow one which has been experimentally located at 0.2 ev below the conduction band. On irradiating *n*-type Ge with a high initial electron concentration n^0, both levels are to some extent occupied until the concentration of defect pairs becomes equal to one-half n^0. Further irradiation favors population of the lower acceptor state until all electrons are trapped therein and conversion to *p*-type occurs. Therefore, at the minimum conductivity, essentially all of the electrons are trapped in a state that has been tentatively identified as one corresponding to a singly ionized interstitial atom. If the defects are randomly distributed and their associated wave functions do not overlap appreciably, a paramagnetic contribution equal to that for n^0 free spins should result. The diamagnetic contribution depends on the radial extent of the wave functions of the trapped electron. Since the interstitial ion has a residual charge, the electron orbit will be considerably decreased over that estimated above for a hydrogen-like impurity and the diamagnetic contribution is expected to be quite small. Should the defect functions overlap, a paramagnetic contribution of much smaller magnitude and temperature dependence would result. Such a condition may exist even for relatively short irradiations if the defects are highly localized in the region of the primary (fast-neutron) collision.

In this picture the vacancy should be occupied by two electrons at the conductivity minimum. Here the diamagnetic contribution might be appreciable. Both the Coulombic repulsion of the electrons and their relatively loose binding (they presumably fill two of the four half-filled orbitals extending into the vacancy) would tend to produce a large orbit. Unfortunately, it is not possible to make a quantitative estimate of their contribution on the basis of present knowledge.

III. EXPERIMENTAL

The magnetic susceptibilities of single-crystal cubes having edge lengths of approximately 5 mm were

[25] A. Kahn, Phys. Rev. **97**, 1647 (1955).

[26] M. H. James and K. Lark-Horovitz, Z. physik. Chem. **198**, 107 (1951).

measured by the Faraday technique using a balance similar to that of McGuire and Lane.[27] In order to increase the balance sensitivity, the phototube-optical system was replaced by a linear differential transformer and the beam suspension was fabricated out of Elgiloy rather than nichrome or phosphor bronze. The sample cubes were suspended from the balance on 0.001-in. diameter molybdenum wire into the fringing field of an Arthur D. Little electromagnet, the field of which could be controlled and reproduced to approximately $\pm 0.01\%$. Sample temperatures were taken as those of the wall of the copper sample tube adjacent to the specimen, helium at a pressure of 125 microns of Hg being used as a heat-exchange medium.

The absolute value of the room temperature susceptibility of each sample was measured using oxygen at a known pressure and temperature as a calibrating agent. The force exerted on a body of volume v and volume susceptibility κ suspended in an inhomogeneous field H is given by

$$F_0 = \tfrac{1}{2}(\kappa - \kappa_0) v \nabla(H^2), \tag{10}$$

where κ_0 is the volume susceptibility of the surrounding medium and $\nabla(H^2)$ is the gradient of the square of the field at the sample. The susceptibility of an irregularly shaped body is given by the expression

$$\kappa = \left[\frac{F_v}{F_v - F_0}\right]\kappa_0, \tag{11}$$

where F_v is the force experienced by the body when suspended in a vacuum and F_0 is the force experienced when suspended in a medium having a susceptibility κ_0.

In this work F_v was measured at four values of the field ranging from 12 to 20 kilo-oersteds. Oxygen was then admitted to the system, the measurements repeated at the same field settings, and κ calculated for each field value. A systematic trend of κ with field was considered an indication of ferromagnetic contamination and the sample was recleaned. Otherwise, the calculated values were averaged to obtain the absolute value of the room temperature susceptibility of each sample. When this technique is used, the absolute accuracy of this point is $\pm 0.6\%$. The susceptibilities at other temperatures were determined relative to this room temperature point with a precision of $\pm 0.1\%$.

Carrier concentrations were obtained from Hall coefficient and conductivity measurements obtained on control specimens which were cut from the original ingot adjacent to the susceptibility cube. In several cases, when inhomogeneity in the impurity distribution was suspected, Hall plates were prepared from successive ingot slices cut radial to the cube and perpendicular to the direction of growth. The average concentration obtained on these plates was used.

One cube, together with its control specimen, was given successive exposures to fast neutrons in a fission chamber in the Oak Ridge Graphite reactor. The irradiations were carried out at $\sim 30°C$ and susceptibility and Hall coefficient measurements were made after each exposure.

IV. RESULTS

A. High-Purity Germanium

For extrinsic carrier concentration $<10^{16}$ cm^{-3}, χ_e is below the limit of detection in the temperature range employed. Consequently, values of χ obtained on high-purity specimens should yield χ_A for Ge directly. The temperature dependence of χ for two n-type specimens ($n = 1\times10^{13}$ cm^{-3} and 1×10^{14} cm^{-3}) is shown in Fig. 1. Because of the absolute precision from one curve to the other of only $\pm 0.6\%$, the curves were adjusted to correspondence at 150°K. As expected, the points for both specimens fall essentially on the same line.

As mentioned above, the atomic diamagnetism is expected to be only slightly temperature-dependent. In contrast, the curve of Fig. 1 exhibits a very appreciable temperature variation. Normally a relative increase of diamagnetism of the same order as the cubical expansion coefficient might be expected. For Ge, however, the dependence is in the opposite direction and the relative change is an order of magnitude greater than the expansion coefficient ($d\log\chi/dT = 2.3\times10^{-4}$ at 300°K). Although we assume that the nature of the binding in the diamond lattice is responsible, the reason for this curious behavior is not yet known. In order to investigate this point further, a specimen of high-purity silicon ($n\sim10^{14}$ cm^{-3}) and a gem-quality diamond were examined. The silicon specimen gave a χ *vs* T curve which is quite similar to that of Ge, while for the diamond χ is temperature independent within experimental error ($\pm 0.1\%$) in this temperature range.

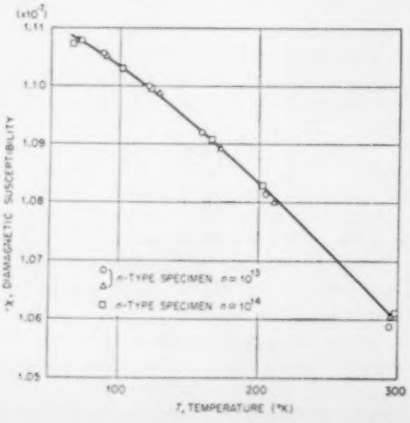

FIG. 1. The diamagnetic susceptibility of two high-purity germanium specimens as a function of temperature. For comparison, the curves are adjusted to correspondence at 150°K.

[27] T. R. McGuire and C. T. Lane, Rev. Sci. Instr. **20**, 489 (1949).

B. *n*-Type Germanium

The diamagnetic susceptibility *vs* temperature curves for a number of *n*-type Ge specimens of known electron concentration are shown in Fig. 2. Also shown for comparison is the curve for a high-purity, zone-refined *n*-type specimen ($n<10^{14}$ cm^{-3}). In every case except the latter the contribution of the extrinsic electrons is evident.

The values of χ_e are obtained for each specimen by subtracting, point by point, the susceptibility of the high-purity specimen. The resulting values for three of the specimens are shown in Fig. 3 in the form of $-\chi_e$ *vs* $1/T$ curves. The curves are essentially linear in the high-temperature range as predicted by Eq. (5). Toward lower temperature the curves begin to fall off, indicating a transition from classical to Fermi-Dirac statistics. In Table I we have summarized the data on *n*-type Ge. The second column lists the high-temperature (low-$1/T$) linear slope. The third column lists the values of n obtained on comparison Hall specimens appropriately corrected for impurity scattering[28] and carrier degeneracy.[29] After such corrections the values of n were found to be temperature independent over the entire range to ~5% with the exception of sample 1. In the fourth column we list the values of $\langle f_e^2\rangle_{Av}$ obtained from the slope and values of n. These values are accurate to about 15%.

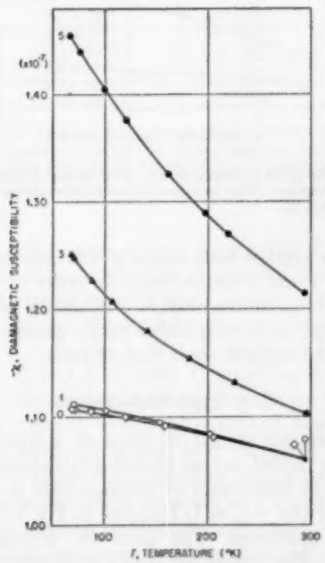

FIG. 2. The diamagnetic susceptibility *vs* temperature curves of four *n*-type germanium specimens. Curve 0 is that for high-purity germanium while the numbers of the other curves correspond to the sample numbers of Table I.

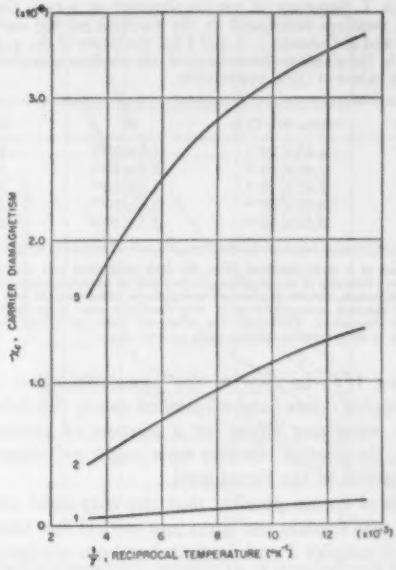

FIG. 3. The carrier diamagnetism *vs* reciprocal temperature for *n*-type germanium. The curve numbers refer to the sample numbers listed in Table I.

It is interesting to note that for the purer specimens agreement of $\langle f_e^2\rangle_{Av}$ with the expected value of 54 is quite reasonable, while with increasing donor concentration the value of $\langle f_e^2\rangle_{Av}$ decreases markedly. Herring[30] has pointed out that the presence of an impurity band which is expected to overlap the conduction band at high donor concentrations would be expected to change the effective mass of the carriers when the overlap becomes appreciable.

Except for sample 1 of Table I, the χ_e *vs* $1/T$ curves of the *n*-type specimens depart from linearity toward the higher $1/T$ values, exhibiting a downward concavity. In the case of samples 2 and 3 this curvature can be accounted for quite adequately on the basis of transition from classical to Fermi-Dirac statistics provided $\omega_c=4$ rather than 8. With this value of ω_c, Eq. (2) yields an acceptable fit to the data over the entire temperature range. The results of this analysis have already been reported[18] and these have been taken as evidence that the minima of the E *vs* k surfaces lie on or within kT of the zone boundary. Attempts to fit the more impure specimens (4 and 5 of Table I) within the framework of the cyclotron resonance results were not successful nor could a suitable correlation be obtained by using Eq. (2) and the experimental values of $\langle f_e^2\rangle_{Av}$ while treating $M_e^{(N)}$ as an adjustable parameter. The experimental curves fall off more rapidly at low temperature than those calculated, in a manner which suggests that the effective mass decreases with in-

[28] V. A. Johnson and K. Lark-Horovitz, Phys. Rev. **82**, 977 (1951).
[29] V. A. Johnson and F.M. Shipley, Phys. Rev. **90**, 523 (1953).
[30] C. Herring (private communication).

TABLE I. Summary of results obtained on n-type Ge. The sample numbers correspond to the numbers on the curves of Figs. 2 and 3. Columns 2, 3, and 4 list the slopes of the χ_e vs $1/T$ curves in the classical (linear) region, the electron concentrations and the values of $\langle f_e^2 \rangle_{Av}$ respectively.

Sample	$-[d\chi_e/d(1/T)]_{cl}$	n^a	$\langle f_e^2 \rangle_{Av}$
1[b]	4.85×10^{-6}	3.1×10^{16}	~43
2	1.46×10^{-6}	7.5×10^{17}	52.6
3	1.45×10^{-6}	1.3×10^{18}	31.6
4	4.57×10^{-6}	5.0×10^{18}	26.4
5	5.59×10^{-6}	1.3×10^{19}	14.0

[a] Values of n were obtained from the Hall coefficient and conductivity curves as a function of temperature, corrections for impurity scattering and, where necessary, carrier degeneracy being made (references 28 and 29).
[b] The electron concentration of this specimen was appreciably temperature dependent. Therefore, the observed value of $\langle f_e^2 \rangle_{Av}$ might be expected to be somewhat smaller than its true one.

creasing $1/T$. In view of the postulated effect of an overlapping donor band mentioned above, this behavior is not surprising since, for a mixture of conduction states, the average effective mass might well depend on the position of the Fermi level.

It is of course possible that impurity-band overlap might also explain the curvature toward low temperature of samples 2 and 3 which has been attributed to carrier degeneracy. In fact, Debye and Conwell[31] have examined the dependence of donor ionization energy on donor concentration in n-type Ge and, within the limitations of necessary assumptions, have shown that the ionization energy becomes zero for net donor concentrations in the neighborhood of 1.5×10^{17} cm^{-3}. If the ionization energy can be taken as an index of band overlap, this would indicate that a mixing of donor and conduction states might also occur in samples 2 and 3. In this regard, Johnson and Shipley[32] have made a careful analysis of the temperature dependence of the Hall coefficient of a specimen containing a net donor concentration of 2.16×10^{18} cm^{-3} and they find an ionization energy of -0.005 ev. Hence the ionizations energies of the specimens in question are expected to lie closer to the band edge than 0.005 ev. For the temperature range in question, since effects of carrier degeneracy are not excessive, we expect the donor states to exert only a small influence on the effective mass of conduction electrons for these specimens. In further support of the choice of $\omega_e=4$, Debye and Conwell find that an average effective mass ratio between 0.2 and 0.5 gives the most consistent fit to all their data. The average effective-mass ratio arising from the density of states expression is $M_e^*=M_e^{(N)}\langle\omega_e\rangle^{\frac{1}{2}}$.

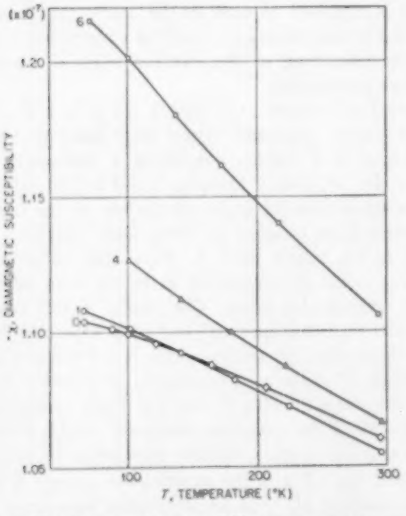

FIG. 4. The diamagnetic susceptibility vs temperature curves of three p-type specimens and one high-purity n-type specimen, curve 0, of germanium. The numbers of the other curves correspond to the sample numbers of Table II.

[31] P. P. Debye and E. M. Conwell, Phys. Rev. **93**, 693 (1954).

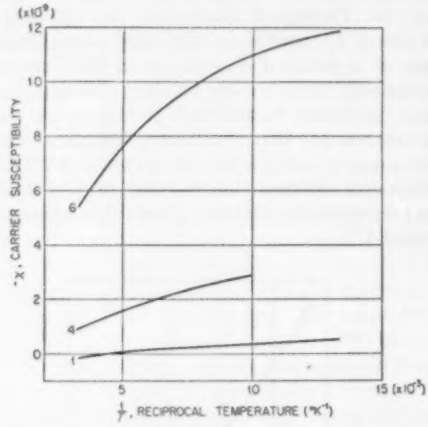

FIG. 5. The carrier diamagnetism vs reciprocal temperature for p-type germanium. The numbers refer to the sample numbers listed in Table II.

This gives average mass ratios of 0.51 and 0.85 for ω_e values of 4 and 8 respectively. In order to establish the value of ω_e conclusively, it is necessary to examine the behavior of χ_e on a higher purity sample ($n\simeq10^{17}$ cm^{-3}) in the range of lower temperatures.

C. p-Type Germanium

Measurements similar to those on n-type material have been carried out on several p-type samples. The temperature dependence of diamagnetism is shown in Fig. 4 and the $-\chi_e$ vs $1/T$ curves in Fig. 5 for representative specimens. The data are summarized in Table II. The values of $\langle f_h^2 \rangle_{Av}$ with one exception (sample 2) are considerably smaller than the value of 31.4 indicated by cyclotron resonance. Again, as for n-type material, this departure from expectation appar-

[32] V. A. Johnson and F. M. Shipley, Report of the Purdue Research Foundation to the Signal Corps, August, 1952 (unpublished).

ently increases with increasing acceptor concentration. Since the deviation seems to set in at a much lower carrier concentration than in n-type material, it is possible that the critical acceptor concentration required for the formation of an overlapping impurity band is smaller than for donors. However, even for 8×10^{16} acceptors cm^{-3} (sample 1 of Table II) the $\langle f_h^2\rangle_{Av}$ is only $\sim$20 and for such a small acceptor concentration an overlapping band does not appear likely. Consequently, we conclude that the discrepancy between observed and expected $\langle f_h^2\rangle_{Av}$ values is real. The reason for the lack of agreement is unknown. It is possible that the energy-surface curvatures in the valence band are sufficiently complex that the cyclotron resonance results obtained at 4°K are no longer applicable in this temperature range. In this connection, it is noteworthy that a detailed analysis of the field dependence of the p-type Ge Hall coefficient,[33] although in agreement with the general features of the valence band as revealed by cyclotron resonance, also fails to give a quantitative correlation. The results of this analysis indicate that

TABLE II. Summary of results obtained on p-type specimens. The sample numbers correspond to those given on the curves of Figs. 4 and 5. Columns 2, 3, and 4 list the classical slopes of the χ_g vs $1/T$ curves, the hole concentrations, and the values of $\langle f_h^2\rangle_{Av}$ respectively.

Sample	$[d\chi_G/d(1/T)]_{cl}$	p^a	$\langle f_h^2\rangle_{Av}$
1	5.2×10^{-6}	7.8×10^{16}	20
2	1.7×10^{-7}	1.9×10^{17}	26
3	2.8×10^{-7}	4.4×10^{17}	18
4	3.2×10^{-7}	5.1×10^{17}	20
5	2.9×10^{-7}	5.4×10^{17}	18
6	2.0×10^{-6}	5.3×10^{18}	12

[a] Although impurity-scattering and carrier-degeneracy corrections were made in obtaining these values, the magnetic field dependence of Hall coefficient, which is known to be appreciable in p-type Ge (reference 31), was not accounted for explicitly. The error involved, however, should not be large.

the fraction of holes in Band 1 is only 0.02 of the total whereas the ratio of effective masses indicates a value of 0.045. A smaller than expected population of Band 1 would also explain the deviation reported here.

Attempts to fit the χ_g vs $1/T$ curves of Fig. 5 for samples 1, 2, and 3 of Table II according to Eq. (2) with experimental carrier masses reveal that there is a significant concave downward curvature toward high $1/T$ values which is too great to be explained by either transition to Fermi-Dirac statistics, higher order terms in H in the susceptibility equation, or a combination of these. Since analysis of Hall coefficient and resistivity data for these specimens indicates that the hole concentrations are essentially constant over the temperature range in question, it appears that $\langle f_h^2\rangle_{Av}$ decreases to some extent with decreasing temperature. Although the contribution to $\langle f_h^2\rangle_{Av}$ of the third valence band is temperature-dependent through a Boltzmann factor

[33] Willardson, Harman, and Beer, Phys. Rev. **96**, 1512 (1954).

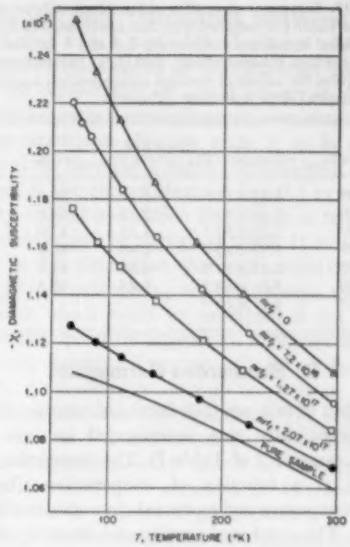

FIG. 6. The diamagnetic susceptibility vs temperature of a fast-neutron-bombarded n-type germanium specimen listed as sample 2 in Table I. The exposures are indicated on the curves. The curve of a pure specimen is shown for comparison.

containing the spin-orbit splitting energy, it was indicated above that this is not expected to introduce appreciable temperature dependence in this temperature range because of the large value that has been indicated for ΔE.

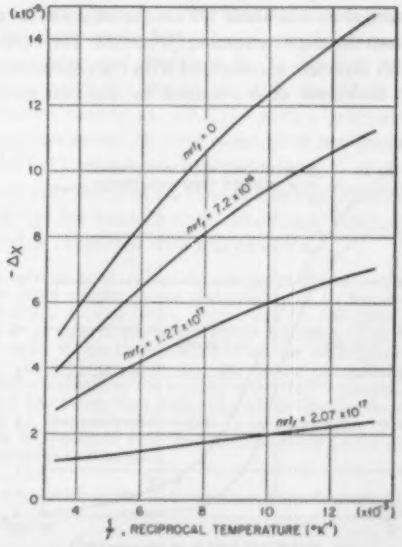

FIG. 7. The carrier plus defect susceptibility vs temperature of the fast-neutron-bombarded germanium sample after the indicated exposures.

TABLE III. Summary of results obtained on n-type specimen (sample 2 of Table I) irradiated with fast neutrons. The integrated fluxes are listed in column 1. Columns 2, 3 and 4 list the classical slopes, the electron concentrations, and $\langle f_c^2 \rangle_{Av}$ values respectively. Column 5 gives the values of electron concentration n_M calculated from the classical slope assuming $\langle f_c^2 \rangle_{Av} = 54$.

Exposure (neutrons/cm²)	$-[d\Delta\chi/d(1/T)]$	$n \times 10^{-17}$ cm^{-3}	$\langle f_c^2 \rangle_{Av}$	$n_M \times 10^{-17}$ cm^{-3}
0.72×10^{17}	1.13×10^{-6}	5.17	59.0	5.68
1.27×10^{17}	5.33×10^{-7}	2.72	53.0	2.68
1.61×10^{17}	2.28×10^{-7}	1.33	47.0	1.15
1.84×10^{17}	1.57×10^{-7}	0.85	50.4	0.79
2.07×10^{17}	1.25×10^{-7}	0.81	42.5	0.63
2.30×10^{17}	8.0×10^{-8}	0.45	48.5	0.40
3.00×10^{17}	1.1×10^{-8}	...	...	0.06

D. Bombarded Germanium

The effect of fast-neutron bombardment on the magnetic susceptibility was investigated on one n-type specimen (sample 2 of Table I). The susceptibility was measured as a function of temperature after each successive exposure and representative results are shown in Fig. 6. The combined carrier and impurity (defect) susceptibilities were obtained by subtracting the values of a pure specimen at each temperature and this, designated as $-\Delta\chi$, is plotted against $1/T$ in Fig. 7. The data are summarized in Table III. Column 1 lists the integrated fast neutron flux, Column 2 the linear slope, the electron concentrations obtained from an analysis of the Hall coefficient and resistivity are given in Column 3 and in Column 4 the values of $\langle f_c^2 \rangle_{Av}$ obtained from the slopes are given. The reciprocal mass ratio is in good agreement with the expected value of 54 and the scatter gives a good indication of experimental error. Also shown in Table III are the values of n calculated from the slopes assuming $\langle f_c^2 \rangle_{Av} = 54$. The variation of n with exposure is compared with the conductivity σ in Fig. 8. Values of n obtained by the two methods

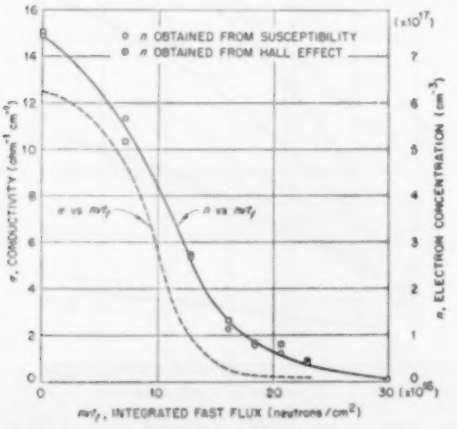

FIG. 8. The electron concentration and conductivity vs integrated fast-neutron flux of the bombarded specimen.

(columns 3 and 5) show a variation with exposure which is quite similar to that of σ.

Examination of the χ vs $1/T$ curves obtained after long exposure (not shown in Fig. 7) reveals that, although the curves are quite linear at low temperature, there is a marked upward concavity at high temperatures (low $1/T$). This behavior may or may not be real. Although it is possible that exposure has decreased the temperature dependence of χ_A in the high-temperature region, thus introducing an apparent curvature into the $\Delta\chi$ vs $1/T$ curves, this behavior may also be explained as being caused by a variation of the sample suspension length with temperature. The thermal expansion of molybdenum, though small, is sufficient between room and dry ice temperatures to move the specimen into a lower region of $H\,dH/dz$ provided the

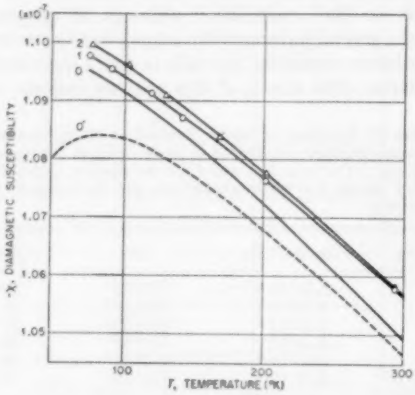

FIG. 9. The diamagnetic susceptibility vs temperature of the bombarded specimen after irradiation into the intrinsic region. Curve 1 is for the specimen with approximately 5×10^{15} electrons per cm³ remaining in the conduction band at 300°K. Curve 2 is after the specimen has become p-type and has less than 10^{15} carriers per cm³ at 300°K. Curve 0 is for a pure specimen, displaced downward by 0.7% for clarity. Curve 0′ is curve 0 to which has been added the expected paramagnetic contribution of 7.5×10^{17} unpaired spins per cm³.

position at room temperature were at the place where the gradient of the square of the field is a maximum. More careful measurements are necessary before this effect can be interpreted. In any event, since molybdenum is a high-temperature metal, its expansion coefficient is quite small below 200°K and the temperature dependence of $\Delta\chi$ in this range (70 to 200°K) should be valid.

It is interesting to note that there is no indication of the temperature-dependent paramagnetism expected to result from unpaired electrons. In Fig. 9 we compare the χ vs T curves for a pure specimen (curve 0) and the two longest exposures (curves 1 and 2) for which essentially all electrons have been trapped. For clarity, Curve 0 has been displaced downward by 0.7% in order to avoid congestion. Also shown (Curve 0′, dashed) is

the expected χ *vs* T curve relative to Curve 0 for a specimen containing 7.5×10^{17} unpaired spins per cm^3. It is clearly evident that such a paramagnetic term is not present in the irradiated specimens. This is taken as evidence that the levels responsible for removing electrons are so dense that they have broadened into degenerate bands. At a concentration of 7.5×10^{17} this does not appear too likely, especially in view of considerations concerning the singly ionized interstitial atom as discussed above. Consequently, we tentatively conclude that the defects are not randomly distributed but rather are to a large extent localized in the region of the primary collision of the fast neutron. The latter situation would produce localized regions of high defect-level density which could be described effectively in terms of degenerate impurity bands. In order to establish this point to any degree of certainty it is necessary to examine lower concentrations of trapped electrons. This can be done quite effectively by extending the range of measurement to liquid helium temperatures. Apparatus is being constructed to this end.

V. SUMMARY

The results have revealed a number of points of interest regarding the magnetic behavior of Ge. The first and most unexpected of these is the temperature dependence of the susceptibility of high-purity specimens. That this is a common property of semiconductors of the diamond-lattice type is suggested by a similar behavior of Si and an indication of such in InSb.[9] It should be noticed, however, that diamond itself has a temperature-independent susceptibility. In view of its existence in the lower melting members of the group (both elements and compounds), it would be worthwhile to re-evaluate the results obtained on α Sn in the light of such a behavior.

The magnetic behavior of *n*-type Ge is consistent with expectation based on results of cyclotron resonance. The appropriate averages of electron mass ratios are in reasonable agreement with those obtained by the Berkeley[14] and Lincoln Laboratory[15] groups for the smaller values of n. At the large n-values the effective masses increase markedly; this increase is probably due to a degenerate donor band which overlaps the bottom of the conduction band. Fitting the data to theory in the range of transition from classical to Fermi-Dirac statics suggests that the energy surfaces of the conduction band are represented by four rather than eight ellipsoids of revolution in **k**-space.

In *p*-type Ge, agreement with cyclotron resonance experiments is not as convincing. We find that generally the values of $\langle f_A^2\rangle_{\text{Av}}$ are smaller by at least 30% than the predicted one. The results of a detailed analysis of the Hall coefficient field dependence in *p*-type Ge also fail to yield quantitative agreement.[33] It is possible that the complex band shapes yield different effective mass ratios at temperatures appreciably above the temperature of liquid helium at which the cyclotron resonance measurements were made. A temperature-dependent effective mass is to be expected because of the lowering of Band 3 by spin-orbit coupling. However, if the energy lowering is $\sim$0.3 ev as is indicated by optical absorption data, such a temperature dependence would be negligibly small. It is interesting to note in this connection that an examination of hole mobility[34] also indicates a variance between theory and experiment which could be explained if the effective mass were temperature dependent. A more careful study of the hole susceptibility, particularly at lower temperature, is necessary to clear up this matter.

Studies of fast-neutron-bombarded Ge reflect only the decrease of electron concentration and reveal no spin paramagnetism which would be expected if the electrons were trapped unpaired in localized states. This behavior is interpreted as indicative of localized fluctuations in the density of fast-neutron-introduced lattice defects.

We are deeply indebted to Miss Louise Roth of Purdue University and to Dr. C. S. Fuller of the Bell Telephone Laboratories who furnished the single crystals of Ge and Si used in these studies. Our thanks also to Mr. Chapman of Kimball's Jewelry, Knoxville, Tennessee, for making available to us the excellent diamond specimen, and Mr. T. R. Green of the Elgin National Watch Company who supplied us with an unheattreated main-spring blank used in the construction of the balance. We finally wish to thank J. C. Pigg, Glenn Craig, and W. T. Adams of this laboratory for their invaluable assistance with instrumentation problems and Professor R. L. Sproull of Cornell University for many valuable discussions and suggestions. One of us, (D.K.S.) wishes to express his appreciation to Dr. H. D. Crockford of the University of North Carolina who, in the capacity of faculty advisor, gave freely of his time and energy in coming to Oak Ridge for consultations concerning much of the early work connected with this problem.

Note added in proof.—Since the completion of this manuscript, another paper relative to the susceptibility of Ge has come to our attention. C. Enz [Helv. Phys. Acta **28**, 158 (1955)] has analyzed the data of Busch and Helfer (reference 17) in the intrinsic range. Within the limitation of certain assumptions concerning the intrinsic range and the lattice susceptibility, he finds that a better fit to the intrinsic susceptibility is obtained by assuming four rather than eight ellipsoids to describe the energy surfaces of the conduction band. It is encouraging that this result is in agreement with that reported above for an entirely different range of behavior.

[34] H. Ehrenreich and A. W. Overhauser, Phys. Rev. **98**, 1533(A) (1955).

Recombination Processes in Tellurium*

DAVID REDFIELD
University of Pennsylvania, Philadelphia, Pennsylvania
(Received August 3, 1955)

Recombination processes in tellurium have been investigated, chiefly by use of the techniques of photoconductivity. Studies were made on single crystals having acceptor densities of about 10^{16} per cm^3. By using pulsed illumination, the decay time constant of photocurrent was found to be 20 μsec, in fairly good agreement with results obtained previously from steady-state photocurrent sensitivity.

The interpretation of the results of the various photoconductivity experiments leads to the conclusion that in Te at 100°K direct recombination dominates over recombination through localized centers (traps) at all light intensities. To explain this unusual result, it is proposed that as a rule in small-energy-gap materials traps should be relatively ineffective as agents of recombination. It follows that small-gap materials should have long lifetimes; thus they should usually be sensitive photoconductors. Furthermore, since the direct recombination probability increases as the gap becomes narrower, there should be some optimum value of energy gap (probably near 0.5 ev) that will give rise to the longest realizable lifetimes. Some confirming data on other materials are cited in support of this proposal.

An attempt to observe radiation which may be emitted in the recombination process was unsuccessful, possibly because of experimental limitations.

I. INTRODUCTION

THE study of recombination processes in semiconductors and insulators is receiving much attention for both theoretical and practical reasons. Experimentally, the most fruitful approach to such studies has been through investigation of photoconductivity, although some new techniques appear promising. This work represents a study of the photoconductive properties of Te with the goals of determining carrier lifetime and obtaining information on the recombination process.

In work on Te reported earlier, steady-state photocurrent experiments were used to determine carrier lifetime as well as the dependence of photosensitivity on temperature, light intensity, and wavelength.[1] The results obtained will be summarized here for our present purposes.

Figure 1 shows the observed dependence of photocurrent i on light intensity I_0 at a wavelength of 3μ for Te at 100°K. On the log-log scales, the slopes 1 and $\frac{1}{2}$ correspond to linear and square root dependence, respectively. In the linear region where the light level is low, carrier lifetime is a well-defined quantity and is a direct measure of the photosensitivity. As shown in reference 1, we may estimate this low-level lifetime τ_0 by using the relation

$$\tau_0 = i/e\mu\mathcal{E}WI_0,$$

where e = magnitude of electronic charge, μ = carrier mobility (properly $\mu_e+\mu_h$), $\mathcal{E}$ = electric field strength in sample, and W = width of sample $\perp$ light flux and field. This method gave a value for τ_0 of 5×10^{-5} sec for a Te crystal at 100°K. Because of the difficulty in calibration of light intensity, this may be regarded only as an order-of-magnitude figure. A similar value was obtained, however, by Aigrain in some apparently unpublished work using the photoelectromagnetic (PEM) techniques.[2]

It is well known that the simple theory of direct recombination of free electrons and holes will lead to just the type of intensity dependence of photocurrent shown in Fig. 1.[3] However, except for phosphorous and possibly selenium, this sort of dependence has never been observed, presumably because trapping states seem to dominate the recombination processes in nearly all known materials. We shall now consider in detail the possible effects of traps using as a basis the statistical treatment of Shockley and Read.[4] (R. N. Hall has arrived at a very similar theory and has found some experimental confirmation.[5])

II. DISCUSSION OF TRAPS

A. General

In considering the effects of traps for our purposes, it is most fruitful to establish the principles involved by treating a single type of trap. Then the possibility of multiple levels may be treated by superposition, and if necessary, some interactions among different levels added later. It is clear on intuitive grounds and is pointed out in reference 4, that recombination through traps may be regarded as a flow through two resistors in series, so independent types of traps may be treated as parallel combinations of such pairs of resistors. In fact, this view allows also the inclusion of direct recombination as a single resistor in parallel with the possible other pairs.

---

* This paper is based on a thesis submitted to the University of Pennsylvania Physics Department in partial fulfillment of the requirements for the degree of Doctor of Philosophy. The work was supported principally by the Socony-Vacuum Oil Company and in part by the U. S. Air Force and the Office of Naval Research.

[1] D. Redfield, *Photoconductivity Conference* (John Wiley and Sons, Inc., New York, to be published).

[2] P. Aigrain (private communication).

[3] See, for example, T. S. Moss, *Photoconductivity* (Academic Press, New York, 1952).

[4] W. Shockley and W. T. Read, Jr., Phys. Rev. **87**, 835 (1952).

[5] R. N. Hall, Phys. Rev. **87**, 387 (1952).

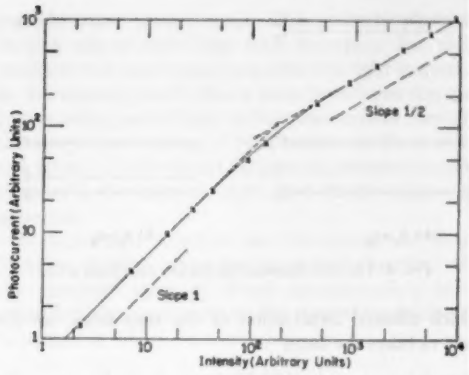

FIG. 1. Photocurrent *vs* light intensity in Te crystal at 100°K (wavelength 3μ).

Therefore, we shall consider now a single set of localized trapping states characterized principally by four quantities: (1) cross section for capture of an electron by the trap when empty, σ_e; (2) cross section for capture of a hole by the trap when occupied, σ_h; (3) energy level of the states, E_t (see Fig. 2); (4) density of traps, N_t. Because of the great difficulty in getting quantitative data on any of these, the approach will be a general one wherever possible so as not to require the assumption of values for these quantities.

B. Shockley and Read Formalism

The recombination of photoelectrons and holes is considered to occur only through the medium of the N_t traps per cm³. The effective lifetime is defined as

$$\tau \equiv \delta n/U, \tag{1}$$

where U = recombination rate density, and δn ($=\delta p$) is the excess electron density over the dark value n_0. This definition for τ embodies both steps of the recombination process. The lifetimes for these two steps are τ_n for free electrons and τ_p for free holes. In general, τ, τ_n, and τ_p may be concentration dependent. However, in the limit of very strongly p-type material all the traps will be empty and τ_n becomes a constant: $\tau_n \rightarrow \tau_{n0} = [B_e N_t]^{-1}$, where $B_e = [\sigma_e v]$ is the "recombination coefficient" for electron capture, and v = thermal velocity. Similarly, in very strongly n-type material all the traps will be full and τ_p becomes a constant: $\tau_p \rightarrow \tau_{p0} = [B_h N_t]^{-1}$, where $B_h = [\sigma_h v]$.

It is shown in reference 4 that for δn small compared to $n_0 + p_0$, τ reduces to a low-level lifetime independent of concentration:

$$\tau_0 = \tau_{p0}\frac{n_0+n_1}{n_0+p_0} + \tau_{n0}\frac{p_0+p_1}{n_0+p_0}, \tag{2}$$

where

$$n_1 = N_c \exp[(E_t - E_c)/kT]$$

and

$$p_1 = N_v \exp[(E_v - E_t)/kT].$$

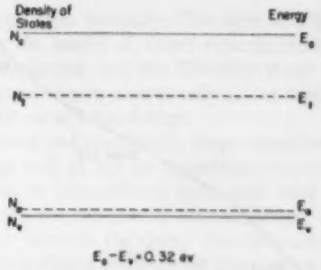

FIG. 2. Energy-level diagram used as a model for Te.

Thus n_1 and p_1 are functions of temperature only for any given trap level. It should be noted that the fact that τ_0 is independent of δn implies that the relation between δn and U (or the excitation rate density f) will be linear as expected at low levels.

For larger values of δn the lifetime becomes dependent on δn in a manner given by

$$\tau = \tau_0 \frac{1+a\delta n}{1+c\delta n}, \tag{3}$$

where

$$c = 1/(n_0+p_0),$$

and

$$a = \frac{\tau_{p0}+\tau_{n0}}{\tau_{p0}(n_0+n_1)+\tau_{n0}(p_0+p_1)}.$$

Note that at high carrier densities $\tau = \tau_0 a/c = \tau_{n0} + \tau_{p0} = \tau_\infty$. Since τ is a measure of the slope of photocurrent as a function of light intensity, Eq. (3) shows that a must be less than c if we are to be able to explain the data of Fig. 1 with this model. Using τ from Eq. (3) in the general relation $\delta n = \tau f$, we find the curve of Fig. 3 relating δn to f. Thus it appears that this model of trapping could account for the data on Te provided only the experimentally available intensities do not reach into the highest region of Fig. 3. We shall now examine the implications of this explanation in view of the known properties of Te.

C. Application to Tellurium

1. *Location of Trap Level*

One useful simplification of the problem results from the fact that at the temperatures of interest (100°K) Te is always strongly p-type, i.e., $p_0 \gg n_0$. Thus Eq. (2) becomes

$$\tau_0 = \tau_{p0}\frac{n_0+n_1}{p_0} + \tau_{n0}\frac{p_0+p_1}{p_0}. \tag{4}$$

Now since $\tau_0 > \tau_\infty = \tau_{n0} + \tau_{p0}$ for $a < c$, it is apparent that either $n_1 > p_0$ or $p_1 > p_0$ may satisfy the condition $a < c$. These cases are shown in Fig. 4. It may be seen that either (a) the trap level must be closer to the conduction band than the Fermi level (in the dark) is to

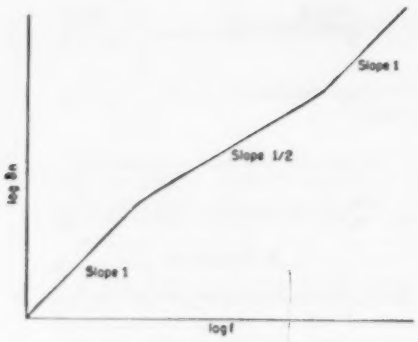

FIG. 3. Plot of δn vs f for $a<c$.

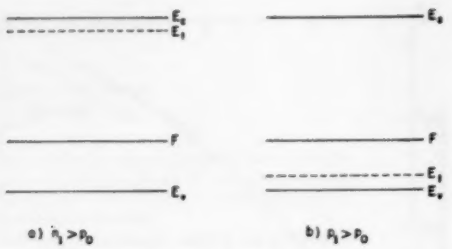

FIG. 4. The two cases satisfying the condition $a<c$.

the valence band; or (b) the trap level must be closer to the valence band than the Fermi level is. Only in these cases can a be less than c. It should be noted that these conclusions are valid regardless of the magnitudes of τ_{n0} or τ_{p0} (hence the capture cross sections).

It is possible, in fact, to obtain some quantitative information on this same basis. Looking again at Fig. 1 we see that the square-root dependence (slope $\frac{1}{2}$) extends over a factor of about 4 in δn. We may estimate the location of the transition point between the linear and square-root regions by extrapolating the two straight lines until they meet. This should correspond to the level at which $\delta n \sim c^{-1}$. Let us suppose that the curve of Fig. 1 is going to bend up to a slope of 1 again as in Fig. 3 just beyond the region of observation. (This transition occurs at $\delta n \sim a^{-1}$.) Then the separation of the two transition points must be at least a factor of 25 on the scale of δn. That is, $c \geq 25a$.

Now it is not difficult to show that this inequality leads to the condition that for case (a) the trap level may lie at most $\frac{1}{5}$ as far from the conduction band as the Fermi level does from the valence band; or for case (b) the trap level may lie at most $\frac{1}{5}$ as far from the valence band as does the Fermi level.

In Te under the conditions of these experiments, a reasonable location of the Fermi level is about $\frac{1}{3}$ of the distance (or about 0.1 ev) up from the bottom of the forbidden gap. Therefore the traps may lie *at most* in the upper or lower 10 percent of the gap, or within 0.03 ev of a band edge.

2. *Sensitivity*

In addition to the foregoing conclusions regarding the location of a trap level which could explain the behavior of Te on the basis of Shockley and Read's model, it is also possible to obtain some qualitative information on the sensitivity, i.e., on τ_0.

Equation (4) for τ_0 may now be further simplified, using the conditions (a) or (b) which must be fulfilled in our present discussion. Using the same arguments which allowed localization of the trap level, we find that τ_0 takes the form

$$\text{Case (a):}\quad \tau_0 = \tau_{p0}(n_1/p_0) + \tau_{n0} \simeq \tau_{p0}(n_1/p_0), \tag{5a}$$

or

$$\text{Case (b):}\quad \tau_0 = \tau_{p0}(n_0/p_0) + \tau_{n0}(p_1/p_0) \simeq \tau_{n0}(p_1/p_0). \tag{5b}$$

Now under the usual assumption (only partly justifiable) that the capture cross sections (hence τ_{n0} and τ_{p0}) are not strongly dependent on temperature,[6] then in the extrinsic region where p_0 is constant, τ_0 will depend on temperature only through n_1 or p_1 in Eqs. (5). It is clear, then, that either n_1 or p_1 will make τ_0 a function which increases exponentially with temperature. In germanium, where traps are well established as the dominant means of recombination, the lifetime is observed to increase exponentially with temperature in most cases.[7] In Te, however, the sensitivity decreases rapidly as the temperature is increased (roughly by a factor of 10^4 between 100°K and 300°K).

Examination of Eqs. (5) will show, as pointed out by Rose,[8] that a trap level close to a band edge leads to a longer lifetime than a distant one. This is because reemission of a trapped carrier is likely before the second step of the recombination process can occur.

D. General Comments

The conclusions reached in the preceding sections have the merit of being based on relatively few assumptions regarding the four quantities which characterize a trap level, τ_{n0}, τ_{p0}, N_t, and E_t. No restrictions at all were placed on E_t initially. The formalism presented requires of N_t only that it be small compared to any one of the four quantities, n_0, p_0, n_1, or p_1.[9] No assumption has been necessary concerning the magnitudes of τ_{n0} or τ_{p0}, although they were assumed to be only slowly varying functions of temperature.

It should be mentioned that there is good evidence that some traps have a negligible capture cross section for one kind of carrier so that both steps necessary for

[6] Some apparently rare circumstances under which this assumption may not be valid are referred to in the thesis.
[7] R. M. Baum and J. F. Battey, Phys. Rev. **98**, 923 (1955).
[8] A. Rose, *Photoconductivity Conference* (John Wiley and Sons, Inc., New York, to be published).
[9] This is proved in Appendix A of reference 4.

recombination cannot occur. This leads to photoconductive effects with long time constants due to reemission from such traps long after the light is shut off. In Te, however, such effects have never been reported. In fact, using pulsed light techniques we have measured the decay time constant of photocurrent in Te at 100°K and found it to be about 20 μsec, in reasonable agreement with the value obtained from steady-state measurements.

It is our next object to use the concepts of recombination through traps just presented, together with the accepted ideas of direct recombination, in an effort to draw conclusions on the type of recombination dominant in Te.

III. CONCLUSIONS ON RECOMBINATION PROCESSES

A. Contributing Factors

It should be stated at the outset that the complexity of the problem of determining the nature of recombination processes is such that even in germanium and silicon which have been so intensively studied, all that can be said with assurance at present is that trapping effects seem to dominate over direct recombination, although both are observed. In nearly all insulators, also, traps seem to be dominant. The nature of the transitions involved is still uncertain and indeed the nature of the traps themselves only slowly coming to light.[10]

Of the important characteristics of these two types of recombination, some general statements may be made. In the first place, direct recombination should be a property of the material involved, whereas trapping effects will be associated with imperfections of a crystal giving rise to "structure sensitivity" of τ such as is found in Ge. In Te there seems no evidence of such structure sensitivity in τ.

A second pertinent factor is the temperature dependence of the sensitivity. As was set forth above, conclusions regarding this dependence require the assumption that capture cross sections are relatively insensitive to temperature.

Unmentioned heretofore is the effect of surfaces on recombination. It is known that the nature of the surface of a germanium crystal can materially alter the effective lifetime.[11] We have therefore made several attempts to observe such effects by using samples with very different surface treatment (see Sec. IV). The negative results of these experiments are taken to be evidence that surface effects are not significant in Te.[12]

Of importance also is the relation between photocurrent and light intensity. The data of Fig. 1 agrees well with the model of direct recombination. It may also be explained by the Shockley-Read theory of traps, but as shown above, only if the trap level lies within 0.03 ev of a band edge.

As pointed out previously, traps sometimes re-emit carriers as well as act as recombination centers, thus giving rise to photoeffects with long time constants even though the free carrier lifetime is very short. The agreement between the decay time constant and lifetime in Te is strong evidence for the absence of at least this kind of trap.

Finally, it has been pointed out by Rose[8] that if the electron and hole lifetimes differ, the steady-state photocurrent will be a measure of the longer of the two lifetimes, whereas the PEM effect (which depends on the diffusion of free *pairs*) measures the shorter of the two. The agreement of the value obtained here with that found by Aigrain[9] in his unpublished measurements of the PEM effect in Te indicates, therefore, that the electron and hole lifetimes are equal.

B. Conclusions

It is apparent that nearly all the available evidence points to direct recombination as the dominant process in Te. This conclusion is very unusual in view of the widespread evidence of traps as the principal agent of recombination in other materials. It is therefore appropriate to seek some reason for this behavior.

The proposed explanation requires some further consideration of traps. It will be argued that trapping states may be present in Te, but their effectiveness as recombination centers is low. Thus, recalling the analogy of a trap level as a pair of resistors in series, we find that the impedance of the pair becomes high. Then the "current flow" (i.e., the recombining carriers) is diverted to the single resistor of direct recombination.

The argument for the ineffectiveness of traps rests on considerations advanced previously showing that any trap level lying near a band edge leads to a long lifetime, that is, less recombination through it. If we consider the regions within 0.03 ev of a band edge in which traps must lie to allow the explanation of Part 1 of Sec. II C, then thermal exchange with the nearby band determines the behavior of the traps at all temperatures of interest here.

It is now proposed that just because of the small energy gap in Te (0.32 ev) any trap level must lie close enough to a band edge to substantially reduce its effectiveness in recombination. Furthermore, the narrow gap aids the direct recombination process because the energy difference between the initial and final states of the transition is small.

Obviously, any such explanation based merely on the size of the energy gap must also be applicable to other materials. It is therefore suggested that on the basis of these considerations we may state a rule that small

[10] J. A. Hornbeck and J. R. Haynes, Phys. Rev. **97**, 311 (1955).
[11] W. Shockley, *Electrons and Holes in Semiconductors* (D. van Nostrand and Company, New York, 1950).
[12] The same conclusions were reached by Hornbeck and Haynes for the silicon samples studied in reference 10. For recent theory relating surface effects to the PEM effect see W. van Roosbroeck, Phys. Rev. **98**, 1533(A) (1955).

energy gap materials in which the bulk properties are dominant should in general have long carrier lifetimes and frequently exhibit direct recombination.

It is not difficult to find some confirmation for these ideas in the literature. In the first place, nearly all states observed as traps in Ge and Si lie at least 0.15 ev (or about $\frac{1}{3}$ the entire gap width of Te) from a band edge.[13] Thus while trap levels may exist closer to the band edges, they do not seem to play a significant role in the recombination.

Furthermore, carrier lifetimes in insulators are as a rule shorter than in semiconductors, often by many orders of magnitude. The longest lifetimes reported (several milliseconds) are in crystals of very pure germanium which has an energy gap of about 0.7 ev. Until recently this was the smallest energy gap of the commonly studied materials. In the last few years a good many new semiconductors of smaller energy gap have been discovered. Nearly all of these are found to be sensitive photoconductors, although much remains to be learned of their properties.

A further consequence of these considerations appears to offer a simple criterion for the selection of materials in device applications. We have seen that "narrowing the energy gap" will lengthen the lifetime due to traps until direct recombination becomes more probable. Further narrowing of the gap, though, will then lead to shorter lifetimes because of the greater ease of the direct recombination. Thus there may be some optimum energy gap (probably near 0.5 ev) that will give the longest lifetime for most types of trap levels. From this it would seem that the effort to produce materials with long lifetimes should be directed toward elimination of trapping states in wide gap materials rather than searching for new small gap materials. On the basis of present knowledge the energy gap of germanium seems to be close to (although somewhat greater than) the realizable optimum for long lifetimes. This probably contributes to its superiority over other known materials for the purposes of most semiconducting devices. On the other hand, for fast response times, small-energy-gap materials should be better than wide gap materials of the same lifetime (although the former usually must be cooled). This is because the possible long-time-constant effects of traps cannot occur in them.

C. Mechanisms of Recombination

The foregoing discussion has been confined to the question of whether recombination in Te occurs principally through traps or direct interband transitions. The actual nature of the transition process is as yet unknown, as is the case in all materials. There are several types of possible mechanisms for a recombination process which might apply to either direct or two-stage processes (although with differing likelihood).

The most obvious process is a simple transition from conduction band to valence band (or trap level) with emission of a photon of the proper energy. In direct recombination this is just the inverse process of the initial optical excitation. That such a process occurs in germanium has been concluded from the observation of emitted light having a peak intensity at a wavelength close to that corresponding to the fundamental absorption edge.[14] Estimates of the magnitude of this effect, however, indicate that it must be a minor one in the over-all recombination. A theoretical analysis of this type of process has been made by van Roosbroeck and Shockley using the known optical properties of germanium and applying the principle of detailed balance.[15] This treatment predicts a lifetime of the order of one second at 300°K if this radiative recombination were the only process. Since this is a factor of 100 greater than the longest observed lifetimes, it is concluded that this process accounts for at most 1 percent of the total recombination in Ge. Because of the difficulties in obtaining any quantitative experimental data from the recombination radiation, all that may be said is that in Ge this process may well represent much less than this 1 percent upper bound.

There is insufficient information available on the optical properties of Te to permit this same calculation to be made rigorously. It is possible, however, to approximate this method using in place of the full spectrum of these optical constants, a cross section for radiative recombination calculated from the equation given by Rose[8]

$$\sigma = 4.5\times10^{-22}K_e\left(\frac{\nu}{\nu_0}\right)^2\frac{kT}{h\nu}\left(\frac{300}{T}\right)^2 \text{ cm}^2,$$

where $h\nu_0 = 1$ electron volt, $h\nu =$ width of forbidden gap, $T =$ absolute temperature, and $K_e =$ absorption constant for photon energy $= h\nu$.[16] This procedure leads to lifetimes of about $\frac{1}{3}$ millisecond at 300°K, and about $\frac{1}{10}$ second at 100°K in p-type Te having about 3×10^{15} acceptors per cm^3 (the approximate sample purities). Although the agreement of these values with observed lifetimes is not good, they might be regarded as possible upper bounds on obtainable lifetimes. The temperature dependence of τ seems in qualitative agreement with observed values, in contrast to the data on Ge.

The van Roosbroeck and Shockley calculation has been carried out recently for some other materials.[17] It has been found, as expected, that the smaller the energy gap, the more likely is the process to occur. The values obtained at 300°K were $\tau\sim$several milliseconds for PbS ($E_G\sim0.4$ ev) and $\tau\sim$a microsecond for InSb ($E_G\sim0.2$ ev) for intrinsic materials. It may be

[13] See, for example, E. Burstein *et al.*, *Photoconductivity Conference* (John Wiley and Sons, Inc., New York, to be published), and W. C. Dunlap, Phys. Rev. **97**, 614 (1955).

[14] J. R. Haynes and H. B. Briggs, Phys. Rev. **86**, 647(A) (1952); R. Newman, Phys. Rev. **91**, 1313 (1953).

[15] W. van Roosbroeck and W. Shockley, Phys. Rev. **94**, 1558 (1954).

[16] The value for this was inferred from data presented by J. J. Loferski, Phys. Rev. **93**, 707 (1954).

[17] G. G. Macfarlane (private communication).

seen that both the energy gap and the lifetime calculated for Te lie between the values in these two materials.

Because of the success in observing recombination radiation in germanium, several attempts were made to detect it in Te. Although the results were all negative, an estimate of the over-all sensitivity of the equipment indicated that experimental limitations might have been responsible.

Of other possible recombination processes (phonon emission, Auger effect), too little is known to allow further conclusions in Te. Thus it may be said, in summary, there is good evidence that recombination in Te is direct although we are not yet in a position to specify the exact mechanism involved.

IV. EXPERIMENTAL CONSIDERATIONS

A. General

The experiments described here were mostly photoconductivity measurements of conventional types. Some of the general features of these experiments will now be mentioned and the more specific considerations of each type presented in the subsequent sections.

In all the photoconductivity experiments, the samples used were single crystals of Te grown in glass tubes. This method produces crystals having rough, pitted surfaces adjacent to the glass, but fairly good uniformity in the bulk. The material used was chemically pure Te (from the Anaconda Copper Company) which was distilled several times. Hall effect measurements on the samples indicated generally that the impurity content was below 10^{16} per cm^3.

Contacts were made to the crystals by letting a hot platinum wire melt its way into the bulk. In the absence of any known method of soldering to Te,[18] this technique has been used successfully also in Hall and resistivity experiments. In order to insure against the complicating effects of rectifying contacts, several current-voltage curves of such samples were taken. In all cases, these were linear and the contacts were presumed to be ohmic. Nevertheless, opaque masks were used to cover the contact areas of all samples to prevent possible photovoltaic effects.

Various treatments were used on the crystal surfaces as mentioned in III A. The various types of surfaces used are: (1) untreated face of a cylindrical crystal having a rough, pitted surface; (2) flat surface ground with No. 600 carborundum; (3) same surface as (2) but etched with about 50 percent HNO_3; (4) untreated cleavage face of a large crystal. The variations in photosensitivity in these cases were no larger than the variations observed from one sample to another having the same type of surface (i.e., a factor of about 2–3). Thus the surface is not considered significant for our purposes.

[18] Ultrasonic soldering, just tried by H. Roth, seems to succeed in wetting Te with ordinary solder.

It has been known for some time that the photosensitivity of Te increases greatly upon cooling.[3,15] For this reason most measurements are made at liquid air temperatures.

B. Steady-State Photoconducitvity

The wavelength, temperature, and intensity dependence of the photoresponse were investigated by use of steady-state photocurrents. The detector used was an indicating amplifier (Electromechanical Research Model 33B) with a noise level about 0.003 μv. (Noise in the sample, however, was often as high as 0.01 μv.) The source of radiation was light emitted from a Beckman IR-2S infrared monochromator using a Nernst glower heated by a current of about $\frac{3}{4}$ amp. The radiation was mechanically "chopped" before entering the monochromator at 10 cps so as to make use of the high sensitivity of the EMR 10-cycle amplifier which has only about a 1-cycle band width.

Intensity variation was achieved by means of a series of optical stops to vary the aperture of the mirror which focusses the glower light onto the monochromator. These permitted intensity variations of a factor of 50 with good reproducibility. Then the effect of varying the slit width could be calibrated by use of the stops. It was found that using two slit settings, each with the full set of stops, a total intensity range of about 5000 was realizable. The calibration of intensity was performed by a Perkin-Elmer radiation thermocouple having a sensitivity of the order of 1 microvolt per microwatt.

C. Transient Photoconductivity

Light from a simple spark gap was used for observation of photocurrent decay. The spark produced at the gap ($\sim\frac{1}{4}$ in. adjustable) had about a 3-μsec decay time constant and was observed to die out completely within 10 μsec. This was true of the light as detected by a 922 phototube and of the rf noise radiated as detected directly on an oscilloscope.

A 40-ohm load in series with the sample was an approximate match to the sample resistance at 100°K. With a gain of 1000 from a pre-amplifier and 0.1 v/cm sensitivity of the oscilloscope, a 500-μv peak signal could be observed after the first 10 μsec of rf noise. The entire decay took $\sim$60 μsec. While the shape of the decay curve could not be analyzed to see if it was truly exponential because of the noise present, it was estimated that an effective time constant of about 20 ± 5 μsec was being observed.

D. Recombination Radiation

If radiation is emitted in a direct recombination process it should peak at the wavelength corresponding to the energy gap. It was therefore decided to use a sample as the source of light for the monochromator

mentioned in IV B and study the spectrum of light output when carriers were excited in the sample. Excitation was produced by illuminating the sample with light from which the wavelengths of interest had been removed by a Pyrex glass filter. This should allow even small amounts of light in the proper range to be observed.

Evaporated films of Te were used in this experiment since they can absorb the high-energy photons (for which $K \sim 10^5$–10^6 cm^{-1}) to produce the excitation, but still transmit the possible light from recombination (for which $K \sim 10^2$ cm^{-1}).

An estimate of the maximum signal that may be expected under the attainable experimental conditions has been made. Assuming that all of the recombination occurs by emission of photons of energy equal to E_g, we should expect about 10^{-9} watt of radiation to strike the detector. With the nominal sensitivity of the detector of 1 μv per μw, this would produce a signal of 10^{-3} μv, about a factor of three below the noise level of the 10-cycle amplifier. Thus, even this rather optimistic estimate of the expected signal is below observable values. On the other hand, it may be hoped that improved experimental techniques can increase the sensitivity by an appreciable amount.

ACKNOWLEDGMENTS

The writer is indebted to Professor P. H. Miller, Jr. for suggesting this work, and for his guidance throughout its course. Several stimulating discussions with Professor B. R. Russell were also very helpful. Thanks are due also to G. D. Long who grew the crystals used in these experiments and made the Hall measurements for determination of their impurity content.

To the Socony Vacuum Oil Company the writer wishes to express his thanks for the generous fellowship which helped support this work. Several parts of this work were also supported by the Office of Naval Research and the U. S. Air Force.

PHYSICAL REVIEW VOLUME 100, NUMBER 4 NOVEMBER 15, 1955

Influence of Crystalline Electric Fields on Antiferromagnetic Transitions

L. D. Roberts, R. B. Murray, and J. W. T. Dabbs
Oak Ridge National Laboratory, Oak Ridge, Tennessee
(Received July 14, 1955)

The Van Vleck two-sublattice treatment of antiferromagnetism predicts theoretically an equality between the transition temperature T_c and the Weiss constant Δ, a prediction which is not usually borne out by experiment. In this paper, through the use of the effective spin Hamiltonian, the treatment of Van Vleck is extended to include a crystalline electric field term. It is shown that Δ and T_c depend on this in an important way, especially at low temperatures, and it is further shown that this term may contribute to the observed inequality of Δ and T_c.

INTRODUCTION

A SIMPLE theoretical treatment of antiferromagnetism, the phenomenon in which equal ionic magnetic moments assume an antiparallel order in a lattice, has been developed by Néel,[1] Bitter,[2] and Van Vleck.[3] In the work of Van Vleck, in particular, the lattice of magnetic ions was assumed to be divisible into two interpenetrating sublattices, each having the properties that (a) an ion on one sublattice would have as nearest neighbors members from the other sublattice only, (b) the ionic moments of the two sublattices would be equal and oppositely oriented, (c) only nearest neighbor interactions would be of importance, and (d) that this interaction could be treated as an effective, or molecular field.

This theory has been further extended by several authors[4–6] to include the effects of next nearest neighbors and more complex lattice structures. These theoretical ideas are quite successful in a qualitative way. For example, Van Vleck[3] showed that, above the antiferromagnetic transition temperature, or Néel point, T_c, the magnetic susceptibility χ^0 should follow a Curie-Weiss law

$$\chi^0 = C/(T+\Delta), \tag{1}$$

where C is the free-ion Curie constant, T is the absolute temperature, and Δ is the Weiss constant. In the simple two-sublattice model, it turns out that $\Delta/T_c = 1$. Experimentally, this ratio is usually found to be different from unity. Values of Δ/T_c different from unity have been obtained theoretically through the use of next nearest neighbor interactions and more complex sublattice structures.[4–6] In the following, we show that crystalline electric field effects may also give $\Delta/T_c \neq 1$.

[1] L. Néel, Ann. phys. **5**, 232 (1936).
[2] F. Bitter, Phys. Rev. **54**, 79 (1937).
[3] J. H. Van Vleck, J. Chem. Phys. **9**, 85 (1941).
[4] L. Néel, Ann. phys. **3**, 137 (1948).
[5] P. W. Anderson, Phys. Rev. **79**, 705 (1950).
[6] J. S. Smart, Phys. Rev. **86**, 968 (1952).

In the above treatments the effect of crystalline electric fields on the transition temperature T_c has not been explicitly included. It has been shown[7,8] that the spin Hamiltonian $\mathcal{H}$ of a number of magnetic ions (for example Mn^{++}, Gd^{+++}, Cr^{+++}, and V^{++}, in a variety of paramagnetic salts) includes a term of the form DS_i^2 arising from the crystalline Stark effect; and in these substances this term is often found to be the leading one in zero magnetic field. Here D is a constant and S_i is the ith of the three components of the effective electron spin operator. In the work presented here, we include this term in the molecular field model of antiferromagnetism, and calculate its effects on the transition temperature, and on the ratio Δ/T_c. As D is usually small, of the order 0.03 cm^{-1}, the effects discussed will be of importance only in the vicinity of 1°K and below. Calculations are presented only for the two-sublattice model of the molecular field theory with isotropic g factors and exchange, but the treatment may be extended to include anisotropy, more complex structures, and, of course, more complex electric field interactions.

We assume that, in the absence of an external field, the effective spin Hamiltonian $\mathcal{H}_i$ for either sublattice may be written[3]

$$\mathcal{H}_i = DS_i^2 - 2Kz\bar{S}_i' S_i, \tag{2}$$

where the sublattice magnetizations are along the ith direction, and where the primed spin operator refers to one of the sublattices and the unprimed operator refers to the other. K is the exchange integral (negative for antiferromagnetism); and z is the number of nearest neighbors. In the Hamiltonian, exchange terms of the form $2Kz\bar{S}_j' S_j$ with $j \neq i$ have been omitted, as for spin orientation along the ith direction $\bar{S}_j' = 0$ in the molecular field approximation. The subscript i may assume any value from 1 to 3; i.e., the direction of antiferromagnetic alignment may be either parallel or perpendicular to the 3 direction, the crystalline electric field symmetry axis. $\bar{S}_i'$ is the average value of the spin operator S_i' and may be defined through the density matrix as

$$\bar{S}_i' = \mathrm{Tr}[S_i' \exp(-\mathcal{H}_i/kT)]/\mathrm{Tr}[\exp(-\mathcal{H}_i/kT)], \tag{3}$$

where k is the Boltzmann constant. Further, we note that for the oppositely oriented sublattices,

$$\bar{S}_i' = -\bar{S}_i. \tag{4}$$

It is convenient to define the effective field H_e by

$$g\beta H_e = -2|K|z\bar{S}_i'. \tag{5}$$

Also we observe that the average magnetization per ion M_i along the ith direction is given by

$$M_i = g\beta\bar{S}_i, \tag{6}$$

where β is the Bohr magneton and g is the effective spectroscopic splitting factor.

In the assumption of the Hamiltonian, Eq. (2), and of the relations, Eqs. (4), (5), and (6), it is implicit that the effective field acting on one of the sublattices is proportional to the magnetization of the other. It follows then, for either sublattice, that the magnetization along the ith direction at the transition temperature T_c is given by

$$M_i = \sigma_i(T_c)H_e, \tag{7}$$

where $\sigma_i(T_c)$ is the susceptibility along the ith direction of the given sublattice at T_c. $\sigma_i(T_c)$ may be obtained through Eqs. (3), (6), and (7).

CALCULATION OF T_c FOR THE CASE WHERE $\langle m|DS_i^2|m\rangle \ll kT_c$

At or above T_c, the effective field H_e as defined above in the molecular field approximation is zero. Then if the electric field term is also small relative to kT_c, we may expand the density matrix in powers of $1/T$. Using the Hamiltonian [Eq. (2)], we then obtain the susceptibilities $\sigma_i(T_c)$ as

$$\sigma_3(T_c) = \frac{g^2\beta^2 S(S+1)}{3k[T_c + D(2S-1)(2S+3)/15k]}, \tag{8a}$$

$$\sigma_{1,2}(T_c) = \frac{g^2\beta^2 S(S+1)}{3k[T_c - D(2S-1)(2S+3)/30k]}, \tag{8b}$$

where σ_3 is the susceptibility per ion along the 3 direction and $\sigma_{1,2}$ is this quantity in the plane perpendicular to the 3 direction. Substituting (8a) and (8b) in Eqs. (5), (6), and (7), we obtain the transition temperatures

$$T_{c,3} = (2|K|zS(S+1)/3k) - D(2S-1)(2S+3)/15k, \tag{9a}$$

$$T_{c,1,2} = (2|K|zS(S+1)/3k) + D(2S-1)(2S+3)/30k. \tag{9b}$$

Thus, if the preferred direction of antiferromagnetic spin orientation is along the electric field symmetry axis, the transition temperature will be $T_{c,3}$; if the spin orientation is perpendicular to this axis, the transition will be at $T_{c,1,2}$. When $D=0$, these temperatures reduce to the transition temperature given by Van Vleck, $T_c = 2|K|zS(S+1)/3k$.

From Eqs. (9a) and (9b) we note that for D positive, $T_{c,1,2}$ will be greater than $T_{c,3}$ with $|K|$ isotropic. Remembering that in transitions from the paramagnetic state, the higher transition temperature will correspond to the lower free energy, the transition will be to an antiferromagnetic state with the spin system oriented perpendicular to the 3 direction. Similarly, with D negative, the spin orientation will be parallel to the electric field symmetry axis.

[7] M. H. L. Pryce, Phys. Rev. **80**, 1107 (1950).
[8] B. Bleaney and K. W. H. Stevens, Repts. Progr. Phys. **16**, 108 (1953).

CALCULATION OF Δ/T_c FOR THE CASE $\langle m|DS_i^2|m\rangle \ll kT_c$

The susceptibilities $\sigma_i(T_c)$ calculated above were for an individual sublattice only. We now wish to obtain the susceptibility χ_i^D for the sample as a whole in the presence of the D term, for $T \geq T_c$. To obtain this we rewrite the Hamiltonian, Eq. 2, to include an external magnetic field H_i along i. In the paramagnetic region,

$$\bar{S}_i' = +\bar{S}_i, \text{ and } \mathcal{H}_i^H = DS_z^2 - g\beta H_e S_i - 2Kz\bar{S}_i' S_i. \quad (10)$$

Including this D term in the Hamiltonian, but following Van Vleck[3] otherwise in all particulars, we obtain

$$\begin{aligned} \chi_z^D &= g^2\beta^2 S(S+1)/ \\ &\quad 3k[T+T_e+D(2S-1)(2S+3)/15k], \\ \chi_{1,2}^D &= g^2\beta^2 S(S+1)/ \\ &\quad 3k[T+T_e-D(2S-1)(2S+3)/30k]. \end{aligned} \quad (11)$$

A similar result has been obtained by Yosida[9] for the special case of spin 5/2.

Thus, the effect of the electric field splitting is to modify T_c and Δ by increments of opposite sign giving a ratio $\Delta/T_c \neq 1$ even for the two sublattice model. With $\lambda \equiv D/kT_e$, we have

$$\left(\frac{\Delta}{T_c}\right)_z = \frac{1+\lambda(2S-1)(2S+3)/15}{1-\lambda(2S-1)(2S+3)/15}, \quad (12a)$$

$$\left(\frac{\Delta}{T_c}\right)_{1,2} = \frac{1-\lambda(2S-1)(2S+3)/30}{1+\lambda(2S-1)(2S+3)/30}. \quad (12b)$$

This ratio Δ/T_c will also be different from unity for a powder sample. For, although the electric field contribution to Δ will average to zero so that $\Delta = T_e$, the effect on T_c will remain as given by Eqs. (9).

To obtain an idea of the possible deviation of Δ/T_c from unity, we assume a T_e of 1°K, $S=5/2$, and $D = -0.03$ cm^{-1}. Then from Eq. (12a), $\Delta/T_c = 0.84$ so the effect is quite appreciable here even though D is small.

CALCULATION OF T_c FOR $\langle m|DS_i^2|m\rangle \sim kT_c$

We note that since H_e is zero at and above T_c, we may write the sublattice susceptibilities at T_c as

$$\sigma_i(T_c) = \left(\frac{\partial M_i}{\partial H_e}\right)_{H_e=0} = kT_c\left[\frac{\partial^2}{\partial H_e^2}\ln Z_i(T_c)\right]_{H_e=0}, \quad (13)$$

where Z_i is the partition function,

$$Z_i = \mathrm{Tr}\exp(-\mathcal{H}_i/kT). \quad (14)$$

Our approach, in this case, is to calculate the partition function using the Hamiltonian of Eq. (2) and with this to form a transcendental equation for T_c through relations (7) and (13). Since the electric field term is here comparable to kT_c, an expansion in terms of $1/T$ as carried out in the previous case is no longer feasible. In addition, for $i \neq 3$, the operators in the Hamiltonian do not commute. A convenient method for dealing with problems of this type has been given by Simon, Rose, and Jauch.[10] Their procedure, which is based on the "interaction representation,"[11] will be used here and is outlined below. Within the molecular field approximation this calculational procedure gives an exact result for T_c.

We wish to expand the operator $\rho = \exp[-\mathcal{H}/kT]$, where $\mathcal{H} = \mathcal{H}_K + \mathcal{H}_j$, in powers of $\mathcal{H}_j/kT$. In general, $\mathcal{H}_K$ and $\mathcal{H}_j$ do not commute. Let $\tau = -1/kT$. Now, if the operator φ obeys

$$\mathcal{H}\varphi = \partial\varphi/\partial\tau, \quad (15)$$

a particular solution is

$$\varphi = \exp(\mathcal{H}\tau) = \rho. \quad (16)$$

We transform to the "interaction representation" by defining a new operator ψ as

$$\psi = [\exp(-\mathcal{H}_K\tau)]\varphi; \quad (17)$$

then it follows that

$$\partial\psi/\partial\tau = \mathcal{H}_j'(\tau)\psi, \quad (18)$$

where

$$\mathcal{H}_j'(\tau) = [\exp(-\mathcal{H}_K\tau)]\mathcal{H}_j[\exp(\mathcal{H}_K\tau)], \quad (19)$$

with

$$\psi(0) = \varphi(0) = 1 \quad \text{and} \quad \varphi = [\exp(\mathcal{H}_K\tau)]\psi.$$

Equation (18) can be solved by an iteration technique in powers of $\mathcal{H}_j(\tau)$ as

$$\psi = \sum_{n=0}^{\infty} T_n(\tau), \quad (20)$$

where

$$T_n(\tau) = \int_0^{\tau} d\tau_1 \int_0^{\tau_1} d\tau_2 \cdots \int_0^{\tau_{n-1}} d\tau_n \mathcal{H}_j'(\tau_1) \times \cdots \mathcal{H}_j'(\tau_n) T_0(\tau_n), \quad (21)$$

and $T_0 = 1$. We may then obtain the partition function as

$$Z = \mathrm{Tr}\{[\exp(\mathcal{H}_K\tau)]\sum_{n=0}^{\infty} T_n(\tau)\}. \quad (22)$$

For our purposes we make the following associations:

$$\mathcal{H}_K = DS_z^2, \quad \mathcal{H}_j = g\beta H_e S_j, \quad (23)$$

where H_e is the effective field along the jth direction.

Further, it is convenient to define the following reduced parameters: $\theta = kT/D$, $h = g\beta H_e/D$, and $t_c = T_c/T_e$. Then from Eqs. (5), (6), (7), and (13), we find

$$t_{ci} = \frac{3\theta_c^2}{S(S+1)}\left[\frac{1}{Z}\left(\frac{\partial^2 Z}{\partial h_i^2}\right)\right]_{h_i=0} \quad (24)$$

[9] K. Yosida, Prog. Theoret. Phys. (Japan) **6**, 691 (1951).

[10] Simon, Rose, and Jauch, Phys. Rev. **84**, 1155 (1951).

[11] J. S. Schwinger, Phys. Rev. **74**, 1448 (1948).

for the reduced critical temperature for orientation along the ith direction.

For the case $\mathcal{H}=DS_3^2+g\beta H_3 S_3$, we obtain the partition function Z_3 corresponding to cooperative ordering along the 3 direction as[12]

$$Z_3=\sum_{m=-S}^{S}[\exp(-m^2/\theta)]\left(1+\frac{1}{2}\frac{m^2h_3^2}{\theta^2}\right), \quad (25)$$

where m is the magnetic quantum number. For t_{c3}, the reduced transition temperature for magnetic order along the 3 direction, this gives

$$t_{c3}=\frac{3}{S(S+1)}\sum_{m=-S}^{S}m^2\exp(-\lambda m^2/t_{c3})/\sum_{m=-S}^{S}\exp(-\lambda m^2/t_{c3}). \quad (26)$$

For magnetic order perpendicular to the 3 direction, the partition function $Z_{1,2}$ for half-integral spins, is[12]

$$Z_{1,2}=\tfrac{1}{2}(h_1^2+h_2^2)\left\{(S(S+1)+\tfrac{1}{4})\left(\frac{e^{-1/4\theta}}{2\theta^2}\right)+\sum_{m=\frac{1}{2}}^{S}[S(S+1)-m(m+1)]\times\frac{\exp(-m^2/\theta)}{2m+1}\left[\frac{1}{\theta}+\frac{e^{-(2m+1)/\theta}-1}{2m+1}\right]\right\}+\sum_{m=-S}^{S}\exp(-m^2/\theta). \quad (27)$$

The transition temperature $t_{c1,2}$ may be found from the relation

$$\frac{\lambda^2S(S+1)}{3}=\frac{t_{c1,2}}{\sum_{m=-S}^{S}\exp(-\lambda m^2/t_{c1,2})}\left\{[S(S+1)+\tfrac{1}{4}]\frac{e^{-\lambda/4t_{c1,2}}}{2(t_{c1,2}/\lambda)^2}+\sum_{m=\frac{1}{2}}^{S}[S(S+1)-m(m+1)]\frac{\exp(-\lambda m^2/t_{c1,2})}{2m+1}\times\left[\frac{\lambda}{t_{c1,2}}+\frac{e^{-(2m+1)\lambda/t_{c1,2}}-1}{2m+1}\right]\right\}. \quad (28)$$

[12] L. D. Roberts and J. W. T. Dabbs, Phys. Rev. **95**, 307 (1954).

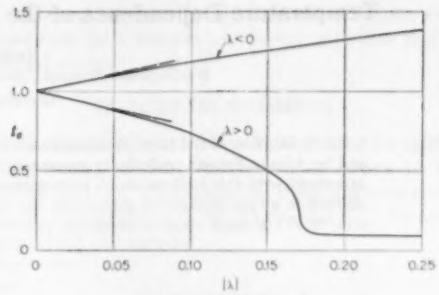

FIG. 1. Dependence of transition temperature on λ.

To learn something of the behavior of this function, Eq. (26) was solved numerically for t_c as a function of λ for spin 5/2. The result is shown in Fig. 1. For $\lambda<0$, i.e., for $D<0$, the transition temperature is found to rise smoothly with $|\lambda|$. This would be the state of lower free energy compared to that described by the lower curve for $\lambda>0$ for isotropic exchange. For a highly anisotropic exchange, the lower curve could be favored, however. Here a quite dramatic dependence of t_c on λ is found. The dotted curves give the behavior for λ near zero as predicted by Eq. (9a).

In the present case, at temperatures immediately above the transition point the susceptibility cannot be described by the Curie-Weiss law. We note, however, that for kT large compared to both the exchange energy and electric field splitting the Curie-Weiss law will apply with the susceptibilities given in Eqs. (11). Comparing the Weiss constants in Eqs. (11) with T_c given by Eqs. (26) or (28) we note that Δ/T_c may deviate markedly from unity; e.g., with $\lambda=-0.25$, $\Delta/T_c\approx\frac{1}{2}$.

The physical mechanism involved in these calculations may be visualized readily. For simplicity we discuss the case where the cooperative orientation of the spins is along the 3 direction and for definiteness we take $S=5/2$. The crystalline electric field term then splits the spin multiplet into three doublets. If D is negative the lowest of these will be the $\pm5/2$ pair. Then, approaching T_{c3} from the high-temperature side, as T falls, the $\pm5/2$ levels will be preferentially populated. Here the susceptibility of a sublattice will be larger at a given T than if $D=0$, and correspondingly the requirements for cooperative ordering expressed through Eq. (7) will be satisfied at a higher temperature than T_c. Similarly, with D positive, the $\pm\frac{1}{2}$ level will be lowest, the susceptibility will be smaller and T_{c3} will be less than with $D=0$.

Temperature Dependence of the Elastoresistance in *n*-Type Germanium

ROBERT W. KEYES
Westinghouse Research Laboratories, East Pittsburgh, Pennsylvania
(Received July 21, 1955)

An explanation of the large elastoresistance effects discovered by Smith has been proposed by Herring and by Adams. Smith's preliminary measurements of the temperature dependence of the effect are not in agreement with this explanation. A more extensive study of the temperature dependence of the elastoresistance in *n*-type germanium shows that the magnitude of the effect is proportional within experimental error to T^{-1}, a result which is consistent with the theory.

I. INTRODUCTION

A LARGE elastoresistance effect in the semiconductors germanium and silicon has been discovered by Smith.[1] The experiments of Smith were performed primarily at room temperature, but the results of preliminary measurements over a limited temperature interval of the temperature dependence of the effect were included. These results were presented by giving the exponent b in the equation $\pi = AT^{-b}$ for a piezoresistance coefficient. The value of b given for *n*-type germanium was 0.8.

The theory of the principal elastoresistance effect in multivalley semiconductors has been given by Herring[2] and by Adams.[3] The effect is due to the fact that the equivalence of the symmetry axes in $\mathbf{k}$ space on which the energy minima are located can be destroyed by elastic strain, allowing the energies of the valleys to shift with respect to one another. This shifting of the valley energies has two results.

(1) The number of electrons in the lower energy valleys is increased at the expense of the number in the higher energy valleys. Because the conductivity of a single valley is very anisotropic, this introduces anisotropy into the total conductivity. The number of electrons transferred is controlled by the Boltzmann factor; therefore, the fractional change in conductivity is proportional to T^{-1}.

(2) The density of final states for the scattering of an electron from one valley to another is changed, since this density is proportional to the square root of the energy of the final state above the minimum energy of the valley. This part of the effect is negligible at sufficiently low temperatures, it is proportional to T^{-1} at temperatures such that $kT \gg \hbar\omega$, the energy of the phonon responsible for intervalley scattering, and in the intermediate temperature region it has an average temperature dependence stronger than T^{-1}.

Because it is difficult to conceive of alternative mechanisms which would lead to dimensionless elastoresistance coefficients of the order of 100, and because the preliminary result of Smith seems inconsistent with the above explanation, a further investigation of the temperature dependence of the effect has been undertaken and is reported herein.

II. EXPERIMENT

The measurements were made using Smith's "arrangement *C*" in which the crystal is strained in tension along a [110] direction, and the change in the resistance along this same [110] direction is observed. This is the arrangement which is sensitive to the largest elastoresistance coefficient. In other matters of technique the methods used closely followed those of Smith, the principal exception being that the crystallographic orientations were only accurate to about 2°. Between 77°K and 300°K, a specimen with a room temperature resistivity of 10 ohm-cm was used. The effects of intrinsic conductivity become important in this material above 300°K. The observations were extended to 380°K with a 0.3 ohm-cm specimen. In all cases the temperature was maintained by immersing the sample and associated apparatus in an appropriate liquid bath.

III. RESULTS

The results are given in Fig. 1. It is seen that the room temperature value of the piezoresistance coefficient is close to that given by Smith, and that this coefficient is proportional, within experimental error,

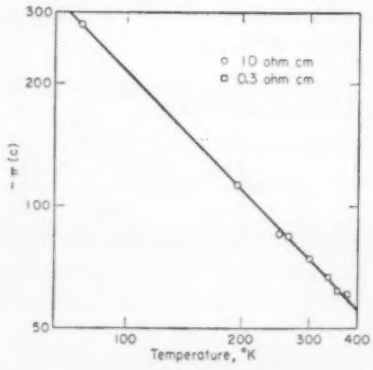

FIG. 1. A logarithmic plot of the piezoresistance coefficient for Smith's arrangement *C*, measured in 10^{-12} cm² dyne^{-1}, *versus* the absolute temperature. The slope of the line is -0.98.

[1] C. S. Smith, Phys. Rev. **94**, 42 (1954).
[2] C. Herring, Bell System Tech. J. **34**, 237 (1955).
[3] E. N. Adams, Chicago Midway Laboratories Technical Note No. CML-TN-P8 (unpublished).

to T^{-1}. Rough calculations show that, in a temperature interval in which the intervalley scattering causes the elastroresistance to have a temperature dependence much stronger than T^{-1}, the mobility should show marked deviations from a $T^{-\frac{1}{2}}$ variation. In the temperature interval considered, the mobility variation is not greatly different from $T^{-\frac{1}{2}}$.[4] Thus, even though the phonon energy $\hbar\omega$ is not known, the observed temperature variation of the elastoresistance is to be expected. We can conclude that the elastoresistance varies with temperature in a manner consistent with the theory described above.

[4] F. Morin, Phys. Rev. **93**, 62 (1953).

IV. ACKNOWLEDGMENTS

The author is indebted to Dr. E. N. Adams for calling the importance of the elastoresistance effects to his attention and for discussions of their interpretation, and to J. P. McKelvey, J. W. Faust, and A. J. Bennett for supplying the samples.

PHYSICAL REVIEW VOLUME 100, NUMBER 4 NOVEMBER 15, 1955

Electroluminescence of Zinc Sulfide Single Crystals

D. R. Frankl
Sylvania Electric Products, Inc., Physics Laboratory, Bayside, New York
(Received May 24, 1955)

Quantitative measurements of the electroluminescent emission from synthetic single crystals of zinc sulfide with silver paint contacts under 60-cycle half-wave voltage excitation have been carried out at several temperatures. Other workers have shown that the emission intensity has two major peaks per cycle, the first coincident with the voltage maximum and the second as the voltage is falling to zero. These peaks have the same color, and both appear to originate throughout the crystals, but they have different voltage dependencies. The second peak is the larger at low-voltage amplitudes, but the first peak grows the more rapidly with increasing voltage amplitude. Emission intensities of the order of 10^{12} photons per second, with energy efficiency of the order of 10^{-4}, were obtained. The total current consists of a displacement current which is linear with voltage and a conduction current which is roughly exponential with voltage. No evidence of space-charge polarization was detected. It is tentatively suggested that excitation occurs by impact of conduction electrons accelerated through internal barriers, that the two emission peaks result, respectively, from immediate recombination and from recombination delayed by trapping of the excited electron, and that the electric field tends to hold the electron in the trap state.

INTRODUCTION

ELECTROLUMINESCENCE may be defined as the emission of visible radiation by a solid at subincandescent temperatures when subjected to an electric field without previous excitation. The latter restriction distinguishes true electroluminescence from a variety of related phenomena which may occur when a field is applied to a phosphor during or after excitation by x-rays, ultraviolet light, etc.

Electroluminescence in silicon carbide was described by Lossew.[1] Other workers[2–10] more recently have studied the phenomenon in a variety of powder phosphors, the powder being suspended in a dielectric between condenser plates. Of the types of phosphors studied, those based on zinc sulfide have received by far the greatest emphasis and have been developed to commercially practical brightness levels.[7]

Electroluminescence of zinc sulfide single crystals has been reported by Piper and Williams[11] (denoted PW below) and by Watson, Dropkin, and Halpin[12] (denoted WDH below). They have shown the emission intensity under sinusoidal exciting voltage to contain two peaks per half cycle, the first in phase with the voltage peak and the second as the voltage is falling to zero. Both PW and WDH attribute the excitation of luminescence to impact on the luminescent centers of fast conduction electrons, the acceleration of these electrons taking place in a macroscopic barrier. PW believe the barrier to be at the cathode, while WDH believe it to lie within the crystal. As for the peaks in emission intensity, PW attribute the in-phase peak to electrons tunneling through the cathode barrier and the out-of-phase peak to electrons released from deep donor levels in the barrier, while WDH attribute these peaks respectively to immediate and delayed recombination with ionized centers, the delay being ascribed

[1] O. Lossew, Wireless World and Radio Review **271**, 93 (1924).
[2] G. Destriau, Phil. Mag. **38**, 700 (1947).
[3] Payne, Mager, and Jerome, Illum. Eng. **45**, 688 (1950).
[4] S. Roberts, J. Opt. Soc. Am. **42**, 850 (1952).
[5] C. W. Jerome and W. C. Gungle, J. Electrochem. Soc. **100**, 34 (1953).
[6] J. F. Waymouth, J. Electrochem. Soc. **100**, 81 (1953).
[7] Homer, Rulon, and Butler, J. Electrochem. Soc. **100**, 566 (1953).
[8] Zalm, Diemer, and Klasens, Philips Research Repts. **9**, 81 (1954).
[9] S. Nudelman and F. Matossi, J. Electrochem. Soc. **101**, 546 (1954).
[10] J. F. Waymouth and F. Bitter, Phys. Rev. **95**, 941 (1954).
[11] W. W. Piper and F. F. Williams, Phys. Rev. **81**, 151 (1952); Brit. J. Appl. Phys., Supplement No. 4, 39 (1955).
[12] Watson, Dropkin, and Halpin, Phys. Rev. **94**, 777(A) (1954); Enlarged Abstracts of the Electrochemical Society Spring Meeting, (1954).

to the removal of the electron from the vicinity of the center. However, our results disagree in several respects with both of these mechanisms, as will be discussed below.

EXPERIMENTAL METHODS

Crystals

The specimens used in this work were synthetic zinc sulfide single crystals grown by Kremheller of our laboratories by deposition from the vapor phase.[13] The crystals obtained to date have shown wide variations in morphology, impurity content, and luminescence characteristics. Rod-shaped crystals of uniform color and uniform blue fluorescence under 3650 A excitation with rapid decay were selected for the present study. Nearly all such crystals are electroluminescent, whereas crystals showing green or orange fluorescence are rarely electroluminescent.

Synthetic zinc sulfide crystals have been shown[14] to be quite complex in structure, containing both cubic and hexagonal regions, and random and periodic stacking faults. The crystals used in the present work covered a wide range of structures, from nearly pure cubic through faulted structures to nearly pure hexagonal. All those whose structure was determined were oriented with the long axis in the $(1\bar{1}0)$ direction referred to the hexagonal coordinate system. The crystals used ranged in length from about 3 to 10 mm and in width from about 0.1 to 0.7 mm, usually having irregular polygonal cross sections.

Emission Intensity Measurements

The crystal is excited to luminescence by the application of a time-varying voltage across its length. In most of the present work, a half-wave-rectified 60-cycle sine wave (denoted "half-wave" below) was used. The light emitted by the crystal was detected by means of a calibrated Type 1P28 photomultiplier tube whose output was displayed on a cathode-ray oscilloscope.

Since the light output is generally too dim for conventional spectroradiometry, the measurement of emitted intensity was carried out in a series of narrow wavelength bands, isolated by means of interference filters. The rate of photon emission in the jth such band is given approximately by

$$n(\lambda_j) = C_j i_j \text{ photons/sec-m}\mu, \tag{1}$$

where

$$C_j = \frac{10^7}{hc}\frac{4\pi R^2}{A}\frac{\lambda_j}{\Delta\lambda_j}\frac{1}{T_j S_j}. \tag{1a}$$

R = distance from crystal to cathode of photomultiplier; A = area of cathode of photomultiplier; λ_j = peak transmission wavelength of filter; $\Delta\lambda_j$ = integrated bandwidth of filter; T_j = peak transmission of filter; S_j = sensitivity of photomultiplier at wavelength λ_j, in amps/watt; i_j = photomultiplier anode current, in amps; and c = velocity of light, 3×10^{17} mμ/sec. Because of various uncertainties in calibration and geometry, the results have only order-of-magnitude precision.

Physical Arrangements

Figure 1 shows the apparatus used for measurements over a range of temperatures. The crystal is cemented by dots of conductive silver paint at its end to a slab of crystalline quartz which provides excellent electrical insulation and good thermal conduction. The silver paint is extended from the crystal so as to hold two small coil springs carrying copper plugs, to which contact is made by quartz-insulated tungsten probes. The slab, together with a copper plate carrying a copper-constantan thermocouple, is bolted to a copper block brazed to the brass base of the chamber. The thermocouple is taken out through one of two tubes through which predried nitrogen can be circulated for prevention of condensation at low temperatures, and the photomultiplier is inserted through a snug-fitting hole in the top of the chamber. Temperature control is provided by an appropriate bath surrounding the lower part of the apparatus.

Some of the work was done in a simpler apparatus, limited to room temperature, but providing more efficient geometry in that the light path was unobstructed. The filter constants C_j of Eq. (1a) were determined for this apparatus, and results obtained in the variable temperature apparatus were corrected by an empirical factor.

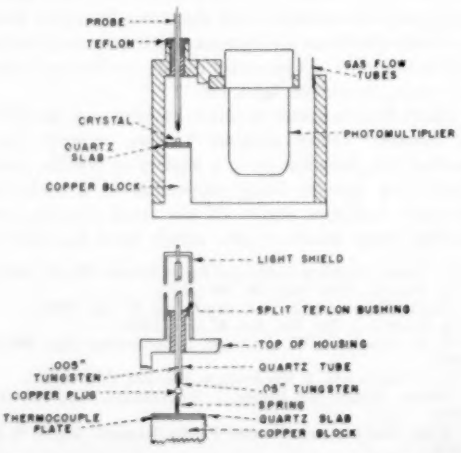

FIG. 1. Apparatus for light and current measurement over a range of temperatures. Top, elevation cross section. Bottom, detail of contacting arrangement, not to scale.

[13] A. Krembeller, Electrochemical Society Spring Meeting, Chicago, Illinois (May 2-6, 1954); Sylvania Technologist **8**, 11 (1955).

[14] L. W. Strock and V. A. Brophy, Am. Mineralogist **40**, 94 (1955).

Current Measurement

A novel feature of the present work is the measurement of the current passing through the crystal under the half-wave voltage. For this purpose, a variable capacitor was used as one arm of a bridge to balance out the displacement current in the crystal and the quartz slab. The crystal and quartz slab formed the second arm, and the other two arms consisted of equal resistors across the inputs of the differential preamplifier of the oscilloscope used as detector. Since the time derivative of the voltage changes abruptly twice in the cycle, balance of the displacement current could readily be detected by the absence of corresponding discontinuities in the net current displayed on the oscilloscope. The capacitor was adjusted under fairly low voltage (a few hundred peak volts) until this condition was achieved, and was thereafter left untouched. Since the two circuits to be balanced actually contain distributed resistance and inductance as well as capacitance, perfect balance cannot be achieved, but the unbalance current is negligible in comparison with the crystal currents obtained under the higher working voltages.

EXPERIMENTAL RESULTS

General Behavior

The steady-state light output from electroluminescent ZnS crystals under 60-cycle half-wave excitation has been described by WDH. Oscillograms are shown in Fig. 2 for a typical crystal at various voltage amplitudes. At low voltages, the emission comes to a peak at about 150 degrees phase,[18] and decays during the second half-cycle. As the voltage is increased, this "150-degree peak" increases in intensity and a new peak at 90 degrees phase emerges. With further increase of voltage, the 90-degree peak grows the more rapidly. In most experiments, the voltage was increased until there was discernible instability in the 90-degree peak, taken as a sign of incipient breakdown. In some crystals, the 150-degree peak contains a 180-degree component, and, more rarely, a small peak at about 130 degrees. These "fine structure" peaks vary in prominence from crystal to crystal, and have not yet been investigated in detail.

The relative colors of the two major peaks have been investigated by measuring the emission through blue and green filters. In general there was no significant color difference between the peaks in a given crystal, although some crystals showed small deviations in either direction. This result contradicts WDH, who found the 90-degree peak to be distinctly bluer than the 150. Subsequent examination of one of their crystals by the writer, however, disclosed that the 90-degree peak contained appreciable ultraviolet due to arcing

[18] It is convenient to refer to the brightness peaks by the location of their maxima in phase degrees with respect to zero phase of the exciting voltage.

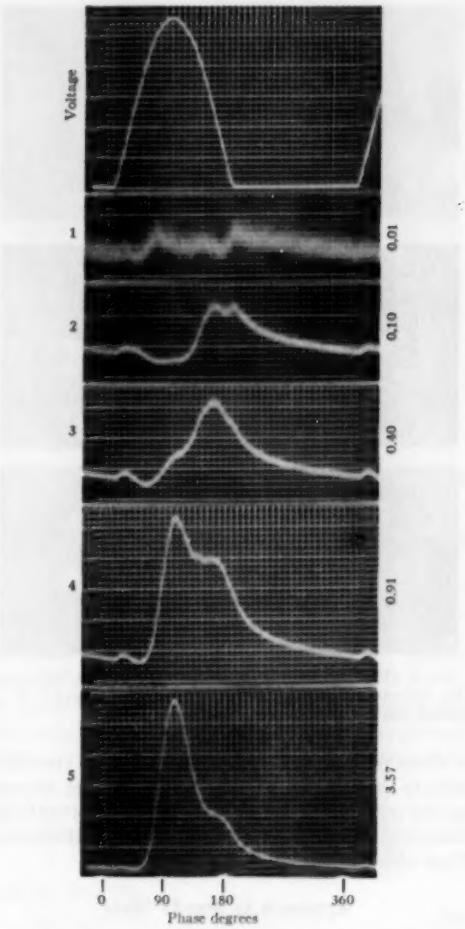

FIG. 2. Half-wave voltage wave form (at top) and oscillograms of electroluminescence of crystal with Ag paint electrodes. Figures at left give voltage amplitudes in kv. Figures at right give scale factors, emission intensity (arbitrary units) per scale division.

in an internal void. This ultraviolet was transmitted by their "blue" filter, giving a spurious result.

Many crystals have been examined microscopically to determine the spatial distribution of the emission. In air, the high refractive index of ZnS results in multiple internal reflection, and the light often appears to originate at the ends or at surface or internal flaws. However, it is significant that in no case was there any appreciable change of distribution with polarity. Furthermore, microscopic observation through a synchronous shutter showed that the spatial distributions of both major peaks were, within limits of visibility, the same. By immersing the crystal in a fluid of refractive index $n_D = 2.0$,[19] the critical angle is increased

[19] "High Series Index of Refraction Liquid 2.0," R. P. Cargille Laboratories, Inc., New York, New York.

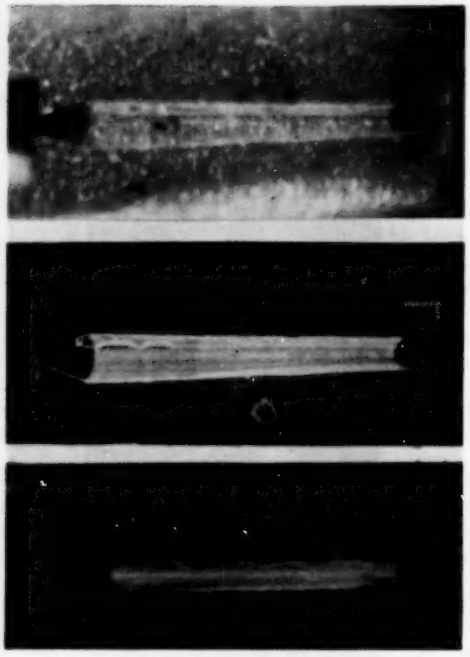

FIG. 3. Photomicrographs of an electroluminescent ZnS crystal. Top, external illumination. Middle, electroluminescence in air. Bottom, electroluminescence in high-index fluid.

to about 60°, and observations under these conditions indicate the emission to be generally uniform throughout the crystal. In a few crystals, poorly resolved bright transverse striations or rows of dots were discernible. These observations are illustrated in Fig. 3.

Approach to Steady State

The first few cycles of emission after sudden application of the half-wave voltage were observed by photographing a triggered single sweep of the oscilloscope. The steady state was reached after some five to ten cycles, during which the residual intensity at the end of the cycle increased while the peak heights usually increased but sometimes decreased slightly. Both infrared irradiation and long resting in the dark failed to give reproducibility in the transient behavior of the peak heights. However, the total change was usally less than twenty percent of the steady-state height; an example is shown in Fig. 4(a). With full-wave excitation, on the other hand, there was a marked build-up in the peaks in the first few cycles, as shown in Fig. 4(b). Presumably this is due to the accumulation of electrons in the conduction band or in traps, since the absence of a zero-field interval such as exists in the half-wave cycles does not give the excitation opportunity to decay. From this comparison of 60-cycle full-wave and half-wave excitation, we may conclude that each cycle of the latter starts with the crystal "nearly" in its ground state, and we may therefore hope to correlate the resulting emission with other physical properties of the "unexcited" crystal.

Steady-State Results

Emission Intensity

Figure 5 shows approximate spectral distributions of the emission from a typical crystal. It is noteworthy that all three curves have about the same shape, confirming the above-mentioned result that there is no appreciable difference in spectral distribution between the two major peaks. The emission is seen to consist mainly of a broad band centered at about 470 mμ, similar to that of a blue-electroluminescent ZnS:Cu powder phosphor.[6]

From the total emission intensities (areas under curves of Fig. 5), we obtain a calibration factor for conversion of the unfiltered photomultiplier response to absolute intensity in photons/sec. This factor should, strictly speaking, be separately determined for each crystal. In view of the many other errors in these measurements, however, the amount of labor involved seemed unwarranted, and the factor used was the average of the values obtained from two crystals.

Figure 6 shows the absolute intensities of the 90-degree peak and the time-average emission from a typical crystal as functions of the voltage amplitude at temperatures of 25°, 0°, and −78°C. All crystals observed to date have shown a progressive deterioration in brightness during the course of a series of measurements. These data were taken after the crystals had been "aged" beyond the initial rapid deterioration.

Current

After balancing out the displacement current under low voltage, as described above, the system remained in balance under all voltages, showing that the displacement current amplitude in the crystal is linear with voltage. The instantaneous net current as function of the instantaneous voltage in the half-wave cycle is shown in Fig. 7. The current is roughly exponential

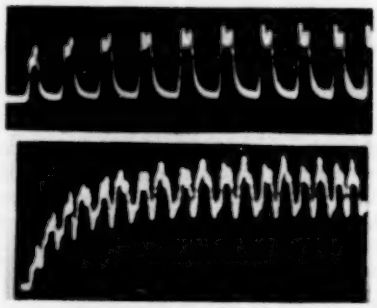

FIG. 4. Initial cycles of electroluminescence of a ZnS single crystal. Top, half-wave excitation. Bottom, full-wave excitation.

with voltage. The falling current is somewhat greater than the rising current, showing that the conductivity of the crystal is temporarily increased by exposure to the peak voltage. It is particularly to be noted that there is no reverse current detected in any part of the cycle. The small current close to 180 degrees cannot be measured due to the unbalance current mentioned above. However, there is no doubt whatever about the existence of forward current at the time of the 150-degree peak.

Efficiency

From the measured light output, current, and voltage, we compute the average efficiency $\bar{\eta}$ of the over-all cycle as

$$\bar{\eta}=h\bar{\nu}\int_0^T Ldt \Big/ \int_0^T iVdt, \tag{2}$$

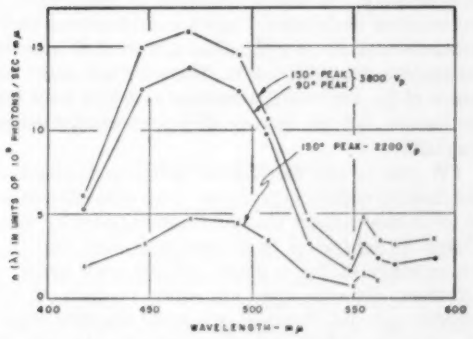

FIG. 5. Photon distributions in electroluminescent emission from a ZnS single crystal.

where

$$L=\int_0^\infty n(\lambda)d\lambda \tag{2a}$$

$=$ instantaneous rate of photon emission,

$$h\bar{\nu}=\frac{1}{L}\int_0^\infty n(\lambda)\frac{hc}{\lambda}d\lambda \tag{2b}$$

$=$ average quantum energy of emitted light.

The value of $h\bar{\nu}$ was obtained by graphical integration of the data of Fig. 5. Values of L, i, and V were scaled off the oscillograms, and the integrations in Eq. (2) were performed numerically.

We may also compute the instantaneous efficiency η_{90} of the 90-degree peak since L, V, and i are all stationary at this instant:

$$\eta_{90}=h\bar{\nu}[L/iV]_{90°}. \tag{3}$$

Also of interest are the photon-electron ratios $\bar{\xi}$ and ξ_{90} for the over-all cycle and the 90-degree peak, given

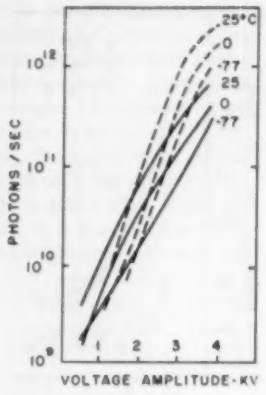

FIG. 6. Absolute intensities of 90-degree peak (broken curves) and time-average (solid curves) electroluminescent emission from a ZnS single crystal.

respectively by

$$\bar{\xi}=\int_0^T Ldt \Big/ \int_0^T idt/e, \tag{4}$$

$$\xi_{90}=e[L/i]_{90°}. \tag{5}$$

The meaning of these ratios requires some discussion. The denominators, current divided by electronic charge, give the total number of electrons per second passing any given transverse plane in the crystal. In general, both free and bound electrons would be included, but the absence of space charge polarization means that only the former are involved here. Now we may *formally* define a reaction cross section in the usual manner,[17] viz.,

$$\sigma=\frac{\text{No. of reactions per second}}{\text{Incident flux}\times\text{No. of reacting centers}}. \tag{6}$$

Thus, we find that

$$\bar{\xi}=\sigma N/A, \tag{6a}$$

where $\sigma=$ cross section of a luminescent center, $N=$ total number of centers in the crystal, and $A=$ cross-sectional

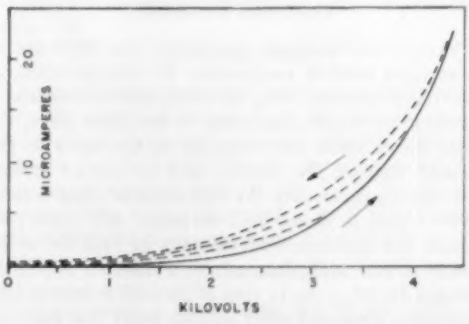

FIG. 7. Instantaneous current *vs* voltage in half-wave cycle for three voltage amplitudes.

[17] See for example, L. I. Schiff, *Quantum Mechanics* (McGraw-Hill Book Company, Inc., New York, 1949), p. 97.

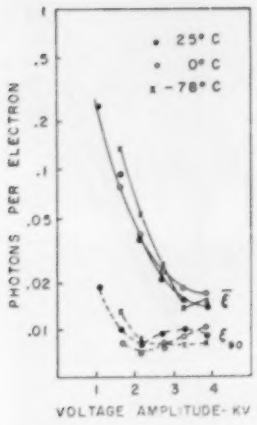

FIG. 8. Photon-electron ratios in 90-degree peak and time-average electroluminescent emission from a ZnS single crystal.

area of crystal. It must be emphasized that σ is purely a formal quantity. But if it can later be shown that excitation occurs by electron impact, then σ will have the physical significance of a collision cross section multiplied by an emission probability.

Figures 8 and 9 show η and ξ for one of the three crystals on which these data were measured. Despite considerable variation among the crystals, certain features seem to be common:

1. ξ_{90} is roughly independent of temperature and increases slowly with voltage.

2. Within a factor of three, $\xi_{90} \cong 0.01$, i.e., the 90-degree peak amounts to about 1 photon per 100 electrons traversing the crystal.

3. η_{90} is also roughly independent of temperature and is roughly constant or a slowly decreasing function of voltage.

4. Within a factor of two, $\eta_{90} \cong 10^{-5}$.

5. Both $\bar{\xi}$ and $\bar{\eta}$ decrease with increasing voltage, since the 150-degree peak increases less rapidly than the current.

DISCUSSION

Excitation Processes

Various authors have recognized that there are at least three possible mechanisms for the excitation of electroluminescence, viz., (a) direct field excitation of luminescent centers, analogous to the Zener effect, (b) injection of holes, and trapping of the latter in the ground state of the centers, and (c) impact of fast electrons on the centers. We shall consider these in turn. With regard to direct field excitation, PW have estimated the required field strength in ZnS:Cu to be 2×10^7 v/cm, while Burns,[18] by a different approach, obtains 3×10^6 v/cm. In view of the high estimated field strengths, these and other authors reject this mechanism. We concur in this conclusion, but for a different reason, since it is entirely conceivable that sufficiently high fields exist in localized regions of a crystal. However, under this mechanism one would expect $\bar{\xi}$ to be of the order of unity at all voltages, since each conduction electron would arise from excitation of a luminescent center. It is hardly conceivable that only a few percent of the electrons arise through this mechanism, since the required high-field regions could not exist in the presence of a parallel conduction mechanism.

Excitation by hole injection through a p-n junction has been observed[19] in silicon carbide crystals. The strongest reason for rejecting this mechansim in zinc sulfide is that it provides no simple way of accounting for the out-of-phase emission peak. This peak is, indeed, absent in the emission oscillograms presented in reference 19. A second reason is that the voltage required in zinc sulfide crystals seems much too high.

Impact excitation was considered in some detail by Curie.[20] Although neither the theory of high-field phenomena in crystals nor our knowledge of the structural details of zinc sulfide is sufficiently advanced for a quantitative evaluation, Curie's considerations make impact excitation seem plausible, and we shall base the subsequent discussion on it. The observed slight increase of ξ_{90} with voltage seems concordant with this mechanism, but the decrease of $\bar{\xi}$ is not readily understandable.

PW also accept the impact excitation mechanism, but limit its region of occurrence to an exhaustion layer at the cathode, where the field is concentrated by space charge. In support of their hypothesis, they find that the intensity of the in-phase emission peak under ac excitation depends upon the work function of the cathode material. However, one would also then expect the emission of light to be localized near the cathode. As described above, we have never observed such localized emission. WDH propose that impact *ionization*

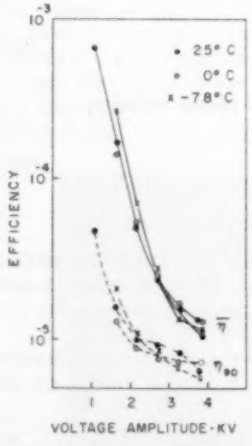

FIG. 9. Efficiency of 90-degree peak and time-average electroluminescent emission from a ZnS single crystal.

[18] L. Burns, J. Electrochem. Soc. **100**, 572 (1953).

[19] Lehovec, Accardo, and Jamgochian, Phys. Rev. **83**, 603 (1951); **89**, 20 (1953).

[20] D. Curie, J. phys. radium **14**, 510 (1953).

occurs in macroscopic barriers within the crystal. Indeed, they found such barriers by a probe method under low dc voltages, and claimed that when the emission is localized its maximum coincides with the barrier. This coincidence, however, may well have been the result of internal reflection in crystals containing macroscopic flaws. Our own observations have disclosed no correlation between the emission and the barriers found by probing.

On the other hand, it seems highly plausible that *microscopic* barriers may play a key role. Ince[21] has found that extremely high magnetic fields fail to quench electroluminescence, showing that the excitation must be localized in small regions. These regions might well be associated with rectifying junctions between regions of different conductivity type, such as *n*- and *p*-type or all *n*-type but with different donor concentrations. The voltage drop would then be concentrated across the alternate junctions which were biased in their reverse direction, and the rapidly increasing current-voltage characteristic would correspond to "breakdown" of the barriers. If there are of the order of 10^3 to 10^4 barriers per cm along the crystal, the emission would appear uniform under any microscopic resolution that it has yet been possible to employ.

Emission Processes

PW attribute the in-phase emission peak to electrons which enter the crystal from the cathode and the out-of-phase peak to electrons released from donor centers in the exhaustion barrier, the emission in both peaks being supposed to occur immediately following excitation. However, in a given half-cycle, the out-of-phase emission would occur *first*; thus, under half-wave excitation there would be a peak near zero rather than near 180 degrees. WDH postulate that the center is ionized and the electron swept away by the field and subsequently trapped. They then attribute the in-phase peak to capture of conduction electrons and the out-of-phase peak to the return of the trapped electrons under the influence of the space-charge field. The critical objection to this mechanism is the absence of reverse current coincident with this peak. The observed height of the 150-degree peak would require readily measurable reverse currents if the electron range is an appreciable fraction of the crystal length. Instead, there is a measurable *forward* current at the time when this peak reaches its maximum.

The observations can be explained by attributing both peaks to excitation which occurs principally during the short time interval about the 90-degree phase when high current flows. The 90-degree peak then arises from "immediate" emission, while the 150-degree peak is delayed by trapping of the excited electron in or near the center. The relative voltage dependencies of the two peaks are then understandable, since a given center could undergo several successive 90-degree processes, but only one 150-degree process in one cycle.

In the 150-degree process, the return of the electron to the ground state is delayed until the applied field is reduced. The delay must be a direct effect of the field rather than simply a result of a long lifetime of the trap, since the phase of the peak remains constant over a wide temperature range, hence over a wide range of trap lifetimes. It appears, therefore, that the electron is in some way held in the trap by the field. This does not imply that the thermal depth of the trap is necessarily increased, but only that the over-all probability of transition from trap to ground state is decreased. If we accept the hypothesis[22] that the luminescent center is a large complex, then the polarization of an excited metastable state might lead to this effect. As a crude picture, the electron would be drawn to the edge of the large center and there could not recombine with the activator atom.

The idea of trap stabilization is consistent with the quenching of emission usually observed when an electric field is applied to a phosphor during or after ultraviolet excitation. The temporary stimulation also observed in such experiments may be a true electroluminescence effect, i.e., excitation of additional centers. However, it must be admitted that these phenomena are extremely complicated, and that quite different ideas which have been advanced to explain them[23] may well turn out to be correct.

Summary of Conclusions

Impact of fast electrons, accelerated through microscopic barriers, appears to be the most plausible mechanism for excitation of the luminescent centers. The excited electron may return to the ground state immediately, or may become trapped in a metastable excited state of the center. In the latter case, the presence of the electric field tends to hold the electron in the trap.

ACKNOWLEDGMENTS

The writer wishes to express his thanks to his Sylvania colleagues and to Professor J. J. Dropkin for many helpful and stimulating discussions. Especial gratitude is due to Dr. A. Kremheller for the crystals and information relating to them; to Mr. V. A. Brophy for the x-ray diffraction studies; and to W. S. Romito and S. R. Kellner for assistance in the experimental work.

[21] A. N. Ince, Proc. Phys. Soc. (London) **B67**, 870 (1954).

[22] G. F. J. Garlick, *Luminescent Materials* (Oxford University Press, London, 1949), p. 119.

[23] See, for example, F. Matossi, Phys. Rev. **94**, 1151 (1954).

Soft X-Ray Absorption of Tellurium and Vitreous and Metallic Selenium*

M. Parker Givens, Charles J. Koester,† and William L. Goffe
Institute of Optics, University of Rochester, Rochester, New York

(Received June 29, 1955)

The absorption of metallic selenium is compared with that of the vitreous form in the region from 200 A to 240 A. For these two forms of selenium and for tellurium, the absorption band is separated into two component bands. This has led to a revised estimate of 1.2 ev for the separation of the M_{IV} and M_V levels of selenium and 1.6 ev for the separation of the N_{IV} and N_V levels of tellurium.

INTRODUCTION

EXPERIMENTAL studies of the soft x-ray absorption of vitreous selenium[1] and of tellurium[2] have been reported previously. The purpose of this paper is to present the results of similar studies on metallic selenium and to give a brief discussion of the results.

The purpose of most soft x-ray absorption measurements is to provide information which may be of value in determining the density of states in the conduction band. In selenium and tellurium, this is complicated by the fact that the lower (or initial) state is double. Therefore, an effort has been made to correct for this doubling and so to reveal the shape which the absorption band should have had if the lower level had been single instead of double.

METHODS

The experimental procedures have been described in the earlier papers[1,2] and only points of special interest are mentioned here. The samples were prepared by vacuum evaporation. The thickness of the selenium films was determined by observing the color of the light reflected from them, a method which has been checked by interferometric measurements. These thickness observations were made with the film in the vitreous state, and it was then converted to the metallic form by heat treatment as described earlier.[3] No measurements were made of the thickness of the samples after their conversion to the metallic state. For this reason, the selenium deposit is here reported in terms of surface density rather than thickness. In bulk selenium, there is a 15% increase in density from the vitreous to the metallic form. Assuming bulk densities, a surface density of 100 $\mu g/cm^2$ corresponds to a thickness of about 2340 A of vitreous selenium or 2090 A of metallic selenium. This estimate, however, may be in some error because of imperfections in the evaporated films and the probability that these imperfections are largely removed by the heat treatment.

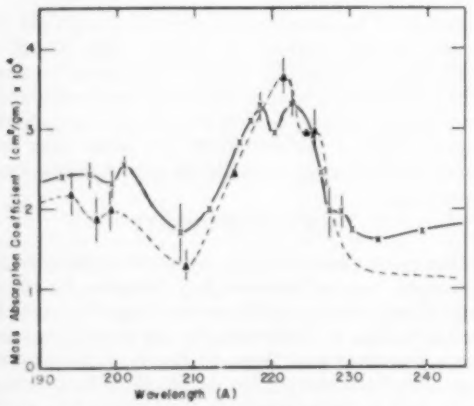

FIG. 1. The soft x-ray absorption band of selenium – – ▲ – – ▲ – – vitreous selenium; ——×——×—— metallic selenium.

The absorption curves for both forms of selenium are given in Fig. 1. In each case there is a strong absorption band in the region around 220 A and this band has a double peak. The detailed features of the two curves are not alike. Notice the apparent change in relative magnitude of the two peaks and the changes in their positions. Outside of the absorption band, the metallic form shows a somewhat higher absorption than the vitreous.

Since each of these curves represents the average of several different runs, vertical lines have been drawn at several points to indicate the standard deviation of the mean at each point. On this basis, it is possible to interpret the vertical separation of the two curves as experimental error. The structure at wavelengths shorter than the absorption band is different for the two forms. The shape of these curves is much better established than Fig. 1 would indicate. In the original work a great

TABLE I. Comparison of the absorption by two forms of selenium.

Feature	Location of feature (angstroms) Vitreous form	Metallic form
Absorption edge	228.1	226.4
Peak at longer wavelength	225.5	222.8
Peak at shorter wavelength	221.6	218.7
Peak separation	3.9	4.1

* This work was supported initially by the Office of Naval Research and recently by the National Science Foundation.

† Now with the American Optical Company, Southbridge, Massachusetts.

[1] M. P. Givens and W. P. Siegmund, Phys. Rev. **85**, 313 (1952).

[2] R. W. Woodruff and M. P. Givens, Phys. Rev. **97**, 52 (1955).

[3] M. P. Givens, Rev. Sci. Instr. **25**, 1130 (1954).

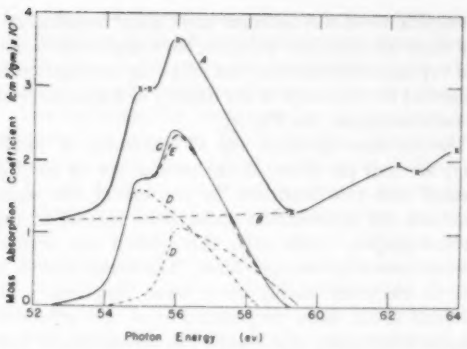

FIG. 2. Structure of the absorption band of vitreous selenium. *A*—Experimental curve. *B*—Background. *C*—Experimental curve minus background. *D*—Suggested individual peaks. *E*—Sum of the suggested peaks.

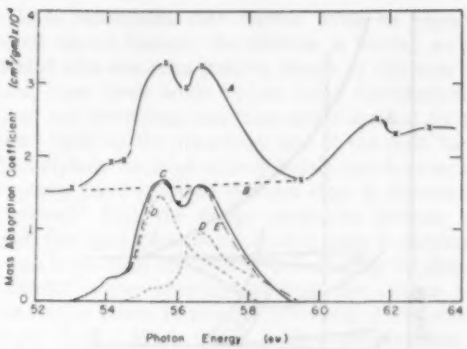

FIG. 3. Structure of the absorption band of metallic selenium. *A*—Experimental curve. *B*—Background. *C*—Experimental curve minus background. *D*—Suggested individual peaks. *E*—Sum of the suggested peaks.

many experimental points were observed, only a few of which are reproduced here. Upon repeating the experiment with a fresh sample a new curve was obtained, which duplicated the original in shape but differed from it in absolute magnitude. It is this uncertainty in absolute magnitude which is indicated by the vertical lines in the figure.

Table I shows some of the interesting features of these curves. The standard deviation of the mean for the location of the edges and peaks shown in the table is about 0.5 A. Since these edges and peaks differ in position between the two forms by considerably more than 0.5 A, the shift is probably real.

Since the doubling of the peaks is due to the separation of the M_{IV} and M_V levels, an effort has been made to resolve the absorption into two bands, each having a shape associated with the density of states within the conduction band. This has been done by using a method described by DuMond.[4]

The method requires that the following assumptions be made: (1) the two absorption bands must be identical in shape and differ only in intensity (i.e., vertical dimension), and (2) there is no other contribution to the absorption except from these two bands. This last assumption is equivalent to assuming there is no third band and that the background absorption can be subtracted out in some simple manner. The first assumption is reasonable because the M_{IV} and M_V levels are both *d* levels, which causes the shape of each absorption curve to be determined by the density of *p*- (and *f*-) type states in the conduction band. The relative intensity of the two bands and their horizontal (or energy) separation must be selected. These two quantities along with the background subtraction provide three parameters which may be adjusted to some extent in an effort to make the method work.

If the method is properly applied, and if the parameters are correctly selected, then the band will be resolved into its two components which may be added together to give the original band within experimental error. Some care must be exercised at this point. If the final recombined curve is required to fit the original more closely than the data justify, then additional structure (presumably extraneous) will appear in the component bands. For this reason, the reconstructed curves do not match exactly the original curves but are within the experimental uncertainty. It might be argued that these reconstructed curves are more meaningful than the original curves which were drawn by eye through the experimental points. In view of the possibilities, it is surprising that the results check as well as they appear to. The curves were plotted on a linear energy scale before beginning the resolution process.

RESULTS

The results of the resolution and recombination are shown in Figs. 2 and 3. The figures show the original curves, the assumed background, the absorption band after subtraction of background, the two separated bands, and finally the recombination of these bands.

For simplicity, the background was assumed to correspond to a straight line connecting the two minima beside the band. Slight variations from this line might have helped the situation somewhat, but any particular choice would have been hard to justify.

Several values of the parameters were tried. Intensity ratios of from 1.4 to 1.6 seemed to work very well. A value of 1.5 was selected, not only because it was near the middle of the satisfactory range but also because this is the relative probability of the transitions from the M_{IV} and M_V levels to the $4p$ levels in isolated selenium atoms.

The energy separation between the two bands represents the separation of the M_{IV} and M_V levels. A casual examination of the absorption curves indicates that this should be approximately one electron volt. A value

[4] J. W. M. DuMond, Revs. Modern Phys. **5**, 1 (1933).

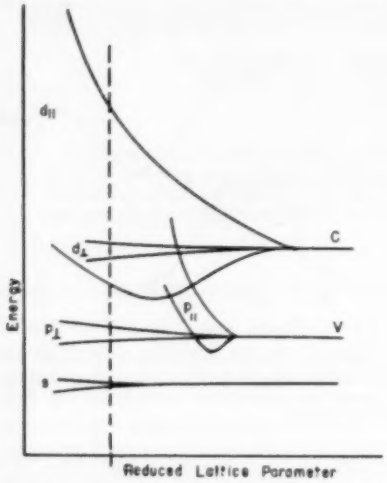

FIG. 4. Schematic diagram of the energy levels of tellurium (after Callen[5]), showing the broadening of the bands as the atoms are brought together. The subscripts indicate that the symmetry of the wave functions is perpendicular or parallel to the chain axis of the crystal. V is the valence band; C is the conduction band.

of 1.2 ev was selected because it could be used for both the metallic and vitreous curves; one should not expect the separation of the M_{IV} and M_V levels to be detectably different in these two cases. This value of 1.2 ev is somewhat larger than the value 0.8 ev predicted by the rule that this separation should be proportional to $(Z-13)^4$.

The separated curves of Figs. 2 and 3 should represent the function $N(E)$ or the density of states in the conduction band. For the two forms of selenium these curves are quite different. Certainly in the case of metallic selenium the curve indicates a narrow band superimposed on a broader weaker band. In view of the

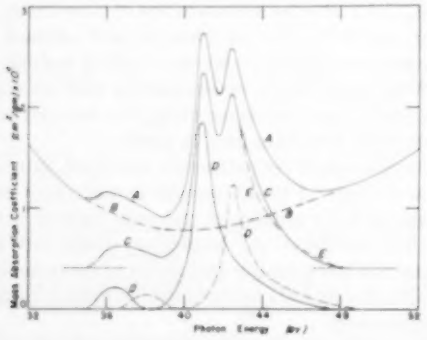

FIG. 5. Structure of the absorption band of tellurium. A—Experimental curve (minus 2×10^4 cm²/g). B—Background. C—Experimental curve minus background. D—Suggested individual peaks. E—Sum of the suggested peaks. Curves C and E have been displaced vertically.

theoretical work of Nussbaum[4] and Callen[5] on tellurium, and since selenium and tellurium have similar electronic and crystalline structures, the following explanation is suggested for the shape of the density of states curve of metallic selenium (see Fig. 4).

The valence electrons are $4p$ electrons, of which there are four per atom. In the crystal, the $4p$ band is divided into two branches. In one branch the wave functions are symmetrical about lines parallel to the crystallographic chain axis; this branch can accommodate two electrons per atom. The other branch is due to electrons having their wave functions symmetrical about lines perpendicular to the crystallographic chain axis; this branch can accommodate four electrons per atom. At normal interatomic distances, the perpendicular branch is filled and the parallel branch is at a much higher energy, so that the latter is empty and takes no part in the absorption band which has been observed.[5] The conduction band arises from states corresponding to $4d$ states of the isolated atom. This band also divides itself into two parts, a narrow band of perpendicular symmetry and a wider band of parallel symmetry. Unlike the p band, these two parts are superimposed rather than separated. The observed absorption is believed to be due to transitions from the $3d$ (i.e., M_{IV-V}) levels to this $4d$ band. The violation of the selection rule $\Delta l=\pm1$ may be ignored on the grounds that this rule is not valid in the solid, or one may recall that the states in the $4d$ band are of mixed character and have some p- or f-type symmetry. In any case, such violations of the selection rule are common in solids. On the basis of this interpretation, the experimental data indicate that the narrow $4d$ perpendicular band begins about 2 ev above the bottom of the broader $4d$ parallel band. This is possible since the work function of selenium[6] is 4.62 ev.

In the case of vitreous selenium, the density-of-states curve is not an obvious superposition of two bands. This is probably due to the fact that the crystal structure is not well formed in vitreous selenium and so it is less meaningful to distinguish between directions parallel and perpendicular to the chains.

The absorption by tellurium is reproduced from the earlier work (Fig. 5). To this has been added the resolution of the band into its two component parts as was done for selenium. The value of 3:2 for the intensity ratio of the two components again proved satisfactory and a separation of 1.6 ev for the N_{IV} and N_V levels gave the best fit. However, a variation of ±0.05 ev in this value was not significant in the analysis. In this case a straight line for the background was entirely unusable, so a "reasonable" background curve was sketched in and the data were reduced.

The density-of-states curve thus obtained showed a strong peak at 40.9 ev, with a secondary peak at 36.5.

[4] A. Nussbaum, Phys. Rev. **94**, 337 (1954).
[5] H. B. Callen, J. Chem. Phys. **22**, 518 (1954).
[6] R. Hamer, J. Opt. Soc. Am. **9**, 256 (1924).

The depth of the minimum between these two peaks was sensitive to the choice of background curve. Shown in the figure is the particular background curve which resulted in a zero minimum between these two maxima.

The interpretation here cannot be as simple as that suggested for selenium. The absorption corresponds to transitions from N_{IV-V} to $5d$. According to Callen,[6] the $5d$ band is made up of a broad band and a narrow band as before. However, the infrared absorption studies of Loferski,[7] interpreted in the light of Callen's work, indicate that the d perpendicular band begins less than 0.$\frac{1}{4}$ ev above the bottom of the d parallel band. Such a small separation would not have been resolved in the present study, so that the main absorption band between 39 ev and 46 ev is probably due to the combined effect of these two bands.

[7] Joseph J. Loferski, Phys. Rev. **93**, 707 (1954).

It is conceivable that exciton levels on impurity levels appear because the electron is leaving an ion behind with one extra positive charge. If this were the case, these levels would lie just below the conduction band and transitions into them might account for the small band on the low-energy side of the main band. This explanation is not entirely satisfactory because the impurity band proposed is wider than is customarily observed.[8] Also, the energy separation between the main band and the impurity band is large, in particular much larger than the 0.324 ev indicated by the data of Loferski as the separation between the valence and conduction bands. In addition, the width of the band is larger than 4.76 ev which is the work function of tellurium.[9]

[8] E.g., L. G. Parratt and E. L. Jossem, Phys. Rev. **97**, 916 (1955).
[9] Apker, Taft, and Dickey, Phys. Rev. **74**, 1462 (1948).

PHYSICAL REVIEW VOLUME 100, NUMBER 4 NOVEMBER 15, 1955

Velocity Analysis of Thermionic Emission from Single-Crystal Tungsten

GEORGE F. SMITH
Electron Tube Laboratory, Hughes Research Laboratories, Culver City, California
(Received June 24, 1955)

Hutson has recently observed a non-Maxwellian distribution of thermionic emission from various crystallographic directions of a tungsten single crystal. It is suggested that the true distribution is Maxwellian, and that the observed distribution is due to an analyzer resolution of 0.24 volt. Factors which might affect resolution are discussed, and Hutson's numerical results are recalculated on the basis of this explanation.

HUTSON[1] has recently reported a careful experiment in which he observed a departure from Maxwell-Boltzmann distribution in the electron emission from single-crystal tungsten. This departure, a low-energy deficit, was the same in various crystallographic directions. As Hutson has pointed out, it is unlikely that the various crystal directions would be patchy in just such a way as to yield identical distributions. He also noted that the reflection coefficient which he uses to account for the distribution has, as yet, no satisfactory theoretical explanation.[2]

We suggest that some extraneous effect in the analyzer might affect analyzer resolution in such a way as to produce the observed distribution. Hutson's experimental points[3] for 2000°K are plotted in Fig. 1, along with a Maxwell-Boltzmann distribution modified by a 0.24-v rectangular resolution. It is seen that the match is very good. The 0.24-v figure was chosen to match the 2000°K data by interpolation from curves for resolutions of 0.2 v and 0.3 v. The same 0.24-v resolution figure was also applied to a Maxwell-Boltzmann distribution for 1700°K. The match to Hutson's experimental points[4] for 1700°K was equally good.

Hutson calculates a tenfold better resolution, 0.024 v, from the dimensions of the analyzer and its operating potential. He states[1,5] that the same distribution was obtained when the resolution was electrically changed to 0.06 v by varying the magnetic field. He concludes that the instrumental resolution was adequate for the detail in the distribution. One might reason instead that the resolution was already limited at 0.24 v by some other factor and that it was not actually being changed by the variation in magnetic field. There is no obvious cause for a spurious loss in resolution. Interconnection of radial and axial energy components, caused by slight misalignment of the analyzer and accelerating diode appears to be ruled out by precision assembly.[1] Stray time-varying magnetic fields were too small to affect the resolution.[1] The presence of patch fields is perhaps the most plausible hypothesis. The configuration of the analyzer is given in reference 1, Fig. 1. A patch field at the central baffle slit would deflect electrons from their normal line focus. A simple order-of-magnitude calculation can be made if patch crystals in the tantalum

[1] A. R. Hutson, Phys. Rev. **98**, 889 (1955).
[2] C. Herring and M. H. Nichols, Revs. Modern Phys. **21**, 185 (1949), Sec. IV.4; D. W. Juenker *et al*, Phys. Rev. **90**, 772 (1953); S. C. Miller, Jr., and R. H. Good, Jr., Phys. Rev. **92**, 1367 (1953).
[3] From reference 1, Fig. 5.
[4] From reference 1, Fig. 11.
[5] A. R. Hutson (private communication).
[6] E. Callen, Phys. Rev. **76**, 1394 (1949).

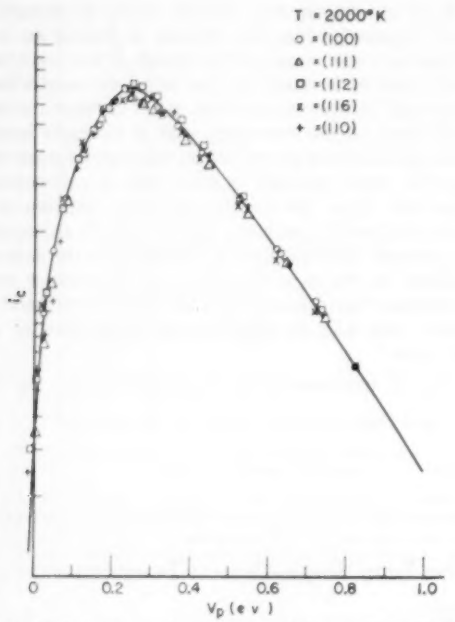

FIG. 1. Hutson's experimental points (reference 3) for 2000°K matched by a Maxwell-Boltzmann distribution modified by 0.24-v analyzer resolution.

baffle wall are comparable in linear dimension to the baffle slit width, 0.2 cm. The deflection at the exit slit would amount to

$$x = R(\Delta V)/2V_0, \tag{1}$$

where R, the trajectory radius, is 3.175 cm; eV_0, the electron trajectory energy, is 3 ev; and ΔV is the patch work function difference. For clean tantalum, a reasonable value of ΔV is 0.5 v. This value gives a deflection ("effective" exit slit width) of 0.26 cm, as compared with actual slit width of 0.026 cm. Since resolution is proportional to exit slit width, 0.26 cm corresponds to 0.24 v resolution. To determine whether Eq. (1) is applicable, Hutson[5] has opened the analyzer tube to measure the crystal grain size at the baffle slit. A photograph of the etched tantalum surface shows grains of a few times 10^{-3} cm in linear size, nearly a hundred times smaller than the slit width. Thus it is unlikely that baffle slit patchiness alone could produce the deflection required to give a resolution of 0.24 v. There is still the possibility that patch effects were enhanced by the presence of contaminants on the tantalum walls. Although great care was taken in the evacuation schedule,[1] it is extremely difficult to thoroughly out-gas large pieces of tantalum. The presence of at least a detectable degree of contamination is indicated by one observed change[1] of analyzer work function due to bombardment heating of the anode. Martin[6] and others have noted that adsorption of contaminants is, in general, extremely sensitive to surface orientation, and that patch contact potentials and hence patch fields are often greatly enhanced by the presence of even small amounts of contaminant.

[6] S. T. Martin, Phys. Rev. **56**, 947 (1939).

TABLE I. Revised summary of single-crystal emission constants. Hutson's values have been altered as required if the distribution shape is due to analyzer resolution.

Direction	$d\phi/dT$ (v/deg)	$A\alpha$ (amp/cm² deg²)
(111)	$+4.9\times10^{-5}$	92
(112)	-6.7×10^{-5}	55
(116)	$+4.9\times10^{-5}$	94
(100)	-0.1×10^{-5}	104

If the shape of the experimental energy distribution curves is attributed to analyzer resolution, Hutson's numerical results are affected as follows: (1) The true work function differences among the various crystal faces[7] are unchanged. (2) The temperature derivatives of the work function[8] are increased by 1.6×10^{-5} v/deg.[9] This is a very small change, being just equal to the stated uncertainty of the measurement. The adjusted temperature derivatives are given in Table I. (3) Hutson's values[10] of $A\alpha$ (A is the emission constant, 120 amp/cm² deg²; α is the energy-independent part of the transmission coefficient) must be recalculated using the new temperature derivatives and assuming no energy-dependent reflection. The new values are given in Table I. (4) The best estimates of true work function[11] for the (111), (112), (116), and (100) directions are increased by 0.08 v, restoring the constant parts to their respective Richardson ϕ^* values. The temperature coefficients must also be replaced by the new values from Table I.

The new values of $A\alpha$ from Table I seem to indicate a value of about 0.8 for α [using the (111), (116), and (001) directions]. This corresponds to an exclusively energy-independent reflection coefficient of 0.2. On the other hand, Nottingham's reflection coefficient, as used by Hutson, gives $\bar{R}=0.52$ at 2000°K. When this is combined with his value of $\alpha=0.9$, a total integrated reflection coefficient of about 0.6 is obtained.[12] It is believed that the new interpretation is in better agreement with theory.[2]

We are indebted to Dr. Hutson for a prepublication copy of his manuscript.

[7] Reference 1, Table I.
[8] Reference 1, Table II.
[9] A. R. Hutson, in private communication, has carried through an accurate general comparison of the two methods of matching curves to obtain values of $d\phi/dT$. He does not refer to the experimental curves except to note that the match of Fig. 1 is satisfactory. We have directly checked the experimental curves of reference 1 with less precision, to show that the two methods give only slightly different results.
[10] Reference 1, Table V.
[11] Reference 1, Table VI.
[12] It is apparently inconsistent that the new method can give a much smaller integrated reflection coefficient from the same values of A^* and only slightly different values of $d\phi/dT$. This is due to a considerable contribution from $d\bar{R}/dT$ in Eq. (6) of reference 1 when Nottingham's reflection coefficient is used.

Dislocation Energies in NaCl†

H. B. HUNTINGTON AND J. E. DICKEY, *Rensselaer Polytechnic Institute, Troy, New York*

AND

ROBB THOMSON, *University of Illinois, Urbana, Illinois*

(Received June 30, 1955)

The energies for both screw and edge dislocations in rock salt have been investigated. The effect of elastic anisotropy has been incorporated into the contribution from the region outside the core. Detailed calculations have been carried out for the energies of the cores themselves as a function of radius, and joined smoothly to the curves of the elastic theory. The core calculations are based on the Born-Mayer model and employ the formulas of Madelung for the potentials of rows of uniformly spaced charges.

For dislocations in the observed plane of slip (110), the constant term associated with the core energy is 1.0×10^5 ev/cm more for the edge than for the screw. Approximate calculations show this term to be appreciably larger for the edge dislocation in the (100) plane. Also, there appears to be large lattice potential barrier for dislocation motion in this plane arising from anion closed shell repulsion. This result may explain why these planes, though close packed, are generally not active in glide for alkali halides. The stability of dislocations with Burger vector longer than the minimum lattice translation is investigated. The possibility of hollow dislocations is also considered.

I. INTRODUCTION

THOUGH the treatment of dislocations within the framework of isotropic elastic theory has proved very fruitful in the past, there has been an increasing need recently to develop specific models for particular materials, which would be detailed enough to take into account the nonelastic distortions in the dislocation core region and the intrinsic anisotropy of the crystal elasticity. The alkali halides present obvious advantages for such a study. From the standpoint of theory a simple and reasonably satisfactory model exists in terms of point charges and short-range, ion-core repulsions which can account quite well for cohesion and for some of the elastic properties. From the standpoint of experiment the slip pattern is well known, namely in the [110] direction on the $(1\bar{1}0)$ planes, but one wonders why slip is not encountered along the close-packed (100) planes, as for the thallium salts and occasionally for AgCl, which shows pencil glide. Also, one is hopeful that a detailed study might throw light on the greater brittleness of alkali halides as compared to the silver salts.

We have calculated the core energies of certain dislocations on the basis of the simple force model. Initially the ion rows are arranged in accord with the isotropic elastic solution, and displacements are allowed to relax to minimize the stored energy. Such a procedure was applied by one of us[1] to the edge dislocation for slip in the (110) plane several years ago. More recently, an analogous calculation for the screw dislocation has been made by another of the authors.[2] The energies of various dislocations in the elastic region outside the cores have been calculated by the third author (R.T.), taking into account the anisotropy of the crystal. From this last it has been possible to draw some conclusions about the stability of dislocations with Burgers vector longer than the shortest translation vector of the lattice. The possibility of "hollow" dislocations is also briefly considered.

II. ELASTIC STRAIN ENERGY OF DISLOCATIONS IN NaCl

In this section, we shall calculate the elastic energy of formation of various types of dislocations in NaCl. We shall assume that the crystal is a continuum, and that the strains are small, say less than ten percent. The core represents just that region near the center of the dislocation where neither of these assumptions is justified, and is dealt with separately. The total energy is, of course, the sum of the two contributions.

Anisotropic elasticity has traditionally been considered to be intractable because of the large mathematical difficulties to be faced. Since the problem has received added attention, general methods have been devised for the treatment of straight dislocations in arbitrary media.[3,4] The elastic calculations in this paper are based on the techniques of Eshelby, Read, and Shockley.[3]

A. (110) Slip Planes

The experimental evidence available shows that the (110) planes in NaCl have a special place with regard to slip. Apparently under certain conditions other planes may be active also, but recent work[5] confirms that at room temperature the (110) planes are the principal active slip planes, and so proves that dislocations are initially present on these planes. (Dommerich[6] has

† This work was supported in part by the United States Air Force.

[1] H. B. Huntington, Phys. Rev. 59, 942 (1941).

[2] J. E. Dickey, M.S. thesis, Rensselaer Polytechnic Institute (unpublished).

[3] Eshelby, Read, and Shockley, Acta Met. 1, 251 (1953).

[4] A. Seeger and G. Schoek, Acta Met. 1, 519 (1953).

[5] P. L. Pratt, Acta Met. 1, 103 (1953).

[6] S. Dommerich, Z. Physik 90, 189 (1934).

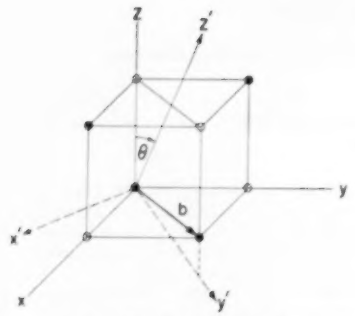

FIG. 1. $(1\bar{1}0)$ slip plane in NaCl.

reported that wetted crystals can glide on (100) planes with a critical shear stress which is approximately three times that observed for (110) planes.) We shall thus begin with a discussion of the elastic strain energy of dislocations on (110) slip planes.

Figure 1 shows the situation in the $(1\bar{1}0)$ slip plane. The unprimed axes represent the cubic coordinate system in NaCl; the primed axes are used for the discussion of a dislocation in the $(1\bar{1}0)$ plane. The (straight) dislocation line is assumed to lie along the z' direction; hence both strain and stress are functions of x' and y' exclusively. The direction of slip in NaCl is also a $[110]$ direction and is indicated in the figure by the Burgers vector b—the shortest distance between like atoms. As the z' axis is rotated from the z direction to the b direction (always in the $(1\bar{1}0)$ plane), the dislocation line gradually changes its character from pure edge to pure screw type.

One of the features of anisotropic elasticity theory might be re-emphasized here. When the Burgers vector is parallel to the dislocation line and points in the z' direction in a crystal of low symmetry, the displacement is not necessarily in the z' direction also, i.e., the dislocation is not a simple screw. A similar result follows when the Burgers vector is perpendicular to the line of the dislocation; the displacement of material is not necessarily normal to the z' direction. In the case of NaCl, however, when z' is either in the z direction or the b direction, the symmetry in the $x'y'$ plane is great enough to ensure the usual pure edge in the first case and pure screw in the second. In the intermediate case, where $\theta \neq 0, \pi/2$, the situation is more complicated than if the material were isotropic, and one does not obtain a simple decomposition into pure edge and pure screw components corresponding to normal and parallel components of the Burgers vector. In order to apply the methods of Eshelby *et al.*, one needs to transform the elastic constants from those given with respect to the xyz system of coordinates to the values suitable to the coordinate system $x'y'z'$. The elastic constants are the components of a fourth-order tensor, and their components in the new coordinate system are given by repeated application of formulas given in the standard references on elasticity.[7]

Calculations have been made with two sets of elastic constants. One set was taken at 80°K by Rose,[8] and the other set was taken at 1000°K by Hunter and Siegel.[9] It is assumed that 1000°K is a typical temperature of annealing, and probably represents the situation during the time that the dislocations have a chance to find their most favorable configuration. The low-temperature values are reasonably valid for a large-temperature interval, from probably zero to several hundred degrees. The results of Hunter and Siegel show an appreciable variation from the low-temperature values beginning at approximately 300–400°K. The elastic constants used are as follows:

80°K: $C_{11}=5.76\times10^{11}$ dynes/cm², $C_{12}=1.17\times10^{11}$ dynes/cm², $C_{44}=1.33\times10^{11}$ dynes/cm.

1000°K: $C_{11}=2.429\times10^{11}$ dynes/cm², $C_{12}=1.070\times10^{11}$ dynes/cm², $C_{44}=1.000\times10^{11}$ dynes/cm.

If τ_{ij} is the elastic stress tensor and b_i is the Burgers vector, it can be shown that the elastic strain energy is

$$E=\tfrac{1}{2}\int \tau_{ij}b_i ds_j, \tag{1}$$

where the integral is a surface integral to be taken over any regular surface bounded by the dislocation "loop." In our case, we consider a single dislocation line imbedded in a large crystal, so that the boundary of the surface in question is made by the dislocation line and the surface of the crystal. No attempt has been made to take account of the boundaries of the crystal in a detailed way. Indeed, if there were only one dislocation in a finite crystal, the stress would have to be relaxed on all boundaries, and small correction terms would thereby be added to the stress configuration near the boundaries themselves. It should be noted that stress relaxation actually destroys one of the basic assumptions—that all the stress and strain components are functions independent of z—because the addition of small stresses near the ends of the crystal where the dislocation breaks the surface destroys the property of plane strain which is always assumed. In this work we assume that the density of dislocations is sufficiently low and random that we can simply use the stress dis-

TABLE I. Elastic strain energy of dislocations on (110) slip planes.

θ	0°	10°	20°	30°	40°	50°	60°	70°	80°	90°
$\frac{E_{80}}{\ln(R/r_0)}$	0.508	0.500	0.490	0.465	0.441	0.424	0.410	0.399	0.388	0.385

[7] W. Voigt, *Lehrbuch der Kristallphysik* (B. G. Teubner, Leipzig, 1910); W. G. Cady, *Piezoelectricity* (McGraw-Hill Book Company, Inc., New York, 1946).
[8] F. C. Rose, Phys. Rev. **49**, 50 (1936).
[9] L. Hunter and S. Siegel, Phys. Rev. **61**, 84 (1942).

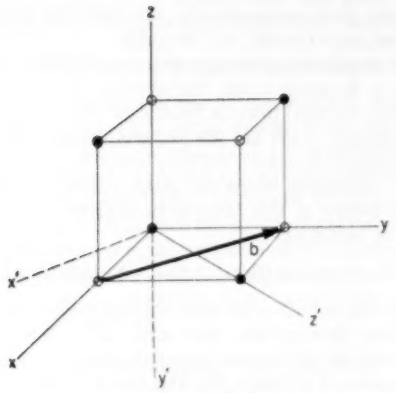

FIG. 2. (001) slip plane, [$\bar{1}$10] Burgers vector.

tribution of an infinite body and arbitrarily cut off integrals at some distance roughly corresponding to the mean distance between dislocations in the real crystal. In an actual well-annealed crystal, the dislocations are probably far from randomly distributed, and, because of the long-range nature of the stress distribution, a particular model may give somewhat different energy values than the ones we have derived.

The calculations were essentially numerical in form, and, with low-temperature elastic constants, were performed for each ten-degree increment in θ from 0° to 90°. The results show a monotonic transition in the value of the energy between the edge ($\theta=0$) and the screw ($\theta=\pi/2$). The results are shown in Table I. E_{80} is given in electron volts per atomic distance along the dislocation line. For NaCl, "atomic distance" is 2.81×10^{-8} cm. The quantity R is the outer cut-off radius discussed above; r_0 is the inner cut-off radius, and corresponds to the limit of elasticity theory; in other words, r_0 is the size of the core of the dislocation.

The results can be approximately represented with a simple cosine variation,

$$E_{80}=(0.454+0.061\cos2\theta)\ln(R/r_0), \qquad (2)$$

with a maximum error of about two percent, which is not much greater than the error of the calculation itself.

We have only made calculations of elastic energy for two values of θ, $\theta=0$ and $\pi/2$, for the temperature 1000°K. We assume that in this case also the variation between the screw and the edge is simple, and using the cosine law above, we find

$$E_{1000}=(0.214+0.032\cos2\theta)\ln(R/r_0). \qquad (3)$$

In a later section, the contribution of the cores of edge and screw dislocations will be added to these values to yield the final strain energy.

B. Elastic Calculations on Other Planes

In order to provide a comparison with other slip planes, we have made calculations for the situation illustrated in Fig. 2. The Burgers vector remains the same as before, but the slip plane is (001). The calculations reported above, when repeated for this case with the same temperatures as before, give for the energy of the edge dislocation,

$$E_{80}=0.456\ln(R/r_0), \quad E_{1000}=0.267\ln(R/r_0). \qquad (4)$$

Note that the corresponding screw dislocation in this case is precisely the same as for the (110) slip planes discussed earlier.

Referring either to Fig. 1 or Fig. 2, one sees that the (110) and (001) planes are only two out of an infinite family of planes which contain the same Burgers vector b. For the sake of completeness, one would like to know the energy of dislocations in these planes where slip is not observed. We have made calculations of the elastic energy of pure edge dislocations in planes inclined at various angles to the observed slip plane. In Fig. 1, if one lets the Burgers vector point in the x' direction, then as θ varies from 0 to $\pi/2$, the slip plane varies from (110) to (001). The elastic energy of pure edge dislocations as a function of slip plane is given in the following Table II for the temperature 80°K. Note that the variation in the elastic energy is again monotonic, and is quite small. We will show later that the core energy probably overbalances the difference in elastic energy shown here between the (110) and (001) slip planes. Since core calculations have been made only for the extreme (110) and (001) types, one cannot predict the actual variation between the two extremes, except to say that the variation in energy of the core is the dominant factor.

The screw dislocation corresponding to each edge dislocation in the above table is in all cases the same, namely the one discussed in Sec. A.

There remains the question of how the dislocation energy varies as one goes from pure edge to pure screw in one of these planes. Only one such calculation has been made, a half-edge, half-screw dislocation whose slip plane is (010). This particular dislocation is discussed later, and its elastic energy is given in Eq. (7).

It is interesting to consider the possibility of other types of Burgers vectors than the [110] in NaCl, even though there seems to be no experimental evidence for them. Calculations of a screw and an edge dislocation with Burgers vectors of type [002] were made with elastic constants appropriate for 80°K and 1000°K. The two types of dislocation considered are shown in Fig. 3.

TABLE II. Elastic energy of pure edge dislocations as a function of slip plane.

θ	0°	10°	20°	30°	40°	50°	60°	70°	80°	90°
$\frac{E_{80}}{\ln(R/r_0)}$	0.508	0.505	0.499	0.490	0.480	0.471	0.463	0.456	0.457	0.456

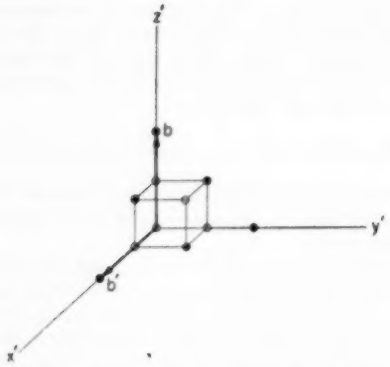

FIG. 3. Large dislocations. The figure shows one edge dislocation and one screw dislocation with the Burgers vectors [002] and [200], respectively. The edge dislocation has a slip plane (010). The dislocation line, in each case, is in the z' direction.

The energies, in the same units as before, were:

$$\begin{aligned}&\text{Edge: } E_{80}=1.013\ln(R/r_0),\quad E_{1000}=0.492\ln(R/r_0).\\&\text{Screw: } E_{80}=0.586\ln(R/r_0),\quad E_{1000}=0.442\ln(R/r_0).\end{aligned}\tag{5}$$

Note that in this case the dislocation Burgers vector reaction

$$\begin{aligned}&[002]\rightarrow[011]+[0\bar{1}1]\\&[002]\rightarrow[101]+[\bar{1}01]\end{aligned}\tag{6}$$

may take place, in which the "large" dislocation breaks up into two component dislocations with the Burgers vectors $[0\bar{1}1]$ and $[011]$. If the energy of the two component dislocations taken together is smaller than the energy of the "large" dislocation, then the breakup will take place spontaneously; otherwise the large dislocation, once formed, will be stable.

The details of the breakup process are shown in Figs. 4 and 5. In order to test the stability with respect to breakup, we need to know the energy of the decomposition product which has the Burgers vector [101] and runs in the z' direction. We have here a half-edge, half-screw, dislocation whose slip plane is (010). The elastic strain energy of this dislocation is given in the same units as before by

$$E_{80}=0.401\ln(R/r_0),\quad E_{1000}=0.233\ln(R/r_0).\tag{7}$$

(Note that in both cases these energies are intermediate in value between the pure edge and screw types.) The stability of the two types of dislocations is best demonstrated in Table III. The first column gives the type of large dislocation, either screw or (010) edge. The third column of Table III gives the elastic strain energy divided by the logarithm term. The large dislocation is stable with respect to breakup if the number in column 4 is larger than the number in column 3. The log factor for the large dislocation is approximately the same as the log factor for the small component. For the large dislocation, r_0 is about two times the r_0 of the small dislocation, because the cutoff has to be taken in each case where the strain is small. However, when the large dislocation breaks up into two, the free area for each dislocation has been effectively cut in half, and hence R for the large dislocation is also about two times the R for the small one. Note that at both the low and high temperatures, the edge is apparently unstable with respect to breakup into either type of component. The screw at first sight seems to be stable. However, since the two energies are so close together, the core energy will be the decisive quantity. One would expect the core energy of the large core to be slightly larger than the combined core energy of the components. Since screw elastic energies per unit length are less than those of

FIG. 4. Breakup of a "large" edge dislocation in a (010) slip plane. The Burgers vector of the large dislocation is [200], and the line of the dislocation is in the z' direction. Two reactions are possible:

$$\begin{aligned}&[200]\rightarrow[101]+[10\bar{1}],\\&[200]\rightarrow[110]+[1\bar{1}0].\end{aligned}$$

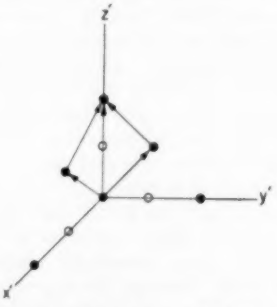

FIG. 5. Breakup of a "large" screw dislocation. The Burgers vector of the large screw dislocation is [002]. Two possible decompositions are possible:

$$\begin{aligned}&[002]\rightarrow[011]+[0\bar{1}1],\\&[002]\rightarrow[101]+[\bar{1}01].\end{aligned}$$

edge dislocations, it is unlikely that any other large dislocations will be more stable than [002] screws.

III. DISLOCATION CORE ENERGIES IN NaCl

To study the dispositions of the atoms in the core region and the associated stress energy, it was advisable to choose a substance where the forces between the atomic constituents were well known and of short range type. The alkali halides are well suited to the problem since one has to deal with the electrostatic forces and, at close range, the repulsive forces of the closed shells. The electrostatic forces are short range also except where logarithmic potentials from rows of ions of the same sign are involved.

A. Edge Dislocation: (110) Slip Plane

The first step in the procedure was to use the displacements predicted by the isotropic elastic solution, even in the core region where they were no longer valid. If the x axis is taken along the slip direction and the y axis along the normal to the slip plane, then u and v the respective components of the displacements along

TABLE III. Stability of large and small dislocations.

Parent type	Temperature	$E_{\text{large}}/\ln(R/r_0)$	$2(E_{\text{small}})/\ln(R/r_0)$	Component type	Stability
Screw	1000°K	0.442	0.466	Mixed (100)	?
Screw	80°K	0.586	0.802	Mixed (100)	Stable
Edge	1000°K	0.492	0.492	(110) edge	Unstable
Edge	1000°K	0.492	0.466	Mixed (100)	Unstable
Edge	80°K	1.016	1.016	(110) edge	Unstable
Edge	80°K	1.016	0.802	Mixed (100)	Unstable

these axes are given by

$$u=\frac{b}{2\pi}\left[\tan^{-1}(y/x)+\left(\frac{\lambda+\mu}{\lambda+2\mu}\right)\frac{xy}{r^2}\right],$$
$$v=\frac{b}{2\pi}\left[-\frac{\mu}{\lambda+2\mu}\log r+\left(\frac{\lambda+\mu}{\lambda+2\mu}\right)\frac{y^2}{r^2}\right], \tag{8}$$

where b is the slip distance and λ and μ are the familiar elastic Lamé constants for an isotropic substance. This sets up a dislocation where the material is compressed for $y>0$ and extended for $y<0$.

In developing the elastic displacements for the various ion rows, it was found expedient to arrange them symmetrically about the yz-plane perpendicular to the direction of slip. Two such arrangements were considered: Configuration I with the symmetry plane passing through two adjacent ion rows on opposite sides of the dislocation center (Fig. 6), and Configuration II with the plane of symmetry half way between the four ion rows nearest the dislocation center (Fig. 7). For slip on the (110) plane the edge dislocations lie parallel to [001] and perpendicular to the slip direction. In the [001] direction, the signs of the ions alternate.

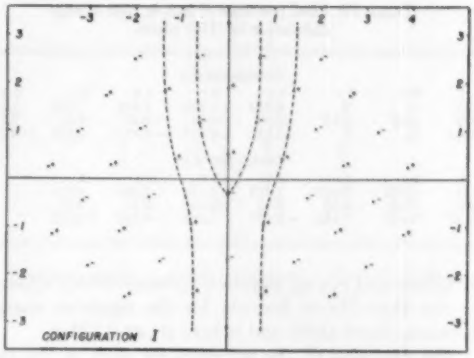

FIG. 6. Edge dislocation for slip in (110) plane—Configuration I.

The electrostatic potential of a row of alternately charged particles, spaced a distance a apart is given by[10]

$$\frac{2e}{a}\sum_{l=1}^{\infty} i\pi H_0\left(\frac{i\pi lr}{a}\right)\cos\left(\frac{2\pi lz}{a}\right). \tag{9}$$

Here e is the magnitude of the charge per ion. Distance from the row is measured by r and distance in the direction of the row by z. For application to NaCl a is 2.81 A. The H_0 is the Hankel function of zero order.

For the energy arising from the repulsion of closed shells a single expression was chosen to represent the interaction between next neighbor ions of opposite sign. The repulsion between like (negative) ions was neglected to keep the calculation as simple and, at the same time, as general as possible, in that the results would not appear as specific for a particular salt. By virtue of the equilibrium condition, the single force law could be written

$$W(x)=\frac{1}{6}\alpha_m\frac{e_\rho^2}{a^2}e^{-(x-a/\rho)}, \tag{10}$$

where α_m is the Madelung number for the NaCl

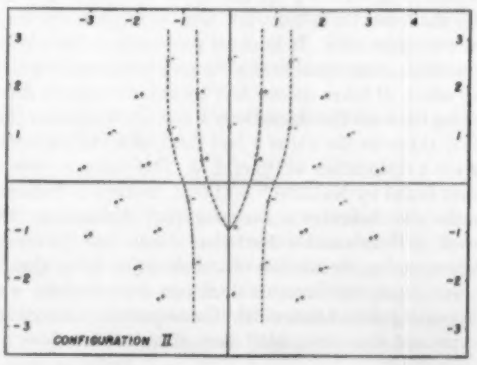

FIG. 7. Edge dislocation for slip in (110) plane—Configuration II.

[10] E. Madelung, Physik. Z. 19, 524 (1918).

TABLE IV. Final positions of ions in core of edge dislocation in (110) plane.

Configuration I							
s	0+	0−	2+	2−	4+	4−	6+
x/b	0	0	0.859	1.195	1.788	2.226	2.762
y/b	0.37	−0.29	0.29	−0.28	0.20	−0.32	0.17
$D(s)$	0	0	−0.141	0.195	−0.212	0.226	−0.238
Configuration II							
s	1+	1−	3+	3−	5+	5−	
x/b	0.431	0.633	1.315	1.710	2.268	2.732	
y/b	0.34	−0.28	0.25	−0.30	0.19	−0.33	
$D(s)$	−0.069	0.133	−0.185	0.210	−0.232	+0.232	

structure and ρ is an empirical constant which appears in the Born-Mayer formula for the repulsion energy between closed shells and is here set at 0.325 A.

The positions of the ion rows for each of the two configurations were next adjusted to a closer approximation by requiring that the interaction of each row with its nearest neighbors and next nearest neighbors be minimized. The procedure was to begin with those rows nearest the center of the dislocation, where the elastic displacements would be most inaccurate, and proceed outward. Except for those rows directly adjoining the dislocation center the displacement corrections were small, of the order of 3 or 4 percent of the interatomic distance, a. The final disposition of the ion rows for both configurations is shown in Fig. 6 and Fig. 7, respectively.

In Table IV are given the final x and y coordinates of the ions directly above and below the slip plane in units of the Burgers vector, $b=\sqrt{2}a$, for both configurations. The ions are indexed by the s number, where $sb/2$ measures the distance to the right or left of the dislocation center at which the ion would be located if no strains were present. The plus or minus sign following the s number indicates whether the ion lies in the upper (compressed) or lower (expanded) half-plane. After the manner of Nabarro[11] we define a displacement function,

$$D(s)=x/b-s/2,$$

where $D(\pm\infty)=\mp\frac{1}{4}$ for the upper half-plane and $\pm\frac{1}{4}$ for the lower half-plane. The form of D gives the shape of the dislocation. It is usual to ascribe a "width" to the dislocation equal to the distance between the points at which D takes on one half its values at $\pm\infty$. Averaging between Configurations I and II, it appears that $|D|$ takes on the value $\frac{1}{8}$ just short of $x=0.75b$, which gives a dislocation width of $1.5b$. This value is close to that found by Nabarro,[11] $b/(1-\sigma)$, where σ is Poisson's ratio and indicates a very compact dislocation. The work of Peierls and Nabarro has shown that the energy hill opposing the motion of a dislocation lying along a crystallographic direction decreases exponentially with increasing dislocation width. Consequently, Cottrell has expressed the viewpoint[12] that actual dislocations are probably broader than $b/(1-\sigma)$ if one is to account for the low observed yield stress in well annealed single crystals. The actual forms for such dislocations have been examined by Foreman, Jaswon, and Wood.[13] It is somewhat disturbing to find this dislocation so compressed. The displacements arising from energy minimization have nevertheless broadened the dislocation appreciably.

The stored energy of the dislocation inside any cylinder coaxial with its center can be determined next from the results of minimizing the energy. (Minimization in general reduced the stored energy by about a factor of $\frac{1}{2}$.) One takes all the interaction energies between rows inside the cylinder and adds to it a half of the interaction energies between rows inside and outside the cylinder. In this way one obtains the stored energy content of cylinders containing a symmetric grouping of rows. In Configuration I, these groupings contained 2, 10, 20, and 24 rows respectively; for Configuration II, 6 and 18. In Fig. 8, the energy content of the cylinders is plotted in units of ev/plane *vs* the cylinder radius R. The radius of the equivalent cylinder is established by

$$\pi R^2=na^2, \tag{11}$$

where n is the number of rows inside the cylinder. From this curve one could obtain the energy of the dislocation core ideally by fitting the curve with the formula

$$E(R)=A\ln(R/a)+B. \tag{12}$$

Actually, one uses instead the value for A, 0.508 ev

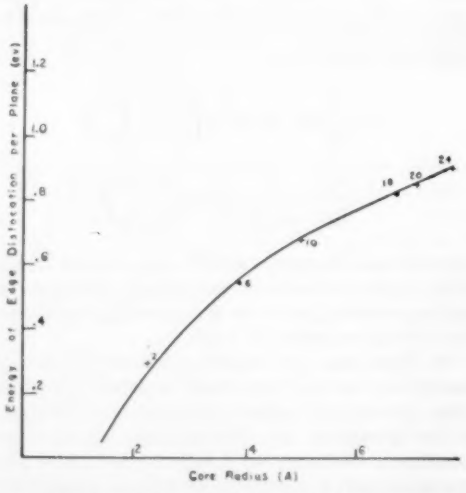

FIG. 8. Edge dislocation for slip in (110) plane—energy *vs* R. Plus signs refer to Configuration I, open circles to Configuration II; nearby numbers show how many ion rows inside cylinder of radius R. Smooth curve is plot of Eq. (12).

[11] F. R. N. Nabarro, Proc. Phys. Soc. (London) **59**, 257 (1947).
[12] A. H. Cottell, *Progress in Metal Physics* (Butterworth Publications, London, 1949), Vol. I, p. 91.
[13] Foreman, Jaswon, and Wood, Proc. Phys. Soc. (London) **64**, 156 (1951); further modification in the Peierls-Nabarro dislocation will shortly be presented by one of us (H.B.H.).

per plane obtained from elastic considerations in Sec. A and fits at the point for greatest R, giving $B=0.392$ ev per plane. The solid line in Fig. 8 is the plot of Eq. (12). It fits the points very well, fortuitously so, because the simplified force model used here, with repulsion only between ions of opposite sign, does not accurately reproduce the elastic constants.

B. Screw Dislocation

The treatment of the screw dislocation likewise involves consideration of two distinct configurations, which we show as Configurations III and IV in Figs. 9 and 10 respectively. They correspond to a screw dislocation along the slip direction $[110]$, so that the ion rows are all composed of ions of the same sign. In Configuration III, the dislocation lies symmetrically at the center of a rectangular prism formed by alternative positive and negative ion rows at the corners. In Configuration IV the dislocation has moved a distance $b/2\sqrt{2}$ along the $[001]$ direction, as would occur for slipping in the $(1\bar{1}0)$ plane. It can be seen that the ion rows are arranged in an alternating rectangular array. Those rows marked by full circles have ions in the plane of the paper, those marked in broken circles have ions in planes above and below the plane of the paper. Individual ion rows will be designated by the numbers along the center lines with abscissa index coming first (e.g., 1, −3 denotes negative row at bottom of Fig. 9 with ions above and below the plane of the figure). The

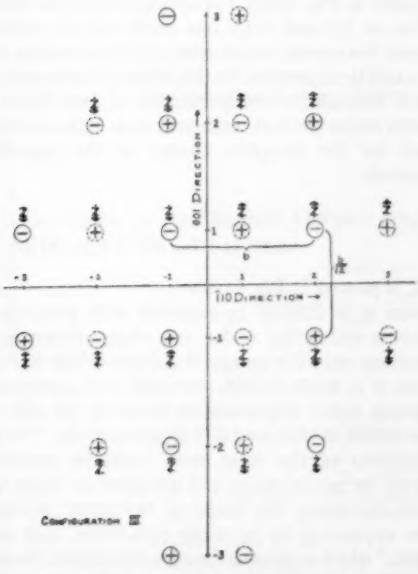

FIG. 9. Screw dislocation—Configuration III. Solid circles denote rows which initially had ion in plane of paper, dashed circles for rows with ions initially $b/2$ above and below the plane. Arrows with superimposed Z indicate direction of $\epsilon_{z\theta}$, the relaxation displacement perpendicular to the paper.

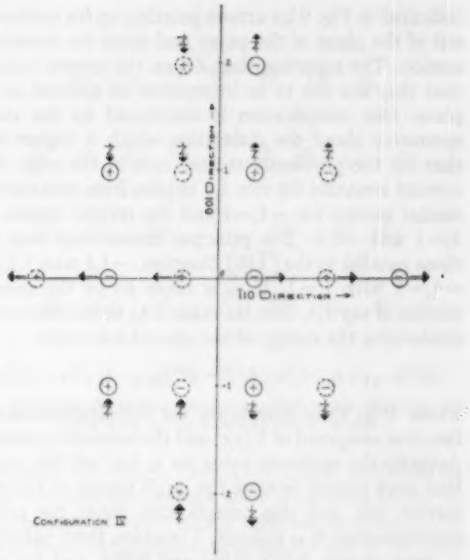

FIG. 10. Screw dislocation—Configuration IV. Same notation as Fig. 9. Outward displacement of ion rows denoted by simple arrow.

distance between rows in the $[\bar{1}10]$ direction is $b/2$, in the $[001]$ direction $b/\sqrt{2}$.

For the interaction energies between the rows the same ion-core repulsion expression, Eq. (10), is used as for the edge dislocation of the preceding section. This interaction is mainly important between rows separated by $b/2$ in the $[\bar{1}10]$ direction. Here every ion in one row is in contact with two ions in the adjoining row, one from the plane above and the other from the plane below. For the electrostatic interaction one uses again a formula due to Madelung[10]

$$V(z,r)=4e/b[\sum_{l=1}^{\infty} K_0(2\pi lr/b)\cos(2\pi lz/b)-\tfrac{1}{2}\ln 2b/r] \quad (13)$$

for the potential at a point a distance r from a line of charges e spaced a distance b apart. The variable z is measured parallel to the line of like charges, with one of the charges at the origin.

The displacements caused by an elastic screw dislocation are simply

$$\epsilon_{z\theta}=b\theta/2\pi,$$

where we have taken θ to be measured counterclockwise from the $[\bar{1}10]$ direction and z is measured + up from the paper. Since the dislocation at this stage introduces only changes in z, the $\ln r$ terms in the electrostatic potential expression are unaffected and the calculation of the stored energy depends only on short-range interactions as before.

For Configuration III, it turns out that the relaxations are principally z-ward motions. These have been

indicated in Fig. 9 by arrows pointing up for motion up out of the plane of the paper and down for downward motion. The superinscribed Z's on the arrows indicate that they are not to be interpreted as motions in the plane. One complication is introduced by the radial symmetry about the dislocation which is higher than that for the previously treated case of the edge. Any upward z-motion for row 1,1 implies from symmetry a similar motion for $-1,-1$ and the reverse motion for $1,-1$ and $-1,1$. The principal interactions here are those parallel to the $[\bar{1}10]$ direction, $-1,1$ with 1,1 and $-1,-1$ with $1,-1$. If ϵ_z is taken to be the upward motion of say 1,1, then its value is to be determined by minimizing the energy of the central four rows,

$$2U(z_{-1,1}-z_{1,1}-2\epsilon_z; b/2)-2U(z_{1,1}-z_{2,1}+\epsilon_z; b/2),$$

where $U(z; r)$ is written for the complete interaction function composed of $V(z,r)$ and the ion-core repulsions. Actually the optimum value for ϵ_z for just the central four rows proved to store too much energy in the rows farther out, and this complication made the precise determination of ϵ_z difficult. Therefore, three values for ϵ_z were chosen, $0.05b$, $0.06b$ and $0.07b$, and for each the optimum values were found for the z-displacements of the other rows. (The results appear later in Fig. 12.) The possibility of outward relaxation in the $[\bar{1}10]$ direction was also investigated after the manner described in the next paragraph, but it was found that there was no appreciable outward relaxation after a z-relaxation of $0.05b$. It is possible that simultaneous variation of ϵ_z and ϵ_r might have given a slightly lower energy minimum at appreciably different coordinates but the labor involved in such a program would have been very considerable. In Table V are given the values of the z displacements for the other ion rows of Configuration III, largely independent of ϵ_z for the central rows.

For Configuration IV, the outward radial displacement of 1,0 and $-1,0$ is particularly important since z-displacements of these rows are ruled out by symmetry. Therefore the technique of investigating this relaxation, which requires some comment, will be discussed here. The variations with r of the first term in Eq. (13) for particular values of z was made available for reference in graphical form. The part of $V(z,r)$ involving $\ln r$ is more difficult to treat, since it is a long range interaction. One needs to know the change in potential energy of a rectangular array of line charges

TABLE V. Z-displacement for outer ion rows in a screw dislocation.

	Configuration III			
Ion row index	2,1	1,2	3,1	2,2
Z-displacement, ϵ_z	$0.06b$	$0.015b$	$0.03b$	$0.02b$
	Configuration IV			
Ion row index	1,1	2,1	1,2	3,1
Z-displacement, ϵ_z	$0.03b$	$0.02b$	$0.01b$	$\sim 0.02b$

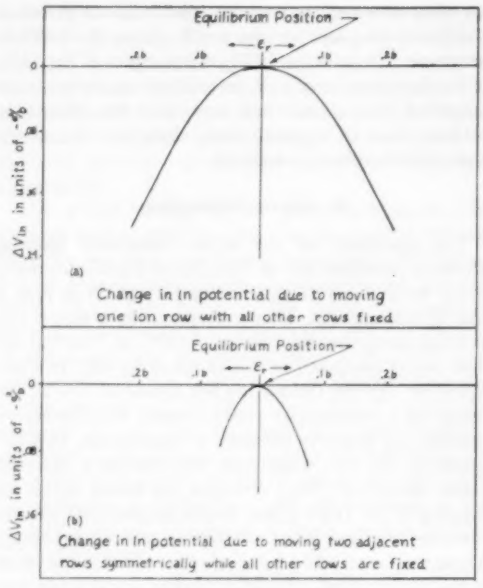

FIG. 11. Variation of ln potentials with ϵ_r.

with alternating sign when one of the array is displaced from its equilibrium position in the direction of one of its neighbors. An expression for this quantity, valid for small displacements, is developed in Appendix I and displayed in Fig. 11(a). For application to the coupled motion of 1,0 and $-1,0$ one needs also to take into account the mutual interaction of the two moving rows. The analytic expression for this interaction is equivalent to the formula for the interaction of two dipole line charges and is given as the second term in the expression below for the complete change in the logarithmic potentials

$$\Delta V_{\ln}=(-2e/b)\{4.756(\epsilon_r/b)^2 +\ln[(1+2\epsilon_r/b)^2/(1+4\epsilon_r/b)]\}. \quad (14)$$

$\Delta V_{\ln}$ is plotted in Fig. 11(b).

Here it is difficult to establish with precision the optimum value for ϵ_r for the whole dislocation by examining only the energy of 1,0 and $-1,0$. For three values of ϵ_r, $0.05b$, $0.055b$, and $0.06b$, the corresponding optimum radial displacements for rows 2,0 and $-2,0$ were $0.010b$, $0.011b$, and $0.012b$ respectively. The z-displacements of the other rows could be determined directly by minimization and are given in Table V.

For discussing the shape of the screw dislocation there appears to be no single parameter, such as the "width" which applies to the edge dislocation. However, the z-relaxations for Configuration III have altered it markedly from the symmetric dislocation of elastic theory. It is now anisotropic and the shear strain in the $(1\bar{1}0)$ plane has been increased at the expense of the

strains in the (001) plane. This distortion tends to lower the barrier for dislocation motion in the (001) plane and conversely raise it for motion in the (1$\bar{1}$0) plane. Again the radial motions of central rows of the Configuration IV tend to reduce the shear strain in the (001) plane and to spread out the dislocation along the [$\bar{1}$10] direction.

The energy results for the screw dislocations are summarized in Fig. 12, where the presentation is closely analogous to Fig. 8 for the edge dislocation. For Configuration III, cylindrical groupings of 4, 12, and 24 rows give 3 values for R for which energy points are plotted for various ϵ_s. Here $R=(n/\pi\sqrt{2})^{\frac{1}{2}}a$. Likewise, Configuration IV gives 3 points for groupings of 2, 8, and 18 rows. The energy curves before relaxation are also shown and it can be seen that the total energy for the twenty innermost rows was decreased by relaxation in the case of Configuration IV by about 65%, in the case of Configuration III by about 35%. Fitting to an equation of the form of Eq. (12) one uses for the coefficient of the elastic term the value of 1.37×10^7 ev/cm found in Sec. A and finds for the constant term 0.38×10^7 ev/cm. These numbers in Eq. (12) give the smooth curve shown in Fig. 12.

C. Edge Dislocation for Slip in the (100) Plane

The elastic results of Sec. II raise a question as to how dislocation theory can account for the observed

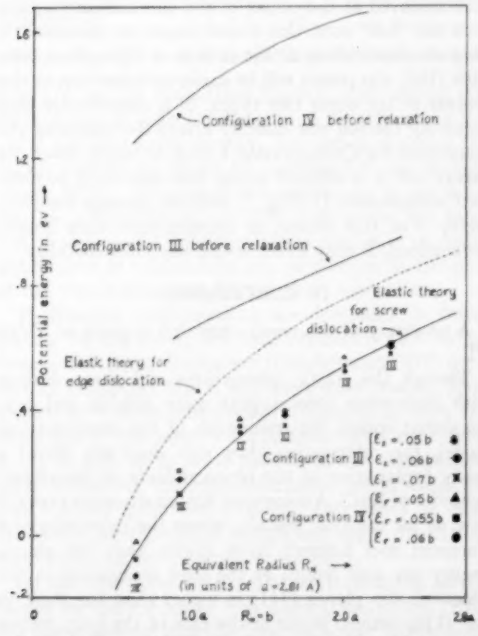

FIG. 12. Screw dislocation—energy vs R. Dotted line gives analogous curve for edge dislocation in (110) plane. Upper lines dicate approximate energies before relaxations.

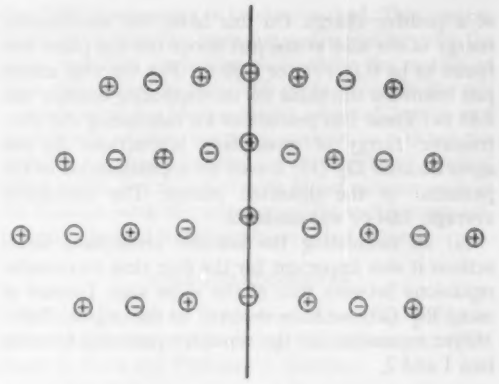

FIG. 13. Edge dislocation for slip in (100) plane. Positions are those given by the isotropic elastic theory.

preference for slip in the (110) planes exhibited by alkali-halide single crystals, since the elastic energy for an edge dislocation for slip in these planes is some 20% higher than for the edge dislocation for slip in the (100) planes. It is uncertain whether the active slip system is determined by the requirement of lowest barrier for dislocation motion or smallest energy per unit length for the appropriate edge dislocation. Believing that the second criterion might be important, we have attempted to estimate the core energy for the edge dislocation for (100) slip. This dislocation is shown in Fig. 13 with ion rows distributed according to the isotropic elastic solution, Eq. (8). One must be content with much more approximate methods here because of the disordered array of positive and negative rows. There is then no easy way to take into account exactly the effect of the long-range log terms. Instead, we have evaluated only a finite number of these, including arbitrarily only nine rows on each side of the slip plane. In estimating the energy of the dislocation four terms were taken into account (i) electrostatic interactions across the slip plane, (ii) ion-core interactions across the slip plane, (iii) short range interactions on the same side of slip plane, and (iv) logarithmic interactions on the same side of the slip plane.

(i) As a first step x-displacements only, corresponding to the elastic dislocation, Eq. (8) were considered. (Effect of y-displacements is small.) Because of complexities no attempt was made to apply variational refinements later. The electrostatic interactions across the slip plane were estimated by considering each atom in the plane directly above the slip to be in the field of a plane of alternating charges arranged in a square array at a distance a below. This potential is given by[10]

$$V(x,y,z)=(e/a)\exp(-\pi z/a)\times\cos(2\pi x/a)\cos(2\pi y/a), \quad (15)$$

where x and y are coordinates in the plane and z is perpendicular to the plane with the origin at the site

of a positive charge. On this basis, the electrostatic energy of the nine atoms just above the slip plane was found to be $0.24\ e^2/a$, or 1.20 ev. For the nine atoms just below the slip plane the corresponding number was 0.88 ev. These two procedures for calculating the electrostatic energy of cross-plane interactions do not agree because Eq. (15) is only an approximation to the potential of the distorted planes. The arithmetic average, 1.04 ev was assumed.

(ii) In calculating the ion-core cross-plane interactions it was important for the first time to consider repulsions between ions of the same sign. Instead of using Eq. (10) we have reverted to the original Born-Mayer expression for the repulsive potential between ions 1 and 2,

$$W'(x) = 10^{-12} \text{ erg} \exp[-(x-r_1-r_2)/\rho], \qquad (16)$$

where the r_i are the radii of the ion cores. Huggins and Mayer's values[14] were used; for sodium 0.875 A and for chlorine 1.475 A. The dislocation displacements increased the repulsions of the Cl−Cl bonds by 0.49 ev and lowered the repulsions of the Na−Cl bonds by 0.39 ev, giving a net increase of 0.10 ev for the cross-plane repulsions.

The Cl−Cl interaction depended slightly on configuration, i.e., on whether the dislocation center lay between two Cl ion rows or two Na ion rows. For the case of no relaxation allowed the difference was evaluated as 0.02 ev, i.e., the amount by which the chlorine-centered configuration lies above the sodium-centered configuration. It is rather unusual to be able to distinguish so clearly by numerical rather than analytic methods, the change in energy of a dislocation in moving half a lattice translation along the slip plane. The minimum resolved shear stress for a slowly moving dislocation to surmount such a sinusoidal barrier would would be 2.2×10^9 dynes/cm^2, or over a thousand times the observed critical shear stress for annealed single crystals. While this value might be greatly reduced in the process of relaxation, it seems doubtful whether the edge dislocations in the (100) slip plane will be mobile for the range of critical shear stress that is experimentally observed.

(iii) The short-range interactions between adjacent rows on the same side of the slip plane is made up of the nonlog term in Eq. (13) and the ion-core repulsions [Eq. (16)], using $z=b/2$. Since the interactions were both repulsive, the energy in the upper half rose by 1.16 ev. Correspondingly, the energy of the ion rows below the slip plane fell by 0.64 ev, leaving a net 0.52 ev.

(iv) The logarithmic terms were calculated separately for both groups of ions. Labor was decreased and accuracy improved by taking analogous pairs above and below together and obtaining the logarithm of the ratio of the distances. The resultant of these terms is −0.31 ev.

[14] M. L. Huggins and J. E. Mayer, J. Chem. Phys. 1, 643 (1933).

Combining the results from all four parts, one obtains 1.73 ev/plane for this edge dislocation. This result may be in error by as much as 50 percent, not only because of the approximate methods used, but also because no variation of the position parameters has been employed to minimize the energy. Also, the selection of ion rows included has not been as systematic as before where the use of the concentric cylindrical surfaces made possible fitting to the elastic solutions at large R. If one takes 1.9 ev as the energy of 16 rows with $R=1.9a$, then the constant term for this dislocation (energy for $R=a$) is 1.5 ev, where the coefficient of $\ln(r_1/r_0)$ is taken to be 0.644 ev per plane (Tables II or VI).

It has been suggested[15] that since the dislocations in NaCl have a Burgers vector which is slightly larger than the shortest distance between neighbors in the crystal, the cores of some types may be hollow.[16] We may make an estimate of the size of the hollow by considering the crystal as a continuum, and assuming that the deleted material creates a surface tension. The radius of the hollow, if we use the elastic energies calculated earlier, turns out to lie between $\frac{1}{2}$ and 1 atomic distances for each of the three main types of dislocations possessing Burgers vector [110]. Hence the question essentially becomes one of determining the core configuration by means of r-wise relaxation. The work reported earlier shows that the "full" dislocation is at least a local minimum for displacements. However, calculations have not been done where a single line of atoms has been removed at the center of the core for comparison with the "full" core. One would expect on electrostatic grounds that hollows at the centers of dislocation lines with (110) slip planes will be easier to form than at the centers of the other two types. It is conceivable that removing the ion row directly above the center of the dislocation for Configuration I (Fig. 6) might lower the energy but it is difficult to see how this could be done for Configuration II (Fig. 7) without altering the symmetry. For this reason, it appears that such hollow dislocations, if they exist, would have low mobility.

IV. CONCLUSIONS

A summary of the results reported is given in Table VI.

Though the elastic calculations and those dealing with dislocation cores appear quite reliable and self-consistent within the framework of the mathematical model, the information they give does not afford a ready explanation of the physical facts of the plastic behavior of NaCl. A somewhat similar situation prevails here as for the f.c.c. metals, where the calculations of Foreman and Lomer[17] have shown that the elastic energy per unit length of the edge dislocation in the observed slip planes (111) is higher than for those in the (110) planes. While in the case of the f.c.c. metals

[15] J. S. Koehler (private communication).
[16] F. C. Frank, Acta Cryst. 4, 497 (1951).
[17] A. J. E. Foreman and W. M. Lomer, Phil. Mag. 46, 73 (1955).

TABLE VI. Dislocation energies—values for A and B [see Eq. (12)].

	Slip plane	Burgers vector	A ev/plane	A 10^7 ev/cm	B ev/plane	B 10^7 ev/cm
80°K						
Edge	(110)	[110]	0.508	1.81	0.39	1.37
Edge	(100)	[110]	0.644	1.62	1.5	3.8
Screw		[110]	0.544	1.37	0.15	0.39
Edge	(010)	[002]	1.016	3.62		
Screw		[002]	0.586	2.09		
1000°K						
Edge	(110)	[110]	0.246	0.875		
Edge	(100)	[110]	0.377	0.950		
Screw		[110]	0.257	0.648		
Edge	(010)	[002]	0.492	1.75		
Screw		[002]	0.442	1.57		

the existence of extended dislocations in the (111) planes is the probable explanation of the preference for slip on these planes, there is little likelihood that extended dislocations are important for alkali halides.

Though a higher value for the dislocation core energy for the (100) slip plane seems clearly indicated from the preceding section, the difference might be considerably reduced by minimization. If one accepts the result calculated for the (100) cores at its face value and cuts off the logarithm term in the elastic energy at a value R corresponding to the distance between dislocations, then one finds that the difference in energy per unit length between the (100) and the (110) dislocations is

$$E_{100}-E_{110}=[2.4+0.19\ln a(\pi N)^{\frac{1}{2}}]\times 10^7 \text{ ev/cm}, \quad (17)$$

where N is the dislocation density. The energy difference goes to zero for N equal to $4\times 10^9/\text{cm}^2$, a low value for dislocation density. For higher densities the energy difference would be positive but varies only slowly with N. In view of the uncertainty in the value for the core energy of the (100) dislocation, the small size of the energy difference found here is of doubtful significance in establishing any preference on the part of the edge dislocations for the (110) slip planes.

If dynamic considerations are dominant in determining the slip plane, one would naturally look to the form of the screw dislocation (Configuration III) for a hint as to the direction it will move most readily. Here the evidence from our model is disquieting since the distortion of the screw's shape from cylindrical symmetry is such as to favor motion in the close-packed plane. Moreover, the edge dislocation core investigated here appears quite concentrated. This tends to raise the barrier for dislocation motion and hence the critical shear stress higher than one would like.

On the other hand the calculations do indicate a high barrier for the motion of edge dislocations in the (100) slip plane, arising from the large repulsive interactions of the closed shells of the anions. In the limit in which one neglects the presence of the alkali atom altogether the (100) plane ceases to be close-packed. This concept provides an intuitive basis for understanding why the anion repulsion prejudices so strongly the motion of edge dislocations in the (100) plane. Though the calculated value for barrier height reported here is not particularly reliable, the result appears to rule out the mobility of these dislocations at the lower applied stress levels. For materials with larger cations, such as the thallous salts, the situation might well become sufficiently changed to favor slip on other planes.

ACKNOWLEDGMENTS

It is a pleasure for the last-named author (R.T.) to acknowledge many stimulating discussions with Professor F. Seitz and Professor J. Koehler.

APPENDIX I. SUMMATION OF Ln POTENTIALS

We wish to develop an expression for the electrostatic potential of a rectangular array of parallel line charges, the lines being alternately positive and negative. The pattern of points formed in a plane perpendicular to the line charges will be an interlocking, face-centered lattice. In particular we are concerned with the curvature of the potential along the principal rectangular axes as experienced by one line charge moving in the field of all the others. Let the equilibrium position of this line be the origin, and, if the translation distances are $2f$ and $2g$, then the radial distance to any other particular line charge is given by

$$r=\{(ng)^2+(mf)^2\}^{\frac{1}{2}}, \quad (A\text{-}1)$$

when the integers n and m are the coordinates of the second line charge in the lattice. At a point ϵ from the origin along the f axis the potential is

$$V(\epsilon)=-2q\sum_{n=-\infty}^{\infty}\sum_{m=-\infty}^{\infty}(-1)^{n+m}\ln[(ng)^2+(mf-\epsilon)^2]^{\frac{1}{2}}, \quad (A\text{-}2)$$

where q is the charge per unit length, if $\epsilon \ll f$

$$\Delta V=V(\epsilon)-V(0)$$

$$\cong q\sum_{n=-\infty}^{\infty}\sum_{m=-\infty}^{\infty}(-1)^{n+m}\left[\frac{-2mf\epsilon+\epsilon^2}{r^2}-\frac{2m^2f^2\epsilon^2}{r^4}\right]. \quad (A\text{-}3)$$

The linear term in ϵ will drop out because its coefficient is odd in m. It can be shown[18] that

$$\sum_{n=1}^{\infty}\frac{(-1)^n}{n^2+k^2}=\frac{\pi}{2k}\operatorname{csch}(k\pi)-\frac{1}{2k^2}$$

and

$$\sum_{m=1}^{\infty}\frac{m^2(-1)^m}{(m^2+d^2)^2}=\frac{\pi}{4d}\left[\frac{\sinh(d\pi)-(d\pi)\cosh(d\pi)}{\sinh^2(d\pi)}\right]; \quad (A\text{-}4)$$

[18] For an ingenious method of handling such summations see M. R. Spiegel, J. Appl. Phys. 23, 906 (1952).

consequently

$$\Delta V \cong -qe^2\left\{\left[\frac{2\pi}{fg}\sum_{m=1}^{\infty}(-1)^m\frac{\operatorname{csch}(mf\pi/g)}{m}-\frac{2\pi^2}{12g^2}\right]+\left[\frac{4\pi^2}{12f^2}-\frac{2\pi}{fg}\sum_{n=1}^{\infty}\frac{(-1)^n}{n}\times\left(\frac{\sinh(ng\pi/f)-(ng\pi/f)\cosh(ng\pi/f)}{\sinh^2(ng\pi/f)}\right)\right]\right\}. \quad \text{(A-5)}$$

For present application, $q=e/b$, $f=b/2$ and $g=b/\sqrt{2}$ so that

$$\Delta V=-\frac{2e}{b}\left(\frac{\epsilon}{b}\right)^2\left\{\frac{\pi^2}{2}+2\pi\sqrt{2}\left[\sum_{n=1}^{\infty}\frac{(-1)^n}{n}\left(\operatorname{csch}\frac{\sqrt{2}\pi n}{2}+\frac{(\sqrt{2}\pi n)\cosh(\sqrt{2}\pi n)-\sinh(\sqrt{2}\pi n)}{\sinh^2(\sqrt{2}\pi n)}\right)\right]\right\}.$$

The series in the square bracket converges very rapidly so that the third term is 0.3% of the first. The final result is

$$\Delta V(\epsilon)\cong -4.76\frac{e}{b}\left(\frac{\epsilon}{b}\right)^2. \quad \text{(A-6)}$$

PHYSICAL REVIEW VOLUME 100, NUMBER 4 NOVEMBER 15, 1955

Longitudinal Photomagnetoelectric Effect in Germanium

JACK ARON AND GERHART GROETZINGER
Lewis Flight Propulsion Laboratory, National Advisory Committee for Aeronautics, Cleveland, Ohio

(Received June 27, 1955)

The emf developed parallel to the gradient of light absorption (Dember emf) in a germanium crystal is reduced by the application of a transverse magnetic field, the diminution being about 10% for a field of 5000 gauss. The size of the effect is approximately quadratic in the field up to about 2000 gauss, is then linear to 4000 gauss, and subsequently saturates.

IT was found earlier by one of us[1] that the photo-emf developed along the direction parallel to the gradient of light absorption in an illuminated cuprous oxide crystal[2] is reduced by the application of a (transverse) magnetic field. In view of the fact that germanium is one of the few elements which are intrinsic semiconductors it seemed of interest to determine whether such an effect exists in this material.

A piece of high-purity polycrystalline *n*-type germanium (resistivity: 50 ohm cm at room temperature)[3] of dimensions 8×8×5 mm was etched in a CP4 solution.[4] It was then placed between the poles of an electromagnet in such a way that the field was parallel to an 8-mm edge and that one of the 8×8 mm faces could be illuminated by a Bausch and Lomb Microscope Illuminator equipped with a 6-v, 18-amp bulb. A point contact of Inconel was held against each 8×8 mm face by spring pressure, the arrangement being such that the position of the point of each contact on the face could be altered. The emf between the two contacts was measured with a potentiometer. A difficulty in looking for the effect described above arises because application of a magnetic field transverse to the light gradient in germanium[5,6] produces an emf along a direction normal to both the field and the gradient. To reduce the contribution of this origin to the emf measured here with the field applied, the crystal was illuminated and the position of the contacts adjusted in such a fashion that the application of a low (250-gauss) magnetic field[7] in either direction produced essentially no change in the emf between them.

With the contacts thus aligned, it was found that the application of a sufficiently high magnetic field in either direction caused a decrease in the emf, e, between the

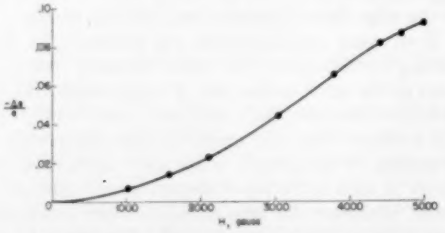

FIG. 1. Longitudinal photomagnetoelectric effect in germanium as a function of the magnetic field strength.

[1] G. Groetzinger, Physik. Z. **36**, 169 (1935); **36**, 216 (1935).
[2] H. Dember, Physik. Z. **33**, 207 (1932).
[3] We are indebted to Dr. M. Selker of the Clevite-Brush Development Company who kindly provided us with the germanium.
R. D. Heidenreich, U. S. patent No. 2619414 (1952).
[5] P. Aigrain and H. Bulliard, Compt. rend. **236**, 595 and 672 (1953).
[6] H. Bulliard, Phys. Rev. **94**, 1564 (1954).
[7] Since the effect sought can be expected to produce a change in the emf proportional to H^2 for small values of H while the interfering emf goes linearly with H, it follows that at sufficiently low values of H only the latter effect will be appreciable.

contacts. Figure 1 shows the size of the relative change $-\Delta e/e$ as a function of $|H|$ averaged for the two field directions for an incident light intensity of about 10^5 lux as measured by a Weston model 757 light meter. The value of e was 0.004 volt in zero field. The general shape of the curve is that to be expected for effects of this sort. For low fields, $-\Delta e/e$ appears to increase approximately quadratically with the magnetic field although the precision in this range is not sufficiently high to permit an exact establishment of the field dependence. The curvature subsequently decreases with increasing field and the relation finally becomes essentially linear between 2500 and 4000 gauss. Above 4000 gauss the slope of the curve diminishes steadily, indicating that $-\Delta e/e$ is approaching a saturation value. The size of the effect in germanium is quite large relative to that in cuprous oxide. In the latter substance, a field of 36 000 gauss decreased the emf by only 0.6%,[1] while in germanium the same percentage change is produced by a field less than 1000 gauss.

It seems desirable to modify the current nomenclature in order to distinguish between the two effects occurring in illuminated semiconductors exposed to a magnetic field. The development of an emf normal to both the light gradient and the magnetic field, first reported by Kikoin and Noskov[8] and Groetzinger,[1] which was called simply the photomagnetoelectric effect by Bulliard,[6] should be designated the transverse photomagnetoelectric effect; and the reduction in the emf parallel to the light gradient first reported by Groetzinger[1] should be called the longitudinal photomagnetoelectric effect or, more specifically in the present case, the longitudinal photomagnetoelectric effect in a transverse magnetic field. This terminology follows the usual convention[9] that the term "longitudinal" or "transverse" modifying the effect designates the relation between the direction of the effect and that of the primary agency.[10]

[8] M. Kikoin and N. Noskov, Physik. Z. Sowietunion 5, 586 (1934).

[9] A. H. Wilson, *The Theory of Metals* (Cambridge University Press, Cambridge, 1953), second edition, p. 209.

[10] Only in those cases in which the name of the effect already implies its longitudinal nature (as in magnetoresistivity) is the term "transverse" or "longitudinal" used to specify the direction of the magnetic field.

PHYSICAL REVIEW VOLUME 100, NUMBER 4 NOVEMBER 15, 1955

Conductivity, Hall Effect, and Magnetoresistance in *n*-Type Germanium, and Their Dependence on Pressure*

GEORGE B. BENEDEK, *Lincoln Laboratory, Massachusetts Institute of Technology, Lexington, Massachusetts*

AND

WILLIAM PAUL AND HARVEY BROOKS, *Division of Applied Science, Harvard University, Cambridge, Massachusetts*

(Received July 29, 1955)

Measurements of the electrical resistance, low-field Hall effect, and low-field longitudinal and transverse magnetoresistance in oriented samples of *n*-type germanium in which the carriers are all of one type have been carried out at 0°C as a function of pressure in the range 1–10 000 kg/cm² by using a nonmagnetic beryllium-copper high-pressure bomb. The experimental results are interpreted in terms of a low-field theory for *n*-type germanium in which the shape parameter $K=m_1/m_2$ of the energy ellipsoids and the dependence of the collision time τ on energy play a central role. The atmospheric-pressure data indicate that K at 0°C is probably different from the low-temperature cyclotron resonance value. Consideration of several possible forms of the energy dependence of τ leads to the adoption for lattice scattering of a phenomenological law of the form $\tau_L=(a/kT)\epsilon^{-p}$. It is found that the inclusion of the effects of even a small amount of impurity scattering plays a significant role in determining the magnitudes of the galvanomagnetic coefficients. By assuming a reasonable amount of impurity scattering in our samples it is possible to obtain an expression for $\tau(\epsilon)$ which is capable of producing the magnitudes of the galvanomagnetic coefficients as well as their temperature dependence. The variation of the galvanomagnetic coefficients with pressure is interpreted in terms of changes in K and the form of the dependence of τ on energy. In particular it is found that K decreases with increasing pressure, indicating that the application of pressure causes the energy ellipsoids to become less prolate. The change in the energy dependence of τ is interpreted in terms of a change in the exponent of the energy in the lattice scattering law.

INTRODUCTION

SINCE the determination of the variation of the energy gap in germanium with pressure,[1] much information both theoretical[3–4] and experimental[5,6] as to the energy-band structure of germanium has become

* The research reported in this document was supported jointly by the Army, Navy, and Air Force under contract with the Massachusetts Institute of Technology and by Harvard University.

[1] See W. Paul and H. Brooks, Phys. Rev. 94, 1128 (1954).

[2] F. Herman, Phys. Rev. 95, 847 (1954).

[3] M. Shibuye, Phys. Rev. 95, 1385 (1954).

[4] B. Abeles and S. Meiboom, Phys. Rev. 95, 31 (1954).

[5] Dresselhaus, Kip, and Kittel, Phys. Rev. 92, 827 (1953).

[6] Lax, Zeiger, Dexter, and Rosenblum, Phys. Rev. 93, 1418 (1954).

available. In the light of this new information the present experiments[7,8] examine the galvanomagnetic properties of *n*-type germanium using the application of high hydrostatic pressure as a means of varying the energy-band structure and thereby the galvanomagnetic coefficients themselves.

I. EXPERIMENTAL METHODS

The measurements were carried out using one of Professor P. W. Bridgman's presses,[9] to which was attached a nonmagnetic beryllium-copper "bomb" capable of containing pressures at least as high as 10 000 kg/cm². Samples obtained through the kindness of the General Electric Research Laboratories, and from the Lincoln Laboratory, Massachusetts Institute of Technology, were mounted inside the bomb by tying them with thread on a fiber support fixed onto the nose of a BeCu seven-terminal electrically insulating plug through which electrical leads are led into the bomb. Temperature stability was achieved by immersing the long BeCu bomb in a well stirred ice bath. Excessive ice melting was avoided by fastening around the neck of the bomb a collar, through which ice water cooled in a separate circuit was continually run, thereby reducing the flow of heat from the press down the bomb into the ice bath. By using this technique, the temperature could be stabilized at 0°C to better than ±0.2°C. Professor E. M. Purcell kindly loaned a magnet whose field was stabilized to within ±3 gauss by manual control of the current through biasing field coils. The current through the biasing coils was determined by continual observation of the nuclear magnetic resonance of protons, the frequency of which as measured on a G. R. Type 616 D Heterodyne frequency meter, served to determine the magnitude of the magnetic field. The magnet as adapted for the present experiments had a pole diameter of 8 in. with a 3-in. gap spacing, resulting in a variation in magnetic field over the sample which was certainly less than 5 gauss. Pressure was measured with a manganin wire gauge[9] connected to a Carey Foster bridge. The gauge, calibrated by using the freezing point of mercury at 0°C and 7640 kg/cm² permitted the determination of pressures accurately to within ±5 kg/cm².

The samples were cut in the form of rectangular parallelepipeds about 9 mm long, 2 mm wide, and 2 mm deep on which contacts were soldered as shown in Fig. 1. When mounted inside the bomb the sample was oriented so that its long axis was perpendicular to the long axis of the bomb which in turn was perpendicular to the magnetic field. The faces on which the Hall probes *A*, *B*, and *C* are soldered were arranged to be in planes parallel to the magnetic field lines. The voltages were measured using a Rubicon, type *B*, dc potentiometer. The current was determined by measuring the voltage across a 100-ohm standard resistor in series with the crystal. The Hall voltages were measured by first balancing the Hall voltage to zero for one direction of field by varying the position of the center tap on a resistor across the two Hall probes *A* and *B* in Fig. 1. The size of this resistor is chosen to be very large compared with the crystal resistance between *A* and *B*. Reversal of the field then produces between the center tap and the probe *C*, a voltage whose magnitude is twice the Hall voltage. Measurement of the Hall voltage permitted final alignment of the crystal so that the magnetic field was perpendicular to the direction of current flow. Specifically, the BeCu bomb was rotated about its long axis until the Hall voltage was maximized. Similarly, alignment of the magnetic field along the current direction was achieved by finding that orientation for which the Hall voltage was zero.

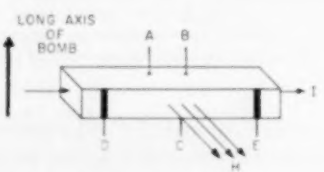

FIG. 1. Diagram of sample geometry.

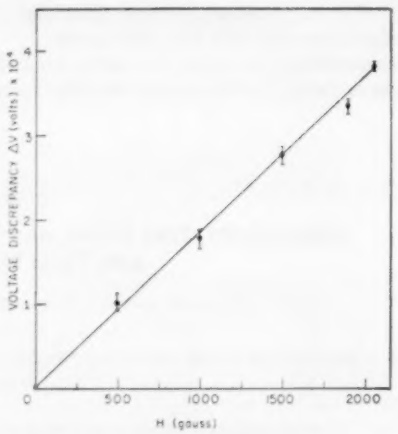

FIG. 2. Voltage discrepancy ΔV *versus* magnetic field strength H at $T=23°C$.

Measurements following the procedures mentioned above showed that the reversal of the magnetic field direction did not leave the magnetoresistive voltage drop along the sample unchanged. The size of the "voltage discrepancy" (i.e., the magnetoresistive voltage drop as measured with the field in one direction minus the magnetoresistance voltage as measured with the field in the opposite direction) was for some samples ~50 microvolts, but for one sample was as large as 260 microvolts, ~20% of the Hall voltage. The effect

[7] Paul, Benedek, and Brooks, Phys. Rev. **94**, 1415 (1954).
[8] Benedek, Paul, and Brooks, Phys. Rev. **98**, 1193(A) (1955).
[9] P. W. Bridgman, *The Physics of High Pressures* (G. Bell and Sons, Ltd., London, 1949).

was much smaller when the current and field directions were parallel than when they were perpendicular. By examining the current and magnetic field dependence of the discrepancy voltage, it was found that the voltage drop between the resistance determining probes could be written as

$$V = iR(H) + biH + \epsilon,$$

where $R(H)$ is the true magnetoresistance, ϵ is the effect of contact potentials, and biH is $\frac{1}{2}$ the discrepancy voltage. Evidence that the field and current dependence of the discrepancy voltage is of the form suggested above is given in Figs. 2 and 3. These measurements of the discrepancy voltage were made on the [100] oriented germanium crystal at room temperature for the transverse orientation of field and current directions.

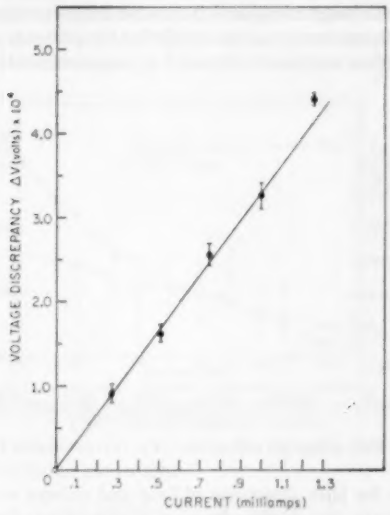

FIG. 3. Voltage discrepancy ΔV *versus* sample current i at $T=23°C$.

It is on this sample that the size of the discrepancy voltage is greatest. While no physical mechanism is suggested to explain the discrepancy voltage, measurements of the magnetoresistive voltage drops for + and − directions of current and field permit elimination of the effects of both the contact potentials and the discrepancy voltage and enable thereby a determination of the true magnetoresistance.

II. EXPERIMENTAL RESULTS

The measurements were made on two samples, one oriented with its long axis in the [100] direction, the other in the [110] direction. The samples were cut from adjacent regions of the same crystal. The conduction properties of the two samples at atmospheric pressure and $T=0°C$ are summarized in Table I. The figure $\pm 8\%$ associated with ρ and μ_H indicates the

TABLE I. Conduction properties of the two samples at atmospheric pressure and $T=0°C$.[a,b]

Sample orientation	Resistivity ρ ohm cm	Hall mobility μ_H cm²/sec volt	Carrier density: n cc⁻¹	Magnetoresistance coefficient $M=\Delta R/RH^2$
100	2.7±8%	4480±8%	~5×10¹⁴	$M_{100}=2.18\times10^{-9}$ $M_{100}^{000}=0.957\times10^{-9}$
110	2.9±8%	4077±8%	~5×10¹⁴	$M_{110}=0.978\times10^{-9}$ $M_{110}^{110}=2.02\times10^{-9}$

[a] In the notation M_A^B, A denotes the direction of the electric current and B the direction of the magnetic field. R is the sample resistance.

[b] It will be noticed that the value 4077 cm²/volt sec for the mobility of the [110] crystal, while in agreement with the Hall mobility of the [100] crystal within the limit of error, is nevertheless much lower than the value we consider the probable one. It seems possible that the reason for the discrepancy lies in a systematic error in the Hall measurement on the [110] sample, although the possibility that there is more impurity scattering in this sample cannot be discounted. However, since the Hall mobility for the [110] crystal has not entered into any of the analyses above, we have not tried to locate possible sources for this discrepancy.

limit of error and is determined by the fact that the width of the soldered voltage probes (D or E in Fig. 1) is 8% of the distance between probes. The high values of the Hall mobility, along with linear plots of the resistance as a function of distance along the crystal, indicate that the impurities were distributed homogeneously within the samples. In all the measurements, the current densities used were small enough (~0.025 amp/cm²) so that the sample voltage was directly proportional to the sample current. Choice of the magnetic field was made by requiring that the Hall voltage per unit current be directly proportional to the strength of the magnetic field, and that the magnetoresistive coefficient be proportional to the square of the magnetic field, i.e., that the measurements correspond to the theoretical low-field region. Evidence that these requirements were met is shown in Figs. 4 and 5.

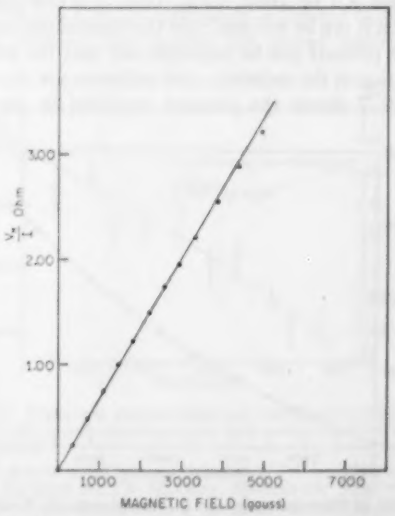

FIG. 4. Hall voltage per unit current (V_H/I) *vs* magnetic field H at $T=22°C$, $P=1$ atmos.

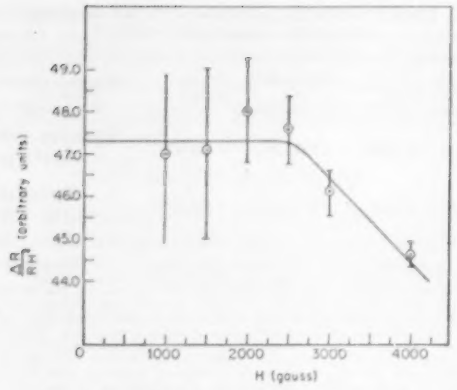

FIG. 5. Magnetoresistance coefficient *versus* field at $T=22°C$, $P=1$ atmos.

Figure 4 shows the Hall voltage per unit current as a function of field at 1 atmosphere and $T\sim22°C$, while Fig. 5 shows $\Delta R/RH^2$ *vs* H at the same temperature and pressure. Measurements of a less precise character than those of Figs. 4 and 5 show that at $T=0°C$ the turnoff point in both curves occurs higher than ~2000 gauss, the field region in which the measurements were made.

Figures 6 through 12 show the effect of pressure on the galvanomagnetic properties. In Fig. 6 the resistance of the [110] crystal as a function of pressure at 0°C is plotted. The pressure variation of the resistivity is found from $\rho=AR/l$, where A is the cross-sectional area of the sample and l the distance between the voltage probes D and E. It is estimated from the volume compressibility[10] that the application of 10 000 kg/cm² changes A/l by about 0.4%. Thus to a first approximation it can be assumed that the dimensional changes under pressure can be neglected and that the pressure variation in the resistivity and resistance are the same. Figure 7 shows the pressure variation in the Hall

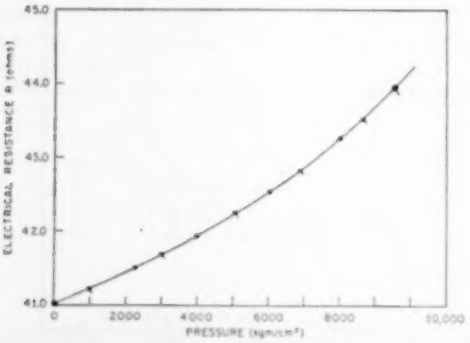

FIG. 6. Electrical resistance R *versus* pressure at $T=0°C$.

[10] E. M. Conwell, Proc. I.R.E. **40**, No. 11 (1952).

voltage per unit current, V_H/I for the [110] crystal. The Hall constant R_H is related to V_H/I via $R_H=(d/H)(V_H/I)$, where d is the crystal dimension in the direction of H. Since d changes by only 0.4% to 10 000 kg/cm², we can to a first approximation again neglect the dimensional changes and assume that Fig. 7 represents closely the pressure variation in the Hall constant, R_H. As an internal experimental check it was found that the pressure variation of the Hall constant and resistivity were the same for both the [110] and [100] crystals. Figure 8 is a plot of the transverse magnetoresistance coefficient *vs* pressure at $T=0°C$ for the [100] crystal. On the left-hand scale is plotted the experimentally measured $\Delta R/R$, while on the right is plotted for convenience $\Delta R/RH^2$. Figure 9 shows the longitudinal magnetoresistance coefficient as a function of pressure at $T=0°C$ for this 100 crystal. For both longitudinal and transverse magnetoresistance coefficients correction was made for the presence of the bIH term mentioned above, i.e., measurements were

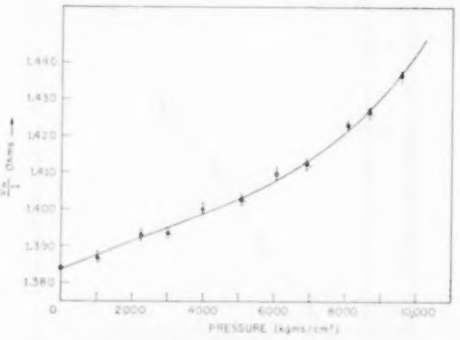

FIG. 7. Hall voltage per unit current (V_H/I) *vs* pressure at $T=0°C$.

made for both directions of field and current so as to eliminate the bIH voltage and determine the true magnetoresistance coefficient. In the case of the [110] crystal the magnitude of the bIH term is much smaller than that for the [100] crystal. Measurements in opposite field directions were made on the [110] crystal during the transverse magnetoresistance run for pressures up to 4000 kg/cm², after which pressure measurements were made using only one direction of field. Figure 10 shows the $(\Delta R/R)_{110}^{110}$ *vs* pressure as deduced using only one direction of field. The measurements including both field directions up to 4000 kg/cm² showed that the discrepancy voltage was approximately independent of pressure. By extrapolating this fact into the rest of the pressure range, the effect of the bIH term can be eliminated and in this way the curve of Fig. 11 is obtained. It can be seen from Fig. 11 that the small bIH correction in this crystal has the effect of raising the entire $(\Delta R/R)_{110}^{110}$ curve up along the ordinate by about 5 percent above the uncorrected curve and has a negligible effect on the shape of the curve. In Fig. 12

the longitudinal magnetoresistance for the [110] crystal is plotted without taking into account any field reversal effects. Since the magnetoresistance coefficients are by definition $\Delta R/R$, dimensional changes under pressure have no effect.

III. THEORY

In order to account quantitatively for the observed size of the magnetoresistance coefficients and ratio of Hall to drift mobility, it is necessary to generalize slightly the theory of Abeles and Meiboom.[4] If (a) the conduction is by carriers of one type and if (b) these carriers are confined to conduction-band minima whose shape is such that the constant energy surfaces are 4 or 8 ellipsoids of revolution about the [111] directions in the crystal, and further if (c) the magnetic field H is small enough so that the Hall constant R_H is independent of the field and the magnetoresistive coefficients $M_A{}^{B\,11}\equiv(\Delta R/RH^2)_A{}^B$ are proportional to the square of the magnetic field, then the theory of Abeles

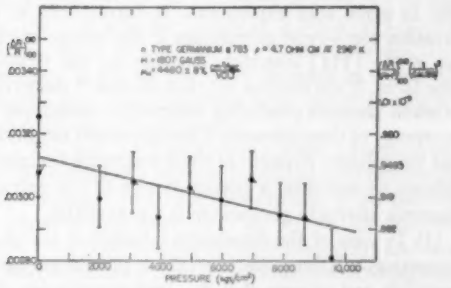

FIG. 8. Transverse magnetoresistance coefficient *vs* pressure for [100] oriented sample at $T=0°C$.

and Meiboom shows that

$$R_H=\frac{1}{Nec}\lambda\frac{3K(K+2)}{(2K+1)^2}\equiv\frac{1}{Nec}\frac{\mu_H}{\mu_D}, \tag{1}$$

$$\frac{M_{100}}{R_H{}^2\sigma_0{}^2}=\frac{2}{3}\eta\frac{(2K+1)(K-1)^2}{K(K+2)^2}\equiv\xi_{100}, \tag{2}$$

$$\frac{M_{100}{}^{010}}{R_H{}^2\sigma_0{}^2}=\eta\frac{(2K+1)^2}{3K(K+2)}-1\equiv\xi_{100}{}^{010}, \tag{3}$$

$$\sigma_0=ne^2\langle\tau\rangle\tfrac{1}{3}(1/m_1+2/m_2), \tag{4}$$

$$M_{110}=\tfrac{1}{2}M_{100}; \tag{5}$$

$$M_{110}{}^{\bar{1}10}=\tfrac{1}{2}M_{100}+M_{100}{}^{010}\quad\text{(symmetry relations)},$$

where N is the total number of electrons in the conduction band, and m_1 and m_2 are respectively the

[11] In the notation $M_A{}^B$: B denotes the direction of the magnetic field, A the direction of the electric current. The absence of the superscript indicates that the current and magnetic field are parallel.

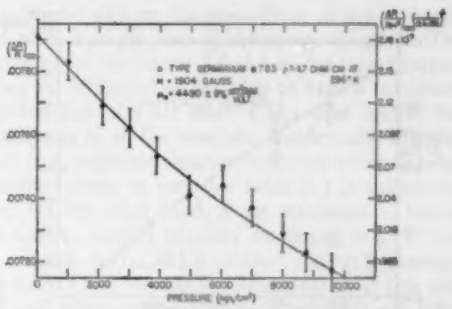

FIG. 9. Longitudinal magnetoresistance coefficient *vs* pressure for [100] oriented sample at $T=0°C$.

longitudinal and transverse masses defined in terms of the shape of the energy surfaces by

$$\epsilon=\tfrac{1}{2}(p_x{}^2/m_1+p_x{}^2/m_2+p_y{}^2/m_2), \tag{6}$$

where the z axis is along the [111] crystal direction.

$$K=m_1/m_2, \tag{7}$$

$$\lambda=\langle\tau^0\rangle\langle\tau^2\rangle/\langle\tau\rangle^2, \tag{8}$$

$$\eta=\langle\tau^1\rangle\langle\tau^3\rangle/\langle\tau^2\rangle^2, \tag{9}$$

$$\langle\tau^n\rangle=\frac{4}{3\sqrt{\pi}}\int_0^\infty\tau^n x^{\frac{1}{2}}e^{-x}dx,\quad x=\epsilon/kT. \tag{10}$$

In order to calculate the magnitudes of the magnetoresistance coefficients, we require the dependence of the scattering time τ on energy so that $\langle\tau^n\rangle$,[12] and thereby λ and η, can be calculated. We have considered three forms of the dependence of the lattice scattering time τ_L on energy.

(1) Intravalley acoustic mode scattering (scattering of an electron only around the energy minimum it

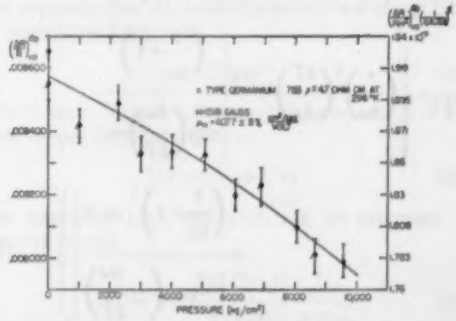

FIG. 10. Transverse magnetoresistance coefficient *vs* pressure for [110] sample uncorrected for field reversal at $T=0°C$.

[12] It is to be noted that our definition of $\langle\tau^n\rangle$ is slightly different from the usual one [W. Shockley, *Electrons and Holes in Semiconductors* (D. Van Nostrand Company, New York, 1950)] in that the v^2 term is automatically included in our weighting factor in the integrand.

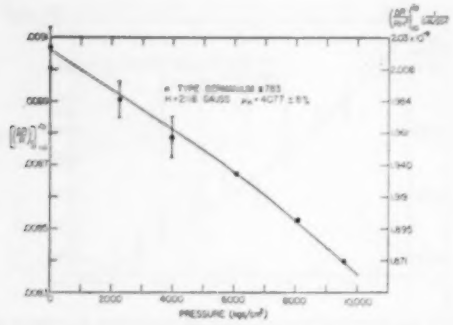

FIG. 11. Transverse magnetoresistance coefficient *vs* pressure for [110] sample corrected for field reversal at $T=0°C$.

momentarily occupies) can be shown[13] to produce for spherical energy surfaces, a dependence of τ_L on ϵ:

$$\tau_L=(l/kT)\epsilon^{-\frac{1}{2}}. \tag{11}$$

By computing μ_L from Eq. (10) and Eq. (11) it is seen that law (11) predicts a $T^{-\frac{1}{2}}$ law for the temperature dependence of the lattice mobility rather than the experimentally observed[14] $T^{-1.66}$ law. Agreement with experiment can be achieved only by assuming a suitable temperature dependence of the effective mass (upon which the constant l depends).

(2) Recently Herring has presented[15] a theory of lattice scattering including both the effects of intravalley scattering and intervalley scattering (i.e., scattering of an electron in one energy minimum to a position of nearly equal energy in the other minima) involving phonon emission and absorption. Using a model which considers absorption and emission of only one type of intervalley phonon, Herring has derived the form of the dependence of τ_L on ϵ in terms of the phonon energy $\hbar\omega$ and the relative probability of intervalley and intravalley scattering w_2/w_1 as

$$w_1\tau_L=\left\{\left(\frac{\epsilon}{\hbar\omega}\right)^{\frac{1}{2}}\left(\frac{kT}{\hbar\omega}\right)+\frac{w_2}{w_1}\left[\frac{\left(\frac{\epsilon}{\hbar\omega}+1\right)^{\frac{1}{2}}}{\exp\left(\frac{\hbar\omega}{kT}\right)-1}+\frac{\left(\frac{\epsilon}{\hbar\omega}-1\right)^{\frac{1}{2}}\text{ or }0}{1-\exp\left(-\frac{\hbar\omega}{kT}\right)}\right]\right\}^{-1}, \tag{12}$$

where the first term on the right-hand side describes intravalley scattering, the second term describes intervalley scattering with absorption of a phonon, and the third term describes intervalley scattering with emission of a phonon. This model would apply to germanium if the energy minima in the [111] directions were on the faces of the Brillouin zone, for it can be shown that in this case only one phonon is effective in producing intervalley transitions.[16] Using law (12), Herring has given plots of the functions λ and η for various amounts of intervalley scattering. Comparison of the temperature dependence of μ_H/μ_D as predicted from this theory with the data of Morin[14] for germanium shows that the predicted temperature-dependence is somewhat different from that which is observed. The drift-mobility data show that μ_H/μ_D is nearly independent of temperature down to liquid nitrogen temperature for *n*-type germanium. Herring's relations imply a much stronger dependence on temperature, at least 20 percent decrease between room temperature and liquid nitrogen. This suggests that one might include in the theory the effects of phonons of several different energies each contributing different amounts to the total scattering. This could have the effect of flattening out the μ_H/μ_D *vs* T plot to agree with experiment. It corresponds to the situation for *n*-type germanium if the energy minima are in the [111] directions but not on the Brillouin zone faces. If the minima are thus located,[17] there could be seven phonons producing intervalley transitions. As the energy of these phonons is not at present established and the relative strength of their scattering function is difficult to estimate, a precise theory of the galvanomagnetic effects in germanium is not available.

(3) In view of the drawbacks inherent in the above theoretical relations, we can take a phenomenological approach and assume that the lattice scattering time τ_L is isotropic and depends on energy and temperature as

$$\tau_L=(a/kT)\epsilon^{-p}, \tag{13}$$

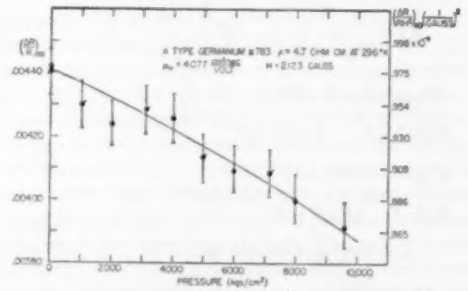

FIG. 12. Longitudinal magnetoresistance for [110] crystal *vs* pressure at $T=0°C$.

[13] J. Bardeen and W. Shockley, Phys. Rev. **80**, 72 (1950).
[14] F. Morin, Phys. Rev. **93**, 62 (1953).
[15] C. Herring, Bell System Tech. J. **34**, No. 2 (1955).
[16] Strictly speaking, two other optical modes could also contribute to the scattering. One corresponds to intervalley scattering and the other to optically induced intravalley scattering. In view of recent work by R. Keyes [Phys. Rev. **99**, 626(A) (1955)], and of the relatively small deviation from the $T^{-\frac{1}{2}}$ mobility law, it seems unlikely that these higher-energy modes can be of much significance.
[17] G. MacFarland and V. Roberts, Phys. Rev. **97**, 1714 (1955).

where it is assumed that a and p are independent of both energy and temperature. In addition to its analytic simplicity, this law has the virtue that with a correct choice of the parameter p it is capable of producing the observed temperature variation in λ, η, and μ_L. Further, from the point of view of the Herring theory, Eq. (13) can be regarded as a representation which except for very low energies describes the superposed effects of intervalley and intravalley scattering by several phonons of different energies. For these reasons we shall, in our subsequent analysis, pursue the consequences of the phenomenological law (13).

Using expression (13) for τ and calculating the quantities λ and η one finds that

$$\lambda=\Gamma(5/2)\Gamma(5/2-2p)/[\Gamma(5/2-p)]^2, \tag{14}$$

$$\eta=\Gamma(5/2-p)\Gamma(5/2-3p)/[\Gamma(5/2-2p)]^2, \tag{15}$$

where the Γ's denote gamma functions of their arguments. That the theory in its present form is not yet applicable to fitting the experimental data can be seen from the fact that for values of $p\geq 5/6$, $\Gamma(5/2-3p)$ diverges, while for $p\geq 5/4$, $\Gamma(5/2-2p)$ diverges. This divergence is due to the rapid increase in τ as ϵ approaches zero. The divergence never occurs in practice for the following three reasons.

(1) The law (13) breaks down when ϵ becomes less than the energy of a phonon associated with intervalley or optical-mode scattering. Specifically, if we consider the Herring expression (12) for τ_L we see that for $\epsilon/\hbar\omega<1$ the phonon emission term disappears and that as $\epsilon/\hbar\omega$ decreases further the intravalley scattering term approaches zero while the intervalley scattering with phonon absorption approaches a constant value. The net result is that τ_L approaches a finite value as $\epsilon\rightarrow 0$.

(2) For sufficiently low energy of the carrier, ionized impurity scattering will predominate, and since this increases with decreasing energy it gives the integrand in Eq. (10) a maximum and allows the integral to converge.

(3) The results, Eqs. (1), (2), and (3), are based on the approximation that the magnetic field is small, strictly that $\omega\tau(\epsilon)=eH\tau(\epsilon)/m_{eff}c\ll 1$ for all values of the energy ϵ. Provided that $p=\frac{1}{2}$, it is readily shown that the part of the energy range where the above relation is not fulfilled makes a negligible contribution to the integral. However, for larger p it is necessary to replace the definitions (8) and (9) by the more exact expressions (16) and (17).

$$\lambda=\left\langle\frac{\tau^2}{1+\omega^2\tau^2}\right\rangle\Big/\langle\tau\rangle\left\langle\frac{\tau}{1+\omega^2\tau^2}\right\rangle, \tag{16}$$

$$\eta=\left\langle\frac{\tau}{1+\omega^2\tau^2}\right\rangle\left\langle\frac{\tau^3}{1+\omega^2\tau^2}\right\rangle\Big/\left\langle\frac{\tau^2}{1+\omega^2\tau^2}\right\rangle^2, \tag{17}$$

where the ω's here have essentially the form eH/mc but they depend also on the orientation of the magnetic field relative to the axes of the energy ellipsoids. The occurrence of the factor $1+\omega^2\tau^2$ in the denominators causes the integrand of Eq. (10) to have a maximum as a function of ϵ for small ϵ and thus insures the convergence of all the integrals. Incidentally, this will result in a magnetoresistance coefficient which is field-dependent down to very low fields if p is sufficiently large. On the other hand, if the maximum τ, taking into account ionized impurity scattering, is such that the criterion $(\omega\tau)_{max}\ll 1$ is fulfilled, then it is unnecessary to take into account the denominators of (16) and (17) and the magnetoresistance coefficients are independent of field over an appreciable range of fields.

In order to calculate values of λ and η which can be compared with the experimental values of the magnetoresistance coefficients, we must decide which of the mechanisms (1), (2), and (3) above are operating to reduce the integrals (10). For our samples of n-type germanium, explicit calculation shows that we can neglect the effect shown in (3) for fields up to 2000 gauss, a value in agreement with the experimental results of Fig. 5. The effectiveness of (1) in reducing (10) is difficult to gauge because the parameters $\hbar\omega_i$ and $(w_3)_i$ needed to describe the effects of the several phonons on the inter- and intravalley scattering are not known. We shall begin then by assuming that effect (2) only is operating, remembering however that in attempting to fit the integrals (10) to their experimental counterparts it may appear necessary to include more impurity scattering than is required by the Brooks-Herring or Conwell-Weisskopf formula, because of the neglect of effect (1) on reducing the integrals (10). The calculation of $\langle\tau^n\rangle$ and thereby λ and η including the effects of scattering by ionized impurities can be made as follows. Writing

$$\tau_L=(\tau_L)_0\epsilon^{-p}, \tag{18}$$

and assuming that the ionized impurity scattering time τ_I depends on energy as

$$\tau_I=(\tau_I)_0\epsilon^{+q} \tag{19}$$

[where again $(\tau_I)_0$ as well as $(\tau_L)_0$ is independent of $\mathbf{k}$], then the net collision time τ is

$$1/\tau=1/\tau_L+1/\tau_I. \tag{20}$$

The quantities $(\tau_L)_0$ and $(\tau_I)_0$ can be expressed in terms of $\langle\tau\rangle$ via

$$\langle\tau_L\rangle=(\tau_L)_0\frac{\Gamma(5/2-p)}{\Gamma(5/2)}\frac{1}{(kT)^p}, \tag{21}$$

$$\langle\tau_I\rangle=(\tau_I)_0\frac{\Gamma(5/2+q)}{\Gamma(5/2)}(kT)^q. \tag{22}$$

Eliminating $(\tau_L)_0$ and $(\tau_I)_0$ from (18) and (19) by using (21) and (22), and substituting the results into

(20), the expression for $\langle\tau^n\rangle$ becomes:

$$\langle\tau^n\rangle=b^n\int_0^\infty \frac{x^{\frac{1}{2}}e^{-x}dx}{\left[x^p+\frac{\Gamma(5/2+q)}{\Gamma(5/2-p)}\left(\frac{\langle\tau_L\rangle}{\langle\tau_I\rangle}\right)x^{-q}\right]^n}, \quad (23)$$

$$b=\langle\tau_L\rangle\Gamma(5/2)/\Gamma(5/2-p).$$

It is seen from the form of the denominator in the integrand of (23), that the divergence difficulty arising out of the low-energy behavior of τ_L is now removed. It is important to note that even a very slight amount of ionized impurity scattering ($\langle\tau_L\rangle/\langle\tau_I\rangle=\langle\mu_L\rangle/\langle\mu_I\rangle\ll1$) can have a marked effect on the $\langle\tau^n\rangle$ integrals (especially for the larger n) because the presence of the x^{-q} term in the denominator can change the form of the integrand from one which increases rapidly near the origin to one that reduces quickly to zero at $x=0$.[18] $\langle\tau^n\rangle$ can be evaluated approximately by noting that the denominator of (23) has a minimum value at $x=x_0$, where

$$x_0=\left[\frac{\Gamma(5/2+q)}{\Gamma(5/2-p)}\frac{\langle\tau_L\rangle}{\langle\tau_I\rangle}\frac{q}{p}\right]^{1/(p+q)}. \quad (24)$$

If x_0 is small, as will be the case when $\langle\tau_L\rangle/\langle\tau_I\rangle$ is small (i.e., the scattering is predominantly lattice but with a small amount of ionized impurity scattering included), then the contribution to the integral in the range $0\rightarrow x_0$ can be assumed small compared to the contribution in the range $x_0\rightarrow\infty$. Further, since for values of $x>x_0$ the denominator behaves predominantly as x^{np}, we can write approximately:

$$\langle\tau^n\rangle\cong b^n\int_{x_0}^\infty x^{\frac{1}{2}-np}e^{-x}dx. \quad (25)$$

This integral is the incomplete gamma function whose value can be calculated approximately with the aid of an integration by parts, resulting in the expression

$$\int_{x_0}^\infty e^{-x}x^{-r}dx=\Gamma(1-r)-\frac{x_0^{1-r}}{1-r}, \quad (26)$$

where the approximations $e^{-x_0}\approx1$ and

$$\int_{x_0}^\infty x^{1-r}e^{-x}dx\cong\int_0^\infty x^{1-r}e^{-x}dx=\Gamma(2-r)$$

have been used. Applying the result shown in Eq. (26) to Eq. (25), we get finally

$$\langle\tau^n(p,x_0)\rangle\cong b^n\left[\Gamma(5/2-np)-\frac{x_0^{5/2-np}}{(5/2-np)}\right], \quad (27)$$

which shows explicitly the correction to the pure lattice scattering that is produced by a small amount of ionized impurity scattering. The accuracy of the approximate expression (27) for an x_0 appropriate to the present crystals, along with the large changes in λ and η that a small amount of ionized impurity scattering produces, will be dealt with in the following section.

[18] The values of $\langle\tau^n\rangle$ for high p become so sensitive to the amount of impurity scattering that the law (13) is of doubtful usefulness in this case.

IV. COMPARISON OF THEORY AND EXPERIMENT

Atmospheric Pressure

The conduction in the present material (3 ohm cm at $T=0°C$) is due almost entirely to impurity-derived electrons moving in the conduction band. The density of holes is estimated as less than 0.1% of the density of electrons, and their effect on the conduction properties can therefore be neglected here. In column 5 of Table II are listed the experimental values of the theoretically significant quantities ξ_{100}, ξ_{100}^{010}, and μ_H/μ_D which are defined in Eqs. (1), (2), and (3). The value of μ_H/μ_D listed in this table is computed from our value of the Hall constant R_H, N being obtained from σ and Prince's[19] value of μ_D. While we present a *limit* of error of 8% for μ_H/μ_D, the measurements of other workers[14] gives $\mu_H/\mu_D=0.99\pm\sim0.02$, and this much smaller estimated error can be expected to give a much more reliable estimate of the range of possible values of μ_H/μ_D appropriate to our sample. It is seen from Eqs. (1), (2), (3), (8), (9), and (27) that if the three quantities: (1) K, defined in Eq. (7) as the ratio of longitudinal to the transverse ellipsoid masses, (2) p, defined in Eq. (13) as the exponent of the energy dependence of τ_L, and (3) x_0, defined in Eq. (24) as the parameter which determines the low-energy cutoff of the scattering time integrals, are known, then ξ_{100}, ξ_{100}^{010}, and μ_H/μ_D can be calculated directly. If K is chosen as 20 from the low-temperature cyclotron resonance data, then in order to get consistency between Eqs. (2) and (3) and the experimental values of $\Delta R/RH^2$, it is necessary to choose $\mu_H=4225$ cm²/sec volt. Since this is a low value for the Hall mobility, it seems likely that at room temperature $K\neq20$. Choosing a value of K consistent with our experimentally determined $\mu_H=4480$ cm²/sec volt, which is only 2% less than that which can be deduced from Morin's data[14] for μ_H/μ_D and Prince's value of

TABLE II. Comparison of theoretical and experimental values of the galvanomagnetic coefficients. The quantities ξ_{100} and ξ_{100}^{010} are defined in Eqs. (2) and (3).

	Calculated (no impurity scattering included)		Calculated (including impurity scattering) $\mu_L/\mu_I=1/220$		Experimental values
	$p=0.50$	$p=0.66$	$p=0.50$	$p=0.66$	
ξ_{100}	1.17	1.74	1.050	1.089	1.086
ξ_{100}^{010}	0.514	1.36	0.465	0.481	0.477
μ_H/μ_D	0.939	1.1	0.9026	0.98	0.99

[19] M. B. Prince, Phys. Rev. 92, 681 (1953).

$\mu_D = 3900$ cm²/volt sec, we find $K = 14.5$. The sensible difference between this and the low-temperature cyclotron resonance value of 20 may be due to a temperature dependence of m_1/m_2 and/or to an anisotropy in τ.[20]

The quantity p in law 13 can be determined independently of the present experiments using the experimentally known variation of the lattice mobility with temperature. From Eqs. (4) and (13) it follows that the conductivity σ_0 is

$$\sigma_0 = ne^2(1/3)(1/m_1+2/m_2) \times \frac{a}{(kT)^{1+p}} \frac{\Gamma(5/2-p)}{\Gamma(5/2)} = ne\mu_D. \quad (28)$$

If the masses m_1 and m_2 and a are assumed independent of temperature, then from the known[14] $T^{-1.66}$ dependence of the mobility on temperature one deduces that $p = 0.66$. On the other hand, if one assumes that the effective masses vary sufficiently with temperature to give the correct temperature dependence, one would choose from law (11) that $p = \frac{1}{2}$.

If the effect of scattering by ionized impurities is neglected, one can calculate ξ_{100}, ξ_{100}^{010}, and μ_H/μ_D

TABLE III. Percentage errors incurred in using Eqs. (27) and (24) instead of an exact integration of Eq. (23).

	Percentage error
λ	+2.3
η	−0.3
$\langle\tau\rangle/b$	−0.08
$\langle\tau^2\rangle/b^2$	+2.1
$\langle\tau^3\rangle/b^3$	+4

using Eqs. (1), (2), (3), (14), and (15). The results of such a calculation are given in columns 1 and 2 of Table II, using $K = 14.5$ for both law (11) and law (13), i.e., $p = \frac{1}{2}$ and $p = 0.66$. It is seen that for $p = 0.66$ the calculated ξ's and μ_H/μ_D are too high, indicating the importance of including the effect of impurity scattering. On the other hand, for $p = \frac{1}{2}$, it is to be noted that while the ξ's are somewhat high the μ_H/μ_D ratio is already too low.

Inclusion of the effects of scattering by ionized impurities can be accomplished if one assumes that the relaxation time for such scattering is $\tau_I \propto \epsilon^q$, i.e., that $q = \frac{3}{2}$. On noting that $\Gamma(5/2+q)/\Gamma(5/2-p) \sim 6$, Eq. (24) for x_0 can be written as

$$x_0 = \left[\frac{9}{p}\frac{\mu_L}{\mu_I}\right]^{1/(1+p)}.$$

If μ_L/μ_I for our samples is known, x_0 and thereby λ, η, ξ_{100}, ξ_{100}^{010} and μ_H/μ_D can be calculated. In order to get the agreement with experiment indicated in column

[20] If one takes into account the anisotropy of τ, K should be replaced by $K = (m_{II}/m_\perp)(\tau_{II}/\tau_\perp)$ [C. Herring (private communication)].

TABLE IV. Check of the symmetry relations: $\frac{1}{3}M_{100} = M_{110}$ and $M_{110}^{\overline{110}} = \frac{1}{3}M_{100} + M_{100}^{010}$, where $M = \Delta\rho/\rho H^2$. [$\frac{1}{3}M_{100}(1) = 1.09 \times 10^{-9}$/gauss²; $M_{110}(1) = 0.987 \times 10^{-9}$/gauss².]

P kg/cm²	$\frac{1}{3}M_{100}+M_{100}^{010}$ (1/gauss)²	$(M_{110}^{\overline{110}})_{\text{exp.}}$ (1/gauss)²	$\frac{M_{110}(P)}{M_{110}(1)}$	$\frac{M_{100}(P)}{M_{100}(1)}$
1	2.05×10^{-9}	2.02×10^{-9}	1	1
2000	2.01	1.99	0.979	0.974
4000	1.97	1.96	0.955	0.952
6000	1.93	1.93	0.933	0.934
8000	1.90	1.90	0.907	0.918
10 000	1.87	1.86	0.879	0.904

4 of Table II, μ_L/μ_I must have the value 1/220, i.e., $x_0 = 0.276$ for $p = 0.66$. This value of μ_L/μ_I corresponds, upon using Prince's data[19] for μ_L to a value of $\mu_I = 9.74 \times 10^5$ cm²/volt sec. Calculation of μ_I from the Brooks-Herring formula for our samples gives this value of μ_I when the effective mass m^* for impurity scattering is taken as $m_0/2.1$. By analysis of Hall mobility data for samples of varying impurity content, Debye and Conwell[21] show that at room temperature the correct effective mass for impurity scattering should be somewhere between $m_0/4$ and m_0. The effect of electron-electron collisions on this estimate will be small[22] because in all their samples lattice scattering is an appreciable part of the total scattering. As an additional point it is to be noted that if one modifies the form of the law (19) with $q = \frac{3}{2}$ to include the logarithmic term present in the Brooks-Herring formula, the expression for x_0 changes somewhat. This change can be expressed by writing μ_I in Eq. (29) as $\mu_I \ln b_0/\ln(b_0 x_0)$. The effect of the $\ln b_0/\ln(b_0 x_0)$ term in our case is to decrease μ_L/μ_I by about 12 percent. The resultant change in m^* required to restore μ_L/μ_I to 1/220 is not so large as to cause it to be outside the range of values given by Debye and Conwell. We can, therefore, conclude that the amount of impurity scattering which must be invoked to explain the magnitudes of the magnetoresistance and Hall effect is entirely reasonable.

The validity of the comparison of the present theory

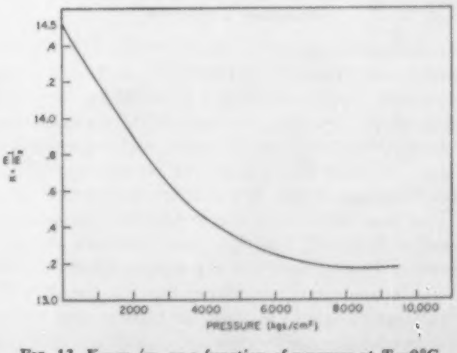

FIG. 13. $K = m_1/m_2$ as a function of pressure at $T = 0$°C.

[21] P. Debye and E. M. Conwell, Phys. Rev. **93**, 693 (1954).
[22] E. M. Conwell (private communication).

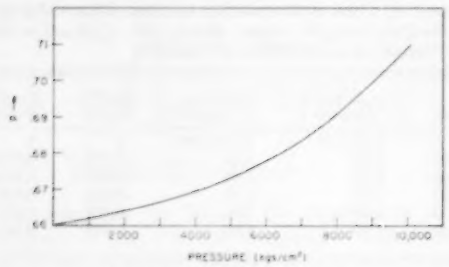

FIG. 14. Plot of ϕ *versus* pressure.

with experiment depends upon the accuracy of the approximation (27) for $\langle\tau^n\rangle$. In Table III are listed the percentage errors in the estimation of τ^n/b^n, λ, η incurred by using the approximate expressions (27) and (24) instead of an exact integration of Eq. (23). The results quoted were obtained by graphical integration methods for the case $p=0.66$, $q=\frac{3}{2}$, $\mu_L/\mu_I=1/220$. A positive percentage error indicates that the approximate expression gives a value greater than the exact one. From the information summarized in Table II we can draw the following conclusions. First, column 1 indicates that a reduction in the values of λ and η predicted by Eq. (14) and Eq. (15) is required in order to account for the observed sizes of ξ_{100}, ξ_{100}^{010}, and μ_H/μ_D. Secondly, from the fact that the amount of impurity scattering which must be invoked to reduce λ and η enough to produce the experimental results is reasonable, we can conclude that our neglect of the effect (1) above (the decrease in the energy dependence of τ at low ϵ) is justified. It is altogether possible, however, that for pure enough samples this effect could be the dominating factor in limiting the integrals (10). Finally, from the fact that even without the inclusion of impurity scattering, law (11) gives values for μ_H/μ_D, which are too low, it can be concluded that law (11) cannot, with $K=14.5$, simultaneously give the experimental values of ξ_{100}, ξ_{100}^{010}, and μ_H/μ_D as can law (13).

Pressure Variation

Since the electrons in the conduction band are derived almost entirely from donor impurities, and since it can be assumed[1] that in the range 1–10 000 kg/cm² these donors do not de-ionize, the number N of electrons in the conduction band can be taken as independent of pressure. In Table IV are listed the experimental values of combinations of the M's at various pressures as a check of the validity of the symmetry relations expressed in Eqs. (5). The agreement between the predictions of Eqs. (5) and the experimental data implies that the assumptions underlying Eqs. (1) through (5) are valid at elevated pressures, at least insofar as the magnetoresistance coefficients are concerned, and suggests the application of these equations to the experimental data on ξ_{100}, ξ_{100}^{010}, and R_H as a function of pressure. Using the experimentally known variation of ξ_{100}^{010}, ξ_{100}, and μ_H/μ_D with pressure in Eqs. (2) and (3), the variation of K with pressure can be deduced independently of the pressure variation of η and is shown in Fig. 13. K can be eliminated between Eqs. (1) and (3), leaving a relation from which ϕ can be deduced. We assume that, despite the change in effective masses and the dielectric constant under pressure, the ratio μ_L/μ_I remains substantially constant and equal to 1/220, and that q is not pressure-dependent. Then, using Eqs. (8), (9), (27), and (29) in conjunction with the experimental values of R_H and M_{100}^{010}, we deduce the variation of ϕ with pressure shown in Fig. 14. It is to be observed that the variation in K and ϕ is quite nonlinear with pressure above about 3000 atmospheres. We believe this may be associated with the onset of interband scattering to [100]-type minima with characteristics in some ways similar to those of the conduction band of silicon. It is believed that this band gets closer in energy to the [111]

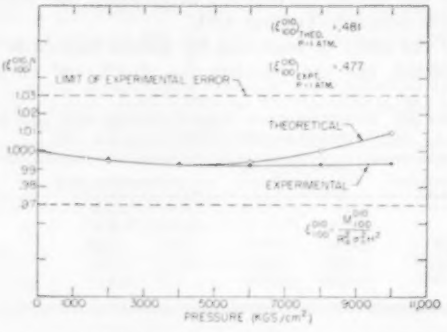

FIG. 15. Comparison of normalized transverse magnetoresistance coefficient $(\xi_{100}^{010})^N$ *versus* pressure. Theory and experiment.

minimum as the pressure increases. Experimental evidence, in a high enough pressure range, on the pressure variation of the galvanomagnetic coefficients is not yet available to test this supposition.

Since we have used three equations to determine two unknowns at each pressure, it is possible to check the consistency of the deduced variation of ϕ and K by calculating ξ_{100}, ξ_{100}^{010}, and R_H at each pressure and comparing with their experimental values. The results of such a procedure are shown in Figs. 15, 16, and 17. A rough estimation of the variation of the individual masses m_1 and m_2 with pressure can be made using the previously deduced variation of K and ϕ and Eq. (28) by inserting therein an expression for a in terms of the deformation potentials, elastic constants, and m_1 and m_2. If the elastic constants and deformation potentials were independent of pressure, then one could deduce from the known variation of the conductivity with pressure that m_1 decreases by $\sim 6\%$ while m_2 increases by ~ 4 percent for 10 000 kg/cm². Since the elastic constants can be expected to increase with pressure,

this would tend to somewhat increase the estimate of the change of m_2 with pressure and somewhat decrease the estimate of the change in m_1 with pressure.

CONCLUSIONS

A generalization of the theory of Abeles and Meiboom has been presented which shows that the galvanomagnetic properties of n-type germanium can be understood in terms of two quantities: $K=m_1/m_2$ which describes the shape of the energy ellipsoids whose axes are assumed in the [111] crystal directions, and $\tau(\epsilon)$, the energy-dependent scattering time.

At atmospheric pressure one can deduce that K has a value of about 14.5, a number sensibly different from the low-temperature cyclotron resonance value of 20, suggesting that K is temperature-dependent and/or that τ is anisotropic. The magnetoresistive coefficients, along with their temperature dependence and the temperature dependence of the lattice scattering mo-

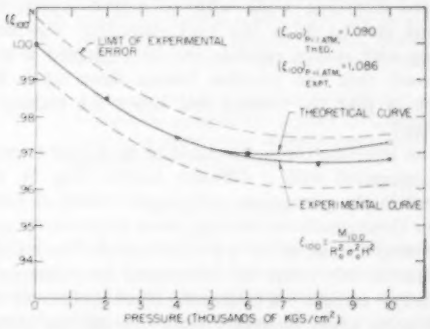

FIG. 16. Comparison of normalized longitudinal magnetoresistance coefficient ξ_{100} *versus* pressure. Theory and experiment.

bility, depend upon the precise form of the energy dependence of τ. After examination of several possibilities, it has been found that all the quantities above can be brought into agreement with experiment simultaneously if the scattering is a combination of lattice and impurity scattering with the lattice scattering law depending upon energy as $\tau_L=(a/kT)\epsilon^{-p}$. Further, it has been shown that the inclusion of even a small amount of impurity scattering can have a marked effect on the magnitudes of the magnetoresistance coefficients and the Hall constant. Experimental examination of the dependence of the galvanomagnetic coefficients on the impurity density can therefore be expected to yield significant information on the scattering processes.

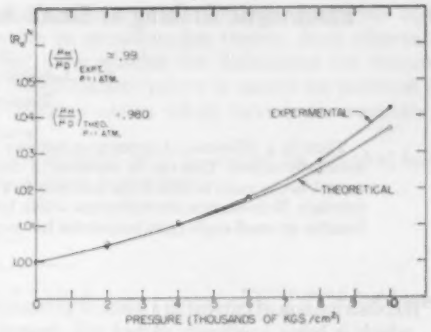

FIG. 17. Comparison of normalized Hall constant $(R_0)^N$ as a function of pressure. Theory and experiment.

The pressure variation in the galvanomagnetic properties can be interpreted in terms of changes in K and $\tau(\epsilon)$. The present experiments indicate that $K=m_1/m_2$ decreases with pressure up to 10 000 kg/cm². An estimate of the changes of the individual masses m_1 and m_2 can be made under the assumption that the elastic constants for germanium are pressure-independent, resulting in the conclusion that the m_1 decreases while m_2 increases—i.e., that the energy ellipsoids become less prolate as the pressure goes up. The apparent energy dependence of the scattering time also increases with pressure. Specifically, if one assumes that under pressure the ratio of lattice to impurity mobility remains substantially constant, then one can interpret the observed change in the dependence of τ on ϵ as a change in the exponent p in the lattice scattering law.

ACKNOWLEDGMENTS

The authors wish to acknowledge with thanks the help of Professor P. W. Bridgman, who kindly lent us one of his high-pressure presses, and Professor E. M. Purcell, who made available to us a magnet and the nonmagnetic beryllium copper bomb. We thank also Dr. Douglas Warschauer for considerable help in diverse ways, and Mr. Robert Powell, for his assistance with the experimental measurements.

Electrolytic Etching at Small-Angle Grain Boundaries in Germanium

S. G. Ellis
RCA Laboratories, Princeton, New Jersey
(Received April 18, 1955)

There is a difference of appearance between *n*-type and *p*-type germanium crystals which have been anodically etched. This can be explained if only the hole current contributes to the etching. An *n*-type crystal can be made to etch in the same way as a *p*-type crystal if injected holes reach the crystal-electrolyte interface. Hole-electron recombination within the crystal can then reduce the rate of etching. Such recombination at small-angle grain boundaries has been demonstrated.

THE distribution of current in a piece of germanium which is being anodically etched will depend in part on the distribution of potential at the surface of the germanium and in part on the variation of the electronic properties (conductivity and lifetime) within the germanium. It might therefore be expected that the shape of the etched surface would reflect in some degree any inhomogeneities within the crystal. An effect of this sort has been found. It demonstrates carrier recombination at dislocations in germanium. It is desirable, for clarity, to preface a description of this effect with an account of some of the general features of the electrolytic etching of germanium.

If a *p*-type germanium crystal is electrolytically etched in a potassium hydroxide solution from a macroscopic viewpoint the removal of material is uniform over the immersed area. At current densities of a few microamperes per cm² the microscopic appearance of the surface is similar to, but not identical with, that of a crystal treated with an alkaline chemical etch.[1] The attack during electrolysis is nucleated where dislocations end at the surface, leading to pit formation at such places. These pits are shallow, seldom exceeding a micron in depth. As the current density is raised, the surface becomes smoother. Electropolishing occurs at current densities of the order of an ampere per cm².

With *n*-type germanium, the attack is quite different if the electrical connection to the crystal is many diffusion lengths away from the crystal-electrolyte interface. (Diffusion length here refers to the diffusion length of minority carriers in the germanium.) Under such conditions a few deep widely-spaced pits are produced, and there seems to be very little, if any, reaction at other points on the surface. The pit depth depends on the charge passed. When the pits are deep a product of the reaction forms within them. It is probably a hydrated form of germanium monoxide. It has been suggested[2] that the deep pits are formed because the monoxide attacks the germanium so that the reaction is self-catalytic. The observations with *p*-type germanium make this explanation improbable.

The current-voltage curves for crystals being etched under such conditions[3] indicate that a junction exists at or near the germanium-electrolyte interface. When a *p*-type crystal is being etched the current passes in the forward direction, while with an *n*-type crystal the etching current is in the back direction. The deep pitting with *n*-type crystals can be explained if it is supposed that the junction breaks down at a few places so that the current and hence the etching is localized.

If an injecting contact is made to an *n*-type crystal, thin compared with a diffusion length (Fig. 1), the current in the germanium will consist chiefly of holes. Under these conditions etching takes place evenly on a macroscopic scale, as for a *p*-type crystal. The etching is apparent only where the holes reach the germanium-electrolyte surface. An interesting effect is observed if a small-angle grain boundary runs through the etched region. Near such a boundary the etching is *less* rapid than elsewhere. See Fig. 2.

This observation can be explained by supposing that the dislocations which form the small-angle grain boundary are the sites of traps which permit hole-electron recombination.[4] The hole current which reaches

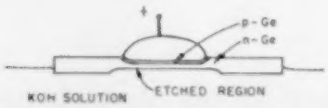

FIG. 1. Etching of a thin *n*-type Ge crystal.

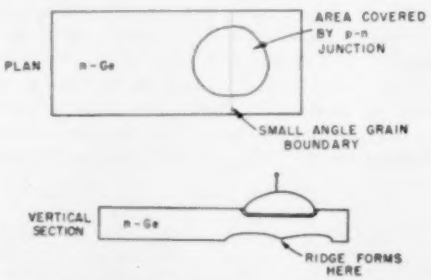

FIG. 2. Effect on etching when a small-angle grain boundary runs through the etched region of a thin *n*-type Ge crystal.

[1] S. G. Ellis, J. Appl. Phys. **26**, 1140 (1955).

[2] F. Jirsa, Z. anorg. u. allgem. Chem. **268**, 84 (1952).

[3] W. H. Brattain and C. G. B. Garrett, Bell System Tech. J. **34**, 129 (1955).

[4] Vogel, Read, and Lovell, Phys. Rev. **94**, 1791 (1954).

the germanium-electrolyte interface near the small-angle grain boundary is therefore reduced and the etching consequently retarded.

The dislocations in such boundaries are commonly of the order of 10^{-4} cm apart. Etching studies[1] show that dislocations of a different character are scattered throughout the crystal with a similar (3-micron) inter-dislocation spacing. The above observation shows, therefore, that not all the dislocations are equally effective as recombination centers. Such observations do not show whether the dislocations are themselves the recombination centers or merely the preferred sites for impurity atoms which behave as recombination centers.

I am indebted to J. J. Gannon for technical help in some of these experiments.

PHYSICAL REVIEW VOLUME 100, NUMBER 4 NOVEMBER 15, 1955

Magnetic Susceptibility of Sodium Metal

RAYMOND BOWERS
Westinghouse Research Laboratories, East Pittsburgh, Pennsylvania
(Received July 27, 1955)

The total susceptibility of sodium metal has been measured from room temperature down to 55°K using the Gouy technique. The mass susceptibility at room temperature was found to be $+(0.70\pm0.03)\times10^{-6}$ cgs units. This result is analyzed by using an estimate of the ion core susceptibility and calculations of the conduction-electron spin contribution. The analysis leads to a conduction-electron orbital diamagnetism which is much smaller than the value obtained from the Landau-Peierls formula. No explanation is given of this disparity.

The susceptibility decreases by 4.5% between room temperature and 55°K. No abnormal behavior was found in the susceptibility between 77°K and 55°K where the Knight shift exhibits an anomaly. An account is given of experimental difficulties which were encountered in an attempt to measure the susceptibility at liquid helium temperatures.

INTRODUCTION

THE total magnetic susceptibility χ of metallic sodium is the sum of three components, namely, the diamagnetism of the core electrons χ_c, the paramagnetism due to the spin of the conduction electrons[1] χ_s, and the diamagnetism due to the orbital motion of the conduction electrons[2] χ_0. In this paper we shall be interested in the magnitude of these components.

For simple metals such as sodium, the contribution due to the core can be determined indirectly from the measured susceptibility of sodium salts[3] and can also be calculated with reasonable confidence using Hartree-Fock wave functions.[4] The determination of the two conduction-electron contributions, particularly the orbital component, is much more difficult. The free-electron calculations, while giving a qualitative understanding of why the susceptibility is almost temperature-independent, are not satisfactory quantitatively. The susceptibility of sodium computed on the basis of the free-electron model[5] leads to a value which is too low by a factor of 3.

A number of recent developments have renewed interest in the susceptibility of sodium metal, particularly concerning the determination of the component susceptibilities. First, an experimental technique has been developed for measuring the spin contribution directly.[6] Only lithium has been studied so far but measurements on sodium are being made currently. Secondly, new theoretical values have been published for the spin contribution. Pines[7] has applied the Bohm and Pines collective-electron theory to this problem. Furthermore, calculations have been made by Townes, Herring and Knight[8] and by Kohn and Kjeldaas[9] of the spin contribution from the experimental value of the Knight shift in sodium.

With the value of ion core susceptibility and these recent values for the spin contribution, an estimate of the orbital contribution can be obtained if the total static susceptibility is known. Since there is a wide scatter in the published data,[10] we have redetermined this total susceptibility.

Apart from the absolute value of the susceptibility at room temperature, we have measured the suscepti-

[1] W. Pauli, Z. Physik. **41**, 81 (1927).
[2] L. Landau, Z. Physik. **64**, 629 (1930). R. E. Peierls, Z. Physik. **80**, 763 (1933); **81**, 186 (1933).
[3] F. E. Hoare and G. W. Brindley, Trans. Faraday Soc. **33**, 268 (1937); Proc. Phys. Soc. (London) **49**, 619 (1937).
[4] A. Sommerfeld and H. Bethe, Handbuch der Physik **24**, Part II, 278 (1933).
[5] N. F. Mott and H. Jones, *The Theory of Metals and Alloys* (Oxford University Press, London, 1936), p. 188.
[6] Schumacher, Carver, and Slichter, Phys. Rev. **95**, 1089 (1954).
[7] D. Pines, Phys. Rev. **95**, 1090 (1954).
[8] Townes, Herring, and Knight, Phys. Rev. **77**, 852 (1950).
[9] T. Kjeldaas and W. Kohn, Phys. Rev. **99**, 623(A) (1955).
[10] A Bernini, Nuovo cimento **7**, 441 (1904); Physik. Z. **6**, 109 (1905); K. Honda, Ann. Physik **32**, 1027 (1910); M. Owen, Ann. Physik. **37**, 657 (1912); W. Sucksmith, Phil. Mag. **2**, 21 (1926); McLennan, Ruedy, and Cohen, Proc. Roy. Soc. (London) **A116**, 468 (1927); C. T. Lane and E. S. Bieler, Proc. Roy. Soc. (Canada) **22**, 117 (1928); W. Klemm and B. Hauschulz, Z. Elektrochem. **45**, 346 (1939).

TABLE I. Details of four specimens and values of the susceptibility obtained with each of them.

Dimensions of sodium		Magnetic force due to Na / Magnetic force due to quartz	Mass susceptibility of Na (cgs units)
Area (cm^2)	Length cm		
0.138	7.6	1.70	0.687×10^{-6}
0.138	7.6	1.80	0.720×10^{-6}
0.108	7.6	1.55	0.708×10^{-6}
0.107	5.4	1.55	0.702×10^{-6}

bility as a function of temperature down to 55°K. In the free-electron picture of the conduction-electron susceptibility, there should be no change apart from the effects of thermal expansion on the Fermi energy. Changes with temperature might occur, however, due to electron-phonon interaction at low temperatures.[11] It is to be noted that Knight[12] has found an anomaly in the Knight shift in sodium below 77°K; if this anomaly is connected with a density of states change, it should be seen in the susceptibility.

METHOD

The measurements of susceptibility have been made using the Gouy technique. A Gulbransen-type microbalance[13] has been used to measure the force on the specimen; the balance is capable of measuring a force of 1 μg with a 3-g load. Due to its great sensitivity, only moderate magnetic fields, less than 4000 gauss, are required for the measurement of susceptibility.

The sodium used for the specimens was supplied by the Ethyl Corporation. According to chemical analysis there was no strongly paramagnetic or ferromagnetic impurity present in concentrations greater than 0.0002%. (The absence of ferromagnetic impurities was demonstrated also by the fact that we found the susceptibility to be independent of the magnetic field. The small change in the susceptibility with temperature found in this work indicates the low level of paramagnetic impurities.) Potassium appeared to be the most abundant impurity, and chemical analysis showed it to be less than 0.01%.

In order to make a specimen from the metal, the oxide was first removed from the sodium under pure benzene. It was placed in a quartz tube and the benzene pumped off. The sodium was then melted under high vacuum. On melting, the sodium breaks any remaining oxide coat; the oxide coat sticks to the wall of the quartz tube and it is very easy to remove the shiny metal from inside. The sodium was allowed to flow out of the oxide and was pushed into a thin-walled quartz tube, the final containing tube, by the pressure of pure helium gas. This quartz tube was sealed off just above the sodium level so as to include some helium gas for thermal exchange. Using this technique we were able to cast cylinders of sodium about 7 cm long and 3½ mm diameter in quartz tubes of various wall thickness ranging between ½ and ¼ mm. The cylinders of sodium produced in this way had very little cavitation and there was no visible oxide. Quartz has been used as a container because its susceptibility has been found to be almost temperature independent, and in addition it has been suggested that sodium reacts slightly with Pyrex, especially at high temperatures, producing free radicals which are paramagnetic.

The quartz tube makes a substantial contribution to the observed force on the specimen (see Table I) so its contribution must be accurately determined. This has been done in two ways. First, the susceptibility of quartz glass has been measured between room temperature and 1.5°K and the container contribution calculated from this and the measured dimensions of the container. Secondly, pieces of quartz which were ultimately to be used for containers were measured independently. The values of the quartz contribution obtained by the two methods were in agreement to 5%. A further check on the accuracy of the correction has been obtained by varying the dimensions of the specimen so as to change the quartz contribution relative to that of the sodium (Table I). No consequent systematic error appeared in the final value for sodium. We are restricted to these methods of determining the quartz contribution since we wished to preserve the final specimens.

The sensitivity of the balance used to measure the magnetic force has been determined using small calibrated weights and also by bouyancy measurements on a specimen of known volume. The magnetic field was measured with a fluxmeter which has been calibrated by proton resonance. In order to check this absolute calibration of the apparatus, we have measured the susceptibilities of: (1) triply distilled water which had been passed through an ion exchange column and boiled to remove air; (2) zinc sulfide with 0.1% manganese incorporated, and (3) oxygen gas. These three calibrations together with the absolute calibration show a scatter of 6%. The calibration used for the final data reduction was the mean of these. Considering the large correction for the quartz container and the scatter of the calibration data, we believe the final data given for the susceptibility at room temperature is accurate to 5%. The relative change in the susceptibility with temperature is accurate to 1%.

The data for the susceptibility below room temperature has been corrected for thermal contraction assuming that the quartz container does not restrain the decrease in cross section of the sodium. (The variation of the magnetic force with temperature, the experimentally determined quantity, is proportional to the product of the susceptibility per unit mass, the density, and the area of cross section of the specimen. If the

[11] M. J. Buckingham, Nature **168**, 281 (1951). M. J. Buckingham and M. R. Schafroth, Proc. Phys. Soc. (London) **67**, 828 (1954).
[12] W. D. Knight, Phys. Rev. **96**, 861 (1954).
[13] E. A. Gulbransen, Rev. Sci. Instr. **15**, 201 (1944); R. Bowers and E. A. Long, Rev. Sci. Instr. **26**, 337 (1955).

container with its negligible contraction had kept the area constant, allowing the sodium to contract in length only, the sole correction would be through the density change, where as our data allows for both density and area changes.) The container may effect the contraction slightly, hence there is some uncertainty in the correction made.

RESULTS

The values obtained for the susceptibility at room temperature are given in Table I. The average value for the mass susceptibility of the four specimens at room temperature is 0.70×10^{-6} cgs units. The variation with temperature down to 55°K is shown in Fig. 1 in the form of the percentage change from the room temperature value. The susceptibility decreases by 4.5% between room temperature and 55°K.

It was originally intended to measure the susceptibility from 300°K to 1.5°K. However, experimental difficulties prevented work in the liquid helium range.

The principal difficulty is due to electromagnetic damping of the specimen in the magnetic field, the damping being proportional to the conductivity of the specimen. At room temperature this is not serious, but because of the purity of the sodium, its electrical resistance may fall by a factor of 1000 between room temperature and 4°K,[14] and the balance becomes seriously over-damped. It is easily calculated that one would have to wait several hours for equilibrium at 4°K for the specimens which we have used. Observation of the damping of the balance at higher temperatures leads us to estimate that 30°K to 40°K would be the lowest temperatures at which measurements could have been made.

One way of overcoming this difficulty is to cut up the specimen and "laminate" it in some way. We have not found a satisfactory way of doing this for sodium (although it is quite easy for metals such as copper) because one wishes to avoid the presence of insulation materials which may react with the sodium, and also because one would have to study carefully the magnetic properties of the insulation. We have also considered the possibility of introducing trace impurities to reduce the conductivity but this would lead to uncertainties in the evaluation of the susceptibility data. There is very little one can do with the balance system, leaving

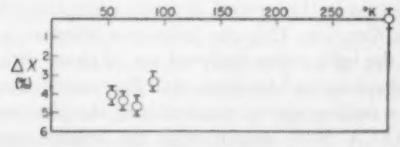

FIG. 1. The variation of the susceptibility of sodium with temperature.

[14] D. K. C. MacDonald and K. Mendelssohn, Proc. Roy. Soc. (London) **A202**, 103 (1950).

TABLE II. Theoretical estimates of the mass susceptibility of sodium,[a] in cgs units.

	I	II
χ_c	-0.23×10^{-6}	-0.23×10^{-6}
χ_s	$+0.68\times10^{-6}$	$+0.86\times10^{-6}$
χ_0	-0.23×10^{-6}	-0.23×10^{-6}
Total χ	$+0.22\times10^{-6}$	$+0.40\times10^{-6}$

[a] Experimental total $\chi = +0.70\times10^{-6}$.

the specimen unchanged, to reduce the damping. A lower sensitivity balance would have a smaller damping time, but the accuracy of measuring the magnetic force would also be smaller. Similarly, reducing the magnetic field reduces the damping but the magnetic force is reduced in the same proportion.

We have observed another effect which renders work at the lower temperatures difficult. Between 77°K and 4.2°K, the sodium ruptured the quartz container of the two specimens which were used. This phenomenon has not been examined in detail but it might be connected with the phase transformation in sodium observed by Barrett[15] in this temperature range. It seems unlikely that the normal difference in thermal contractions could be the cause because the bulk of the volume changes occur between room temperature and 77°K and it is quite certain that the rupture did not occur in this range.

DISCUSSION

We shall first discuss the value of the susceptibility at room temperature. The value we obtain is slightly higher than the two most recent previous determinations of the susceptibility[10]; it is 6% higher than the value due to Klemm and Hauschulz, and 7% higher than that due to Lane and Bieler. Our value is at least 17% higher than that found in any work previous to these authors.

In Table II we have constructed two theoretical values which may be compared with our experimental value. Column I uses the free electron value for the spin contribution while Column II uses the value due to Pines and Kohn and Kjeldaas. The value for the core susceptibility is a mean value derived from measurements on sodium salts and also direct calculations from the electronic wave functions. The orbital contribution used in both columns is the Landau-Peierls free electron value. It can be seen that there is a serious disparity between these calculated values and the experimental value. Indeed no experimental value for sodium has been reported in the literature as low as these calculated values.

It seems unlikely that the disparity can be due to the value for the ion core. The observed susceptibility of neon, which has the Na^+ configuration, suggests that it is unlikely to be in error by more than 20%. With regard to the spin contribution, Kohn and Kjeldaas

[15] C. S. Barrett (private communication).

claim a 5% accuracy for their calculation while Pines claims 20% for his. Unfortunately, we do not have as yet an independent experimental value for this spin contribution. However, these two different types of calculation do give the same result, and in the case of lithium, for which χ_s has been measured, the calculations are in good agreement with the experimental value.

Thus we conclude, that if the value of the orbital contribution is that given by the Landau-Peierls formula, the susceptibility of sodium is anomalously high.

If either of the values for $\chi_s+\chi_c$ in Table II are accepted as correct, then our experimental value is seen to imply a surprisingly small value for the orbital diamagnetism. Using the free electron χ_s, we obtain $\chi_0=+(0.25\times10^{-6})$; using the Kohn and Kjeldaas value, we obtain $\chi_0=+(0.07\times10^{-6})$. The value of $-(0.23\times10^{-6})$, expected on the free-electron theory, differs from both of these by several times the estimated error.

We have no explanation of these disparities. While it is true that according to the band theory of metals, the Landau-Peierls formula does not give the complete orbital susceptibility,[16] it would be surprising if the correction terms were responsible.

Finally, we shall discuss the low-temperature data. The decrease in susceptibility by 4.5% from room temperature to 55°K is roughly what is to be expected from the change in the Fermi level with density. Below 77°K, we have found no sign of an anomaly similar to that found in the Knight shift in sodium[12] which changes by 5% between 77°K to 55°K. Thus we conclude that, at least in the limited temperature range 77°K to 55°K, the behavior of the Knight shift is not due to a rapid change in the density of states.

Note added in proof.—After submitting this paper, we received a preprint of a paper by Schumacher and Slichter which gives the results of their measurement of the conduction electron spin susceptibility in sodium. (This paper is to appear soon in *The Physical Review.*) They obtain for χ_s a value per g of $(0.96\pm0.1)\times10^{-6}$ cgs units corrected to room temperature. If one uses the value of 0.96×10^{-6} to calculate the orbital diamagnetism as described in the discussion above, one obtains $\chi_0=-0.03\times10^{-6}$. This is still much less than the free electron value of -0.23×10^{-6}. However, the uncertainties in the values of χ_s, χ_c and the total χ are now such that a combination of extreme values of these quantities can lead to a χ_0 close to the free electron value. Hence, the existence of a substantial deviation of the actual orbital diamagnetism from the free electron value, while appearing most likely from the data, is not definitely established.

ACKNOWLEDGMENTS

We wish to acknowledge the helpful discussions we have had with E. N. Adams, T. Kjeldaas, and W. Kohn.

[16] A. H. Wilson, Proc. Cambridge Phil. Soc. **49**, 292 (1953); E. N. Adams, Phys. Rev. **89**, 633 (1953).

PHYSICAL REVIEW VOLUME 100, NUMBER 4 NOVEMBER 15, 1955

Electroluminescence of GaP

G. A. Wolff, R. A. Hebert, and J. D. Broder
Signal Corps Engineering Laboratories, Fort Monmouth, New Jersey

(Received June 10, 1955)

Electroluminescence has been observed in GaP single crystals. Above a threshold current the intensity of the emitted light is proportional to the ac and dc passing through the crystals. The orange color of the light emission probably is due to the presence of Ga as activator, while the brilliant, deep red luminescence is observed in crystals where Zn is a possible activator. The temperature dependence of the luminescence is negligible in the range from liquid nitrogen temperature to 160°C. The impact excitation mechanism of Piper and Williams is proposed.

SINGLE crystals of GaP have been prepared[1] which were found to emit orange-colored light when either dc, or ac (up to 20 000 cps) is applied. Massive In, Ga, Hg, Cd, Zn, Pb, conducting glass, and point contacts of W were used as electrodes. Above a threshold current, the light intensity is proportional to the ac and dc passing through the crystals (Fig. 1), as has been found for SiC [2] and ZnS:Cu [3]; it increases exponentially with voltage. Since rectification is found in the crystals, the light output in the forward direction is less than in the reverse direction. This also holds true when ac is applied; the light pulses observed are in phase with the applied voltage and are sinusoidal. This was determined with an oscilloscope by synchronizing the photomultiplier (RCA 5819) output with the voltage applied (Fig. 2). There were no out-of-phase pulses observed. The decay time, as derived from the ac measurements, is less than 25 μsec. Using dc, the light emitted from the majority of the crystals appears in the vicinity of the

[1] Wolff, Keck, and Broder, Phys. Rev. **94**, 753 (1954).
[2] Lehovec, Accardo, and Jamgochian, Phys. Rev. **83**, 603 (1951); **89**, 20 (1953).
[3] W. W. Piper and F. E. Williams, Phys. Rev. **87**, 151 (1952).

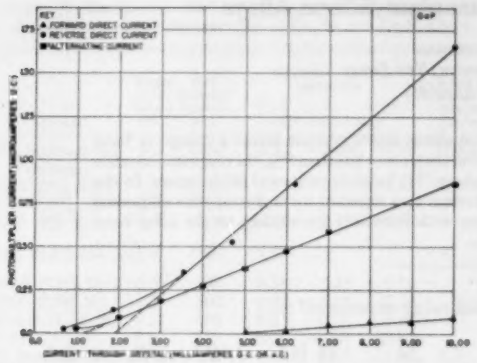

FIG. 1. The intensity of the electroluminescence, given as the photomultiplier current, as a function of the current passing through the crystal.

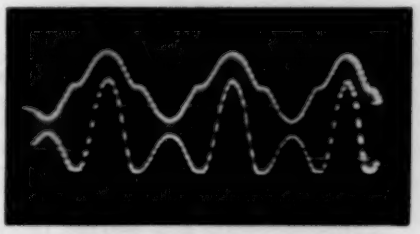

FIG. 2. Oscillogram of photomultiplier current (lower curve) synchronized with the current through the crystal (60 cps; upper curve). The current is nonsinusoidal due to nonohmic characteristic and rectification in the crystal. More intense emission is observed during the reverse current interval.

cathode. The temperature dependence of the luminescence is negligible. Light is also emitted when a layer of GaP powder, or a layer of a suspension of GaP powder in a dielectric, is placed between a metal and a conducting-glass electrode. When GaP crystals are bombarded with electrons from a Van de Graaff generator, the same orange-colored luminescence resulted. Neither fluorescence, phosphorescence, thermoluminescence in the visible range, nor photoconductivity has been observed.

The electroluminescence begins at 5600 A, which is close to the end of the absorption edge of GaP (5300 A). It can be concluded from this that the emission is a direct electron-hole recombination but it is more likely an electron-hole recombination through an activator, having the energy term close to the valence band. The GaP crystal might very well be self-activated, since it has been grown from a solution in Ga.[1] As a result of adding Zn or Cu to the Ga solvent prior to preparing the GaP solution and crystallization, GaP crystals having a brilliant, deep red electroluminescence were obtained and these were of a much higher efficiency than the crystals showing the orange luminescence. The spectral range of the red luminescence begins at about 6800 A as was found from the spectra recorded photographically. In this instance, there was definite shift of the emission toward longer wavelengths. Probably the spectra extend beyond 8900 A, where the film sensitivity is negligible.[4] Whether or not Zn or Cu was the activator responsible for the red luminescence is yet to be determined, but the evidence points to Zn in relatively small amounts. The crystals were prepared in quartz tubes, which would indicate the possibility of Si as a coactivator. There was no noticeable effect upon the orange luminescence as a result of doping the crystals with elementary C, Si, Ge, Mn, or S.

GaP:Zn corresponds very largely to ZnS:Cu. GaP is isoelectronic with ZnS and has the same crystallographic structure. Among the colored III-V compouuds, AlP (light yellow), AlAs (brown) and GaP (orange),[5] there is strong indication that GaP will have good luminescent properties since it is closely related to ZnS. Since, however, GaP has a much lower energy gap than ZnS—close to that of CdS—and the semiconductor properties are more pronounced, with the bonding energy much higher than ZnS, basic differences in the properties of these two luminescent materials are to be expected.

It is proposed that impact excitation as suggested by Piper and Williams[5,6] for ZnS:Cu, causes the electroluminescence in GaP at the metal-semiconductor barrier. It was found that in one out of ten cases luminescence did not occur in the vicinity of the cathode. From this, it may be concluded that recombination of injected minority carriers from a *p-n* junction captured by the activator system[2,7] is a second possibility for luminescence, although it is as yet impossible to prepare *p-n* junctions in GaP crystals to confirm this point. By doping with S, *n*-type material only was obtained. It was dark in color and had relatively low resistivity.

It might be worthwhile to mention that electroluminescence was also observed in GaAs and Si by means of a snooperscope, but the luminescence was irregular, fading, disappearing and reappearing as the current passed through the crystals.

We are indebted to Miss M. Minamoto for providing some of the GaP crystals. Thanks are also due to Dr. W. J. Ramm, Mr. L. McSherry, and Mr. M. N. Stein for their help with the Van de Graaff generator. The authors also wish to thank Mr. M. J. Katz for his help in determining the optical absorption of the compounds mentioned.

[4] *Note added in proof.*—A second type of luminescence of a yellow-green color, seen in Zn-doped crystals, consists of the red band mentioned in the text and a band in the range of 5300 A to 6300 A, with a maximum at 5900 A.

[5] Absorption edges as determined in our laboratory are located at about 4000 A, 5730 A, and 5200 A which corresponds to energy gaps of approximately 3.1 ev, of 2.16 and 2.39 ev.

[6] W. W. Piper and F. E. Williams, Brit. J. Appl. Phys. Supplement 4, 39 (1955); F. E. Williams, Advances in Electronics 5, 158 (1953).

[7] M. Schoen, Z. Naturforsch. 8a, 442 (1953).

Magnetoresistance of Germanium-Silicon Alloys

MAURICE GLICKSMAN
RCA Laboratories, Princeton, New Jersey
(Received July 25, 1955)

Magnetoresistance measurements of *n*-type germanium-silicon single crystals reveal a change in band structure occurring at about 14% silicon content. For silicon contents of less than 8%, the magnetoresistance is that of a crystal with ellipsoidal conduction minima along [111] axes in reciprocal lattice space. In the region 11–14% silicon, the magnetoresistance changes toward that expected for a crystal with ellipsoidal conduction minima along [100] axes. These results agree with Herman's speculations on the alloy band structure.

ALLOYS of germanium and silicon have been prepared[1–3] in homogeneous form, and a number of the physical and electrical properties measured. In particular, measurements of the optical band gap reported by Johnson and Christian[3] showed that the alloys have a forbidden band gap which may be represented by the equations:

$$E=0.72+1.5x \text{ ev} \tag{1}$$

in the region of x between 0 and 14%, and

$$E=0.89+0.31x \text{ ev} \tag{2}$$

in the region of x between 14 and 100%. Here x is the mole percent of silicon in the germanium.

To explain this behavior of the forbidden band gap, Herman suggested[4] that the alloys exhibit a band structure like germanium and silicon. Germanium has a conduction band with minima along the [111] axes[5] in the reduced zone; the conduction minima in silicon are along the [100] axes[5,6] in the reduced zone. Herman suggested that in germanium, beside the [111] states which are the lowest conduction minima, there are [100] minima about 0.17 ev above the [111] states. As we add silicon to form the alloys, both the [111] and the [100] minima move away from the valence band, at rates given respectively by Eqs. (1) and (2). Therefore, with less than 14% silicon we have conduction in [111] minima; for greater alloy compositions we would expect conduction in [100] minima.

In order to test this suggestion of Herman's, magnetoresistance measurements are being made on single-crystal samples of germanium-silicon alloys. This is a preliminary report on the results obtained to date.

For cubic crystals, the change of resistivity upon application of a magnetic field can be represented by the following expression[7]:

$$\frac{\Delta\rho}{\rho H^2}=b+c\frac{(\mathbf{I}\cdot\mathbf{H})^2}{I^2H^2}+d\frac{I_1^2H_1^2+I_2^2H_2^2+I_3^2H_3^2}{I^2H^2} \tag{3}$$

where ρ is the resistivity, $\mathbf{I}$ and $\mathbf{H}$ the electric current and magnetic field, respectively, with the components taken along the crystal axes. The constants b, c, and d can be determined from the measurement of the magnetoresistance for certain directions of $\mathbf{I}$ and $\mathbf{H}$, and compared with theory. If we assume a relaxation time dependent on the energy only and conduction minima ellipsoidal in shape and oriented along the [100] axes of the [111] axes in the reduced zone, we obtain the following predictions[8]:

$$\begin{aligned}&[100]\text{ axes: } b+c+d=0, \quad d<0;\\ &[111]\text{ axes: } b+c=0, \quad d>0.\end{aligned} \tag{4}$$

To a first approximation, the data for silicon satisfy the first condition; those for germanium, the second. The constants b, c, and d are functions of the scattering law assumed, the ratio of the effective masses in the minima, and the Hall mobility R/ρ. However, the above symmetry relations [Eqs. (4)] do not depend on these quantities.

In the region where the two levels may be of the order of kT apart, both bands will contribute to the conduction. The magnetoresistance observed will be intermediate between the two cases. A calculation shows that there is no simple symmetry relation as in the cases where one set of valleys alone takes part. However, there is a condition among the constants b, c, and d which involves the effective masses of the valleys.

Oriented samples of germanium, silicon, and germanium-silicon alloys, *n*-type in conductivity, were cut in a bridge shape.[9] The resistivity, Hall coefficient, and magnetoresistance were measured at about 290°K. Details of the samples and results of the measurements

[1] H. Stöhr and W. Klemm, Z. anorg. u. allgem. Chem. **241**, 305 (1939).
[2] C. C. Wang and B. H. Alexander, American Institute of Mining and Metallurgical Engineers Symposium on Semiconductors, New York, February 15–18, 1954 (unpublished).
[3] E. R. Johnson and S. M. Christian, Phys. Rev. **95**, 560 (1954).
[4] F. Herman, Phys. Rev. **95**, 847 (1954).
[5] Dresselhaus, Kip, and Kittel, Phys. Rev. **98**, 368 (1955) and previous notes by both the California and the Lincoln Laboratory groups, referred to in above paper.
[6] G. L. Pearson and C. Herring, Physica **20**, 975 (1954).
[7] G. L. Pearson and H. Suhl, Phys. Rev. **83**, 768 (1951).
[8] B. Abeles and S. Meiboom, Phys. Rev. **95**, 31 (1954); M. Shibuya, Phys. Rev. **95**, 1385 (1954).
[9] Similar in shape to those used by Pearson and Suhl (reference 7), except that two additional probes were at the center of the sample bar and were used for Hall measurements.

TABLE I. Resistivity, Hall mobility, and magnetoresistance measurements on various samples of Ge, Si, and Ge-Si alloys.

Crystal	Resistivity (ohm-cm)	Hall mobility (cm^2/v-sec)	Magnetoresistance constants (10^8 cm^4/v^2-sec^2) b	c	d	Ratio of effective masses (m_l/m_t)
Ge (average for 5 samples)	5–7	4250	8.57	−7.99	17.99	12.3±3
106*T* (6% Si)	1.5	2330	2.31	−2.27	5.42	12.8±3
87*J* (7.5% Si)	0.6	2100	1.72			12
87*H* (8% Si)	0.9	2110	1.61	−1.43	3.60	9 ±3
87*E* (8.5% Si)	1.0	2100	1.57			8 $^{+3}_{-2}$
106*H* (12% Si)	6.2	840	0.55	−0.45	0.70	
106*G* (13% Si)	8.3	580	0.29	−0.18	0.24	
106*D* (13.5% Si)	9.2	540	0.21	−0.11	0.12	
106*F* (14% Si)	9.4	510	0.17	−0.09	−0.10	
Si (average for 6 samples)	8–10	1570	1.59	0.55	−2.05	5.5

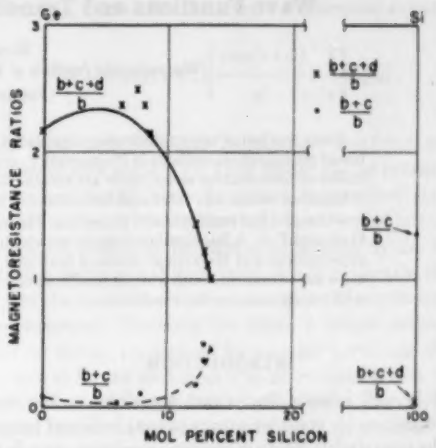

FIG. 1. The variation of the ratios $(b+c+d)/b$ and $(b+c)/b$ with composition in the germanium-silicon alloys. The curves drawn are for illustration purposes only.

are given in Table I. The composition of the alloy samples was estimated indirectly from measurements of the optical band gap[9] and x-ray determination of the lattice spacing.[1,3]

The mobility of these samples falls off very rapidly with the addition of silicon; indeed at 14% we are down to a mobility one-third that of pure silicon. This is in sharp contrast to measurements of R/ρ for p-type samples, where the decrease is less rapid in this region.[10,11] Mobility measurements on the p-type samples have been interpreted[11] in terms of a combination of alloy scattering and a lattice scattering which varies continuously from germanium to silicon. The rapid decrease in the n-type mobility may be due to additional scattering processes or an abrupt change in the lattice scattering or a combination of these. Measurements of the temperature dependence of the mobility are being made in the hope of clarifying this situation.

It is possible to estimate K, the ratio of longitudinal to transverse effective masses from the data, in the case where only one set of valleys need be considered. These values are given in the last column in Table I. The value 5.5 for silicon is in good agreement with previous measurements. However, the value 12.3±3 for germanium is to be compared with a ratio of 14.6 given by Benedek[12] and the value 19.3 determined from the cyclotron resonance measurements.[5] The errors in the magnetoresistance value of K for germanium are large because of a high sensitivity of this constant to the experimental data. However, an examination of the values for the crystals in the range 6–8.5% silicon shows a tendency for K to decrease, from 12.8±3 at 6%, to 8^{+3}_{-2} at 8.5%. This question will be examined in more detail when more data are available in the range 0–10%.

In the region 11.5–14% silicon, the magnetoresistance exhibits the changes in symmetry conditions expected for a competition of [111] and [100] minima. This behavior can be seen in Fig. 1, where are plotted $(b+c+d)/b$ and $(b+c)/b$ *versus* alloy composition. Since the constants b, c, and d are proportional to $(R/\rho)^2$, dividing by b eliminates the mobility variation from these functions. In the region 11–14%, $(b+c+d)/b$ drops off towards its value in silicon, whereas $(b+c)/b$ rises significantly from the low germanium value. This trend is well outside the estimated experimental error and tends to support Herman's speculations on the alloys' band structure.

If reasonable values are assumed for the effective masses of the valleys in this region, we can estimate the separation of the two sets of valleys. Some rough estimates indicate that samples 106*H*, 106*G*, 106*F*, and 106*D* have the [111] minima below the [100], with the two sets of the order of kT or less apart. The magnetoresistance data satisfy the new symmetry relation but are rather insensitive to changes in the effective masses of the [100] and [111] valleys. When more data become available, it may be possible to say something about the shape of the valleys in this region.

Especial thanks are due to Dr. S. M. Christian and R. Jensen who grew the alloy crystals used here, and to J. J. Gannon who did much of the sample preparation. The author is indebted to Dr. J. Kurshan, who began these experiments, and to Dr. A. Moore and Dr. F. Herman for much helpful discussion and encouragement.

[10] Similar measurements are being made on p-type alloy single crystals and will be reported later.
[11] A. Levitas, Phys. Rev. **99**, 1810 (1955).
[12] G. B. Benedek (private communication).

Wave Functions and Transition Probabilities for Light Atoms*

HUSEYIN YILMAZ†
Massachusetts Institute of Technology, Cambridge, Massachusetts
(Received July 12, 1955)

A new method of taking electronic correlations into account is presented. This method differs from conventional configuration methods in its generality, simplicity, and interpretation. However, due to the particular choice of perturbation series, there are substantial similarities. The computation is based on a function, the *S*-function, which was tabulated beforehand. This function is a bilinear Laplace transform of the Green's function and has various useful properties. The method is applied to the $(1s^2 2s^2 2p^2)$ configuration of C I, N II, O III, and F IV. A few significant terms are identified which take care of 60–80% of the discrepancy between experimental and theoretical values of multiplet separations. The spin-orbit separations and nebular transitions are calculated. With a slight modification of the $2p$ wave function it is seen that substantial agreement with experiment can be obtained.

INTRODUCTION

IT is well known that exact solutions to the wave equation for complex atoms cannot be found because of the inseparable electron-electron repulsion term in the Hamiltonian. Consequently, one must use some kind of an approximation. The approximate wave functions so far developed are either analytical or numerical in nature. The methods of Slater[1] and of Morse, Young, and Haurevitz[2] (hereafter referred to as M.Y.H.) give analytical wave functions. Hartree[3] self-consistent field wave functions are numerical and they do not take the exchange effect into account. Hartree-Fock[4] self-consistent field wave functions are also numerical and they take exchange into account. All these methods give separable wave functions, i.e., they do not take into account the inseparable effect of the electron-electron repulsion term in the Hamiltonian. But in most cases of physical interest, one needs sufficiently accurate wave functions for use in calculations such as transition probability, hyperfine structure, polarizability, and spin-orbit splittings, so that the inseparability must be included. Especially the multiplet separations and, therefore, the spin-orbit energies, and magnetic dipole radiations are strongly affected by the inseparability.[5]

One way of taking the inseparability into account is to include factors of the form

$$1+\alpha r_{12}+\beta(r_1-r_2)^2+\cdots$$

as is done in the Hylleraas's wave functions for helium. This procedure introduces a large number of variation parameters and becomes impractical for many electron configurations due to the difficulties of making the wave functions antisymmetric and orthonormal. A second way is the so-called configuration interaction method which is essentially a complicated perturbation expansion. To do this correctly one has to find good wave functions for a large number of higher configurations in addition to the actual state in question. Unfortunately, the perturbation of these states gives tedius expressions, which make the examination of a sufficient number of terms prohibitively difficult. It seems that in order to make further progress possible in this field, an easier way must be found. The purpose of this paper is to suggest a simpler way of taking the inseparability into account. This is a perturbation expansion based on the variational wave functions discussed in M.Y.H. In fact, this work may be considered as a continuation of M.Y.H. to include the inseparable effect of electronic repulsion terms. The perturbation functions are strictly hydrogenic one-electron wave functions and are automatically selected as soon as the zeroth-order variational wave function is given.

The main feature of the M.Y.H. variational method is to take the antisymmetric combinations of the one-electron functions

$$u=N(\textstyle\sum_k A_k r^k e^{-a_k r}) r^\lambda P_\lambda^m(\cos\theta) e^{im\phi},$$

and determine the parameters a_k from a variational principle. The resulting functions have been shown to be fairly good by various calculations.[6] The necessary integrals were tabulated so that one could do the minimization of each multiplet numerically. Because of the increasing need and interest, the earlier tables have been extended by the present author to include $3d$ electrons in addition to $1s$, $2s$, and $2p$ electrons and recomputed on I.B.M. machines in a wider range and closer spacing of the parameters. It is hoped that these tables, by P. M. Morse and the author, appropriate for calculations of the sort discussed in this paper, will be published in the near future.

The zeroth-order wave functions that we have used in the present work are obtained by a graphical minimization over the machines computation. Since the varia-

* Work supported by the Office of Naval Research.
† Now at Stevens Institute of Technology, Hoboken, New Jersey.
[1] J. C. Slater, Phys. Rev. **36**, 1 (1930); **42**, 33 (1931); **34**, 10 (1929).
[2] Morse, Young, and Haurwitz, Phys. Rev. **48**, 948 (1935).
[3] Hartree, Hartree, and Swirles, Trans. Roy. Soc. (London) **A238**, 229 (1939).
[4] D. R. Hartree, Proc. Roy. Soc. (London) **A150**, 9 (1935).
[5] A. P. Yutsis, J. Exptl. Theoret. Phys. (U.S.S.R.) **19**, 565 (1949).
[6] A. P. Yutsis and G. K. Tsuyunaitis, Zhur. Eksptl. i Teort. Fiz. (U.S.S.R.) **23**, No. 5 (11), 512 (1952); P. Gombas and R. Gaspar, Acta Phys. Hungarica **1**, 295, No. 3 (1952).

tional energies are quite close to the true energies, one needs to consider only the first-order terms in the perturbation scheme. Further, the elaborate parts of the calculation have been eliminated by the use of a function, the S-function, which was calculated and tabulated beforehand. The S-function was investigated by the present author quite extensively; many useful expressions, recursion formulas, and a simple approximation have been found. A few of its properties which are of continual use throughout this work are given in the Appendix. The tables and the properties of the S-functions and the special choice of perturbation functions as strictly hydrogenic single-electron wave functions greatly facilitate the examination of a large number of perturbation terms. Since it is recognized that configuration interaction series are slowly convergent in atoms,[7] the advantage of the present method should be evident.

A. Correction Terms

The zeroth-order wave function is the variational wave function Ψ_0 in its determinantal form, obtained by the method of M.Y.H. The correction terms are appropriate combinations of the u's of M.Y.H. and of the set

$$\psi_{n\lambda m}(r)=N_{n\lambda m}\xi_{n\lambda}{}^{\lambda}\exp(-\tfrac{1}{2}\xi_{n\lambda}) \times P_\lambda{}^m(\cos\theta)e^{im\varphi}L_{n-\lambda-1}{}^{2\lambda+1}(\xi_{n\lambda}), \quad (1)$$

where $\xi_{n\lambda}=2\mu a_\lambda(\lambda+1)r/n$, $a_0=a$, $a_1=c$, $\psi_{100}=u_1$, $\psi_{210}=u_3$, $\psi_{211}=u_4$, and $\psi_{21-1}=u_5$ of M.Y.H. N is the normalization factor

$$N_{n\lambda m}=\left[\left(\frac{2a_\lambda(\lambda+1)\mu}{n}\right)^3\frac{2\lambda+1}{8\pi n} \times\frac{(\lambda-m)!(n-\lambda-1)!}{(\lambda+m)![(n+\lambda)!]^3}\right]^{\frac{1}{2}}. \quad (2)$$

The functions L are the Laguerre polynomials. These functions are orthogonal to the basic variational functions u_2, and to each other.

If there are $2s$ electrons in the zeroth-order wave function, then ψ_{200}, ψ_{300}, $\cdots$, ψ_{n00} cannot be used because these are not orthogonal to u_2. But we can build up a proper set ϕ_n as a linear combination of ψ_{200}, ψ_{300}, $\cdots\psi_{n00}$:

$$\phi_2=u_2, \quad \phi_n=\sum_{\sigma=2}^{n}A_\sigma\psi_{\sigma 00}, \quad \int\tilde{\phi}_i\phi_k d\tau=\delta_{ik}. \quad (3)$$

This requires only the following integrals:

$$\zeta_n=\int u_2\psi_{n00}d\tau. \quad (4)$$

[7] Green, Mulder, and Milner, Phys. Rev. **91**, 35 (1953).

The set (1) satisfies the simple differential equation

$$\nabla^2\psi(r)=\mu a_\lambda(\lambda+1)\left[\frac{\mu a_\lambda(\lambda+1)}{n^2}-\frac{2}{r}\right]\psi(r). \quad (5)$$

Thus these functions are hydrogenic functions with effective charge $\mu a_\lambda(\lambda+1)$. They would not be proper to use as variational wave functions for excited states because many of these functions have no adjustable parameters, their only parameter being fixed by the first variation (orthogonality to u's). Mathematically they are just the correction terms to correct the zeroth-order wave function. Therefore for those ψ whose orthogonality to the u_n are secured by angular parts, one does not have to fix the parameters so as to make ψ look like an excited state, but rather so as to make the convergence of the perturbation series as rapid as possible.

B. Single and Pair Substitutions

Correction terms Ψ_s are obtained by substituting for each basic function u in the zeroth-order determinantal wave function a ψ with its parameter and its quantum number chosen to be orthogonal to the function replaced. These are the "single substitution terms." It is also possible for each pair of u's to be replaced by a suitably chosen pair of ψ's. These are called "pair substitution terms." Since the z-component of the total angular momentum is a good quantum number, a single substitution function should be so chosen that its m_l and m_s are equal to that of the replaced u. Similarly the $\sum m_l$ and $\sum m_s$ of the pair substitution terms must be equal to the $\sum m_l$ and $\sum m_s$ of the replaced basic functions. As a matter of fact, all the other possible substitutions (triple and higher substitutions, substitutions with different $\sum m_s$, etc.) give zero contributions to the energy.

C. Perturbation Scheme

Let Ψ be a linear combination of the variational wave function Ψ_0 and the correction terms Ψ_s:

$$\Psi=a_0\Psi_0+\sum_s a_s\Psi_s+\sum_\sigma a_\sigma\Psi_\sigma, \quad (6)$$

where the Latin indices represent the single substitutions and the Greek indices represent the pair substitutions. Since the energy computed with the zeroth-order wave function Ψ_0 is quite close to the true energy, we have $a_0\simeq 1$, $a_s\ll 1$ and $a_\sigma\ll 1$. Therefore we consider only the first-order terms in the perturbation.

The equation to be solved is

$$H\Psi=W\Psi. \quad (7)$$

Premultiplying this equation by Ψ_s or Ψ_σ, integrating over the space of all the electronic coordinates, and

neglecting the higher order terms, we obtain

$$a_s\left(W-\int\bar{\Psi}_sH\Psi_s d\tau\right)=a_0\int\bar{\Psi}_sH\Psi_0 d\tau,$$
$$a_s\left(W-\int\bar{\Psi}_sH\Psi_s d\tau\right)=a_0\int\bar{\Psi}_sH\Psi_0 d\tau, \tag{8}$$

with $W\simeq W_0$. The ratios a_s/a_0 and a_σ/a_0 are determined from these equations. Then the normalization condition,

$$a_0^2+\sum_s a_s^2+\sum_\sigma a_\sigma^2=1, \tag{9}$$

gives the actual values of the coefficients.

D. The Integrals Involved

The integrals $H_{ss}=\int\bar{\Psi}_sH\Psi_s d\tau$, and $H_{s\sigma}=\int\bar{\Psi}_sH\Psi_\sigma d\tau$ in (8) are of the same kind as defined by M.Y.H. The integrals $H_{0s}=\int\bar{\Psi}_sH\Psi_0 d\tau$ and $H_{0\sigma}=\int\bar{\Psi}_\sigma H\Psi_0 d\tau$ are different. We generalize the integrals discussed by M.Y.H. to include these new possibilities:

$$X_{mn,\,m'n'}=\int\bar{u}_m(1)\bar{u}_n(2)\frac{2}{r_{12}}u_{m'}(1)u_{n'}(2)d\tau_1 d\tau_2, \tag{10}$$

$$V_n^{n'}=\int\bar{u}_n(\mathbf{r})\frac{2}{r}u_{n'}(\mathbf{r})d\tau,$$
$$T_n^{n'}=-\int\bar{u}_n(\mathbf{r})\nabla^2u_{n'}(\mathbf{r})d\tau. \tag{11}$$

We see that $X_{mn,\,mn}=V_{mn}$, $X_{mn,\,nn}=X_{mn}$, $V_n^n=V_n$, $T_n^n=T_n$, etc. In order to keep the evaluation of H_{0s} similar to M.Y.H., we also put

$$X_{mn,\,mn'}=V_{m,\,nn'} \quad\text{and}\quad X_{mn,\,n'm}=X_{m,\,nn'}.$$

Most of these integrals are zero, according to the rules of Table I. Now it is easily seen that if the primes denote the substitution functions ψ the H_{0s} and $H_{0\sigma}$ are

$$H_{0s}=\mu^2T_n^{n'}-Z\mu V_n^{n'}+\mu\sum_{m\neq n}(V_{m,\,nn'}-X_{m,\,nn'}), \tag{12}$$

$$H_{0\sigma}=\mu[X_{mn,\,m'n'}-X_{mn,\,n'm'}]. \tag{13}$$

The T's are given as

$$T_n=a_\lambda(\lambda+1)\left[V_n-\frac{a_\lambda(\lambda+1)}{n^2}\right], \tag{14}$$

$$T_n^{n'}=a_\lambda(\lambda+1)V_n^{n'}. \tag{15}$$

E. Correction of the Energy and μ

From (8) we have

$$a_s=\frac{a_0H_{0s}}{W_0-H_{ss}},\quad a_\sigma=\frac{a_0H_{0\sigma}}{W_0-H_{\sigma\sigma}}. \tag{16}$$

We can calculate the corrected energy and the corrected μ similarly to M.Y.H., considering μ as a variation parameter. This gives

$$\mu=-\frac{V_0+2\sum a_sV_{0s}+2\sum a_\sigma V_{0\sigma}-\sum a_s^2(V_0-V_{ss})-\sum a_\sigma^2(V_0-V_{\sigma\sigma})}{2[T_0+2\sum a_sT_{0s}-\sum a_s^2(T_0-T_{ss})-\sum a_\sigma^2(T_0-T_{\sigma\sigma})]}, \tag{17}$$

$$W=-\frac{[V_0+2\sum a_sV_{0s}+2\sum a_\sigma V_{0\sigma}-\sum a_s^2(V_0-V_{ss})-\sum a_\sigma^2(V_0-V_{\sigma\sigma})]^2}{4[T_0+2\sum a_sT_{0s}-\sum a_s^2(T_0-T_{ss})-\sum a_\sigma^2(T_0-T_{\sigma\sigma})]}. \tag{18}$$

The values of a_s and a_σ can be recorrected using the corrected μ instead of μ_0. An approximate expression for W is

$$W=-\frac{V_0^2}{4T_0}-\sum_s\frac{H_{0s}^2}{H_{ss}-W_0}-\sum_\sigma\frac{H_{0\sigma}^2}{H_{\sigma\sigma}-W_0}. \tag{19}$$

F. Results for $2p^2$ Configuration

The method developed in the previous sections was applied to obtain the wave functions for the ^1D, ^3P, and ^1S states of the $(1s^22s^22p^2)$ configuration of C I, N II, O III, and F IV. Single substitutions up to $n=5$, $\lambda=4$ and double substitutions up to $n=5$, $\lambda=2$ were considered. Most of them give negligible contributions. The terms which give the largest contributions are given in Table II in the case of O III.

The ratios $\rho=(PS)/(DS)$ are compared with the experimental values in Table III.

G. Nebular Lines

The wave functions thus obtained are used to calculate the spin-orbit, spin-other orbit, and spin-spin interactions, and finally the intensity of the forbidden nebular transitions. Electric dipole transitions are still forbidden because of parity considerations. The method used for the magnetic dipole transitions is a generalization of Condon's work.[8] For the electric quadripole transitions, we used the formulae of Aller, Menzel, and Shortley[9] after a suitable generalization. Calculation of spin-other orbit and spin-spin interactions are similar to the method used by Marvin,[10] Araki,[11] and Garstang.[12]

[8] E. U. Condon, Astrophys. J. **79-80**, 217 (1934).

[9] *Physical Processes in Gaseous Nebulae*, D. H. Menzel, L. H. Aller, J. G. Baker, M. H. Hebb, and G. H. Shortley (Harvard College Observatory, Reprints from the Astrophysical Journal, Vol. 85, No. 4, 1937).

[10] H. H. Marvin, Phys. Rev. **71**, 102 (1947).

[11] G. Araki, Progr. Theoret. Phys. (Japan) **3**, 152, 262 (1948).

[12] R. H. Garstang, Monthly Notices Royal Astron. Soc. **111**, 1, 115 (1951).

TABLE I. Integrals.

	Parity	Σm_l	Σm_s
$X_{nn'n''n'''}=0$ unless	$p(l_n+l_{n'})=p(l_{n''}+l_{n'''})$	$(m_l)_{n''}+(m_l)_{n'''}=(m_l)_n+(m_l)_{n'}$	$(m_s)_{n''}=(m_s)_n$, $(m_s)_{n'''}=(m_s)_{n'}$
$V_{nn'}=0$ unless	$p(l_n+l_{n'})=$even	$(m_l)_n=(m_l)_{n'}$	$(m_s)_n=(m_s)_{n'}$
$X_{nn'n''n'''}=0$ unless	$p(l_n)=p(l_{n'})$	$(m_l)_n=(m_l)_{n'}$	$(m_s)_n=(m_s)_n=(m_s)_{n'}$
$X_{nn'}=0$ unless	...	...	$(m_s)_n=(m_s)_n$
$V_{nn'}=T_{nn'}=0$ unless	$l_n=l_{n'}$	$(m_l)_n=(m_l)_{n'}$	$(m_s)_n=(m_s)_{n'}$

The spin-orbit term requires wave functions accurate near the origin.[13] For this reason the $2p$ function is modified slightly by effective charge considerations. In principle, such a modification could be achieved by considering a large number of correction terms, which would improve the wave function in all respects. The modification consists of adding to $2p$ wave function another exponential as $u_3 \rightarrow N\cos\theta(e^{-\mu cr}+e^{-\mu\alpha r})$ and adjusting α such that when $r\rightarrow 0$, $\mu c+\mu\alpha=Z$. The effect of this is comparatively small for various physical quantities except spin-orbit interaction in which case the matrix elements are close to the experimentally expected ones. The results of the calculations for the nebular lines are given in the Table IV together with the spin-orbit splittings, and are compared with empirical values given by Garstang.[12]

H. Discussion

In this work the substitutions such as $2s\rightarrow\phi_n$, $1s2s\rightarrow\phi_n\phi_m$, etc., which would give the same contributions to all three multiplets are not considered because these are not important for the second part of the calculation (spin-orbit interactions depend mainly on the intermultiplet separations). However, a rough estimate of the contributions of these substitutions was made which yields approximately 0.7 a.u. (atomic units). This is rather small (about 14% of the difference between the experimental and the theoretical values of the energy). Together with the other substitutions, the total improvement is about 28% averaged over the ^1D, ^3P, and ^1S states. In comparison, the improvement in the intermultiplet separation is much better, 65% for ($^3P-^1D$) and 82% for ($^3P-^1S$). The remaining discrepancies may be attributed to the following facts. (a) The method is approximate; instead of diagonalizing a large determinant, we have made use of the approximations (8). (b) Only a few of the perturbation terms are examined (up to $n=5$, $l=4$ for single substitutions, $n=5$, $l=2$ for double substitutions). Convergence seems to be good as judged by individual sequences, but after a certain l the number of possible substitutions increase so rapidly that the contributions spread over a large number of states. (c) Perhaps the most important omission is the contributions from the continium states, which presumeably would account for another 30% of the discrepancy between the experimental and the theoretical values of the energy. (d) Finally, as a consequence of choosing strictly hydrogen like wave functions for perturbation series, some of the substitution terms cannot be used. For example, $u_1^+u_1^-\rightarrow\psi_{211}^+\psi_{21-1}^-$ and $u_3^+u_3^-\rightarrow\psi_{211}^+\psi_{21-1}^-$ cannot be employed because these are already in the determinant of the zeroth-order wave function. Therefore, the improvement of inner parts of the wave function is left to substitution functions with higher quantum numbers This makes the convergence very slow in this respect and is mainly responsible for the modified form of the $2p$ wave function mentioned above The modified $2p$ wave function, $u_3=N(e^{-\mu cr}+e^{-\mu\alpha r})\cos\theta$ essentially resembles self-consistent field wave functions near the origin and thereby improves the inner part of the wave function. In conclusion, the present method gives contributions which are in the right directions and of the right orders of magnitudes as far as the energy and the multiplet separations are concerned. Further, after the inner behavior of the $2p$ wave function is modified, calculation

TABLE II. Contributions from various substitutions.

Single substitutions	^1D		^1P		^1S	
$u\rightarrow\psi$	a_n/a_0	$H_{0n}^2/\Delta W$	a_n/a_0	$H_{0n}^2/\Delta W$	a_n/a_0	$H_{0n}^2/\Delta W$
$2p\rightarrow 3p$	−0.0690	2×0.0129	−0.046	2×0.0063	−0.104	2×0.0265
$2p\rightarrow 4p$	−0.0197	2×0.0014	−0.015	2×0.0008	−0.032	2×0.0038
$2s\rightarrow 3d$	0.0226	2×0.0030	−0.010	2×0.0007	−0.012	2×0.0080
Double substitutions	^1D		^1P		^1S	
$2p^2\rightarrow(321)^2$	−0.021	0.0042	−0.025	0.0058	−0.0429	0.0158
$2p^2\rightarrow(320)(322)$	0.018	2×0.0028	−0.020	0.0039	−0.0328	2×0.0092
$2p^2\rightarrow 3p^2$	−0.015	0.0017	−0.004	0.0001	−0.0304	0.0059

[13] S. Pasternack, Astrophys. J. 92, 129 (1940).

TABLE III. Multiplet ratios.[a]

ρ	C I	N II	O III	F IV
Variational	2.47	2.48	2.48	2.47
Improved	2.33	2.27	2.25	2.25
Experimental	2.13	2.14	2.14	2.14

[a] Slater's perturbation scheme gives $\rho=2.50$.

TABLE IV. Transition probabilities.

		C I	N II	O III	F IV
$A(D_2,P_2)$	m	$0.0^{2}18$	0.0027	0.0195	0.0937
$A(D_2,P_2)$	e	$0.0^{2}15$	$0.0^{2}114$	$0.0^{2}51$	$0.0^{2}161$
$A(D_2,P_1)$	m	$0.0^{2}60$	$0.0^{2}92$	0.0066	0.034
$A(D_2,P_1)$	e	$0.0^{2}21$	$0.0^{2}176$	$0.0^{2}78$	$0.0^{2}26$
$A(D_2,P_0)$	e	$0.0^{2}32$	$0.0^{2}30$	$0.0^{2}14$	$0.0^{2}47$
$A(S_0,D_2)$	e	0.62	1.350	2.00	2.60
$A(S_0,P_1)$	m	0.002	0.030	0.214	0.94
$A(S_0,P_2)$	e	$0.0^{2}23$	$0.0^{2}16$	$0.0^{2}89$	0.0028

for the absolute intensities of the nebular transitions are quite satisfactory.

ACKNOWLEDGMENTS

The author wishes to express his gratitude to Professor Phillip M. Morse who suggested this problem and to Professor William P. Allis and Dr. Harold Zirin for many illuminating discussions.

APPENDIX: THE S-FUNCTION

Let $f(\mathbf{r})$ and $g(\mathbf{r}')$ be any two polynomials and $G(\mathbf{r}|\mathbf{r}')$ a Green's function. The following integral must be of interest for many physical applications:

$$V(f,\alpha|g,\beta)=\int f(\mathbf{r})e^{-\alpha r}G(\mathbf{r}|\mathbf{r}')g(\mathbf{r}')e^{-\beta r'}d\tau d\tau'. \quad (1)$$

In our case $G(\mathbf{r}_1|\mathbf{r}_2)=1/r_{12}$. From (10) we see that the substitutions $f(\mathbf{r}_1)=r_1^{\,p}$, $P_\lambda(\cos\theta_1)$ and $g(\mathbf{r}_2)=r_2^{\,q}$, $P_\lambda(\cos\theta_2)$ would suffice for our purpose.

$$V_\lambda(p,\alpha|q,\beta)=\int r_1^{\,p}P_\lambda(\cos\theta_1)e^{-\alpha r_1}G(\mathbf{r}_1|\mathbf{r}_2) \times r_2^{\,q}P_\lambda(\cos\theta_2)e^{-\beta r_2}d\tau_1 d\tau_2. \quad (2)$$

The angular parts can be integrated at once:

$$V_\lambda(p,\alpha|q,\beta)=\frac{16\pi^2}{(2\lambda+1)^2}S_\lambda(p,\alpha|q,\beta), \quad (3)$$

where the function S is defined as

$$S_\lambda(p,\alpha|q,\beta)=\int_0^\infty e^{-\alpha r_1}r_1^{\,2}dr_1\left\{\int_{r_1}^\infty r_1^{\,p}r_2^{\,q}\frac{r_1^{\,\lambda}}{r_2^{\,\lambda+1}}e^{-\beta r_2}r_2^{\,2}dr_2 + \int_0^{r_1} r_1^{\,p}r_2^{\,q}\frac{r_2^{\,\lambda}}{r_1^{\,\lambda+1}}e^{-\beta r_2}r_2^{\,2}dr_2\right\}. \quad (4)$$

This function has interesting mathematical properties. The most helpful ones for the calculations are the following[14]:

$$\begin{aligned}
&\text{(a)} && S_\lambda(p,\alpha|q,\beta)=S_\lambda(q,\beta|p,\alpha),\\
&\text{(b)} && S_\lambda(p,\mu\alpha|q,\mu\beta)=\mu^{-p-q-5}S_\lambda(p,\alpha|q,\beta),\\
&\text{(c)} && S_\lambda(p+1,\alpha|q,\beta)=-\frac{\partial}{\partial\alpha}S_\lambda(p,\alpha|q,\beta),\\
&\text{(d)} && S_\lambda(\lambda-1,\alpha|\lambda-1,\beta)=\frac{(2\lambda+1)!}{\alpha\beta(\alpha+\beta)^{2\lambda+1}},\\
&\text{(e)} && S_\lambda(p,\alpha|q,\beta)=\frac{(p+q+3)!}{(\alpha+\beta)^{p+q+4}}\left[\frac{1}{\alpha}F(\alpha,\beta,p,q) + \frac{1}{\beta}F(\beta,\alpha,q,p)\right],\\
&\text{(f)} && S_\lambda(p,\alpha+\epsilon|q,\beta)=\sum_{n=0}^{\infty}\frac{(-1)^n\epsilon^n}{n!}S_\lambda(p+n,\alpha|q,\beta),\\
&\text{(g)} && S_\lambda(p,\alpha|q,\beta)\cong\frac{\Gamma(\xi_p')\Gamma(\xi_q')}{\alpha^{\xi_p}\beta^{\xi_q}},
\end{aligned} \quad (5)$$

where $F(\alpha,\beta,p,q)$ is the hypergeometric function $F(-p-1+\lambda,1|-p-q-3|1+\beta/\alpha)$, $\epsilon\ll\alpha/(p+3)$, $\xi_p=p+2-\lambda+(2\lambda+1)\alpha^2/(\alpha^2+\beta^2)$, $\xi_p'=p+2-\lambda+(2\lambda+1)\alpha^2/(\alpha^2+\gamma\beta^2)$ and $\gamma=(3.4+p+q+\lambda)/(1+p+q+\lambda)$. Quite a large number of problems can be handled with these functions such as variational calculations, improvement of variational wave functions, perturbations, Hylleraas type of calculations, etc.

Here we give also some specific formulas for some of the integrals involved:

$$\begin{aligned}
V_1^{\,n}&=\frac{8a(n-1)^{n-1}\sqrt{n}}{(n+1)^{n+1}};\quad T_1^{\,n}=aV_1^{\,n},\\
V_2^{\,n}&=\frac{8a^2n}{(3anN)^{\frac{1}{2}}}\frac{2n^2(a-1)(n-a)^{n-2}}{(n+a)^{n+2}} + \frac{3(a+b)^{\frac{1}{2}}(nb-a)^{n-1}}{(a+1)^4(nb+a)^{n+1}},\quad T_2^{\,n}=aV_2^{\,n},\\
V_3^{\,n}&=\frac{128nc(n-2)^{n-2}}{(n+2)^{n+2}}\left(\frac{n(n^2-1)}{6}\right)^{\frac{1}{2}},\quad T_3^{\,n}=2cV_3^{\,n},
\end{aligned} \quad (6)$$

where 1, 2, 3 represents u_1, u_2, u_3 (M.Y.H.), and n is the radial quantum number of the substitution term. The integral (4) is given as

[14] Some of these properties have also been derived by S. F. Boys, Proc. Roy. Soc. (London) **A201**, 125 (1950).

$$\zeta_n=8a^5n^2\left(\frac{3n}{aN_n}\right)^{\frac{1}{2}}\left\{\frac{(n-a)^{n-2}}{(n+a)^{n+2}}\left[n^2(1-2a)+\frac{2n^2+1}{3}\right]\right.$$
$$\left.+\frac{(a-b)(a+b)(nb-a)^{n-2}}{(a+1)^4(nb+a)^{n+2}}\right\}. \quad (7)$$

For the calculation of V_m and V_{nm}, the following integrals may be useful:

$$\int_0^\infty r^s e^{-(\mu+1)r}[L_m^a(r)]^2dr$$
$$=\frac{[(m+a)!]^2}{m!(\mu+1)^{s+2+2m}}F(-m,-m-a|1|\mu^2),$$

$$\int_0^\infty r^s e^{-\mu r}[L_m^a(r)]^2dr \quad (8)$$
$$\times\left\{\int_0^r r'^s e^{-\mu r'}dr'+r\int_r^\infty e^{-\mu r'}dr'\right\}$$
$$=\frac{[(m+a)!]^2}{m!\mu^2}$$
$$\times\left\{1-\frac{1}{(\mu+1)^{s+2+2m}}F(-m,-m-a|1|\mu^2)\right\}.$$

PHYSICAL REVIEW VOLUME 100, NUMBER 4 NOVEMBER 15, 1955

Fine Structure of Singly Ionized Helium*†

ROBERT NOVICK, EDGAR LIPWORTH, AND PAUL F. YERGIN‡
Columbia Radiation Laboratory, Columbia University, New York, New York
(Received July 15, 1955)

The energy difference ($\mathcal{S}$) between the $2\,^2S_{\frac{1}{2}}$ and $2\,^2P_{\frac{1}{2}}$ states of ionized helium has been measured by a pulsed microwave method. Helium atoms are excited to the metastable $2\,^2S_{\frac{1}{2}}$ state of the ion by a microsecond pulse of electrons of about 250-ev energy. After bombardment and after the atoms and ions excited to nonmetastable states have decayed to their respective ground states, a pulse of microwave power is applied to induce the $2\,^2S_{\frac{1}{2}}-2\,^2P_{\frac{1}{2}}$ transition. This transition is followed immediately by spontaneous emission of a 40.8-ev photon associated with the $2\,^2P_{\frac{1}{2}}-1\,^2S_{\frac{1}{2}}$ transition. The photons are observed by counting photoelectrons with high-speed counters gated on synchronously with the pulses of microwave power. Two different levels of rf power are used alternately to provide a means of normalizing the data for variations in the population of the $2\,^2S_{\frac{1}{2}}$ state.

The present value of $\mathcal{S}$ for He^+ is 14 043±13 Mc/sec. The stated uncertainty is equal to three times the standard deviation plus an estimated 3 Mc/sec for the uncertainty in the corrections for systematic effects. This result, consistent with previous results, is in agreement with the best available theoretical value of 14 043.2±3.0 Mc/sec.

A. INTRODUCTION

THE energy difference ($\mathcal{S}$) between the $2\,^2S_{\frac{1}{2}}$ and $2\,^2P_{\frac{1}{2}}$ states of hydrogen and singly ionized helium is of purely radiative origin. It therefore provides a sensitive test of the theoretical predictions of quantum electrodynamics. Since the nuclear charge of ionized helium is twice that of hydrogen, the relativistic terms in the theory of the radiative shift are of greater importance in helium than they are in hydrogen. Thus the ionized helium spectrum provides a more critical test of these terms than does the hydrogen spectrum. In the present formulation of quantum electrodynamics, the radiative corrections to the energy levels of hydrogenic atoms are obtained as a double power series expansion in the parameters α and αZ, where α is the fine structure constant and Z is the nuclear charge. A number of these terms has been computed and found to give an excellent, but not perfect, account of the observed value of $\mathcal{S}$ in hydrogen. The 0.65-Mc/sec difference between the observed value of the shift in hydrogen (1057.77 Mc/sec) (H V, p. 104)[1] and the theoretical value (1057.12 Mc/sec)[2] is six times the experimental uncertainty. If this difference arises because of a missing or incomplete term in the theory, then a sufficiently precise measure-

* Work supported jointly by the Signal Corps, the Office of Naval Research, the Air Research and Development Command, and the National Science Foundation.

† Submitted by Robert Novick in partial fulfillment of the requirements for the degree of Doctor of Philosophy, in the Faculty of Pure Science, Columbia University.

‡ Present address: Department of Physics, University of Pennsylvania, Philadelphia 4, Pennsylvania.

[1] The series of papers on the hydrogen experiments will be referred to as H I, H II, H III, H IV, H V, and H VI. These are: H I, W. E. Lamb, Jr., and R. C. Retherford, Phys. Rev. **79**, 549 (1950). H II, W. E. Lamb, Jr., and R. C. Retherford, Phys. Rev. **81**, 222 (1951). H III, W. E. Lamb, Jr., Phys. Rev. **85**, 259 (1952). H IV, W. E. Lamb, Jr., and R. C. Retherford, Phys. Rev. **86**, 1014 (1952). H V, Triebwasser, Dayhoff, and Lamb, Phys. Rev. **89**, 98 (1953). H VI, Dayhoff, Triebwasser, and Lamb, Phys. Rev. **89**, 106 (1953).

[2] E. E. Salpeter, Phys. Rev. **89**, 92 (1953). The 0.07 Mc/sec difference between the theoretical value of $\mathcal{S}_H$ as given by Salpeter and as given in the present paper results from the inclusion, in the present value, of the reduced mass correction to the second order magnetic moment term (see Table V).

ment of δ in He^+ will indicate the Z dependence of the term and thereby give a clue to its nature.

In 1950, Lamb and Skinner[3] made the first high-resolution measurement of δ for singly ionized helium. They obtained a value of $14\,020\pm100$ Mc/sec. Since neither their method nor their apparatus was suited for very precise measurements, a new apparatus was constructed and a new method devised for a redetermination of δ in He^+. In 1953, Yergin *et al.*[4] obtained a preliminary value of $14\,020\pm60$ Mc/sec with their new apparatus. At the time, accuracy was limited by a poor signal-to-noise ratio and by lack of a detailed theory of the line shape. Such a theory is necessary, since the natural width of the observed resonance is about 1600 Mc/sec. To obtain a result for He^+ with a fractional uncertainty which is no greater than the present fractional discrepancy between the observed and theoretical value of δ in hydrogen, it is necessary to make a meaningful determination of the center of the observed line to within 1% or less of the line width. This requires a full understanding of the various systematic effects that may distort and shift the resonance curve. Subsequent to Yergin's work, the signal-to-noise ratio has been increased tenfold by an improvement of the detection efficiency. In addition, a careful study has been made of the various phenomena that determine the shape of the resonance curve. As a result of this study, a number of corrections to the observed resonance center have been discovered and evaluated. About one-fourth of the uncertainty in the results of the present experiment arises from the estimated uncertainties in these corrections; the remainder of the uncertainty is of a statistical nature.

B. METHOD

The atomic beam method developed by Lamb and Retherford (H I, p. 552) for the measurement of δ in the hydrogens is not applicable to singly ionized helium because the particles are charged. In the method adopted for this experiment, an atmosphere of helium gas at low pressure is bombarded with electrons for a period of about one microsecond (see Fig. 1). After the bombardment, there is a waiting period of about one-quarter microsecond, during which all of the ions and atoms excited to shortlived states decay to their respective ground states. Thus, at the end of the waiting period, the bombarded cloud contains ions in the ground state and the metastable $2\,^2S_{\frac{1}{2}}$ state,[5] as well as the two metastable atomic states (see Fig. 2). After the waiting period, an rf power source and a photomultiplier and counting channel are gated on for a period of about one microsecond. The rf electric field induces transitions from the metastable $2\,^2S_{\frac{1}{2}}$ state to the $2\,^2P_{\frac{1}{2}}$ state; the $2\,^2P_{\frac{1}{2}}$ state decays with a lifetime of 10^{-10} second to the ground state of the ion with the emission of λ303.8 A photon. This decay photon is detected and recorded by the photomultiplier tube and counting channel.

The above cycle of events is repeated at a rate of 10^5 cycles per second. The ions and metastable atoms diffuse to the walls of the apparatus during the eight-microsecond interval between the end of each rf pulse and the beginning of the next bombardment pulse. In addition to the "delayed" counting channel, described above, there is also an "undelayed" counting channel which is turned on in coincidence with the bombarding pulse. The undelayed count provides a convenient reference signal for normalizing the delayed count. This normalization procedure greatly reduces the effects of changes in detection efficiency, helium pressure, bombarding current, and counting time and thereby substantially improves the quality of the rf quenching data. Hereafter, the undelayed and delayed counting channels will be referred to as channel I and channel II respectively.

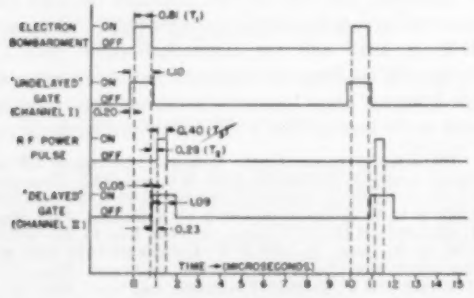

FIG. 1. Pulse-timing sequence.

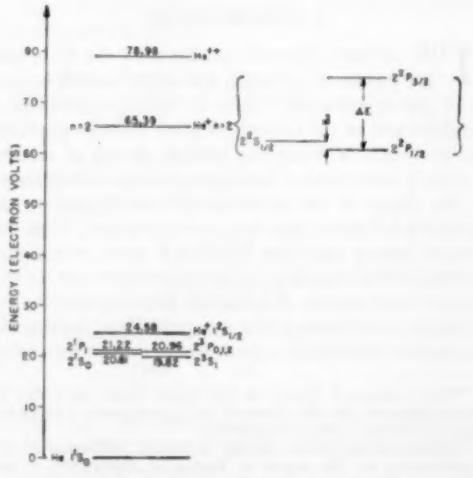

FIG. 2. Energy levels of helium.

[3] W. E. Lamb, Jr., and M. Skinner, Phys. Rev. **78**, 539 (1950). This paper will be referred to hereafter as He I.

[4] Yergin, Lamb, Lipworth, and Novick, Phys. Rev. **90**, 377(A) (1953).

[5] The metastability of the $2\,^2S_{\frac{1}{2}}$ state is discussed in Sec. E1a.

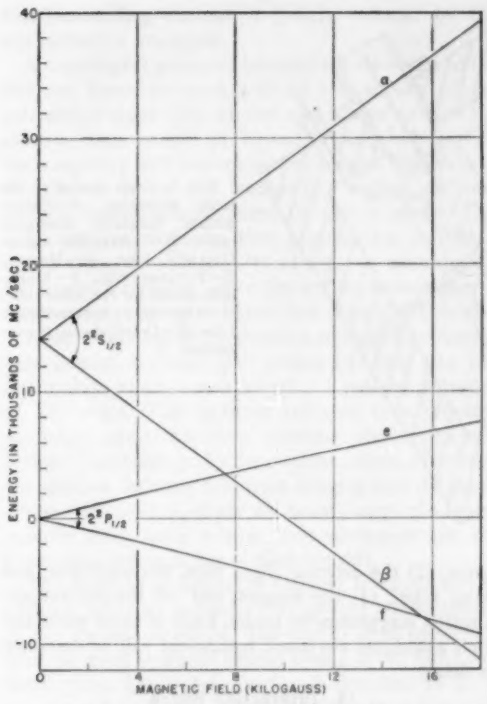

FIG. 3. Zeeman splitting of the $2\,^2S_{\frac{1}{2}}$ and $2\,^2P_{\frac{1}{2}}$ states.

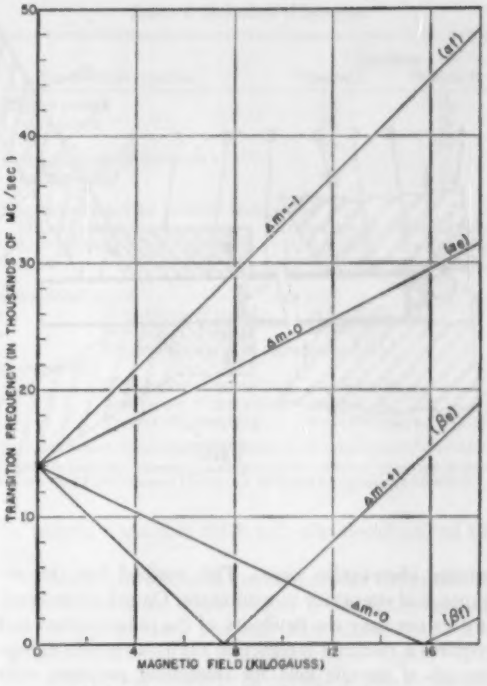

FIG. 4. Zeeman transition frequencies as a function of the magnetic field.

The experiment is performed in a magnetic field primarily in order to make use of the Zeeman effect to obtain resonance between the transition frequency and a fixed frequency microwave oscillator (see Fig. 3 and Fig. 4). The alternative procedure of using a variable frequency oscillator would require the maintenance of power constant to within a fraction of one percent as the oscillator is tuned over a 10% band. Such performance would be difficult to achieve with available microwave techniques.

Resonance data are obtained in the following manner: At selected magnetic field values, three sets of channel I and channel II counts are obtained. The first set is taken with high enough rf power to quench essentially all of the metastable ions during the rf pulse. This provides a measure of the number of metastables formed at the chosen field. The second set is taken with a sufficiently low rf power, so that no more than 30% of the metastables are quenched at the peak of the resonance. This provides the basic resonance data. The third set is taken with zero rf power. This provides a measure of the background to be subtracted from each of the first two observations. Each of the channel II counts is divided by the corresponding channel I count to reduce the effect of changes in the parameters listed above. The percent rf quenching (f) at each field value is obtained from the relation

$$f=100(l-b)/(h-b), \tag{1}$$

where h, l, and b are the normalized channel II counts with high, low, and zero rf power (see Table I). The values of f, so obtained form a resonance curve. The value of δ is readily computed from the observed center of the resonance curve and the known oscillator frequency.

The present pulsing and waiting method has an advantage over the simultaneous bombardment and observation method of Lamb and Skinner (He I, p. 540), in that the large background arising from the shortlived ionic and atomic levels has been eliminated. This has led to a thirty-fold improvement in the signal-to-background ratio. The background from the atomic states is additionally suppressed, as in the Lamb-Skinner experiment (He I, p. 543), by resonant scattering from normal helium atoms in the path between the bombardment chamber and the detector.

The background from the short-lived atomic and ionic states may also be reduced by combining the Lamb-Skinner method with a modulated rf oscillator and a lock-in type rectifier in the output of the photodetector. With comparable observation time, the lock-in scheme should yield about the same signal-to-noise ratio as the pulse method (about 300 to 1 for a five-

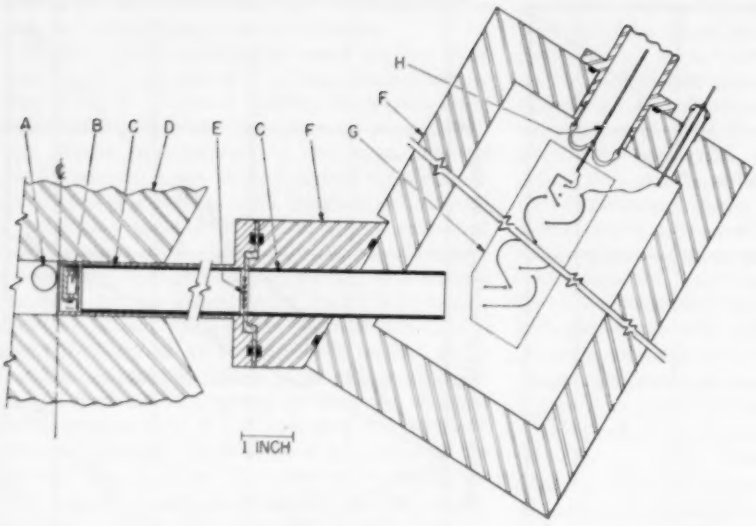

FIG. 5. Cross section of the main apparatus. *A*—Proton nuclear magnetic resonance probe. *B*—Interaction region. *C*—Light pipe. *D*—Magnet. *E*—Formvar film. *F*—Magnetic shield for the Allen tube. *G*—Allen type photomultiplier tube. *H*—Detector output connection.

minute observation time). This method has the advantage of simplicity in equipment. On the other hand, it does not have the flexibility of the pulse method and requires a resonant interaction cavity to attain a large enough rf electric field for quenching purposes with existing microwave CW sources.

C. APPARATUS

A cross section of the main apparatus is shown in Fig. 5. The essential parts are: (1) the interaction space, (2) the detector (light pipe, Formvar film, and Allen tube), (3) the magnet, and (4) the nuclear absorption magnetometer probe. Each of these parts and their associated electronic equipment will be described in detail.

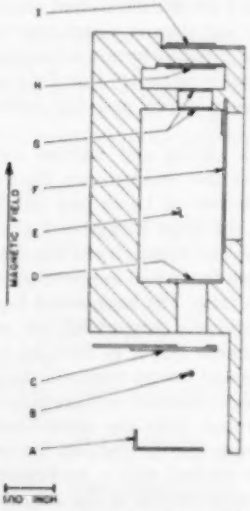

FIG. 6. Cross section of the interaction region. *A*—Filament shield. *B*—Filament. *C*—Control grid. *D*—Grid. *E*—Interaction space. *F*—Photon grid. *G*—Double grid. *H*—Electron collector. *I*—Electrical connection to collector.

1. Interaction Space

A cross section of the interaction space is shown in Fig. 6. The body of the interaction space consists of a piece of modified *K*-band wave guide (0.170×0.340 inch, inside dimensions). Attached to the wave guide are an electron gun, an electron beam collector system and a viewing grid to permit the $2\,^2P_{\frac{1}{2}}-1\,^2S_{\frac{1}{2}}$ decay photons to enter the detector. The electrical connections to the interaction space are shown in Fig. 7. The electron beam bombarding energy is determined by the steady voltage applied between the filament and the interaction space.

A hot tungsten filament 0.010 in. in diameter and 1.040 in. long serves as the electron gun cathode. The filament is heated by passing approximately 6 amp of 100 kc/sec alternating current through it. The use of the rf heating eleiminates the annoying filament-bending associated with dc heating, the vibration associated with low-frequency heating, thereby preventing possible line shape distortion resulting from displacement of the electron beam in the interaction space as the magnetic field is varied.

The filament is operated in the temperature-limited region. Thus the bombarding current may be controlled independently of the bombarding voltage and control grid bias. The heating current, and consequently the emission current, may be adjusted by varying the plate voltage of the rf filament supply oscillator.

The bombarding current is stable to better than 1% over a five-minute period. The effect of fluctuations in

the bombarding current is greatly reduced by the normalization procedure.

A control grid is located between the filament and the electron beam entrance grid at the bottom of the interaction space. The control grid is used to turn the electron beam on and off. Normally the grid is held 50 volts negative with respect to the filament. This voltage is sufficient to cut the bombarding current off completely. During bombardment the grid is pulsed to 25 volts positive, to insure that a saturation current is drawn from the cathode. No attempt is made to use electrostatic focusing, since the entire electron gun is immersed in a strong magnetic field (about 7600 gauss).

After traversing the interaction region, the electrons pass through a double grid system and then to a collector plate which is maintained at a positive potential of 225 volts. This positive collector bias prevents secondary electrons from entering the interaction region. The double grid in front of the collector prevents the electron collector field from fringing into the interaction region. Thus, except for space charge effects and possible stray fields arising from contamination, the interaction region is free of electric fields.

The shield underneath the filament is maintained at cathode potential and serves to prevent bombardment of the vacuum envelope. The control grid pulser has been designed to insure precise timing of the bombardment pulse. The pulse duration is constant to 0.1% over a period of several hours; the effective switching time is estimated to be less than 0.05 microsecond.

2. Detector

The detector consists of an eleven-stage Allen type electron multiplier tube[6] which responds to λ303.8 A photons from the $2\,^2P_{\frac{1}{2}}-1\,^2S_{\frac{1}{2}}$ transition in the ion. Since the Allen tube must be placed outside the magnetic field, it subtends a small solid angle at the interaction space. The effective solid angle has been increased by installing a gold light pipe[7,8] between the interaction space and the Allen tube cathode. On the basis of the published data on the reflectivity of gold,[9] the light pipe was estimated to increase the effective solid angle by a factor of eighteen. After nearly one year's use, the light pipe "gain" was observed to be approximately twelve.

The Allen tube is provided with a platinum photocathode in order to reduce its sensitivity to soft photons from the electron gun filament and to reduce the thermionic background count of the multiplier. The stray magnetic field in the neighborhood of the Allen tube was reduced from about 100 gauss to less than 2 gauss by placing a one-inch-thick soft iron shield around the tube.

TABLE I. Definition of notation.

Experimental condition	Counts in Channel I	Counts in Channel II
High rf power	U_h	D_h
Low rf power	U_l	D_l
rf off	U_b	D_b
Bombardment off (detector background)[a]	U_d	D_d
Counts corrected for detector background		
High rf power	$U_h'=U_h-U_d$	$H=D_h-D_d$
Low rf power	$U_l'=U_l-U_d$	$L=D_l-D_d$
rf off	$U_b'=U_b-U_d$	$B=D_b-D_d$
Normalized signals		
High-power rf signal	$=h=H/U_h'$	
Low-power rf signal	$=l=L/U_l'$	
Delayed background signal	$=b=B/U_b'$	
rf *quenching*		
High-power rf quenching	$=\phi_h=h-b$	
Low-power rf quenching	$=\phi_l=l-b$	
Percent rf quenching	$=f=100\times\phi_l/\phi_h$	

[a] Aside from the differences arising from the different observation times the channel I and channel II detector background signals are identical.

A thin Formvar film is located between the multiplier and the interaction space in order to prevent metastable helium atoms from reaching the photocathode and thereby producing a large background signal.[10] This film also prevents the flow of normal helium atoms into the multiplier chamber. As a precaution against rupture, the film was mounted on a flat 150-mesh nickel grid. With this mounting the helium pressure in the multiplier is about one hundredth of the pressure in the interaction region. The thickness of the film is estimated to be about 500 A. By comparing its performance with that of a collodion film of known transmission,[11] the λ303.8 A transmission of the film has been estimated to be about 25%. Formvar was used in preference to collodion because of its greater mechanical strength.

The long column of helium in the section of the light pipe between the interaction space and the Formvar film serves to reduce by resonant scattering[12] the signal from the excited states of atomic helium (He I, p. 550).

3. Counting System

A block diagram of the counting system is shown in Fig. 8. The two discriminator circuits are used in

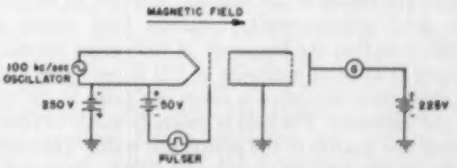

FIG. 7. Electron bombarder potentials.

[6] J. S. Allen, Rev. Sci. Instr. **18**, 739 (1947).
[7] The light pipe consisted of a glass tube coated internally with a gold reflecting film.
[8] F. P. Bundy and H. M. Strong, J. Opt. Soc. Am. **39**, 393 (1949).
[9] H. M. O'Bryan, Phys. Rev. **38**, 32 (1931).
[10] R. Dorrstein, Physica **9**, 433 and 447 (1942).
[11] H. M. O'Bryan, J. Opt. Soc. Am. **22**, 739 (1932).
[12] T. Holstein, Phys. Rev. **72**, 1212 (1947).

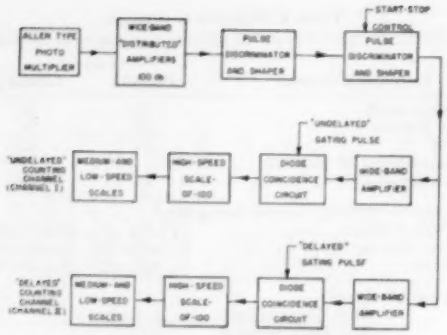

FIG. 8. Block diagram of the detector circuit and counting channels.

cascade in order to increase the uniformity of the signal pulses. As in the case of the gun pulse, the gate pulse duration is stable to 0.1% over a period of several hours.

The dead time for the entire detection and counting system is 0.16 microsecond. The entire counting process can be started and stopped by switching the discrimination level in the second pulse-height discriminator. The normalization procedure eliminates the effects of changes in the counting time.

The gain and band width of the amplifier chain are such that the Johnson noise and tube noise in the first amplifier are not quite large enough to trigger the first pulse-height discriminator. The total detector background signal is about 2.4 counts per second (gated). The gain of the amplifier chain is continuously monitored by a noise voltmeter connected to the grid of the first pulse-height discriminator.

4. Magnetic Field

The magnetic field is produced by an electromagnet with pole pieces $6\frac{1}{4}$ in. in diameter, tapered to 4 in. in diameter, with a gap length of 1 in. The magnet current is supplied by a motor generator set. The current is regulated by the same regulator used by Lamb and Retherford in the hydrogen experiment. (H II, p. 224.) This circuit holds the magnet field current steady to about one part in ten thousand.

The magnetic field is measured with a Pound-type proton resonance absorption apparatus.[13] The water sample and interaction region are symmetrically located about the center of the magnet. In order to facilitate the field measurements, magnetic field values are selected so that the frequency of the proton resonance occurs at integral multiples of 100 kc/sec. The width of the proton resonance is about one gauss at the base of the resonance. The field is generally stable to plus or minus one quarter of the proton line width. The uncertainty in the field measurement has been estimated to be plus or minus one gauss.

[13] R. V. Pound and W. D. Knight, Rev. Sci. Instr. **21**, 219 (1950).

5. Radio-Frequency Equipment

A block diagram of the radio-frequency apparatus is shown in Fig. 9. The source of the rf power is a Raytheon type QK 289 klystron. About 250 milliwatts peak power is obtained by pulsing the klystron beam voltage to 4.5 kv. This power is barely sufficient for the purposes of the high-power rf-quenching measurement, although it is several times the rated power of the tube. The power entering the interaction region is reduced by a factor of ten for the low-power quenching measurement by inserting the attenuator. The wave-guide gate switch cuts off the power for the rf off observation.

The rf components between the interaction region and the bolometer were designed in such a way as to maintain a stable and reproducible relation between the rf field in the interaction space and the power absorbed by the bolometer.

The rf power is measured with a Polytechnic Research and Development model 618 bolometer and a model 650-A bolometer bridge. The sensitivity of the bolometer is adjusted between two fixed levels for the high power and low power measurements by manipulating the two-way rotary switch. In the high-power position, an attenuator is placed between the interaction region and the bolometer; in the low-power position, the power enters the bolometer directly from the interaction region. The power level is generally stable to a fraction of 1%.

A small fraction of the klystron power is fed into an rf envelope viewer and an rf spectrum analyzer. The shapes of the envelope and the spectrum are continuously monitored during each observation. The spectrum analyzer is also used for measuring the klystron frequency. This is accomplished by superimposing a pip

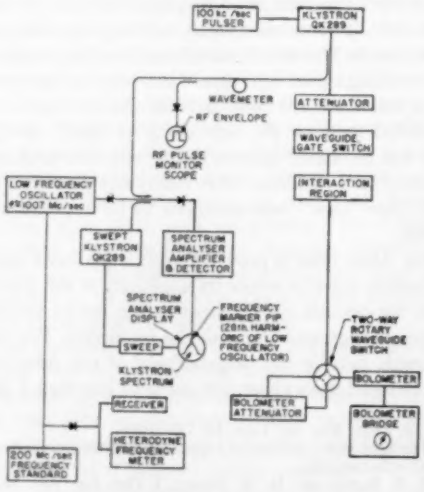

FIG. 9. Block diagram of the rf apparatus.

from the 28th harmonic of a low-frequency CW oscillator on the klystron spectrum. The frequency of the CW oscillator is determined by standard heterodyne methods. The width of the rf spectrum is close to the theoretical value of 5 Mc/sec for a 0.4-microsecond pulse. The klystron frequency is stable to plus or minus one quarter of the spectrum width. The uncertainty in the klystron frequency is estimated to be ±2.0 Mc/sec.

As an additional check on the magnetic field and klystron frequency, the electron cyclotron resonance was observed in the interaction region. Within the stated precision of the field and frequency measurements, the resonance occurred at the theoretical value

$$f_0 = eH/2\pi mc, \tag{2}$$

where f_0 is the resonant frequency, H is the magnetic field, e is the electronic charge, m is the mass of the electron and c is the velocity of light. The electron cyclotron resonance manifests itself as a large increase in the channel II high-power rf signal (h) as stray electrons are accelerated, by the resonant rf field, to the optical excitation energy of helium.

6. Timing Circuits

The various gates and pulses are controlled by a timing circuit which generates triggering impulses properly spaced in time (see Fig. 10). A 100-kc/sec sine wave from a frequency standard establishes the repetition rate of the timing cycle. The 100-kc/sec signal is squared and differentiated, and the resulting pulses drive pulse-sharpening circuits which feed two lumped constant delay lines. The trigger pulses are picked off the delay lines at times adjustable in steps of 0.1 microsecond. Four different independently adjustable trigger outputs are available. The trigger pulses from the delay lines drive sharpening circuits which reform the pulses which have been somewhat distorted by their passage through the lines. The relative timing of the various pulses is monitored continuously on an oscilloscope.

D. OPERATING CHARACTERISTICS

A careful study has been made of the operating characteristics of the apparatus. A few of the more important results of this study are presented below.

1. Signal Strength

The estimated number of high-power rf induced counts per bombardment pulse is given by

$$N = \tfrac{1}{2}\sigma^+(2S) \frac{I}{e} L n^0 T_1 \eta_{PG}\eta_F\eta_{PE} C \frac{\omega}{4\pi} G, \tag{3}$$

where $\sigma^+(2S)$ is the cross section for the excitation to the $2\,^2S_{\frac{1}{2}}$ state of the ion by 250 volt electrons, I is the bombarding current, e is the electronic charge, L is the length of the electron beam exposed to the detector, n^0 is the density of helium atoms in the interaction space, T_1 is the length of the bombarding pulse, η_F is the transmission of the Formvar film and support grid, η_{PE} is the photoelectric yield of the photocathode, η_{PG} is the transmission of the photon grid, ω is the solid angle subtended by the photocathode at the interaction space, G is the light pipe "gain" and C is the fraction of photoelectrons that are recorded by the scalers.

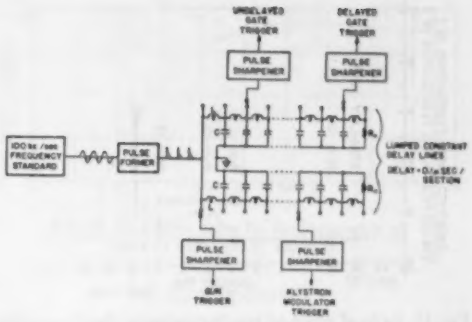

FIG. 10. Pulse-timing circuits.

Lamb and Skinner (He I, p. 548) have estimated $\sigma^+(2s)$ to be

$$\sigma^+(2s) = 0.37\times10^{-2}\pi a_0^2, \tag{4}$$

where a_0 is the Bohr radius. Typical values for the other parameters are: $I = 740$ microamperes, $L = 0.902$ centimeter, $n^0 = 0.746\times10^{14}$ atoms per cm^3, $T_1 = 0.81$ microsecond, $\eta_{PG} = \frac{1}{4}$, $\eta_F = \frac{1}{4}\times\frac{1}{2} = \frac{1}{8}$ [$\frac{1}{4}$ for the film (see above) and $\frac{1}{2}$ for the grid], $\eta_{PE} = 0.05$ (Walker and Wainfan[14]) $C = \frac{1}{4}$ (see below), $\omega = 8.4\times10^{-6}$, and $G = 18$ (see above). Using these values, a value for N of 0.099 rf induced counts per bombardment is calculated. The observed value for N is 0.024 rf induced counts per bombardment. Thus the observed signal is about one-fourth of the estimated signal. This difference is well within the uncertainties in the cross section, the film transmission, and the photoefficiency.

2. Noise

Ideally, the fluctuations in the rf quenching data should be only slightly greater than those imposed by the shot noise in the cathode current of the photomultiplier tube. Some difficulty was encountered in achieving this theoretical limit. A large body of the data was obtained in which the observed fluctuation level was approximately ten times the theoretical value. In obtaining these data a magnetron was used as the source of rf power and the interaction region was exposed to a relatively high density of organic vapors

[14] W. C. Walker and N. Wainfan, Phys. Rev. 92, 533(A) (1953), and private communication.

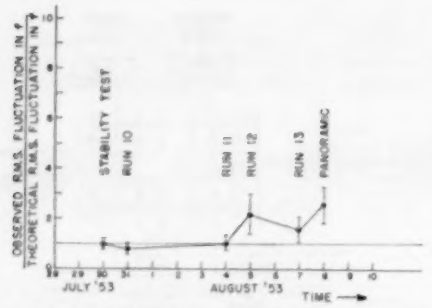

FIG. 11. Ratio of observed rms fluctuation in the rf quenching data to the theoretical fluctuation, as observed on six different occasions.

from rubber "O" rings.[15,16] Upon replacing the rubber "O" rings with Teflon "O" rings and the magnetron with a klystron, the fluctuation level in the rf quenching data dropped to the theoretical value. It is not known how much of this improvement was due to the improved rf and how much was due to the reduced contamination of the interaction region. The ratio of observed rms fluctuation in the rf quenching data to the theoretical rms fluctuation, on six different occasions, is shown in Fig. 11. The data of July 30, 1953 were taken immediately after the improvements noted above were made. These data were taken for the purpose of studying the stability of the apparatus. Since the individual signals often changed by several percent during the course of a run, the excellent agreement between the theoretical and observed fluctuations in the rf signal could not have been achieved without the normalization procedure. The source of the large fluctuations in the individual signals is believed to be either in the Allen tube or in the amplifier and counting circuits.

3. Allen Tube Characteristic

The variation of the undelayed signal (U_b'), delayed background (B) and detector background (D_d) with Allen tube voltage is shown in Fig. 12. These curves were taken with the amplifier gain and discriminator setting adjusted so that the amplifier noise did not quite trigger the scalers. The rather high degree of saturation exhibited by the undelayed and delayed background counts is an indication that a large fraction of the photoelectrons is recorded by the scalers. The value of ½, used for the counting efficiency (C) in the signal strength calculation, is based on the residual slope of these curves at the high-voltage limit. The fact that the voltage dependence of the delayed background (channel II rf off count) is very nearly the same as that of the undelayed signal shows that there is not an appreciable number of multiplier satellites having a delay of 0.05 microsecond or more.[17] It should be noted that, when the Allen tube was contaminated, there was evidence of an appreciable number of satellites at voltages as low as 2.1 kv.

The detector background count is obtained by turning off the electron gun, and then counting in the normal manner. This background is satisfactorily low and is assumed to be due to thermionic and high field emission from the photomultiplier dynodes.

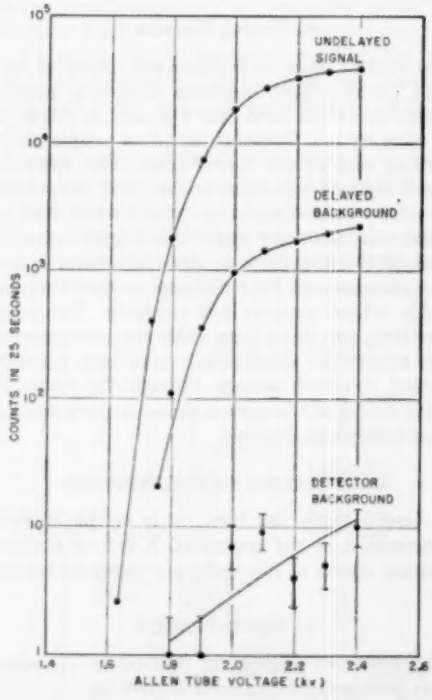

FIG. 12. Variation of the undelayed (U_b'), delayed background (B) and detector background (U_d) signals with Allen tube voltage. The symbols refer to the appropriate definitions in Table I.

[15] The magnetron was of low voltage, CW design, built expressly for this experiment. At the high duty cycle required in this experiment, this magnetron exhibited very severe back bombardment of the cathode with consequent instability of operation.

[16] It is believed that organic vapors condense on the walls of the interaction regions where they form charged insulating films. The electric fields from such films could easily cause significant motion of the ions in one microsecond. In support of this hypothesis, it has been observed that heavy black deposits formed on all surfaces exposed to electron bombardment. The electrical resistance of these films is in the megohm range. These films cannot be removed by extended heating in a hydrogen atmosphere at temperatures up to 1300°C. However, they can be removed by a rather short heating in air at about 700°C. From these observations it is concluded that the films are probably carbonaceous. See J. Blears, J. Sci. Instr. Suppl. No. 1, 36 (1951), and H. A. Wilcox, Phys. Rev. **74**, 1743 (1948), reference 9.

[17] Mueller, Best, Jackson, and Singletary, Nucleonics **10**, 53 (June, 1952). We are indebted to D. W. Mueller for pointing out to us that the satellite ratio depends on the photomultiplier operating voltage.

4. Excitation Functions

Excitation curves for the undelayed signal, the delayed background, and the rf induced signal are shown in Figs. 13, 14, and 15. The observed thresholds for atomic and ionic radiation occur close to the expected values of 21 volts and 65 volts (see Fig. 2). The suppression of atomic radiation by resonance scattering and possible selective absorption in the Formvar film (He I, p. 545) are clearly evident in Figs. 13 and 14. Without this suppression the atomic radiation would be many times stronger than the ionic radiation and the threshold at 65 volts would not be visible (He I, Fig. 6, p. 544). The low voltage peak in the delayed background excitation curve is reproducible, but its origin is unknown. It is clear from Fig. 14 that most of the delayed background arises from ionic radiation. The excitation function for the metastable state of the ion (Fig. 15) does not show the sharp rise indicated in Fig. 7 of Lamb and Skinner (He I, p. 544). The reason for this is that Lamb and Skinner have plotted the ratio of the rf induced signal to background signal, and since both of these signals have very nearly the same energy dependence the resulting curve is approximately a step function. The bombarding energy used in the remainder of the experiment corresponds to the maximum of the metastable excitation function.

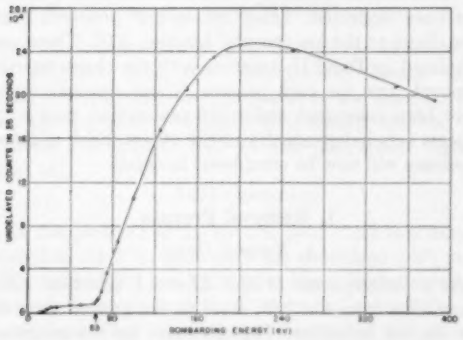

FIG. 13. Excitation curve for the undelayed signal (U_b', Table I).

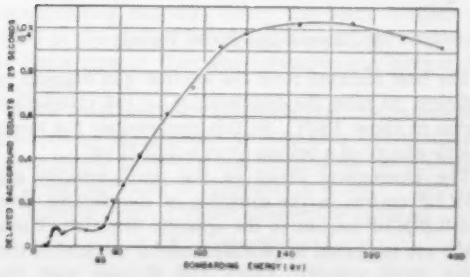

FIG. 14. Excitation curve for the delayed background signal (B, Table I).

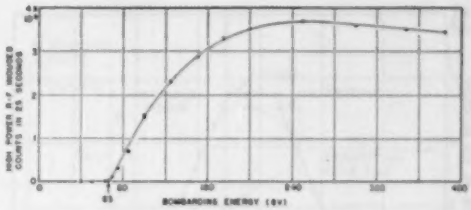

FIG. 15. Excitation curve for the high-power rf induced signal (H-B, Table I).

5. Timing Curves

The variation of the undelayed signal with channel I trigger delay setting is shown in Fig. 16. The trapezoidal shape of this curve results from the rectangular shape of the gun pulse and the gate pulse. The residual signal at large delay settings is due to the delayed background. This curve very graphically shows the reduction in background obtained with the present pulsing technique compared to the background obtained by Lamb and Skinner. The background in the latter experiment corresponds to the peak value of the undelayed signal, while the background in the present experiment corresponds to the signal at a delay setting of 2.4 μsec. Since the rf induced signal is nearly the same in the two cases, the pulsing technique results in a substantial improvement in the signal-to-background ratio. The absence of a signal at the very early delay settings shows that there are no excited particles remaining in the interaction region from bombardment to bombardment.

The variation of the delayed background and the high-power rf induced signal with the delay setting of channel II is shown in Fig. 17. The form of the delayed background curve is identical with that of the undelayed signal (see Fig. 16). The rf curve exhibits three interesting features. They are: (1) the extended flat top, (2) the nonlinear tail, and (3) the negative value at the largest delay setting. The first two features are a consequence of the fact that the curve was obtained with high rf power. Under this condition the lifetime of the metastable state is very short (roughly 0.10 microsecond in the present case), and essentially all of the rf induced counts are obtained in the early part of the rf pulse. Similar curves, taken with lower rf power and therefore a greater metastable lifetime, exhibit a shorter flat region on top. The negative value for the rf signal at the largest delay setting results from radiative collision quenching of metastable ions by normal atoms. Since this phenomenon is of only minor importance to the present experiment, though it is of some interest in its own right, a detailed discussion of the effect will be presented in a separate paper.

E. LINE SHAPE

If all of the metastable ions were exposed to the rf field for the same time (t), then aside from certain small

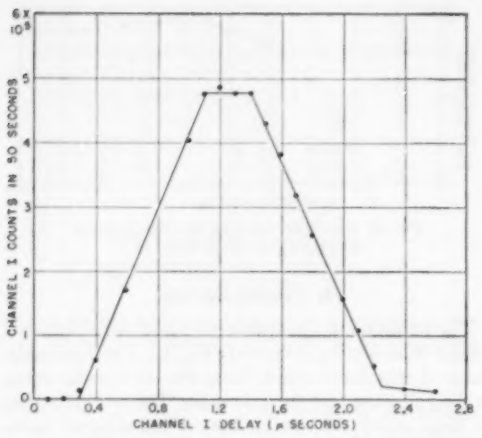

FIG. 16. Variation of the undelayed signal (U_0', Table I) with the channel I trigger delay setting.

corrections, the shape of the resulting rf quenching function would be given by

$$\phi(\mu)=N_0(1-e^{-\mu t}), \tag{5}$$

where N_0 is proportional to the number of metastables formed per bombardment and the transition rate μ is given by

$$\mu=\frac{2\pi S_0}{\hbar\omega}\frac{e^2}{\hbar c}\frac{\gamma\omega}{(\omega-\omega_0)^2+(\gamma/2)^2}|\mathbf{r}\cdot\mathbf{E}|^2, \tag{6}$$

where $1/\gamma$ is the mean life of the P state, ω_0 the resonant frequency and ω the frequency of the rf, both in radians per second, S_0 is the incident power in ergs/cm²/sec, $\mathbf{r}$ is a vector whose components are the matrix elements for the transition, and $\mathbf{E}$ is a unit vector along the direction of rf polarization. Since it was desired to study the σ transition af, ($2\,^2S_{\frac{1}{2}}$, $m=+\frac{1}{2}-2\,^2P_{\frac{1}{2}}$, $m=-\frac{1}{2}$), the interaction space was oriented so that the rf electric field was at right angles to the magnetic field. In this case we require the matrix element of the coordinate X between the α state and the f state. This matrix element is

$$X_{\alpha f}=(\sqrt{3}/2)a_0, \tag{7}$$

where a_0 is the Bohr radius.

In practice there is a distribution of interaction times (t). Thus, if the number of metastable ions in the interaction region decreases monotonically after the end of the gun pulse, then

$$\phi(\mu)=\mu\int_{T_2}^{T_2+T_3}N(t)e^{-\mu(t-T_2)}dt, \tag{8}$$

where $N(t)$ is proportional to the number of metastables in the interaction space at the time t (measured from the end of the gun pulse), T_2 is the delay from the end of the gun pulse to the beginning of the rf pulse and T_3 is the length of the rf pulse (Fig. 1). In deriving the above expression, the spatial variation of the transition rate μ has been approximated by a rectangular function having the same peak value and the same area as the true function (Fig. 18). In addition, the variation of the detection efficiency across the detector window has been neglected. There are several processes that contribute to the ion removal function $N(t)$. These are tabulated in Table II, together with the characteristic removal time for each process. These removal times have been computed under the assumption that each process acts independently of the others. Each of these processes will now be considered in detail.

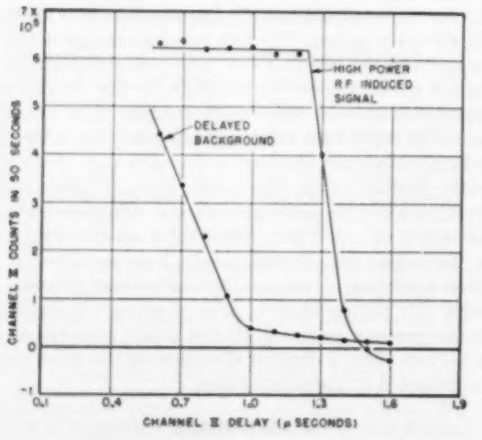

FIG. 17. Variation of the delayed background signal (B, Table I) and the high-power rf induced signal (H-B Table I) with the channel II trigger delay setting.

1. Removal Process

a. Natural Decay

As a consequence of the $\Delta L=\pm 1$ selection rule, transitions from the $2\,^2S_{\frac{1}{2}}$ state to the ground state of the ion are forbidden. This accounts for the metastability of the $2\,^2S_{\frac{1}{2}}$ state. The most probable decay mechanism for this state is believed to be two-quantum decay, for which the lifetime is 2.2×10^{-3} sec.[18]

b. Thermal and Recoil Velocity

The heat radiated from the electron gun filament is sufficient to raise the temperature of the interaction region to about 130°C. At this temperature the mean kinetic energy of a helium atom is 0.0521 ev.

The kinematical limits on the recoil velocity are 2.8×10^5 cm/sec in the direction of the electron flow and 0.28×10^5 cm/sec in the opposite direction. These limits are too broad to provide a useful measure of the mean recoil velocity. Lamb and Skinner used the

[18] G. Breit and E. Teller, Astrophys. J. 91, 215 (1940).

"sudden" approximation to estimate the excitation cross section of the metastable state of the ion (He I, p. 548). This approximation is consistent with the assumption that the recoil momentum of the ion is equal to the momentum of the ejected electron in its normal state at the instant of impact. The mean value of this momentum is

$$P=Z_{\text{eff}}\alpha mc, \tag{9}$$

where $Z_{\text{eff}}=1.69$ is the effective value of the nuclear charge, α is the fine structure constant, m is the electronic mass, and c is the velocity of light. The corresponding recoil velocity and recoil energy are

$$v_R=0.507\times10^5 \text{ cm/sec}, \quad E_R=0.00534 \text{ ev}. \tag{10}$$

Since this energy is only about 10% of the thermal energy and since the angular distribution of the recoil velocity is not known, it is assumed that the net effect of the thermal and recoil velocities may be represented by an effective temperature of the metastable ions. This effective temperature is chosen so that the effective kinetic energy of the ions is equal to the sum of the above thermal and recoil energies. The temperature is

$$T_{\text{eff}}=440°\text{K}. \tag{11}$$

The corresponding rms transverse and longitudinal velocities are

$$v_T=1.36\times10^5 \text{ cm/sec}, \quad v_L=0.961\times10^5 \text{ cm/sec}. \tag{12}$$

Since the ions are free to move only in the direction of the magnetic field, the characteristic thermal and recoil removal time may be taken as the time for an ion, moving with a velocity of 0.96×10^5 cm/sec, to traverse the central half of the interaction region (Fig. 18).

c. Stark Quenching

In the presence of an electric field there is a Stark mixing of the $2\,^2S_{\frac{1}{2}}$ state with the shortlived $2\,^2P_{\frac{1}{2}}$ and $2\,^2P_{\frac{3}{2}}$ states. The resulting state has a lifetime somewhere between that of the S state and that of the P state. Lamb has developed a theory for this Stark quenching of the S states. The lifetime of the mixed state is given in H I, Eq. (76), p. 571.

It may be shown that for the same electric field and corresponding magnetic fields, the Stark lifetime of either of the ionized helium S states is approximately 64 times greater than the corresponding lifetime in hydrogen.

Aside from possible stray fields, the ions experience space charge and motional electric fields. The maximum values for the transverse and longitudinal space charge fields are estimated in Appendix I to be 7.9 and 2.5 v/cm respectively. The motional field is given by

$$\mathbf{E}_m=(\mathbf{V}\times\mathbf{H})/c, \tag{13}$$

where $\mathbf{V}$ is the velocity of the ion, and $\mathbf{H}$ is the magnetic field. We may obtain an upper bound to the effective electric field by adding the motional field corresponding to a velocity of 1.36×10^5 cm/sec [Eq. (12)] to the above space-charge field. The lifetimes of the α and β states resulting from this limiting field are shown as a function of the magnetic field in Fig. 19. The sharp minimum in the lifetime of the β state at a field of 7596 gauss is a result of the crossing of the β and ϵ states at this field.

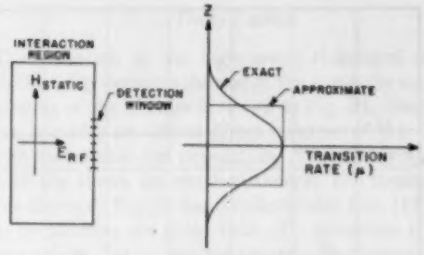

FIG. 18. Spatial variation of the rf transition rate.

Since the Stark lifetime of the α state, as computed above, is very much greater than the other removal times (Table II), we need not seek a more refined value for the α state Stark lifetime. In the case of the β state, it appears that the Stark quenching is the dominant removal process. Fortunately, the results of the present experiment do not depend upon a precise knowledge of the lifetime of the β state. This is because the frequency of the rf field is so far removed from any of the β-state transition frequencies that, even in the high-power observation, only a negligible number of β-state ions are quenched by the rf.

d. Gas Collisions

Metastable ions are lost through encounters with normal atoms: (1) by elastic collisions which cause the ions to diffuse out of the interaction chamber and (2) by inelastic collisions which result in the quenching of the metastable ions.

Unfortunately, no estimate exists for the elastic scattering cross sections of a metastable ion by a normal atom. Hornbeck and Wannier[19] have estimated from mobility measurements that the effective cross section

TABLE II. Metastable ion loss processes.

Loss process	Characteristic loss time (μsec)
Natural decay	2200.0
Thermal and recoil velocities	4.5
Stark quenching[a]	170.0
Gas quenching	8.6
Transverse space charge motion	8.8
Longitudinal space charge motion	0.846

[a] This is for the α state. The Stark lifetime of the β state is very much less than this value.

[19] J. A. Hornbeck and G. H. Wannier, Phys. Rev. **82**, 458 (1951). J. A. Hornbeck, Phys. Rev. **84**, 615 (1951).

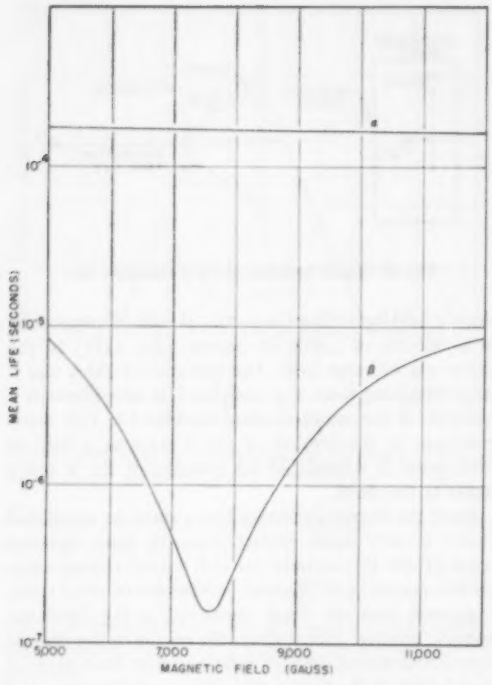

FIG. 19. Dependence of the net lifetime of the α and β states on the magnetic field.

for the collision of a normal ion with a normal atom is $61.8\pi a_0^2$. It seems reasonable to assume that the corresponding cross section for the metastable ion is of the same order or perhaps smaller than the above value. Under this assumption the elastic mean free path of a metastable ion is 2.5 cm at a gas density of 0.748×10^{14} atoms/cc (this density corresponds to the normal experimental conditions). Since the entire experiment takes place in a region having a maximum dimension of 0.5 cm, it is permissible to neglect elastic collisions in discussing the motion of the ions.

There are two classes of quenching collisions which are important in the present range of pressure and velocity. In the first, the ion returns to its ground state with its excitation energy of 40.8 ev used to ionize the helium atom with the ejection of an electron with 16.2-ev energy. In the second, the helium atom remains in its ground state but the $2\,^2S_{\frac{1}{2}}$ ion is transferred to the nearby $2\,^2P_{\frac{1}{2}}$ or $2\,^2P_{\frac{3}{2}}$ states. Since the ions transferred to the P states quickly decay to the ground state, with the emission of a λ303.8 A photon, the latter process accounts for the observed radiative collision quenching of metastable ions by normal atoms (see Sec. D5). Lamb and Sternberg[20] have estimated that, at a velocity of 3×10^5 cm/sec and a gas density of 0.748×10^{14} atoms/cc, the cross sections and mean lifetimes for the above processes are:

$$\begin{aligned}&\sigma_e=18\pi a_0^2, \quad \tau_e=28\ \mu\text{sec},\\ &\sigma_r=41\pi a_0^2, \quad \tau_r=12\ \mu\text{sec},\\ &\sigma_q=59\pi a_0^2, \quad \tau_q=8.6\ \mu\text{sec}.\end{aligned} \tag{14}$$

where the subscript e refers to the ejection process, r to the radiative process, and q to the combined effect of both processes. The velocity used in the above calculation is believed to be representative of the collision velocity. It is the sum of the mean thermal velocity of the atoms and the mean ion velocity resulting from space charge explosion (see Appendix I).

e. Space-Charge Effects

In the absence of positive ions, the electron beam forms a potential well approximately 0.65 ev deep in the interaction region. Since the combined thermal and recoil energy of the ions is about 0.057 ev, this potential well traps the ions as they are formed. The rate of ionization is such that neutralization occurs only slightly before the end of the gun pulse; thus essentially all of the ions are trapped. Since the bombarding electrons have a velocity of 0.93×10^9 cm/sec, the density of these electrons drops to zero as soon as the electron beam is turned off by the control grid. It is assumed that the secondary electrons liberated in the gas have a velocity corresponding to the recoil momentum in Eq. (9).

$$V_s=Z_{ef}\alpha c=3.7\times10^8\ \text{cm/sec}, \tag{15}$$

where V_s is the velocity of the secondary gas electrons. Most of these electrons leave the interaction region during the bombardment pulse. Thus at the end of the gun pulse there is a pure positive ion space charge cloud in the interaction region. The dominant mode of decay of such a cloud is a Coulomb explosion along the magnetic field lines. In addition, there is a transverse cycloidal motion resulting from the combined action of the magnetic field and the transverse space charge electric field. This cycloidal motion results in a transverse shearing of the ion cloud in the direction of rf propagation.

In Appendix I a detailed estimate is made of both the Coulomb explosion and the transverse shearing of the ion cloud. It is shown that as a result of the Coulomb explosion the ion density decreases as

$$\rho(t)=\rho_0\{1/[1+(t/T)^2]\}, \tag{16}$$

where $\rho(t)$ is the ion density at the line t, measured from the end of the gun pulse; ρ_0 is the initial ion density, and the characteristic time T is 0.846 μsec for a typical set of experimental conditions. It is further shown that, for the same set of conditions and in the absence of the longitudinal Coulomb explosion, the shearing motion causes the number of ions exposed to the detector to drop to half the initial number in 8.8 μsec.

[20] W. E. Lamb, Jr., and D. Sternberg (private communication).

2. Theoretical Quenching Function

From the above discussion it is evident that the Coulomb explosion of the ion cloud is the dominant ion removal mechanism. Accordingly, a theory of the rf quenching function has been developed in which the motion of the ions is given by Eq. (24). This theory includes the radiative and nonradiative gas quenching discussed above. It is also possible to include Stark quenching and natural decays. However, since these are such slow processes there is little point in considering them further. The resulting rf quenching function is

$$\phi(\mu)=(\mu+\lambda_r)\phi_0 e^{-\lambda_g T_2}\int_{T_2}^{T_2+T_3} dt\frac{e^{-(\mu+\lambda_g)(t-T_2)}}{1+(t/T)^2}, \quad (17)$$

where μ is defined in Eq. (6), T is defined in Eq. (25), ϕ_0 is a normalization constant, T_2 and T_3 are defined in Fig. 1. $\lambda_r=1/\tau_r$ is the rate of radiative gas quenching

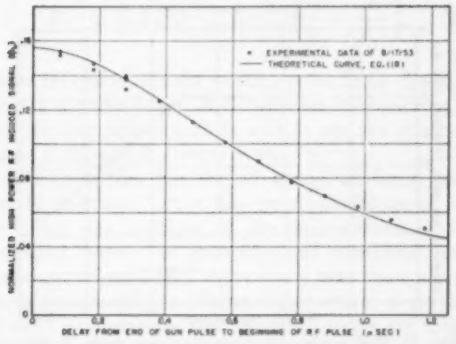
EXPERIMENTAL DATA OF 8/17/53
THEORETICAL CURVE, EQ. (10)
NORMALIZED HIGH POWER R F INDUCED SIGNAL (φ0)
DELAY FROM END OF GUN PULSE TO BEGINNING OF R F PULSE (μ SEC)

FIG. 20. Rf delay curve showing the dependence of the normalized high-power rf-induced signal (ϕ_0, Table I) on the delay between the end of the gun pulse and the beginning of the rf pulse.

and $\lambda_g=1/\tau_g$ is the total rate of gas quenching [τ_r and τ_g are given in Eq. (14)]. The quantity that is experimentally observed is the rf induced signal; by definition this is the difference between channel II count taken with and without rf. This quantity, $F(\mu)$, is related to the above quenching function by

$$F(\mu)=\phi(\mu)-\phi(0). \quad (18)$$

The percent rf quenching defined in Eq. (1) is given by

$$f=100\times\frac{F(\mu_l)}{F(\mu_h)}=100\times\frac{\phi(\mu_l)-\phi(0)}{\phi(\mu_h)-\phi(0)}, \quad (19)$$

where μ_l is the rf transition rate corresponding to the low rf power and μ_h is the same quantity with high rf power.

3. Comparison with Experiment

The above quenching theory has been tested experimentally in three different ways.

a. Delay Curves

The variation of the high-power rf-induced signal with the delay between the end of the gun pulse and the beginning of the rf pulse is shown in Fig. 20. Since this curve provides an almost direct measure of the decay of the metastable ion population, it serves as a good test of the above ion removal theory. The theoretical curve shown in Fig. 20 was obtained from Eqs. (17) and (18) by allowing the delay time (T_2) to assume appropriate values. The agreement between the observed and theoretical values is probably better than might be expected for such a rough theory. Data obtained in April, 1953, under similar conditions, showed comparable agreement. On two occasions rf delay curves were obtained with one-tenth the normal bombarding current. In such a case it is expected that the characteristic loss time would be increased by a factor of $\sqrt{10}=3.16$ [Eq. (25)], but unfortunately neither of these curves showed the expected increase. In one there was an increase of approximately a factor of 2, while in the other there was almost no increase. The former result may be consistent with the theory if thermal and recoil velocities are taken into account. The latter result is not understood. It may be the result of contamination in the interaction space, since the data were obtained after nearly three weeks of continuous running.[21] It should be noted that the precision resonance data were obtained soon after a thorough cleaning of the interaction space.

b. Quenching Curves

The variation of the rf-induced signal with rf power is shown in Fig. 21. The data obtained at magnetic field values other than the resonance value were shifted on the power scale in accordance with Eq. (6) so that

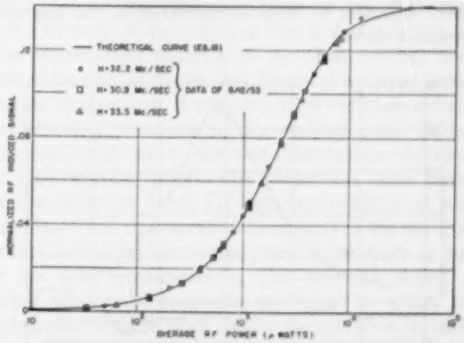

FIG. 21. Quenching curves showing the variation of the normalized rf-induced signal with rf power at three values of the magnetic field corresponding to resonance and the two working points.

[21] An inspection of the interaction space immediately after these data were obtained revealed a slight black deposit on the electron collector.

they could be compared with the resonance data. The agreement of the curves obtained at different field values is an indication that there are no major asymmetries in the experimental resonance curve. Unfortunately, such a test is not precise enough for the purposes of the present experiment.

The theoretical quenching function given in Eq. (18) is also shown in Fig. 21. The only adjustable parameters in the theoretical curve are the vertical and horizontal scale factors. Since the curves are plotted against the logarithm of the rf power, the horizontal scale factor does not affect the shape of the curves. The agreement between the observed and the theoretical curves is quite satisfactory.

The effective rf power in the interaction region, determined by fitting the theoretical quenching function to the observed quenching curves, is roughly 1.5 times greater than the power indicated by the bolometer. This difference can be accounted for by rf losses in the waveguide between the interaction region and the bolometer.

c. *Panoramic Resonance Curves*

The field dependence of the observed percent rf quenching is shown in Fig. 22, together with a theoretical curve obtained from Eq. (19). In deriving the theoretical curve, allowance was made for the field dependence of the matrix element (H III, p. 270), for the exact dependence of the transition frequency on the magnetic field (H III, p. 265), and for the width of the klystron spectrum. The transition frequency for the theoretical curve was based on the theoretical value of δ (Table V). The power scale factor was adjusted for the best fit at the resonance peak. In this fitting, the ratio of the high-power to low-power transition rate was held equal to the observed ratio of high rf power to to low rf power. As in the case of the quenching curves, the agreement between the observed and theoretical curves indicates no large asymmetries in the observed resonance curve.

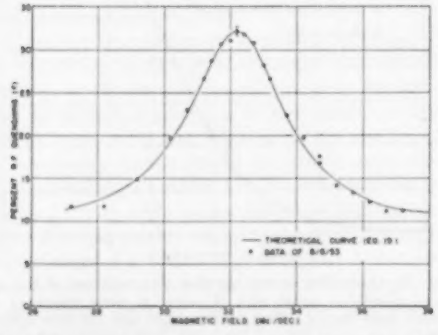

FIG. 22. Panoramic resonance curve for the αf transition showing the dependence of the percent rf quenching (f, Table I) on the magnetic field. The vertical bar indicates the standard deviation of each point.

The field dependence of the high-power rf-induced signal is shown in Fig. 23. This curve shows the degree of rf saturation actually achieved in the high-power observations. The curve is quite flat in the region where the precision resonance data is obtained (30.5 to 33.5 Mc/sec). The only effect of the incomplete saturation of the high power rf quenching data is to broaden the percent rf quenching resonance curve.

Since the channel I signal is somewhat field dependent, the normalization procedure introduces a field dependent distortion into the low-power and high-power rf-induced signals. For this reason it is not feasible to compare the observed field dependence of the rf-induced signals with theoretical curves. Since this distortion affects the low-power and high-power signals in the same manner, there is no net distortion of the percent rf quenching data.

The field dependence of the delayed background signal is shown in Fig. 24. The field-dependent part of this background arises from the Stark quenching of

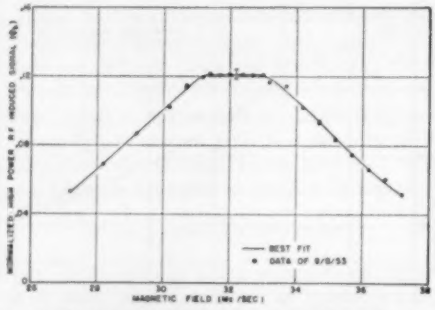

FIG. 23. High-power panoramic resonance curve showing the dependence of the normalized high-power rf-induced signal (ϕ_a, Table I) on magnetic field. The vertical bar indicates the standard deviation of each point.

metastable ions formed in the β state. Close to the βe crossing point (Fig. 19), most of these ions decay before the channel II gate is turned on and thus make only a small contribution to the delayed background; as the field is varied the Stark lifetime increases, so that more of these ions decay during the channel II gate and thereby increases the delayed background; as the field is varied still further from the crossing point, the lifetime becomes long compared with the channel II gate length and the β-state contribution to the delayed background decreases again. No quantitative theory for the field dependence of the delayed background signal was made since such a theory requires detailed knowledge of the electric fields in the interaction region as well as precise knowledge of the relative excitation and detection efficiencies of the various levels.

F. PRECISION RESONANCE DATA

The precision resonance data were obtained and treated by a method similar to that used by Lamb and

Retherford (H IV, p. 1017). Precise data are obtained at two points on the resonance curve known as working points; these are selected to fall close to the inflection points of the curve. Somewhat less precise data are obtained at two sets of points known as slope points; each set of slope points brackets a working point. Several short observations are made close to the center of the resonance. These are used to determine the peak height of the resonance and to provide a measure of the instrumental fluctuations (Fig. 11). If the values of the rf quenching at the two working points are exactly equal, then the resonant field is equal to the mean value of the two working point fields. In general the rf quenching values at the working points are not exactly equal: in such a case it is necessary to use the observed slopes of the resonance curve to extrapolate the working point fields to values which would yield equal quenching. The resonant field (H_0) is equal to the mean value of the corrected working point fields.

$$H_0=\tfrac{1}{2}(H_1+H_2)-\tfrac{1}{4}(\bar{f}_1-\bar{f}_2)\left(\frac{1}{S_1}+\frac{1}{|S_2|}\right), \quad (20)$$

where H_1 and H_2 are the working point fields, $\bar{f}_1$ and $\bar{f}_2$ are the average values of the percent rf quenching at the working points, and S_1 and S_2 are the observed slopes at H_1 and H_2, respectively.

This procedure has the advantage of being completely objective, but it has the disadvantage of not providing any measure of the asymmetries in the resonance curve. The quenching and panoramic resonance curves discussed above show that there are no major asymmetries in the resonance curve. A number of small asymmetries and resonance shifts are investigated theoretically in the next section.

Generally, each run consisted of two observations at each working point, one observation at each slope point, and six observations at the resonance peak. Each observation consisted of a high-rf power, a low-rf power and an rf-off reading. The counting time for each reading was five minutes at the working points, three minutes at the slope points, and one minute at the resonance peak. The resonance curve is traversed in a zig-zag pattern to reduce the effects of the instrumental drifts. The observations at the resonance peak were taken between alternate pairs of the other observations. The comparatively small number of observations at each field value is a result of the somewhat cumbersome field measuring and stabilizing equipment, approximately five minutes being required to set up a particular field value. Typical operating conditions for a run are: Electron bombarding energy = 250 ev; electron bombarding current = 742 μa (peak); positive grid pulse = 24 v; negative grid bias = 50 v; electron collector bias = 225 v; gun pulse length = 0.81 μsec; rf pulse length = 0.40 μsec; gate I length = 1.104 μsec; gate II length = 1.089 μsec; pulse repetition rate = 10^6 pulses/sec; helium pressure = 3.1×10^{-4} mm Hg; Allen tube voltage = 2.30 kv; Allen tube pressure = 1.5×10^{-4} mm Hg (N_2 equiv.); klystron beam voltage = 4.8 kv; klystron beam current = 38 ma (peak); high-rf power = 0.250 w (peak), and low-rf power = 0.025 w (peak).

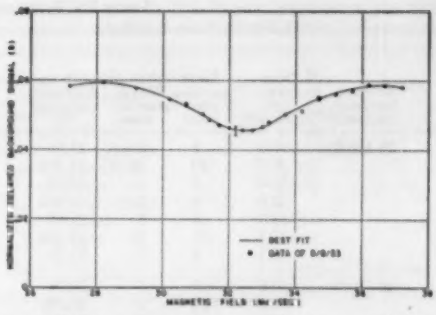

FIG. 24. Field dependence of the normalized delayed background signal (*b*, Table I). The vertical bar indicates the standard deviation of each point. The position of the minimum does not coincide with the position of the maximum in Fig. 22 since the klystron frequency was selected so that the resonant field for the αf transition did not correspond to the βe crossing field (Fig. 3).

The resonance field was selected close to the βe crossing point in order to minimize resonance distortion arising from β-state transitions. This is accomplished for the following reasons: (1) at the crossing, the β-state population is minimized due to the rapid Stark quenching (Fig. 19), (2) the βe-αf overlap is smallest at this field, and (3) the field dependence of the βe transition is symmetrical with respect to the αf resonance.

The results of the precision runs are shown in Table III. Appropriate dead time corrections have been applied to these data.[22] The theoretical quenching uncertainties listed in Table III are based on the theoretical rms uncertainty in each of the observed counts. The ratio of the observed rms fluctuation in the percent rf quenching at the resonance peak to the theoretical value for each of the precision runs is shown in Fig. 11. The approximate equality of the observed and theoretical fluctuation shows that there are no large instrumental fluctuations. A comparison of the observed and theoretical fluctuations in the working point data is less significant, since only two observations are made at each working point. The theoretical slope uncertainties listed in Table III include the effects of both the theoretical rms uncertainty in each of the observed counts and an estimated one gauss uncertainty in each of the field measurements. The observed slopes on either side of the resonance are equal to within the theoretical uncertainties in the slopes. This is taken as a further indication of a symmetrical resonance curve.

[22] Each run was reduced both with and without the dead time corrections. In no case did the dead time corrections change the value of S by more than 1 Mc/sec. The dead time corrections are entirely negligible for the quenching and panoramic resonance curves.

TABLE III. Summary of precision data and results.[a]

Run	Klystron frequency (Mc/sec)	Magnetic field (Mc/sec)	Total counting time (min)	No. of observations	Average fractional quenching (%)	Theor. quenching uncertainty (%)	Obs. quenching uncertainty (%)	Resonance slope (% per Mc/sec)	Theor. slope uncertainty (% per Mc/sec)	Uncorrected value of δ (Mc/sec)	Wt.	Theor. uncertainty in δ (Mc/sec)
10	28 196.0	30.5	3	1	22.31	0.14						
		30.7	10	2	24.294	0.073	0.27	8.80	0.51			
		30.9	3	1	25.83	0.13						
		32.0	6	6	31.496	0.097	0.078			14 038.0	1	3.8
		33.1	3	1	25.18	0.14						
		33.3	11	3	23.564	0.062	0.21	8.70	0.49			
		33.5	3	1	21.70	0.13						
11	28 350.9	30.8	3	1	24.23	0.15						
		31.0	10	2	26.380	0.074	0.033	9.70	0.52			
		31.2	3	1	28.11	0.14						
		32.3	7	7	33.846	0.090	0.095			14 046.0	1	3.8
		33.4	3	1	27.80	0.15						
		33.6	10	2	26.132	0.072	0.17	8.63	0.51			
		33.8	3	1	24.35	0.14						
12	28 294.0	30.7	3	1	21.08	0.13						
		30.9	5	1	22.65	0.10		7.33	0.45			
		31.1	3	1	24.01	0.12						
		32.2	5	5	30.472	0.093	0.20			14 058.1	½	5.0
		33.3	3	1	23.47	0.12						
		33.5	5	1	21.61	0.095		8.05	0.46			
		33.7	3	1	20.25	0.12						
13	28 305.8	30.7	3	1	23.01	0.14						
		30.9	10	2	23.945	0.076	0.14	9.65	0.49			
		31.1	3	1	26.87	0.13						
		32.2	6	6	32.460	0.094	0.15			14 042.2	1	3.8
		33.3	3	1	26.60	0.13						
		33.5	10	2	23.841	0.073	0.012	8.35	0.48			
		33.7	3	1	23.26	0.14						
										$\langle\delta\rangle_{Av}=14\,044.3$		

[a] The magnetic field values are given in terms of the proton resonance absorption frequency. The uncertainties in the quenching values, the slopes, and the values of δ are rms deviations.

The theory of the Zeeman effect, as given by Lamb (H III, p. 265), is used to determine the value of δ from the observed value of the resonant magnetic field and the observed klystron frequency. The fine structure splitting (ΔE) for the $n=2$ states of He^4 is given by

$$\Delta E=\frac{\alpha^2 cR_{H_\infty}Z^4}{16}\left(1+\frac{\alpha}{\pi}-5.946\frac{\alpha^2}{\pi^2}+\frac{5}{8}\alpha^2Z^2\right),$$

where α is the fine structure constant, c is the velocity of light, R_{H_∞} is the Rydberg constant in wave numbers for He^4, and $Z=2$ in the nuclear charge. Using the 1953 constants of DuMond and Cohen,[23] the mass of He^4 as determined by Mattauch and Bieri,[24] and the ratio of the proton moment (uncorrected) to the Bohr magneton as determined by Gardner,[25] the Zeeman constants appropriate to He^4 are:

$$H_1=355.217\pm0.009 \text{ Mc/sec},$$
$$H_{1\alpha}=355.672\pm0.009 \text{ Mc/sec},$$
$$H_{1\alpha}=355.900\pm0.009 \text{ Mc/sec},$$
$$T=-0.002558689\pm0.000000027,$$
$$f_1=\tfrac{2}{3}\Delta E=117\,056.6\pm2.6 \text{ Mc/sec}.$$

[23] J. W. M. DuMond and E. R. Cohen, Revs. Modern Phys. **25**, 691 (1953).
[24] J. Mattauch and R. Bieri, Z. Naturforsch. **9a**, 303 (1954).
[25] J. H. Gardner, Phys. Rev. **83**, 996 (1951).

The notation is that of Lamb (H III, p. 265), except that the unit fields are expressed in terms of the proton resonance absorption frequency. The uncertainties in the above constants produce a negligible contribution to the uncertainty in δ. The theoretical values for the rms uncertainty in δ, listed in Table III, include the effects of an estimated two megacycle per second uncertainty in the klystron frequency, an estimated one gauss uncertainty in the working point field values, the theoretical uncertainty in the working point quenching values and the theoretical uncertainty in the resonance slopes.

Run 12 has been given a weight of one-half since as a result of equipment failure only half of the normal working point data were obtained. The theoretical rms uncertainty in the weighted mean value of $\delta(\langle\delta\rangle_{Av})$ is

$$\Delta_T\langle\delta\rangle_{Av}=2.0 \text{ Mc/sec}. \quad (21)$$

The rms deviation in $\langle\delta\rangle_{Av}$, as determined from the individual values of δ, is

$$\Delta_0\langle\delta\rangle_{Av}=3.4 \text{ Mc/sec}. \quad (22)$$

The theoretical uncertainty in $\Delta_0\langle\delta\rangle_{Av}$ is 2.2 Mc/sec, thus the observed uncertainty in $\langle\delta\rangle_{Av}$ is consistant with the theoretical uncertainty. The larger of the two above values of $\Delta\langle\delta\rangle_{Av}$ is used for estimating the over-all reliability of the final result.

G. CORRECTIONS

A number of corrections to the observed value of δ have been discovered and evaluated (Table IV). These corrections are discussed below. Except for the space-charge corrections, the quenching function given by Eq. (5) is used when it is necessary to consider saturation effects in the evaluation of a correction, and the interaction time (t) is taken equal to the rf pulse duration (T_3).

1. Matrix Element Variation

The form of the $2\,^3P_1$ wave function changes as the magnetic field is varied, and this produces a field-dependent variation of the matrix elements that appear in Eq. (6). This variation may be expressed in terms of correction factors to the matrix elements evaluated in weak field. These correction factors are given by Lamb [H III, p. 270, Eqs. (200) to (201)]. The appropriate unit field for the X that appears in these equations is listed above as H_1.

2. Zeeman Curvature

Since the relation between magnetic field and transition frequency is not quite linear (H III, p. 265), there is a small difference between the true resonant transition frequency and the value obtained in Sec. F by linear interpolation of the corrected working point fields. The Zeeman curvature correction is equal to the difference between the mean value of the transition frequencies corresponding to the corrected working point fields and the transition frequency corresponding to the mean field (H_0).

3. Overlap with Other Resonances

In addition to the desired αf transition, the rf electric field may also induce βe, αe and βf transitions (Fig. 4). The last two transitions require a component of rf electric field along the magnetic field (π polarization). If any of the undesired transitions do in fact occur, the observed resonance curve will be distorted and the value of δ so obtained will be in error. The largest correction is expected to arise from overlap with the αe resonance since it is separated by only 7000 Mc/sec or roughly nine half-half widths from the αf resonance at the operating field. The βf resonance is separated by about 21 000 Mc/sec, and the βe by about 28 000 Mc/sec. The intensity of π radiation in the interaction region is believed to be less than 10% of the intensity of the desired σ radiation. Taking the relative intensity of the π radiation as 10%, and ignoring the rapid Stark quenching of the β state in the neighborhood of the αf resonance (Fig. 19), the resulting overlap corrections are $+0.20$ Mc/sec for αe overlap, -0.02 Mc/sec for βf overlap, and <0.01 Mc/sec for βe overlap. Since these are believed to be extreme upper bounds to the true corrections, the value adopted was $+0.1\pm0.01$ Mc/sec.

TABLE IV. Corrections to δ in Mc/sec calculated at the working points of the resonance curve.

Matrix element variation	-1.56
Zeeman curvature	-0.25
Overlap	$+0.10\pm0.10$
Doppler effect	±0.02
Field inhomogeneity	-0.24 ± 0.60
Static stark effect	<0.01
rf stark effect	<0.01
Space-charge effects	
longitudinal	$+0.02$
transverse	$+0.21$
Total correction	-1.72 ± 0.72 Mc/sec

If the electron cyclotron resonance overlaps the desired αf resonance, there will be a distortion of the observed resonance and the value of δ will be in error. It may be shown that, in the neighborhood of the αf resonance, the energy acquired by electrons from the rf field is about 2×10^{-4} ev. Since this energy is much less than the lowest excitation energy of helium, there is no electronic contribution to the rf induced signal and consequently no distortion of the αf resonance curve.

4. Doppler Effect

In Appendix I, it is shown that, as a result of the transverse space charge fields, there is a net transport of about one-fifth of the ion cloud in the direction of rf propagation. The magnitude of the resulting Doppler shift is about 0.10 Mc/sec. The sign of the shift is not known because the sign of the magnetic field was not determined. Since only one-fifth of the ions are affected the correction is taken to be ±0.02 Mc/sec.

5. Field Inhomogeneity

As a result of the spatial separation of the interaction region and the proton nuclear magnetic resonance probe, there is a slight difference between the field at the probe and the field in the interaction region. The field in the interaction region was calibrated in terms of the field at the proton probe. This was done by replacing the interaction region with a second probe and observing the difference in resonant frequencies for the two probes at a given field setting. The result of this measurement is that the field in the interaction region is higher by 0.12 ± 0.30 gauss than the field in the probe. The diamagnetic corrections to the proton field values are negligible.[25]

6. Stark Effect

For the same electric field and corresponding magnetic fields, the Stark shift in ionized helium is 1/64 of the corresponding shift in hydrogen. At a field of 11 v/cm, the Stark shift of the α state is less than 0.01 Mc/sec and is therefore negligible.

[25] W. E. Lamb, Jr., Phys. Rev. **60**, 817 (1941). N. F. Ramsey, Phys. Rev. **77**, 567 (1950).

7. Rf Stark Effect

The rf electric field used to produce the observed quenching also causes a small Stark displacement of the energy levels. The theory of this effect has been developed by Lamb (H III, p. 275). An rf electric field of 30 v/cm is used for the high-power rf quenching measurement. This field causes a 0.006 Mc/sec shift of the αf resonance; this displacement is entirely negligible.

8. Field Dependence of Removal Processes

a. Gas Quenching

The magnetic field dependence of the gas quenching cross section discussed in Sec. E has been evaluated by a first-order method that gives the total cross section to within 10% of the value obtained by Lamb and Sternberg.[20] The cross sections given in Eq. (14) change by less than one part in 10^4 as the field is varied from one working point to the other. This effect is entirely negligible.

b. Space-Charge Effects

Since the ions move under the combined action of the space charge electric field and the applied magnetic field, it might be expected that the ion loss rate depends strongly upon the strength of the magnetic field. To first order, the ion explosion rate is independent of the magnetic field. The reason for this is simply that the explosive motion takes place along the field lines and is therefore independent of the field strength. The transverse ion less rate varies as H^{-1}, where H is the magnetic field strength. Since the transverse motion is slow, this strong field dependence produces only a small correction to δ. These qualitative arguments are supported by detailed estimates in Appendix II of the correction to δ resulting from the field dependence of the space charge removal processes. It is shown that that for a specific space-charge model, the corrections to δ resulting from the field dependence of the ion explosion rate and the transverse shearing motion are $+0.018$ Mc/sec and $+0.21$ Mc/sec, respectively. The model used for these estimates is admittedly rather crude; however, since the resulting corrections are so small there appears to be no need for a more refined calculation.

TABLE V. Terms contributing to the theoretical value of the separation of the $2\,^2S_{\frac{1}{2}}$ and $2\,^2P_{\frac{1}{2}}$ levels of hydrogen-like atoms, and their values in megacycles per second for singly ionized helium.

Second-order radiative shift[a–e]	
$L\left(1-3\frac{m}{M}\right)\left(2\ln\frac{1}{\alpha}+\frac{m}{M}-2\ln Z+\frac{11}{24}-\ln\frac{K_0(2,0)}{K_0(2,1)}\right)Z^5$	+13 168.8
Second-order vacuum polarization[a–c, e]	
$L\left(1-3\frac{m}{M}\right)(-\frac{1}{5})Z^4$	−433.9
Second-order magnetic moment[a–c, f]	
$L\left(1-2.75\frac{m}{M}\right)(\frac{1}{4})Z^4$	+1084.7
Second-order relativistic shift[c, e]	
$L\left(1-3\frac{m}{M}\right)(3\pi\alpha)\left(1+\frac{11}{128}-\frac{1}{2}\ln 2+\frac{5}{192}\right)Z^5$	+228.4
Fourth-order radiative shift[b]	
$L(3\alpha/2\pi)(0.52)Z^4$	+3.9
Fourth-order vacuum polarization[i]	
$L(-41\alpha/54\pi)Z^4$	−3.8
Fourth-order magnetic moment[j]	
$L(-2.973\alpha/\pi)Z^4$	−15.0
Finite mass effect[k]	
$L(m/M)(5.3684-\frac{1}{4}\ln Z)Z^5$	+3.0
Finite size effect[c, e, l]	
$\frac{1}{24\pi}\frac{e^2}{a_0\hbar}\left(\frac{a_0}{a_0}\right)^2Z^5$	+7.1
Total splitting	$\delta=14\,043.2\pm3.0$
Lamb constant[e]	
$L=\alpha^3R_\infty C/3\pi=135.6388\pm0.0045$ Mc/sec	
Excitation energies[d, e]	
$K_0(2,0)=(16.646\pm0.007)Z^2R_{\mathrm{He}}hc$	
$K_0(2,1)=(0.9704\pm0.0002)Z^2R_{\mathrm{He}}hc$	

[a] See reference 27.
[b] See reference 28.
[c] See reference 29.
[d] See reference 30.
[e] See reference 31.
[f] See reference 32.
[g] See reference 33.
[h] See reference 34.
[i] See reference 35.
[j] See reference 36.
[k] See reference 37.
[l] See reference 38.

H. RESULTS AND DISCUSSION

The final corrected value of δ is $14\,043\pm13$ Mc/sec. The 13-Mc/sec uncertainty is believed to represent the limit of error; it is equal to three times the observed standard deviation of the mean value of δ [Eq. (22)], plus an estimated 2.7 Mc/sec for the uncertainty in the corrections (0.7 Mc/sec for the uncertainty in the corrections listed in Table IV, 1.0 Mc/sec for the uncertainty in the dead time corrections, and 1.0 Mc/sec for the possible effects of the thermal and recoil velocities).

The values of the various terms that contribute to the theoretical value of δ are listed in Table V.[27–38]

[27] N. M. Kroll and W. E. Lamb, Jr., Phys. Rev. **75**, 388 (1949).
[28] J. B. French and V. F. Weisskopf, Phys. Rev. **75**, 1240 (1949).
[29] Karplus, Klein, and Schwinger, Phys. Rev. **86**, 288 (1952).
[30] Bethe, Brown, and Stehn, Phys. Rev. **77**, 370 (1950).
[31] E. E. Salpeter, Phys. Rev. **89**, 92 (1953).
[32] N. M. Kroll and W. E. Lamb, Jr., unpublished calculation of the reduced mass correction to the second-order magnetic moment contribution to δ_T.
[33] M. Baranger, Phys. Rev. **84**, 866 (1951). Baranger, Bethe, and Feynman, Phys. Rev. **92**, 482 (1953).
[34] Bershon, Weneser, and Kroll, Phys. Rev. **86**, 596(A) (1952); Phys. Rev. **91**, 1257 (1953).
[35] Baranger, Dyson, and Salpeter, Phys. Rev. **88**, 680 (1952).
[36] R. Karplus and N. M. Kroll, Phys. Rev. **77**, 536 (1950).
[37] E. E. Salpeter, Phys. Rev. **87**, 328 (1952).
[38] Hofstadter, McAllister, and Wiener, Phys. Rev. **96**, 854(A) (1954). We are indebted to Professor R. Hofstadter for communicating to us the more recent value $(1.50\pm0.25)\times10^{-13}$ cm for the rms charge radius of the α particle.

These values are based on the 1953 atomic constants of Dumond and Cohen[22] and the mass of He^4 as determined by Mattauch and Bieri.[24] The sum of these terms is $S_T = 14\,043.2 \pm 3.0$ Mc/sec.[39,40] The uncertainty in S_T arises from the uncertainties in the nuclear charge radius (2.3 Mc/sec), the fourth-order radiative shift (1.5 Mc/sec), the excitation energies (1.0 Mc/sec) and the physical constants (0.5 Mc/sec). It does not include any allowance for the contributions from terms that have not been evaluated. The essentially exact agreement of the theoretical and observed values is fortuitous.

If it is assumed that the difference between the observed and theoretical values of δ for hydrogen is due to missing terms in the theory, then by comparing the present results with the hydrogen results it is possible to place limits on the charge (Z) dependence of these terms. If we let $\delta(Z)$ represent these additional theoretical terms, from the hydrogen results we have $\delta(1) = +0.65 \pm 0.26$ Mc/sec and from the present results $\delta(2) = 0 \pm 16$ Mc/sec. The uncertainties in $\delta(z)$ are obtained by adding the theoretical and experimental uncertainties. It has been suggested[23] that the hydrogen difference might be accounted for by a relativistic term of the order $Z^6 \ln \alpha Z$. If the coefficient of this term is adjusted to fit the hydrogen data then the corresponding term for helium is $\delta(2) = 36 \pm 14$ Mc/sec. This value is not consistent with the present result. Thus we conclude that the hydrogen difference is not due to a single term of order $Z^6 \ln \alpha Z$ or higher. It is possible to reconcile the hydrogen and helium results with a single term of order Z^4 or Z^5. However, the coefficient for such a term must be at least $+0.39$ Mc/sec.

ACKNOWLEDGMENTS

The authors wish to thank Professor N. M. Kroll, Professor P. Kusch, and Professor W. E. Lamb, Jr., for their continued support and guidance in this experiment. We wish to thank the members of the Columbia Radiation Laboratory staff for their wholehearted cooperation, and especially to A. H. Barrett, A. W. Costello, C. Dechert, and H. Scharfstein.

APPENDIX I. SPACE-CHARGE REMOVAL PROCESSES

For the purpose of estimating the rate of space-charge explosion, a model consisting of a uniform rectangular cloud of ions constrained to move along the magnetic field lines is considered. It is assumed that the ions are initially at rest and that the Coulomb repulsion is "turned on" at a time corresponding to the end of the gun pulse (Fig. 25). Since an exact treatment of even this model is difficult, the following simplifying assumptions are made: (1) the ions continue to move with their initial acceleration and (2) the image charges in the interaction region walls are neglected. It may be shown that, for the dimensions of interest, the initial longitudinal space-charge field is given approximately by

$$E_Z = 8\rho_0 Z_0 \tan^{-1}(w/a), \tag{23}$$

where ρ_0 is the initial ion space-charge density, Z_0 is the initial coordinate of the particle that experiences the field E_Z, w is the thickness of the cloud, and a is the height of the cloud (Fig. 25). Under the assumption that the ions move with their initial acceleration, the trajectories of the ions are given by

$$Z = Z_0[1 + (t^2/T^2)], \tag{24}$$

where Z_0 is the initial Z coordinate of an ion, t is measured from the beginning of the explosion, and T is given by

$$T = \left(4\frac{e}{M}\rho_0 \tan^{-1}\frac{w}{a}\right)^{-\frac{1}{2}}, \tag{25}$$

where ρ_0, w, and a are defined above and e/M is the charge to mass ratio of the ion. The velocity of the ions resulting from the space charge explosion is

$$\dot{Z} = 2Z_0 t/T^2, \tag{26}$$

where Z_0, t and T are defined above. [The mean velocity used in the section on gas quenching was obtained by evaluating Eq. (26) at a time corresponding to the middle of the rf pulse and at a position corresponding to the center of each of the exploding segments.] Under the above conditions, the ion cloud expands in such a manner that the charge density decreases uniformly:

$$\rho(t) = \rho_0[1 + (t/T)^2]^{-1}, \tag{27}$$

where $\rho(t)$ is the charge density at the time (t) and ρ_0, t and T are defined above. In computing ρ_0, it is necessary to include the contribution from both ground-state

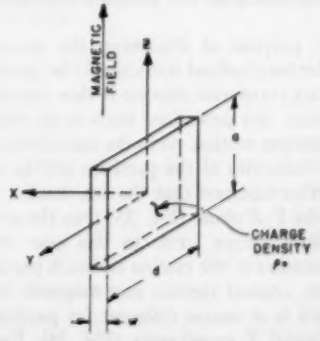

FIG. 25. Space-charge model and coordinate system used for discussing the space-charge explosion.

[39] Novick, Lipworth, and Yergin, Phys. Rev. 99, 612(A) (1955). The difference between the present theoretical value of δ and the value quoted in the above paper results from a small numerical error in the latter value.

[40] *Note added in proof.*—Professor Salpeter has kindly informed us of a small numerical error in the coefficient of the finite mass term. The corrected value of this term is $+2.8$ Mc/sec. The corrected value of S_T is $14\,043.0 \pm 3.0$ Mc/sec.

and metastable ions. Lamb and Skinner estimate that one hundred ground-state ions are formed for every metastable ion (He I, p. 549). The initial charge density is given by

$$\rho_0 = n^0[\sigma^+(1s)+\sigma^+(2s)]J^-T_1, \tag{28}$$

where n^0 is the gas density, $\sigma^+(1s)$ is the ionization cross section, $\sigma^+(2s)$ is the cross section for excitation to the metastable state of the ion, J^- is the electron beam current density and T_1 is the length of the gun pulse. Typical values for the constants appearing in Eqs. (23)–(28) are:

$$n^0 = 0.748\times10^{14} \text{ atom/cc},$$
$$\sigma^+(1s) = 0.37\pi a_0^2 \text{ (He I, p. 549)},$$
$$\sigma^+(2s) = 0.37\times10^{-2}\pi a_0^2 \text{ (He I, p. 549)},$$
$$J^- = 8.40\times10^7 \text{ esu/cm}^2\text{/sec},$$
$$T_1 = 0.81\times10^{-6} \text{ sec},$$
$$a = 0.865 \text{ cm}, \quad w = 0.0254 \text{ cm},$$

and

$$e/M = 7.227\times10^{13} \text{ esu/g}.$$

The corresponding values for ρ_0 and T are

$$\rho_0 = 0.165 \text{ esu/cc}, \quad T = 0.846 \text{ microsecond}. \tag{29}$$

Thus, in the above model, the ion density drops to one half of its initial value in 0.846 microsecond. The maximum value of the longitudinal electric field acting on those ions exposed to the detector is (see Sec. E1*c*)

$$E_{Z\,\max} = 8\rho_0(a/4)\tan^{-1}(w/a) = 2.52 \text{ v/cm}. \tag{30}$$

Estimates have been made of the errors introduced by the above approximations. It has been found that, if allowance is made for the change in acceleration, the effective value of T, the ion explosion time, is increased by about ten percent. Inclusion of the first twenty images similarly increases T by about 10%. Thus as a result of these two approximations the apparent explosion rate is about twenty percent too fast. No estimate has been made of the effect of the initial thermal and recoil velocities, but it is expected that these initial velocities will hasten the dispersal of the ion cloud.

For the purpose of discussing the transverse ion motion, the longitudinal motion will be ignored. Since the resulting transverse motion is slow compared with the explosion, this procedure leads to an overestimate of the transverse motion. As in the case of the explosion, the initial velocities of the particles will be neglected. If it is further assumed that the ion cloud is of infinite extent in the Y–Z plane (Fig. 25) then the motion is of a particularly simple form. In this case the electric field is a constant of the motion and each particle moves in constant, crossed electric and magnetic fields. The electric field is of course different for particles having different initial X coordinates (Fig. 25). Under these conditions the particle trajectories are cycloids, the average drift velocity of an ion across the field is

$$\bar{v}_y = cE_x/H, \tag{31}$$

where c is the velocity of light, H is the magnetic field, and E_x is given by

$$E_x = 4\pi\rho_0 X_0, \tag{32}$$

where ρ_0 is the initial ion density, and X_0 is the initial X coordinate of the ion (Fig. 25). The maximum value of this transverse field occurs at the edge of the cloud (see Sec. E1*c*)

$$E_{x\,\max} = 4\pi\rho_0 w/2 = 7.90 \text{ v/cm}. \tag{33}$$

Since the transverse drift velocity of each layer of ions is proportional to the initial displacement of the layer from the center of the cloud, the various layers slip past each other and the cloud undergoes a shearing distortion, the shear axis being parallel to the Y axis (Fig. 25). If the cloud is truly of infinite extent in the Y–Z plane (Fig. 25) and if two conducting sheets are placed parallel to the broad faces of the cloud then there is no change in the above description of the motion. If, however, account is taken of the finite extent of the cloud and its asymmetrical location between the broad faces of the interaction regions, then it is found that the plane of zero slip moves from the center of the cloud to a point about $W/10$ from the center toward the remote wall of the interaction region. Thus there is a net transport of about twenty percent of the cloud along the Y axis (Fig. 25), since this is also the direction of rf propagation this effect leads to a slight Doppler shift.

If the ion cloud extended well beyong the edges of the detection window in the Y direction then the transverse motion would not lead to any net loss of ions; in the actual apparatus at least one edge of the ion cloud is close to the edge of the detection window, this asymmetry results from an asymmetrical electron gun filament temperature distribution. For the purpose of obtaining an upper bound to the ion loss resulting from this transverse motion, it is assumed that both ends of the ion cloud coincide exactly with the edges of the detector window, and it is also assumed that the motion of the ions near the ends of the cloud is the same as it would be for a cloud of infinite extent. Under these conditions the number of ions exposed to the detector is given by

$$N = N_0[1-\pi(\rho_0 cwt/Hd)], \tag{34}$$

where N_0 is the number of particles in the field of view at the end of the gun pulse, H is the magnet field, d is the length of the detection window, ρ_0 is the charge density, w is the wdith of the cloud, and t is the time measured from the end of the gun pulse. Taking $d = 0.953$ cm, $w = 0.025$ cm, $\rho_0 = 0.165$ esu/cc, and $H = 7600$ gauss, it is found that the number of particles exposed to the detector dropes to half of the initial value in 8.8 microseconds.

APPENDIX II. FIELD DEPENDENCE OF SPACE-CHARGE REMOVAL PROCESSES

The dependence of the ion explosion time (T) upon the ion charge density and the dimensions of the ion cloud is given by Eq. (25). The ratio of the cloud width (w) to height (a) is about 1/34, thus Eq. (25) may be expanded in power of (w/a). It is also convenient to express the charge density in terms of the total charge in the ion cloud (Q_0). Thus Eq. (25) may be rewritten as

$$T=\left(4\frac{e}{M}\frac{Q_0}{a^2d}\right)^{-\frac{1}{2}}\left(1+\frac{1}{6}\frac{w^2}{a^2}\right), \tag{35}$$

where Q_0 is the total initial charge in the cloud, and w, a, and d are the thickness, height, and depth of the cloud (Fig. 25). Since the electron collector current is held constant as the magnetic field is varied any field dependence in Q_0 must arise from field dependent changes in either the ionization efficiency or the electron collection efficiency. There are good theoretical reasons for believing that the ionization and excitation cross sections are field independent. Since the bombarding electrons follow helical paths and since the diameter of the helices depend upon the magnetic field it might be expected that the ionization efficiency depends upon the magnetic field; however, since the electron spiralling frequency (cyclotron frequency) increases at the same rate as the helix diameter decreases the rectified electron path length is independent of field. Therefore the ionization efficiency is believed to be field independent. The bombarding electrons pass through a double grid system in going from the interaction region to the collection plate. Since the diameters of the electron helices are inversely proportional to the field, there is a small field dependence in the grid transmission factor and in the electron collection efficiency. A larger fraction of the electrons passes through the grid system at high fields than at low fields. The change in grid transmission has been estimated by assuming that the effective size of the grid wires is equal to the geometrical wire diameter plus one electron helix diameter, the helix diameter being computed from the transverse thermal velocity of the electrons. The grid transmission increases by about 0.067% as the field is varied from the low-field working point to the high-field working point. The correction to δ resulting from this effect is +0.02 Mc/sec.[41]

As a result of the transverse cycloidal motion the width of the cloud (w) depends slightly upon the magnetic field; at high fields the cloud width is less than at low fields. For the purpose of estimating a correction to δ it is assumed that w is inversely proportional to the field. With this assumption the explosion time (T) changes by about 0.0025% between the two working point fields. The corresponding correction to δ is −0.002 Mc/sec. The quenching function given by Eq. (19) was used for the evaluation of the above space charge corrections, the gas quenching processes were neglected in this calculation.

In estimating the correction to δ resulting from the field dependence of the transverse ion motion, the explosive motion of the ions is ignored. In this manner an upper bound to the correction is obtained. For the purpose of evaluating this correction, a quenching function has been developed which is based on the ion loss function given by Eq. (34). This quenching function is

$$\phi(\mu)=N_0\left\{\left(1-\frac{T_2}{\tau}-\frac{1}{\mu\tau}\right)(1-e^{-\mu T_1})+\frac{T_1}{\tau}e^{-\mu T_1}\right\}, \tag{36}$$

where N_0 is the number of metastable ions in the interaction region at the end of the gun pulse, μ is the quenching amplitude given by Eq. (6), T_1 is the length of the rf pulse, T_2 is the delay between the end of the gun pulse and the beginning of the rf pulse and the removal time τ is given by

$$\tau=Hd/\pi\rho_0 cw, \tag{37}$$

where H is the magnetic field, ρ_0 is the ion charge density, and d and w are the depth and width of the ion cloud respectively (Fig. 25). The field dependence of the removal time τ shifts the center of the resonance, as determined at the working point fields, by 0.21 Mc/sec.

[41] The principal effect on δ arising from the variation in collection efficiency is due to its effect on T [Eq. (35)]. The normalization procedure eliminates the other effects which the variation would have.

Pure Quadrupole Spectra of CH_3I and CF_3I Vapors*

FRED STERZER† AND YARDLEY BEERS
Physics Department, College of Engineering, New York University, University Heights, New York, New York
(Received April 27, 1955)

This paper first gives the theory of $\Delta J=0$, $\Delta F=\pm 1$ transitions of symmetric top molecules having a nucleus with a large quadrupole moment on the axis. The manner in which the gaseous state spectrum converges on the pure quadrupole sold state spectrum as J becomes infinite is discussed. Also is described an absorption experiment in which six quadrupole lines of CH_3I and one of CF_3I were observed in the region between 290 and 520 Mc/sec. The experiment yielded values of the quadrupole coupling constants of -1933.99 ± 0.25 Mc/sec and -2142.5 ± 1.8 Mc/sec respectively for CH_3I and CF_3I. These values are in agreement with previous values obtained elsewhere from rotational transitions.

INTRODUCTION

THIS paper[1] is concerned with the observation by an absorption method of the so-called "pure quadrupole" transitions in the vapors of symmetrical top molecules containing a nucleus with a large quadrupole interaction on the molecular symmetry axis. These are transitions arising from the reorientation of the nucleus with respect to the rotational angular momentum vector while the rotational quantum numbers J and K remain constant.

A more detailed description of these transitions may be given with reference to Fig. 1, which is an angular momentum vector diagram. **K** represents the quantized component of rotational angular momentum along the molecular axis. This precesses around the total rotational angular momentum vector **J**. The nuclear spin **I** is coupled to **J**, and these two vectors precess around their resultant **F**. In pure quadrupole transitions, the relative orientation of the nucleus and **J** changes such that the spin vector changes from **I** to **I'** with a new resultant angular momentum **F'**, as shown in Fig. 1, assuming a frame of reference fixed to **J**. At the same time the nuclear quadrupole moment changes in orientation with respect to the electric field of the molecule, involving a change in the energy, which is accompanied by the emission or absorption of radiation. These transitions, then may be seen to be those defined by the selection rules $\Delta J=0$, $\Delta K=0$, and $\Delta F=\pm 1$.

Quadrupole coupling constants may be determined very accurately from these observations since these are the principal parameters determining the frequencies.

The conventional method of determining quadrupole coupling constants of vapors is from observations of the hyperfine splitting of rotational transitions. Those occur at much higher frequencies and are usually much easier to detect. However, sometimes quadrupole coupling constants cannot be determined very accurately since they are related to hyperfine splittings which represent only a small fraction of the frequency. This situation is particularly true for high-J transitions.

Mainly because pure quadrupole spectra exist at frequencies below 1000 Mc/sec, they have low intensities and are hard to observe. However, the recent development of a spectrometer for these frequencies in this laboratory[2,3] has made possible the observation of these spectra in a few favorable cases.

While pure quadrupole transitions in vapors have not been studied generally, the analogous transitions in the solid state have been observed very widely since their discovery by Dehmelt and Kruger.[4] Those are transitions arising from the reorientation of a quadrupolar nucleus with respect to the gradient of a crystalline electric field. The spectra of solids are very simple as the electric field is invariant, while with vapors the spectra are complex since the effective value of the gradient of the electric field is different with each rotational state. Although they are also at low frequencies, the solid state spectra are easy to observe, partly because the available intensity is concentrated in a very few lines and partly because it is practical to work with samples containing many more molecules. Since the quadrupole coupling constant has slightly different numerical values for the solid and vapor, the observations made in the two states are not equivalent. Although the spectra in the vapor state are complex, as will be shown later, they are very simply related theoretically to the spectra obtained in the corresponding solids if the change in the magnitude of the constant is neglected.

While the frequencies of the pure quadrupole lines are determined by nuclear quadrupolar interactions, the intensities are fortunately determined by changes in the effective electric dipole moments of the molecules. If the intensities were determined by the interaction of the nuclear quadrupoles with electromagnetic radiation, they would be much too weak to be observed.

The mechanism for the interaction of the dipole moment **P** with the radiation may be seen by reference

* Supported by the Office of Naval Research, and by the United States Air Force, through the Office of Scientific Research of the Air Development Command.
† Present address, Radio Corporation of America, Harrison, New Jersey.
[1] A preliminary report of this work has been published: F. Sterzer and Y. Beers, Phys. Rev. **94**, 1410(A) (1954).
[2] Y. Beers and S. Weisbaum, Phys. Rev. **91**, 1014 (1953).
[3] Weisbaum, Beers, and Herrmann, J. Chem. Phys. **23**, 1601 (1955).
[4] H. G. Dehmelt and H. Kruger, Naturwiss, **37**, 111 (1950).

again to Fig. 1. **P** is parallel to **K** and has a component $\mathbf{P}_J$ which persists with respect to the precession of **K** about **J**. $\mathbf{P}_J$ in turn has a component $\mathbf{P}_F$ which persists with respect to the precession of **J** about **F**. When the transition takes place, this persistent component changes to a new value $\mathbf{P}_{F'}$ because of the change in the angle between **J** and the resultant angular momentum **F**. Thus there is a change in this persistant component, which is the effective value of the dipole moment.

This discussion indicates that the strongest lines occur with $K=J$ and that the intensities are zero when J and K are mutually perpendicular: that is, when $K=0$. Since a linear molecule in a ground vibrational state is equivalent to a symmetric top molecule with $K=0$, no transitions will be observable with such a molecule. The discussion also indicates that the strongest lines are obtained with I and J as nearly parallel as possible: that is, in the group of transitions $F=I+J-1$ to $F=I+J$. Another reason why this group of lines tends to have the greatest intensities is that for each given J and I the levels have the highest possible statistical weights. These qualitative conclusions are generally supported by quantum-mechanical calculations, but these indicate that there are a few transitions of other types which are relatively strong.

CALCULATION OF SPECTRA[6]

The interaction energy of a nuclear quadrupole moment Q located upon the axis of a symmetric top molecule as given by a first order quantum mechanical perturbation calculation is well known[6,7]

$$E_Q=\frac{eq_JQ}{2I(2I-1)J(2J-1)}\left[\tfrac{3}{4}C(C+1)-I(I+1)J(J+1)\right], \quad (1)$$

where F, J, and I are respectively the quantum numbers associated with total angular momentum, total rotational angular momentum, and nuclear spin. e is the charge of the electron. By definition,

$$C=F(F+1)-I(I+1)-J(J+1).$$

q_J is the second derivative of the electrostatic potential at the nucleus with respect to a linear coordinate measured along a space-fixed axis, as averaged over the state with the quantum numbers J, K, and $m_J=J$. This potential is the result of the other charged particles in the molecule. The value of q_J is given by

$$q_J=\frac{J}{2J+3}\left[\frac{3K^2}{J(J+1)}-1\right]q, \quad (2)$$

where q is the second derivative of the electrostatic potential at the nucleus with respect to a coordinate measured along the axis of symmetry of the molecule.

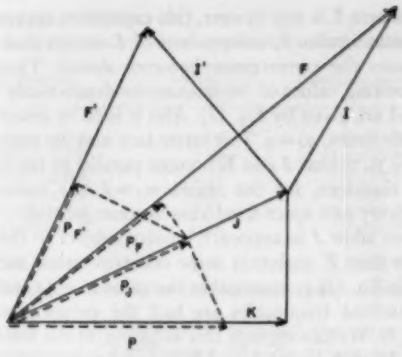

FIG. 1. Vector diagram of symmetric top molecule in frame of reference fixed to the total rotational angular momentum J.

If the quadrupole coupling constant eQq is expressed in frequency units, the frequency of a spectral line is obtained by expressing the energies of the two levels by Eqs. (1) and (2) and taking the difference. In general, the selection rules for electric dipole transitions are $\Delta J=0,\pm1$ (except $J=0\rightarrow0$), $\Delta K=0$, and $\Delta F=0,\pm1$, but in this paper by definition we are restricted to only those lines for which $\Delta J=0$ and $\Delta F=\pm1$.

To discuss the spectra resulting from these latter selection rules, it is convenient to arrange the lines into groups. The allowed values of F may be written as $F=J+M$. Here M is to be considered as a mathematical parameter which takes on a sequence of values in integral steps ranging from $-I$ to I. According to our selection rules, a transition occurs between some level labeled by K, J, and M-1 and a level labeled by K, J, and M. We define a group of lines by giving M some fixed value and allowing J and K to vary.

First left us consider the $K=J$ groups, which, as we have said, tend to have the greatest intensities. For low values of J, the frequencies vary rapidly with J, but as J becomes very large, they converge upon definite limits. These limits may be determined by writing down the expression for the frequency in terms of J, K, and M and passing to the limit when $K=J$ becomes infinite. The resulting expression is

$$f_{\text{lim}}=3eQq(2|M|-1)/4I(2I-1). \quad (3)$$

In considering groups for which $K\neq J$, we note that the only dependence of the frequency upon K is through the expression in the brackets in Eq. (2). If J and K approach infinity subject to the condition that $J-K$

[6] While preparing this manuscript we have learned that some calculations on these spectra have been made by T. Itoh of the University of Tokyo but most of the details of his calculations are unknown to us. See S. Kojima, Symposium on Molecular Physics at Nikko, 1953, p. 98.

[6] See for example, N. F. Ramsey, *Nuclear Moments* (John Wiley and Sons, Inc., New York, 1953).

[7] Gordy, Smith, and Trambarulo, *Microwave Spectroscopy* (John Wiley and Sons, Inc., New York, 1953).

$=L$, where L is any integer, this expression approaches a constant value 2, independent of L except that as L increases the convergence becomes slower. Therefore the limiting values of the frequencies depend only upon M and are given by Eq. (3). Also it is to be noted that in such limits, $q_J=q$. This latter fact may be explained by the facts that **J** and **K** become parallel in the limits, and, therefore, for the states $m_J=J$ the molecular-symmetry and space-fixed axes become parallel.

If we allow J to approach infinity subject to the condition that K maintain some constant value, we note that in Eq. (2) q_J approaches the value of $-\frac{1}{2}q$ and that the limiting frequencies are half the values given by Eq. (3). We can explain this behavior in the following way. In such limits **J** and **K** become perpendicular to one another while for the states $m_J=J$, **J** becomes parallel to the space-fixed axis. Therefore the molecular symmetry axis becomes perpendicular to the space-fixed axis. Hence the property of the electrostatic field which persists with respect to the precession of the various angular momentum vectors is the second spatial derivative of the potential with respect to a direction perpendicular to the symmetry axis. Since the potential must satisfy Laplace's equation and have axial symmetry, the second derivative with respect to a direction at right angles to the axis is equal to the second derivative along the axis multiplied by this factor $-\frac{1}{2}$.

Many of these remarks have been illustrated in Fig. 2 for the case when $I=5/2$, which pertains to the experimental work to be described later. The frequencies of the five $K=J$ groups of lines are plotted against J in the solid curves. Two of these approach the limit 0.30 eQq from below; two others approach the limit 0.15 eQq, one from above and one from below; and the fifth group approaches zero in the limit. The frequencies of one of the $K=J-1$ groups are plotted also with a dashed line, and this curve is seen to converge upon the same limit as the corresponding $K=J$ curve but somewhat more slowly.

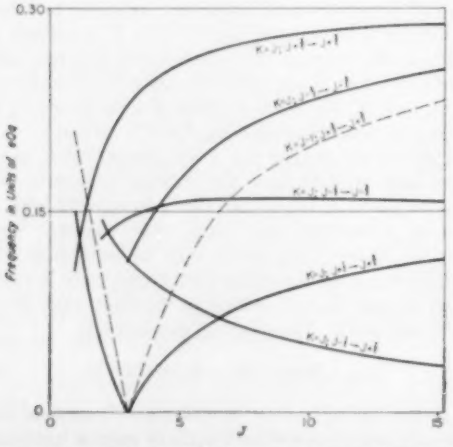

FIG. 2. Frequencies of principal groups of pure quadrupole lines of the vapor of a symmetric-top molecule with a nucleus having a spin $I=5/2$ plotted as a function of J.

RELATION OF THE SPECTRA OF THE GASEOUS AND SOLID STATES

The physical significance of the limiting frequencies for large J as given by Eq. (3) may be seen by considering pure quadrupole transitions in the solid state which result from the change in orientation of a nucleus of spin I with respect to a crystalline electric field with axial symmetry. The theory of these transitions has been given by Pound,[8] and he has shown that the frequencies are given by a formula identical with Eq. (3). Here, however, M must be redefined as the quantum number giving the projection of I along the crystalline axis, and Q must be redefined as the second derivative of the electrostatic potential with respect to a linear coordinate measured along the crystalline axis.

The quantum mechanical theories for both the gaseous and solid states are, of course, based upon the same classical theory. It is not surprising that they should give results which coincide when we recall the discussion of the correspondence principle in many textbooks on quantum theory in which it is shown that when the angular momentum becomes large many of the quantities associated with the motion take on values which approach the classical ones. In fact Feld and Lamb[9] have used this approach to evaluate quadrupole splittings of diatomic molecules which have been been observed to make magnetic dipole transitions in molecular beam experiments. Also in his paper, Pound[8] suggested that such an approach could be used for the crystalline state but he did not use it because in practical situations the theory must include provision for asymmetry of the field.

In the transitions which we are considering for the gaseous state the principal agent reacting with the radiation field is the electric dipole moment of the molecule while in the solid state the agent is the magnetic dipole moment of the nucleus. These facts may be reconciled by reference to Fig. 1 and by considering the case in which J becomes infinite while $J-K=L$. Then the vectors **J** and **K** become parallel, and their principal role is to define a direction which is the analog of the crystalline axis. At the same time the effective value of the dipole moment P_F approaches a constant value P, and, since it does not change in the transition, it becomes inactive. Then the role of principal agent must pass to the next higher available multipole which is the magnetic dipole moment of the nucleus.

HIGHER ORDER INTERACTIONS

The previous discussion is based upon a first-order perturbation theory which assumes that the quadrupole

[8] R. V. Pound, Phys. Rev. **79**, 685 (1950).
[9] B. T. Feld and W. E. Lamb, Phys. Rev. **67**, 15 (1945).

TABLE I. Measured pure quadrupole transitions of CH_3I and CF_3I.

$J=K$	Transition of F	Measured frequency Mc/sec	Calculated eqQ Mc/sec	Second order correction Mc/sec	Calculated intensity cm^{-1}
		(a) CH_3I			
1	3/2→5/2	292.5 ±0.4	−1934.6 ±2.3	2.29	2.8×10^{-10}
2	9/2→7/2	375.0 ±0.3	−1934.0 ±1.7	3.48	3.8×10^{-10}
3	11/2→9/2	444.76±0.10	−1934.0 ±0.4	1.55	7.9×10^{-10}
4	13/2→11/2	481.05±0.10	−1933.8 ±0.4	1.14	3.3×10^{-10}
5	15/2→13/2	503.05±0.15	−1934.4 ±0.6	0.85	2.5×10^{-10}
6	17/2→15/2	517.3 ±0.4	−1933.95±1.2	0.65	3.5×10^{-10}
		(b) CF_3I			
3	11/2→9/2	500.4 ±0.4	−2142.5 ±1.8	9.39	1.7×10^{-11}

splittings are very small compared to the rotational splittings. However, pure quadrupole spectra are only observable with very large quadrupole interactions and this assumption is not completely valid. Corrections must be made by an application of the second order theory due to Bardeen and Townes.[10] The calculations of these corrections is straight-forward and will not be given in detail. As can be seen in Table I, these corrections amounted to several Mc/sec in the experiments which will be described.

The sign of the quadrupole coupling constant may be determined from a study of the second-order corrections. These corrections, depending upon the square of this constant, are independent of the sign. However, in the first-order theory a reversal of sign inverts the order of the two levels. Thus whether the second-order correction is to be added or subtracted to the frequency calculated from first-order theory depends on the sign. Therefore, both the magnitude and sign of the constant may be determined if two or more lines are measured accurately.

While the observation of quadrupole spectra affords a method of obtaining accurate values of quadrupole coupling constants, it does not seem to be a favorable method under present conditions for investigating the magnetic dipole ($\mathbf{I}\cdot\mathbf{J}$) interaction. The theory of this interaction has been developed by Henderson and Van Vleck.[11] With our present techniques we have been able to observe only $K=J$ and $F=I+J\rightarrow F=I+J-1$ transitions. Except for $J=1$ and $J=2$, the change in frequency due to this interaction varies very slowly from line to line in this group. Furthermore, if we assume the interaction constants in CH_3I are not larger than those of NH_3, we cannot expect the total effect to be greater than about 50 kc/sec. Such an effect would be obscured by experimental errors.

CALCULATION OF INTENSITIES

The intensities can be calculated by methods given in standard texts.[7] However, a direct calculation required the evaluation of the matrix element of the molecular dipole moment P between the state JKF and the state JKF^*, where $F^*=F\pm1$, but we were unable to locate any explicit evaluation of these matrix elements. Therefore we devised a procedure employing standard reference material whereby these matrix elements were evaluated indirectly.

This procedure consisted of two principal steps. The first consisted of calculating the intensity of a fictitious transition connecting two states with the same J and K without any nuclear hyperfine splitting but occurring at the actual frequency of the spectral line. (An actual transition of this type, of course, would occur at zero frequency and therefore would have zero intensity.) This intensity could be calculated directly with matrix elements whose values are well known. The second step introduced the effect of hyperfine splitting. The intensity calculated in the first step was multiplied by the ratio of the relative intensity $I_{F\rightarrow F^*}$ of the transition from F to F^* to $\sum I$, the sum of all the intensities connecting all of the levels with the same J and K. These quantities have been calculated by several authors,[13-14] and numerical tables have been reprinted in several standard textbooks. By combining these two steps and evaluating all constants, the following final result was obtained:

$$\alpha=\frac{3.86\times10^{-14}(2J+1)K^2\nu^2BA^{\frac{1}{2}}\sigma g f_v P^2 I_{F\rightarrow F^*}}{T^{3/2}(\Delta\nu)_1 J(J+1)\sum I}$$

$$\times\exp\{-4.80\times10^{-8}[BJ(J+1)+(A-B)K^2]/T\}, \quad (4)$$

where α = absorption coefficient at center of line in cm^{-1}, ν = frequency in Mc/sec, B = rotational constant with respect to the principal axis of inertia parallel to the symmetry axis in Mc/sec, A = rotational constant with respect to a principal axis of inertia perpendicular to the symmetry axis in Mc/sec, f_v = fraction of the molecules in vibrational state in which the transitions take place, P = dipole moment in Debye units (1 Debye unit = 10^{-18} esu), T = temperature of the gas in degrees Kelvin, and $(\Delta\nu)_1$ = half-line width at half-maximum at 300°K and 1 mm Hg pressure expressed in Mc/sec.

[10] J. H. Bardeen and C. H. Townes, Phys. Rev. 73, 627 and 1204 (1948).
[11] R. S. Henderson and J. H. Van Vleck, Phys. Rev. 74, 106 (1948).
[13] R. De Kronig, Z. Physik. 31, 885 (1925); 33, 261 (1925).
[13] E. L. Hill, Proc. Natl. Acad. Sci. U. S. 15, 779 (1929).
[14] H. E. White and A. Y. Eliason, Phys. Rev. 44, 753 (1933).

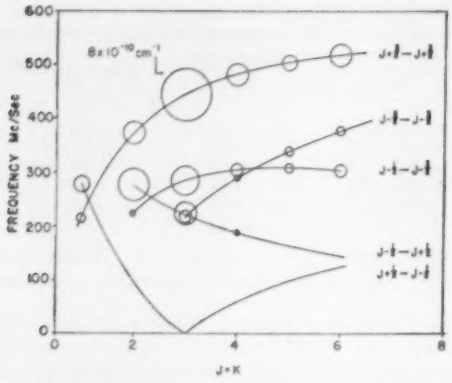

FIG. 3. The frequencies of the principal pure quadrupole lines of CH_3I plotted against J. The intensities at room temperature are indicated by the diameters of the circles.

The values of g and σ in Eq. (4) can be evaluated as follows[7]:

$$g = g_I g_K, \tag{5}$$

where

$$g_K = 1 \text{ for } K = 0, \quad g_K = 2 \text{ for } K \neq 0. \tag{6}$$

For molecules with a threefold axis of symmetry with one set of three identical "off-axis" nuclei having spin I, $\sigma = 3$, and

$$g_I = \tfrac{1}{3}[1 + 2/(2I+1)^2] \quad \text{for } K \text{ divisible by 3, including } K = 0,$$
$$g_I = \tfrac{1}{3}[1 - 1/(2I+1)^2] \quad \text{for } K \text{ not divisible by 3.} \tag{7}$$

To determine which pure quadrupole transitions are likely to be the most intense ones, we note from Eq. (4) that the absorption coefficient is proportional to the square of the frequency. In general, the highest frequency lines are the $F = I + J - 1 \rightarrow F = I + J$ transitions, as indicated in Fig. 2. These are the transitions which we predicted from the vector model to be the strongest. Also in accord with the vector model, we note that for a given J, the intensity is proportional to K^2, and therefore, even aside from considerations of frequency, generally the strongest lines for a given J will occur for $K = J$.

For low values of $K = J$ the intensity increases with J because of the predominant effect is the increasing statistical weights. For large values of $K = J$, this effect is outweighed by the decrease in the ratio $I_{F \rightarrow F'}/(\sum I)$ in Eq. (4), and the net effect is to cause the intensity decrease rapidly with J. A further decrease is caused by the Boltzmann factor.

In Fig. 3 are shown the frequencies of the principal pure quadrupole lines of methyl iodide, CH_3I, plotted against J. Centered upon the appropriate points are circles whose diameters are proportional to the intensities at room temperature, the strongest line being the $K = J = 3$, $F = 11/2 \rightarrow 9/2$ with an intensity of 8×10^{-10} cm^{-1}. Mainly because the ratio $I_{F \rightarrow F'}/(\sum I)$ is small compared to unity, these intensities are generally considerably smaller than those of rotational transitions in the same frequency region. (For example, the $5_5 \rightarrow 5_3$ line of HDO, which was observed in this laboratory[3] at 486.50 ± 0.15 Mc/sec, has a computed intensity of 1.5×10^{-8} cm^{-1}.) The smallness of this ratio is to be attributed to the fact that here we are dealing with "nondiagonal" $\Delta F = \pm 1$ transitions. On the other hand, it is to be noted in Fig. 1 that a few low-J lines not in the $F = J + I \rightarrow F = J + I - 1$ group have comparatively large intensities. This fact is explained by the existence of abnormally large values of this ratio.

EXPERIMENTAL TECHNIQUES

The experimental investigation employed a Stark-modulated spectroscope with a 3 in.$\times 1\frac{1}{2}$ in.$\times 20$ ft absorption cell. The details of the instrument itself are given elsewhere[2,3] and will not be given here. However, because of the very low intensities of the lines it was necessary to operate the equipment in an unorthodox fashion at the cost of resolution.

To obtain high sensitivity, it was necessary to operate at high-power levels, corresponding to rectified crystal detector currents of about 0.5 Ma. To avoid power saturation it was necessary to use high gas pressures such that the line width was comparable to the bandwidth of the rf system. Therefore it was not practical to operate at fixed pressure and sweep the frequency in the usual way. On the other hand, the high degree of absolute frequency stability obtainable at low frequencies made another procedure possible.

The system was tuned up near to the expected frequency of a line. The cell was filled with gas at such high pressure that the Stark modulation completely failed because of the absence of any resolution of the Stark components. The corresponding deflection of the output meter gave the zero. Then the pump was turned on, and the meter deflected as the pressure decreased. This deflection went through a maximum and ultimately decreased because of the onset power saturation. It was assumed this deflection decreased in the limit to the

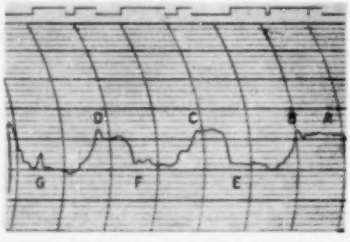

FIG. 4. Illustration of the pressure variation method. The zero is shown at A. With the gas at high pressure, the pump is turned on at B causing downward deflections followed by the beginning of a slow recovery. At E the pump is turned off and gas is admitted. The cycle is repeated at CF and again at DG. These data were obtained on the $K = J = 4$, $F = 13/2 \rightarrow 11/2$ line of CH_3I at 480.8 Mc/sec.

same value as that at high pressure, although it was impractical to verify this assumption since it would have required pumping such a long time that other factors could not be assumed to remain constant. This effect and its reproducibility is illustrated in Fig. 4. At A, the deflection is that pertaining to high pressure. Then at B, the pump was turned on, and the output deflected downward, and, after reaching a stationary value, tended to recover slowly to the value at A. After a few minutes at E, the pump was turned off and gas at high pressure was readmitted. The deflection returned to that at A. Then this cycle was repeated twice, C and D corresponded to B, and the F and G corresponded to E.

On a recording such as shown in Fig. 4 we observed either the maximum deflection, or, by the use of the pressure calibration which was introduced on to the record by the chronometer pen, we determined the deflection at some preassigned pressure. In either case some of the effects of noise were eliminated by smoothing. Having obtained either the maximum deflection or the deflection at some pressure at the original frequency, we repeated the process at other frequencies maintaining constant power. Then the line contour was obtained by plotting the deflections against frequency. Such a contour, obtained by the maximum deflection procedure, with the $K=J=3$, $F=11/2\rightarrow 9/2$ line of CH_3I is shown in Fig. 5. The validity of these procedures for obtaining the line frequency may be illustrated by the fact that four values, two obtained by maximum deflection and two by the constant pressure method, lay within 70 kc/sec of their average value while we have assigned a probable error of 100 kc/sec to our final value of this frequency.

Confirmation of the identities of two of the CH_3I lines was obtained by observing some of their Stark components. A few of the measurements were made by this same pressure variation technique, but a better method proved to be the one where at a constant frequency and pressure the Stark voltage was swept while the output was recorded as shown in Fig. 6. Because of a gradual change in stray pick-up, the base line has a large slope, but superimposed upon it are three small peaks corresponding to three of the components of the $K=J=3$, $F=11/2\rightarrow 9/2$ line of CH_3I. Small as these peaks were, they were reproducible, and their positions changed with frequency in a manner consistent with their calculated Stark coefficient.

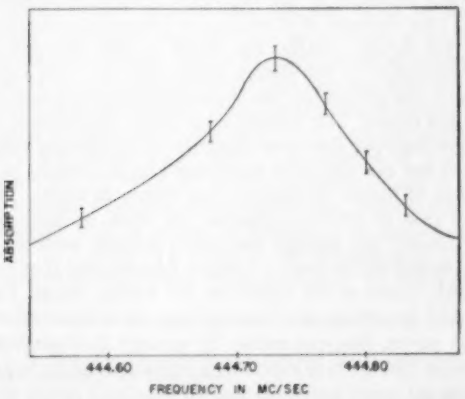

FIG. 5. Line contour computed from deflections obtained by pressure variation method as illustrated in Fig. 4. This is a plot of the $K=J=3$, $F=11/2\rightarrow 9/2$ line of CH_3I.

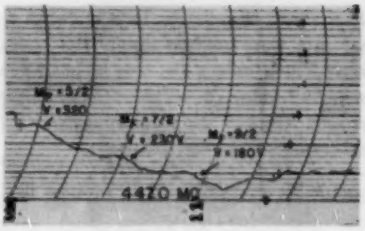

FIG. 6. Some Stark components of the $K=J=3$, $F=11/2\rightarrow 9/2$ line of CH_3I by sweeping Stark voltage at a constant frequency of 447.0 Mc/sec.

Whereas these techniques were developed for use in this low-frequency region, one of the present authors has also employed them to good advantage in observing the $J=0\rightarrow 1$ rotational spectrum of trifluoriodomethane in the S-band.[15]

EXPERIMENTAL RESULTS

Observations were made upon two molecules, CH_3I and CF_3I. The CF_3I was obtained from the reaction of trifluroacetic acid with silver iodide. After partial distillation, the sample was observed to have the correct boiling point for CF_3I.

Listed in Table I are the measured frequencies and the corresponding values of eQq for the six lines which were observed for CH_3I. The weighted average is -1933.99 ± 0.25 Mc/sec, which is in good agreement with the value of -1934 Mc/sec obtained by Gordy, Simmons, and Smith[16] from the observation of microwave rotational transitions.

The spectrum of CF_3I is very much weaker than that of CH_3I mainly because of the less favorable population of the same energy levels, and it was possible to observe only one line, whose frequency is also listed in Table I. The corresponding value of eqQ is -2142.4 ± 2 Mc/sec in good agreement with the value of -2143.8 ± 2 Mc/sec obtained from the experiment on the $J=0\rightarrow 1$ rotational transition mentioned above.[15] These values,

[15] F. Sterzer, J. Chem. Phys. 22, 2094 (1954); 23, 762 (E) (1955).

[16] Gordy, Simmons, and Smith, Phys. Rev. 74, 243 (1948).

however, are not completely independent, since the rotational data were used to supply the second-order correction.[16] These values are also in good agreement with the earlier value of -2150 Mc/sec obtained by Sheridan and Gordy[17] from observations of higher rotational transitions in the K-band.

[17] J. Sheridan and W. Gordy, J. Chem. Phys. **20**, 591 (1952).

ACKNOWLEDGMENTS

The authors wish to express their appreciation to the New Products Division of the Minnesota Mining and Manufacturing Company for advice on the preparation of CF_3I and for the gift of some trifluroacetic acid. Thanks are due also to Mr. William C. Meluch of the Chemistry Department, New York University, University Heights, for the actual preparation of CF_3I.

PHYSICAL REVIEW VOLUME 100, NUMBER 4 NOVEMBER 15, 1955

Threshold Law for Multiple Ionization

G. H. WANNIER
Bell Telephone Laboratories, Murray Nill, New Jersey
(Received July 22, 1955)

On the basis of evidence from single ionization, an approximate threshold law for multiple ionization is derived.

TWO years ago, in a paper on the threshold law for single ionization[1] a serious effort was made to take into account the three-body character of the ionization process. It is a result of that calculation that the interaction of the two electrons is a relatively minor effect as far as the power law is concerned, the reason being that the two slow electrons, upon emerging from the ion, keep to opposite sides of it. A simplified type of reasoning which neglects the interaction of the emerging electrons outside the reaction zone has thus semi-quantitative value. If it is applied to double ionization a quadratic dependence of the yield on the energy excess results. This was communicated to Fox, Hickam, and Kjeldaas and is mentioned in their paper.[2] It appears that these ideas are of some interest to the experimental workers in the field, and the derivation of this approximate threshold law will therefore be presented here.

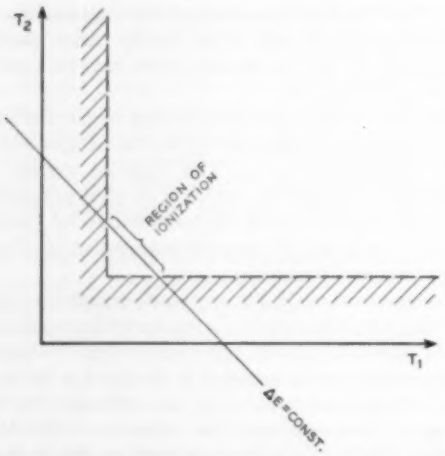

FIG. 1. Region in which ionization occurs in the case of single ionization. T_1 and T_2 are the kinetic energies of the two emerging electrons, and ΔE is the energy excess.

Draw around the ion a spherical surface (whose radius b is, as is usual in this type of argument, unspecified) and let the electrons emerge from the sphere with "switched off" mutual interaction. Each electron must then have a kinetic energy T greater than e^2/b in order to escape. In Fig. 1, the case of single ionization is illustrated. The kinetic energies T_1 and T_2 of the two emerging electrons are plotted on abscissa and ordinate. The region in which ionization occurs is limited by two straight lines parallel to the axes. Now a line of constant energy excess ΔE in this diagram is straight and of slope -1; the segment of it leading to ionization is marked in the figure. Clearly, the length of this segment is proportional to the energy excess and so is the yield unless the probability distribution has a strong anomaly in the corner. This possibility is highly improbable. If more than two electrons emerge from the reaction zone, then one can plot their respective kinetic energies in a space of higher dimensions, and reason as above. For the case of double ionization, we work in three dimensions: the straight line ΔE=constant becomes a plane and the segment a triangle. Its area, and thus the yield, varies as the square of the energy excess. For n-fold ionization, the threshold law thus becomes the nth power. One can reason by analogy to single ionization that the true exponent is probably slightly larger than n.

[1] G. H. Wannier, Phys. Rev. **90**, 817 (1953).

[2] Hickam, Fox, and Kjeldaas, Phys. Rev. **96**, 65 (1954).

Stark Fields from Ions in a Plasma*

A. A. BROYLES
The Rand Corporation, Santa Monica, California
(Received July 5, 1955)

A method is described here for determining the probability of obtaining a given electric field on an ion in a plasma. This quantity is essential for computing the broadening of spectral lines from neighboring ions and therefore for their contributions to the opacity. The Pines-Bohm method of separation into long-range Coulomb interactions has been employed. It is argued that the formulas give the line width for iron at one kilovolt and normal density to ±3%.

I. INTRODUCTION

IT is often essential to know the breadths and shapes of spectral lines to compute the absorption coefficients and Rosseland mean opacities[1] of substances at high temperatures. An understanding of the causes of line broadening also aids the interpretation of the spectra of the sun and stars.[1] Several experiments[1] have been performed for the purpose of observing line shapes under conditions that are controlled enough to check theoretical calculations.

Some of the causes of line broadening[2] are (1) the natural width due to the coupling of the atom with the electromagnetic field, (2) Doppler broadening, (3) electron collisions with the atom, and (4) the Stark effect shift of the atomic levels by fields from neighboring ions.

To compute the line broadening by Stark fields from neighboring ions, it is essential to know the probability $P(\epsilon)d\epsilon$ of finding a given electric field of magnitude ϵ at a radiating ion due to the displacement of neighboring ions. This paper is concerned with the calculation of this probability.

In the past, the Holtsmark distribution[3] has often been used for $P(\epsilon)$. It is obtained by neglecting the Boltzman factor and thus ignores the fact that one ion is hindered from approaching another by the electrostatic repulsion. This is a good approximation when the potential energy of two ions, exerting fields of the largest interesting magnitude on each other, is much less than the thermal energy kT. This potential energy must be at least as great as that for two ions separated by their average spacing. Thus, the Holtsmark approximation is good when the number of ions per cubic centimeter $n \ll 10^{11} T^3/Z^6$ with T in degrees or when $n \ll 10^{23} (kT)^3/Z^6$ with kT in electron volts, where Z is the number of electron charges on the ion. In some cases the upper limit on n may be lowered by as much as a factor 10^{-1}, since the wings of the spectral lines are generated by large Stark displacements of the levels of the ions, and, therefore, by close collisions between ions. These conditions are well satisfied in the reversal layers of normal stars and in laboratory experiments that are known by the author to have been performed to observe line broadening. They are not satisfied, however, in stellar interiors. Here the radiation transport may be computed with the aid of the Rosseland mean opacity which will, in some cases, depend strongly on the widths of the lines. For these cases, then, the Boltzmann factor must be taken into account.

The problem may be considerably simplified by employing the following model. The electrons are assumed to be either attached to an ion or free to move through the plasma. Since the free electrons move so much more rapidly than the ions, they may be treated as a smeared negative charge. For simplicity this smeared charge will be assumed uniform in density and to be undistorted by displacements of the ions. The ions will all be taken to have the same charge.

With this model, a certain set of units appears to be natural. For the unit of length, it is convenient to take the "ion sphere radius." This is the radius of a sphere that, on the average, contains exactly one ion. The unit of field strength then will be taken to be the magnitude of the field exerted on one ion by another ion a unit distance away, and the unit of energy will be the difference in potential energy of two ions when separated by unit distance and when separated by infinite distance. This is equivalent to using the charge on the ions as the unit charge.

Mayer[2] has made two approximations to $P(\epsilon)$ that take account of the Boltzmann factor. The first is useful when θ is much less than one, where θ is the temperature measured in the above energy units. In this case, the ions tend to remain at their equilibrium positions at the center of their respective ion spheres and to feel a restoring force proportional to their displacements. Thus, they move like three-dimensional simple harmonic oscillators (SHO). For very large fields and large θ's, the approximation must break down since an ion will get out of its own ion sphere.

Mayer's second approximation is for large fields and takes account of the fact that the Boltzmann factor and the available volume in configuration space make it more probable to obtain large fields by the close

* This work was sponsored by the U. S. Atomic Energy Commission.

[1] L. H. Aller, *The Atmospheres of the Sun and Stars* (The Ronald Press Company, New York, 1953).

[2] H. Mayer, Los Alamos Scientific Laboratory Report LA-647, 1947 (unpublished).

[3] J. Holtsmark, Ann. Physik **58**, 577 (1919); Physik Z. **20**, 162 (1919); Physik Z. **25**, 73 (1924); S. Chandrasekhar and J. von Neumann, Astrophys. J. **95**, 489 (1942).

approach of a single nearest neighbor than by the cooperative action of several nearby ions. Thus, the contributions to the field at the radiating ion by other than the nearest neighbor are neglected. It is not clear, however, how to normalize this approximation since $P(\epsilon)$ is not represented well in the neighborhood of its maximum.

To determine $P(\epsilon)$ over the entire range of ϵ and to check the normalization used by H. Mayer in his nearest neighbor approximation, it is necessary to consider other methods of treating a plasma than those mentioned above. Another simple approximation may be obtained by visualizing the high-energy ions as being free particles in a box. This gas is made up of ions having sufficient energy to make an approach to another ion close enough to exert the required field on it. The Holtsmark distribution can then be applied to this reduced number of ions to obtain $P(\epsilon)$. The level of the bottom of the box, however, still remains as an undetermined constant and the approximation is only good for large fields.

The work of Pines and Bohm[4] has suggested a very effective way of treating the ions in a plasma. They show how to separate the Coulomb forces into long and short range components and to convert the system of ions in an electron sea into a system of particles interacting with short range forces and a set of waves whose amplitudes become independent coordinates. The wave part of the system is quite easy to treat. The particle part is much more difficult and so formulas have been obtained that give upper and lower limits to $P(\epsilon)$.

All the approximations have been compared for the case of iron at normal density (7.83 g/cm^3) and one kilovolt temperature ($\theta=0.186$) and all but one have been compared at infinite temperature where the Holtsmark distribution gives the correct values of $P(\epsilon)$. An ionic charge of 23 electron charges has been assumed. To compute the Rosseland mean opacity, it is essential to know how far the tail is from the line center when its absorption is equal to the continuous background. For the important lines in iron at one kilovolt, this occurs when $P(\epsilon)$ has values of the order of 10^{-6}. Values of $P(\epsilon)$ smaller than this are of little interest.

The accurate determination of the probability, $Q(\epsilon)d\epsilon$, of finding an electric field ϵ at the radiating ion would require an evaluation of the expression,

$$Q(\epsilon)=\frac{\int\cdots\int \exp\left(-\frac{V}{\theta}\right)\delta\left(\epsilon+\sum_i \frac{\mathbf{r}_i}{r_i^3}\right)d\mathbf{r}_1\cdots d\mathbf{r}_N}{\int\cdots\int \exp\left(-\frac{V}{\theta}\right)d\mathbf{r}_1\cdots d\mathbf{r}_N}, \quad (1)$$

where θ is the temperature in energy units, V the potential energy of the system, N the number of ions, and $\mathbf{r}_i$ the position vector of the ith ion. The numerator of Q is merely the sum over all configurations having fields in the range $d\epsilon$ around ϵ as selected by the Dirac delta function. If N is very large, the limit of this integral may be taken when N and the volume of the system increase without limit in such a way that the number of particles per unit volume remains constant. The radiating ion is placed at the origin of coordinates since a shift in position of this ion will merely give the same configurations of the other ions with the same probabilities (except for surface effects).

It is convenient to expand the delta function in terms of plane waves so that

$$Q(\epsilon)=\frac{1}{(2\pi)^3}\int T(\mathbf{l})\exp(i\epsilon\cdot\mathbf{l})d\mathbf{l},$$

$$T(\mathbf{l})=\frac{\int\cdots\int \exp\left(-\frac{V}{\theta}+i\mathbf{l}\cdot\sum_i \frac{\mathbf{r}_i}{r_i^3}\right)d\mathbf{r}_1\cdots d\mathbf{r}_N}{\int\cdots\int \exp\left(-\frac{V}{\theta}\right)d\mathbf{r}_1\cdots d\mathbf{r}_N}. \quad (2)$$

Since $T(\mathbf{l})$ is a function of the magnitude of $\mathbf{l}$ alone, the probability density of finding a field of a given magnitude ϵ is

$$P(\epsilon)=4\pi\epsilon^2Q(\epsilon)=\frac{2\epsilon}{\pi}\int_0^\infty l\sin(l\epsilon)T(\mathbf{l})dl. \quad (3)$$

II. SHO AND NEAREST NEIGHBOR APPROXIMATIONS

For Mayer's[2] SHO approximation, the radiating ion will be attracted toward the center of its ion sphere by the negative smeared electron charge. If r is its displacement from this center, its potential energy is $\frac{1}{2}r^2$, and the electric field on it has magnitude r. For this case, then

$$P(\epsilon)=(2/\pi)^{\frac{1}{2}}(\epsilon^2/\theta^{\frac{1}{2}})\exp(-\epsilon^2/2\theta). \quad (4)$$

For large fields, Mayer makes the assumption that only the nearest neighbor to the ion at the origin makes a contribution to the field there. Thus he is able to relate $P(\epsilon)$ to the probability density,[5] $4\pi r^2ng(r)$, that an ion will lie a certain distance from the origin. The function[5] $g(r)$ is the "radial distribution function." Instead of this probability, the probability of the *nearest neighbor* lying at distance r should be used but the difference is small for large fields. When the nearest neighbor is near the origin, $d\epsilon=-[(2/r^3)+1]dr$. Thus, we find that

$$P(\epsilon)=4\pi r^2ng\Big/\left(\frac{2}{r^3}+1\right), \quad \epsilon=r^{-2}-r. \quad (5)$$

The first term in ϵ comes from the interaction between the ions and the second from the shielding of the elec-

[4] D. Pines and D. Bohm, Phys. Rev. **85**, 338 (1952).

[5] Hirshfelder, Curtis, and Bird, *Molecular Theory of Gases and Liquids* (John Wiley and Sons, Inc., New York, 1954), pp. 84, 321.

trons. For a system of particles interacting in pairs with short range forces, g may be approximated[5] by $\exp\{-u(r)/\theta\}$ where u is the potential energy between a pair of particles and must go to zero more rapidly than r^{-2} for large r. Because of the shielding effect of the plasma, such a short range interaction appears to be a possibility and the separation of the Coulomb interactions into short and long range components demonstrates that this is essentially the case. For close approach of the two ions u may be approximated by $r^{-1}+\frac{1}{2}r^2+$constant. Since u is not known over its entire range, it is not clear what the constant should be. Since it enters an exponent, $P(\epsilon)$ is quite sensitive to its value. Mayer chose the value $-\frac{3}{2}$ and obtained the formula:

$$P(\epsilon)=[3r^2/(2r^{-3}+1)]\exp[-(r^{-1}+\tfrac{1}{2}r^2-\tfrac{3}{2})/\theta], \qquad \epsilon=r^{-2}-r. \tag{6}$$

The constant $-\frac{3}{2}$ corresponds to including in u the interaction of the nearest neighbor with the central ion and with the electrons in a sphere of unit radius around the origin and with nothing else.

The values of $P(\epsilon)$ given by Eq. (6) are shown in Fig. 1 for iron at normal density and temperatures of one kilovolt and infinity.

III. MODIFIED HOLTSMARK DISTRIBUTION

It is possible to get another simple approximation to $P(\epsilon)$ at large ϵ by modifying the Holtsmark distribution to take account of the Boltzmann factor. Most of the ions moving around in a plasma may well be quite confined by the action of other charges on them. However, there must be a few ions with very high energies that move around quite freely and that only notice the presence of other charges when they approach quite close to another ion. It is also true that only these ions have sufficient energy to approach a second ion closely enough to exert a large field on it. Thus $P(\epsilon)$ may be calculated for large fields from an equivalent system of a reduced number of ions in a box whose bottom has some average potential energy $\bar{V}$. We may again place the radiating ion at the origin and then the potential energy of an ion on close approach will be $r^{-1}+\frac{1}{2}r^2-\bar{V}$. Thus only those ions with energy greater than

$$E=r_0^{-1}+\tfrac{1}{2}r_0^2-\bar{V}, \tag{7}$$

where $\epsilon=r_0^{-2}-r_0$, will contribute to $P(\epsilon)$.

The number of ions per unit volume in the Holtsmark distribution must be reduced by the fraction $S(E/\theta)$ given by the Maxwell Boltzmann law:

$$S(E/\theta)=\frac{4}{\sqrt{\pi}}\int_{\sqrt{(E/\theta)}}^{\infty}\exp(-x^2)x^2dx. \tag{8}$$

The density of particles has been taken into account by the unit of length mentioned in Sec. I. This unit is the ion sphere radius and must be increased by the factor $S^{-\frac{1}{3}}$ when the number of ions is reduced. Thus the field strength unit is proportional to $S^{\frac{1}{3}}$, and $P(\epsilon)$ is proportional to $S^{-\frac{1}{3}}$. If $H(\epsilon)$ is the Holtsmark distribution, the modified distribution is

$$P(\epsilon)\approx H(\epsilon/S^{\frac{1}{3}})/S^{\frac{1}{3}}. \tag{9}$$

As in the case of Mayer's nearest-neighbor approximation, it is not clear what value should be assigned to $\bar{V}$. The points on Fig. 1 correspond to $\bar{V}=\frac{3}{2}$.

IV. SEPARATION INTO SHORT AND LONG RANGE INTERACTIONS

Pines and Bohm[4] have suggested a way of splitting the electrostatic forces into long and short range terms and have found a way of treating the long range interactions quite accurately. A similar procedure will be adopted here.

Suppose we have a plasma of essentially infinite extent, and suppose we consider that portion which lies within a large cube containing N ions. We shall limit this system to one having an electrostatically equipotential boundary. This means that the average field on a test charge as it moves across the cube from one side to the other is zero. The potential for such a system that is electrically neutral is

$$\Phi=4\pi\sum_{\mathbf{k}}{}'\sum_{j}\frac{e^{i\mathbf{k}\cdot(\mathbf{r}-\mathbf{r}_j)}}{k^2}, \tag{10}$$

and the charge density is

$$\rho=\sum_{\mathbf{k}}{}'\rho_{\mathbf{k}}e^{i\mathbf{k}\cdot\mathbf{r}}, \quad \rho_{\mathbf{k}}=\sum_{j}e^{-i\mathbf{k}\cdot\mathbf{r}_j}, \tag{11}$$

where unit volume is taken for the Fourier expansion. These quantities give a potential energy to the system of

$$V=2\pi\sum_{\mathbf{k}}{}'\frac{\rho_{\mathbf{k}}\rho_{\mathbf{k}}^*}{k^2}. \tag{12}$$

The primes indicate the omission of $k=0$ from the sums.[4]

The separation into short and long range parts is accomplished by splitting V into two sums, one over k's larger than k_c, the other over k's less than k_c. The sum over large k's may then be evaluated to give the short-range potential energy,

$$V_{s.r.}=\sum_{i<j}v(R_{ij}), \tag{13}$$

where

$$\mathbf{R}_{ij}=k_c(\mathbf{r}_i-\mathbf{r}_j),$$

$$v(R)=\frac{k_c}{R}\left[1-\frac{2}{\pi}\,\mathrm{Si}(R)\right],$$

$\mathrm{Si}(x)$ being the sine integral.

The electric field at the origin is the negative gradient

of the potential energy with respect to the coordinates of the particle at the origin. Then

$$\sum_i \frac{\mathbf{r}_i}{r_i^3} = 4\pi i \sum_{|\mathbf{k}|<k_c} \frac{\mathbf{k}}{k^2}\rho_{\mathbf{k}} - k_c \sum_{j=1}^{n} \frac{\mathbf{R}_j}{R_j}\frac{dv}{dR_j}, \tag{14}$$

$$\mathbf{R}_j = k_c \mathbf{r}_j.$$

The essential quantities for $Q(\epsilon)$ (Eq. (2)) have now been expressed in terms of the two sets of coordinates made up of the $\rho_{\mathbf{k}}$'s and $\mathbf{r}_j$'s. An approximation to the Jacobian of the transformation from one set of coordinates to the other may be obtained in the following manner. From Eq. (11), it is clear that $\rho_{\mathbf{k}}$ may be thought of as a sum of two dimensional unit vectors at various orientations. While the $\mathbf{r}_j$'s are ranging through the volume of the system for the integrations in $Q(\epsilon)$, the $\rho_{\mathbf{k}}$'s should be points in the complex plane whose density is essentially that given by the solution of a two dimensional random walk problem. Thus, if k_c is chosen so that the number of k's less than k_c is equal to the number of $\mathbf{r}_i$'s, we may write approximately that[6] (to within a constant factor)

$$d\mathbf{r}_1 \cdots d\mathbf{r}_n \rightarrow \prod_{|\mathbf{k}|<k_c} \exp(-\rho_{\mathbf{k}}\rho_{\mathbf{k}}^*/2n) dx_{\mathbf{k}} dy_{\mathbf{k}}, \tag{15}$$

where $\rho_{\mathbf{k}} = x_{\mathbf{k}} + iy_{\mathbf{k}}$ and n is the number of ions per unit volume.

Unfortunately, the expressions for $\sum_i(\mathbf{r}_i/r_i^3)$ and V [Eqs. (12), (13), and (14)] contain both $\mathbf{r}_j$'s and $\rho_{\mathbf{k}}$'s so that we need both sets of coordinates. Thus the number of coordinates is too large. Actually, however, the number of $\mathbf{r}_j$'s required is small since they appear only in short-range terms and only those particles near to the origin can contribute to the field there. To circumvent this difficulty, we shall alter the system in an unessential way by placing around the origin an impenetrable barrier in the form of a sphere containing a large number N of ions but a very small number compared to the total number of ions in the system. The number of ions inside the impenetrable sphere will be determined so that the average number per unit volume is equal to that for the whole system. This device will serve to keep the number of coordinates from becoming excessive.

The electrostatic field and potential energy are now separated into short and long range terms. The long range terms depend only on the $\rho_{\mathbf{k}}$'s and the short range terms on the $\mathbf{r}_j$'s. With these approximations, the transform $T(\mathbf{l})$ [Eq. (2)] is factorable into a T_p for particles and a T_w for waves. For T_w there still remains a restriction on the $\rho_{\mathbf{k}}$'s arising from the fact that ρ is a real quantity. Thus

$$\rho_{-\mathbf{k}} = \rho_{\mathbf{k}}^*. \tag{16}$$

For this reason we shall take only those $\rho_{\mathbf{k}}$'s to be independent that belong to $\mathbf{k}$'s having a positive Z component and indicate a sum or product over these $\mathbf{k}$'s by a plus sign superscript. This transform can now be reduced to

$$T_w = \prod_{|\mathbf{k}|<k_c}^{+} \frac{\int_{-\infty}^{\infty}\int_{-\infty}^{\infty} \exp\left\{\left[-\frac{4\pi}{\theta}\frac{1}{k^2}-\frac{1}{n}\right](x_{\mathbf{k}}^2+y_{\mathbf{k}}^2)+8\pi i\frac{\mathbf{l}\cdot\mathbf{k}}{k^2}y_{\mathbf{k}}\right\} dx_{\mathbf{k}}dy_{\mathbf{k}}}{\int_{-\infty}^{\infty}\int_{-\infty}^{\infty} \exp\left\{\left[-\frac{4\pi}{\theta}\frac{1}{k^2}-\frac{1}{n}\right](x_{\mathbf{k}}^2+y_{\mathbf{k}}^2)\right\} dx_{\mathbf{k}}dy_{\mathbf{k}}} = \exp(-\gamma l^2), \tag{17}$$

where

$$\gamma = \frac{k_c}{\pi}[1-(3/k_c^2\theta)^{\frac{1}{2}}\tan^{-1}(k_c^2\theta/3)^{\frac{1}{2}}].$$

In the units mentioned in Sec. I, the number of ions per unit volume n is equal to $(4\pi/3)^{-1}$ and $k_c^3 = 9\pi/2$. This k_c was determined so that the number of wave degrees of freedom equals the number of particles in the whole system. For the particles, we obtain

$$T_p = \frac{\int\cdots\int \exp\left\{-\sum_{i<j}[v(R_{ij})/\theta] - ik_c\sum_{j=1}^{n}\frac{\mathbf{R}_j\cdot\mathbf{l}}{R_j}\frac{dv}{dR_j}\right\} d\mathbf{R}_1\cdots d\mathbf{R}_N}{\int\cdots\int \exp\{-\sum_{i<j} v(R_{ij})/\theta\} d\mathbf{R}_1\cdots d\mathbf{R}_N}. \tag{18}$$

The approximations up to this point do not appear to be particularly drastic. The formulas above might be expected to give a reasonably good approximation to $P(\epsilon)$. In Eq. (18), however, we run into the age-old difficulty of noncentral interactions. These interactions have been reduced by the above approximations but are not eliminated. Monte Carlo techniques would probably do a good job of evaluating these integrals.

[6] This is the same transformation obtained by Pines and Bohm in their Appendix I.

To reduce them by analytic methods, it is necessary to replace the potential energy by a function involving only central interactions. Since the particle nature seems so important at this stage, approximations similar to that used by Hartree to treat the atom do not appear promising. One thing that can be done is simply to neglect interactions that do not involve the central particle. Another possibility is to neglect short-range contributions to the potential energy and electric field at the origin due to all ions except the ion at the origin and its nearest neighbor.

V. SHORT-RANGE CENTRAL-INTERACTIONS APPROXIMATION

If we neglect interactions that do not involve the central ion, the multiple integrals in T_p [Eq. (18)] then reduce to a product of integrals:

$$T_p=\left[\frac{\int \exp\left\{-\frac{v(R)}{\theta}-ik_e\frac{\mathbf{R}\cdot\mathbf{l}}{R}\frac{dv}{dR}\right\}d\mathbf{R}}{\int \exp\left\{-\frac{v(R)}{\theta}\right\}d\mathbf{R}}\right]^N. \quad (19)$$

The limit of T_p, as N and the volume go to infinity so that their ratio is n, is

$$T_p=\lim\left[\frac{\text{vol}-\int\left\{1-\exp\left[-\frac{v}{\theta}-ik_e\frac{\mathbf{R}\cdot\mathbf{l}}{R}\frac{dv}{dR}\right]\right\}d\mathbf{R}}{\text{vol}-\int\left\{1-\exp\left[-\frac{v}{\theta}\right]\right\}d\mathbf{R}}\right]^N$$

$$=\exp\left\{-\frac{4\pi n}{k_e^3}I(l,\theta)\right\}, \quad (20)$$

$$I(l,\theta)=\int_0^\infty\left\{1-\left[\sin\left(lk_e\frac{dv}{dR}\right)\Big/\left(lk_e\frac{dv}{dR}\right)\right]\right\}\times\exp(-v/\theta)R^2dR.$$

Combining Eqs. (20), (17), and (3) gives

$$P(\epsilon)=\frac{2\epsilon}{\pi}\int_0^\infty l\sin(l\epsilon)\exp\left\{-\gamma l^2-\frac{3}{k_e^3}I(l,\theta)\right\}dl. \quad (21)$$

These formulas have been evaluated to obtain $P(\epsilon)$ for the case of iron at a temperature of one kilovolt and normal density (see Fig. 1).

VI. SHORT-RANGE NEAREST NEIGHBOR APPROXIMATION

If we neglect all terms in the exponent in the integrand of T_p [Eq. (18)] that involve particles other than the one at the origin and its nearest neighbor we obtain

$$T_p\approx\frac{\int_{|\mathbf{R}_1|>0}\int_{|\mathbf{R}_2|>|\mathbf{R}_1|}\cdots\int_{|\mathbf{R}_N|>|\mathbf{R}_1|}\exp\left\{-v(R_1)/\theta-ik_e\mathbf{l}\cdot\frac{\mathbf{R}_1}{R_1}\frac{dv}{dR_1}\right\}d\mathbf{R}_N\cdots d\mathbf{R}_1}{\int_{|\mathbf{R}_1|>0}\int_{|\mathbf{R}_2|>|\mathbf{R}_1|}\cdots\int_{|\mathbf{R}_N|>|\mathbf{R}_1|}\exp\{-v(R_1)/\theta\}d\mathbf{R}_N\cdots d\mathbf{R}_1}. \quad (22)$$

Taking the limit of T_p, as N and the volume go to infinity, and substituting this into Eq. (17) and Eq. (3) leaves

$$P(\epsilon)\approx\epsilon J/[2k_e(\pi\gamma)^{\frac{1}{2}}K],$$

$$J=\int_0^\infty(R^2/v')\exp\{-(R/k_e)^3-(v/\theta)\}\times\{\exp[-(k_ev'-\epsilon)^2/4\gamma] \quad (23)$$
$$-\exp[-(k_ev'+\epsilon)^2/4\gamma]\}dR,$$

$$K=\int_0^\infty R^2\exp[-(R/k_e)^3-(v/\theta)]dR.$$

Both J and K may be approximated by the method of steepest descents.

For evaluating J [Eq. (23)] at large values of ϵ, only the variation in v' in the exponent of the second term of the integrand is significant. The first term is negligible and the other quantities may be replaced by their values at $R=R_1$ where R_1 is that value of R that makes $k_ev'+\epsilon=0$. Also v' may be replaced by $v_1'+v_1''(R-R_1)$ in the exponent. These approximations together with the steepest descents approximation for K give

$$P(\epsilon)\approx[(-\epsilon R_1^2/(k_e^2R_0^2v_1'v_1'')](g_0''/2\pi)^{\frac{1}{2}}\times\exp\{-[(R_1^3-R_0^3)/k_e^3]-[(v_1-v_0)/\theta]\}, \quad (24)$$
$$g_0''=(6R_0/k_e^3)+(v_0''/\theta)+(2/R_0^2),$$

where R_0 is the location of the saddle point in the integrand of K and the subscripts 1 and 0 indicate arguments of R_1 and R_0.

For small values of ϵ, the rapidly changing part of the integrand of J is the same as the integrand of K. If R_0 is the location of the saddle point of the integrand of K, then

$$P(\epsilon)\approx[\epsilon/(2k_ev_0'\sqrt{\pi\gamma})]\{\exp[-(k_ev_0'-\epsilon)^2/4\gamma]-\exp[-(k_ev_0'+\epsilon)^2/4\gamma]\}. \quad (25)$$

Comparisons between these approximations and the accurate formulas of Eq. (23) are made in Table I.

TABLE I. Comparison of approximations to the short-range nearest neighbor (SRNN) formula with accurate evaluation.

	ϵ	0.3	0.5	1	1.5	2	3	4	5	6	8	10
$\theta=1$ kev	Accurate SRNN Eq. (23)	0.63	1.13	0.66	0.147	0.043	0.0056	0.00082	0.000155	0.0000375	0.0000036	
	Large ϵ approximation Eq. (24)				0.064	0.024	0.0037	0.00067	0.000144	0.0000342	0.0000032	
	Small ϵ approximation Eq. (25)	0.78	1.36	0.61	0.034							
$\theta=\infty$	Accurate SRNN Eq. (23)		0.066	0.20	0.33	0.36	0.225	0.087	0.032	0.018	0.0086	0.0046
	Large ϵ approximation Eq. (24)							0.030	0.019	0.013	0.0068	0.0040
	Small ϵ approximation Eq. (25)		0.084	0.27	0.42	0.45	0.227	0.050				

VII. COMPARISON WITH HOLTSMARK

The Holtsmark distribution is the accurate determination of $P(\epsilon)$ corresponding to the exact evaluation of Eq. (1) for $Q(\epsilon)$ for infinite temperature. For this reason, it is particularly interesting to compare the approximations mentioned above at infinite temperature with the Holtsmark distribution.

Even at infinite temperatures, the "short-range central interaction" approximation [Sec. V, Eq. (21)] requires considerable numerical work. However, it can be shown that it reduces to the Holtsmark distribution in the limit of large fields. In this limit, close approaches of the ions are important and v may be approximated by $1/r$. Setting θ equal to infinity and neglecting γ, we obtain

$$I(l,\infty)=l^{\frac{1}{3}}k_c^{\frac{2}{3}}2(2\pi)^{\frac{1}{2}}/15,$$

$$P(\epsilon)=\frac{2}{\pi\epsilon}\int_0^\infty x\sin x\exp\{-(2(2\pi)^{\frac{1}{2}}/5)(x/\epsilon)^{\frac{1}{2}}\}dx. \tag{26}$$

This is the formula for the Holtsmark distribution as given by Chanrdasekar and von Neumann[3] except for the small difference between $2(2\pi)^{\frac{1}{2}}/5$ and unity arising from a slight difference in units for ϵ. This is actually a convenient derivation of the Holtsmark distribution.

Curves are shown in Figs. 1 and 2 for the "short-range nearest neighbor" (SRNN) approximation [Sec. VI, Eq. (23)] at infinite temperature and for the "nearest neighbor" (NN) approximation [Sec. II, Eq. (6)]. The latter approximation does not have long-range and short-range separation for forces and potential energy.

The "modified Holtsmark" approximation goes over into the Holtsmark distribution at infinite temperature.

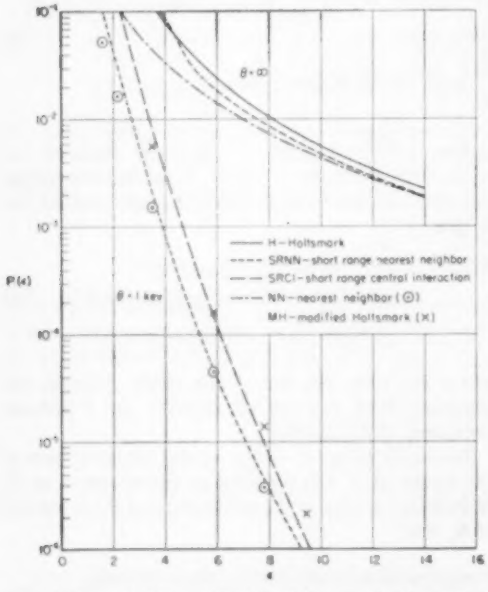

FIG. 1. The probability of obtaining field strengths of magnitude ϵ for $\theta=\infty$ and $\theta=1$ kev for iron at normal density for large values of ϵ. Only approximations good in this region are shown. The correct curve at $\theta=1$ kev is believed to lie between the SRNN and SRCI curves.

VIII. DISCUSSION AND CONCLUSIONS

The two approximations involving separation of the Coulomb interaction into short- and long-range components must bracket the correct evaluation of $P(\epsilon)$. The short-range central-interaction approximation (SRCI) in Sec. V gives $P(\epsilon)$ correctly for a system of particles that has no short range interactions between particles other than those involving the ion at the origin. Thus, the Boltzmann factor is too large when two or more particles are near the origin, and the probability of large fields is higher for this system than for the true plasma.

The short-range nearest neighbor approximation (SRNN) (Sec. VI) replaces the plasma by a system where the short-range forces act only between the nearest neighbor and the central ion. Since the short-range contributions to the field at the origin due to other than the nearest neighbor are neglected, the probabilities of large fields should be smaller than that for the true plasma. This is confirmed for the case of infinite temperatures since the SRNN curve in Fig. 1 lies below the Holtsmark for large ϵ.

The nearest neighbor approximation made by Mayer[2]

(Sec. II) is a remarkably good one in view of the uncertainty in the constant appearing in the potential energy. The large field approximation [Eq. (24)] to the SRNN formulas is very close to the NN formula [Eq. (6)] when v is set equal to k_e/R. Mayer's formula is given further justification from the fact that the short-range potential $v(R)$ [Eq. (13)] can be expanded for small R to give

$$v=(1/r)-1.54\ldots+\tfrac{1}{2}r^2+\cdots. \tag{27}$$

The constant 1.54 is very close to the $\frac{3}{2}$ used in Eq. (6) for the NN approximation.

The modified Holtsmark (MH) approximation provides a simple means of computing $P(\epsilon)$ for large fields that is probably good to roughly a factor of two in the parameter ranges considered here. However, it does not seem to be as accurate as the NN approximation [Eq. (6)] and is somewhat more difficult to compute. Nevertheless, since the approximations used in it are different from those used in the (NN) approximation, it can serve as a check on those formulas.

The widths of the spectral lines from the broadening due to electric fields of other ions is bracketed by the SRNN [Eq. (24)] and SRCI [Eq. (21)] approximations so that the widths are determined to $\pm 3\%$ for iron at one kilovolt and normal density. Under these assumptions, the NN approximation [Eq. (6)] provides a simple formula for determining the widths to better than 6% while the MH approximation [Eq. (9)] may serve as a simple check.

The uncertainties stated above do not include any errors arising from the neglect of the supplementary conditions that should be imposed because of the extra coordinates present when the potential is separated into long and short range components. This error is believed to be small because of the arguments presented in Sec. IV below Eq. (15).

The value of $P(\epsilon)$ around its maximum is not well determined but might be expected to lie near the SRNN curve because of the close agreement between it and the SHO curve in this region and its good agreement with the Holtsmark curve at infinite temperature. Accurate evaluation of T_p [Eq. (18)] is required to determine $P(\epsilon)$ more accurately. Monte Carlo methods might accomplish this.

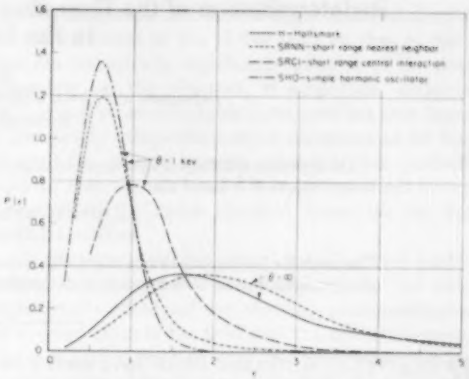

FIG. 2. The probability of obtaining field strengths of magnitude ϵ for $\theta=\infty$ and $\theta=1$ kev for iron at normal density for small values of ϵ. Only approximations good in this region are shown. The correct curve for $\theta=1$ is believed to lie between the SRNN and SRCI curves but nearer to the SRNN curve.

IX. ACKNOWLEDGMENTS

Considerable aid and direction for carrying out the numerical work involved here was given by Dr. Glenn H. Peebles.

The author also wishes to thank Mr. C. Lowery for assisting in the preparation of formulas and the numerical calculations.

The author is also particularly indebted to Dr. R. Ferrell and to his colleagues in the Nuclear Energy Division of The Rand Corporation for many helpful discussions.

Redetermination of the Hyperfine Splittings of Hydrogen and Deuterium in the Ground State*

P. Kusch
Department of Physics, Columbia University, New York, New York
(Received August 12, 1955)

The hyperfine splittings of hydrogen and deuterium in the $1^2S_{\frac{1}{2}}$ state have been remeasured by the atomic beam method. It is found that

$$\Delta\nu(\mathrm{H}) = (1420.40573 \pm 0.00005) \times 10^6 \text{ sec}^{-1},$$
$$\Delta\nu(\mathrm{D}) = (327.384302 \pm 0.000030) \times 10^6 \text{ sec}^{-1}.$$

The result for hydrogen is in agreement with a recent measurement of Wittke and Dicke. It is in significant disagreement with an earlier atomic beam measurement.

RECENTLY, Wittke and Dicke[1] have made a new determination of the hyperfine splitting of hydrogen in the ground state. The result is in disagreement with an earlier result of Prodell and Kusch[2] by almost three times the sum of the stated uncertainties of the two results. While no interpretation of the experimental value of the hfs splitting itself is concerned with the discrepancy because of a lack of knowledge of the fine structure constant to a precision comparable to the discrepancy between the two results, the resolution of the discrepancy is, nevertheless, of importance in the comparison[3] of the hyperfine structure separation of hydrogen in the 1*S* and 2*S* states and in the search for a differential hfs anomaly for hydrogen and deuterium in the 1*S* and 2*S* states.

Dicke[4] has suggested that a systematic error may have occurred in the atomic beam method through a continuous change in phase of the rf magnetic field along the rf circuit (hairpin) traversed by the atom. Such a change of phase can occur through a differential resistance or radiation at the two ends of the hairpin. The change in phase may be reversed by mechanical reversal of the hairpin with respect to the direction of the beam provided that the whole electrical environment of the hairpin, including its shielding, is reversed. In the previous modification of the experiment, no complete reversal was possible. In the present experiment, the hairpin was rigidly and symmetrically mounted in a rigid shield with minimal apertures to allow transit of the beam and the whole system could readily be reversed with respect to the beam. The apparatus generally was as previously described.[2] However, the Pirani gauge had been remarkably improved in steadiness and a much better frequency standard was available for the present work. The wire deflecting magnets had been replaced by conventional iron magnets of increased deflecting power.

The oscillator output was beat against a signal, derived from the frequency atandard, of 1420 and 328 Mc/sec for H and D, respectively. The beat frequencies of about 405 and 615 kc/sec were measured on a *BC* 221 frequency meter which was, in turn, calibrated against the standard. The oscillators themselves were as previously described. The rf amplitude was adjusted to values in the neighborhood of the optimum value where the line has its theoretical transit-time width and the probability of transition at the line center is a maximum. A probe in the coaxial line which fed the hairpin was connected through a crystal to a galvanometer. In most cases a detectable change in the galvanometer current occurred as the oscillator frequency was varied over several times the line width. The observed effect is, of course, a result both of variation of the rf current in the hairpin and of the frequency-dependent characteristics of the detecting circuit. The effect of a variable rf field amplitude will be discussed in the section on errors.

To determine the central frequency of the line, pairs of observations were made of the frequencies on both sides of the intensity maximum at which the readings of the galvanometer in the Pirani gauge circuit were equal. Since the Pirani gauge circuit had, for long periods of time, a slow and constant thermal drift, alternate pairs of readings were made for an opposite direction of traverse of the line frequency and effects of drift were thus cancelled out. In a random way and at the discretion of the observer, the center was measured for a range of widths whose extremes differed by a factor of five though a statistically significant body of data is not available for widths which differ by this large factor. The data for H were taken on eight days and those for D on six. The adjustment of all available parameters (rf circuit, rf amplitude, deflecting fields, beam intensity, etc.) was changed between different days and sometimes within a given day. Data were taken for both directions of traverse of the hairpin by the beam and by five different observers.

For hydrogen the line (1,0; 0,0) was measured. The frequency of the line is very nearly independent of magnetic field at low field, but a small correction, quadratically dependent on field, must be subtracted

* This research was supported in part by the Office of Naval Research.

[1] J. P. Wittke and R. H. Dicke, Phys. Rev. **96**, 530 (1954); J. P. Wittke, dissertation, Princeton University, 1955 (unpublished).
[2] A. G. Prodell and P. Kusch, Phys. Rev. **88**, 184 (1952).
[3] Reich, Heberle, and Kusch, Phys. Rev. **98**, 1194 (1955).
[4] R. H. Dicke (private communication).

from the line frequency to determine the zero-field hfs separation. To determine the field, about 0.32 gauss, the frequency of the line (1,0; 1,−1) was measured. The quadratic correction was about 280 cps. For deuterium, the central frequency of a doublet was measured. The doublet is unresolved, and at the fields used in these experiments the separation of the components is about 400 cps. The line of lower frequency, $(\frac{3}{2},\frac{1}{2};\frac{1}{2},-\frac{1}{2})$, and that of higher frequency $(\frac{3}{2},-\frac{1}{2};\frac{1}{2},\frac{1}{2})$ are characterized[5] by matrix elements proportional to the rf amplitude and $(1\pm x)$ respectively. In the present case x, the usual magnetic field parameter, is about 0.0026. If the rf amplitude is less than its optimum value, the component with a larger matrix element will be characterized by both a greater width and a higher probability of transition at the center than will the component of the smaller matrix element. If, however, the rf field is greater than its optimum value, the line of larger matrix element has a lower probability of transition at the center and a greater width than does the other line.

Salwen[6] has given tables of both the transition probability and line width as a function of rf amplitude. It is easily shown that over a considerable range of rf amplitude about its optimum value, the shift of the center of the doublet arising from the differential transition probabilities is wholly negligible (~1 cps). Atoms with a very low velocity may make such large excusions in their trajectories that they may collide with the surfaces of the deflecting magnets or with other obstacles. In the present case, however, the magnetic moment of atoms in the terminal states of the two transitions are so nearly identical that no significant loss of intensity in either of the two lines with respect to the other can occur.

For D, the magnetic field was determined from the frequency of the line $(\frac{3}{2},-\frac{1}{2};\frac{3}{2},-\frac{3}{2})$. The quadratic field correction was of the order of 1000 cps.

RESULTS, CORRECTIONS, AND UNCERTAINTIES

The following results are obtained:

$$\Delta\nu(\mathrm{H}) = (1420.40573\pm 0.00005)\times 10^6 \text{ sec}^{-1},$$

$$\Delta\nu(\mathrm{D}) = (327.384302\pm 0.000030)\times 10^6 \text{ sec}^{-1}.$$

In each case the result depends on the determination of the center of an observed line to about 1 part in 750 of the line width. A detailed consideration of the various uncertainties follows.

(a) *Statistical uncertainty.*—A total of 440 observations was made for H and 360 for D. The probable error of the mean value of $\Delta\nu$ was 12 cps for hydrogen and 6 cps for deuterium. The difference occurs because the H line is broader than the D line, because of a better absolute frequency stability of the oscillator used for D than of that used for H and because uncertainties in the frequency standard have a larger absolute effect on the measurement of the H line than on that of the D line. No statistically significant variation of the result dependent on the observer, rf amplitude, deflecting field, or any other adjustable parameter has been found. A completely independent set of observations for both H and D, with a hairpin somewhat less perfectly shielded than the one finally used, gave a result in both cases within the limits specified above for the final result.

(b) *Magnetic field determination.*—The lines used to determine the magnetic field have a linear frequency dependence on field and the frequency presumably gives an average value of the field over the transition region. The quadratic correction term, however, depends on the average value of the square of the field and it has been assumed that this is equal to the square of the average field. The lines with a linear field dependence had their natural half-width, in the case of D about 25 kc/sec. While no theoretical or experimental investigations of the effects of field inhomogeneity exist, it seems reasonable to assume that the inhomogeneity does not exceed 10% of the total field, which, for D, would give a frequency spread in the line of about 28 kc/sec. If the field is assumed to vary linearly from one end of the hairpin to the other with an extreme variation of 10%, the difference between $\langle H^2\rangle_{\mathrm{Av}}$ and $\langle H\rangle^2$ is about 0.075%. If the variation is assumed to be quadratic with a total variation of 10% and a minimum field at the center of the hairpin, the difference is 0.083%. The effect is thus less than 1 cps for D and very much less for H.

A random fluctuation of the field of the order of a few milligauss was noted. The fluctuations were so rapid that a critical measurement of the half-width of the field-dependent line could not be made in a single observation. However, sufficient measurements of the low-frequency, field-dependent line were made to insure that an average applicable to the calculation of the quadratic correction was found.

(c) *Doublet error.*—It is estimated that an upper limit to the displacement of the apparent center of the deuterium doublet from the true center is ±3 cps.

(d) *Overlap error.*—The rf field had a direction relative to that of the constant field such that both σ and π transitions could be excited. Only those lines were observable, however, which correspond to the high-field transitions $\Delta m_J=\pm 1$, since the deflecting magnets operate at a field where high-field quantization occurs. Therefore the line (1,1; 0,0) but not the line (1,−1; 0,0) occurs for H. The line (1,1; 0,0), at higher frequency than the line (1,0; 0,0) under observation is separated from it by about 13 line widths. The overlap of the lines then shifts the central frequency at half-intensity of the line (1,0; 0,0) upwards by 8 cps and the true $\Delta\nu$ is then the apparent $\Delta\nu$ reduced by 8±4 cps. In the case of D, the two adjacent σ lines are both observable and symmetrically spaced on either side of the doublet under observation. These lines, therefore, give no overlap

[5] H. C. Torrey, Phys. Rev. 59, 293 (1941).
[6] H. Salwen (to be published).

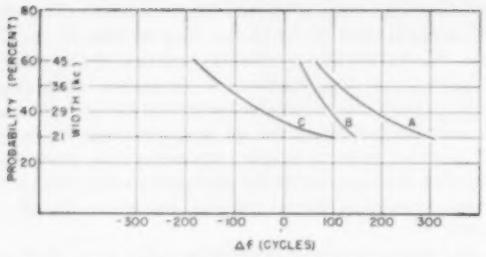

FIG. 1. The shift in the resonance line of hydrogen when the rf amplitude varies linearly. Curves A and B correspond to an optimum value of the amplitude and a 5 and 2.5% variation over 35 kc/sec respectively. Curve C corresponds to an amplitude about 1.3 times the optimum value and a variation of 5% over 35 kc/sec. The sequence in which the widths are shown should be inverted; i.e., a probability of 60% corresponds to a width of 21 kc/sec.

correction. The line $(\frac{3}{2},\frac{3}{2};\frac{1}{2},\frac{1}{2})$ however gives an overlap correction of 1 ± 1 cps.

(e) *Nonconstant* rf *amplitude.*—It is inevitable that some variation of the rf amplitude will occur over the width of the line and this variation may shift the apparent center of the line. The effect may be calculated from Salwen's[6] tabulation of line widths and transition probabilities in a beam which issues from a source containing atoms in thermal equilibrium. In Fig. 1 are shown some results for a resonance line whose natural half-width is 35 kc/sec. The curves A and B are calculated for an optimum rf amplitude at the center of the line and a linear variation of 5 and 2.5% respectively over a range of 35 kc/sec. The line widths which correspond to the probabilities are indicated. The curve C corresponds to an amplitude at the line center of 1.3 times the optimum value and a variation of the amplitude of 5% over 35 kc/sec. It is to be noted that the shift reverses in sign with respect to A and B for the same sign in the change of amplitude and for widths near the half-width. All available evidence suggests that the amplitude did not vary by more than 0.5% over the line width in hydrogen. Moreover, the variation had a variable sign and the rf amplitude at the line center had a variable magnitude from run to run. Accordingly a maximum error of 20 cps at the half-width point is assigned. The data of each run were analyzed to detect a statistically significant variation of $\Delta\nu$ as measured at the narrow and wide portions of the resonance line. In no case was an effect discovered. In the case of H, the 100 observations in the total body of data taken at the smallest widths, with a mean width of 22.7 kc/sec differed in mean frequency from the 100 observations at the greatest width, with a mean width of 40.8 kc/sec by 28 cps. The difference is much less than the statistical uncertainties allow. For hydrogen we allow, however, an uncertainty of ±20 cps arising from the effect under discussion. For deuterium, where the line is narrower we allow ±15 cps.

(f) *Phase change in the hairpin.*—There is no statistically significant variation of the apparent $\Delta\nu$ as the direction of traverse of the beam through the hairpin is reversed. Any effect of a continuous change in phase over the length of the hairpin should average out in the reversal. Nevertheless, an identical traverse in both directions is limited by mechanical tolerances. We assign ±5 cps as a maximum residual error for both H and D.

(g) *Frequency errors.*—Frequent comparison was made of the local frequency standard with WWV and the standard was always within 2 parts in 10^8 of WWV. Because the local standard was frequently reset, the residual error was random in magnitude and presumably in sign. A generous estimate of error arising from the difference between our standard and WWV is, therefore, ±28 cps for H and ±7 cps for D.

In the course of his measurements of the hfs of hydrogen, Wittke[1] has made a study of the possibility of systematic error in the intercomparison of a local standard of frequency and WWV due to a diurnal variation of a Doppler shift in the transmitted signal. He concludes that there is no detectable systematic effect at Princeton, New Jersey and we assume that no significant error occurs in New York. Finally, the signal transmitted by WWV is corrected whenever the deviation from the nominal frequency is greater than 1 part in 10^8. The maximum error for H is thus ±14 cps and for D, ±3 cps.

All the estimates of possible systematic error appear to be rather generous in magnitude. The rms sum of the uncertainties is ±40 cps for H and ±20 cps for D. We, however, give in the final result a somewhat larger uncertainty to allow for an unfavorable accumulation of error.

At the present time the origin of the error in the previous determination of $\Delta\nu$(H) by the atomic beam method is not clear. It appears, however, that inadequate shielding of the hairpin, with a consequent differential radiation at the two ends may have been responsible for the error. Our present result is in satisfactory agreement with the result, $\Delta\nu(\mathrm{H})=(1420.40580\pm0.00005)\times10^6$ sec^{-1} of Wittke and Dicke. If it is assumed that there is no significant dependence of $\Delta\nu$ on the pressure of the molecular hydrogen into which the atomic hydrogen is mixed, the data of Wittke and Dicke give for $\Delta\nu$(H) the value 1420.40571 Mc/sec. It is not wholly clear, both from the data and from theoretical estimates, that the pressure dependence of $\Delta\nu$(H) is as great as found by Wittke and Dicke.

The hyperfine structure anomaly as previously defined[2] and with the same values of the auxiliary constants is now $(1.703\pm0.005)\times10^{-4}$.

It is a pleasure to acknowledge the important aid of T. Eck, J. Hendrie, A. Lurio, and A. Prodell in the accumulation of the large body of data on which the present result depends.

PHYSICAL REVIEW VOLUME 100, NUMBER 4 NOVEMBER 15, 1955

Resonance Transitions Induced by Perturbations at Two or More Different Frequencies

NORMAN F. RAMSEY*
Lyman Physics Laboratory, Harvard University, and Ecole d'Eté de Physique Théorique, Les Houches, Hte-Savoie, France
(Received August 15, 1955)

Resonance transition probabilities for a system in the presence of oscillatory perturbations at two or more different frequencies are discussed. It is shown that if resonance transitions are induced by a perturbation at one frequency, then the presence of the other perturbations at nonresonant frequencies alters the resonance frequency for the first perturbation. Theoretical expressions for the alteration of the resonance frequency are derived. Various applications of the derived formulas are discussed, including resonance experiments with more than one oscillatory field, molecular beam experiments in a nonuniform constant field, evaluation of "collision-narrowing" effects in nuclear paramagnetic resonance, etc. The effects of the extraneous oscillatory perturbations are shown to be especially important if their frequencies are close to Bohr frequencies for the perturbation.

I. INTRODUCTION

IN many cases, resonance transitions are studied in the presence of more than one oscillatory field. For example, in nuclear resonance experiments the transitions are often induced by a high harmonic of an oscillator at a low fundamental frequency. In such a case the other harmonics are often also present and the question arises as to the effects that the oscillatory magnetic fields of the other harmonics may have on the apparent resonance frequency. Likewise, in a molecular beam experiment, the transitions are induced by an applied oscillatory field while the molecules pass through a fixed field. If the fixed field is not completely uniform, the motion of the molecule through the varying field gives rise to an apparent oscillatory field at the molecule in addition to the one specifically applied.[1] As a still different example, if a molecule is subjected to many collisions, the magnetic field of say one nucleus at the position of the other fluctuates in time and one Fourier component of this fluctuating field will appear as an oscillating magnetic field; if an externally produced oscillating field is produced to induce a resonance transition, the transition then actually occurs in the presence of perturbations at more than one frequency.

One special case of the simultaneous presence of two perturbations has been discussed by Bloch and Siegert,[2] Stevenson,[3] and Winter[4]: that of a magnetic moment acted upon by two fields rotating at equal frequencies but with opposite directions of rotation. The more general results derived in the present paper will be shown to agree with those of Bloch and Siegert in the special case to which their result applies.

In the present paper, it will be shown that if resonance transitions are induced by a perturbation at one frequency, then the presence of the other perturbations at nonresonant frequencies will alter the resonance frequency for the first perturbation. Since most resonance experiments involve only single quantum transitions rather than the multiple quantum transitions that have occasionally been discussed,[4-10] the present discussion will be limited to single quantum transitions, i.e., the assumption will be made that one of the oscillatory perturbations is approximately at the resonance frequency of an allowed transition while the other perturbations are not at resonance frequencies.

The results reported here were first obtained in 1950 and have been privately circulated[5] and quoted in various publications.[1,5-7] The present report is the subsequent paper promised in one of these earlier publications.

II. MAGNETIC MOMENT IN TWO ROTATING FIELDS

A particularly easy case to discuss is that of a magnetic moment $\gamma\hbar\mathbf{I}$ acted upon by a fixed field H_0 about which as an axis two fields H_1 and H_2, perpendicular to H_0, rotate with angular velocities $-\omega$ and $-\omega_2$.

In the absence of H_2, the magnetic resonance frequency for ω would be equal to the Larmor frequency,

$$\omega_0=\gamma H_0. \tag{1}$$

It now remains to see how the presence of H_2 rotating at frequency $-\omega_2$ affects the position of the resonance frequency for ω. This problem can easily be analyzed by the use of a rotating coordinate system.[11]

Consider the problem from the point of view of a coordinate system rotating with angular velocity $-\omega_2$. Then, as discussed by Rabi, Ramsey, and Schwinger,[11]

* John Simon Guggenheim Fellow.
[1] Kolsky, Phipps, Ramsey, and Silsbee, Phys. Rev. **81**, 106 (1951); **87**, 400 (1952).
[2] F. Bloch and A. Siegert, Phys. Rev. **57**, 522 (1940).
[3] A. J. Stevenson, Phys. Rev. **58**, 1061 (1940).
[4] N. Winter (private communication). Dr. Winter's calculations were made without his knowledge of the existence of the work reported in the present paper. Dr. Winter's results will be reported in *Comptes rendus hebdomadaires des séances de l'académie des sciences, Paris*.
[5] N. F. Ramsey (private communications and public lectures, 1950) (unpublished).
[6] H. Silsbee, Ph.D. thesis, Harvard University, 1950.
[7] N. F. Ramsey, *Molecular Beams* (Oxford University Press, Oxford, 1955).
[8] P. Kusch, Phys. Rev. **93**, 1022 (1954).
[9] Brossel, Cagnac, and Kastler, Comptes rend. **237**, 984 (1953).
[10] Besset, Horowitz, Messiah, and Winter, J. phys. radium **15**, 251 (1954).
[11] Rabi, Ramsey, and Schwinger, Revs. Modern Phys. **26**, 167 (1954).

on this rotating coordinate system the effective magnetic field H_{er} from H_0, H_2, and the rotation will have the magnitude

$$H_{er}=[(H_0-\omega_2/\gamma)^2+H_2^2]^{\frac{1}{2}}. \quad (2)$$

However, on this rotating coordinate system the apparent rotational frequency of H_1 will be $-(\omega-\omega_2)$. Hence, if the magnitude of $H_0-\omega_2/\gamma$ is much greater than either H_2 or H_1, the resonance frequency will be at

$$\omega-\omega_2=\gamma H_{er}=\gamma[(H_0-\omega_2/\gamma)^2+H_2^2]^{\frac{1}{2}} \quad (3)$$

or for $\omega_0-\omega\gg\gamma H_2$

$$\begin{aligned}\omega&=\omega_0+(\omega_0-\omega_2)\{[1+(\gamma H_2)^2/(\omega_0-\omega_2)^2]^{\frac{1}{2}}-1\}\\&=\omega_0+(\gamma H_2)^2/2(\omega_0-\omega_2).\end{aligned} \quad (4)$$

Consequently it is apparent that the presence of the perturbation of amplitude γH_2 shifts the resonance away from the Larmor frequency ω_0.

The special case considered by Bloch and Siegert[2] and by Stevenson[4] was that for which $\omega_2=-\omega_0$ and $H_2=H_1$, in which case the above reduces to

$$\omega=\omega_0+(\gamma H_1)^2/4\omega_0, \quad (5)$$

which is just the result of Bloch and Siegert. It is also apparent from Eq. (4) that the selection of $\omega_2=-\omega_0$ is one for which the extra oscillatory field is particularly ineffective, in agreement with the conclusion of Bloch and Siegert that their term was ordinarily small. On the other hand, if $\omega_2\approx\omega_0$ the shift of the resonance frequency can become significant in some cases.

III. GENERAL CASE FOR TWO EIGENSTATES

The discussion in the preceeding section was limited to a magnetic moment in a magnetic field. In the present section the result will be generalized to transitions involving any two eigenstates p and q. However, the discussion in this section will be limited to the case of only two levels being involved. In the next section, the effects of the presence of more than two eigenstates will be considered.

The calculation can be performed in several different ways. One is to consider directly a case for which the result is relevant, namely the case of the separated oscillatory field method of molecular beam resonance described in a previous paper.[12] The calculation is thereby simplified since the two oscillatory fields can be considered to be applied at separate times, yet the results for the shift in resonance frequency is applicable equally to the case when the two perturbing frequencies are applied simultaneously since for levels of fixed separation the resonance frequency in the separated oscillatory field method is the same[12] as in the method with a single oscillatory field. Consideration of the separated oscillatory field problem in this section has the further advantage that the results show the consistency of the conclusions of the present section with those of the preceding section for which the perturbations are simultaneously applied.

The problem then is that of an atom or molecule with energy eigenvalues W_p and W_q which is first perturbed for a time τ by a perturbation of the form

$$V_{pq}=\hbar be^{i\omega t},\quad V_{qp}=\hbar be^{-i\omega t},\quad V_{pp}=V_{qq}=0, \quad (6)$$

where the notation here and subsequently is that of reference 12. Then the atom enters a region where (unlike the usual case[12]) it is subjected to a perturbation

$$V_{pq}=\hbar b_2e^{i(\omega_2 t+\phi)},\quad V_{qp}=\hbar b_2e^{-i(\omega_2 t+\phi)},\quad V_{pp}=V_{qq}=0, \quad (7)$$

for the time T. Finally the atom is again perturbed as in Eq. (6) for a time τ. Without loss of generality in the calculation of the shift of resonance frequency, τ (but not $b\tau$) can be taken as very small and $|2b|\gg|\omega_0-\omega$. For simplicity, it will be assumed that $|\omega_0-\omega_2|\gg 2b_2$ though some generality is lost by this assumption. At time $t=0$ the system will be assumed to be in the state $C_q=0$, $C_p=1$.

For these assumptions, $\sin\Theta=1$, $\cos\Theta=0$, $\sin\Theta_2=0$, $\cos\Theta_2=1$, and $a=2b$, so the equations analogous to Eqs. (8a–f) of reference 12 become the following:

$$\begin{aligned}
C_p(\tau)&=\cos b\tau,\\
C_q(\tau)&=-i\sin b\tau,\\
C_p(\tau+T)&=[i\sin\tfrac{1}{2}a_2T+\cos\tfrac{1}{2}a_2T]C_p(\tau)\\
&\quad\times\exp\{i[\tfrac{1}{2}\omega_2-(W_p+W_q)/2\hbar]T\}\\
&=C_p(\tau)\exp\{i[\tfrac{1}{2}a_2+\tfrac{1}{2}\omega_2\\
&\quad-(W_p+W_q)/2\hbar]T\},\\
C_q(\tau+T)&=[-i\sin\tfrac{1}{2}a_2T+\cos\tfrac{1}{2}a_2T]C_q(\tau)\\
&\quad\times\exp\{i[-\tfrac{1}{2}\omega_2-(W_p+W_q)/2\hbar]T\}\\
&=C_q(\tau)\exp\{i[-\tfrac{1}{2}a_2-\tfrac{1}{2}\omega_2\\
&\quad-(W_p+W_q)/2\hbar]T\},\\
C_p(2\tau+T)&=\cos b\tau C_p(\tau+T)\\
&\quad-i\sin b\tau\exp(i\omega T)C_q(\tau+T),\\
C_q(2\tau+T)&=-i\sin b\tau\exp(-i\omega T)C_p(\tau+T)\\
&\quad+\cos b\tau C_q(\tau+T).
\end{aligned} \quad (8)$$

The nonappearence of ϕ in the above equations can be seen from the equivalence of ϕ to ωt_1 in reference 12 and from the fact that ωt_1 terms do not appear in Eq. (4) of reference 12 with the above assumption of $\sin\Theta_2=0$. Therefore,

$$\begin{aligned}
C_q(2\tau+T)&=-i\sin b\tau\cos b\tau\exp\{i[\tfrac{1}{2}a_2+\tfrac{1}{2}\omega_2\\
&\quad-\omega-(W_p+W_q)/2\hbar]T\}-i\sin b\tau\cos b\tau\\
&\quad\times\exp\{i[-\tfrac{1}{2}a_2-\tfrac{1}{2}\omega_2-(W_p+W_q)/2\hbar]T\}\\
&=-2i\sin b\tau\cos b\tau\cos\tfrac{1}{2}\lambda_2T\\
&\quad\times\exp\{-[\omega+(W_p+W_q)/\hbar]T/2\},
\end{aligned} \quad (9)$$

where

$$\lambda_2=a_2+\omega_2-\omega. \quad (10)$$

[12] N. F. Ramsey, Phys. Rev. 78, 695 (1950).

Therefore, the transition probability is

$$P_{p,q}=4\sin^2 b\tau\cos^2 b\tau\cos^2(\tfrac{1}{2}\lambda_2 T)$$
$$=\sin^2(2b\tau)\cos^2(\tfrac{1}{2}\lambda_2 T). \quad (11)$$

It is apparent from Eq. (11) that the transition probability of Eq. (11) will be a maximum for $\lambda_2=0$. A discussion of the effect of a molecular beam velocity distribution on a function of this form is given in reference 12, Eq. (14), ff. The resonance frequency ω for maximum transition probability, from Eq. (10) above and from Eq. (5) of reference 12, then is

$$\omega=a_2+\omega_2=[(\omega_0-\omega_2)^2+(2b_2)^2]^{\frac{1}{2}}+\omega_2$$
$$=\omega_0+(\omega_0-\omega_2)\{[1+(2b_2)^2/(\omega_0-\omega_2)^2]^{\frac{1}{2}}-1\}$$
$$=\omega_0+(2b_2)^2/2(\omega_0-\omega_2). \quad (12)$$

In the special case of magnetic moments,[12] $2b_2=\gamma H_2$ and the above reduces to Eq. (4), which was derived for magnetic moments only but with the two perturbations applied simultaneously instead of successively as in the separated oscillatory field method.

If $|\omega_0|\gg|\omega_2|$, Eq. (12) can also be written as

$$\omega=\omega_0+(2b_2)^2/2\omega_0+(2b_2)^2\omega_2/2\omega_0^2+(2b_2)^2\omega_2^2/2\omega_0^3. \quad (12a)$$

On the other hand, if $|\omega_0|\ll|\omega_2|$,

$$\omega=\omega_0-(2b_2)^2/2\omega_2+(2b_2)^2\omega_0/2\omega_2^2. \quad (12b)$$

From these equations it is apparent, when oscillatory instead of rotating fields are used and when ω_2 is far from ω_0, that the first terms dependent on ω_2 are mutually cancelled by the positive and negative rotating components into which the oscillatory field can be resolved.[2] Nearer the resonance frequency, however, this partial cancellation is much less complete.

IV. MORE THAN TWO EIGENSTATES

Now consider the case of four levels p, q, r, and s with the primary resonance observed at frequency ω being that for transitions from p to q while there are also present nonresonant perturbations with the matrix elements

$$V_{pr}=\hbar b_r e^{i(\omega_r t+\phi_r)},$$
$$V_{sq}=\hbar b_s e^{i(\omega_s t+\phi_s)}, \quad (13)$$

between the levels p and r and between the levels s and q. ω_r and ω_s could of course be equal and for a two-frequency problem they would have to be, with the two frequencies being ω and $\omega_1=\omega_r=\omega_s$.

With the same approximations as in the preceding section, this problem can be solved as in that section; in fact the same Eqs. (8) apply except that the middle two equations are replaced by

$$C_p(\tau+T)=C_p(\tau)\exp\{i[\tfrac{1}{2}a_r+\tfrac{1}{2}\omega_r-(W_p+W_r)/2\hbar]T\},$$
$$C_q(\tau+T)=C_q(\tau)\exp\{i[-\tfrac{1}{2}a_s-\tfrac{1}{2}\omega_s-(W_s+W_q)/2\hbar]T\}. \quad (14)$$

Consequently, Eq. (9) is replaced by

$$C_q(2\tau+T)=-i\sin b\tau\cos b\tau\exp\{i[\tfrac{1}{2}a_r+\tfrac{1}{2}\omega_r-\omega-(W_p+W_r)/2\hbar]T\}-i\sin b\tau\cos b\tau\times\exp\{i[-\tfrac{1}{2}a_s-\tfrac{1}{2}\omega_s-(W_s+W_q)/2\hbar]T\}$$
$$=2i\sin b\tau\cos b\tau\cos\tfrac{1}{2}\lambda_{rs}T\times\exp\{-i[\omega+\tfrac{1}{2}(a_s-a_r)+\tfrac{1}{2}(\omega_s-\omega_r)+(W_p+W_s+W_r+W_q)/2\hbar]T/2\}, \quad (15)$$

where

$$\lambda_{rs}=\tfrac{1}{2}(a_r+a_s)+\tfrac{1}{2}(\omega_r+\omega_s)-\omega-(W_p-W_q+W_r-W_s)/2\hbar. \quad (16)$$

The transition probability $P_{p,q}$ is then given by

$$P_{p,q}=\sin^2(2b\tau)\cdot\cos^2(\tfrac{1}{2}\lambda_{rs}T). \quad (17)$$

Just as in the previous section then, the resonance frequency is

$$\omega=\tfrac{1}{2}[a_r+\omega_r-(W_p+W_r)/\hbar]+\tfrac{1}{2}[a_s+\omega_s-(W_q+W_s)/\hbar]$$
$$=(W_q-W_p)/\hbar+\tfrac{1}{2}\{(W_r-W_p)/\hbar-\omega_r\}\times\{[1+(2b_r)^2/((W_r-W_p)/\hbar-\omega_r)^2]^{\frac{1}{2}}-1\}+\tfrac{1}{2}\{(W_q-W_s)/\hbar-\omega_s\}\times\{[1+(2b_s)^2/((W_q-W_s)/\hbar-\omega_s)^2]^{\frac{1}{2}}-1\}$$
$$=\omega_0+(2b_r)^2/4[(W_r-W_p)/\hbar-\omega_r]+(2b_s)^2/4[(W_q-W_s)/\hbar-\omega_s]. \quad (18)$$

It is of interest to note that Eq. (18) equals Eq. (12) in the case that $W_p=W_s$, $W_q=W_r$, and $\omega_2=\omega_r=\omega_s$.

Equations (12) and (18) may be combined to provide the net resonance frequency in the general case of the presence of several nonresonant perturbations to different eigenstates. Let ω be the resonance transition frequency between the two levels p and q. Let the level p be perturbed by a matrix element to the state r at frequency ω_i such as

$${}_iV_{pr}=\hbar\,{}_ib_{pr}\,e^{i(\omega_i t+{}_i\phi_{pr})}, \quad (19)$$

while q is perturbed by

$${}_iV_{rq}=\hbar\,{}_ib_{rq}\,e^{i(\omega_i t+{}_i\phi_{rq})}. \quad (20)$$

Then, from Eqs. (12) and (18),

$$\omega-\omega_0=\textstyle\sum_i(2\,{}_ib_{pq})^2/2(\omega_0-\omega_i)+\sum_i\sum_r{}''(2\,{}_ib_{pr})^2/4[(W_r-W_p)/\hbar-\omega_i]+\sum_i\sum_r{}''(2\,{}_ib_{rq})^2/4[(W_q-W_r)/\hbar-\omega_i], \quad (21)$$

where the symbol $\sum_r{}''$ indicates that the summation does not include $r=p$ or q. Expansions similar to Eqs. (12a) and (12b) can also be made for Eq. (21) when desired.

V. APPLICATIONS

The relations derived above are applicable to a number of different present and contemplated experiments. In molecular-beam magnetic-resonance experiments, the oscillatory magnetic fields are often produced as high harmonics of a much lower frequency funda-

mental. In such experiments undesired harmonics are often present along with the fundamental. Equation (21) can then be used to estimate the distortion caused by the unwanted oscillations. As shown by the above formulas, these effects can be serious if the unwanted frequency is at all close to a Bohr frequency of the system. It should be noted in the application of Eqs. (12) and (21) that for perturbation frequencies far from resonance, the positive and negative rotating components partially cancel each other as discussed in conjunction with Eqs. (12a) and (12b); however, this is not true for the components closer to the resonance condition.

The above formulas can also be applied to the case of a molecular beam resonance experiment for which the constant magnetic field is not exactly uniform and unidirectional. By field measurements, the fluctuating magnetic field components perpendicular to $\mathbf{H}_0$ can be estimated as well as the characteristic cyclic distances d_2 for the variation of the direction of these components. If v is the velocity of the molecule, then the characteristic frequencies for the fluctuating components are v/d_2. Equations (4), (12), or (21) can then be used to evaluate the displacement of the resonance frequency. For the molecular beam case, in the averaging of such relations as Eq. (11) over the molecular beam velocity to obtain the experimental line shape, it should be noted that ω_2 and hence λ_2 are velocity-dependent. In the frequently occurring case that expansions such as Eq. (12a) are applicable, the $\cos^2(\frac{1}{2}\lambda_2 T)$ of Eq. (11) becomes for a particular velocity v and for $T=L/v$,

$$\begin{aligned}\cos^2(\tfrac{1}{2}\lambda_2 T) &= \cos^2\{\tfrac{1}{2}[\omega_0-\omega+(2b_2)^2/2\omega_0+(2b_2)^2v/2\omega_0^2d_2 \\ &\qquad +(2b_2)^2v^2/2\omega_0^3d_2^2+\cdots]\} \\ &= \cos^2\{\tfrac{1}{2}[\omega_0+(2b_2)^2/2\omega_0-\omega]L/v \\ &\qquad +(2b_2)^2L/2\omega_0^2d_2 \\ &\qquad +(2b_2)^2Lv/2\omega_0^3d_2^2+\cdots\}. \quad (22)\end{aligned}$$

From this, it is apparent that the first term in Eq. (12a) that is dependent on the frequency ω_2 becomes a velocity-independent phase shift $(2b_2)^2L/2\omega_0^2d_2$ in Eq. (22). The effects of such velocity-independent phase shifts on the average resonance line shape have been discussed by Ramsey and Silsbee.[13]

The above formulas may also be applied to a discussion of "collision narrowing" in nuclear paramagnetic resonance.[14] In a free molecule, the nuclear magnetic resonance frequency depends on the orientation state of the molecule, due to the various magnetic interactions within the molecule. Furthermore, because of the even-order perturbations of these interactions, the average frequency of the resonance lines in the vicinity of the nuclear Larmor frequency is not equal to the Larmor frequency in the average magnetic field at the nucleus (the external magnetic field corrected for the magnetic shielding of the molecule). The average nuclear resonance frequency for the free molecule is in fact closer to the Larmor frequency in the average magnitude of the field at the nucleus rather than in the magnitude of the average field (these differ since the internal fields are not always parallel to the external field). If the molecule on the other hand is subjected to many collisions which change the molecular orientation, the separate resonance lines are averaged to a single one by the process[14] of "collision narrowing." However, it is not immediately obvious that the collision-narrowed line is at the Larmor frequency of the nucleus in the magnitude of the average field at the nucleus rather than in the average magnitude of the field; indeed, the latter corresponds more nearly to the average of the resonance frequencies for the free molecule.

The discussion of the previous sections can be applied to show that it is the magnitude of the average field rather than the average of the magnitudes that is relevant when the molecule is subject to frequent collisions. Although the collisions cause a randomly fluctuating field, the field can be Fourier-analyzed into components at angular frequency ω_i, where ω_i is of the order of the collision frequency or of the inverse of the correlation time[15] τ_c. Then the nondiagonal matrix elements can be taken to be of the form of Eqs. (19) and (20), and Eq. (21) applies. However, in most cases of collision narrowing,

$$\omega_i \gg (W_r-W_p)/\hbar \gg 2\,|b_{pr}| \approx \gamma H_c,$$

where H_c is a typical instantaneous component of the molecular magnetic field perpendicular to the direction of the external field H_0. Consequently, in this limit, $\omega=\omega_0$. On the other hand, in the absence of collisions a typical frequency ω_i would be the Larmor precession frequency of the molecular rotational magnetic moment; this is not necessarily larger than $(W_r-W_p)/\hbar$ so the terms on the right side of Eq. (21) become important and $\omega \neq \omega_0$.

Finally, it should be added that there are resonance experiments in which several different oscillatory frequencies are deliberately, instead of accidentally, introduced. In such cases, the formulas of the preceding sections may be directly applied to estimate the shifts of the resonance frequencies. In some precision experiments, these shifts can be important.

[13] N. F. Ramsey and H. B. Silsbee, Phys. Rev. **84**, 506 (1951).
[14] Bloembergen, Purcell, and Pound, Phys. Rev. **73**, 699 (1948).
[15] N. F. Ramsey, Phys. Rev. **58**, 226 (1940).

Electron Affinity of Boron, Carbon, Nitrogen, and Oxygen Atoms

TA-YOU WU
Division of Pure Physics, National Research Council, Ottawa, Canada
(Received July 11, 1955)

The electron affinity of boron, carbon, nitrogen, and oxygen atoms has been calculated by the method of Bacher and Goudsmit which enables the energy of a state in an n-electron configuration to be calculated in terms of the spectroscopic values of the energies of states of the $(n-1)$-, $(n-2)$-, ..., 1-electron ions. The negative ions of boron and nitrogen are found to be unstable, the electron affinity being *ca* -0.14 and -0.72 ev, respectively. The electron affinities of carbon and oxygen atoms are 1.75 and 1.13 ev, respectively. The last value is in fair agreement with the recently observed values, 1.48 ev found by Branscomb and Smith, and 1.05 found by Schüler and Bingel.

VARIOUS theoretical calculations have been suggested for the estimation of the electron affinity of various atoms.[1] For the simplest of atomic systems, namely the negative ion of the hydrogen atom, accurate calculations have been carried out by the variational method. For ions involving more than two electrons, calculations of similar accuracy (i.e., with the use of Hylleraas wave functions) would be excessively lengthy. Calculations with the Hartree-Fock method would be simpler, but that method is not suitable for the accurate determination of the rather small difference between the rather large total energies of the n- and $(n-1)$-electron systems. Extrapolation methods based on some polynomial expressions for the ionization potentials of an isoelectronic sequence in powers of the nuclear charge Z have also been used; but the disadvantage with this method is that the coefficients of terms like $1/Z$, $1/Z^2$ determined from the higher positive ions in the sequence may not be accurate for the extrapolation to the negative ion.

It was first suggested by Bacher and Goudsmit[2] and by the writer[3] that the method of Bacher and Goudsmit,[2] which expresses the energy of a state in an n-electron atom in terms of the energies of various states of the preceding ions, may be useful for the estimation of electron affinity of atoms. The method is the more accurate the further one can go back in the series of $(n-1)$-, $(n-2)$-, $(n-3)$-, $\cdots$, 1-electron ions. The method has been applied to the case of the fluorine atom.[3,4] The limitation of the method is, apart from the approximate nature of the method itself, that in most cases not all the states of the higher ions have been found spectroscopically. In the case of the fluorine atom, this method seems more satisfactory than other calculations of comparable simplicity. In the present note, the Bacher-Goudsmit method has been applied to boron, carbon, nitrogen, and oxygen atoms.

In each case, the energy difference between the ground state of the negative ion and that of the neutral atom is calculated from the spectroscopic term values of the preceding ions.[5] For a multiplet, say ^3P, the "center of gravity" of the components $^3P_{0,1,2}$ is employed. Table I summarizes the spectroscopic data and the result of the calculation. For B^- and C^-, the lowest state, namely, $1s^22s^22p^2\,^3P$ and $1s^22s^22p^3\,^4S$ respectively, can be calculated from the expressions for these states in terms of the ions up to $1s^2\,^1S$ given in the paper by Bacher and Goudsmit and the spectroscopic values given in Table I. For N^-, the expression for the state $1s^22s^22p^4\,^3P$ is also given in that paper. As the states of $1s^22s2p^4\,^3P$ of N I and of $1s^22p^4\,^3P$ of N II have not yet been observed, these states are in turn expressed in terms of the states of their preceding ions. The final expression is

$$\begin{aligned}1s^22s^22p^4\,^3P&=\tfrac{1}{3}(s^2p^3)[4\,^4S+5\,^2D+3\,^2P]+(4/3)(sp^4)\,^4P\\&\quad-\tfrac{1}{3}(s^2p^2)[12\,^3P+5\,^1D+^1S]-(1/9)(sp^3)\\&\quad\times[15\,^5S+^3S+20\,^3D+12\,^3P]+4(s^2p)\,^2P\\&\quad+(4/9)(sp^2)[11(^4P)+^2P+5(^2D)+^2S]\\&\quad-(s^3)\,^1S-\tfrac{1}{3}(sp)[14\,^3P+2\,^1P]+(4/3)(s)\,^2S.\end{aligned}$$

From Table I, it is seen that the electron affinity of nitrogen is ~ -5850 cm^{-1} $= -0.72$ ev and no stable N^- exists. This is of considerable interest in connection with the problem of the positive β-decay of the O^{14} nucleus.[6]

For C^-, the electron affinity calculated is 14 169 cm^{-1} or 1.75 ev. For B^-, it is -1135 cm^{-1} or -0.14 ev so that B^- is unstable.

To obtain an idea of the accuracy of this method of calculation, we have calculated the energy of the $1s^22s^22p^3\,^4S$ from the energies of the states of preceding ions by means of the expression for $s^2p^3\,^4S$. The calculated value of $E(1s^22s^22p^3\,^4S)$ of N I is $-2\,154\,261$ cm^{-1}, referred to the state $1s^2\,^1S$ of N VI, compared with the observed value $-2\,153\,201$. The error is -1060 cm^{-1} or 0.13 ev.

For O^-, the expression for the state $1s^22s^22p^5\,^2P$ given in Bacher-Goudsmit contain the term $1s^22p^5\,^2P$ in O II which has not yet been observed. We shall hence make use of the expression for $1s^22s2p^5\,^2P$ of O I in terms of

[1] See H. S. W. Massey, *Negative Ions* (Cambridge University Press, London, 1950).
[2] R. F. Bacher and S. A. Goudsmit, Phys. Rev. **46**, 948 (1934).
[3] T. Y. Wu, Phil. Mag. **22**, 837 (1936).
[4] J. L. Margrave, J. Chem. Phys. **22**, 636 (1954).
[5] C. E. Moore, *Atomic Energy Levels* (National Bureau of Standards, Washington, D. C., 1949).
[6] M. E. Rose, Phys. Rev. **90**, 1123 (1953).

TABLE I. Term values in cm^{-1} referred to the state $1s^2\,{}^1S$.

Atom	B	C	N	O
$1s^2\,{}^1S$	0	0	0	0
$1s^22p\,{}^2P$	257 550	455 622	708 970	
$1s^22s\,{}^2S$	305 931	520 178	789 533	1 114 000
$1s^22p^2\,{}^1D$	406 464			
$\quad{}^3P$	409 900	768 911	1 238 786	
$1s^22s2p\,{}^1P$	435 430	803 986	1 283 689	1 873 904
$\quad{}^3P$	471 478	853 971	1 347 111	1 950 289
$1s^22s^2\,{}^1S$	508 826	906 338	1 414 384	2 032 702
$1s^22p^3\,{}^4S$		960 972	1 610 207	
$1s^22s2p^2\,{}^2P$	503 213	992 344	1 651 060	2 476 455
$\quad{}^2S$			1 666 006	2 492 731
$\quad{}^2D$	527 900		1 695 983	2 530 156
$\quad{}^4P$	546 946	1 059 964	1 739 727	2 585 719
$1s^22s^22p\,{}^2P$	575 756	1 102 997	1 796 835	2 657 098
$1s^22s2p^3\,{}^1P$				2 889 833
$\quad{}^3S$		1 088 074	1 880 726	2 903 205
$\quad{}^1D$				2 913 242
$\quad{}^3P$			1 926 636	2 957 908
$\quad{}^3D$			1 943 606	2 980 250
$\quad{}^5S$		1 160 140	1 988 689	3 039 979
$1s^22s^22p^2\,{}^1S$			2 003 169	3 057 108
$\quad{}^1D$	569 120 calc.		2 020 540	3 080 021
$\quad{}^3P$	B⁻ 574 621 calc.	1 193 875	2 035 767	3 100 292
$1s^22s2p^4\,{}^2P$				3 171 193
$\quad{}^2S$				3 188 132
$\quad{}^2D$				3 217 851
$\quad{}^4P$			2 065 066	3 263 909
$1s^22s^22p^3\,{}^3P$			2 124 361	3 343 375
$\quad{}^3D$			2 133 974	3 357 026
$\quad{}^5S$		C⁻ 1 208 044 calc.	2 153 201	3 383 842
$1s^22s2p^5\,{}^1P$				3 303 842
$\quad{}^3P$				3 367 375
$1s^22s^22p^4\,{}^1S$				3 459 887
$\quad{}^1D$				3 447 811
$\quad{}^3P$			N⁻ 2 147 351 calc.	3 493 679
$1s^22s^22p^5\,{}^3P$				O⁻ 3 502 808 calc.

the states of the preceding ions, and obtain

$$
\begin{aligned}
s^2p^5\,{}^2P = {} & \tfrac{1}{3}(s^2p^4)[9\,{}^3P+5\,{}^1D+{}^1S]+\tfrac{1}{2}(sp^5)[3\,{}^3P-{}^1P] \\
& -(s^2p^3)[2\,{}^4S+5\,{}^2D+3\,{}^2P] \\
& -\tfrac{1}{2}(sp^4)[12\,{}^4P-3\,{}^3P+5\,{}^2D+{}^2S] \\
& +\tfrac{1}{2}(s^2p^2)[18\,{}^3P+10\,{}^1D+2\,{}^1P] \\
& +\tfrac{1}{2}(sp^3)[5\,{}^5S-{}^3S+10\,{}^3D+6\,{}^3P] \\
& -5(s^2p)\,{}^2P-\tfrac{1}{3}(sp^2)[18\,{}^4P+10\,{}^2D+2\,{}^2S] \\
& +(s^2)\,{}^1S+\tfrac{1}{2}(sp)[9\,{}^3P+{}^1P]-(s)\,{}^2S.
\end{aligned}
$$

The calculated energy for $1s^22s^22p^5\,{}^2P$ of O^- is $-3\,502\,808$ cm^{-1} referred to $1s^2\,{}^1S$ of O VI, and this leads to an electron affinity of 9129 cm^{-1} or 1.13 ev which is in fair agreement with the recent observed values, 1.05 ev found by Schüler and Bingel[7] and 1.48 ev found by Branscomb and Smith.[8]

[7] V. H. Schüler and W. Bingal, Z. Naturforsch. **10A**, 252 (1955).
[8] L. M. Branscomb and S. J. Smith, Phys. Rev. **98**, 1127 (1955), and private communication (to appear in J. Research Natl. Bur. Standards).

Statistical Theory of Delayed-Coincidence Experiments*

Z. Bay,† V. P. Henri,‡ and H. Kanner§
The George Washington University, Washington, D. C.

(Received October 15, 1953; revised manuscript received June 30, 1955)

The consistent use of a general statistical theory makes possible the elimination of ambiguities and of idealizing assumptions from the interpretation of delayed-coincidence experiments. Introduction of the concept of the "total coincidence counting rate" (which can be determined experimentally) makes possible the definition of resolving time, thereby eliminating discrepancies between earlier definitions; it also provides means for relating the coincidence efficiencies directly to the number of source events.

The effect of random time lags on coincidence curves is calculated and experimental methods for the determination of time lags are derived. The statistical errors in the determination of moments of a coincidence curve are calculated and outlined in detail for first moment investigations. It is shown that: (1) the best choice of the resolving time is a (experimentally measurable) weighted rms of all time delays present in the measurement; (2) using the best choice of the resolving time the standard error of the centroid, obtained by successive measurements of the points of a coincidence curve, is approximately twice the least theoretical standard error (that could be obtained for the total time of observation); (3) the moment method can be applied generally for the determination of mean time delays; other methods, while applicable with some restrictions, can lead to similar or greater statistical errors.

I. GENERAL CONSIDERATIONS

A CONSEQUENCE of recent improvements[1–10] in coincidence counting techniques is that a reformulation of some basic definitions has become necessary. For example, two hitherto equivalent definitions of the resolving time of a coincidence circuit are no longer equivalent or even, strictly speaking, meaningful. We shall demonstrate that a consistent and unambiguous set of definitions for all parameters needed in the interpretation of delayed-coincidence measurements can be formulated in terms of experimentally observable quantities without any idealizing assumptions or approximations.

The basic equation for delayed coincidence experiments is given by the convolution integral[11–15]:

$$N(T)=\int_{-\infty}^{+\infty} P(T-t)w(t)dt, \qquad (1)$$

where T is the inserted time delay, $N(T)$ is the coincidence curve for the source whose decay time is to be measured, $P(T)$ (usually termed a "prompt" curve) is the coincidence curve for a source of simultaneous events, and $w(t)$ is the normalized probability density for the time interval t between entry of particles of the source to be measured into the respective detectors. $P(T)$ and $N(T)$ are meant to be taken with the same source strength. Equation (1) is valid under the following conditions: (a) the quantities t and T are interchangeable, i.e., the inserted delay mechanism does not materially affect the pulse shapes; (b) the pulse shape distributions in the respective channels are the same for both sources. Condition (a) usually offers no experimental difficulty, as one generally uses short delay cables with negligible attenuation. Condition (b) can be met either by assuring that the same type and energy of radiation enters the detectors from both sources,[9] or by eliminating the effect of any discrepancy between the radiations by proper pulse shaping or pulse height selection.

As has been pointed out earlier,[14] a consequence of Eq. (1) is that the moments of N can be expressed in terms of those of P and w by the relations

$$M_r(N)=\sum_{k=0}^{r}\frac{r!}{k!(r-k)!}M_{r-k}(P)M_k(w), \qquad (2)$$

where

$$M_r(N)=\int_{-\infty}^{+\infty} T^r N(T)dT.$$

This set of equations can be solved for the moments of w, thus determining the latter function. If w is known except for the values of a finite set of parameters, as many of Eqs. (2) will be needed as there are parameters to be evaluated. It is convenient to rewrite Eqs. (2) in terms of the normalized moments $\mu_r=M_r/M_0$. Since

* This work was supported by the joint program of the Office of Naval Research and the U. S. Atomic Energy Commission.
† Now at National Bureau of Standards, Washington D. C.
‡ Now at Northeastern University Boston, Massachusetts.
§ Now at Shell Research and Development, Houston, Texas.
[1] Z. Bay and G. Papp, Rev. Sci. Instr. **19**, 565 (1948).
[2] R. E. Bell and H. E. Petch, Phys. Rev. **76**, 1409 (1949).
[3] Meyer, Baldinger, and Huber, Helv. Phys. Acta **23**, 121 (1950).
[4] R. Hofstadter and J. A. McIntyre, Phys. Rev. **78**, 24 (1950).
[5] M. Deutsch and W. E. Wright, Phys. Rev. **77**, 139 (1950); Phys. Rev. **82**, 277 (1951).
[6] F. K. McGowan, doctoral thesis, Oak Ridge National Laboratory Report ORNL-952, 1951 (unpublished).
[7] Z. Bay, Rev. Sci. Instr. **22**, 397 (1951).
[8] S. De Benedetti, Rev. Sci. Instr. **23**, 37 (1952).
[9] Bell, Graham, and Petch, Can. J. Phys. **30**, 35 (1952).
[10] R. L. Graham and R. E. Bell, Can. J. Phys. **31**, 377 (1953).
[11] H. Bradt and P. Scherrer, Helv. Phys. Acta **16**, 251 (1943); **16**, 259 (1943).
[12] F. W. Van Name, Phys. Rev. **75**, 100 (1949).
[13] D. Binder, Phys. Rev. **76**, 856 (1949).
[14] Z. Bay, Phys. Rev. **77**, 419 (1950).
[15] T. D. Newton, Phys. Rev. **78**, 490 (1950).

$M_0(N)=M_0(P)$ for equal source strengths, one obtains

$$\mu_r(N)=\sum_{k=0}^{r}\frac{r!}{k!(r-k)!}\mu_{r-k}(P)\mu_k(w). \tag{3}$$

Since the normalized moments are independent of the source strengths, Eq. (3) is valid for any source strength.

Another parameter, the "total coincidence counting rate," to be denoted by C, will be needed for a clear understanding of the phenomena involved.[16] In particular, it is necessary for the definition and determination of resolving time and efficiency and for the investigation of time lags and statistical errors. We define a "coincidence-countable" pulse pair to be a pair of pulses, one from each detector, having the property that they will produce a coincidence count for some range or set of ranges of T of nonzero measure. The property that a pair of pulses be coincidence-countable is then dependent on the shapes of both pulses and the operation of the coincidence circuit but independent of the relative time orientation of the two pulses. The quantity C is then defined to be the number of coincidence-countable pulse pairs which originate in unit time from related events at the source.

The description of the following thought experiment may serve to clarify the definition of C. Let a multichannel delayed-coincidence apparatus observe the pulses from two detectors, using a source of related events. By a multichannel apparatus is meant a system in which the detector outputs are branched and simultaneously observed by a number of delayed-coincidence circuits, each having a different fixed value of T but being otherwise identical. Thus, a finite set of points spanning the delay curve is obtained in one measurement. Now, let the discriminator outputs of all the coincidence circuits go to one scaling circuit of sufficiently great dead time that only one count will be registered for one source event, regardless of how many of the coincidence circuits respond to it. Then the counting rate registered by the scaler will (after substraction of the chance coincidence counting rate in the usual way) asymptotically approach C as the number of channels is increased indefinitely with a proportional decrease in ΔT, the interval between adjacent T values.

Note.—The operational conditions of the coincidence circuit change from time to time because of internal noise. Therefore it may happen (in the case of small pulses) that the same pulse pair which is coincidence countable in one state of noise is not coincidence countable in another state. The quantity C, given by the above definition and appearing as the result of the above thought experiment, is an expectation over the pulse-shape distribution and over the distribution of all noise parameters inherent in the coincidence circuit.

Practical methods for the direct experimental measurement of C have been devised[17,18]; the general principle will be described briefly in Sec. IV and the methods presented in detail in another paper.[19]

The theory can further be developed most simply in terms of $p(T)=P(T)/C$ and $n(T)=N(T)/C$, which will be called "reduced coincidence curves." These functions define the probability of a single coincidence-countable pulse pair producing a delayed coincidence count for a delay of value T. In terms of p and n, Eq. (1) can be rewritten as

$$n(T)=\int_{-\infty}^{+\infty}p(T-t)w(t)dt. \tag{4}$$

By applying the moment theorem of Eq. (2) to p and n, one obtains the important result:

$$M_0(n)=M_0(p), \tag{5}$$

i.e., the area under a reduced coincidence curve is independent of the source strength and independent of time delays at the source. Furthermore, since the coincidence circuit cannot distinguish time delays at the source from those introduced by the detectors or the coincidence device, the above statement can be extended to read; the area under a reduced coincidence curve is independent of all time delays, regardless of origin. For a given coincidence circuit, this area depends only on the pulse-shape distributions.

Application of Eq. (2) to a simple parent-daughter decay is straightforward.[14] If one detector responds only to one of the particles, which case will be called "asymmetric" (as, for example, in a $\beta-\gamma$ experiment), then

$$\mu_1(N)=\mu_1(P)+\theta, \tag{6}$$

i.e., the mean life θ is given by the displacement of the centroids of the N and P curves.

In the event that both detectors have the same response to either particles, which case is termed "symmetric" (as is true in a $\gamma-\gamma$ experiment with γ's of similar energy), and in a coordinate system in which $\mu_1(P)=0$, Eq. (3) yields

$$\mu_2(N)=\mu_2(P)+2\theta^2. \tag{7}$$

The generalization of the theory to the analysis of the mean lives of a radioactive family will be given in Appendix A.

II. RESOLVING TIME

A careful analysis shows that two different time magnitudes are needed to describe the resolution of a coincidence device and the statistical accuracy of time measurements[16] and by their use the inconsistencies between several earlier definitions of the resolving time can be eliminated. The problems encountered in attempting to define the resolving time of a coincidence circuit can best be appreciated by considering some simple cases.

First, let us assume that all pulses in a given channel are of the same shape and that no random time lags between events and pulses are introduced by the equipment. Then there will be a well-defined interval in the time coordinate describing the separation of the members of a pulse pair for which a coincidence will be

[16] Z. Bay, Phys. Rev. **87**, 194 (1952).
[17] Z. Bay, Phys. Rev. **83**, 242 (1951).
[18] Bay, Meijer, and Papp, Nucleonics **10**, No. 3, 38 (1952).
[19] Bay, Henri, and McLernon (to be published).

recorded. Without loss in generality the possibility that this interval consists of several separate subintervals can be disregarded here. The resolving time, τ, is customarily defined as half of the magnitude of this interval, and could be measured experimentally in two ways. One could either measure the coincidence curve for a prompt source, obtaining a rectangular curve of width 2τ, or one could observe the chance coincidence counting rate, N_c, for unrelated sequences of pulses in the two channels, obtaining

$$N_c = N_A N_B \cdot 2\tau, \tag{8}$$

where N_A and N_B are the respective "singles" counting rates.

Now, let us introduce random time lags between the actual events and the pulses which come from them. The value of τ will be unchanged, and can be determined as before from Eq. (8), since the chance coincidence counting rate will not be influenced by the random lags. However, the prompt coincidence curve will be broadened and will no longer be of rectangular shape. The maximum of the prompt curve will even be lowered if *any* of the random time lags exceed τ. Despite the distortion of the coincidence curve, there is a convenient functional of it that will yield τ. Noting that in the absence of random time lags, the height of the rectangular coincidence curve will be C, the area of the curve divided by C will be 2τ. Now, invoking the principle expressed by Eq. (5), that the area of a reduced coincidence curve is independent of time delays, we can write

$$\tau = \frac{1}{2C}\int_{-\infty}^{+\infty} P(T)dT = \frac{1}{2}\int_{-\infty}^{+\infty} p(T)dT, \tag{9}$$

which is also valid if $P(T)$ is replaced by $N(T)$, the coincidence curve for any source of related events, prompt or otherwise.

On the other hand, we see that the width of the coincidence curve is no longer given by the resolving time, τ. Nevertheless, the width of the prompt coincidence curve determines the statistical accuracy of the measurement of time delays. Therefore, it is desirable to introduce a second characteristic time, τ', that is a measure of this width. Theoretically, the best choice would be the square root of the normalized second moment about the mean of the prompt curve, $\sigma = \{\mu_2 - \mu_1^2\}^{\frac{1}{2}}$, which appears in the calculations of statistical accuracy. However, in practice, one prefers to choose a quantity which is easier and quicker to calculate from the data. Therefore we choose the definition

$$\tau' = \frac{1}{2p_{\max}}\int_{-\infty}^{+\infty} p(T)dT = \frac{1}{2P_{\max}}\int_{-\infty}^{+\infty} P(T)dT, \tag{10}$$

which has the virtues that τ' reduces to τ in the absence of time lags, and that τ' is usually very close to the half-width at half-maximum of the coincidence curve, being the half-width of the rectangle that has the same height and area as the curve.

If one writes

$$\tau'^2 = \alpha\sigma^2, \tag{11}$$

the constant α is of the order of magnitude unity for the types of delay curves usually obtained. This can be seen from the examination of a few analytical functions. For example, for a simple exponential $\alpha = 1$, for an isoceles triangle $\alpha = \frac{2}{3}$, for a Gaussian $\alpha = \pi/2$, and for the extreme case of a rectangle $\alpha = 3$. Therefore, in the estimation of statistical error one is often justified in using τ' instead of σ.

The final step is to extend the definitions to the general case in which each channel receives a distribution of pulse shapes. Then a resolving time can be defined in the original manner for every possible kind of coincidence-countable pulse pairs, and τ should be the average of these resolving times over the pulse shape distributions. We again consider first the case of no random time lags, and describe all possible coincidence-countable pulse pairs by a running index "k." Letting C_k be the number of "type k" pulse pairs appearing in unit time, the prompt coincidence curve will be given by

$$\Psi(T) = \sum_k C_k \psi_k(T), \tag{12}$$

where ψ_k is the coincidence curve for a single "type k" pulse pair, i.e., a rectangle of unit height and of the width $2\tau_k$. Without loss in generality, we can assume here that all $\psi_k(T)$ have the same centroid, as failure to meet this condition can be compensated for by introduction of appropriate time lags. Then, since $\sum C_k = C$, the maximum of $\Psi(T)$ will be C, and the average resolving time, τ, will be given by

$$\tau = \frac{\sum C_k \tau_k}{\sum C_k} = \frac{1}{2C}\sum C_k \int_{-\infty}^{+\infty} \psi_k(T)dT = \frac{1}{2C}\int_{-\infty}^{+\infty} \Psi(T)dT, \tag{13}$$

as before.

The internal noise of the coincidence circuit causes fluctuations in τ_k. These will be taken into consideration in Sec. III. Replacing τ_k in Eq. (13) by its average for "type k" pulse pairs, Eq. (13) and the above derivation remain valid for the general case.

The argument already given for the case of uniform pulses again serves to extend Eq. (9) to apply to coincidence curves influenced by random time lags. Thus, 2τ is always given by the area of the reduced coincidence curve $p(T)$ or $n(T)$.

The chance coincidence counting rate will still be given by Eq. (8), provided the quantity $N_A N_B$ only includes coincidence-countable pulse pairs.

The definition of τ' is based on the shape alone of the observed prompt coincidence curve and will also be given in the general case by Eq. (10). In the literature

both τ [defined by Eq. (8)] and τ' have occasionally been called "resolving time." We suggest calling τ the "resolving time" and τ' either the "practical resolving time" or, better, just the "half-width of the prompt curve." Since $p_{max} \leq C$, one always has $\tau' \gg \tau$.

III. EFFECT OF TIME LAGS ON COINCIDENCE CURVES

We will investigate the effect of time lags originating (1) in the detectors and (2) in the rest of the equipment. First we consider prompt events.

(1) The pulses of a "type k" pulse pair both appear with some time delay after the events; the difference of these time delays will be denoted by t_k'. It must be noted that the definition of t_k' is arbitrary since no unique definition for the timing of pulses of different shape can be given. (For example, one can define the time of appearance of a pulse as the center of gravity of a voltage curve or as the time at which the output voltage, or current, rises to a given level, etc.). However, when changing from one definition to another, only the origin of the t_k' axis will change and the variance $v(t_k')$, which is the quantity of greater interest in the investigation of time lags, remains unaltered.

(2) The "type k" pulse pairs for which $t_k'=0$ produce a prompt curve which will be denoted by $P_{k0}(T)$. If there were no statistical fluctuations in the coincidence circuits, P_{k0} would be a rectangle of height C_k, width $2\tau_k$, with its center at (say) T_k. One could then regard $T_k=t_k''$ (where $T=0$ corresponds to equal inserted time delays in the two channels of the coincidence circuit) as the time lag originating in the coincidence equipment (excluding the detectors). One should note that while t_k'' depends on the definition used for t_k', the sum $t_k'+t_k''$ (for prompt events) is independent of that definition.

Now, if $\rho_k'(t_k')$ is the probability density for t_k' and if $t_k=t_k'+t_k''$, the probability density for t_k will be $\rho_k(t_k)=\rho_k'(t_k')$ since t_k'' is a constant. Therefore, when ignoring the fluctuations (noise) of the coincidence circuit,

$$P_k(T)=C_k\int_{-\infty}^{+\infty}\psi_k(T-t_k)\rho_k(t_k)dt_k, \tag{14}$$

where $\psi_k(T)$ is a rectangle of height unity, width $2\tau_k$, with its center at $T=0$.

The prompt curve for all types of pulse pairs is

$$P(T)=\sum_k C_k\int_{-\infty}^{+\infty}\psi_k(T-t_k)\rho_k(t_k)dt_k, \tag{15}$$

its centroid is

$$\mu_1(P)=\frac{\sum C_k 2\tau_k\mu_1(\rho_k)}{\sum C_k 2\tau_k}=\frac{\sum C_k 2\tau_k \bar{t}_k}{\sum C_k 2\tau_k}, \tag{16}$$

and using the notation $\sigma^2=\mu_2-\mu_1^2$, one has

$$\sigma^2(P)-\sigma^2(\Psi)=\frac{\sum C_k 2\tau_k\{v(t_k')+[\bar{t}_k-\mu_1(P)]^2\}}{\sum C_k 2\tau_k}$$

$$=\frac{\sum C_k 2\tau_k\langle[t_k-\mu_1(P)]^2\rangle_{Av}}{\sum C_k 2\tau_k}, \tag{17}$$

where

$$\Psi(T)=\sum_k C_k\psi_k(T). \tag{18}$$

The right-hand sides of Eqs. (16) and (17) represent the weighted mean and weighted mean square deviation of the time lags, with the weighting factors $2\tau_k$ for t_k.

Now, to take into account also the effect of statistical fluctuations originating in the coincidence circuit, we consider again the "type k" pulse pairs for which $t_k'=0$. Identical pulse pairs now produce different coincidence curves, depending on the state of internal noise of the coincidence circuit. If one distinguishes by a running index l the different states of noise of the circuit, each determined by a set of values of all the noise parameters, then for each such "state l" there will be a $\psi_{kl}(T)$ rectangular curve of height unity and width $2\tau_{kl}$ around $T=0$, a C_{kl} total coincidence rate, and a t_{kl}'' time lag. The prompt curve $P_{k0}(T)$ will therefore be

$$P_{k0}(T)=\sum_l C_{kl}\psi_{kl}(T-t_{kl}''), \tag{19}$$

and

$$P_k(T)=\sum_l C_{kl}\int_{-\infty}^{+\infty}\psi_{kl}[T-(t_k'+t_{kl}'')]\rho_k'(t_k')dt_k'. \tag{20}$$

The centroid is given by

$$\mu_1(P_k)=\frac{\sum_l C_{kl}2\tau_{kl}\{\mu_1(\rho_k')+t_{kl}''\}}{\sum_l C_{kl}2\tau_{kl}}=\frac{\sum_l C_{kl}2\tau_{kl}\bar{t}_{kl}}{\sum_l C_{kl}2\tau_{kl}}, \tag{21}$$

and

$$\sigma^2(P_k)-\sigma^2(\Psi_k)$$

$$=\frac{\sum_l C_{kl}2\tau_{kl}\{v(t_k')+[\bar{t}_{kl}-\mu_1(P_k)]^2}{\sum_l C_{kl}2\tau_{kl}}, \tag{22}$$

where

$$\Psi_k(T)=\sum_l C_{kl}\psi_{kl}.$$

The prompt curve $P(T)$ in the general case for all types of pulse pairs is

$$P(T)=\sum_k P_k(T)$$

$$=\sum_k\sum_l C_{kl}\int_{-\infty}^{+\infty}\psi_{kl}[T-(t_k'+t_{kl}'')]\rho_k'(t_k')dt_k', \tag{23}$$

the centroid is

$$\mu_1(P)=\frac{\sum_k\sum_l C_{kl}2\tau_{kl}\bar{t}_{kl}}{\sum_k\sum_l C_{kl}2\tau_{kl}}=\frac{\sum_k C_k 2\bar{\tau}_k\bar{t}_k}{\sum_k C_k 2\bar{\tau}_k}, \tag{24}$$

and

$$\sigma^2(P)-\sigma^2(\Psi) = \frac{\sum_k\sum_l C_{kl}2\tau_{kl}\{v(t_k')+[\bar{t}_{kl}-\mu_1(P)]^2\}}{\sum_k\sum_l C_{kl}2\tau_{kl}}, \quad (25)$$

where

$$\Psi(T)=\sum_k\Psi_k(T)=\sum_k\sum_l C_{kl}\psi_{kl}.$$

Equations (24) and (25) show that, also in the general case, when time delays of all origins are taken into account, the coincidence equipment "sees" the weighted average and weighted mean square deviation of the time lags, with the weighting factors equal to the individual resolving times. In addition, one can see that the effect of internal noise in the coincidence circuits is (1) to change the form of $\Psi(T)$ and (2) to introduce additional time lags appearing as fluctuations of t_k''.

The occurrence of these weighted statistics in the operation of the coincidence equipment can readily be understood in the following way: In a multichannel arrangement consisting of a large number of identical coincidence circuits with an inserted time delay ΔT between them, every "type k" input pulse pair would give a coincidence output simultaneously in $2\tau_k/\Delta T$ channels. Therefore in the calculation of the area and of higher moments of the $P(T)$ curve a "type k" pulse pair occurs with the relative frequency $C_k2\tau_k/\Sigma C_k2\tau_k$ instead of $C_k/\Sigma C_k$. What is true for a multichannel equipment is also true for the one-channel equipment since it gives a similar $P(T)$ coincidence curve in the successive measurements.

In Eq. (25), $\sigma^2(\Psi)$ represents the smallest possible width of the prompt curve compatible with the given pulse shape distribution and resolving times τ_{kl} of the equipment (i.e., a prompt curve without time lags, which could be called "prompt-prompt" curve) and the right side of the equation describes the broadening of the prompt curve by time lags. Introducing now the symbol $\bar{t}^2$ for the right sides of Eqs. (17) and (25), one can write

$$\sigma^2(P)=\sigma^2(\Psi)+\bar{t}^2. \quad (26)$$

It should be noted that $\Psi(T)$ can be determined in principle (e.g., by pulse-shape selection, approximated by pulse-height selection) but in most cases it is sufficient simply to write

$$\sigma^2(\Psi)=(1/\alpha)\tau^2, \quad (27)$$

and consequently

$$\sigma^2(P)=(1/\alpha)\tau^2+\bar{t}^2, \quad (28)$$

where α is the same as in Eq. (11), and can be estimated fairly well with some knowledge of the amplitude distribution.

Generalization to the case of the $N(T)$ curve can be obtained simply by adding the first and second moments of the $w(t)$ curve. Therefore,

$$\sigma^2(N)=(1/\alpha)\tau^2+\bar{t}^2+\sigma^2(w). \quad (29)$$

The problem of the variation of $\sigma^2(P)$ with varying conditions in the coincidence circuit is important for Sec. VI. There are methods for varying τ; $v(t_k')$ cannot be reduced below some theoretical limits for scintillation counters and little is known about the time lags $\bar{t}_k=\bar{t}_k'+\bar{t}_k''$ for different pulse shapes (or amplitudes).

The variation of $\bar{t}$ for different values of τ was investigated in a differential coincidence circuit. Using $\gamma-\gamma$ coincidences from Ni^{60} (established as "prompt" within 10^{-11} second[29]) and stilbene scintillators, τ alone was varied and the reduced coincidence curves taken. For τ varying from 7.9×10^{-10} second to 1.65×10^{-10} second, $\bar{t}$, calculated from Eq. (26) with $\alpha=\pi/2$ (i.e., taking Ψ to be Gaussian, since no pulse height selection was used), varied by less than 2 percent around its mean value 10.5×10^{-10} second. Thus for the differential coincidence circuit the functional dependence of $\sigma^2(P)$ on τ as given in Eq. (28) with constant α and constant $\bar{t}$ can be used.

Equations (17) or (25) can be used to obtain an estimate of time fluctuations of scintillation counters. This is important since, to our knowledge, no other methods are at present available to determine these time fluctuations.

For symmetric excitations of the two detectors, as in the above experiment, one can regard $\bar{t}/\sqrt{2}$ as the weighted rms of the time lags related to one channel. This gives 7.5×10^{-10} second for stilbene, 6.5×10^{-10} second for diphenyl acetylene and 3.5×10^{-10} second for diphenyl acetylene when a pulse-clipping method is used (anode pulses shorted by dynode pulses[31]). Since these values are near to the theoretical expectations for the scintillators[22,33] plus time lags in photomultipliers, one can conclude that the spread of time lags attributable to the varying pulse shapes is small ($\sim10^{-10}$ second or less), at least in the differential coincidence circuit. Using Čerenkov counters,[34] $\bar{t}/\sqrt{2}\sim2\times10^{-10}$ second was obtained, this can be attributed to the photomultipliers. Time lags due to the fluctuations of t_k'' have been investigated by the use of pulses branched from one detector (where $t_k'=0$) and were found to be of the order of a few times 10^{-11} second for a differential coincidence circuit, i.e., about one order of magnitude smaller than the time lags $\sqrt{v(t_k')}$ for scintillation counters.

To obtain results more specialized than the above weighted averages, e.g., for scintillation counters, and in particular to obtain the dependency of $v(t_k')$ on the total number of photoelectrons utilized, one has to apply Eqs. (17) or (25) with pulse-height selection in the experiment.

IV. EXPERIMENTAL DETERMINATION OF C

Figure 1 illustrates a possible scheme for obtaining the coincidence curve $N(T)$ and the value of C appro-

[29] Bay, Henri, and McLernon, Phys. Rev. **97**, 561 (1955).
[31] Bay, Henri, and McLernon, Phys. Rev. **90**, 371 (1953).
[33] R. F. Post, Nucleonics **10**, No. 5, 46 (1952).
[22] R. F. Post and L. I. Schiff, Phys. Rev. **80**, 1113 (1950).
[34] Bay, Cleland, and McLernon, Phys. Rev. **87**, 901 (1952).

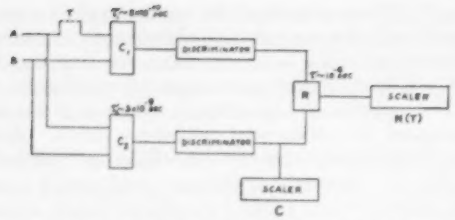

FIG. 1. Block diagram of the equipment for the determination of C.

priate to that curve. In the figure, C_1 represents the fast circuit, with a resolving time τ_1, that yields the coincidence curve; C_2 represents a similar circuit having a resolving time τ_2 at least an order of magnitude greater than both θ and $\bar{l}$. The type of coincidence circuits used for C_1 and C_2 in this measurement is immaterial. In Fig. 1, $\tau_1 \sim 2\times10^{-10}$ second and $\tau_2 \sim 3\times10^{-9}$ second are shown as used in an actual experiment. The level of the discriminator following C_2 is set sufficiently high and that of C_1 sufficiently low (even tolerating noise pulses in C_1), that any pulse pair yielding an output from C_2 great enough to trigger C_2's discriminator is certain to produce an output from C_1's discriminator if the delay time, T, is correctly chosen. R represents a far slower coincidence circuit, the purpose of which is to determine whether a pair of outputs from C_1 and C_2 stem from the same source events. The output counting rate of R as a function of T will be the coincidence curve $N(T)$, and the counting rate of the discriminator following C_2 will be C. In actual experiments,[20,25] we used for C_1 a differential coincident circuit in which one can vary τ independently of the pulse length.

Having determined C, one can use the reduced coincidence curve which is normalized to one pair of events, and present the following advantages:

(1) No correction is needed for the decrease in strength of a radioactive source while making a measurement.

(2) The change of solid angle and thereby counting efficiency introduced by displacing the source, as is done in some time-of-flight measurements, does not affect the reduced coincidence curve.

(3) If instead of utilizing the moments of the coincidence curves for the time measurements one uses a portion of the steep part of the curves (slope method), then if one measures C it is not necessary to normalize the prompt and delayed curves to the same area and therefore one does not need to measure the entire coincidence curves.

(4) If an initially unknown number of prompt coincidences is mixed with the desired pulses whose lifetime is to be measured, then one attempts to find out the ratio of mixing by introducing some changes in the experimental conditions. In such a case it is easier and faster to record changes of C than changes of areas of the coincidence curves.

(5) The C_2 circuit monitors the equipment and diminishes the effect of temporal fluctuations during the experiment.

[25] Bay, Henri, and McLernon, Phys. Rev. **97**, 1710 (1955).

V. COINCIDENCE EFFICIENCY

The chance coincidence counting rate was given in Eq. (8) as $N_A N_B \cdot 2\tau$, valid only if all pulse pairs are coincidence-countable. Equation (8) can be written in terms of the disintegration rate, ν, of the source by introduction of ϵ_A and ϵ_B, the efficiencies for the counting of singles:

$$N_c = \nu^2 \epsilon_A \epsilon_B \cdot 2\tau. \tag{30}$$

It should be noted that N_c as used in this section contains only chance coincidences originating from the source events. Other types of chance coincidences may be present in a given experiment and N_c should be corrected for them.

In practice, not all pulse pairs are coincidence-countable, and Eq. (30) must be modified to

$$N_c = \nu^2 \epsilon_A \epsilon_B \epsilon_c \cdot 2\tau, \tag{31}$$

where ϵ_c is a proportionality factor for the pulse pairs that are coincidence-countable. Although it is common practice to regard a quantity such as ϵ_c as the efficiency of the coincidence circuit proper, ϵ_c has no fixed value for a given circuit since it depends on the values of ϵ_A and ϵ_B, which in turn are determined by arbitrary discrimination levels. (In fact, it is possible to choose ϵ_A and ϵ_B in such a manner that ϵ_c is greater than unity.) However, the product $\epsilon = \epsilon_A \epsilon_B \epsilon_c$ is well defined, being the fraction of source events yielding coincidence-countable pulse pairs.

For the experimental determination of ϵ, we use the relation

$$C = \nu\epsilon. \tag{32}$$

By Eqs. (9), (31), and (32), ϵ can be expressed in terms of experimentally observable quantities as

$$\epsilon = C\int_{-\infty}^{+\infty} N(T)dT \Big/ N_c$$

$$= \left[\int_{-\infty}^{+\infty} N(T)dT\right]^2 \Big/ 2\tau N_c. \tag{33}$$

Equation (33) shows that ϵ is independent of time magnitudes such as $\bar{l}$, θ, and τ, and that it is also independent of the source strength ν and can be determined experimentally without knowledge of the source strength. Furthermore, ϵ (being independent of θ) is the same for the prompt and decaying sources. Since ϵ is the ratio of the number of coincidence-countable pulse pairs to the number of source events [Eq. (32)], we call it the coincidence yield of the experiment.

The ordinates of the reduced coincidence curves $n(T)$ and $p(T)$ give the fraction of coincidence-countable pairs which are in the proper time-delay interval (given by 2τ) around T and which therefore will be counted. It is usual to call $p_{max}=P_{max}/C$ the "coincidence efficiency" (as in reference 9). In general, one can call $p(T)$ and $n(T)$ the "coincidence-counting efficiencies" at T, which are related to the number of coincidence-countable pulse pairs. One also can directly relate the counting efficiencies to the number of source events by multiplying $p(T)$ and $n(T)$ by the coincidence yield ϵ.

VI. STATISTICAL ACCURACY OF MEAN-LIFE DETERMINATIONS

In the measurement of an individual point at T_i of a curve $N(T)$, $n_i=n(T_i)$ is the probability of obtaining a coincidence count per countable pulse pair. Let the duration of observation for one point be $[t]$ and let the number of countable pulse pairs occurring during $[t]$ be $\mathfrak{C}$ and the number of observed counts be $\mathfrak{N}_i$. Then, $\mathfrak{N}_i$ may be regarded as the number of successes in $\mathfrak{C}$ trials, with an *a priori* probability of success n_i. For a given $\mathfrak{C}$, $\mathfrak{N}_i$ follows a Bernoulli distribution, its mean being $\mathfrak{C}n_i$ and its variance $v(\mathfrak{N}_i)=\mathfrak{C}n_i(1-n_i)$.

In the following, we have to distinguish between two different cases.

(1) *C is not measured.*—The number of trials $\mathfrak{C}$ during $[t]$ fluctuates from point to point and

$$v(\mathfrak{N}_i)=\langle\mathfrak{C}\rangle_{Av}n_i(1-n_i)+n_i^2v(\mathfrak{C}). \tag{34}$$

With a Poisson distribution for $\mathfrak{C}$ around its mean value

$$\langle\mathfrak{C}\rangle_{Av}=[t]C,$$

the variance is found to be

$$v(\mathfrak{N}_i)=[t]Cn_i; \tag{35}$$

or, if one regards sampling values as experimental estimates for population values, and uses the same notation for sampling and population values, one gets

$$v(\mathfrak{N}_i)\cong\mathfrak{N}_i, \tag{36}$$

$$v(N_i)\cong N_i/[t], \tag{37}$$

$$v(n_i)\cong n_i/[t]C. \tag{38}$$

If the coincidence curve is obtained from a set of $\mathfrak{N}_i$'s taken at equidistant T_i values, μ_r can be approximated by $\sum T_i^rN_i/\sum N_i$. Taking the same $[t]$ for each point and employing the usual method of treatment of the propagation of errors,

$$\sigma^2(\mu_r)=\frac{\sum(T_i^r-\mu_r)^2N_i}{(\sum N_i)^2[t]}=\frac{\mu_{2r}-\mu_r^2}{\mathfrak{N}}, \tag{39}$$

where $\mathfrak{N}=\sum\mathfrak{N}_i$ is the total number of counts observed along the entire coincidence curve.

The variance of θ in terms of those of the moments used is

$$v(\theta)=\sigma^2[\mu_1(N)]+\sigma^2[\mu_1(P)] \tag{40}$$

for the asymmetric case, and

$$v(\theta)=\frac{1}{16\theta^2}\{\sigma^2[\mu_2(N)]+\sigma^2[\mu_2(P)]\} \tag{41}$$

for the symmetric case.

Simple formulas, particularly useful for order-of-magnitude estimates when planning experiments, result from the use of an approximation. This consists of fitting a Gaussian to the prompt-coincidence curve $P(T)$ and expressing all pertinent moments of $P(T)$ and $N(T)$ in terms of τ'/θ.[26] If one also takes $\mathfrak{N}$ to be the same for the two curves, then

$$\frac{v(\theta)}{\theta^2}=\frac{1}{\mathfrak{N}}\left\{1+\frac{4}{\pi}\left(\frac{\tau'}{\theta}\right)^2\right\} \tag{42}$$

for the asymmetric case, and

$$\frac{v(\theta)}{\theta^2}=\frac{1}{\mathfrak{N}}\left\{\frac{5}{4}+\frac{1}{\pi}\left(\frac{\tau'}{\theta}\right)^2+\frac{1}{\pi^2}\left(\frac{\tau'}{\theta}\right)^4\right\} \tag{43}$$

for the symmetric case.

Valuable information is obtainable from Eq. (39) concerning the optimal use of coincidence equipments among given circumstances. We restrict our discussion to the statistical error of μ_1, in the asymmetric case.

We determine first how to choose the best value of the resolving time for measuring a given lifetime and for a given time of observation. We assume that $\bar{l}$ is unaffected by the variation of τ as was shown to be the case for a differential coincidence circuit (Sec. III).

Using the notations of Eqs. (11), (26), and (28), one can write

$$\sigma^2[\mu_1(P)]=\frac{\mu_2(\Psi)+\bar{l}^2}{\mathfrak{N}}=\frac{\alpha^{-1}\tau^2+\bar{l}^2}{\mathfrak{N}}. \tag{44}$$

For $\mathfrak{N}$ we substitute

$$\mathfrak{N}=[t]C\sum n_i=[t]C2\tau/\Delta T, \tag{45}$$

where ΔT is the distance between two adjacent points. The measured points m are distributed along the length T_m-T_1 which is proportional to the width of the coincidence curve. Thus, writing

$$T_m-T_1=2\kappa\{\mu_2(P)-\mu_1^2(P)\}^{\frac{1}{2}}, \tag{46}$$

we have

$$\sigma^2[\mu_1(P)]=\frac{\kappa}{[T]C}\frac{(\alpha^{-1}\tau^2+\bar{l}^2)^{\frac{1}{2}}}{\tau}, \tag{47}$$

where $[T]=m[t]$ is the total time of observation for the entire coincidence curve. The value of κ will be

[26] Kanner, Bay, and Henri, Phys. Rev. **90**, 371 (1953).

discussed later. Equation (47) yields the optimal τ, denoted by τ_0, for which $\sigma^2[\mu_1(P)]$ is a minimum. We have

$$\tau_0^2=\tfrac{1}{2}\alpha\bar{l}^2, \tag{48}$$

and

$$\sigma^2[\mu_1(P)]=\left[\frac{3}{\alpha}\right]^{\frac{1}{3}}\frac{\kappa}{2[T]}. \tag{49}$$

When $\Psi(T)$ is a Gaussian, $\alpha=\pi/2$. When it is a rectangle, $\alpha=3$. Since $\Psi(T)$ is most probably between these two extreme cases, it is safe to write Eq. (48) as

$$\tau_0^2\sim\bar{l}^2 \tag{50}$$

for the $P(T)$ curve and

$$\tau_0^2\sim\bar{l}^2+\theta^2 \tag{51}$$

for the $N(T)$ curve. Thus the best choice for τ is the weighted rms of the time delays present in the measurement. This choice of τ corresponds to a $p_{\max}$ being ~ 60 to 70 percent of C [depending somewhat on the shape of the $\Psi(T)$ curve].

Since both $P(T)$ and $N(T)$ are involved in the measurement of a lifetime, the resulting optimal choice for τ will be determined by $\bar{l}, \theta$, and the intensities of the prompt and decaying sources.

With τ_0, and $\alpha\sim 2$, one can write

$$\sigma^2[\mu_1(P)]\sim\frac{2\kappa}{[T]C}\bar{l}^2, \tag{52}$$

and

$$\sigma^2[\mu_1(N)]\sim\frac{2\kappa}{[T]C}(\bar{l}^2+\theta^2). \tag{53}$$

The factor κ is the range of the measured interval relative to the width of the curve. It is of practical interest to have κ as small as possible, i.e., to avoid long measurements with small counting efficiencies. Utilizing some geometrical properties present in individual cases, one finds means to shorten T_m-T_1. In practice one seldom needs $\kappa>3$ (or T_m-T_1 three times the half-width of the curve between half-maxima).

Larger reduction in κ can be achieved in the case of a pure parent-daughter exponential decay (if one is also sure that no mixture of other, e.g., prompt, coincidences is present). Using the differential equation

$$N(T)-P(T)=-\theta(dN/dT), \tag{54}$$

derived by Newton,[18] and its integrated form

$$\int_{T_1}^{T_m}N(T)dT-\int_{T_1}^{T_m}P(T)dT=\theta[N_1-N_m], \tag{55}$$

where $N_1=N(T_1)$ and $N_m=N(T_m)$, and choosing T_1, and T_m such that $N_1=N_m$, one finds that the areas of the two curves within the section T_m-T_1 are equal, i.e., the two curves can be normalized without measuring the outer parts. Calculating the first moments $\mu_1(N)$ and $\mu_1(P)$ for the measured sections, one obtains:

$$\theta=[\mu_1(N)-\mu_1(P)]\frac{1}{1-N_m(T_m-T_1)/A}, \tag{56}$$

where A represents the area of $N(T)$ or $P(T)$ within the measured section. With $N_m(T_m-T_1)/A$ small compared to unity, the variance of θ will be

$$v(\theta)\sim\frac{\mu_2(N)-\mu_1^2(N)}{\mathfrak{N}_N}+\frac{\mu_2(P)-\mu_1^2(P)}{\mathfrak{N}_P}+\frac{\theta^2(T_m-T_1)^2}{A^2}\frac{N_m^2}{\mathfrak{N}_1+\mathfrak{N}_m}. \tag{57}$$

By proper choice of T_1 and T_m the small additional error due to the third term in Eq. (57) can be overcompensated by the gain in $\mathfrak{N}_N$ and $\mathfrak{N}_P$.

Instead of measuring the first moments of the measured sections, one can utilize Eqs. (54) and (55) directly to calculate θ.[18] Dividing the measured sections into two intervals T_0-T_1 and T_m-T_0, where T_0 is the abscissa of the intersection of $N(T)$ and $P(T)$, one obtains

$$\theta=\frac{A_2-A_1-(a_2-a_1)\eta}{2N_0-(N_1+N_m)}, \tag{58}$$

where A_1 and A_2 are the areas under the $N(T)$ curve for the two intervals, a_1 and a_2 are the corresponding areas under the $P(T)$ curve, and $\eta=(A_1+A_2)/(a_1+a_2)$ is the normalizing factor. Disregarding the statistical error of η, one obtains, for $N_m\ll N_0$,

$$v(\theta)=\frac{(A_1+A_2)^2}{4N_0^2\mathfrak{N}_n}+\frac{(A_1+A_2)^2}{4N_0^2\mathfrak{N}_p}+\theta^2\left(\frac{N_m}{N_0}\right)^2\frac{1}{\mathfrak{N}_1+\mathfrak{N}_m}+\frac{\theta^2}{\mathfrak{N}_0}. \tag{59}$$

The first three terms are of the same order as in Eq. (57) since $(A_1+A_2)/2N_0$ represents the width of the $N(T)$ curve and $A\sim(T_m-T_1)N_0/2$. Except for $\theta\ll\tau'$ the additional term is not small ($\mathfrak{N}_0\ll\mathfrak{N}$), and therefore the total error is greater than that obtained with the moment method.

We next examine the following question: Is it possible to improve the accuracy by utilizing the total time of observation $[T]$ in a better way, using unequal counting times at the various delays T_i?

Rewriting Eq. (39) in the following form:

$$\sigma^2[\mu_1(N)]=\frac{\sum(T_i-\mu_1)^2N_i\sqrt{[t_i]}}{(\sum N_i)^2}, \tag{60}$$

where $[t_i]$ is now the time of observation for the point T_i, and minimizing the expression on the right in

Eq. (60) with the condition

$$\sum [t_i]=[T]=\text{constant}, \tag{61}$$

results in the time schedule

$$[t_i]=[T]\frac{|T_i-\mu_1|\sqrt{N_i}}{\sum |T_i-\mu_1|\sqrt{N_i}}, \tag{62}$$

and

$$\sigma^2[\mu_1(N)]=\frac{1}{[T]}\left(\frac{\sum |T_i-\mu_1|\sqrt{N_i}}{\sum N_i}\right)^2. \tag{63}$$

A comparison of Eqs. (63) and (52) for a Gaussian and for an experimental coincidence curve gives in both cases, when utilizing the time schedule of Eq. (62), a rather small improvement ($\sim$10 percent).

(2) *C is measured.*—The ordinate of the reduced coincidence curve is calculated as $n_i=\mathfrak{N}_i/\mathfrak{C}$ and its variance is

$$v(n_i)\cong n_i(1-n_i)/\mathfrak{C}. \tag{64}$$

In the successive measurements of individual points of a coincidence curve the observations are made either for a constant $\mathfrak{C}$ ("preset count") or for a constant $[t]$ ("preset time"). Since n_i is always calculated from correlated values of $\mathfrak{N}_i$ and $\mathfrak{C}$, Eq. (64) is valid for all separate points and in the calculation of errors $\mathfrak{C}$ can be replaced by its average value $[t]C$. Thus

$$v(n_i)\cong n_i(1-n_i)/([t]C). \tag{65}$$

A comparison of Eqs. (65) and (38) shows that the statistical error is smaller when C is measured.

The expression for $\sigma^2[\mu_1(n)]$ is:

$$\sigma^2[\mu_1(n)]=\frac{\sum (T_i-\mu_1)^2 n_i(1-n_i)}{[t]C(\sum n_i)^2}$$

$$=\frac{1}{[t]C\sum n_i}\left\{\mu_2-\mu_1^2-\frac{\sum (T_i-\mu_1)^2 n_i^2}{\sum n_i}\right\}. \tag{66}$$

The first term in the bracket is the same as in Eq. (39) and the term to be subtracted from it is always positive. Calculation for a Gaussian curve and for actual coincidence curves showed that the second term is $\sim$30 percent of the first term when $\tau=\tau_0$.

Other advantages of the measurement of C have been pointed out in Sec. IV.

It is interesting to compare the errors given in Eqs. (52), (63), and (66) with the least possible error obtainable during $[T]$ in the presence of time lags characterized by $\bar{l}$ and in the presence of the time delay function $w(t)$. The least possible error would be obtained with a multichannel coincidence system consisting of channels having a negligibly small τ, and of a sufficiently large number to cover, without overlap, the entire range of the coincidence curve. In such a system none of the $[T]C$ coincidences would be missed being counted, the variance of $\mu_1(P)$ would be

$$\sigma^2[\mu_1(P)]=\bar{l}^2/([T]C), \tag{67}$$

and the variance of $\mu_1(N)$ would be

$$\sigma^2[\mu_1(N)]=(\bar{l}^2+\theta^2)/([T]C). \tag{68}$$

With $\kappa=3$, the factor appearing in front of $\bar{l}^2/([T]C)$ in Eq. (52) is $\sim$6, i.e., the one-channel method yields, in about six times larger a time of observation, the same accuracy as the (infinite) many-channel system. By the use of unequal times [Eq. (63)] this factor is reduced to $\sim$5.5, and by the measurement of C to $\sim$4 [Eq. (66)]. It can be further reduced by methods diminishing κ. Therefore, related to the same time of observation, the standard error obtained with the one-channel equipment is approximately twice $(2\kappa)^{\frac{1}{2}}$ the least theoretical standard error.

Slope Method

One can utilize the slope of a coincidence curve to measure time delays when:

(a) $w(t)$ is a simple exponential function. In this case θ can be determined [Eq. (54)] as[16]:

$$\theta=\frac{N(T)-P(T)}{dN/dT}. \tag{69}$$

(b) $w(t)$ is of a general form but its entire range is not longer than the linear part of the prompt curve. It has been shown[27] in this case, that

$$\mu_1(w)\cong\frac{N(T)-P(T)}{dP/dT}. \tag{70}$$

As was pointed out in Sec. IV, the slope method is simple only if one avoids the normalization procedure, i.e., if one measures C (denoted by C_n and C_p for the two curves). We will therefore relate the slope s to the reduced coincidence curves. We approximate s by

$$s=(n_1-n_2)/(T_1-T_2), \tag{71}$$

where T_1 and T_2 are two separate points chosen around T, and obtain for the variance of θ

$$v(\theta)=\frac{1}{s^2}\left\{\frac{n(1-n)}{[t_n]C_n}+\frac{p(1-p)}{[t_p]C_p}\right\}$$

$$+\frac{\theta^2}{s^2(T_1-T_2)^2}\left\{\frac{n_1(1-n_1)}{[t_1]C_n}+\frac{n_2(1-n_2)}{[t_2]C_n}\right\}. \tag{72}$$

The second term in Eq. (72) shows that the method is feasible only for very small θ's. Namely, T_1-T_2 must be small compared to $\bar{l}$ to avoid a large systematic error in the determination of s. On the other hand, large $\theta^2/(T_1-T_2)^2$ introduces large statistical errors. For

[27] Bay, Meijer, and Papp, Phys. Rev. 82, 754 (1951).

$\theta \ll \bar{t}$ the second term in Eq. (72) can be neglected and we calculate the first term for the highest slope s_{max} of the $n(T)$ curve.

Since $n(T)$ is a threefold convolution integral of $\psi(T)$, $\rho(t)$ (we take here the time lag function to be uniform for all pulse pairs), and $w(t)$, it follows that s_{max} cannot exceed $(d\psi/dT)_{max}$, ρ_{max}, or w_{max}.

For the ideal case where $(d\psi/dT)_{max}=\infty$ [rectangular $\psi(T)$, with uniform τ for all pulse pairs], when τ is large enough to cover the entire range of $\rho(t)$ and when $\theta \ll \bar{t}$, we have $s_{max} \cong \rho_{max}$ and

$$n(T) \sim p(T) \sim \int_{-\infty}^{T} \rho(t)dt. \tag{73}$$

Writing

$$\rho_{max}=1/(2\alpha^{\frac{1}{2}}\bar{t}), \tag{74}$$

we obtain for each of the coincidence curves

$$v(n/s) \sim \alpha \bar{t}^2/([T]C), \tag{75}$$

where the measured ordinates of n or p are taken as $\frac{1}{2}$, corresponding to the nodal point of the $\rho(t)$ curve.

A comparison of Eq. (75) with Eq. (67) shows the important fact that the ultimate determining factor for the accuracy of very short time measurements is also $\bar{t}$ when using the slope method.

In practice $(d\psi/dT)_{max}$ is finite, $s_{max}<1/(2\alpha^{\frac{1}{2}}\bar{t})$, and the actual statistical error may be similar to that obtained by the moment method, Eq. (52) corrected as in Eq. (66).

The convenience of the slope method makes it very useful for the *detection* of very short time delays.[25]

Tail Method

For large T's where $N(T) \gg P(T)$, the tail of the coincidence curve approaches an exponential for both the asymmetric and the symmetric parent-daughter cases. θ can be determined by fitting a straight line by least squares through a semilog plot of the experimental points. This leads to the slope[26]:

$$\lambda=-\frac{1}{\theta}=\frac{\sum N_i(T_i-\bar{T})(y_i-\bar{y})}{\sum N_i(T_i-\bar{T})^2}, \tag{76}$$

where $\bar{T}=\sum N_iT_i/\sum N_i$, $y_i=\log N_i$, $\bar{y}=\sum N_iy_i/\sum N_i$, and the points of the plot are weighted by N_i to satisfy the condition

$$N_iv(y_i)=1/[t]=\text{constant}, \tag{77}$$

if $[t]$ is the same for all points.

The variance of θ is

$$v(\theta)=\theta^4\frac{1}{[t]\sum N_i(T_i-\bar{T})^2}, \tag{78}$$

or, when measuring at equidistant T_i's,

$$v(\theta)=\frac{\theta^2}{\mathfrak{N}}\frac{\theta^2}{\mu_2-\mu_1^2}, \tag{79}$$

where μ_2 and μ_1 are the normalized moments of the measured section. For $T_m-T_1 \gg \theta$, $v(\theta)$ approaches $\theta^2/\mathfrak{N}$, which is just the variance of the center of gravity of the measured section. Thus the moment method with the use of Eqs. (56) and (57) having here $P(T)=0$, choosing a coordinate system such that $T_1=0$, and omitting $\mathfrak{N}_1$ in Eq. (57), leads to similar statistical accuracy.

The determination of θ from the tail has the advantage of involving only one coincidence curve. There is therefore no need to be concerned here with pulse shape distributions [Sec. I, condition (b)]. Of course in this case $\mathfrak{N}$, being dependent on τ, τ', θ, and T_m-T_1, is generally a rather small fraction of $C[T]$. This restricts the practical use of the method to $\theta \gg \tau'$.

Summarizing the results of statistical error calculations for the different methods, one can conclude that the moment methods can be used generally. Other methods, applicable only with some restrictions, can lead to similar statistical accuracy as the moment method.

Effect of Chance Coincidences

The chance coincidence counting rate is measured at $T=\infty$ and its mean value subtracted from all the measured counting rates along the coincidence curves. Again we consider two cases:

(1) *C is not measured.*—N_i is obtained by measuring $\mathfrak{N}_i'=\mathfrak{N}_i+\mathfrak{N}_c$ for the time $[t]$ and calculating

$$N_i=\frac{\mathfrak{N}_i+\mathfrak{N}_c}{[t]}-N_c, \tag{80}$$

where $\mathfrak{N}_c$ is the number of chance coincidences occurring during $[t]$ and N_c is the chance-coincidence background, determined separately at $T=\infty$, during the time $[t_c]$. The variance of N_i is

$$v(N_i)=\frac{N_i}{[t]}+\frac{N_c}{[t]}+\frac{N_c}{[t_c]}, \tag{81}$$

and since the last term of Eq. (81) is common for all points of the coincidence curve, the variance of μ_r is

$$\sigma^2(\mu_r)=\frac{\mu_{2r}-\mu_r^2}{\mathfrak{N}}+\frac{N_c}{[t](\sum N_i)^2}\sum (T_i^r-\mu_r)^2 + \frac{N_c}{[t_c](\sum N_i)^2}(\sum T_i^r-\mu_r)^2. \tag{82}$$

[25] For example see R. H. Bacon, Am. J. Phys. 21, 428 (1953).

For μ_1, Eq. (82) gives

$$\sigma^2(\mu_1)=\frac{1}{\mathfrak{N}}\Big\{(\mu_2-\mu_1^2)+\frac{N_c}{\langle N_i\rangle_{Av}}\Big[\frac{1}{3}\Big(\frac{T_m-T_1}{2}\Big)^2+\Big(\frac{T_m+T_1}{2}-\mu_1\Big)^2\Big]\Big\}+\Big(\frac{T_m+T_1}{2}-\mu_1\Big)^2\frac{N_c}{\langle N_i\rangle_{Av}^2}\frac{1}{[t_c]}. \quad (83)$$

A similar expression is valid for the $P(T)$ curve. The first term of the right-hand side of Eq. (83) shows that the additional error caused by the statistical fluctuation of the number of chance coincidences during the measurement of the individual points, is proportional to $N_c/\langle N_i\rangle_{Av}$. The second term depends on the time $[t_c]$ spent in the determination of N_c. It is interesting to note that the second term can be suppressed by taking the measured interval T_m-T_1 symmetrically around μ_1. In this case even a statistically poor determination of N_c is sufficient, and one can write

$$\sigma^2(\mu_1)=\frac{\mu_2-\mu_1^2}{\mathfrak{N}}\Big(1+\frac{\kappa^2}{3}\frac{N_c}{\langle N_i\rangle_{Av}}\Big), \quad (84)$$

where κ is defined in Eq. (46).

Since $\langle N_i\rangle_{Av}\sim\frac{1}{2}N_{\max}=\frac{1}{2}C\tau/\tau'$ and $\tau/\tau'=1/\sqrt{3}$ for $\tau=\tau_0$, and $\kappa=3$, one can estimate that, for $N_c/C=1\%$, the variance of μ_1 increases by $\sim 5\%$ or the standard error by $\sim 2.5\%$.

If only chance coincidences originating from source events are present, then N_c/C can be calculated and one obtains

$$N_c/C=\nu\cdot 2\tau, \quad (85)$$

which can be used as an estimate when designing experiments.

(2) *C is measured.*—Here n_i is calculated as follows:

$$n_i=\frac{(1/[t])(\mathfrak{N}_i+\mathfrak{N}_c')-N_c'}{(1/[t])(\mathfrak{C}+\mathfrak{N}_c'+\mathfrak{N}_c'')-N_c}, \quad (86)$$

where $\mathfrak{N}_c'$ is the number of chance coincidences appearing in the circuit with the resolving time τ_1, within the time $[t]$, and $\mathfrak{N}_c'+\mathfrak{N}_c''=\mathfrak{N}_c$ is the number of chance coincidences appearing with $\mathfrak{C}$ in the other circuit (resolving time τ_2).

The corresponding chance coincidence counting rates are measured at $T=\infty$ during the respective times of observation $[t_c']$ and $[t_c]$. The $\mathfrak{N}_c'$ counts appear in both circuits and $N_c'/N_c=\tau_1/\tau_2$. A simple calculation gives

$$v(n_i)=\frac{n_i(1-n_i)}{[t]C}+\frac{N_c}{C^2}\Big\{(1-n_i)^2\frac{\tau_1}{\tau_2}\Big(\frac{1}{[t]}+\frac{1}{[t_c']}\Big)+n_i^2\Big(1-\frac{\tau_1}{\tau_2}\Big)\Big(\frac{1}{[t]}+\frac{1}{[t_c]}\Big)\Big\}. \quad (87)$$

Comparing Eq. (87) with Eq. (81) rewritten in the form:

$$v(n_i)=v\Big(\frac{N_i}{C}\Big)=\frac{n_i}{[t]C}+\frac{N_c'}{C^2}\Big(\frac{1}{[t]}+\frac{1}{[t_c']}\Big), \quad (88)$$

one can see that for all practical cases where $N_c<C$ and $[t_c]\sim[t_c']$ the variance shown in Eq. (87) is less than that given by Eq. (88).

VII. APPENDIX A

To illustrate the application of Eqs. (1) and (4) to more complicated cases, we will now treat the case of parent-daughter-granddaughter decay and will then make the obvious generalization to larger radioactive families.

Let us denote the mean life of the daughter by θ_1 and that of the granddaughter by θ_2. Without loss in generality, we can restrict the problem to the case in which only the radiation of the parent and granddaughter decays can excite the detectors.

The $w(t)$ function for the time interval between the parent and granddaughter decays will be the superposition of the two exponential decay functions with the respective mean lives θ_1, and θ_2. The $w(t)$ function and hence its moments will be symmetric in θ_1, and θ_2. The moments, μ_r, will be given by

$$\begin{aligned}\mu_1&=\theta_1+\theta_2=S_1,\\ \mu_2&=2[\theta_1^2+\theta_1\theta_2+\theta_2^2]=2[S_1^2-S_2],\\ \mu_3&=6[\theta_1^3+\theta_1^2\theta_2+\theta_1\theta_2^2+\theta_2^3]=6[S_1^3-2S_1S_2],\\ \mu_4&=24[\theta_1^4+\theta_1^3\theta_2+\theta_1^2\theta_2^2+\theta_1\theta_2^3+\theta_2^4]\\ &=24[S_1^4-3S_1^2S_2+S_2^2],\end{aligned} \quad (A1)$$

etc.;

where $S_1=\theta_1+\theta_2$, $S_2=\theta_1\theta_2$ are the elementary symmetric functions of the θ's. Now, for an asymmetric experiment, the first moment of $w(t)$ will yield S_1, the second moment and the known value of S_1 will yield S_2, and θ_1 and θ_2 will be the roots of the second-degree equation:

$$\theta^2-S_1\theta+S_2=0. \quad (A2)$$

The generalization to the analysis of an asymmetric experiment performed on a family of N members is straightforward. We denote the N elementary symmetric functions of the θ's by S_{kN} $(k=1\cdots N)$. Since $\mu_n(w)$ is a symmetric function of the nth degree in the θ's, μ_n can always be expressed as a function of the S_{kN} such that

$$\mu_n(w)=\Phi_n(S_{1N},\cdots,S_{nN}), \quad (A3)$$

where Φ_n does not contain any S_{kN} for $k>n$. Thus the first N moments of w utilized in ascending order will yield the S_{kN}'s by simple substitution, since the right hand side of Eqs. (A3) will be a triangular array in the S_{kN}'s. By a well-known theorem of algebra, θ_1, θ_2,

$\cdots, \theta_N$ will be the roots of the Nth-degree equation

$$\sum_{k=0}^{n} (-1)^k S_{kN} \theta^{N-k} = 0. \tag{A4}$$

The $w(t)$ function obtained in a symmetric experiment differs in that all the odd moments are zero. The even moments, however, will be the same as those obtained in an asymmetric experiment. Thus, for the parent-daughter-granddaughter case, S_1 and S_2 can be determined by inserting μ_2 and μ_4 in Eqs. (A1). While the previous triangular array is no longer available, Eq. (A2) is still valid and yields θ_1, and θ_2.

For the case of a symmetric experiment performed on a family of N members, we use the first N even moments $\mu_2, \mu_4, \cdots, \mu_{2N}$ from which we determine S_{kN}, $k=1, \cdots, N$. Then Eq. (A4) can be solved for $\theta_1, \theta_2, \cdots, \theta_N$ as before.

PHYSICAL REVIEW VOLUME 100, NUMBER 4 NOVEMBER 15, 1955

Inadmissible Auxiliary Conditions in Quantized Linear Systems

J. K. PERCUS
Institute of Mathematical Sciences, New York University, New York City, New York

(Received June 27, 1955)

Methods of applying supplementary linear conditions to quantized linear systems are reviewed; it is seen that such a procedure is self-consistent for Fermi-Dirac systems in general, and for Einstein-Bose systems possessing positive definite constants of the motion. Possible modifications are discussed for those cases in which the operator conditions to be added appear intrinsically inconsistent with the commutation relations. Alterations of the commutation relations which maintain the invariance properties of the system are found to be generally inapplicable. Increasing the number of side conditions achieves the desired objective, but at the expense of reducing drastically the class of constants of motion. Finally the introduction of a restricted set of field variables is explored. It is shown that the new variables, in terms of which all pertinent field quantities may be expressed, permit a consistent formulation to be realized; the case of a massless spin s boson field is treated in this manner.

INTRODUCTION

IT is often necessary to augment the equations of motion of a physical system by relations of a more peripheral nature. The effect, and frequently the intent, is to reduce some symmetry of the problem and so negate the attendant decoupling of properties which appear correlated in nature, such as internal and external angular momentum for the vector meson without Lorentz condition. Whereas in the classical situation the additional equations may simply be tacked on as dynamical conditions, this option is not available, in an operator sense, when the original system is presented together with appropriate commutation relations; instead one may judiciously modify the commutation relations, construct a new Lagrangian which implies all relations, or perhaps use more specialized methods[1] in the case of linear systems. However, perverse situations arise in which none of these approaches can be reconciled with the maintaining of important invariance properties and the associated constants of the motion; the usual cure is to apply the truculent side condition only to the quantum states of the system. Another possible approach, with admittedly limited applicability, is to formulate the theory in terms of variables of presumably more direct physical significance, such as field strengths in electromagnetic theory, and thereby, in some mysterious way, banish the associated difficulties. We shall examine, in detail, considerations leading to the latter method, applying it to linear systems, in which its inherent imperfections are well camouflaged.

A quantization formalism for linear systems previously employed[1-3] by the writer will be of considerable aid. Briefly, the recipe runs as follows. A real linear system is determined by

$$\sum_s M_{rs}\psi_s(x) = 0, \tag{1}$$

or $M\psi = 0$, where $M = (M_{rs})$ is a real matric differential operator and x refers to the full set of space-time coordinates. Then if the basic commutator (or anticommutator) $\psi_\alpha(x)\cdot\psi_\beta(x') \equiv \psi_\alpha(x)\psi_\beta(x') + J\psi_\beta(x')\psi_\alpha(x)$, with $J = \pm 1$, is a c-number, the full set of pertinent commutation relations may be written succinctly as

$$\mathcal{T}(\omega,\psi)\cdot F\psi = F\omega; \tag{2}$$

here ω is any c-number solution of $M\omega = 0$, F is any linear operator, $\mathcal{T}(\omega,\psi)$ is bilinear in ω and ψ and coordinate independent. Further, if U, real, is an invariant transformation in the sense that $M(U\psi) = 0$, whenever $M\psi = 0$, and if U satisfies $\mathcal{T}(\omega,U\psi) + \mathcal{T}(U\omega,\psi) = 0$ as well,

[1] J. K. Percus, Phys. Rev. 97, 1406 (1955).

[2] J. K. Percus, Phys. Rev. 96, 1147 (1954).

[3] J. K. Percus, Columbia University dissertation, 1954 (unpublished).

then

$$Q_U=\tfrac{1}{2}i\hbar\mathcal{T}(\psi,U\psi) \tag{3}$$

may be taken as the constant of motion corresponding to U. The commutation and transformation properties of Q_U are precisely as expected.

APPLICATION OF AUXILIARY CONDITIONS

Before proceeding to auxiliary condition of the more troublesome variety, let us review the situation in which only a simple modification of the commutation relations is required. Since an added condition

$$S\psi=0 \tag{4}$$

serves to reduce the space of solutions of (1), we may assume that S is an invariant linear operator or a set thereof. First, we had better see what the commutation relations were originally. For this purpose, it is helpful to introduce a coordinate-independent basis $\{F_\alpha\psi\}$ for quantities of the form $F\psi$, where F is a linear operator and ψ satisfies (1); thus "any" $F\psi$ can be expressed uniquely as

$$(F\psi)_s=\sum_\alpha f_{\alpha s}(x)F_\alpha\psi, \tag{5}$$

$\sum_\alpha$ denoting both summation and integration, as required. Utilizing the $F_\alpha\psi$, the bilinear expression $\mathcal{T}(\omega,\psi)$ may be written explicitly as

$$\mathcal{T}(\omega,\psi)=\sum F_\alpha\omega\tau_{\alpha\beta}F_\beta\psi; \tag{6}$$

if the commutation relations are specified, as they may be, by the set

$$F_\alpha\psi\cdot F_\beta\psi=\mathfrak{F}_{\alpha\beta}, \tag{7}$$

$\mathfrak{F}_{\alpha\beta}$ a pure number, then it is readily shown that (2) reduces to the matrix equation

$$\mathfrak{F}=\tau^{-1}, \tag{8}$$

and this is our desired relation. We note parenthetically that

$$\tau^T=J\tau \tag{9}$$

follows directly from (7) and (8), A^T denoting the transpose of the matrix A, while

$$(\tau^*)_{\alpha\beta}=J\tau_{\alpha\beta} \tag{10}$$

follows from (7) and (8) by applying the Hermitian adjoint.

Let us now insert the supplementary condition (4); then the $F_\alpha\psi$ are no longer independent, and the consequent linear relations existing between them show at once that the set of commutation relations (7) is no longer applicable. There is of course no unique prescription for the modification of (7), but a number of eminently reasonable ones turn out to be equivalent. Thus, if we assume merely that the expressions for the constants of motion in terms of ψ are unchanged, the maintenance of their properties requires that the expression for $\mathcal{T}(\omega,\psi)$ be unchanged as well, and the modified commutation relations become completely determined. Suppose then that under condition (4), we obtain the reduced basis $\{G_\beta\psi\}$ for the quantities of the form $F\psi$; in particular, then, one can write

$$F_\alpha\psi=\sum_\beta\Gamma_{\alpha\beta}G_\beta\psi \tag{11}$$

for some "rectangular" matrix Γ. Note that on the other hand, using only the fact that (1) still holds, we have as well

$$G_\beta\psi=\sum_\beta\Omega_{\alpha\beta}F_\beta\psi, \tag{12}$$

from which it follows that $\Omega\Gamma=1$. Since

$$\begin{aligned}\mathcal{T}(\omega,\psi)&=\sum F_\alpha\omega\tau_{\alpha\gamma}F_\gamma\psi=\sum G_\beta\psi\Gamma_{\alpha\beta}\tau_{\alpha\gamma}\Gamma_{\gamma\delta}G_\delta\psi\\&=\sum G_\beta\psi(\Gamma^T\mathfrak{F}^{-1}\Gamma)_{\beta\delta}G_\delta\psi,\end{aligned}$$

the new commutation relations become simply

$$G_\beta\psi\cdot G_\gamma\psi=(\Gamma^T\mathfrak{F}^{-1}\Gamma)_{\beta\gamma}{}^{-1} \tag{13}$$

provided that the inverse matrix exists. There remains only the task of rewriting (13) in the form

$$F_\alpha\psi\cdot F_\beta\psi=\mathfrak{F}_{\alpha\beta}', \tag{14}$$

appropriate to our original basis, but a glance at (11) assures us that we need only choose

$$\mathfrak{F}'=\Gamma(\Gamma^T\mathfrak{F}^{-1}\Gamma)^{-1}\Gamma^T, \tag{15}$$

which is our basic result.

Equation (15) is a rather poor one, computationwise, so that equivalent formulations may be more useful. We observe, for the sake of completeness, a simple and powerful restatement of (15) which was obtained in reference 1. First, since an invariant transformation U, with respect to the system (1), permutes the set of $F\psi$, we may represent U by a matrix of constant elements $U_{\alpha\beta}$ defined by

$$F_\alpha U\psi=\sum U_{\alpha\beta}F_\beta\psi. \tag{16}$$

Then if ρ, an invariant operator, projects the solutions of $M\psi=0$ onto those of $M\psi=S\psi=0$ in the sense that if $\{\psi\}$ is the complete set of solutions of $M\psi=0$, then $\{\rho\psi\}$ is the complete set of solutions of the supplemented relations, and if furthermore ρ satisfies

$$\mathcal{T}(\omega,\rho\psi)=\mathcal{T}(\rho\omega,\psi)$$

(this determines ρ uniquely), we have simply, in matrix form,

$$\mathfrak{F}'=\rho\mathfrak{F}. \tag{17}$$

The existence of a ρ satisfying the above conditions and of an inverse for $\Gamma^T\mathfrak{F}^{-1}\Gamma$ are thus equivalent concepts.

It is natural to inquire whether there are conditions which ensure that the process leading to (15) [or, equivalently, to (17)] can be carried out; one such condition possessing the advantages of generality and of dealing with quantities of direct physical import is readily obtained. For the purposes of this derivation, the bases $\{F_\alpha\psi\}$, $\{G_\beta\psi\}$ and so the transformation Γ, are chosen as real. We first observe, from (9), that

$[\exp\pi(1-J)/4]\tau$ is a pure real matrix. Suppose then that there exists a real transformation T which is invariant both with respect to the system (1) and to (1) augmented by (4), and for which $[\exp\pi(1-J)/4]\tau T$ is positive definite. Since T is invariant with respect to both systems, we can write not only $F_\alpha T\psi=\sum T_{\alpha\beta}F_\beta\psi$, but also $G_\alpha T\psi=\sum T_{\alpha\beta}'G_\beta\psi$; thus $\sum(\Gamma T')_{\alpha\beta}G_\beta\psi=F_\alpha T\psi=\sum T_{\alpha\beta}\Gamma_{\beta\gamma}G_\gamma\psi$, or

$$\Gamma T'=T\Gamma. \tag{18}$$

But $[\exp\pi(1-J)/4]\tau T$ being positive definite implies that $[\exp\pi(1-J)/4]\Gamma^\tau\tau T\Gamma$ is likewise positive definite, and this, according to (18), may be written as

$$[\exp\pi(1-J)/4]\Gamma^\tau\tau\Gamma T',$$

which is then certainly invertible; thus $(\Gamma^\tau\tau\Gamma)^{-1}=T'(\Gamma^\tau\tau\Gamma T')^{-1}$ exists, as desired. Summing up:

> If for some real T, invariant for both $M\psi=0$ and for $M\psi=S\psi=0$, $\exp\pi(1-J)/4\ \tau T$ is positive definite, then commutation relations for $M\psi=S\psi=0$ exist and are determined by (15) or (17). (19)

Statement (19) is subject to immediate physical interpretation. First consider Einstein-Bose (E.B.) statistics ($J=-1$); then coupling (9) with the fact that τT is to be a symmetric matrix, we find that $\mathcal{T}(\omega,T\psi)+\mathcal{T}(T\omega,\psi)$ vanishes, as required for (3). Further, the positive definiteness of the matrix $i\tau T$ implies that of the quadratic form[4] Q_T in (3). We conclude that, in brief:

> For E.B. statistics, the condition in (19) may be replaced by the positive definiteness of any quadratic constant of the motion. (20)

For example, an E.B. system in which all energy quanta are positive may be supplemented with impunity.

On the other hand, for Fermi-Dirac (F.D.) statistics, if we assume as is customary that the scalar product associated with the Hermitian conjugate is positive definite, then the matrix $\mathfrak{F}$, and so τ itself, will be positive definite.[5] Hence (19), is automatically satisfied by $T=1$:

> For F.D. statistics and positive-definite scalar product, the condition (19) is always satisfied. (21)

In our analysis of the inapplicability or supplementary conditions, we might thus restrict ourselves to E.B. systems.

METHOD OF MODIFIED COMMUTATIONS RELATIONS

We shall now turn to those cases in which, despite the confidence engendered by (19) and (20), the system (including commutation relations) being considered refuses to countenance the direct application [as in (15) or (17)] of the desired auxiliary relations. Three remedial tactics, in order of increasing effectiveness, will be set forth.

As the first approach, we may note that since it is apparently the form of the original commutation relations which produces the difficulties in appending the subsidiary conditions, the possibility of a slight but appropriate modification of the commutation relations at once suggests itself. To this end, we first introduce the τ-adjoint U^τ of an invariant transformation U, defined by

$$\mathcal{T}(\omega,U^\tau\psi)=\mathcal{T}(U\omega,\psi), \quad \text{or} \quad U^\tau=\tau^{-1}U\tau, \tag{22}$$

and possessing the usual properties of an adjoint. Now two sets of commutation relations for $M\psi=0$ differ only in the associated expressions for $\mathcal{T}(\omega,\psi)$ or equivalently in the invertible matrices τ. It is then clear that any modified commutation relations may be determined from

$$\mathcal{T}'(\omega,\psi)=\mathcal{T}(\omega,P\psi), \quad \text{or} \quad \tau'=\tau P, \tag{23}$$

for some invertible invariant P which is restricted solely by (9) applied to both τ and τ', or using (22), by

$$P=P^\tau. \tag{24}$$

The arbitrariness inherent in (24) cannot however be maintained against desired invariance of the commutation relations under a set of physically significant infinitesimal transformations. In fact, applying such an infinitesimal U to (7), we have $F_\alpha U\psi\cdot F_\beta\psi+F_\alpha\psi\cdot F_\beta U\psi=0$, or $U^\tau\mathfrak{F}+\mathfrak{F}U=0$, from which

$$U^\tau=-U \tag{25}$$

is the required condition for invariance under U; this is observed to coincide, as expected, with the requirement that U generate a constant of the motion, as in (3). Now the interrelation between τ and τ' adjoints, obtained directly from (22) and (23), is that

$$U^{\tau'}=P^{-1}U^\tau P; \tag{26}$$

coupling $U^{\tau'}=-U=U^\tau$ through (26), we find that both sets of commutation relations can be invariant under U only if

$$UP=PU \tag{27}$$

is satisfied (on the space of solutions of $M\psi=0$).

The requirement that P commute with all transformations under which the quantum relations are to be invariant is of course a rather severe one, illustrating incidentally the high degree of uniqueness of the commutation relations when invariance considerations are taken into account. If, for example, the complete problem is to remain invariant under the inhomogeneous Lorentz group connected to the identity, and if $\Box^2$ is a constant on solution space, then the coordinate dependence of P can be generally through $\operatorname{sgn}(\partial/\partial t)$

---

[4] The criterion of positive definiteness of Q_T holds the same implication for c or q-number ψ.

[5] From $F_\alpha\psi F_\beta\psi+F_\beta\psi F_\alpha\psi=\mathfrak{F}_{\alpha\beta}$, we have for numerical χ_α, $\sum\mathfrak{F}_{\alpha\beta}\chi_\alpha\chi_\beta=2(\sum F_\alpha\psi\chi_\alpha)^2$, which, for a real basis $\{F_\alpha\psi\}$, must exceed zero.

alone, and this operator has the drastic effect of changing signs of energy quanta. In brief, we conclude that a modification of $\mathcal{T}(\omega,\psi)$ is most often inapplicable per se and so can certainly not be used as a stratagem in exorcising difficulties associated with supplementary conditions.[6]

METHOD OF ADDED SUPPLEMENTARY CONDITIONS

The matrix $\Gamma^T\tau\Gamma$ of (13) and (15) may be written in a more instructive form by a suitable transformation of basis. Again defining the $\{G_\beta\psi\}$ as spanning the set of $F\psi$ when both $M\psi=0$ and $S\psi=0$, we may clearly choose the corresponding basis $\{F_\alpha\psi\}$ (when $M\psi=0$ alone) to consist of the $\{G_\beta\psi\}$, augmented by a set $\{H_\gamma\psi\}$, where $H_\gamma\psi=0$ when $M\psi=S\psi=0$. In this event, we may form the partitioned matrix

$$\tau=\begin{pmatrix}\tau^{11} & \tau^{12}\\ \tau^{21} & \tau^{22}\end{pmatrix}, \tag{28}$$

where superscript 1 refers to the $\{G_\beta\psi\}$, 2 to the $\{H_\gamma\psi\}$; it then follows that

$$\Gamma^T\tau\Gamma=\tau^{11}. \tag{29}$$

In other words, $\Gamma^T\tau\Gamma$ is some principal minor of τ, and its invertibility is of course not implied by that of τ. There arises, however, the possibility of extending this liability to an asset, for a further supplementary condition may then select a nonsingular minor of τ^{11}.

To implement this approach, let us suppose that the basis $\{G_\beta\psi\}$ has been chosen such that it may be subdivided into sets $\{K_\lambda\psi\}$ and $\{L_\rho\psi\}$ in terms of which τ^{11} achieves the form

$$\tau^{11}=\begin{pmatrix}\bar{\tau} & 0\\ 0 & 0\end{pmatrix}, \tag{30}$$

$\bar{\tau}$ nonsingular; the first rows and columns refer to the $\{K_\lambda\psi\}$ and the second to the $\{L_\rho\psi\}$. Since τ, and so τ^{11} may be chosen as a numerical multiple of a real symmetric or skew matrix, this procedure can be carried out, but not in a unique manner. It is now apparent that if we introduce the additional set of restrictions

$$L_\rho\psi=0, \tag{31}$$

then the $\{K_\lambda\psi\}$ alone will form a complete basis for the $F\psi$ and

$$\mathcal{T}(\omega,\psi)=\sum K_\lambda\omega\bar{\tau}_{\lambda\lambda'}K_{\lambda'}\psi \tag{32}$$

will be represented by the nonsingular $\bar{\tau}$; the recipes of (15) and (17) thus become applicable.

To obtain the $L_\rho\psi$, it is not necessary to retrace the steps just described; in fact we need only remark that the $L\psi$ which are to be equated to zero all satisfy

$$\mathcal{T}(\omega,L\psi)=0, \tag{33}$$

whenever ω and ψ are solutions of both $M\psi=0$ and $S\psi=0$. Since the set of additional relations can generally be reduced to a single supplementary condition, it suffices to obtain one L satisfying (33). There are a large number of L's available, essentially equivalent to the choices of basis $\{G_\beta\psi\}$; however, in each case, one must ascertain that L "catches" all of the null operators corresponding to the basis which is intrinsically used. This is most easily done by requiring that any L chosen have the same rank (when the term may be reasonably defined) as that L of highest rank possible (with greatest number of independent conditions on solution space). The lack of uniqueness of L implies an inherent lack of symmetry which indeed makes itself painfully felt in that the set of physical invariant transformations often is greatly reduced by application of $L\psi=0$.[7]

As an example, we may consider the electromagnetic field, given by

$$(\partial^2/\partial x_\mu\partial x^\mu)A_\nu=0, \tag{34}$$

with supplementary $(\partial/\partial x_\nu)A_\nu=0$. Let us first apply the method of (31); it is easily shown that for standard commutation relations for the vector meson with normalized mass $\kappa=mc/\hbar$, we have on any space of fixed wave number k, $\tau_{\mu\mu'}\propto\delta_{\mu\mu'}$. Thus applying the Lorentz condition $A_0=\sum(k_i/k_0)A_i$,

$$\tau_{ii'}{}^{11}\propto(k_0{}^2\delta_{ii'}-k_ik_{i'}). \tag{35}$$

Now letting $\kappa\to0$, so that $k_0\to\pm|k|$, the null space of the resulting matrix $k_0{}^2\delta_{ii'}-k_ik_{i'}$ consists of multiples of the vector (k_1,k_2,k_3); the corresponding additional supplementary condition is then

$$\sum k_iA_i=0, \tag{36}$$

or equivalently $\partial A_0/\partial t=0$.

More generally, we employ (33); again limiting ourselves to vectors of fixed wave number,

$$\mathcal{T}(B,LA)\to B_i{}^*L_{ij}A_j-B_0{}^*L_{0j}A_j+B_i{}^*L_{i0}A_0-B_0{}^*L_{00}A_0 \tag{37}$$

with dummy 3-indices i and j $[B_i{}^*(k)=B_i(-k)]$. Thus setting $A_0=(k_j/k_0)A_j$, $B_0=(k_i/k_0)B_i$, (37) is identically zero when

$$L_{ij}-(k_i/k_0)L_{0j}+(k_j/k_0)L_{i0}-(k_ik_j/k_0{}^2)L_{00}=0. \tag{38}$$

Solving (38) for L_{ij}, the relation $LA=0$ then becomes

$$(L_{0i}A_i+L_{00}A_0,\ (k_i/k_0)L_{0i}A_i-(L_{10}/k_0k_i)A_i+(k_1/k_0)(L_{00}/k_0k_i)A_i+L_{10}A_0,\ \cdots)=0,$$

which is equivalent to the pair

$$k_iA_i-k_0A_0=0,\quad L_{0i}A_i+L_{00}A_0=0; \tag{39}$$

[6] Even assuming the existence of an extensive class of P satisfying (27), our position *vis-à-vis* criterion (19) is not thereby improved: if a multiple of $\tau'U$ were positive definite, then so would have been $\tau(PU)$ in the unmodified formulation.

[7] An invariant U will remain invariant on adjunction of $L\psi=0$ if, matrically, $LU=KL$ for some K.

the maximum rank of L is clearly two, and so any L will do,[8] except those cases (rank 1) in which $L_{00}=L_{0i}=0$. However, this is no better than the more special case $A_0=0$, for it does not retain the Lorentz transformations as invariant, and so is not of greater physical interest.

REDUCTION OF FIELD VARIABLES

The method (31) of compelling the $\{K_\lambda\psi\}$ of the discussion following (30) to constitute a complete basis for the $F\psi$, with $M\psi=S\psi=0$, has been seen to present difficulties in principle. However, another possibility quickly arises: Could ψ itself no longer be an appropriate field variable after the adjunction of the supplementary relation $S\psi=0$? If, for example, the new variable is chosen to be $\Lambda\psi$ for some (invariant) linear operator Λ, it is conceivable that the $L_\lambda\psi$ of (31) are not members of the set of $F\Lambda\psi$, so that the problem of the $L_\lambda\psi$ becomes ephemeral. Of course, care must be taken lest the operator Λ, palpably singular, be so singular that various quantities of importance cannot be expressed in terms of $\Lambda\psi$.

We may readily formalize the preceding comments. Operating in the basis of the $\{K_\lambda\psi\}$ and $\{L_\lambda\psi\}$, we need only define

$$\tilde{\psi}=\Lambda\psi, \tag{40}$$

where, in the notation of (30), Λ is represented by

$$\Lambda=\begin{pmatrix}1 & 0\\ 0 & 0\end{pmatrix}, \tag{41}$$

precisely the projection onto the space of $\{K_\lambda\psi\}$. This clearly results in

$$K_\lambda\tilde{\psi}=K_\lambda\psi, \quad L_\lambda\tilde{\psi}=0, \tag{42}$$

whence the $\{K_\lambda\tilde{\psi}\}$ alone form a basis for the $F\tilde{\psi}$. Then retaining the initial expression for $\mathcal{T}(\omega,\psi)$ so that the various constants of motion are unchanged in form, we observe that

$$\mathcal{T}(\tilde{\omega},\tilde{\psi})\equiv\sum K_\lambda\omega\bar{\tau}_{\lambda\lambda'}K_{\lambda'}\psi=\sum K_\lambda\tilde{\omega}\bar{\tau}_{\lambda\lambda'}K_{\lambda'}\tilde{\psi};$$

thus the matrix of $\mathcal{T}(\tilde{\omega},\tilde{\psi})$ is invertible (and again $\bar{\tau}^T=J\bar{\tau}$), yielding a unique set of commutation relations.

This approach is most easily effected if we note that our new field quantities may be taken as any set, operations upon which generate precisely the set of $F\tilde{\psi}$, and these, as we have seen, are none other than the set of $K_\lambda\psi$. But then, from $\mathcal{T}(\omega,\psi)=\sum K_\lambda\omega\bar{\tau}_{\lambda\lambda'}K_{\lambda'}\psi$, it follows that

> The $\{K_\lambda\psi\}$ are the space generated by $\mathcal{T}(\omega,\psi)$ as ω varies over all numerical solutions of $M\omega=S\omega=0$, (43)

which is the desired criterion. The uniqueness made evident by (43) portends the absence of invariance difficulties which reduced the previous two methods to impotence. More explicitly, we wish to ascertain that, corresponding to each invariant transformation U on the ψ for which $M\psi=S\psi=0$, there exists a U', invariant on the related set of $\tilde{\psi}$, such that U and U' have the same effect upon the system: $U\psi\to U'\tilde{\psi}$ as $\psi\to\tilde{\psi}$, or

$$\Lambda U\psi=U'\Lambda\psi; \tag{44}$$

in such a case, constants of the motion will be maintained, as will invariance of the commutation relations. To verify (44), we recall, according to (22) and (25), that the invariant transformations of consequence when $M\psi=0$ are determined by $\tau U+U^T\tau=0$; applying $S\psi=0$ as well, under which U is assumed to remain invariant, we may examine this condition in the basis of $\{K_\lambda\psi\}$, $\{L_\lambda\psi\}$. Then if

$$U=\begin{pmatrix}U^{11} & U^{12}\\ U^{21} & U^{22}\end{pmatrix},$$

we find at once, employing (30), that $\bar{\tau}U^{11}+(U^{11})^T\bar{\tau}=0$, $U^{12}=0$, an immediate consequence being that $\Lambda U=\Lambda U\Lambda$. Thus, in (44) we may choose either of

$$U'=\Lambda U, \quad \text{or} \quad U'=\Lambda U\Lambda; \tag{45}$$

examination of U' in the light of the $\{K_\lambda\psi\}\{L_\lambda\psi\}$ basis assures us that $\tau U'+(U')^T\tau=0$ is again satisfied. We conclude that the process (43) does not destroy invariance properties of the system.

As an application of (43), consider the spin s Boson field[9] in which the mass $\kappa\to 0$:

$$(\partial/\partial x^\alpha\partial/\partial x_\alpha-\kappa^2)U^{\alpha\beta\gamma\cdots}(x)=0. \tag{46}$$

U is an sth-rank tensor, and supplementary conditions are:

$$U^{\alpha\beta\gamma\cdots}\ \text{symmetric}, \quad \partial/\partial x^\alpha U^{\alpha\beta\gamma\cdots}=0, \tag{47}$$

and

$$U_\beta{}^{\beta\gamma\cdots}=0.$$

In this case, the matrix conditions of symmetry and vanishing trace do not contribute to inconsistency of the commutation relations, and so we shall concentrate upon the effect of the Lorentz condition. Again dropping dependence upon wave number k, it is readily found that, for (46),

$$\mathcal{T}(V,U)\to V_{\alpha\beta\gamma\cdots}{}^*U^{\alpha\beta\gamma\cdots}; \tag{48}$$

since V is restricted by $V_{0\beta\gamma\cdots}=(k_i/k_0)V_{i\beta\gamma\cdots}$, $V_{00\gamma\cdots}=[k_ik_j/(k_0)^2]V_{ij\gamma\cdots}$, and so forth, (48) becomes

$$V_{ijl\cdots}{}^*[U^{ijl\cdots}-(k^i/k^0)U^{0jl\cdots}-\cdots +k^ik^j/(k^0)^2U^{00l\cdots}+\cdots], \tag{49}$$

which is generated by the quantities

$$[\delta_\alpha{}^i-(k^i/k^0)\delta_\alpha{}^0][\delta_\beta{}^j-(k^j/k^0)\delta_\beta{}^0]\cdots U^{\alpha\beta\gamma\cdots}. \tag{50}$$

[8] Different L yield Lorentz-equivalent conditions.

[9] M. Fierz, Helv. Phys. Acta 12, 3 (1939).

If the Lorentz condition, and ultimately the symmetry and trace conditions, are taken into account, there are a large number of sets of variables which will generate the same space, but most obvious and superficially the simplest is the set

$$f^{ijl\cdots}=(i)^s(k^0\delta_\alpha{}^i-k^i\delta_\alpha{}^0)(k^0\delta_\beta{}^j-k^j\delta_\beta{}^0)\cdots U^{\alpha\beta\gamma\cdots}, \quad (51)$$

which, since the Lorentz transformations are still invariant, may be extended at once to

$$f^{\alpha'\beta'\gamma'\cdots\alpha''\beta''\gamma''\cdots}=(i)^s(k^{\alpha''}\delta_\alpha{}^{\alpha'}-k^{\alpha'}\delta_\alpha{}^{\alpha''}) \times(k^{\beta''}\delta_\beta{}^{\beta'}-k^{\beta'}\delta_\beta{}^{\beta''})\cdots U^{\alpha\beta\gamma\cdots}. \quad (52)$$

We observe in passing that symmetry of $U^{\alpha\beta\gamma\cdots}$ now yields symmetry among primed indices or among doubly primed indices of f, and antisymmetry between them; since $k^\alpha k_\alpha=0$ and $k^\alpha U_\alpha{}^{\beta\gamma\cdots}=0$, the trace condition may be extended to any pair of indices; finally, again using $k^\alpha k_\alpha=0$, the Lorentz condition holds for any index. It must of course be possible to express $\mathcal{T}(V,U)$ in terms of f and g [where g is derived from V from V by the scheme of (52)]; the identity

$$\sum_{\alpha\beta\cdots\alpha'\beta'\cdots}g_{\alpha\beta\gamma\cdots\alpha'\beta'\gamma'\cdots}{}^*(k)\delta_{\alpha\alpha}\delta_{\beta\beta}\cdots \times f^{\alpha\beta\gamma\cdots\alpha'\beta'\gamma'\cdots}(k)=2^s(k_0)^{2s}V_{\alpha\beta\gamma\cdots}{}^*U^{\alpha\beta\gamma\cdots}, \quad (53)$$

which is readily demonstrated, shows how this may be done.

All quadratic constants of motion, as well as the pertinent commutators, are now expressible in terms of the $\{K_\lambda\psi\}$; further, according to (41), $K_\lambda(1-\Lambda)H\psi=0$ for all invariant H. Thus, we may say that the general case under consideration is characterized by its invariance under the extended gauge transformations

$$\psi\rightarrow\psi+(1-\Lambda)H\psi, \quad (54)$$

whose correlation with zero mass is quite clear. A similar procedure has recently been delineated for application to nonlinear fields,[10] but the computational simplicity of the above approach is of course not generally attainable in such cases.

[10] P. G. Bergmann and I. Goldberg, Phys. Rev. **98**, 531 (1955).

Letters to the Editor

PUBLICATION of brief reports of important discoveries in physics may be secured by addressing them to this department. The closing date for this department is five weeks prior to the date of issue. No proof will be sent to the authors. The Board of Editors does not hold itself responsible for the opinions expressed by the correspondents. Communications should not exceed 600 words in length and should be submitted in duplicate.

Irradiation of Graphite at Liquid Helium Temperatures

STANLEY B. AUSTERMAN AND JOHN E. HOVE

Nuclear Engineering and Manufacturing, North American Aviation, Downey, California

(Received October 3, 1955)

IN a recent paper,[1] a model for the damage produced in graphite by particle bombardment was presented. This was based to a considerable extent on information obtained from neutron and proton irradiations at nominal liquid nitrogen temperatures; it was further postulated that the damage retained at this temperature represents essentially all the damage formed. This postulate implies that none of the damage centers move, or are altered, below liquid nitrogen temperatures and that irradiation at liquid nitrogen temperature does not affect the damage centers already formed. To verify this assumption, it is necessary to irradiate at still lower temperatures and the present note describes recent bombardments of graphite (type *AWG*) at liquid helium temperatures with 1.25-Mev electrons at integrated fluxes of about 20 and 40 microampere-hours. Following irradiation, the specimen was given one-minute annealing pulses at successively higher temperatures to room temperature and resistivity measurements made at 4°K following each annealing pulse. Two samples were irradiated, one showing a change of 7% in resistivity, the second a change of 4%. During the first run (7% change), the sample temperature was not observed during irradiation. There was some concern about possible specimen heating, so the second sample was irradiated with a reduced beam current and the temperature continuously monitored during irradiation; for the most part the temperature remained very close to 4°K, occasionally reaching a maximum of about 10°K. Because of the similarity of the two annealing runs, it is deduced that the sample temperature also remained low during the first run.

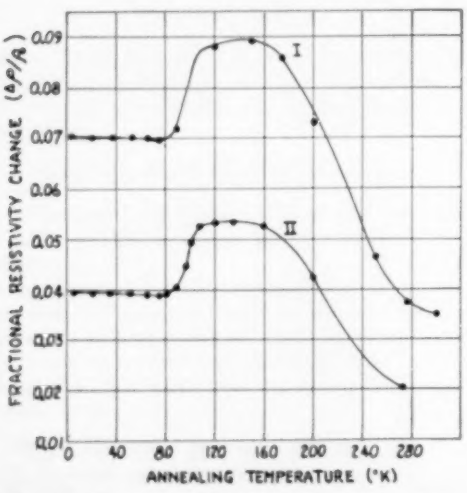

FIG. 1. Pulse annealing of two graphite samples irradiated at liquid helium temperature with 1.25-Mev electrons. Resistivity measured at 4°K.

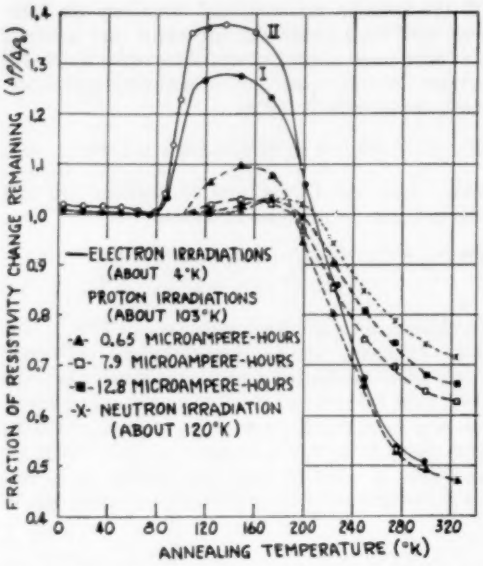

FIG. 2. Comparison of pulse annealing behavior with that observed in previous proton and neutron irradiations of graphite at the temperatures indicated. $\Delta\rho_0$ refers to the value at 78°K.

The two annealing curves are shown in Fig. 1. As can be seen, there is practically no effect below about 80°K. A small amount of annealing may take place, but is too small to warrant discussion, especially when compared to the striking behavior at higher temperatures. Note the abruptness of the annealing between 80°K and 110°K. The actual temperatures during the nominal "liquid nitrogen" irradiations were in the range of 103°K (cyclotron) to 125°K (Brookhaven Reactor), which are high enough that most of the annealing in the region 80°K–110°K must have taken place during irradiation. Figure 2 compares our results with those obtained previously by Deegan[2] following irradiation with protons and neutrons. The neutron irradiation corre-

sponds approximately to 3×10^{18} fast neutrons per cm², while one microampere-hour is 2.3×10^{16} protons (8 Mev) per cm². The smaller peaks of the latter data are presumably due in part to the annealing at the higher irradiation temperatures, although there is also some dependence of the annealing behavior on the total exposure. On the basis of this comparison, it may be concluded that, although the assumption of reference 1 (that all the damage is retained at the nominal liquid nitrogen exposures) is not literally justified, probably no new type of damage center is introduced by the lower temperature irradiation. In other words, the previous annealing experiments revealed some of the behavior that we have reported, but not all of it. From the standpoint of radiation damage studies, it is of interest to note that, if the specimen temperature is carefully held below 80°K, a liquid nitrogen temperature irradiation is sufficient to inhibit all thermal annealing of the damage centers.

At the present time, we do not wish to discuss the annealing mechanism in the 80–110°K region except to point out that presumably it is due either to a release of trapped electrons or a decomposition of interstitial clusters, both of which will increase the resistivity in graphite.

We wish to express our appreciation to T. G. Berlincourt for much invaluable discussion and assistance. In addition we wish to acknowledge discussions with D. B. Bowen and the help of H. Kenworthy and L. Bienvenue in performing the irradiations.

[1] G. R. Hennig and J. E. Hove, "Interpretation of Radiation Damage in Graphite," presented at the International Conference on the Peaceful Uses of Atomic Energy in Geneva on August 15, 1955 (unpublished).
[2] G. E. Deegan (unpublished).

Superconductivity at Millimeter Wave Frequencies*

GILBERT S. BLEVINS, WALTER GORDY, AND WILLIAM M. FAIRBANK
Department of Physics, Duke University, Durham, North Carolina
(Received October 3, 1955)

THE interesting phenomenon of superconductivity discovered by Onnes[1] in 1911 is still incompletely understood. London[2] has emphasized that somehow the superconducting electrons must fall into a quantum state of long-range order, a "macroscopic quantum state." The discovery of the isotopic effect[3] and the theories of Fröhlich[4] and Bardeen[5] have linked superconductivity to the zero-point vibrational energies of the atoms and have thus indicated a possible mechanism for a superconducting quantum state. The postulate of a superconducting quantum state implies an energy gap of the order of kT_c between the superconducting and the normal state. The substances for which superconductivity occurs in the easily workable temperature range of 2° to 5°K might, therefore, have a quantum gap corresponding to absorption frequencies of the order of 40 to 100 kMc/sec. Previous superconductivity measurements[6] of Sn up to frequencies of 36 kMc/sec failed to reveal an energy gap, although measurements[7] in the infrared region indicate that Sn is not superconducting at optical frequencies. The development[8] at Duke University of refined millimeter wave techniques for the 1- to 5-mm region has made possible investigations in the

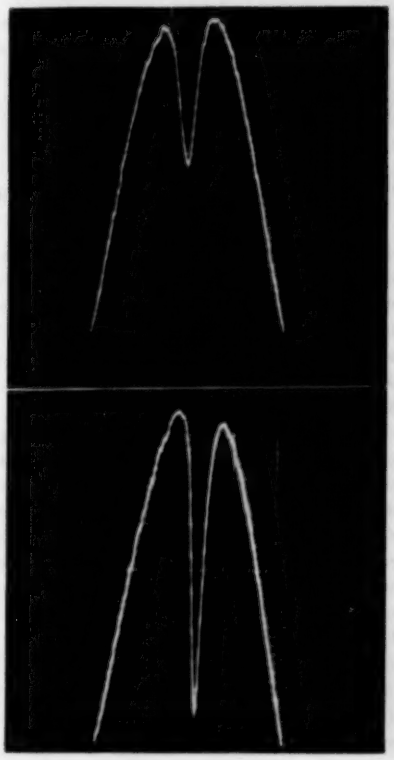

FIG. 1. Cathode-ray display of a resonance curve of a tinplated cylindrical cavity operating in TE_{011} mode at 4-mm wavelength and at 2.6°K; (a) with magnetic field applied to prevent superconductivity, (b) without magnetic field.

frequency range where the supposed energy gap might be measured for several substances including Sn, Al, and Cd. We have consequently undertaken a study of these metals. The rather suggestive preliminary results obtained for Sn will be briefly described here.

For Sn, $kT_c/h=77$ kMc/sec. Measurements have been made at wavelengths of 2, 2.5, 3, and 4 mm (77 kMc/sec to 150 kMc/sec). Superconductivity, but with some residual resistance, has been observed at all these frequencies for temperatures well below T_c. See, for example, Fig. 1. However, at temperatures not far below

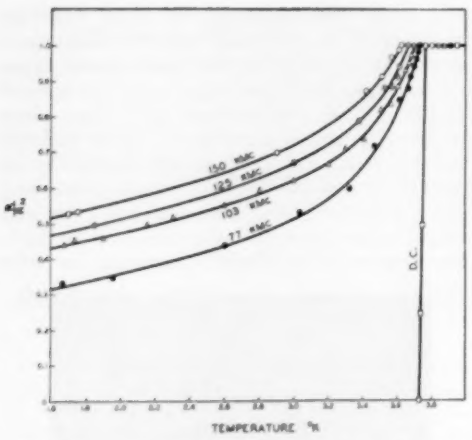

FIG. 2. Temperature variation of resistance of tin for dc and for the millimeter wave frequencies as indicated (wavelengths 2, 2.5, 3, and 4 mm).

T_c where there is already complete dc superconductivity, no evidence for superconductivity was found at any of these frequencies. The onset of superconductivity was found to depend on the frequency in a manner indicated by Figs. 2 and 3. The higher the frequency, the lower the temperature (below T_c) required to start the decrease in resistance.

The results indicate that the effective energy gap between the superconducting and normal states increases as temperature is decreased below the critical temperature T_c. As the gap becomes wider (temperature lower), higher and higher frequencies are required to prevent the onset of superconductivity. The energy gap seems, therefore, not to be defined except at a fixed temperature or at temperatures well below T_c. From our data, Fig. 3, we obtain a value of 77 kMc/sec or 3.9 mm for the maximum gap at the temperature, 3.72°K at which dc superconductivity becomes complete. Interestingly, this value is exactly kT_c/h. We have not yet measured at frequencies high enough to ascertain the maximum gap when $T \ll T_c$. However, our results indicate at very low temperatures the effective gap is appreciably greater than it is at 3.72°K. At temperatures only 0.1°K below 3.72°K it is already greater by a factor of 2. The projection of our data indicates it is an order of magnitude greater at $T=0$.

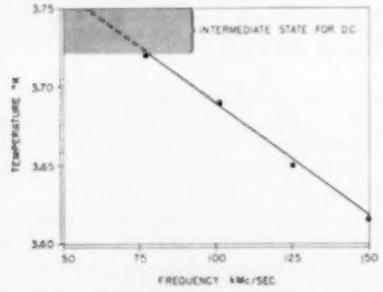

FIG. 3. Plot showing how the temperature for the onset of superconductivity depends on frequency of the conducted wave.

The measurements of Figs. 2 and 3 were made simply by observation of the change in resistance of an H_1-band wave guide. The same wave guide and hence the same superconducting surface was employed for all four frequencies. Measurements at 3 and 4 mm were also made with a resonant cavity operating in the TE_{01N} mode. From the measured value of the unloaded Q of the cavity the absolute (but not highly accurate) value of the surface resistance, R, could be calculated in both the normal and superconducting state. The value of R_N measured with the cavity was used to calculate R/R_N from the wave-guide measurements. For 2.0 and 2.5 mm, extrapolated values of R_N were used. A comparison of the value of R/R_N in Fig. 2 with the values obtained at longer wavelengths[9] suggests that R may not become zero at absolute zero for these frequencies. However, this is a highly tentative conclusion. Additional measurements are being made to make more certain the absolute values of R.

We wish to thank Dr. M. J. Buckingham and Professor L. W. Nordheim for helpful discussions of this work.

* This research was supported by the United States Air Force through the Office of Scientific Research of the Air Research and Development Command and by the Office of Ordnance Research, Department of the Army.

[1] H. Kamerlingh Onnes, Leiden Comm. **122b**, **124c** (1911).
[2] F. London and H. London, Physica **2**, 341 (1935); F. London, *Superfluids* (John Wiley and Sons, Inc., New York, 1950), Vol. 1.
[3] E. Maxwell, Phys. Rev. **78**, 477 (1950); Serin, Reynolds, and Nesbitt, Phys. Rev. **78**, 813 (1950).
[4] H. Fröhlich, Phys. Rev. **79**, 845 (1950).
[5] J. Bardeen, Phys. Rev. **80**, 567 (1950).
[6] E. Fawcett, Proc. Phys. Soc. (London) **A66**, 1071 (1953).
[7] Daunt, Keeley, and Mendelssohn, Phil. Mag. **23**, 264 (1937); K. G. Ramanathan, Proc. Phys. Soc. (London) **A65**, 532 (1952).
[8] W. C. King and W. Gordy, Phys. Rev. **90**, 319 (1953); **93**, 407 (1954).
[9] A. B. Pippard, *Advances in Electronics and Electron Physics* (Academic Press, Inc., New York, 1954), Vol. 6, pp. 1–45.

Cyclotron Absorption in Bismuth*

R. N. DEXTER† AND BENJAMIN LAX
Lincoln Laboratory, Massachusetts Institute of Technology, Lexington, Massachusetts
(Received October 3, 1955)

MICROWAVE experiments similar to those of cyclotron resonance in semiconductors[1] have been performed on bismuth single crystals at 23 000 Mc/sec and temperatures down to 1.3°K. The measurements were made in a microwave cavity operating in a TE_{111} mode with a linear polarized rf field at 45° to the plane of rotation of the dc magnetic field. The sample was

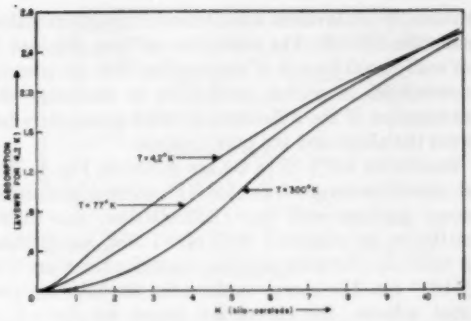

FIG. 1. Absorption in bismuth as a function of magnetic field. The curves at 77°K and 300°K were normalized so that the maximum absorption at 11 000 oersteds was scaled equal to that at 4.2°K. The ΔVSWR from 0 to 11 000 gauss was 0.83 and 0.12 for 77°K and 300°K, respectively.

mounted with Wood's metal at one end of the cavity with an exposed surface of approximately 6 mm in diameter. The cleaved surface of the crystal was metallurgically polished and etched through several cycles and finally polished.

Absorption traces as a function of magnetic field up to 11 000 oersteds were obtained at various temperatures as shown in Fig. 1. At low magnetic fields the curves showed sharper curvature and increased absorption, due to decreased lattice scattering, as the temperature was reduced. In this sample,[2] further increase in absorption and curvature was produced at 1.3°K. Although it appears[2] that $\omega\tau > 1$ at 4°K, the absorption is nonresonant. Resonance in metals at microwave frequencies is obscured because of high carrier concentration.[4]

Detailed analysis of the real part of the Poynting vector at a metallic interface with a transverse magnetic field shows that for a single isotropic carrier the absorption curve has an inflection point at

$$\omega_c \approx \omega + K/\tau, \tag{1}$$

where $\omega_c = eH/m^*c$ is the cyclotron frequency; ω, the rf frequency; τ, the collision time; and K, a constant of the order of unity. Thus, for high $\omega\tau$, $\omega_c \approx \omega$. Similar analysis for a single isotropic carrier with H parallel to the metal interface gives no magnetoabsorption for energy independent τ. For two or more carriers there is magnetoconductivity and an inflection point. The theory suggests the possibility of measuring effective masses and examining band structure of metals and semimetals by looking at dP/dH, the derivative of the absorption with respect to magnetic field.

Figure 2(a) shows an experimental trace of dP/dH for very pure bismuth[5] with the magnetic field perpendicular to the sample surface and parallel to the trigonal axis. The derivative curves were obtained by superposing a small magnetic field modulation at 34 cps on the applied dc field. Phase detection of the reflected signal yielded the traces shown. The magnified trace of Fig. 2(b), at low magnetic fields shows one peak at ~150 oersteds and another at ~480 oersteds. If we interpret these in accordance with Eq. (1), we obtain effective masses of 0.018 m_0 and 0.058 m_0, where m_0 is the free electron mass. Figure 3 shows a second trace with the magnetic field in the plane of the sample with peaks at about 100 oersteds, 250 oersteds, and 450 oersteds, corresponding to effective masses 0.012 m_0, 0.03 m_0, and 0.055 m_0. Similar traces were obtained at intermediate angles between H and the surface of the sample. Peaks of varying intensities appeared at $m^* \approx 0.02\ m_0$, $0.03\ m_0$, and $0.06\ m_0$ with some anisotropy.

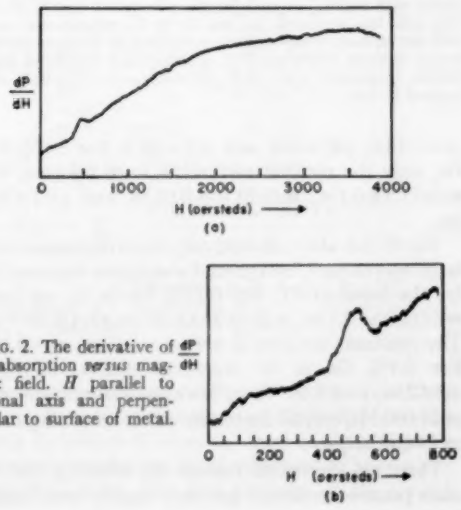

FIG. 2. The derivative of $\frac{dP}{dH}$ the absorption *versus* magnetic field. H parallel to trigonal axis and perpendicular to surface of metal.

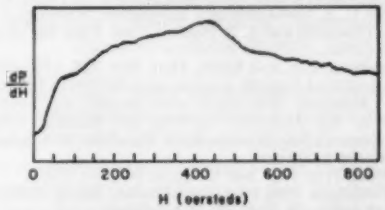

FIG. 3. Derivative of absorption *versus* magnetic field. H in the trigonal plane and parallel to surface of metal.

From the peak at about 450 oersteds, Fig. 2(b), a crude estimate of τ is made by assuming that $\Delta H \approx 150$ oersteds. From $\Delta H/H = 2/\omega\tau$, we estimate $\omega\tau \approx 6$. This yields a value of $\tau \approx 4 \times 10^{-11}$ sec, which is in reasonable agreement with Chambers and Pippard.[3]

This preliminary experiment has demonstrated the possibilities of the inflection point method for measuring effective masses of carriers in metals by microwaves. No convenient scheme for studying orientation effects was possible with the existing setup. A modification of the cavity and a refinement of the experiment will be made

for investigating possible anisotropy in oriented crystals. The preliminary data agree in order of magnitude with the results deduced by Jones[6] and Blackman[7] from the magnetic susceptibility experiments. However, their ellipsoidal models do not appear to explain our data. The interpretation of our results for multiple carriers is quite involved, particularly for the magnetic field parallel to the metal surface.[8] The simplest situation occurs for transverse H and circular polarization,[9] which would also permit the distinction between holes and electrons. More complicated cases involving ellipsoidal models are being analyzed. The theory which excludes the phenomenon of anomalous skin effect will have to be further refined.

We would like to thank Dr. H. J. Zeiger and Mrs. Laura M. Roth for many helpful suggestions and discussions and Mr. W. M. Walsh, Jr. for assisting with some of the experiments.

* The research reported in this document was supported jointly by the Army, the Navy, and the Air Force, under contract with the Massachusetts Institute of Technology.

† Now at the Department of Physics, University of Wisconsin, Madison, Wisconsin.

[1] Lax, Zeiger, and Dexter, Physica **20**, 818 (1954); and Dresselhaus, Kip, and Kittel, Phys. Rev. **98**, 368 (1955).

[5] This crystal of pure bismuth was supplied by Dr. E. I. Salkovitz of the U. S. Naval Research Laboratory, Washington, D. C.

[2] R. G. Chambers and A. B. Pippard, Proc. Phys. Soc. (London) **A65**, 955 (1952).

[4] Dresselhaus, Kip, and Kittel, Phys. Rev. **100**, 618 (1955).

[5] This crystal of bismuth was prepared by Mr. P. L. Moody of Lincoln Laboratory. The highly pure bismuth was kindly contributed by the American Smelting and Refining Company, Central Research Laboratories, South Plainfield, New Jersey, and was zone-refined 60 times.

[6] H. Jones, Proc. Roy. Soc. (London) **147**, 396 (1934).

[7] M. Blackman, Proc. Roy. Soc. (London) **166**, 1 (1938).

[8] B. Lax and L. M. Roth (to be published).

[9] A. F. Kip, Physica **20**, 813 (1954).

Cyclotron Resonance in Ge-Si Alloys*

G. Dresselhaus, A. F. Kip, Han-Ying Ku, and G. Wagoner,
Department of Physics, University of California, Berkeley, California

and

Schuyler M. Christian, *RCA Laboratories, Princeton, New Jersey*

(Received July 27, 1955; revised manuscript received August 31, 1955)

We have observed cyclotron resonance at 4°K and at 24 000 and 48 000 Mc/sec in four alloys prepared by the RCA Laboratories: in atomic percent, 0.4 and 0.75 Ge in Si; 0.8 and 5.4 Si in Ge. The experimental technique generally has been described earlier,[1] but the 6-mm apparatus is new and utilizes a transmission cavity; the power is produced as the second harmonic from a germanium crystal point-contact rectifier, with a K-band klystron as primary source. The striking feature of the results is that it is possible to resolve cyclotron lines with as much as 5% Si in Ge, whereas 10^{-4}% of trivalent or pentavalent substitutional impurities makes resolution difficult. The resolution we have obtained is not really good enough in conjunction with the present uncertainties in crystal orientation to encourage the examination of the differences in mass parameters between the alloys and the pure crystals.

Results for 0.8% Si in Ge are shown in Fig. 1. The calculated curves are drawn for ⟨111⟩ spheroidal electron energy surfaces with $m_l=(1.59\pm0.05)m$, $m_t=(0.086\pm0.002)m$, as compared with $m_l=1.58m$, $m_t=0.082m$ for pure Ge. The alloy electron relaxation times are 2 to 4×10^{-11} sec. The energy surfaces for the holes are two fluted spheres: the curves are drawn for $A=-11.8\pm0.1$, $|B|=7.4\pm0.1$, and $|C|=10.5\pm0.4$, all in units of $\hbar^2/2m$; the constants for pure germanium[1] are

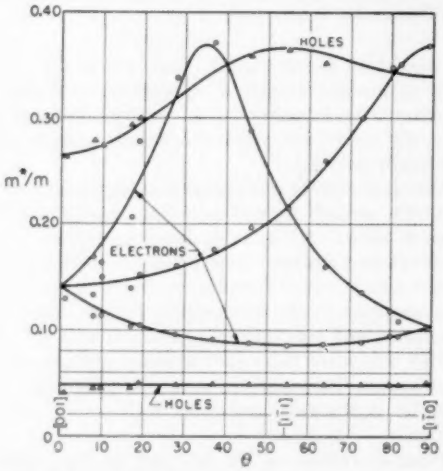

Fig. 1. Variation of effective masses for electrons and holes in the Ge-rich alloy 0.8% Si in Ge with the angle that the magnetic field makes with a [001] crystal direction; frequency 48 000 Mc/sec. The solid line represents the best fit to the experimental points with the parameters $m_l=0.086m$, $m_t=1.59m$ for electron constant-energy surfaces which are ⟨111⟩ spheroids and the fluted energy surface parameters $A=-11.8$, $|B|=7.4$, and $|C|=10.5$, all in units of $\hbar^2/2m$.

$A=-13.0$, $|B|=8.9$, and $|C|=10.3$. For 5.4% Si in Ge, only the electron resonances were resolved, with $m_l\cong(1.5\pm0.1)m$, $m_t\cong(0.10\pm0.01)m$, and $\tau\approx1\times10^{-11}$ sec.

The Si-rich alloys showed only electron resonances: a large nonresonant background absorption suggests that for the holes $\omega\tau\ll1$. For 0.75% Ge in Si, we found $m_l\cong(1.10\pm0.1)m$; $m_t\cong(0.20\pm0.01)m$; $\tau\approx1\times10^{-11}$ sec. The constants for pure Si are: $m_l=0.97m$; $m_t=0.19m$. For 0.4% Ge in Si: $m_l\cong(0.83\pm0.2)m$; $m_t\cong(0.18\pm0.02)m$; $\tau\approx1\times10^{-11}$ sec; this alloy was measured only at 24 000 Mc/sec; all the results on the other alloys refer to 48 000 Mc/sec.

There are theoretical reasons for believing that the mass parameters should not vary rapidly with compo-

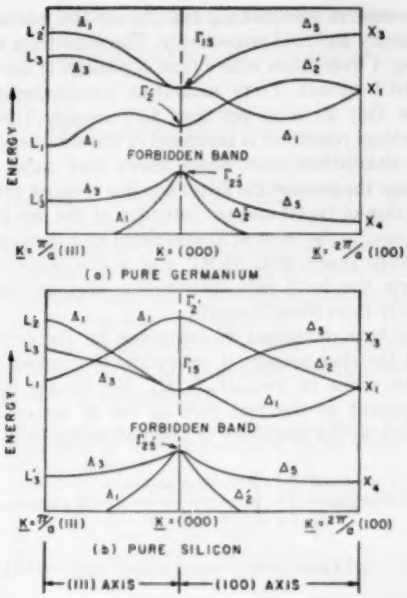

FIG. 2. Schematic diagrams of the energy band contours in perfect Ge and Si crystals along [111] and [100] axes in the reduced zone as suggested by Herman.[3] The removal of the degeneracy by spin-orbit interaction is not shown.

sition. If the conduction band minima are a Δ_1 state in Si and an L_1 state in Ge, as suggested by Herman,[3] then perturbation theory about the minimum gives

$$E=\frac{\hbar^2}{2}\left(\frac{k_1^2}{m_l}+\frac{k_2^2+k_3^2}{m_t}\right), \tag{1}$$

where for the Δ_1, $\mathbf{k}=k(100)$, minimum:

$$\frac{m}{m_l}=1+\frac{2}{m}\sum_{l=\Delta_1}{}'\frac{|(\Psi_{100}{}^0|p_x|\Psi_{100}{}^l)|^2}{E_0-E_l}; \tag{2}$$

$$\frac{m}{m_t}=1+\frac{2}{m}\sum_{l=\Delta_1}\frac{|(\Psi_{100}{}^0|p_y|\Psi_{100}{}^l)|^2}{E_0-E_l}. \tag{3}$$

For the L_1, $\mathbf{k}=(\pi/a)(111)$, minimum:

$$\frac{m}{m_l}=1+\frac{2}{3m}\sum_{l=L_2'}\frac{|(\Psi_{111}{}^0|p_x+p_y+p_z|\Psi_{111}{}^l)|^2}{E_0-E_l}; \tag{4}$$

$$\frac{m}{m_t}=1+\frac{2}{3m}\sum_{l=L_2'}\frac{|(\Psi_{111}{}^0|p_x+\omega p_y+\omega^2 p_z|\Psi_{111}{}^l)|^2}{E_0-E_l}, \tag{5}$$

where $\omega^3=1$.

Herman's[3] explanation (Fig. 2) of the optical gap change observed by Johnson and Christian[3] does not show a Δ_1 level in Si or an L_2' level in Ge sufficiently close to the conduction band minimum to have a profound effect on m_l. The data for holes on the Ge-rich side indicate that the levels at $\mathbf{k}=0$ are separating in an orderly fashion.

There was some suggestion in the results at 24 000 Mc/sec that alloy scattering processes may tend to mix the different ellipsoids together, producing less anisotropy in the observed electron mass parameter. Such an effect, if it exists, would be most effective under conditions of low resolution ($\omega\tau\approx 1$). Our present practice for crystal orientation involves certain resonance degeneracy checks *in situ*, and such a procedure does not work effectively when the resolution is poor.

We are indebted to Mr. Robert Behringer for assistance with the measurements and to Dr. F. Herman and Professor C. Kittel for discussion of the results.

* The work at Berkeley was assisted by the Office of Naval Research and the U. S. Signal Corps.

[1] Dresselhaus, Kip, and Kittel, Phys. Rev. 98, 368 (1955).
[2] F. Herman, Phys. Rev. 95, 847 (1954).
[3] E. R. Johnson and S. M. Christian, Phys. Rev. 95, 660 (1954).

Rapid Passage Effects in Electron Spin Resonance

A. M. PORTIS

Sarah Mellon Scaife Radiation Laboratory and Physics Department, University of Pittsburgh, Pittsburgh, Pennsylvania

(Received September 26, 1955)

RELAXATION effects which have been observed in electron spin resonance from F centers in alkali halides[1] and from donor states in silicon[2] are interpreted here in terms of the rapid passage theory of Bloch.[3] The distinguishing feature of the two cases in which these effects have been observed is that the line broadening is of the inhomogeneous type,[4,5] arising from hyperfine interaction.

In Fig. 1 we show the dispersion signal obtained at room temperature from a sample of LiF irradiated with

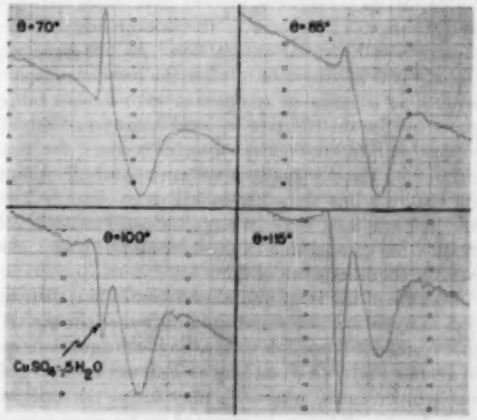

FIG. 1. Dispersion signal in LiF as a function of magnetic field for several values of θ, the phase angle between modulation field and reference signal.

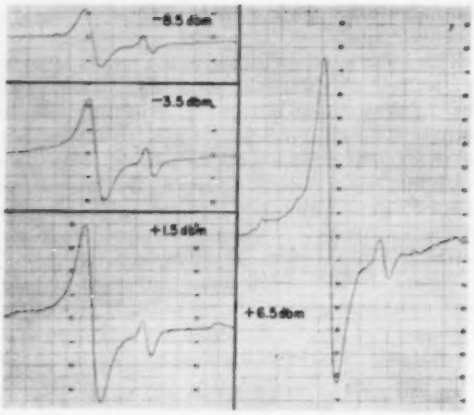

FIG. 2. Absorption signal in KCl as a function of magnetic field for several values of power incident on the microwave cavity. The low field signal is copper sulfate.

220-kev x-rays for a period of 18 hours. The signal is obtained by superimposing a small modulation field at a frequency of 280 cps on the static magnetic field and then detecting the component of the real part of the rf susceptibility which varies at this frequency. Two surprising results are evident from an examination of these curves:

1. The LiF signal lags the modulation field by nearly 90°.

2. The line shape of the LiF resonance more closely resembles an absorption curve than it does the derivative of a dispersion curve.

On the other hand, the copper sulfate signal appears quite normal. The difference between the primary sources of line broadening for these two samples suggests the reason for the difference in their behavior. It is well established that the source of the line width in $CuSO_4 \cdot 5H_2O$ is magnetic dipolar broadening narrowed by exchange. The source of the line broadening in F centers is a hyperfine interaction.[5] As has been suggested,[4] it is appropriate to view the resonance from F centers as a *series* of resonances with a distribution given by the distribution in local hyperfine fields. In copper sulfate, resonance absorption must be associated with the electron spin system as a whole. Assuming that the line structure in LiF is as described one may ask whether, with an amplitude of magnetic field modulation comparable to the over-all line width, slow passage conditions can obtain.

Because of the large and almost continuous distribution in hyperfine fields and the dilution of the electron spin system, it is possible to use the Bloch equations and to assume that $T_2 = T_1$ as long as T_1 is not excessive. At low temperatures, where T_1 may be of the order of seconds, the situation is expected to be more complicated. Under saturation conditions the time of passage is of the order of $H_1/\omega_m H_m$, where $2H_1$ is the peak transverse rf field and ω_m and H_m are the modulation frequency and field respectively. The recordings shown in Fig. 1 were taken with a time of passage of the order of 10^{-5} second. From saturation measurements we know that T_1 is longer than 10^{-4} second. Then, an individual resonance is traversed in less than one-tenth of a spin-lattice time. Bloch shows that under rapid passage the sense of the dispersion line reverses with the direction of travel and the intensity of the line is proportional to the value of S_z associated with the line. The observed phase shift of 90° and a line shape which reflects the local field distribution may be inferred directly from Bloch's results.

We have developed an expression for the deviation from the slow-passage rf susceptibility expressed as a power series in $\epsilon = \omega_m H_m T_1/H_1$. We obtain for the component of the real part of the rf susceptibility periodic at the frequency of the modulation field:

$$\chi'(\omega) = \tfrac{1}{2}\pi\chi_0\omega \frac{\partial}{\partial\omega_0}\left\{\frac{2}{\pi}\int_0^\infty \frac{\omega' h(\omega',\omega_0)\,d\omega'}{\omega'^2-\omega^2}\right\}\gamma H_m \cos(\omega_m t)$$

$$+\tfrac{1}{4}\pi\chi_0\omega\epsilon\cos\phi_1\, h(\omega,\omega_0)\sin(\omega t-\phi_1)+O(\epsilon^3), \quad (1)$$

where $h(\omega,\omega_0)$ is the normalized distribution in local magnetic fields centered about the applied field, $H_0=\omega_0/\gamma$, and $\phi_1=\tan^{-1}(\omega_m T_1)$. The first term on the right is simply the derivative of the dispersion envelope associated with the field distribution. The first-order correction introduces the field distribution itself, shifted in phase by nearly 90°.

In order to obtain an experimental check of Eq. (1) we have re-examined the electron resonance from F centers in KCl. Figure 2 shows the peculiar saturation behavior of the absorption which has already been discussed.[4] From the data obtained we have determined that $T_1 = 5\times10^{-6}$ sec at room temperature. Then $\epsilon = 0.4$

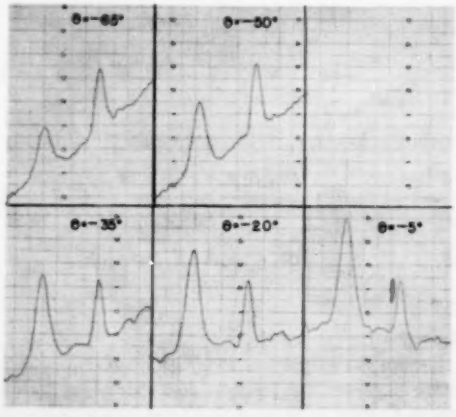

FIG. 3. Dispersion signal in KCl as a function of magnetic field for several values of θ, the phase angle between modulation field and reference signal. The low field signal is copper sulfate.

and at the line center, taking a shape of the form

$$h(\omega,\omega_0)=(T_2^*/\pi)\exp[-T_2^{*2}(\omega-\omega_0)^2/\pi],$$

we have

$$\chi'(\omega)=\tfrac{1}{2}(0.62)\chi_0\omega T_2^*(\gamma H_m T_2^*)\cos(\omega_m t) +\tfrac{1}{4}\chi_0\omega T_2^*\epsilon\sin(\omega_m t)+O(\epsilon^3). \quad (2)$$

The lag angle, $\phi=\tan^{-1}(0.81/\gamma H_m T_2^*)\sim 45°$ for $\Delta H=1/\gamma T_2^*=19$ oersteds. In Fig. 3 we show the set of dispersion curves for KCl. The phase shift as determined from these curves is consistent with the above estimate. This confirms that rapid passage conditions are responsible for the observed effects.

It is a pleasure to thank Dr. F. Keffer for his interest in this work and Mr. D. Shaltiel for assisting with the preliminary measurements.

* This research was supported by the United States Air Force through the Office of Scientific Research of the Air Research and Development Command.

[1] A preliminary account of the experimental work was given by A. M. Portis and D. Shaltiel, Phys. Rev. **98**, 264(A) (1955).
[2] A. F. Kip (private communication).
[3] F. Bloch, Phys. Rev. **70**, 460 (1946).
[4] A. M. Portis, Phys. Rev. **91**, 1071 (1953).
[5] Fletcher, Yager, Pearson, and Merritt, Phys. Rev. **95**, 844 (1954).
[6] Kip, Kittel, Levy, and Portis, Phys. Rev. **91**, 1066 (1953).

Phenomenological Equations for Superconductors

M. R. Schafroth and J. M. Blatt

The F. B. S. Falkiner Nuclear Research and Adolph Basser Computing Laboratories, School of Physics, The University of Sydney, Sydney, N. S. W. Australia*

(Received May 9, 1955)

In every physical system at finite temperature the momenta of distant particles are uncorrelated—that is, there exists a "correlation length" Λ such that particles which are farther apart than Λ have rapidly decreasing momentum correlation.[1] Λ is very large in a lattice of particles; for nearly freely moving particles Λ is usually of the order of several mean free paths against collisions, although there are exceptional systems in which it can be much longer. No matter what the size of the correlation length, its very existence has important effects on the behavior of a system in temperature equilibrium when this system is rotated uniformly, or when it is put into a magnetic field.

It has been shown[2] that London's equation,[3]

$$-\lambda c\,\mathrm{curl}\mathbf{j}_s=\mathbf{B}, \quad (1)$$

is incompatible with the existence of a finite correlation length; i.e., (1) implies an infinite correlation length (more precisely a correlation length proportional to the size of the container). This is illustrated by the fact that the only model known to obey Eq. (1), the ideal Bose-Einstein gas of charged particles below its condensation point,[4] does indeed have an infinite correlation length: the momenta of bosons occupying the ground state are correlated over the whole volume of the container.

It is therefore necessary to modify the London equation so as to be consistent with a finite correlation length Λ. This can be done by rewriting (1) in terms of the magnetization vector $\mathbf{M}$ rather than the supercurrent density vector $\mathbf{j}_s$. The two vectors are related through

$$\mathbf{j}_s=c\,\mathrm{curl}\mathbf{M}, \quad (2)$$

so that Eq. (1) becomes

$$-\lambda c^2\,\mathrm{curl}\,\mathrm{curl}\mathbf{M}=\mathbf{B}. \quad (3)$$

We now expand in an orthonormal set of vector eigenfunctions $\mathbf{u}_q(\mathbf{r})$ defined by

$$\mathrm{curl}\,\mathrm{curl}\mathbf{u}_q=q^2\mathbf{u}_q, \quad (4a)$$

$\mathbf{u}_q$ is normal to the surface of the superconductor, (4b)

and

$$\int(\mathbf{u}_q)^2 d^3\mathbf{r}=1, \quad (4c)$$

where the last integral extends over the volume of the superconductor. These functions form a complete set. We write

$$\mathbf{M}(\mathbf{r})=\textstyle\sum_q M_q\mathbf{u}_q(\mathbf{r}), \quad \mathbf{B}(\mathbf{r})=\sum_q B_q\mathbf{u}_q(\mathbf{r}). \quad (5)$$

Equation (3) becomes

$$M_q=-(\lambda c^2 q^2)^{-1}B_q. \quad (6)$$

In this form the equation can be modified. We introduce a "kernel" $K(q)$ which is a (so far unknown) continuous function of q, and write

$$M_q=-(\lambda c^2)^{-1}K(q)B_q. \quad (7)$$

The values of q which appear in (7) are the discrete eigenvalues of Eq. (4) for the particular shape and volume of the superconductor under study. The construction of Eq. (7) in terms of the eigenfunctions (4) ensures automatically that the supercurrent is parallel to the superconductor at its surface, provided only that $K(q)$ decreases sufficiently rapidly for large q.

It can be shown that, in terms of the kernel $K(q)$, the existence of a finite correlation length implies that the quantity $qK(q)$ must not become infinite as q approaches 0. Thus the London equation (6) gives an infinite correlation length. An additional clue to the form of $K(q)$ can be derived from the observed agreement between the London equation and the Meissner-Ochsenfeld effect. This indicates that $K(q)$ must behave like q^{-2} in the relevant region of q, i.e., for $q\sim d^{-1}$, where $d=c(\lambda/4\pi)^{\frac{1}{2}}$ is the London penetration depth. A simple kernel which satisfies both requirements is

$$K(q)=1/[q(q+\mu)], \quad (8)$$

where μ is an inverse length, such that μ^{-1} is comparable

to the correlation length Λ. In order that (8) be consistent with (1) in the region $q \sim d^{-1}$, the correlation length Λ must be much larger than the penetration depth d.

It is well known that London's second equation,

$$\lambda \partial \mathbf{j}_s / \partial t = \mathbf{E}, \tag{9}$$

cannot be derived from (1) in general. However, a partial derivation can be made as follows: We assume that all relaxation times are small compared to the time intervals of interest, so that we are allowed to differentiate the equilibrium equation (1) with respect to time. We then use Maxwell's equations to get the curl of (9). The divergence of both sides of (9) is automatically zero. The terms omitted in this quasi-derivation

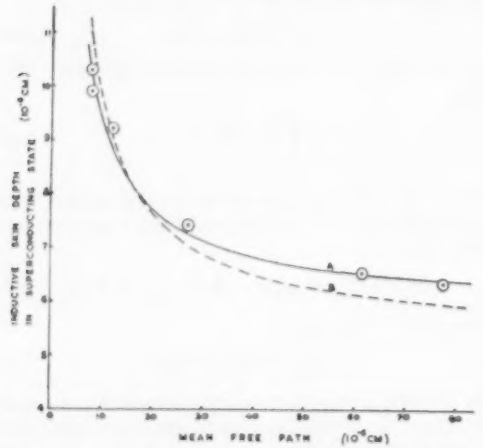

FIG. 1. Inductive skin depth d_{eff} of a superconductor *vs* mean free path ξ of the conduction electrons. The points are Pippard's measured values. Curve A is the best theoretical curve, with a correlation length $\Lambda \approx 3\xi$, and $\lim_{\xi \to \infty} d_{eff} = d = 5.9 \times 10^{-6}$ cm. Curve B is the best curve under the assumption $d = 5.3 \times 10^{-6}$ cm, which is the value for very pure tin determined by Pippard in another measurement; the correlation length for curve B is $\Lambda \approx 2\xi$.

are precisely the ones responsible for supercurrent charge transport (constant vector fields in a simply connected region, "streamline flow" fields in a multiply connected superconductor). However, the method outlined here is presumably sufficient for the discussion of phenomena in which there is no actual charge transport. Straightforward application of this method to our modified equations (7) and (8) is therefore sufficient to discuss microwave measurements on superconductors.

Equations (7) and (8) yield a static field penetration different from (1), but the penetration depth measured with small spheres in colloidal suspension remains equal to $d = c(\lambda/4\pi)^{\frac{1}{2}}$. At microwave frequencies, however, there are significant differences. The inductive skin depth determined from the inductive part of the surface impedance of superconductors is no longer equal to the statically measured penetration depth. The ratio between the inductive skin depth d_{eff} and the static penetration depth d can be used to determine the quantity μ in Eq. (8), i.e., to estimate the size of the correlation length Λ.

This provides a natural explanation for an effect found experimentally by Pippard.[5] Pippard observed a strong dependence of the measured penetration depth on the mean free path ξ of the electrons in the metal in its normal state. The measurements of Pippard are compared with our theory in Fig. 1. Curve A is the best fit and corresponds to a static penetration depth $d = 5.9 \times 10^{-6}$ cm, and $\mu\xi = 0.291$ (i.e., a correlation length $\Lambda \cong \mu^{-1}$ slightly more than 3 times the mean free path ξ). Not only is the ratio of correlation length to mean free path very reasonable, but the extrapolated static penetration depth d agrees quite well with Pippard's microwave value $d = 5.3 \times 10^{-6}$ cm in very pure tin (for which Λ is very large, and hence $d_{eff} = d$). It is difficult to determine whether the difference between these two values of d is significant, since the experiments are subject to considerable uncertainty. However, in curve B we show the best fit assuming $d = 5.3 \times 10^{-6}$ cm; the corresponding value of the product $\mu\xi = 0.493$, i.e., the correlation length Λ is equal to twice the mean free path ξ.

In view of the fact that the experimental measurements are subject to unknown errors, and that our theoretical kernel (8) is merely one possibility out of many others, this agreement between theory and experiment is entirely satisfactory.

It should be mentioned that the modified kernel (8) is basically different from the one proposed by Pippard himself in order to account for his measurements. Our modification cuts down the contributions from the *long*-wavelength parts ($q^{-1} \gg \Lambda$) of the magnetic field; Pippard's[5] equation (7) gives a smearing over small regions of space, i.e., a cutoff for the *short*-wavelength parts of the field. Pippard's equation, therefore, although in agreement with his experiments, contradicts the existence of a finite correlation length just as much as London's equation (1).

Similarly, Bardeen's[6] equation is inconsistent with a finite correlation length and can therefore not be accepted. Bardeen obtains his equation by assuming a finite energy gap between the lowest state of the electron gas and all excited states. Such an energy gap cannot occur in a system of finite correlation length.

We would like to thank Dr. S. T. Butler for valuable discussions.

* Also supported by the Nuclear Research Foundation within the University of Sydney.

[1] The concept of a correlation length was introduced in connection with work on the statistical mechanics of rotating systems by Blatt, Butler, and Schafroth, Phys. Rev. **100**, 481 (1955).

[2] M. R. Schafroth, Phys. Rev. **100**, 502 (1955).

[3] F. London, *Superfluids* (John Wiley and Sons, Inc., New York, 1950), Vol. I.

[4] M. R. Schafroth, Phys. Rev. **96**, 1149 (1954); **100**, 463 (1955).

[5] A. B. Pippard, Proc. Roy. Soc. (London) **A216**, 547 (1953).

[6] J. Bardeen, Phys. Rev. **97**, 1724 (1955).

Magnetic Second-Order Transitions

K. J. TAUER* AND R. J. WEISS
Ordnance Materials Research Office, Watertown Arsenal, Watertown, Massachusetts
(Received October 4, 1955)

WE have recently examined the thermodynamic functions of pure iron with the purpose of extending the functions to the calculation of the phase diagrams of iron rich alloys.[1] In this study we have examined the specific heat curves of a number of ferromagnets and antiferromagnets to establish correlations between the magnetic enthalpy and magnetic entropy, as well as relationships between the critical temperature and magnetic moments. The purpose of this note is to point out several interesting correlations observed.

Our general method consisted of fitting the (previously published) measured specific heat, at temperatures sufficiently removed from the Curie or Néel temperature, by Debye functions corrected to C_p for lattice expansion (and electronic terms when applicable). Figure 1 shows several representative curves. The difference between measured and constructed specific heats were then integrated for magnetic enthalpy and magnetic entropy. Table I summarizes the pertinent data.[2-8]

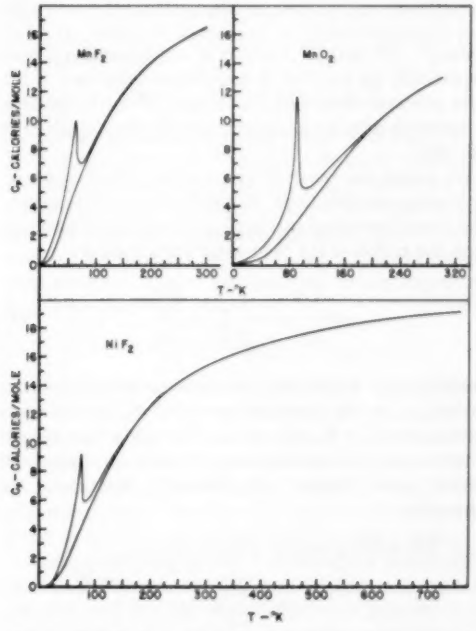

FIG. 1. Specific heat *versus* temperature for 3 representative antiferromagnets. The calculated curves using Debye temperatures given in Table I are included.

The sixth column of Table I shows that the magnetic enthalpy is given by the average thermal energy at the critical temperature and that this is essentially the energy required to uncouple the magnetic moments.

The seventh column shows that the magnetic entropy is given by the statistical expression $R\ln(2s+1)$, where $2s$ is the number of unpaired electrons recently indicated

TABLE I. Magnetic enthalpy and entropy for various substances shown in relation to the Curie or Néel temperature. The Debye temperatures are those used to determine the lattice contribution to the specific treat.

Substance	Debye θ(°K)		T_c (°K) Curie or Néel temp.	H_{mag} enthalpy (cal/mole)	S_{mag} entropy (cal/mole deg)	H/RT_c	$S_{mag}/R\ln(2s+1)$
αFe[a]		420	1043	1925	2.18	0.926	0.943
MnF_2[b]	θ(Mn)	200	63	135	3.37	1.07	0.946
	θ(F)	600					
MnO_2[c]	θ(Mn)	475	92	195	2.60	1.06	0.942
	θ(O)	950					
NiF_2[d]	θ(Ni)	300	77	141	2.26	0.922	1.03
	θ(F)	700					
VCl_2[e]	θ(V)	300	104	195	2.10	0.937	0.960
	θ(Cl)	425					
V_2O_3[f]	θ(V)	500	169	640	4.55	0.953	1.04
	θ(O)	875					
Cr_2O_3[g]	θ(Cr)	500	306	1270	5.43	1.04	0.984
	θ(O)	1150					

[a] See reference 2. [d] See reference 5. [f] See reference 7.
[b] See reference 3. [e] See reference 6. [g] See reference 8.
[c] See reference 4.

TABLE II. Ratio of total magnetic enthalpy to magnetic entropy tabulated for face-centered cubic and body-centered cubic substances.[a]

Face-centered cubic substances		$T_c/\ln(2s+1)$	Body-centered cubic substances		$T_c/\ln(2s+1)$
	Composition			Composition	
NiCo	0% Ni	1400	FeCr	30% Fe	875
	25% Ni	1410		50	910
	50% Ni	1420		70	882
	75% Ni	1380		100	900
	100% Ni	1330			
			FeCo	85	970
NiCu	50% Ni	1270			
			FeAl	70	970
NiCr	90% Ni	1400			
			FeMn	84	895
NiMo	95.73% Ni	1300			av 905±20
NiSi	91.4% Ni	1240			
NiZn	88.1% Ni	1460			
NiW	85% Ni	1420			
CoMo	95% Co	1320			
CoCr	95% Co	1350			
		av 1360±50			

[a] All data taken from R. Bozorth, *Ferromagnetism* (D. Van Nostrand Company, Inc., New York, 1951).

in the case of NiF_2 by Catalano and Stout.[4] In the case of αFe the moment is the measured value, i.e., 2.2 Bohr magnetons, while the moment of the transition elements in their compounds is taken as follows in (for example) MnF_2. Manganese has seven electrons outside the argon core of which two are associated with the two fluorines leaving five electrons. These, by Hund's rule, are of like spin and result in a moment, i.e., $2s$ equal to 5 Bohr magnetons. The statistical entropy is then $R\ln 6$, equal to 3.56 entropy units.

Another interesting correlation is between Curie temperature and magnetic moment for face-centered cubic and body-centered cubic metals illustrated in Table II, and expressed as the ratio between total enthalpy, RT_c, and total entropy, $R\ln(2s+1)$.

Since the ratios are in proportion to the number of nearest neighbors, $1360/905=12/8$, the proportionality can be expressed for both body-centered and face-centered lattices as $T_c/\ln(2s+1)=113Z$ where Z is the number of nearest neighbors. Although the data for hexagonal close-packed and antiferromagnetic lattices are quite limited, the following modification of this formula appears to cover the general case for *transition metals:*

$$T_c/\ln(2s+1)=113|Z_\uparrow-Z_\downarrow|,$$

where $Z_\uparrow$ and $Z_\downarrow$ are the number of nearest neighbors with spin up and spin down.

* Chemistry Department, Boston College, Boston, Massachusetts.

[1] K. J. Tauer and R. J. Weiss (to be published).
[2] L. S. Darken and R. P. Smith, Ind. Eng. Chem. **43**, 1815 (1951).
[3] J. W. Stout and H. E. Adams, J. Am. Chem. Soc. **64**, 1535 (1942).
[4] K. K. Kelley and G. E. Moore, J. Am. Chem. Soc. **65**, 782 (1943).
[5] E. Catalano and J. W. Stout, J. Chem. Phys. **23**, 1284 (1955).
[6] C. H. Shumate, J. Am. Chem. Soc. **69**, 220 (1947).
[7] C. T. Anderson, J. Am. Chem. Soc. **58**, 564 (1936).
[8] C. T. Anderson, J. Am. Chem. Soc. **59**, 488 (1937).

Thermodynamics of Irreversible Processes and the Overhauser Nuclear Polarization Effect

W. A. Barker* and A. Mencher†
Swiss Federal Institute of Technology, Zürich, Switzerland
(Received September 6, 1955)

WE have treated the Overhauser nuclear polarization effect[1] from the point of view of the thermodynamics of irreversible processes and the Onsager relations. For this purpose it is convenient to think of the relaxation processes of the electrons as chemical reactions and consider that the totality of spins, electronic and nuclear, constitutes a system containing the four components n_m, n_{m-1}, and $e_{\pm\frac{1}{2}}$, where n_m denotes a nucleus with component m of the spin angular momentum I in the direction of the external magnetic field H_0, and $e_{\pm\frac{1}{2}}$ refers to electrons whose spin components are parallel (+) or antiparallel (−) to H_0. The population of each of these components is denoted by M_m, M_{m-1}, and $N_{\pm\frac{1}{2}}$, respectively.

We may now say that there are two independent "chemical" reactions, one in which the electron spin relaxes accompanied by a nuclear spin flip and the other in which the electron spin relaxes without an accompanying nuclear spin flip. It is assumed that the nuclear relaxation may take place (1) accompanied by an electron spin flip in the opposite sense, (2) accompanied by an electron spin flip in the same sense, or (3) without an accompanying electron spin flip, and that the total number of electrons equals the total number of nuclei.

The two processes may be represented by the following reaction equations:

$$(f^{(1)}-f^{(2)})e_{\frac{1}{2}}+n_{m-1}\rightleftarrows(f^{(1)}-f^{(2)})e_{-\frac{1}{2}}+n_m, \qquad \text{(A)}$$

$$f^{(B)}e_{\frac{1}{2}}\rightleftarrows f^{(B)}e_{-\frac{1}{2}}, \qquad \text{(B)}$$

where $f^{(1)}$, $f^{(2)}$, and $f^{(3)}$, the sum of which is unity, denote respectively the fraction of nuclei relaxing by each of the three processes described above, and $f^{(B)}$ is the fraction of electrons relaxing without an accompanying nuclear spin flip.

We adopt the point of view of De Groot[2] and use, with minor modifications, his terminology and notation. The internal entropy production per unit time resulting from the action of the "chemical" processes is

$$\sigma\equiv\frac{d_iS}{dt}=-\frac{1}{T}\sum_{k=1}^{4}\mu_k\frac{dN_k}{dt}, \qquad (1)$$

where T is the temperature of the surroundings (i.e., the lattice), μ_k is the chemical potential of the kth component, and $N_1=N_{\frac{1}{2}}$, $N_2=M_{m-1}$, $N_3=N_{-\frac{1}{2}}$, $N_4=M_m$. In order to cast (1) into the form of a sum of products of "forces" and "fluxes," the following definitions are convenient.

(i) The affinity for the jth reaction is

$$A_j\equiv-\sum_{k=1}^{4}\mu_k\nu_{kj},$$

where the ν_{kj} are the stoichiometric coefficients.

(ii) The "forces" are

$$X_j\equiv A_j/T.$$

(iii) The reaction rates or "fluxes" are

$$J_j\equiv\frac{1}{\nu_{kj}}\frac{d_jN_k}{dt}, \quad \text{where} \quad \sum_j d_jN_k=dN_k.$$

Equation (1) may now be written in the desired form $\sigma=\sum_j X_jJ_j$.

We now make the usual assumption that a linear relationship holds between the "forces" and the "fluxes":

$$J_A = L_{AA}X_A + L_{AB}X_B,$$
$$J_B = L_{BA}X_A + L_{BB}X_B. \quad (2)$$

According to the general theory, the Onsager relations hold with the above definitions of forces and fluxes. It is, however, an interesting and important fact that the Onsager relations are automatically satisfied in a trivial way by the condition of the independence of the two reactions, which requires that $L_{AB}=L_{BA}=0$.

We may apply the above considerations to the situation in which the spins are subject to a static magnetic field and in addition to a time-varying magnetic field of constant amplitude which resonates the electron spin system and forces it out of its thermal equilibrium distribution. The chemical potential of the component $e_{+\frac{1}{2}}$ no longer equals that of the component $e_{-\frac{1}{2}}$ as is the case for thermal equilibrium. The difference between the chemical potentials is maintained by the time varying field, the effect of which may be represented by a fixed "chemical" "force,"

$$X_B = A_B/T = f^{(B)}(\mu_{\frac{1}{2}} - \mu_{-\frac{1}{2}})/T.$$

The properties of the stationary state resulting from the time-varying magnetic field may be found by calculating the minimum entropy production subject to the constraints imposed on the system which here take the form X_B=constant. The required condition $\partial\sigma/\partial X_A = 0$ is satisfied if $J_A = L_{AA}X_A = 0$ or $A_A = 0$. Using (1), we then obtain the equation of reaction equilibrium corresponding to reaction (A):

$$f^{(A)}(f^{(1)} - f^{(2)})(\mu_{\frac{1}{2}} - \mu_{-\frac{1}{2}}) = f^{(A)}(\mu_m - \mu_{m-1}).$$

This equation forms the principal pillar supporting the thermodynamic and statistical arguments leading respectively to Eq. (1) of our previous communication[3] and to an analogous expression for the case of Fermi-Dirac statistics. The details of the justification of these arguments and of the discussion presented above will be given in an article to be submitted to this Journal.

It should be emphasized that the above results apply both to Boltzmann and to Fermi-Dirac statistics for the electrons and that the only restriction is imposed by the assumption of the validity of the linear relations (3). The condition is that the chemical affinities A_j be small compared to kT. For the most stringent case of complete saturation of the electron spin system, the results are the same for both statistics and lead to the requirement that

$$2f^{(B)}|\mu_e|H \ll kT. \quad (3)$$

To the extent that this is fulfilled, the results of the theory of the thermodynamics of irreversible processes are valid, and in particular the principle of minimum entropy production applies.[4] Since $f^{(B)}$ decreases sharply with decreasing temperature because of the inverse dependence of the corresponding relaxation time upon temperature,[5] it may be expected that the condition (3) will be fulfilled over essentially the entire range of field and temperature at which the related measurements may be performed.

We wish to express our appreciation to Professor W. Pauli and Professor G. Busch for comments and encouragement, and to A. Thellung and C. Enz for helpful discussions.

* Present address: St. Louis University, St. Louis, Missouri.
† Fellow in Switzerland of the Institute for International Education.
[1] Albert W. Overhauser, Phys. Rev. **92**, 411 (1953).
[2] S. R. De Groot, *Thermodynamics of Irreversible Processes* (Interscience Publishers, Inc., New York, 1952).
[3] W. A. Barker and A. Mencher, Phys. Rev. **98**, 1868 (1955).
[4] The Overhauser effect for nonmetals has recently been discussed from the point of view of the principle of minimum entropy production by Martin Klein [Phys. Rev. **98**, 1736 (1955)] who finds two restricting conditions rather than one. Although both conditions are necessary from a formal point of view, from a physical point of view satisfaction of the second condition $2|\mu_e|H \ll kT$ insures satisfaction of the first condition $N_{\frac{1}{2}} \approx N_{-\frac{1}{2}}$ as well, since the effect of saturation is always to reduce population differences in the electron spin system. More important is the presence of the factor $f^{(B)}$ in our expression (3) which reduces considerably the severity of the restriction imposed by Klein's second condition.
[5] Albert W. Overhauser, Phys. Rev. **89**, 689 (1953); R. J. Elliott, Phys. Rev. **96**, 266 (1954); Y. Yafet (private communication).

Interpretation of the Stored Energy of Irradiated Graphite in Terms of Elastic Energy Associated with Microscopic Strains*

ALFRED E. AUSTIN AND RALPH J. HARRISON
Battelle Memorial Institute, Columbus, Ohio
(Received August 15, 1955; revised manuscript received September 14, 1955)

IT has been known from the earliest work with graphite-moderated nuclear reactors that fast neutrons produce rather drastic disarrangements in the graphite crystal lattice.[1] There is a marked change in the unit cell dimensions, an expansion taking place in the direction of the c axis, while a contraction takes place in the direction of the a axis. The fractional change in a is about eight times smaller than the fractional change in c. That other distortions take place was also indicated by the fact that the x-ray diffraction lines were considerably broadened.

In the course of an extensive study at Battelle of irradiation effects in graphite, an attempt was made to get a clearer picture of the exact nature of these distortions in irradiated graphite by using the Fourier analysis technique[2] to analyze in detail the shape of the (110) x-ray diffraction lines. Most of the attention was given to the nature of the distortions parallel to the graphite layer planes. Warren and Chipman[3] have used these x-ray techniques to study the distortions in the

TABLE I. Mean square strain and stored energy of irradiated and annealed graphite.[a]

Annealing temperature	Sample A		Sample B	
	Mean square strain $\langle \epsilon^2 \rangle_{Av}$	Strain energy cal/cm³	Mean square strain $\langle \epsilon^2 \rangle_{Av}$	Strain energy cal/cm³
Room temperature	0.00026	40	0.00070	107
200°C	0.000077	12	0.00015	23
400°C	0.000068	10.5	0.00010	15
500°C	0.000054	8.2	0.000094	14
600°C	0.000033	5	0.000076	11.5
1000°C	0.000013	2	0.000055	8.4

[a] Sample *A* had an exposure of approximately 2×10^{19} *nvt*. Sample *B* was irradiated approximately 2.5 times as long as Sample *A*. The value of c_0 for Sample *A* after irradiation at a temperature of 30–60°C with only room-temperature annealing was 6.927 A. The value of c_0 for Sample *B* under these conditions was 7.174 A. After annealing at 2500°C, the value of c_0 for both samples was 6.732 A. The values of a_0 for Sample *A* and Sample *B* were 2.4560 A and 2.4408 A, respectively, after irradiation and 2.4612 A after annealing at 2500°C.

direction parallel to the *c* axis. The present authors have profited a great deal by the close contact with their work that has been made possible through the U. S. Atomic Energy Commission.

One of the results obtained in the present study was the determination with higher precision than heretofore of the amount of contraction of the a_0 dimension and its behavior on annealing. It is hoped to publish elsewhere a more detailed account of these and other results of these experiments.

It is the purpose of the present letter to point out that the observed intralayer distortions have more the character of strains as opposed to crystal breakup, at least for the range of exposures reported on. Because only the (110) line could be studied in the present work,[4] the separation of particle size effect and strain cannot be made with complete certainty. The shape of the experimentally determined curve of the Fourier coefficients of line shape *versus* order of the coefficient appears however to be inconsistent with the hypothesis that a major portion of the line broadening can be accounted for by crystal breakup. On the basis of any particle size distribution that would be at all consistent with the observed data and that would account for an appreciable part of the line broadening, there would be a large number of particles of small size, less than about 20 A; on the other hand, a significant fraction of the graphite would be associated with crystallites having dimensions more than 100 A, yet both the large and the small crystallites would be characterized by the same amount of contraction in their average a_0 dimension. This seems unreasonable from a physical point of view.

By neglecting particle size broadening, the observed line shapes can be used to compute the mean and the root-mean-square distance between the atoms as a function of their distance apart. The deviations from the undistorted positions represent strains which are presumably associated in part with the interstitials and vacancies present in irradiated graphite. On the assumption that the distortions could be represented by a strain given as a continuous function of distance within the crystal—which assumption is not quite correct in the present instance where the apparent strain varies quite appreciably within a distance of only a few atom spacings—one can obtain an average value for the square of this strain. Using this value of the mean square strain together with an estimate[5] of the elastic modulus governing displacements of atoms parallel to the graphite layer planes, one can obtain an approximation to the elastic stored energy associated with the observed distortion.

Table I lists values of the mean square strain and computed stored energy for graphites with two different periods of irradiation and subjected to different annealing treatments. The irradiations were carried out at Hanford[6] in a test facility having a nominal temperature of 30–60°C. The value of the c_0 unit-cell dimension after irradiation as well as approximate *nvt* units are listed as a measure of the amount of irradiation. The annealing treatments were carried out by quickly heating the specimens to the temperatures indicated, without overshoot, and maintaining temperature for one hour before cooling to room temperature.

The most significant feature of the data given in Table I appears to be the relatively large proportion of stored energy which is released at the 200-degree annealing temperature. Although the values of the stored energy tabulated are based entirely on calculation from the x-ray diffraction patterns, they do agree quite well in order of magnitude with experimental measurements of stored energy release.[7]

Because of the nature of the estimates entering into this calculation of stored energy, this agreement cannot be regarded as conclusive. Nevertheless, the present data do seem to establish that the elastic energy associated with observed intralayer strains in irradiated graphite can very possibly account for a significant portion of the observed stored energy released upon annealing below 400°C.

* Work performed under contract with the U. S. Atomic Energy Commission.

[1] See historical review given by F. Seitz, Phys. Today **5** (6), 6 (1952). Also see papers presented by G. R. Hennig and J. E. Hove, by W. K. Woods, and by G. H. Kinchin at the 1955 International Conference on Peaceful Uses of Atomic Energy summarizing recent United States and British work, respectively, on irradiation effects in graphite (unpublished).

[2] B. E. Warren and B. L. Averbach, J. Appl. Phys. **21**, 595 (1950).

[3] B. E. Warren and D. R. Chipman (unpublished).

[4] A highly oriented specimen of artificial graphite has been irradiated at several exposures and line shapes recorded but not yet analyzed, with fairly good resolution of the (210) (100) (200) lines as well as the (00*l*) lines.

[5] The value of the elastic modulus parallel to the layer planes which was used was estimated from data given by D. R. Riley, Proc. Phys. Soc. (London) **57**, 486 (1945) together with the assumption of Cauchy's rule. The value used was 0.64×10^{12} dynes/cm². This is in satisfactory agreement with the value estimated by K. Komatsu and T. Nagamiya, J. Phys. Soc. Japan **6**, 428 (1951), who use 0.853×10^{12} dynes/cm². No correction was attempted for the effect of irradiation on modulus.

[6] The irradiated specimens were kindly furnished us by Hanford.

[7] See for example the papers of Hennig and Hove, and Kinchin referred to in reference 1.

Possibility of a Zener Effect

GREGORY H. WANNIER*
Bell Telephone Laboratories, Murray Hill, New Jersey
(Received September 12, 1955)

THE motion of an electron in a crystal under the action of a static uniform field is a problem which has been treated since the early days of quantum mechanics. New insight into it can be gained, however, if account is taken of the fact that the field modifies the band structure. An elegant procedure consists in constructing an auxiliary equation from the Schrödinger equation of the problem; this equation is obtained by replacing $\mathbf{x}$ by $\mathbf{x}+i\partial/\partial\mathbf{k}$ in the (scalar or vector) potential defining the field. This auxiliary equation is periodic and has Bloch-type solutions $b_q(\mathbf{x};\mathbf{k})$ with stationary energies $W_q(\mathbf{k})$. It is then found that if the state of a particle was at one time describable by a single function $b_q(\mathbf{x},\mathbf{k})$ this property is preserved in time, the complete solution being

$$\psi_q(\mathbf{x},t;\mathbf{k})=b_q\left(\mathbf{x};\mathbf{k}+\frac{e\mathbf{A}}{\hbar c}\right)\exp\left[-\frac{i}{\hbar}\int W_q\left(\mathbf{k}+\frac{e\mathbf{A}}{\hbar c}\right)dt\right].$$

In interpreting this formula, the antisymmetric gauge must be taken for the magnetic case and the time gauge for the electric case. (This is a different one from the one used in defining the b's.)

Little has been done up to this time in interpreting the result for the magnetic case. In the electric case, the result means that interband transitions have disappeared and that the entire change of the wave function in time is summed up by the linear increase of $\mathbf{k}$ with t. This implies that whenever bands are separated by energy gaps transitions across them are rigorously excluded by a selection rule; this situation presumably prevails for the usual field strengths. For those situations, therefore, the result of Zener[1] is wrong and no tunneling through the forbidden band is possible. It is possible to show, however, that for very high fields the band gaps all have disappeared; the above equation must then be read to imply a smooth acceleration from band to band, as for a free particle. Thus the Zener effect is to be replaced by a picture whereby no current whatever takes place up to a threshold field, whereupon conduction becomes metallic. As a restriction to this, it should be added that processes of the Zener type are still possible in crystals whose periodicity has been disturbed, for instance by lattice defects or the inhomogeneity of the field itself. The process is then of a higher order, however, with a probability which is decreased correspondingly.

In conclusion we want to add that we have not yet succeeded in constructing an example which demonstrates explicitly that the electric field closes the bands as it becomes large. This particular feature is therefore inferred from the other pieces of information.

I want to thank Dr. C. Herring for calling my attention to the qualitative change taking place at high fields.

* Now at the University of Geneva, Geneva, Switzerland.
[1] C. Zener, Proc. Roy. Soc. (London) **A145**, 523 (1934).

PHYSICAL REVIEW VOLUME 100, NUMBER 4 NOVEMBER 15, 1955

Proceedings of the American Physical Society

ABSTRACTS OF PAPERS PRESENTED AT THE EIGHTH ANNUAL GASEOUS ELECTRONICS CONFERENCE HELD AT SCHENECTADY, NEW YORK, OCTOBER 20–22, 1955*

A. Breakdown

A1. First and Second Townsend Coefficients in Hydrogen and Nitrogen.* D. J. DEBITETTO AND L. H. FISHER, *New York University.*–Ionization currents were measured in uniform fields in hydrogen and nitrogen at pressures from 100 to 400 and 300 mm Hg, respectively. Log i *vs* δ curves yielded accurate values of α/p in the low E/p region reproducible to 2%. Current-voltage measurements taken in the same gas samples to within 0.05% of the sparking potential check the consistency of the α/p measurements and provided numerous evaluations of γ. The values of γ are about 10^{-3} in both gases (nickel cathode) and are independent of E/p in the range covered. The values of γ are reproducible to within 20% and are not affected by breakdown or by large changes in initial current. At all pressures studied, self-sustained currents of the order of 10^{-7} amp were obtained in both gases and in nitrogen

* *Note.*—The usual preamble to these abstracts will be published in the Bulletin early in 1956. Abstracts of meetings in 1956 and subsequent years will not be published in *The Physical Review.*

these were associated with an anode glow. The values of α/p obtained in nitrogen are in excellent agreement with those of Dutton, Haydon, and Llewellyn Jones[1]; however, the values of γ obtained in nitrogen are about five times larger. The measurements in both gases verify the Townsend criterion for breakdown to within experimental error.

* Supported by the Office of Naval Research.
[1] Dutton, Haydon, and Llewellyn Jones, Proc. Roy. Soc. (London) **A213**, 203 (1952).

A2. Semiempirical Calculation of the Townsend α. PETER L. AUER *General Electric Research Laboratory.*—Studies concerning the rapid estimation of polyatomic molecules' ionization coefficient reported on at last year's meeting[1] has been extended in the present paper by an application of the molecular formalism given by Kihara.[2] The Maxwellian model is used to describe elastic scattering, while empirical relations are used to describe inelastic scattering. In the first-order approximation it is found that below excitation threshold energies the velocity distribution is of Maxwellian form with an adjusted temperature value. Above excitation threshold the velocity distribution is expressed in terms of confluent hypergeometric functions for a class of inelastic scattering formulas. Application of this formalism to helium gas yields results in agreement with previous calculations.[3] Some justification is obtained for the empirical formula

$$\alpha = AP \exp(-BP/E),$$

where B may be related explicitly to molecular parameters. The calculation of the factor A and the determination of its dependence on the variable (E/P) is in general a difficult task. For correlative purposes, however, the estimation of B is usually sufficient.

[1] R. W. Crowe and J. C. Devins, Gaseous Electronics Conference, New York, New York, October 14–16, 1954.
[2] Taro Kihara, Revs. Modern Phys. **24**, 45 (1952).
[3] J. Abdelnabi and H. S. W. Massey, Proc. Phys. Soc. (London) **A66**, 285 (1953).

A3. Formative Time Lags of Positive Point-to-Plane Corona in Nitrogen and Argon.* L. A. BORNSTEIN AND L. H. FISHER, *New York University.*—Previous positive point-to-plane corona measurements in air[1] showed formative times so short as to preclude a secondary cathode mechanism in corona formation. Nitrogen and argon have been studied from 100 to 700 mm Hg with a variety of points and gaps. In nitrogen, with pulsed voltage resulting in localized corona at the point, lags have been found from 10 μsec to 0.1 sec at overvoltages of a few percent to a few tenths of a percent, respectively. At overvoltages of about 0.1%, with pulsed ultraviolet irradiation, lags up to 10 minutes have been observed. Reduction of ultraviolet irradiation produces a marked increase in lags. In argon, at low overvoltages leading to a glow corona near the point, no sharp breakdown has been found. Synchroscope studies indicate a gradual development of this discharge in argon. Both nitrogen and argon at about 10% overvoltage show filamentary breakdown with lags between 0.1 and 1 μsec, independent of overvoltage. It is concluded that positive localized corona formation in nitrogen and argon is cathode dependent.

*Supported by the Office of Naval Research.
[1] M. Menes and L. H. Fisher, Phys. Rev. **94**, 1 (1954).

A4. Formative Breakdown Delays in Noble Gases at Small Overvoltages. B. T. MCCLURE, *Bell Telephone Laboratories.*—During most of the time between the application of a small overvoltage, ΔV, and the attainment of a current recognized as breakdown, the current increases exponentially with a single time constant, θ. For sufficiently small overvoltages, $\theta\Delta V$ is observed to be constant and too large to be explained solely on the basis of ion transit times. Explicit consideration of the effect of metastables returning to the cathode of a plane parallel discharge leads to a theoretical expression for $\theta\Delta V$. The metastables are assumed to be lost by diffusion to the electrodes as well as by destruction in the volume.[1] For neon Rogowski[2] gives the metastable production coefficient as a function of E/p_0. The breakdown delays of a plane parallel discharge in neon have been measured for $1<p_0d<11$. The values of $\theta\Delta V$ derived from these data are in excellent quantitative agreement with the theory.

[1] A. V. Phelps and J. P. Molnar, Phys. Rev. **89**, 1202 (1953).
[2] W. Rogowski, Z. Physik **115**, 257 (1940).

A6. High-Frequency Gas Discharge Breakdown in Neon-Argon Mixtures. H. J. OSKAM, *Philips Research Laboratories, Eindhoven-Netherlands* (presented by W. Elenbaas).—Breakdown electric fields in a wave guide at 9500 Mc/sec are presented for neon-argon mixtures at various pressures. The purity and constancy of the gas mixtures were checked in two ways. In contrast with measurements of Penning, who found for dc discharges two minima in the E_b *versus* p curves, in the hf discharge only one minimum is found. This can be explained by the difference in the energy build-up process in the dc and hf discharge. Plotting the minima of E_b *versus* p curves against the argon concentration gives a smooth curve (with a minimum at 5.10^{-3}% A), in contrast with measurements of MacDonald [Phys. Rev. **98**, 1070 (1955)] carried out at 2800 Mc/sec. The behavior of the curve is due to a dependence on the argon concentration of the number of ionizing collisions of metastable neon with argon and the energy losses of electrons by excitation collisions with argon. Plotting breakdown fields at fixed pressures against the argon concentration shows that for higher pressures the argon concentration giving the lowest breakdown field decreases. The behavior of the curve giving this dependence can be explained by considering the number of the collisions of metastable neon with argon atoms as a function of the pressure.

A7. Pressure Limits of the High-Frequency Secondary Electron Resonance Breakdown Mechanism.* ALBERT J. HATCH AND H. BARTEL WILLIAMS, *New Mexico College of Agriculture and Mechanic Arts.*—Experimental studies have been made of the transition region between the gas controlled diffusion mechanism and the electrode surface controlled secondary electron resonance mechanism of high-frequency breakdown multipacting in order to determine the pressure limits of the latter mechanism. Plane parallel internal metal electrodes were used (1) at 53 Mc/sec and 1- to 5-cm separation in undried air at pressures of 10^{-4} to 1 mm Hg and (2) at 100 to 170 Mc/sec and 1-cm separation in dry air at pressures of 10^{-6} to 10 mm Hg. Plots of breakdown field strength as a function of pressure exhibit typical Paschen minima at pressures of the order of 0.1 mm Hg with a steep rise on the low-pressure side when only the diffusion mechanism is operative, i.e., below the secondary electron resonance cut-off frequency. At frequencies above cutoff, however, the minima occur at much lower field strengths and the rise on the low-pressure side terminates in pressure independent plateaus extending from approximately 10^{-2} to 10^{-6} mm Hg. These plateaus are characteristic of the secondary electron resonance breakdown mechanism and establish the pressure limits of this mechanism. Erratic behavior of the plateaus at about 10^{-3} mm Hg in (2) operating near cut-off frequency is due to variations in the secondary electron emission coefficient.

* Supported by the Navy Bureau of Ordnance.

A8. Semirandom Sparking in a Short Air Gap. C. D. MALDONADO AND R. C. RETHERFORD, *University of Wisconsin.*—Erratic post-breakdown currents are sometimes observed with short air gaps. Closer examination shows that the current consists of sharp pulses occurring in semirandom sequence.

The phemomenon may be satisfactorily described in terms of relaxation oscillations having a fluctuating time interval between pulses. In this respect it is similar to that reported by Skolnik and Puckett.[1] However in the present case, operation is at a much lower average current, well below that of the steady glow discharge. In a typical case a planar gap 0.003 in. in length was used between brass electrodes 0.187 in. in diameter. The current was limited by a 66-megohm resistance and the stray capacitance shunting the gap was 11 micromicrofarads. Under these conditions the current was 2 to 4 microamperes. The sparking potential was found to be about 700 volts and the extinction potential about 460 volts. Oscilloscopic observation readily shows that fluctuation of the extinction potential account for much of the variation in the interval between pulses. Fluctuation of the sparking potential is considerably less. Factors influencing the phenomenon will be discussed.

[1] M. I. Skolnik and H. R. Puckett, Jr., J. Appl. Phys. **26**, 74 (1955).

A9. Negative-Ion Formation in Iodine by Electron Capture. R. E. Fox, *Westinghouse Research Laboratories.*—The techniques for obtaining monoenergetic electrons[1] have been applied to the study of negative ions in iodine vapor. Preliminary studies indicate that the maximum cross section for the dissociative attachment process $I_2+e\rightarrow I^-+I+K.E.$ occurs at an electron energy of less than 0.1 ev. This is in disagreement with earlier work by Buchdahl[2] who found a sharp decrease at lower energies from a maximum cross section occurring at about 0.4 ev. However, these results agree with those of Biondi[3] who found a large cross section for electron attachment at thermal energies (0.04 ev) in the afterglow of a microwave discharge. The energy scale for the electrons in the present work was calibrated by observing the appearance potential for SF_6^-.[4] The results were complicated by the formation of HI in the apparatus which also yields a negative ion by the dissociative process $HI+e\rightarrow I^-+H+K.E.$ This and other experimental difficulties associated with the study of halogen molecules will be discussed briefly.

[1] Fox, Hickam, Kjeldaas, and Grove, Phys. Rev. **84**, 859 (1951).
[2] R. Buchdahl, J. Chem. Phys. **9**, 146 (1941).
[3] M. A. Biondi, Phys. Rev. **89**, 337(A) (1953).
[4] W. M. Hickam and R. E. Fox, Phys. Rev. **98**, 557(A) (1955).

B. Elastic Collisions and Mobility

B1. Low-Energy Scattering of Electrons by Atoms.* J. Hammer, H. Malamud, and B. Bederson, *New York University.*—An atomic beam method for obtaining hitherto unavailable data on low-energy electron scattering has been devised. Specifically this method allows the determination of the total electron scattering cross section for atoms normally bound in a molecule. Two rectangular beams are made to cross at right angles. One of these beams consists of electrons and the other consists of the atoms or molecules whose scattering cross section is being investigated. The electron beam is produced by an electrostatically focused gun and the atomic beam by a slit in a quartz tube containing the gas under investigation. An electrodeless discharge in the tube produces a beam of high atomic content which reaches the scattering region after suitable collimation. The atomic beam is mechanically modulated at 24 cps and the scattered electrons are collected by a Faraday chamber and measured by a phase-sensitive narrow band-width amplifier. Data obtained using an H^2 beam are in good agreement with the results of the Ramsauer method and can be used as a calibration to yield absolute values for the cross sections. Preliminary measurements on atomic hydrogen will be discussed.

* Work supported in part by the Office of Naval Research and the Research Corporation.

B2. Drift Velocity of Electrons in Helium and Hydrogen at Low Fields. J. L. Pack and A. V. Phelps, *Westinghouse Research Laboratories.*—Measurements of drift velocity of electrons in helium and hydrogen have been made at 300°K for E/p between 0.001 and 0.2. Data obtained with a tube of the Nielson[1] type using modern pulse techniques will be presented. Good agreement is obtained with previous data of Hornbeck[2] and Nielson[3] in helium at an E/p of 0.1 and above. A comparison is made between the experimental drift velocity in helium and the theory of Margenau[4] using a constant collision probability obtained from microwave experiments of Gould and Brown.[5] Good agreement is obtained with previous data of Bradbury and Nielson at an E/p of 0.03 and above in hydrogen.

[1] N. E. Bradbury and R. A. Nielson, Phys. Rev. **49**, 388 (1936).
[2] J. A. Hornbeck, Phys. Rev. **83**, 374 (1951).
[3] R. A. Nielson, Phys. Rev. **50**, 950 (1936).
[4] H. Margenau, Phys. Rev. **69**, 508 (1946).
[5] L. Gould and S. C. Brown, Phys. Rev. **95**, 897 (1954).

B3. Microwave Studies of Slow Electron Collision Processes in Helium Plasmas.* J. M. Anderson and L. Goldstein, *University of Illinois.*—The method of interaction of microwaves in plasmas, previously described,[1] has been applied to the determination of the momentum transfer collision cross sections of helium atoms, q_m, and positive ions, q_i, with free electrons. A controlled variation of the mean energy of the electrons permitted the determination of the *variation* of q_m with electron energy from 4/100 to 4/10 ev. For these experiments guided microwaves in the X-band (~9000 Mc/s) have been propagated in plasmas with electron densities of the order of 10^{11} elec./cc. Under these conditions appropriate charge interactions have been considered. The "effective" cross section of the helium atoms for electrons of 4/100 ev was found to be 6.6×10^{-16} cm². The mean fraction of excess energy loss factor of the electrons upon collision, G, was found to be $\sim2.7\times10^{-4}$, the expected 2m/M value. In the isothermal plasma at 300°K, q_i was found $\sim2\times10^{-10}$ cm² for electron densities $\sim10^{11}$ elec./cc.

* Work supported by The Air Force Cambridge Research Center.
[1] Goldstein, Anderson, and Clark, Phys. Rev. **90**, 151 (1953).

B4. Collision Cross Section of Nitrogen Molecules with Slow Electrons.* J. Goldstein and J. M. Anderson, *Electrical Engineering Research Laboratory, University of Illinois.*—The method of interaction of microwaves in plasmas has been applied to the determination of momentum transfer collision cross section, q_m, of nitrogen molecules with free electrons. The mean energy of the electrons was varied from 4/100 to

46/100 ev. At 4/100 ev q_m was found $\sim 17\times10^{-16}$ cm^2 and decreased to $\sim 8\times10^{-16}$ cm^2 at 0.5 ev. The mean fractional *excess* energy loss of the electrons, G, was found to extrapolate to $\sim 4\times10^{-4}$ at 4/100 ev and to fall to $\sim 2\times10^{-4}$ at 0.5 ev. The mean fractional energy loss of the slow electrons, λ, related to G by

$$\lambda = G\left(1-\frac{\epsilon_m}{\epsilon_e}\right),$$

where ϵ_m and ϵ_e are the mean energies of the molecules and electrons respectively, is then ~ 5.5 in units of $2m/M$. This is in agreement with the theory proposed by Gerjuoy and Stein[1] if the above found q_m is used in an adoption of the theory to compare with experiment.

* Work supported by The Air Force Cambridge Research Center.
[1] E. Gerjouy and S. Stein, Phys. Rev. **97**, 1671 (1955).

B5. Deviations from Blanc's Law of Ionic Mobilities: Ne^+ in Neon-Helium Mixtures. MANFRED A. BIONDI AND LORNE M. CHANIN, *Westinghouse Research Laboratories.*—According to Blanc's law the reciprocal of the mobility of an ion moving in a gas mixture varies linearly with the fractional concentration of constituent gases. In the present experiment deviations from Blanc's law have been found for the case of Ne^+ in neon-helium mixtures. It is found that the curve of $1/\mu$ *vs* neon concentration exhibits a concave-downward shape and at its midpoint deviates by 6% from the straight line joining the end points of the curve. In general, deviations from Blanc's law have been ascribed to "clustering," i.e., the formation of weakly bound complex molecules. In the present case of Ne^+ and helium atoms such clustering appears unlikely in view of the small polarizability of helium. Theoretical calculations[1] indicate that small deviations from Blanc's law in the direction observed can arise as a result of special ion-atom interactions.

[1] T. Holstein (following abstract.)

B6. Mobility of Positive Ions in Gas Mixtures. T. HOLSTEIN, *Westinghouse Research Laboratories.*—It has generally been assumed that the mobility of positive ions in a mixture of two gases, A and B, obeys Blanc's law,

$$\frac{1}{\mu}=\frac{f_A}{\mu_A}+\frac{1-f_A}{\mu_B}$$

where f_A is the fractional concentration of gas A. In the present work, the validity of this relationship has been investigated by the use of a variational treatment of Boltzmann's transport equation. The result may be expressed in the standard form[1] $\mu=\mu_1/(1-\epsilon_0)$, where μ_1, the first-order Chapman-Enskog mobility formula, obeys Blanc's law, and ϵ_0 is a positive quantity. It is found that $d^2\mu_1\epsilon_0/df^2>0$, from which it follows that ϵ_0 does not exceed the larger of the two extremes, $\mu_1\epsilon_{0A}$ or $\mu_1\epsilon_{0B}$. This condition generally suffices to limit deviations from Blanc's law to a few percent.

[1] Cf. Massey and Burhop, *Electronic and Ionic Impact Phenomena*, Eqs. (7), (8), and (9), p. 367.

B7. Temperature Dependence of Ionic Mobilities: Ne^+ and Ne_2^+ in Neon. LORNE M. CHANIN AND MANFRED A. BIONDI, *Westinghouse Research Laboratories.*—Measurements have been made of the mobilities of Ne^+ and Ne_2^+ ions moving in neon gas at 300°K, 195°K, and 77°K. The mobility tube[1] permits measurements at sufficiently low values of E/p so that the ions are very nearly in thermal equilibrium with the gas. The results for Ne^+ are compared with theoretical calculations based on Holstein's theory[2] in the following table:

T(°K)	300°	195°	77°
μ_0 (exptl.) cm^2/volt sec	4.0	4.3	5.3
μ_0 (theoret.)	4.1	4.7	6.0

As in the case of He^+ in helium[3] the experimental values lie below the theoretical values, the difference being greatest at low temperatures. The experimental values for Ne_2^+ in neon at 300°, 195°, and 77°K are 6.5, 7.3, and 6.8 cm^2/volt sec, respectively.

[1] M. A. Biondi and L. M. Chanin, Phys. Rev. **94**, 910 (1954).
[2] T. Holstein, J. Phys. Chem. **56**, 832 (1952).
[3] L. M. Chanin and M. A. Biondi, Phys. Rev. **99**, 1658(A) (1955).

C. Excitation and Afterglow

C1. Lifetime of Imprisoned Resonance Radiation in Neon. A. V. PHELPS, *Westinghouse Research Laboratories.*—Absorption studies of the lowest metastable and radiating states of neon have shown that the concentration of excited atoms in the resonance state is sufficient to cause an appreciable reduction in the rates of metastable destruction compared with the values which would be present in the absence of imprisonment.[1] We have made use of this fact to determine the effective lifetime of atoms in the resonance state, i.e., the lifetime of the imprisoned resonance radiation. Measurements show that the lifetime is independent of the neutral gas density to within the experimental error and that it varies inversely as the square root of the radius of the absorption cell as predicted by Holstein's theory.[2] The natural lifetime of the $2p^53s^1P_1$ state as calculated from these measurements is 2×10^{-8} sec compared to a value of $1.6\pm0.8\times10^{-8}$ sec obtained from measurements by Shütz of the natural line breadth of the $2p^53s^1P_1$ state[3] and Shortley's calculation of the relative natural lifetimes for the two resonance states.[4]

[1] A. V. Phelps, Phys. Rev. **99**, 1657(A) (1955).
[2] T. Holstein, Phys. Rev. **72**, 1212 (1947); **83**, 1159 (1951).
[3] W. Shütz, Ann. Physik **18**, 705 (1933).
[4] G. H. Shortley, Phys. Rev. **47**, 295 (1935).

C2. Radiation Temperature of a Plasma. FRANCIS BITTER,* *MIT*, AND JOHN F. WAYMOUTH, *Sylvania Electric Products Inc.*—We have found the concept of a "radiation temperature" helpful in computing certain limits for the resonance radiation emitted from an electrically excited vapor. This is defined as the temperature at which the ratio of concentrations of atoms in the excited and ground states would be in equilibrium. This radiation temperature will have its maximum value at the center of a lamp and decrease toward the surface. It will necessarily be less than the electron temperature. If the radiation temperature were uniform, the spectral intensity radiated near the center of the resonance line would be that of a blackbody at that temperature. The line width radiated by a lamp would be determined by the condition that quanta having frequencies at the edges of the line can escape from the center of the lamp without being absorbed. If the radiation temperature is not uniform, the spectral intensity at any particular wavelength will be determined by some average of the optical temperature of the atoms radiating that wavelength out of the lamp without absorption.

* This work was done at the Sylvania Electric Products Inc. plant in Salem, Massachusetts.

C3. UV Continuum of the Xe HG′ Molecule. CARL KENTY, *General Electric Company, Nela Park.*—In a study of the excitation of metal vapors by active nitrogen as obtained in a high pressure of rare gas,[1] the case of Hg has proved of interest in several respects. A 3-sec afterglow of a 1- to 10-ma diffuse discharge in a mixture of 100 mm Xe, 0.3 mm N_2 and Hg at R.T. reveals besides Hg lines an intense continuum from ~2537 to beyond 3000 A with a broad maximum at ~2700 A. The same continuum occurs in the discharge itself, and in fluorescence under excitation by 2537. The intensity but not the breadth of the continuum increases with Xe pressure. A somewhat similar continuum[2] extending from ~2537 to beyond 2700 A was found with Kr as the main gas, and a still narrower one[2] in the case of A. Continua and bands associated with 2537 of Hg, emitted by Van der Waals molecules in the rare gases, chiefly other than Xe, were studied by Oldenberg[2] and others.[3] The continuum here found in Xe is unique in its large extent and intensity and in having a maximum ~200 A removed from 2537. Broad red continua frequently present in these experiments are in some cases due to rare gas molecules, but in some cases are unexplained. The discharges studied are unusual in that the voltage is strongly lowered by the addition of N_2 to a Hg rare gas mixture. In the case of 23 cm of Xe with Hg at 3°C, 0.3 mm N_2 lowered the voltage from 1400 to 400. The result can be explained in terms of a high concentration of the N_2 metastables[1] a' and w.

[1] C. Kenty, Phys. Rev. **98**, 563 (1955).
[2] O. Oldenberg, Z. Physik **55**, 1 (1929).
[3] See W. Finkelnburg *Continuerlich Spektren* (Verlag Julius Springer, Berlin, 1938), p. 214.

C4. Light Absorption and Photoionization in NO and N_2O. W. C. WALKER AND G. L. WEISSLER, *University of Southern California.*—Total absorption cross sections, photoionization efficiencies and cross sections of NO and N_2O have been measured in the wavelength region between the ionization onset and 680 A using techniques previously described.[1] In NO the ionization onset was found at 1347±5 A or 9.20±0.03 ev in agreement with other work.[2] The cross sections found were independent of pressure. However, because of their rapid variation with wavelength due to the presence of diffuse bands, it was not possible to establish with any degree of certainty the contour of the NO ionization continuum. In N_2O the ionization onset was measured at 695±5 A or 12.83±0.07 ev, in agreement with electron impact results[3] and Duncan's Rydberg series value.[4] The cross sections showed some pressure dependence indicative of resonance bands which were sharp in comparison to the width of the radiation band passed by the exit slit. In spite of this difficulty it was still possible to assign a tentative contour to the N_2O ionization continuum. Preliminary results on the identification of photoionization products will be discussed.

[1] Wainfan, Walker, and Weissler, Phys. Rev. **99**, 542 (1955).
[2] K. Watanabe, J. Chem. Phys. **22**, 1564 (1954); H. D. Hagstrum, Revs. Modern Phys. **23**, 185 (1951).
[3] H. D. Smyth and E. C. G. Stueckelberg, Phys. Rev. **36**, 478 (1930).
[4] A. B. F. Duncan, J. Chem. Phys. **4**, 638 (1936).

C5. Theory of Ionization Probability Near Threshold.* SYDNEY GELTMAN, *Applied Physics Laboratory, The Johns Hopkins University.*—The behavior of the cross section for ionization by electron impact is investigated in the vicinity of threshold by means of the quantum theory for inelastic scattering. A Coulomb-modified form of the Born approximation is used to calculate the S-wave ionization cross sections for H^+, He^+, and He^{++}. The electron-nuclear interaction is included in the unperturbed Hamiltonian for the problem while the interaction between the incident and ejected electrons is considered as the perturbation. It can be shown that the limiting law for the ionization of a hydrogen atom by electron impact has a linear dependence on the excess incident energy. The absolute cross sections evaluated are in good agreement with experiment. Generalization of the threshold law for multiple (n-fold) ionization is found to yield the forms E_{ex}^n for ionization by electron impact and E_{ex}^{n-1} for photoionization.

* This work was supported by the Bureau of Ordnance, Department of the Navy, under NOrd 7386.

C6. Formation of Metastable Ar^+, Kr^+, and Xe^+ by Electron Impact. HOMER D. HAGSTRUM, *Bell Telephone Laboratories, Inc.*—Metastably excited, singly charged ions of argon, krypton, and xenon formed by single electron impact have been detected by their greater ability, with respect to unexcited ions, to eject electrons from an atomically clean metal surface. The yield (γ_i) of electrons ejected per ion by all singly charged ions has been measured as a function of electron energy. γ_i is found to be constant only up to electron energies near 32.2, 28.9, and 24.0 ev for Ar, Kr, and Xe, respectively, above which energies ions in the lowest lying metastable levels ($4D_{7/2}$) can be formed. At greater energies the increase in γ_i above that for unexcited ions gives directly the form of the cross section for formation of the excited ions. To determine the absolute magnitude of the cross section one must estimate γ_i for the excited ions. Assuming this to be equal to that measured for doubly charged ions (an upper bound), one calculates a lower bound of about 0.02 for the ratio of the cross sections for the formation of metastable ions and unexcited ions at the second ionization energy.

C8. Transient Behavior Following Breakdown and its Relation to Afterglow Processes.* DONALD E. KERR AND ELDRED F. TUBBS, *The Johns Hopkins University.*—Following application of a pulse of microwave power to form a helium discharge in a resonant cavity, there is a period of about one millisecond which is characterized by a transient behavior of both emitted light and rf properties, particularly transmitted power. In general atomic radiation first rises sharply, then undergoes quasi-oscillatory behavior in approaching a stationary value. During the pulse, molecular radiation is generally weak but rises many-fold at the end of the pulse. Detailed measurements of certain transitions show atomic light falling abruptly in the afterglow; but molecular light rises sharply then falls more slowly. The radiation is usually characterized by more than one time constant, the larger one being markedly dependent upon pulse length and pressure. The abrupt rise of molecular radiation at the end of the breakdown pulse is strongly dependent upon pulse length. Consequently the relative predominance of molecular or atomic radiation can be controlled by pulse length. This fact casts doubt on interpretations of afterglow mechanisms which depend upon predominance of either type of spectrum. Other rare gases are under study.

* This work was supported by the Office of Scientific Research, U. S. Air Force.

C9. Low-Pressure Afterglow Studies in Nitrogen. A. C. FAIRE AND GEORGE W. GRIFFING, *Air Force Cambridge Research Center.*—Quantitative laboratory studies have been conducted on the afterglow following a pulsed microwave[1] discharge in N_2+He, N_2+Ne, and N_2+A at partial pressures of nitrogen below 20 microns Hg. These measurements extend the work previously reported for partial pressures of nitrogen in the range of 20 microns to 3 mm Hg.[2,3] A discussion of the loss mechanism at early times in the afterglow is presented.

[1] M. A. Biondi and S. C. Brown, Phys. Rev. **76**, 1697 (1949).
[2] Faire, Fundingsland, and Aden, Gaseous Electronics Conference Paper, October, 1953, Washington, D. C.
[3] Faire, Fundingsland, and Aden, Conference on Electron Physics, June, 1954, University of Birmingham, Birmingham, England.

C10. Scattering of Low-Energy H^- Ions in Helium.* T. L. BAILEY AND E. E. MUSCHLITZ, *University of Florida.*—

Measurements have been made by the method of Simons and co-workers[1] on the scattering of H^- ions in helium gas at incident ion energies of 4 ev to 300 ev. Both elastic and total inelastic cross sections have been determined as functions of ion energy. The results are similar to those for the scattering of H^- ions in H_2.[2,3] From the elastic cross-section data below about 50 ev, a potential law is calculated which is characteristic of an ion-induced dipole interaction. From 100 ev to 300 ev the apparent elastic cross section increases slightly with ion energy; this increase is attributed to the electronic excitation of He atoms by the incident H^- ions. The inelastic cross section for the electron detachment process $H^-+He=H+He+\epsilon^-$ is nearly constant from 300 ev to about 200 ev. Below 20 ev the detachment cross section drops sharply but seems to persist to incident ion energies as low as 2 ev.

* Supported by the Office of Naval Research.
[1] Simons, Muschlitz, and Unger, J. Chem. Phys. **11**, 307 (1943).
[2] E. E. Muschlitz, Phys. Rev. **95**, 635 (A) (1954).
[3] Muschlitz, Bailey, and Simons (to be published).

D. Arcs

Invited Paper

D1. Past and Present Ideas about Cold Arcs. A. VON ENGEL, *Oxford University.*

D3. Short Arcs. L. H. GERMER AND W. S. BOYLE, *Bell Telephone Laboratories, Inc.*—Short field emission arcs are of two types, those which vaporize metal predominantly from the anode by electron bombardment, and those in which the metal of the arc is supplied from the cathode by melting points by field emission currents flowing through them. These are appropriately called "anode arcs" and "cathode arcs." An anode arc erodes a pit in the anode, and leaves a roughened area on the cathode. A cathode arc leaves on the cathode a dispersed array of pits which lie largely along scratches; often there is no mark on the anode. These arcs differ in arc voltage, higher for cathode arcs, and other ways. Both types have been observed for many metals. For clean palladium all arcs are cathode arcs at 400 volts, but at 300 and lower voltages anode arcs occur also, becoming more frequent at lower voltages. For surfaces activated by carbonaceous material only cathode arcs occur at all potentials. In anode arcs metal is transferred in both directions, as measured by radioactive tracers, with net transfer from anode to cathode. Cathode arcs transfer from cathode to anode only, and less metal per unit of arc energy than is transferred in anode arcs.

D4. Some Properties of Arc Cathode Spots in Magnetic Fields. DINO ZEI,* ROBERT ST. JOHN,† AND J. G. WINANS *University of Wisconsin.*—The velocity of the cathode spot of a mercury arc in a transverse magnetic field has been measured with the arc spot in a groove above the junction line between the metal cathode and mercury. The approximate doubling of velocity[1] at fields about 11 000 to 15 000 oersteds does not take place under these conditions. However, the velocity is always greater than when the arc spot is at the mercury-electrode junction. Spectra of the arc showed some Hg II lines enhanced at the arc spot. There was no broadening of the Hg I lines like that observed when the arc spot was at the junction between mercury and metal.

* Now at State Teachers College, St. Cloud, Minnesota.
† Now at The University of Oklahoma, Norman, Oklahoma.
[1] Robert St. John and J. G. Winans, Phys. Rev. **98**, 1664 (1955).

D6. Glow-to-Arc Transitions in the Column of the High-Pressure Glow in Hydrogen. W. A. GAMBLING,* *University of Liverpool.*—By using relatively cool copper or tungsten electrodes in hydrogen it is possible to obtain a transition from glow to arc in the column of a high-pressure (1 atmos) discharge while the cathode regions remain in the glow state. Experiment shows that the column transition is governed by thermal considerations, in accordance with the predictions of King[1] and others. Excitation temperature and other measurements indicate that in the glow column, as at low pressure, the electron temperature is very high and the gas temperature low. With increasing current the electron temperature falls and the gas temperature rises until the transition to an arc column occurs. The current density is now higher, and the voltage gradient lower than in the glow column but the electron temperature is still appreciably higher than that of the gas, and the measured ion density does not agree with that calculated using the Saha equation. As the current or the pressure increases the gas and electron temperature difference falls and the measured ion density approaches more closely that given by the Saha equation.

* Now at The Department of Electrical Engineering, University of British Columbia, Vancouver, British Columbia.
[1] L. King, Nature **174**, 1008 (1954).

D7. On Pronounced Deviations from the Maxwellian Velocity Distribution of the Electrons in Hollow Hot Cathode Diodes* with Ne Filling. GUSTAV MEDICUS, *Wright-Patterson Air Force Base.*—At pressures of the order of 1 mm Hg and diode currents between about 10 to 20 ma the velocity distribution of the electrons in the vicinity of the cathode, derived from automatically plotted probe curves[1] by the Druyvesteyn method,[2] has a pronounced minimum (≈ 0) which clearly separates a fast group from a slow group of electrons. The fast group has a sharp onset between 16 and 17 volts and rises steeply to a maximum nearby. The onset of this group probably is determined by the metastable level of Ne at 16.7 ev; the electrons from a hot cathode have to be accelerated by a "cathode fall" of this magnitude to provide a high enough density of the metastables for cumulative ionization. The potential of the plasma near the opening of the hollow cathode measured by the same probe curves checks satisfactorily with this cathode fall. The slow group of electrons formed by the secondaries in itself is Maxwellian, corresponding to a temperature of about 3000°K. The numbers in the two groups have the same order of magnitude. With increasing current the distribution function becomes smoothed out more and more and approaches a Maxwellian to some degree.

* G. Medicus, J. Appl. Phys. **24**, 233 (1953).
[1] G. Wehner and G. Medicus, J. Appl. Phys. **23**, 1035 (1952).
[2] M. J. Druyvesteyn, Z. Physik **64**, 781 (1930).

D8. Influence of Electron Emission on the Cathode Processes of the Arc. G. ECKER,* *University of Bonn.*—The contraction theory of the arc discharge in the regions in front of the electrodes is distinguished from other theories[1–6] chiefly by its program. Instead of attempting to justify a preconceived doubtful model, the problem is attacked in as

complete generality as possible, employing the conservation laws and the basic laws of electrodynamics and thermodynamics. The predictions achieved are in adequate agreement with experimental knowledge and, moreover, the theory accounts for the attraction phenomenon, the origin of the charge carriers, the distinction between cathode and anode regions, and finally the two cathode types observed by Seeliger and his co-workers. A recent extension of this theory to include electron emission has been based largely upon an improved formulation of the energy balance between gas and cathode. The stabilization diagram for normal arc currents is only slightly affected by the inclusion of electron emission. However, at large currents the extended theory predicts an extra uncontracted stabilization point, which explains in detail our prior observation of an arc existing without a cathode spot.

* Now at the University of Oklahoma, Norman, Oklahoma.
[1] G. Ecker, Z. Physik **132**, 248 (1952).
[2] G. Ecker, Z. Physik **135**, 105 (1953).
[3] G. Ecker, Z. Physik **136**, 1 (1953).
[4] G. Ecker, Z. Physik **136**, 556 (1954).
[5] G. Ecker, Z. Physik **142**, 444 (1955).
[6] G. Ecker, Ber. Arbeitstagung Gasentladungsphysik, Halle, 148 (1953).

E. Magnetic Field Effects and Miscellaneous

E1. Isotopic Separation by Magneto-Ionic Expansion. JOSEPH SLEPIAN, *Westinghouse Research Laboratories.*—A metallic gas, at a high temperature, 100 000°C or higher, and therefore ionized, is sent down a tube of increasing cross section, and precipitates on insulated slats. It is prevented from precipitating on the side walls by a combination of a strong enough magnetic field set parallel to the walls and perpendicular to the discharge of gas, and an electric potential between the side walls, drawing current from the one wall to the other wall. It is prevented from precipitating on the insulated end walls by the large separation of these walls from the point of inlet of the ionized gas.[1] The potential for uranium, for example, may be a few hundred volts, the magnetic field about 6000 gauss, the tube length a foot or two, the tube egress section some 20 square feet. The current to the side walls, if the magnetic field and electric potential are high enough, is negligibly small. All the precipitation is among the insulated slats. The isotopes become separated there, the deposit on the insulated slat adjacent to the negative side wall being richer in the ligher isotope, and the deposit on the insulated slat adjacent to the positive side wall being richer in the heavier isotope. The enrichment is proportional approximately to the square of the distance between the two side walls at the insulated slat egress end. This isotope separator will offer isotopes of metals more cheaply than any other device known to me.

[1] Proc. Natl. Acad. Sci. July, 1955.

E2. Ion Diffusion in a Uniform Magnetic Field.* K. S. W. CHAMPION AND A. B. DE SAINT MAURICE, *Tufts University.*—A new method has been used to measure ion diffusion coefficients in the presence of a magnetic field. A high-power pulse discharge was produced in a small diameter quartz tube inserted into a long cylindrical microwave cavity. The TM_{010} mode was used to produce the discharge and the TE_{111} mode utilized to measure the electron density in the afterglow. A specially designed coil was used to produce a uniform magnetic field. Considerable care was taken with the vacuum technique to insure the purity of the hydrogen gas used in the measurements. The values obtained for the ion diffusion coefficient when B/p was small were in agreement with classical theory for diffusion in the presence of a magnetic field. On the other hand, values measured when B/p was large were consistent with the theory of Simon.[1] It seems probable that there is a steady transition from ordinary ambipolar conditions, with small B/p, to Simon's free ion diffusion conditions, with large B/p. The transition may also be a function of p or, at least, of the ratio of mean free path to the tube dimensions.

* This work was sponsored by the Geophysics Research Directorate, Air Force Cambridge Research Center, Air Research and Development Command.
[1] A. Simon, Phys. Rev. **98**, 317 (1955).

E3. Resonant Power Transfer within a Plasma in a Magnetic Field.* J. E. DRUMMOND AND L. WILCOX, *Sylvania Electric Products, Inc.*—This paper presents the results of a study of conditions under which power can be transferred to or from a small oscillating electric field within the body of a plasma in a magnetic field. By Lagrange's method of characteristics, the linearized Boltzmann equation is solved under the assumption that the collision rate between electrons and neutral gas molecules is much less than the cyclotron frequency. From this and Maxwell's equations, a conductivity tensor, $\sigma(\omega)$, is derived and a set of resonant frequencies is found for which the power transfer $\mathbf{E}_\omega \cdot \sigma(\omega) \cdot \mathbf{E}_\omega$ can become large. When the kinetic energy density of the electrons is much less than the energy density of the static magnetic field, the resonant frequencies for power transfer reduce to integral multiples of the electron cyclotron frequency. Thus, additional physical insight is provided concerning the "gaps" in the electromagnetic propagation at these frequencies obtained by E. P. Gross. For plasmas with relatively large kinetic energy densities, the electromagnetic vector potential, which was dropped by Gross, becomes important and significant deviations from the cyclotron multiples are predicted for the first several resonances. A practical upper limit is found to the spectrum of resonant frequencies for which significant energy transfer occurs.

* This work was performed under Signal Corps Contract No. DA-36-039-sc-31435.

E4. Cyclotron Resonance of Electrons in Gaseous Discharge Plasmas.* M. GILDEN AND L. GOLDSTEIN, *University of Illinois.*—Resonance phenomena in gyromagnetic gaseous discharge plasmas can be particularly useful for investigating certain fundamental processes in plasmas. A study was made of such phenomena at microwave frequencies (10 000 Mc) in noble gases at pressures of the order of 10 mm Hg and plasma electron densities of the order of 10^{11} e/cc. The gases were contained in a discharge tube which passed through a section of wave guide located in a periodically varying magnetic field. The results indicated that the principal resonance was the cyclotron resonance of free electrons. The widths of these resonances gave values for the probabilities of collision for electrons with molecules at room temperature (300°K) which are in agreement with other published determinations. These values were also found to be consistent with the experimentally determined increases in the electron collision frequency resulting from the enhanced heating of the electron gas during resonance. Also found, were additional "resonance-like" effects at the higher electron densities which may be associated with the intrinsic behavior of gyromagnetic plasmas.

* Work sponsored by the Air Force Cambridge Research Center.

E5. High-Intensity Ion Sources. C. B. MILLS. *Curtiss-Wright Research Division.*—High-intensity ion sources consist of the source plasma, acceleration region, and ion beam. Processes in the plasma of high-production ion sources are discussed and a particular ion source developed with the use of these processes is described. The processes are described

by dc probe measurement in and ion currents from a plasma with 10^{14} ions/cc and a temperature of 40 ev. Results of pressure and electric gradient analyses, using the formula of Chapman and Cowling,

$$\bar{\omega}=\left(e\frac{E_z}{m}-\frac{1}{\rho}\frac{\partial p}{\partial z}\right)\frac{\tau}{1+\omega^2\tau^2},$$

with argon gas give a diffusion velocity in the plasma (near the meniscus) of 6100 cm/sec. The experimental value from current measurement, $I=ne\bar{\omega}$, was 5900 cm/sec. Other points of interest are that the acceleration due to the electric gradient was $\frac{1}{4}$ of that due to the pressure gradient; and that transverse diffusion, $\bar{\nu}=\omega r\bar{\omega}$, is the major component of ion and electron velocity across the magnetic field.

E6. Statistical Mechanics of Cathode Sputtering. DON E. HARRISON, JR., *University of Louisville.*—In an earlier paper, the author has discussed a theory of cathode sputtering.[1] The equal mass restriction, made in this earlier work, has now been removed. The results appear as a convergent series of exponential functions of the logarithmic energy. In most cases the first term dominates completely. The final expression for the sputtering ratio depends upon four parameters, only two of which are even approximately experimentally known, but the theoretical curves are extremely sensitive to the choice of parameters, and the required values are consistent with what we know of the physical system. Agreement with Keywell's experimental data[2] is satisfactory, although much of the fitting is to curves formed from three or four experimental points. The present theory is not completely satisfactory for systems of small mass ratio, but the cause of breakdown is apparent from the behavior of the curves. Extension of the theory to cover these cases is possible, but hardly warranted at this time.

[1] Don E. Harrison, Jr., Phys. Rev. **93**, 652(A) (1954).
[2] Frank Keywell, Phys. Rev. **87**, 160 (1952); Phys. Rev. **97**, 1611 (1955).

E7. Minimum Quenching Times of Low Voltage, Non-Self-Quenching Geiger Counters. ROGER D. ERICKSON *Honeywell Research Center.*—The general problem of quenching is examined to determine some factors contributing to the minimum quenching time, τ_m, of non-self-quenching Geiger counters. Experimental data were obtained using Geiger tubes filled with neon-argon mixtures. The data showed that τ_m is proportional to the gas pressure from 3 mm Hg to 125 mm Hg; it also indicated that τ_m was independent of the gas mixtures tested (neon with 0.05% to 1.00% argon). No dependence of τ_m on the quenching voltage was observed. τ_m was found to be inversely proportional to the absolute temperature with a constant gas density. The plateau lengths were determined by τ_m when a given quenching circuit was used. The experimental evidence indicates that secondary electrons produced by the diffusion of metastable atoms to the cathode are responsible for the relatively long minimum quenching times observed (0.01 to 0.30 sec).

E8. Electrical Characteristics of Low-Pressure Spark Discharges.* R. J. LEE, *Melpar, Inc.*, AND R. G. FOWLER, *University of Oklahoma.*—Precise investigations have been made of the current and voltage characteristics of spark discharges in helium, neon, argon, and xenon at pressures ranging from 1 mm Hg to 100 mm Hg. The derived quantities power and resistance have been calculated, and an analysis has been made of the resistance curves so obtained. It is found that initially the resistance is governed by the need to develop an ion concentration sufficient to carry the current, but that after this is accomplished, the resistance varies inversely as the current until the discharge has waned to a point that recombination exceeds ion production. The course of the resistance curve is wholly interpretable in terms of fundamental gas constants.

* Work sponsored by the Office of Naval Research.

F. Positive Columns and Plasmas

F1. Inclusion of Coulomb Interactions in the Boltzmann Equation.* H. DREICER† AND W. P. ALLIS, *MIT.*—The Fokker-Planck method has been used to extend the Boltzmann transport equation to include the random Coulomb interactions in an ionized gas. The time rate of change of the particle distribution function due to these interactions is expressed as the divergence of a flow vector in velocity space, and consists of two parts: (1) the flow resulting from the average retarding force, and (2) a diffusion-like flow in velocity space resulting from the fluctuations in the interaction force. An expansion of the distribution function in spherical harmonics is used to derive the equation satisfied by the spherical part of the electron distribution function, and a criterion is derived for the degree of ionization at which Coulomb interactions first exceed the effects of inelastic collisions and external electric fields. Above this degree of ionization the distribution becomes Maxwellian, but the average electron energy and the rate of ionization are not altered appreciably from their values at low electron density. It is shown that charged particles in a fully ionized gas can be accelerated indefinitely by an external electric field provided their velocities are larger than a critical barrier velocity.

* This work has been supported in part by the Signal Corps, Air Material Command, and the Office of Naval Research.
† Now at the University of California Los Alamos Scientific Laboratory, Los Alamos, New Mexico.

F2. Production and Loss of Excited Atoms in the Helium Positive Column. L. S. FROST AND A. V. PHELPS, *Westinghouse Research Laboratories.*—Measurements of the important parameters of a helium positive column reported previously[1] have been refined and extended over wider ranges of electron density and pressure. Electron density is measured by microwave techniques; the density of singlet and triplet metastable atoms and of atoms in the resonance state are measured by means of optical absorption; the axial electric field and the average electron energy are measured with fine wire probes. A power balance is presented, comparing the total input power per electron to the sum of power losses associated with diffusing ions, electrons and metastables, with resonance radiation and with elastic recoil. Agreement is obtained within limits defined by experimental accuracy and uncertainties in necessary coefficients. The data at low electron densities indicate somewhat smaller deviations from ambipolar diffusion than predicted by the transition diffusion theory of Allis and Rose.[2] A comparison is made between the combined rate of excitation and ionization given by the theory of Reder and Brown,[3] and the sum of loss rates calculated from our measurements. Again, reasonable agreement is obtained.

[1] L. S. Frost and A. V. Phelps, Phys. Rev. **98**, 559 (1955).
[2] W. P. Allis and D. J. Rose, Phys. Rev. **93**, 84 (1954).
[3] F. H. Reder and S. C. Brown, Phys. Rev. **95**, 885 (1954).

F3. Failure of Schottky Theory for the Positive Column of O_2† D. S. BURCH, G. H. DUNN, R. GEBALLE, AND V. M. MADSEN, *University of Washington.*—Measurements of the potential gradient in the uniform positive column of the O_2 glow discharge have been made using cold probes. The results are in agreement with those of Guntherschulze[1] and in the range $0.2<pR<2.4$ mm cm lie between 23 and 15 volts/cm mm. The Schottky theory for the uniform positive column has been extended to include electronegative gases. This extension predicts a lower limit to E/p corresponding to a value for which the attachment coefficient and the ionization coefficient are equal. In oxygen, equality occurs for $E/p=35$,[2] considerably higher than the above measured values. Oscillographic studies of the current and light emission show rapid time variation,[3] implying that the column does not have the uniformity on which the theory is based. N_2 has been subjected to the same observations. Measured fields in this gas do agree with predictions of Schottky theory. No current and light variation is found in N_2 in the range of current and pR for which the theory is valid.

† This work has been supported in part by the U. S. Office of Ordnance Research.
[1] A. Guntherschulze, Z. Physik **42**, 763 (1927).
[2] M. A. Harrison and R. Geballe, Phys. Rev. **91**, 1 (1953).
[3] E.g., T. Donahue and G. H. Dieke, Phys. Rev. **81**, 248 (1951); A. B. Stewart, J. Opt. Soc. Am. **45**, 651 (1955); N. L. Oleson, Phys. Rev. **98**, 559 (1955).

F4. Oscillating Glow Discharge Plasma.* A. B. STEWART AND G. E. OWEN, *Antioch College.*—The plasma potential, electron temperature, and electron concentration have been measured as functions of both time and position in the positive column of an argon glow discharge with moving striations. Plane circular tungsten probes 0.5 mm in diameter that could be saturated in the electron collecting region were used. The variations of potential, electron temperature, and charge obtained demonstrate that the moving striations in the glow discharge are closely related in their electrical properties to the striations in the argon arc studied by Pupp.[1] In the glow discharge however, in addition to the positive striations, there are weak light flashes that travel with speeds greater than 10^3 m/sec. The plasma potential is observed to drop about 10 volts within ½ of a period after the flash. Although space charge concentrations with maxima approximately 5 times the average concentration in the plasma accompany the positive striations, no increase in concentration was observed at the time of the light flash. The reliability of the probe measurements and the bearing of the results on theories of the moving striations will be discussed.

* Supported by the National Science Foundation.
[1] W. Pupp, Z. Physik **36**, 61 (1935).

F7. Derivation from Boltzmann's Equation of the Similarity Laws for Ionized Gases. T. E. VANZANDT, *Sandia Corporation.*—The similarity laws for ionized gases are derived by requiring that the Boltzmann equations for the normalized particle distribution functions of two similar discharges be the same. The results are, in addition to the usual similarity laws, that the product of the magnetic field strength times the characteristic length be the same for both discharges.

ABSTRACTS OF PAPERS TO BE PRESENTED AT THE 1955 THANKSGIVING MEETING AT THE UNIVERSITY OF CHICAGO, CHICAGO, ILLINOIS, NOVEMBER 25 AND 26, 1955*

(Corresponding to *Bulletin of the American Physical Society*, Vol. 30, No. 7)

Errata Pertaining to Abstracts C6, I5, Q3, V12, V13, and Y6

C6, by J. Joseph. In line 19, instead of "$4\alpha r_0^3 \ln(2\gamma)[\ln(2\gamma)+1]/\gamma$," read "$+\alpha r_0^3 \ln(2\gamma)[\ln(2\gamma)+1]/\gamma$."

I5, by V. E. Pilcher, J. A. Harvey, and K. K. Seth. The daggered reference should read: "Research Collaborator, on leave from Radiation Laboratory, University of Pittsburgh.

Q3, by W. A. Wallenmeyer. In line 12, instead of "41:12:7," read "41:12:57."

V12, by I. C. Gupta, W. Y. Chang, and A. Snyder. In line 7, instead of "66 events," read "64 events." In lines 16 to 17, instead of "31 events have been classified as θ^0 particles, 30 as Λ^0 particles," read "32 have been classified as θ^0 particles, 27 as Λ^0 particles."

V13, by A. Snyder, W. Y. Chang, and I. C. Gupta. In line 4, instead of "31 θ^0 particles," read "32 θ^0 particles"; instead of "30 Λ^0 particles," read "27 Λ^0 particles." In lines 18 to 20, instead of "for the 31 θ^0 particles . . . to be $(1.83^{+0.35}_{-0.25})\times10^{-10}$ sec, and for the 30 Λ^0 particles $(3.47^{+0.70}_{-0.49})\times10^{-10}$ sec," read "for the 32 θ^0 particles . . . to be $(1.4^{+0.3}_{-0.2})\times10^{-10}$ sec, and for the 27 Λ^0 particles, $(3.8^{+1.0}_{-0.6})\times10^{-10}$ sec."

On page 1268 "(R. H. Crane presiding)" should read "(H. R. Crane presiding)."

Y6, by E. D. Courant, R. R. Kassner, E. C. Raka, Lloyd Smith, and J. Spiro. In line 17 instead of "$2\nu_0+\nu_y$" read "$\nu_x+2\nu_y$."

* The usual preamble to these abstracts will be published in the Bulletin early in 1956. Abstracts of meetings in 1956 and subsequent years will not be published in *The Physical Review.*

PROGRAMME

FRIDAY MORNING AT 10:00

Eckhart 133

(A. C. G. MITCHELL presiding)

Radioactive Nuclei

A1. Decay of Ca^{49} (8.4-min).* DAVID W. MARTIN, S. BRADLEY BURSON, AND JAMES M. CORK, *Argonne National Laboratory.*—The beta and gamma radiations of radioactive Ca^{49} have been studied with the Argonne 256-channel coincidence scintillation spectrometer. Sources were prepared by irradiation in the Argonne reactor (CP 5) of samples enriched to about 12% in Ca^{48}. Gamma rays of 3.24 ± 0.05 and 4.30 ± 0.05 Mev were observed to decay with the 8.4 ± 0.1-minute period in the NaI (Tl) pulse-height distribution, in which a well collimated geometry was used. The 4.30-Mev gamma ray has an intensity of about 5% that of the 3.24-Mev transition. Calibration was based on the 4.45-Mev gamma ray of C^{13} excited by an (α,n) reaction in a shielded Po-Be source.[1] A beta ray with an end-point energy of 1.93 ± 0.10 Mev is found to be in coincidence with the 3.24-Mev gamma ray from a coincidence absorption curve. A softer beta ray in the neighborhood of 1 Mev is in coincidence with the 4.30-Mev gamma ray. The indicated decay energy of 5.1 ± 0.2 Mev is consistent with the beta decay systematics of this region of the nuclide chart.[2]

* Work performed under auspices of U. S. Atomic Energy Commission.
[1] R. J. Breen and M. R. Hertz, Phys. Rev. **98**, 599 (1955).
[2] K. Way and M. Wood, Phys. Rev. **94**, 119 (1954).

A2. Scandium-50. H. MORINAGA AND E. BLEULER, *Purdue University.*—In order to look for Sc^{50} which can be produced by an (n,p) reaction on Ti^{50}, titanium metal and TiO_2 were bombarded with Be-d neutrons from the cyclotron. The gamma-ray spectrum showed a line at 1.56 Mev which decayed with a half-life of 1.5 min. Also, beta rays with a maximum energy of about 3.5 Mev and the same half-life were detected. The intensities of the beta and gamma rays are about the same. No other radiations with a half-life between several seconds and several days were found, except for those from known isotopes expected to be produced by neutron bombardment of the samples used. This 1.5-min activity is thus assigned to Sc^{50} since no possible impurities can produce such an activity and because the energy of the gamma ray coincides well with the energy of the first excited state of Ti^{50}. Since no other gamma ray of 1.5-min half-life was found, the decay must proceed to the 2^+ first excited state ($\log ft=5$) indicating that the spin of Sc^{50} is most likely to be 2^+. This would be an example of the violation of Nordheim's rule.

A3. Radiations from Mo^{91}.* NORWOOD GOVE, FRED A. SMITH, AND R. A. BECKER, *University of Illinois.*—A detailed study has been made of the disintegration scheme of Mo^{91} (produced by a gamma-n reaction with the 22-Mev betatron) during the past year. Gamma-radiation energies were measured at 1540 ± 20, 1210 ± 30, and 658 ± 3 kev, all of which are associated with the 65.5-second activity. Three positron groups were found to be involved in the above activity and a single group was found to be associated with the 15.5-min decay. Coincidences were detected between positrons, and the first two gamma rays listed in the foregoing. The third gamma ray is not involved in coincidences. A tentative decay scheme will be discussed.

* This work was supported by the joint program of the Office of Naval Research and the U. S. Atomic Energy Commission.

A4. Disintegration of Te^{129}. WILLIAM E. GRAVES AND ALLAN C. G. MITCHELL, *Indiana University.**—The disintegration of Te^{129} has been investigated with the help of a magnetic lens spectrometer, permanent field spectrometer with photographic recording, and scintillation counters. The half-lives of the isomeric states in the parent were found to be 41 days and 74 minutes, respectively. The 74 minute state decays to I^{129} with the emission of beta-ray groups whose end-point energies and relative abundances are 1.453 Mev (71%), 0.989 Mev (15%), 0.69 Mev (4%), and 0.29 Mev (10%). Gamma rays of 0.027, 0.212, 0.475, 0.725, and 1.12 Mev were found. The 41 day state decays, for the most part, to the 74 minute state of Te^{129} with the emission of a highly internally converted gamma ray of energy 106.3 ± 0.1 kev for which the K/L ratio is unity. A beta-ray transition, of low intensity, from the 41 day state of Te^{129} to the ground state of the product is postulated. Gamma-gamma and beta-gamma coincidence experiments using scintillation spectrometers served to indicate the probable level shceme of I^{129}. A discussion of the disintegration scheme will be given suggesting probable spins and parities of the levels.

* Supported by the joint program of the Office of Naval Research and the U. S. Atomic Energy Commission.

A5. Decay of 72 Second and 49 Day In^{114}.* LEE GRODZINS AND HENRY MOTZ, *Brookhaven National Laboratory.*—Scintillation counter coincidence experiments were performed on the 72 sec activity produced by p,n and $d,2n$ cyclotron bombardments of enriched Cd^{114} and the 49 day In^{114} produced by neutron capture of enriched In^{113}. By comparing the K x-ray, 722 coincidences per x-ray for 72 sec and 49 day In^{114}, the ground state K branch to the 1278 state in Cd^{114} was found to be $\leqslant 0.2\%$ confirming the assignment of $4+$.[1] Using 49 day In^{114} the previously reported 1300–556 coincidences[2] were not confirmed, the upper limit being 0.1% of the 722–556 coincidences. The gamma ray of ~1300 kev was found to be in coincidence with a 700 kev beta spectrum with a branching ratio of 0.09%. The $\log ft$ value of 5.73 is consistent with a $2+$ assignment for the 1300 kev level in Sn^{114}, in agreement with the systematics of even-even nuclei. A 3.5% K-branch was found from the 72 sec In^{114}, presumably to the ground state of Cd^{114}.

* Work performed under contract with the U. S. Atomic Energy Commission.
[1] N. Brazos and R. Steffen, Phys. Rev. **99**, 1645(A) (1955).
[2] Johns, McMullen, Donnelly, and Nable, Can. J. Phys. **31**, 225 (1953)

A6. Decay of Cs^{138}.* R. B. DUFFIELD,† M. E. BUNKER, J. P. MIZE, AND J. W. STARNER, *Los Alamos Scientific Laboratory.*—The decay of the fission product Cs^{138} (32.0 min) has been studied with beta- and gamma-scintillation spectrometers and a 141-gauss, 180° permanent magnet spectrograph. As observed previously,[1] there is no detectable ground-state beta transition. Twelve gamma rays were found with energies of 0.1389, 0.1931, 0.2289, 0.4106, 0.4626, 0.5495, 0.87, 1.010, 1.426, 2.21, 2.63, and 3.34 Mev. The intensities of the gamma rays relative to the total number of disintegrations were found to be 2, 1, 2, 3, 26, 8, 4, 25, 73, 18, 9, and 0.5%, respectively. Internal conversion measurements indicate that

the multipolarity of the 0.1389-Mev transition is predominantly $M1$. On the basis of the above data and the results of a number of gamma-gamma and beta-gamma coincidence studies, a consistent decay scheme is proposed which involves levels in Ba^{130} at 1.426, 1.89, 2.21, 2.30, 2.44, 2.63, and 3.34 Mev. The angular correlation of the 1.010 Mev—1.426 Mev cascade has been measured. The experimental results are in best agreement with a $0(Q)2(D)3$ correlation. The spin and parity assignment for the ground state of Cs^{133} which is most consistent with the established features of the decay scheme is 3−.

* Work performed under the auspices of the U. S. Atomic Energy Commission.
† Permanent address: Department of Physics, University of Illinois, Urbana, Illinois.
[1] Langer, Duffield, and Stanley, Phys. Rev. **89**, 907 (1953).

A7. Nuclear Levels in Tm^{169}, Lu^{175}, and Lu^{177} as Derived from the Radioactive Isotopes of Yb. J. M. Cork, M. K. Brice, D. W. Martin, L. C. Schmid, and R. G. Helmer, *University of Michigan.*—Using Yb of high purity (99.8%) irradiated in the maximum flux of the Argonne pile and studied by scintillation and magnetic photographic spectrometers, a re-evaluation of the energies of the radiations has been made. Several previously unreported gamma rays are found and nuclear level schemes for Tm^{169}, Lu^{175}, and Lu^{177} proposed. Several of the levels appear to be rotational states in the unified nuclear model. Yb^{169} decays with a half-life of 30.6 days by K capture, followed by eleven gamma rays in Tm^{169}. Rotational levels lie at 8.4, 118.3, and 139.1 kev. The gamma energies are 8.4, 20.6, 63.2, 93.6, 109.9, 118.3, 130.7, 177.7, 198.6, 261.0, and 308.3 kev. Yb^{176} decays with a half-life of 4.2 days by beta emission (474 kev max) followed by five gamma rays in Lu^{176}. Rotational levels exist at 114.1 and 251.9 kev. The gamma energies are 114.1, 137.8, 145.0, 282.9, and 397.0 kev. Yb^{177} decays with a half-life of 1.88 hours by beta emission followed by gamma transitions in Lu^{177}. In addition to any lower energy gamma rays, two high energy transitions are found at 1.080 and 1.228 Mev. The latter is a cross-over for the 1.080- and 0.148-Mev gammas which are in coincidence. The expected well-known daughter product Lu^{177}, if present at all, is too weak to be observed by the magnetic spectrometers, which suggests some possible error in the assignment of masses in the stable isotopes.

A8. Electron Capture Decay of Os^{185} and the Excited States of Re^{185}.* Charles H. Pruett and Roger G. Wilkinson, *Indiana University.*—The 95 day orbital electron capture decay of Os^{185} has been studied using magnetic beta-ray spectrometers and scintillation spectrometer techniques. The measurements disclosed the presence of gamma rays at 72.5 and 125 kev which have not been previously reported. With the information obtained from coincidence and intensity measurements it is possible to include these two gamma transitions in a decay scheme with the previously reported 875, 647, 234, and 162 kev transitions. Use was made of internal conversion coefficients, K/L ratios, and lifetimes of transitions to determine the multipolarities of the gamma rays. These determinations permit assignment of spins and parities to the various excited levels of Re^{185}. Levels at 125, 647, 809, and 875 kev are given the assignments of $g_{7/2}$, 1/2+, 1/2+, and 3/2+, respectively. The 125 kev level is interpreted as the first rotational level in Re^{185}. Arguments based on the relative intensities of capture to the excited levels and ground state of Re^{185} indicate an assignment of $p_{3/2}$ to the ground state of Os^{185}.

* Supported by joint program of the Office of Naval Research and the U. S. Atomic Energy Commission.

A9. Energy Determination of Au^{198} Conversion Electrons.* D. R. Connors, W. C. Miller, and B. Waldman, *University of Notre Dame.*—The same 90° cylindrical electrostatic analyzer which was used to measure the photothresholds of Be and D[1] and the conversion lines of Cs^{137} [2] has been used to measure the conversion lines of Au^{198}. An absolute energy measurement, with an accuracy of 0.1%, can be made with this analyzer. A 1 mg/cm² layer of gold was evaporated onto a thin aluminum foil and was irradiated in the Argonne reactor. In the observed spectrum the K, L_I, L_{II}, L_{III}, M, and N lines were resolved. The K line had an intensity of ten times the beta background. The transition energy is found to be 411.8±0.3 kev in excellent agreement with the value of Muller, Hoyt, Klein, and Dumond.[3] The L_I:L_{II}:L_{III} intensity ratios are found to be in good agreement with the theoretical values of Rose and Goertzel.[4]

* Supported in part by the joint program of the U. S. Atomic Energy Commission and the Office of Naval Research.
[1] Noyes, Van Hoomissen, Miller, and Waldman, Phys. Rev. **95**, 396 (1954).
[2] Bhattacherjee, Waldman, and Miller, Phys. Rev. **95**, 404 (1954).
[3] Miller, Hoyt, Klein, and Dumond, Phys. Rev. **88**, 775 (1952).
[4] K. Siegbahn, *Beta and Gamma Ray Spectroscopy* (Interscience Publishers, Inc., New York, 1955), p. 905.

A10. Directional and Polarization-Direction Correlations in Pb 208 γ-γ Cascades.* G. T. Wood† and P. S. Jastram,‡ *Washington University.*—Direction-direction correlations and polarization-direction correlations have been measured for γ-γ cascades in Pb-208 following the decay of ThB. Together with previously measured internal conversion coefficients,[1,2] the present results yield spin and parity assignments of 3⁻, 5⁻, 4⁻, and 5⁻, respectively, to the 2.62, 3.20, 3.48, and 3.71 Mev levels in Pb-208, and multipolarity character assignments of $E3$, $E2$, $M1+E2$ ($\delta=-0.20\pm0.05$), and $M1+E2$ ($\delta=-0.028\pm0.010$), for the 2.62, 0.58, 0.51, and 0.86 Mev gamma rays, where δ is the ratio of the reduced quadrupole to dipole nuclear matrix elements. Assignments are based on angular correlation measurements between the 2.62–0.58 Mev, 0.58–0.51 Mev, and 2.62–0.86 Mev γ-γ cascades and on polarization distributions of the 2.62, 0.86, 0.51, and 0.51+0.58 Mev gammas. With the exception of the mixing ratio for the 0.51 Mev gamma our results are in agreement with the decay scheme previously proposed.[3]

* Supported in part by the joint program of the Office of Naval Research and the U. S. Atomic Energy Commission.
† University Fellow in Physics.
‡ Now at Ohio State University.
[1] D. G. E. Martin and H. O. W. Richardson, Proc. Roy. Soc. (London) **A195**, 287 (1948).
[2] Elliott, Graham, Walker, and Wolfson, Phys. Rev. **93**, 356 (1954).

A11. Alpha Decay of Np^{237}. L. B. Magnusson, D. W. Engelkemeir, M. S. Freedman, F. T. Porter, and F. Wagner, Jr., *Argonne National Laboratory.*—Nine alpha groups from the decay of Np^{237} have been detected by ion pulse analysis[1]: 4.872 Mev (3.1%), 4.816 (3.5), 4.787 (53), 4.767 (29), 4.713 (1.7), 4.674 (3.3), 4.644 (6.0), 4.589 (0.5), 4.52 (0.02). Alpha standards were Th^{230} (4.682 Mev) and Po^{210} (4.877 Mev). Using scintillation, proportional and magnetic spectrometers, we observed transitions (kev, *photons/disintegration*, e^-): (20, *0*, L?, M?) (29, *0.14*, L_{12}, L_3, M), (56.8, *0*, L_2, L_3, M), (86.9, *0.14*, L_{12}, L_3, M, N), (145, *0.008*, K, L), (175, *0.001*, K), (200, *0.003*, K, L); also the Pa x-rays at (13, *0.9*), (16, *0.4*) and (92, *0.05*). Transition assignments were derived from α-e^-, α-γ, and γ-γ coincidences. The 4.872 alpha-particle emission leads to the Pa^{233} ground state. The 86 kev and most of the 30 kev transitions depopulate the second excited state (3.7×10^{-6} sec).[2] A fraction (which is "prompt") of the 30 kev, the 145, and complex (unresolved) 200 kev radiation arise from levels above 160 kev. This work was sponsored by the U. S. Atomic Energy Commission.

[1] D. W. Engelkemeir and L. B. Magnusson, Rev. Sci. Instr. **26**, 295 (1955).
[2] D. W. Engelkemeir and L. B. Magnusson, Phys. Rev. **94**, 1395 (1954).

A12. Energy Levels of Pu^{239} Populated by the Beta Decay of Np^{239}. J. M. HOLLANDER AND W. G. SMITH, *University of California*, AND J. W. MIHELICH, *Notre Dame University*.—The conversion-electron spectrum observed from the beta decay of 2.33-day Np^{239} to Pu^{239} has been studied with three 180° permanent-magnet photographic spectrographs. The Np^{239} was prepared by irradiation of U^{238} in the Livermore reactor followed by chemical separation of the neptunium. The following transitions, with multipolarities where known, were observed: 0.04464 ($M1+E2$), 0.04940 ($M1+E2$), 0.05725 ($E2$), 0.0614 ($E1$), 0.06782 ($E2$), 0.09832, 0.1033, 0.10610 ($E1$), 0.1064, 0.1253, 0.1818, 0.2099 ($M1$), 0.2264, 0.2264, 0.2284 ($M1$), 0.2546, 0.2731, 0.2777 ($M1$), 0.2856, 0.3161, and 0.3345 Mev. The energy-level scheme of Asaro, Thompson, and Perlman[1] has been found to describe some of the features of the decay but the observation of certain transitions requires the postulation of additional energy levels. An energy-level scheme based on transition energy sums and relative internal conversions will be presented. This work was performed under the auspices of the U. S. Atomic Energy Commission.

[1] Asaro, Thompson, and Perlman, Phys. Rev. **92**, 694 (1953).

A13. Gamma-Ray Induced Isomers with Half-Lives between 10^{-5} and 10^{-1} Second.* STANLEY H. VEGORS, JR., AND PETER AXEL, *University of Illinois*.—A technique was developed for the detection of radioactivity between the x-ray yield pulses of the University of Illinois 22 Mev betatron, and was applied to the measurement of radioactivities in the half-life range between 10^{-5} and 10^{-1} second. The validity of this approach was investigated by observing the known isomeric transitions in this range of half-lives in Pb^{204m}, Zn^{67m}, Ta^{181m}, and Y^{89m}. A search was undertaken to determine whether any undetected isomers exist in this range of half-lives. Twenty-two elements are investigated, and seven previously unreported activities were found. The elements, gamma-ray energies, and half-lives are as follows: As, 315 kev, approximately 14×10^{-3} sec; Mo, 98 kev, 16.5×10^{-6} sec; Pd, 160 and 300 kev, 33×10^{-6} sec; W, 370 kev, 16×10^{-6} sec; Tl, 410 kev and 720 kev, 65×10^{-6} sec; Tl, 520 kev, 5.3×10^{-4} sec; and Bi, 545 kev and 1.065 Mev, 2.7×10^{-6} sec. Negative results were obtained in a search for W^{180m} and Na^{23m} activities. The (γ,n) thresholds for the production of Pb^{204m}, Pb^{207m}, Y^{89m}, and the 16.5×10^{-6} sec. Mo activity is also measured.

* This work was supported by the joint program of the Office of Naval Research and the U. S. Atomic Energy Commission.

FRIDAY MORNING AT 10:00

Mandel Hall

(D. W. KERST presiding)

Apparatus and Techniques, I

B1. Angular Momentum and Energy of the Ions in the Magneto-Ionic Isotope Separator. JOSEPH SLEPIAN, *Westinghouse Research Laboratories*.—In the magneto-ionic expander isotope separator,[1] the net current taken by the collectors is zero, and that by the impressed voltage bearing side walls is negligibly small. Hence, the total moment of momentum of the ions received by each collector is zero, and the total kinetic energy of the ions and electrons is the same at the collectors as it was at the input end. The increase in length of the discharge as it terminates upon the collectors, and the reduction in the temperature of the ions there, are both responsible for the high enrichment observed there, the deposit upon the collector adjacent to the negative wall being enriched in the lighter ion, and that upon the collector adjacent to the positive wall being enriched in the heavier ion. The method will offer isotopes of the metals more cheaply than any other method known to me.

[1] J. Slepian, Proc. Natl. Acad. Sci. 451–457 (July 15, 1955).

B2. Transmission Secondary Electron Multiplication for High Resolution Counting and Imaging. E. J. STERNGLASS AND M. M. WACHTEL, *Westinghouse Research Laboratories*.—Weak currents may be amplified with high space and time resolution using secondary electron multiplication through a series of plane-parallel insulating films, each covered with a thin layer of a heavy metal. The metallic layer serves to scatter the incident electrons so that they enter the insulator at large angles. The long secondary electron diffusion length in the insulator results in high yields and permits the use of relatively thick films, thereby keeping the number of fast transmitted electrons small. In order to allow reasonably low voltages between stages, the films must be very thin. The films used consist of a supporting film of SiO about 100 A thick, followed by ~20 A of Au and 400–600 A KCl. To obtain sufficient mechanical strength, they are carried by electro-formed screens of fine mesh and 50% open area. With this screen open area, a yield of 4 per stage was obtained at 2 to 3 kev. Less than 10% of the emerging electrons exceeded an energy of 6 ev, indicating that the homogeneity is adequate for high image and time resolution. Time response tests were carried out using the technique developed by R. V. Smith. A seven stage device with a 50Ω coaxial output and 0.75 inch diam screens spaced 0.20 inch apart gave a transit time of 3×10^{-9} sec and a rise time of $\lesssim1\times10^{-9}$ sec at 3 kv per stage.

B3. New Method for Determining the Range of Low-Energy Electrons in Solids. J. E. HOLLIDAY AND E. J. STERNGLASS, *Westinghouse Research Laboratories*.—The range of electrons at energies in the kilovolt region and below may be determined by measuring the number of backscattered electrons from composite layers as a function of the incident energy. This technique is especially useful at low energies, where the energy loss in supporting foils becomes appreciable. The material studied is deposited as a film on a thick base having greatly different backscattering properties. Using a monoenergetic electron beam, the fraction η of backscattered electrons is determined with a plane-parallel collector system that rejects the secondaries of <50 ev. For low primary energies, η is characteristic of the surface film. As the energy is increased, electrons penetrate to the base material. When the energy of the primaries is such that the range in the surface material is equal to twice its thickness, a marked change in η occurs. Using a series of aluminum layers of different thicknesses on a gold backing and observing the energy at which η begins to change, it was possible to obtain a range-energy curve for aluminum between 2 and 17 kev. The results are in good agreement with Bethe's theory of stoppping and the experimental results of Lane and Zaffarano who utilized the

onset of penetration through layers carried by thin organic foils.

B4. Bistable Solid State Opto-Electronic Devices. E. E. LOEBNER, *Sylvania Electric Products, Inc.*—The bistable operation of ac circuits containing optically coupled and impedance matched electroluminescent and photoconductive elements has been investigated as a function of amplitude and frequency of the applied voltage, circuit current, and bias illumination. It was found that a series circuit of an electroluminescent and a photoconductive cell will stabilize either at a low-current and nonemitting or at a high-current and light-emitting operating condition within a range of voltages, whose mean magnitude and spread decreases with increasing illuminance bias. Selection of the desired operating mode can occur by means of electrical or optical or combined input signals. The time needed for switching into the other stable condition varies from few milliseconds to several seconds and depends not only on the operation and the time constants of the cells, as well on the strength and duration of the signal pulses, but also on the accompanying electro-photoluminescent and infrared quenching effects. Several logic networks, capable of computer operations, were built using series and parallel arrangements of electroluminescent and photoconductive cells and selecting light channels between them.

B5. Evapor-Ion Pump Behavior with Noble Gases. IGOR ALEXEFF AND EDWARD C. PETERSON, *University of Wisconsin.**—With the Evapor-ion pump, as previously described, relatively high pumping speeds for chemically active gases are easily attained. For inert gases which must be ionized and driven into the walls, high speeds have been difficult to reach. During the past year, various arrangements of electric and magnetic fields have been tried in attempts to improve ionization efficiency. The most effective arrangement produced a pumping speed for argon of 250 liters/sec at 1 ampere of ionization current. A high transparency grid and an axial magnetic field were used. The Evapor-ion pump is an efficient leak detector because of the difference in pumping speeds for air and inert gases. Spraying a leak with helium, for example, causes a sudden marked pressure rise.

* Work supported by the Wisconsin Alumni Research Foundation and the U. S. Atomic Energy Commission.

B6. Negative Hydrogen Ion Source. J. A. WEINMAN, J. R. CAMERON, AND R. G. HERB, *University of Wisconsin.**—Positive hydrogen ions from a magnetic ion source[1] are accelerated to an energy of 20 kev. The ions then pass through a capillary tube into the center of which hydrogen is introduced.[2] The negative ions emerging from this tube are accelerated by an additional 30 kv, while the emerging secondary electrons are electrostatically repelled. The negative ions are then focused by an electrostatic "saddle-field" lens,[3] and separated by a magnetic analyzer. Currents measured in a collector after passing through the magnetic analyzer can readily be maintained at 20 to 25 microamperes and the source has yielded a maximum of 30 microamperes of negative hydrogen ions. The beam at the collector cup is normally $\frac{1}{8}$ to $\frac{1}{4}$ inch in diameter. A pressure of 10^{-3} to 10^{-4} mm Hg is maintained in the negative hydrogen ion source container by an Evapor-ion pump,[4] which gives pumping speeds of approximately 7000 liters per second.

* Work supported by the U. S. Atomic Energy Commission and the Wisconsin Alumni Research Foundation.
[1] J. Kistemaker and H. L. Douwes Dekker, Physica XVI **3**, 198 (1950).
[2] A. C. Whittier, Can. J. Phys. **32**, 275 (1954).
[3] O. Klemperer, *Electron Optics* (Cambridge University Press, Cambridge, New York, 1953), p. 64.
[4] R. H. Davis and A. S. Divatia, Rev. Sci. Instr. **25**, 1193 (1954).

B7. Energy Resolution Obtainable with a 2 Mev H_2^+ Beam. D. F. HERRING, R. A. DOUGLAS, E. A. SILVERSTEIN, AND REN CHIBA, *University of Wisconsin.**—The energy resolution obtainable with a diatomic hydrogen ion beam is appreciably inferior to that available with the atomic ion beam. The ion beams were provided by an electrostatic generator and defined in energy by a 90° cylindrical electrostatic analyzer. The resolution was investigated by observing the very narrow 0.993 Mev (p,γ) resonance in Al^{27} first for 0.993-Mev protons and then for 1.986-Mev diatomic ions. The resolution for the atomic ions was measured to be 0.09%, while that of the diatomic beam was 0.25%. Preliminary calculations of the resolution for values for the internal energy of the H_2^+ system less than the dissociation energy (2.65 ev) indicate that the bulk of the effect can be attributed to doppler broadening resulting from the internal motion in the H_2^+ ion.

* Work supported in part by the U. S. Atomic Energy Commission and the Wisconsin Alumni Research Foundation.

B8. Investigation of Boron Trimethyl Counters. G. A. FERGUSON, C. W. PETERS, AND F. E. JABLONSKI, *U. S. Naval Research Laboratory.*—The use of boron trimethyl, $B(CH_3)_3$, as a counting gas has been reported.[1] The nonelectronegative character of its decomposition products is desirable for extended counter life. We have prepared $B(CH_3)_3$ according to a procedure similar to that described by Brown[2] using BF_3 generated from the nonenriched complex $CaF_2 \cdot BF_3$. Impurities were removed by a method suggested by Dr. M. Taylor of Howard University. A sample of the purified gas was analyzed by infrared spectroscopy and bands were found at locations indicated for boron trimethyl.[3] A cylindrical brass-walled counter, one inch in diameter and six inches in length, having a 4.5 mil tungsten anode was filled with purified, nonenriched boron trimethyl to pressures in the range 5–30 cm Hg. The response of these proportional counters, in a flux of Po-Be neutrons moderated in paraffin, has been compared with the response of a similar filling of BF_3. Differential pulse-height spectra have been observed for the two fillings. The resolution is roughly 30% for a 30-cm Hg pressure.

[1] O. H. Hauser, Z. Naturforsch. **7a**, 781 (1952).
[2] H. C. Brown, J. Am. Chem. Soc. **67**, 374 (1945).
[3] J. Goubeau and H. Becher, Z. anorg. u. allgem. Chem. **268**, 1 (1952).

B9. Recoil-Coincidence Method for Producing Monoenergetic *d-d* Neutrons. W. FRANZEN,* *University of Rochester*, AND P. HUBER AND L. SCHELLENBERG, *University of Basel.*—A method has been developed for eliminating background neutrons from a *d-d* neutron source. For this purpose, neutrons emitted from a deuterium gas target are observed in coincidence with the He^3 recoils also produced in the reaction. The gas volume is confined by means of a 0.5 mg/cm² Ni foil, and the recoil counter consists of a layer of ZnS crystals on the face of a photomultiplier mounted behind a system of apertures at 90±3° to the direction of incidence of the deuterons. A cylinder of Scintillon plastic attached to a photomultiplier mounted on a movable frame is used as a neutron counter. The factors influencing the energy resolution of the system have been analyzed. For a gas pressure of 3.5 cm Hg, the geometry of the system is designed to achieve a neutron energy spread of less than 10 kev for a deuteron bombarding energy between 400 and 1000 kev. This device is now in use for the measurement of total neutron cross sections, and its operation will be described in detail.

* On leave 1954–1955 at the University of Basel, Switzerland.

B10. Characteristics of the New Argonne Fast Neutron Chopper.* L. M. BOLLINGER, R. E. COTÉ, AND J. M. LEBLANC, *Argonne National Laboratory.*—A fast neutron chopper having unique features has been completed and is operating at reactor CP-5. It consists of a rotor of a new design spun about

a vertical axis at 15 000 rpm by a direct coupled dc motor. The rotor is a 10-inch diameter monel cylinder with a uranium core of 3 inch diameter. Two sets of 7 slits perpendicular to the axis of rotation intersect at 90° in the core. All slits are cigar-shaped, being 0.025 inch wide at both ends and 0.055 inch in the middle. This shape produces neutron bursts which, for a given speed, are twice as narrow as those given by conventional fast chopper slit designs. At full speed the average burst width is 2 μsec, giving a resolution of about 0.04 μsec with a 60-meter flight path. The shape of the cut-off function may be varied over a wide range by adjustment of collimator positions. The large slit area of the present rotor is to give a high flux for partial cross section measurements. A second rotor under construction, giving narrower neutron bursts, is intended for transmission measurements.

* Work done under the auspices of the U. S. Atomic Energy Commission.
† The drive system is similar to that of the Brookhaven chopper.

B11. Third-Order Aberration and Focusing with Sector-Shaped Magnetic Field.* D. F. DEMPSEY, W. C. MILLER, AND B. WALDMAN, *University of Notre Dame.*—Magnetic focusing computations have been carried out which extend the first-order results of Herzog[1] and the second-order results of Hintenberger[2] for magnets whose edges are in the shape of straight lines or arcs of circles. The general formula obtained evaluates the transverse aberration of order α^3 which occurs at the focus of second-order instruments. It contains as a factor a term which may be equated to zero to yield parameters which result in third-order focusing. These have been plotted as design curves which allow a choice of many third-order magnets.

* Supported in part by the Office of Naval Research and the U. S. Atomic Energy Commission.
[1] R. Herzog, Z. Physik **89**, 447, 786 (1934).
[2] H. Hintenberger, Z. Naturforsch. **3a**, 125, 669 (1948); **6a**, 275 (1951); Rev. Sci. Instr. **20**, 748 (1949).

B12. Attenuation of 1-cm Microwaves by Abnormal dc Discharge in Helium.* Z. GELLER AND W. LOW,† *The Hebrew University.*—The attenuation of 1 cm microwave was measured as a function of the distance from the cathode of a cold cathode dc discharge. Measurements were made for various pressures and current densities in the abnormal discharge region. The attenuation reaches a maximum before the beginning of the negative glow, falling off to small values in the positive column. Electron densities calculated from the attenuation data agree roughly with those found by other methods. Near the beginning of the negative glow negative attenuation or amplification was observed in a very narrow layer in about the same region where Merrill and Webb[1] have observed oscillations. The amplification increases with current density. The calculated density at this region corresponds to that obtained if the plasma were to oscillate with the microwave frequency. A possible explanation is a coupling between the microwave field and the longitudinal plasma oscillations which makes the microwaves grow as they traverse the discharge tube.

* Assigned to a Friday session at the request of one of the authors.
† Present address: Institute for Nuclear Studies, University of Chicago.
[1] H. J. Merrill and H. W. Webb, Phys. Rev. **55**, 1191 (1939).

FRIDAY MORNING AT 10:00

Cobb 110

(D. C. PEASLEE presiding)

Theoretical Physics, I

C1. Self-Consistent Treatment of the Nuclear Independent Particle Model. G. E. TAUBER* AND T. Y. WU, *National Research Council.*—A general central nucleon-nucleon interaction $V(|\mathbf{r}_i-\mathbf{r}_j|)$ including all possible central interactions, such as Wigner, Bartlett, Majorana, and Heinsenberg, has been chosen to satisfy the saturation requirements and to be consistent with some of the properties of the two-nucleon system, but contains the strength V_0 as an adjustable parameter. The wave function of the nucleus is an antisymmetric combination of products of the single-nucleon wave function ψ_ν. The ψ_ν and V_0 are determined by the Ritz variational principle and the empirical value of the total binding energy of the nucleus. It is then possible to find the "central field" $V(\mathbf{r})$ for a nucleon in any shell, and to calculate its binding energy from the Hartree-Fock equations. Calculations have been carried out for the O^{16} nucleus. With the value of V_0 so obtained, the total binding energies of O^{15} and O^{17} and the binding energy of the "last" nucleon has been calculated. The result that the last neutron in O^{17} outside the closed shells is weakly bound compared with the nucleons in the closed shells in O^{16} is consistent with the usual basic ideas in the shell model.

* Present address: Department of Physics, Western Reserve University, Cleveland, Ohio.

C2. *L-S* Interaction in Nuclei. L. S. KISSLINGER,* *Indiana University.*—The spin-orbit interaction in nuclei is derived from the two-body nucleon-nucleon interaction. Firstly, a calculation is made using only the tensor interaction, which is known to be present in the nucleon-nucleon interaction. Using a nuclear surface which is currently accepted, this calculation gives an interaction which is not in disagreement with experiment. Secondly, a more general approach is taken, one which is more nearly in accord with the spirit of the "coherent" model of the nucleus[1]. In this case the general nonrelativistic nucleon-nucleon scattering operator is used, and from this it is shown that a splitting arises which is consistent with observations. The mixed density function for the nucleus is evaluated as part of the calculation.

* National Science Foundation Predoctoral Fellow.
[1] Brueckner, Levinson, and Mahmoud, Phys. Rev. **95**, 217 (1954); K. A. Brueckner, Phys. Rev. **97**, 1353 (1955); and other recent publications by Brueckner *et al.*

C3. Hole-Particle Relations and *j-j* Coupling. R. W. KING *Purdue University.*—Odd-odd spins and β decay matrix elements involving neutrons and protons in $l+\frac{1}{2}$ orbits show marked departures from hole-particle equivalence in the *j-j* coupling scheme. The less abundant data on $l-\frac{1}{2}$ shells reveal no such marked departures for either odd-odd spins or β decay transition probabilities. This behavior shows that the spin-orbit interaction does not lead to *j-j* coupling over the complete shell. It appears that mutual interactions large enough to prevent *j-j* coupling are achieved when only a few particles are present in a shell. As particles are added the mutual interactions become less specific, and the average

tendency to j-j coupling re-emerges. A good approximation to j-j coupling is reached near the closure of an $l+\frac{1}{2}$ shell. The $l-\frac{1}{2}$ shells are forced to be j-j coupled by the exclusion principle. This point of view leads to a consideration of β transition probabilities as a function of the percent of shell crossed with the satisfying result that the image transitions appear as limiting cases of a continuous trend. Implications for individual orbital forbiddenness in (d,p) reactions and β decay are also apparent.

C4. Proton-Proton Scattering at 1 Bev.* WILLIAM RARITA,‡ *Case Institute of Technology.*—By using the partial wave analysis reported at the last Washington meeting[1] and limiting the l value to 3 we obtain a good fit to the experimental elastic angular distribution of protons scattered by protons at 1 Bev. The elastic cross section σ_e can then be evaluated. $\sigma_e=22.3$ mb and the absorption cross section $\sigma_a=25.7$ mb. $\sigma_a/\sigma_e=1.15$. By making the more restrictive assumption that the phase shifts δ_l depend solely on l and not j we find that the δ_l can be determined in terms of a single parameter. Usually three parameters would be needed to express the phase shifts. But the inequality relation between the forward angle scattering and the total cross section is best fitted at the minimum and thus gives two additional conditions. An unusual result is that for all values of the remaining parameter the absorption in the S state is less than that in the D state contrary to the expectation of the ray approximation of the optical model. On the other hand, the P and F state phase shifts behave well according to such a model and give a reasonable radius of interaction.

* Supported by U. S. Atomic Energy Commission.
‡ On sabbatical leave from Brooklyn College.
[1] William Rarita, Phys. Rev. **99**, 630(A) (1955).

C5. Phase Shift Analysis of Nucleon-Nucleon Scattering at 150 Mev.* SHOROKU OHNUMA AND DAVID FELDMAN, *University of Rochester.*—A phase shift analysis of the unpolarized n-p and p-p scattering as well as the polarized p-p scattering data at 150 Mev has been carried out on the assumption that nuclear forces are charge independent and that only states with total angular momentum $J\leq 2$ contribute; $^3P_2-{}^3F_2$ and $^3S_1-{}^3D_1$ coupling have been neglected, however. The formulas used to estimate the Coulomb-nuclear interference in p-p scattering are essentially nonrelativistic (although they include a kinematic correction so as to give agreement with the Møller formula at small angles). Those nuclear phase shifts which are common to the p-p and n-p systems are not identical to one another because of the Coulomb interaction; the differences between these two kinds of phase shifts have been estimated, assuming only a range for the nucleon-nucleon force, and have been found to be small. Polarized n-p scattering cross sections have been calculated for the same energy using the sets of phase shifts thus obtained and they will be compared with the experimental data. The implications of the analysis for the nature of the nucleon-nucleon interaction will also be discussed.

* This research was supported, in part, by the U. S. Atomic Energy Commission.

C6. Multiple Photon Production from Electron Pair Annihilation. J. JOSEPH, *State University of Iowa.*—Gupta[1] estimated the cross section for N-photon production, assuming that the principal contributions come from very soft photons (infrared divergence) *and* small scattering angles. Gupta justified these assumptions by an independent estimate of three-photon production. He regarded the latter as more reliable. Specializing his general result to $N=3$ one finds a discrepancy of a factor $\frac{1}{3}$. We have estimated N-photon production assuming *only* the infrared limiting form,[2] introducing this approximation at an earlier stage of the calculation. Our results agree with Gupta's, giving $\sigma_N\simeq\sigma_3[2\alpha\pi^{-1}\ \ln(\gamma/\epsilon)\times\ln(2\gamma)]^{N-3}/(N-2)!$ where γm is the electron energy in the laboratory system and ϵm is the experimental energy resolution. Moreover, we applied the substitution law to the double Compton[3] process to obtain three-photon pair annihilation. This result *agrees* with the general formula, differing from Gupta's value by a factor $\frac{1}{3}$. We also estimated the next terms in the high-energy expansion for $N=3$: $4\alpha r_0^2\ \ln(2\gamma)[\ln(2\gamma)+1]/\gamma$.

[1] S. N. Gupta, Phys. Rev. **98**, 1502 (1955).
[2] J. M. Jauch and F. Rohrlich, Helv. Phys. Acta **27**, 613 (1954).
[3] F. Mandl and T. H. R. Skyrme, Proc. Roy. Soc. (London) **A215**, 497 (1952).

C7. Contribution of the Electron to Pair Production in Atomic Hydrogen. F. ROHRLICH AND J. JOSEPH, *State University of Iowa.*—The total cross section for pair production by γ rays on a free electron in the high energy limit is (in units of αr_0^2) $\sigma=(28/9)\ln(2\omega/m)-106/9$, which includes recoil and exchange effects. The constant term is the result of an exact integration of Votruba's[1] formulas, who estimated it to be $-(102\pm 4)/9$. Extracting the electron recoil distribution from Votruba's work permits one to correct the screening calculations of Wheeler and Lamb.[2] They neglected the recoil energy and exchange and found for complete screening in atomic hydrogen $\sigma_{coh}=16.4$ and $\sigma_{incoh}=19.8$ for the coherent and incoherent total cross sections. We find that the recoil energy is indeed negligible, but that exchange modifies their results to $\sigma_{coh}=-(28/9)\ln 2\alpha+(97\pm 10)/27=16.8\pm 0.4$ and $\sigma_{incoh}=-(28/9)\ln 2\alpha+77/27=16.1$. Exchange gives a smaller electronic momentum transfer distribution and therefore decreases the incoherent cross section, but increases slightly the coherent cross section due to the (negative) interference term between nuclear and electronic momentum transfer.

[1] V. Votruba, Bull. intern. acad. tech. Sci. **49**, 19 (1948).
[2] J. A. Wheeler and W. E. Lamb, Phys. Rev. **55**, 858 (1939).

C8. High-Energy Photoneutron-Proton Pair Ejection from Nuclei.* ALLEN ODIAN,† BERNARD FELD, WILLIAM RANKIN, PETER STEIN, ALBERT WATTENBERG, AND ROY WEINSTEIN, *Massachusetts Institute of Technology.*—The high-energy photoproduction of neutron-proton pairs from nuclei has been compared to the photodisintegration of the deuteron for 260 Mev photons. The differential cross sections for the production of these pairs from lithium and oxygen was compared with that for the photodisintegration of the free deuteron at proton angles of 35°, 60°, 90°, and 135° in the center of mass of the deuteron. The relative angular distribution from lithium and oxygen to deuterium was found to be flat within the experimental error. This indicates that if the mechanism for the photodisintegration of the real and *quasi*-deuterons is the same, then the relative angular momentum of a neutron and proton in a *quasi*-deuteron is the same as that in a free deuteron. The process shows a cross section dependence of $\sigma_{quasi\text{-}deuteron}=CNZ\sigma/A$ free deuteron where C is between 2.5 and 4 indicating that the mechanisms for the two processes are the same.

* Supported in part by the U. S. Atomic Energy Commission Office of Naval Research.
† Now at the University of Illinois, Urbana, Illinois.

C9. Electric-Monopole Transitions in Atomic Nuclei. E. L. CHURCH* AND J. WENESER,† *Brookhaven National Laboratory.*‡—Low-energy electric-monopole, or $E0$ transitions, ($\Delta I=0$, *no*), proceed solely by internal conversion, with zero units of angular momentum transferred to the ejected electron. Gamma-ray emission of this multipole order is strictly forbidden, although $E0$ pair production is possible for transition energies $>2\ mc^2$. It is pointed out that (1) the electric-mono-

pole mode of de-excitation is available between any two equal-parity states of the same spin, zero or otherwise, (2) that in such cases, $E0$ internal conversion may compete favorably with the paralleling magnetic-dipole and electric-quadrupole radiative transitions in heavy nuclei, and (3) that monopole matrix elements, $\langle i|\Sigma r_p^2|f\rangle$, may be particularly useful in the study of nuclear structure. The relative and absolute conversion properties of electric-monopole transitions have been calculated relativistically, including the effects of the finite nuclear size and atomic screening. These results have been used to analyze the available experimental data on the $2^+ \rightarrow 2^+$ transitions in Pt^{194} and Hg^{198}, and to determine upper limits for the monopole matrix elements. These limits appear appreciably smaller than the values deduced for the well-known monopole transitions of the $0^+ \rightarrow 0^+$ type. The possible significance of these results is considered with reference to current nuclear models.

* On leave from Frankford Arsenal, Philadelphia, Pennsylvania.
† Now on leave at the University of Illinois, Urbana, Illinois.
‡ Work performed under the auspices of the U. S. Atomic Energy Commission.

C10. Strength Function of Nuclear Energy Levels. H. H. BARSCHALL AND S. E. DARDEN, *University of Wisconsin.**—Measurements of the strength function (ratio of average reduced neutron width to level spacing) for levels in the compound nucleus have been continued.[1] Deviations from exponential attenuation of neutrons at average energies between 60 and 225 kev were observed. For manganese, a large effect found at all energies provides evidence for the S-wave peak in the strength function predicted by the complex square well model.[2] For selenium and niobium, the strength function computed assuming only S-wave interactions increases rapidly with neutron energy suggesting appreciable interactions of P-wave neutrons. An analysis of the data taking into account the effect of P-waves yields for selenium and niobium a P-wave strength function in qualitative agreement with calculations based on the complex square well theory which predicts a P-wave maximum at low neutron energies for these elements.

* Work supported by the U. S. Atomic Energy Commission and the Wisconsin Alumni Research Foundation.
[1] S. E. Darden, Phys. Rev. **99**, 748 (1955).
[2] Feshbach, Porter, and Weisskopf, Phys. Rev. **96**, 448 (1954).

FRIDAY MORNING AT 10:00

Kent 106

(G. E. PAKE presiding)

Magnetism; Magnetic Resonance

D1. A Low Voltage Magnet and Regulated Power Supply.* R. C. MOBLEY, C. H. BLAKEWOOD,† AND D. C. RALPH, *Louisiana State University.*—An electrogmanet constructed for use as an ion buncher[1] and its associated power supply will be described. The magnet produces a field of 15 kilogauss across a gap of ½ inch over an area of 100 sq in. The power supply is capable of delivering controlled currents up to 150 amperes at 20 volts to two series connected strip wound magnet coils. The current control circuit consists of a high gain closed loop servo system using a self-balancing electronic amplifier and a two stage single magnetic amplifier to yield the magnet coil current. The high internal gain of the system and the excellent zero stability of the self-balancing amplifier limits excursions in current to $\pm 0.01\%$. The design and operating characteristics of the control circuit will be discussed.

* Supported by the Office of Naval Research and the U. S. Atomic Energy Commission.
† Now at Yale University.
[1] R. C. Mobley, Phys. Rev. **88**, 360 (1952).

D2. Magnetic Properties of Murdochite, Cu_6PbO_8. PALMER L. EDWARDS, *Naval Ordnance Laboratory.*—The paramagnetic susceptibility of Cu^{++}, octahedrally surrounded[1] by O^{--}, as found in the mineral murdochite,[2] was determined from 77°K to 845°K. Above room temperature the Curie-Weiss law is satisfied with $\theta = -700° \pm 50°$K. Below room temperature the reciprocal susceptibility curve bends slightly toward the temperature axis. From the linear portion of the curve the effective magnetic moment per Cu^{++} ion was found to be $1.75 \pm 0.02 \mu_B$, which is very near the value for complete orbital quenching. The large negative θ indicates that murdochite may be antiferromagnetic, although no transition temperature was observed in the susceptibility curve. A molecular-field analysis showed that the possible arrangements of the magnetic ions below a transition temperature would be such that the ions are antiferromagnetically arranged on each of three sublattices.

[1] C. L. Christ and Joan R. Clark (to be published in *American Mineralogist*).
[2] Kindly loaned by C. L. Christ of the U. S. Geological Survey, Washington, D. C.

D3. New Magnetic Transition in Mn_3ZnC. B. N. BROCKHOUSE, *Chalk River Laboratory,* AND H. P. MYERS, *University of British Columbia.*—Alloys with the approximate compositon Mn_3ZnC are ferromagnetic but the saturation magnetization shows a maximum in the region of 230°K. X-ray studies have shown that below 231°K the normal cubic structure becomes tetragonal with a c/a ratio changing smoothly from 0.994 at 77°K to 1.000 at 231°K. Neutron diffraction studies have shown that a set of lines which can be indexed as 111, 311, and 331 lines of a unit cell of double the normal size appear below 231°K. These lines have an intensity which increases steadily with decreasing temperature and are ascribed to magnetic scattering. Above 231°K the 100 line (normal cell) has an intensity which can be accounted for by simple ferromagnetism of equivalent manganese atoms. Below 231°K the intensity of the 100 line is greater than can be accounted for on this basis. Above the normal Curie temperature (~400°K) the diffuse scattering suggests moments of about $1.5 \mu_B$ per manganese atom, consistent with the saturation magnetization above 231°K. Mn_3ZnC therefore appears to be a normal ferromagnetic material above 231°K. At this temperature a second-order transition occurs, involving a complex ordering of the manganese ions. Possible magnetic structures will be discussed.

D4. Magnetic Superexchange Interaction.* DAVID A. KOTTWITZ, *University of Pennsylvania.*—A straightforward formulation of the theory of superexchange for the standard tri-

atomic model has been carried out. Explicit determinantal wave functions are employed in a routine configuration interaction calculation based on perturbation theory. Orthogonal atomic orbitals are assumed, but, following Slater, are considered as disposable parameters. Our program is threefold in purpose: (1) to set up a formalism generalizable to "degenerate superexchange" and other indirect magnetic interactions; (2) to include within the analysis the hitherto neglected direct exchange interaction between the excited magnetic cation and the excited anion; (3) to obtain a formalism which permits us to test the sensitivity of results to the choice of perturbing excited states. It is found that inclusion of the direct exchange interaction referred to above does not essentially alter the previously given expressions[1,2] for superexchange coupling. The simple intuitive significance of this result will be discussed. The choice of excited states suitable for the perturbation calculation will also be discussed.

* This work was supported by the Office of Naval Research.
[1] P. W. Anderson, Phys. Rev. **79**, 350 (1950).
[2] J. H. Van Vleck, J. phys. radium **12**, 262 (1951).

D5. Microwave Resonance Relations in Anisotropic Single Crystal Ferrites.* J. O. ARTMAN, *Lincoln Laboratory*.—The ferromagnetic resonance relations in magnetically anisotropic single crystal ferrites have been re-examined. The basic theory has been considered previously by Smit[1] and Zeiger.[2] Generalized nomograms are presented which relate the microwave resonance frequency to the magnetic field, anisotropy parameter K/M, and magnetization M. These curves are derived for both negative and positive anisotropy spherical specimens oriented so that both the static and microwave magnetic fields lie in a (110) crystal plane. Results are given for calculations made on the assumption that the specimen exists as a single magnetic domain. The nature of the gradual alignment of M to the static magnetic field H is discussed in detail. Simplified formulas are given for the "quasi-line up" region in which the angle between M and H becomes small. The occurrence of multiple domain structures below magnetic saturation is also considered. The domains are assumed to be lamellas of two varieties arranged alternately. Resonance relations are derived for both negative and positive anisotropy crystals when H is applied along a [110] direction. These results are compared with recent experiments.

* The research reported in this document was supported jointly by the Army, Navy, and Air Force under contract with Massachusetts Institute of Technology.
[1] J. Smit and H. G. Beljers, Philips Research Repts. **10**, No. 2, 113-130 (April, 1955).
[2] H. J. Zeiger, Lincoln Laboratory (private communication).

D6. A Lagrangian Formulation of the Gyromagnetic Equation of the Magnetization Field. T. L. GILBERT, *Armour Research Foundation of Illinois Institute of Technology*.—The gyromagnetic equation, $d\mathbf{M}/dt = \gamma \mathbf{M} \times \mathfrak{H}$, for the motion of the magnetization field, $\mathbf{M}(\mathbf{r})$, in a ferromagnetic material can be derived from a variational principle, as first shown by Döring.[1] Here $\mathfrak{H}$ is the effective internal field, including the magnetic field and contributions from exchange, anisotropy, and magnetoelastic effects. Using this variational principle, the equations of motion can be recast into a Lagrangian form. This makes possible a consistent derivation of the equations of motion of the magnetization field and other fields to which it may be coupled (e.g., the displacement field of the lattice and the electromagnetic field). It also permits the introduction of viscous damping effects in a consistent manner using the Rayleigh dissipation function. It is shown that viscous damping of the magnetization field leads to an equation of motion which reduces to the Landau-Lifshitz equation only when the damping is small. It is also shown that this Lagrangian formalism permits the introduction of damping due to disaccommodation in a consistent and very general way.

[1] W. Döring, Z. Naturforsch. **3a**, 374 (1948).

D7. Anisotropic Paramagnetic Absorption Spectrum of Manganous Ion in Cubic Zinc Sulfide. LAWRENCE M. MATARRESE, *United States Naval Research Laboratory*, AND CHIHIRO KIKUCHI, *University of Michigan*.—We have investigated the paramagnetic absorption spectrum of manganous ion in a natural crystal of cubic zinc sulfide and have found the anisotropy to be unusually pronounced. The maximum width of a hfs group is 45 gauss with the densities of the components approximately in the ratio 8:5:9:5:8. This pattern of density distribution is to be expected when quartic terms in the crystalline electric field potential predominate. The spectra were obtained at fields in the vicinity of 8500 gauss and at a microwave frequency of approximately 24 000 mc/sec. The angular dependence was investigated by varying the direction of the magnetic field in the (100), (110), and (111) planes of the crystal. Experimental results indicate that the symmetry of the crystalline electric field about the manganous ion is cubic. The cubic anisotropy constant, A, is -1.37, the sign being determined from the dependence of the hfs pattern upon the nuclear magnetic quantum number. The relationships among the anisotropy constant, the hfs coupling constant, and anion coordination will be discussed for several compounds.

D8. The Doublet Structure in Paramagnetic Absorption Spectra of Mn^{++} in Calcite.* CHIHIRO KIKUCHI, *Engineering Research Institute*.—Hurd, Sachs, and Hershberger[1] observed that some of the paramagnetic absorption lines of Mn^{++} in calcite are split into doublets for certain orientations of the magnetic field with respect to the crystal trigonal axis. According to their observations, the doublet separation is maximum near 60° and vanishes at 0° and 90°. The present paper suggests that this doublet splitting is due to the nonequivalent trigonal fields at the two calcium sites occupied by Mn^{++}. The present theory gives (1) $P_4^3(\cos\theta)$ for the angular dependence of the doublet splittings, (2) 23 gauss for the maximum splitting, (3) the ratio 5:4 for the splittings of the strong to weak doublets, and (4) isotropic absorption spectrum when the magnetic field varies in the equatorial plane. These results are in good agreement with experiment. The possible occurrence of the doublet splitting in other crystals will be discussed.

* This investigation was carried out under a contract with the Signal Corps. During the initial phases the author was associated with the Nucleonics Division, Naval Research Laboratory, Washington, D. C.
[1] Hurd, Sachs, and Hershberger, Phys. Rev. **93**, 373 (1954).

D9. Nuclear Magnetic Relaxation Times in Polyethylene.* I. J. LOWE, L. O. BOWEN, AND R. E. NORBERG, *Washington University*.—Direct measurements of T_1 and T_2 for the proton magnetic resonance in polyethylene have been made from observations of Bloch decays and spin echoes produced by microsecond pulses of 30 mc/sec radio-frequency power. Observations were made at temperatures between 240°K and 392°K using the same commercial stock material as Wilson and Pake.[1] The results are in substantial agreement with the relaxation times postulated by Wilson and Pake and show the coexistence of several very distinct T_2's between 260°K and 295°K. The T_2 values measured ranged from 4 microseconds near 240°K to 0.1 second in a molten sample at 392°K. Over much of this temperature range T_1 was measured to be of the order of 0.1 second with T_2 becoming nearly equal to T_1 at 392°K. The short T_2 component visible on the Bloch decays grows progressively weaker as the temperature is raised, becoming nearly undetectable by 340°K. Near 280°K there is a weak "slow-beat" structure on the Bloch decays.

* Supported by the Office of Naval Research and the U. S. Air Force through the O.S.R. of the Air Force Research and Development Command.
[1] C. W. Wilson and G. E. Pake, J. Polymer Sci. **10**, 503 (1953); C. W. Wilson, thesis (unpublished) Washington University, 1952.

FRIDAY MORNING AT 10:00

Oriental 104

(S. K. ALLISON presiding)

General Nuclear Physics

E1. Elastic Scattering of Protons from Na^{23}.* N. P. BAUMANN, F. W. PROSSER, JR., AND R. W. KRONE, *University of Kansas.*—The elastic scattering of protons from Na^{23} at an angle of 155° has been observed in the energy interval 780 kev to 1500 kev. Targets were made by evaporating metallic sodium onto thin organic backings inside the target chamber. A zinc sulfide screen and photomultiplier tube were used for particle detection. For some of the stronger resonances unambiguous spin and parity assignments were made. These resonance assignments are: $E_p=877$ kev, $1+$; $E_p=1022$ kev, $2-$; $E_p=1176$ kev, $1+$; $E_p=1321$ kev, $3+$, and $E_p=1398$ kev, $3+$. Two strong resonances at $E_p=1288$ kev and $E_p=1460$ kev, which decay strongly by ground-state alpha particles, could not be given assignments compatible with those required for the observed angular distribution of the alpha particles. Simultaneously with the elastic scattering, the excitation curve for emission of ground-state alpha particles was obtained, verifying the results of Stelson[1] above 1 Mev. In addition three resonances, which show no evidence of gamma decay, at proton energies of 797 kev, 815 kev, and 922 kev were found which correspond to levels of Mg^{24} obtained by elastic scattering of alpha particles from neon.[2]

* Supported in part by the Office of Naval Research and the National Science Foundation.
[1] P. H. Stelson and W. M. Preston, Phys. Rev. **96**, 974 (1954).
[2] Goldberg, Haeberli, Galonsky, and Douglas, Phys. Rev. **93**, 799 (1954).

E2. Polarization in *P-α* Elastic Scattering.* MARY JEAN SCOTT† AND RALPH E. SEGEL,† *Brookhaven National Laboratory.*—The polarization of protons elastically scattered by alpha particles was observed by measuring the left-right asymmetry obtained by doubly scattering protons in helium. Protons at 3.0 Mev entered a helium filled double scattering chamber through a thin nickel window. Protons whose first scattering was at 90° (c.m.) and second scattering at ±73°, ±100°, and ±125° (c.m.) were detected by 50 μ Kodak NTA emulsions. The polarization was calculated from the ratio of the number of tracks on symmetrically placed plates using the formula: $R=(1+P_1P_2)/(1-P_1P_2)$ where P_1 and P_2 are the polarizations in the first and second scatterings, respectively. The resultant polarizations are compared below to those calculated from the single scattering phase shifts given by Critchfield and Dodder.[1] The two results are seen to be in agreement, with the error in the calculated polarizations being quite large due to the great sensitivity of the polarization to variations in the phase shifts.

R (observed)	P_1P_2 (observed)	P_1P_2 (calculated)
2.19 ± 0.09	0.37 ± 0.05	0.48 ± 0.11
1.94 ± 0.09	0.32 ± 0.05	0.35 ± 0.09
1.57 ± 0.08	0.22 ± 0.05	0.18 ± 0.05

Preliminary data taken at an incident proton energy of 3.5 Mev indicate similar results.

* Work performed under the auspices of the U. S. Atomic Energy Commission.
† On leave from Johns Hopkins University.
[1] C. L. Critchfield and D. C. Dodder, Phys. Rev. **76**, 602 (1949).

E3. *T-T* Elastic Scattering from 1.6 to 2.0 Mev. DALE M. HOLM AND H. V. ARGO, *Los Alamos Scientific Laboratory.*—A magnetically analyzed triton beam from an electrostatic generator has been scattered from tritium in a 14-inch scattering chamber and the differential cross sections measured in 10° steps from 20° to 140° in the c.m. system for incident energies of 1.8 and 2.0 Mev. Two proportional counters with a fixed angular separation of 90° were used in coincidence to detect both the scattered and recoil tritons for the laboratory angular range from 45° to 70°, with an absolute probable error of ±3%. A single counter was used for laboratory angles between 10° and 20°, with resultant probable errors of +5, −15%. Excitation functions in 100 kev steps from 1.6 to 2.0 Mev for c.m. angles of 60° and 90° show no evidence for an excited state in this region. The c.m. angular distributions in barns per steradian are as follows: 1.800 Mev: 20°, 2.90; 30°, 0.60; 40°, 0.1790; 50°, 0.1007; 70°, 0.0891; 80°, 0.0831; 90°, 0.0824. 2.013 Mev: 30°, 0.41; 40°, 0.159; 50°, 0.1103; 70°, 0.0815; 80°, 0.0881; 90°, 0.0795.

E4. Elastic Scattering of 40-Mev Alpha Particles from Light Nuclei.* G. IGO, H. E. WEGNER, AND R. M. EISBERG,* *Brookhaven National Laboratory.*—Thin foils of light and intermediate weight elements have been bombarded with alpha particles of energy 41±0.3 Mev. The angular distributions of elastically scattered alpha particles have been measured. In qualitative distinction to the differential cross section for elastic scattering of alpha particles from heavy elements, the lightest elements investigated show strong maxima and minima. The ratio, $(d\sigma/d\Omega)_{obs}/(d\sigma/d\Omega)_{Coul}$, oscillates about a value approximately equal to one. The quantity, $(d\sigma/d\Omega)_{Coul}$, is the cross section in the field of a point charge. In Cu and Al, the maxima occur at approximately ten degree intervals from 20° to 100°, the angular region investigated. The data for Cu and Al fit the diffraction formula: $kR\Delta(\sin\theta/2)=\pi/2$, where $R=1.3A^{\frac{1}{3}}+1.5$. In the intermediate weight elements such as Mo, the maxima and minima in $(d\sigma/d\Omega)_{obs}/(d\sigma/d\Omega)_{Coul}$ are less prominent and are superimposed on an exponentially decreasing function. The exponential decrease in Mo is comparable to the decrease[1] observed in elastic scattering from the heavier element, Ta, which shows no maxima or minima at this energy. A comparison will be made between these data and data taken at other energies.

* Work performed under the auspices of the U. S. Atomic Energy Commission.
† Now at the University of Minnesota.
[1] Wegner, Eisberg, and Igo, Phys. Rev. **99**, 825 (1955).

E5. Absolute Cross Sections for the Coulomb Scattering of 1.00-, 1.75-, and 2.50-Mev Electrons.* V. SPIEGEL, JR.,† B. WALDMAN, AND W. C. MILLER, *University of Notre Dame.*—Electrons from our electrostatic generator were scattered from thin foils of aluminum, nickel, silver, and gold. The scattered electrons were analyzed by means of a 90° magnetic spectrometer using a scintillation detector. The cross sections were measured at 30°, 60°, and 90° with an estimated error of ±2% and at 120° and 150° with an estimated error of ±5%. A comparison of these results with the Mott theory as evaluated by Curr shows deviations of 5% to 10%, the experimental results being low. Corrections for nuclear size and screening and the radiative correction of Schwinger seem to be needed to remove this discrepancy.

* Assisted by the joint program of the Office of Naval Research and the U. S. Atomic Energy Commission.
† Now at the National Bureau of Standards.

E6. Plural Scattering of Fast Electrons.* B. WALDMAN, V. SPIEGEL, JR.,† AND W. C. MILLER, *University of Notre Dame.*—We have evaluated the effect of plural scattering in

our experiments on the Coulomb scattering of electrons. Electrons of energy 1.00, 1.75, and 2.50 Mev were scattered by aluminum, nickel, silver, and gold foils. The foils were in the transmission position for scattering angles of 30°, 60°, and 90°, and in reflection position for angles of 90°, 120°, and 150°. Data were taken as a function of foil thickness in the range 0.3 to 3 mg/cm². As expected the effect of plural scattering increased with decreasing electron energy and increasing atomic number.

* Assisted by the joint program of the Office of Naval Research and the U. S. Atomic Energy Commission.
† Now at the National Bureau of Standards.

E7. Nuclear Gamma-Ray Scattering Techniques.* G. E. Pugh, R. Gomez, D. H. Frisch, and G. S. Janes, *M. I. T.*—We have made further studies of an energy sensitive γ-ray detection system previously reported for use with scattered gamma rays in the 50 to 150 Mev range.[1] The system consists of a conventional gamma-ray telescope for identification, followed by a large liquid scintillation counter to measure the energy lost by an electron pair made in the lead converter by the gamma ray. A new telescope and large counter have been subjected to a more careful electron calibration using several converter thicknesses and many electron energies. This gives the telescope efficiency, somewhat lower at low energies than was previously assumed, as well as the pulse height response in the large counter. This data, together with the experimental pair cross sections, allows us to predict the response to an arbitrary gamma-ray spectrum. Assuming a bremsstrahlung distribution of gamma rays, the calculated response was in good agreement with the observed response when the counter was placed in the direct beam of the M. I. T. synchrotron. Difficulties of the order of 15% have arisen in our absolute normalization and are not yet understood.

* This work was supported in part by the joint program of the Office of Naval Research and the U. S. Atomic Energy Commission.
[1] Pugh, Frisch, and Gomez, Rev. Sci. Instr. **25**, 1124 (1954).

E8. Gamma-Ray Scattering by Complex Nuclei.* R. Gomez, G. E. Pugh, D. H. Frisch, and G. S. Janes, *M. I. T.*—Data is now available at 45° from several elements. In the pulse height region corresponding to 80-Mev gamma rays and above, the counting rate is a factor of two to three below that expected from a Thompson-type cross section. The cross section itself could dip to a considerably lower minimum and not be observed because of the width of the counter response. The low energy cross section at 45° is obscured by large numbers of low-energy gamma rays for which the counting rate is linear in target thickness. These produce a counting rate whose magnitude and dependence on angle, energy, and peak machine energy is consistent with a rough estimate of internal bremsstrahlung from pair creation. No theoretical calculation is available for comparison. The data at 90° and 135° also indicate some excess in scattering at low energy which may be attributed to the giant resonance.[1] After form factor correction, the high-energy data are almost consistent with Thompson, but there appears to be an excess of about 20 to 30% at 135° relative to 90°. Our knowledge of the radius and our absolute normalization may not be good enough to say which is out of line. It is probable that a systematic error in our previous data may have caused us to over-estimate the excess at 135°.[2]

* This work was supported in part by the joint program of the Office of Naval Research and the U. S. Atomic Energy Commission.
[1] E. Hayward, Proc. Photonuclear Conf., Case Institute of Technology, May 23, 1955, p. 23.
[2] Pugh, Frisch, and Gomez, Phys. Rev. **95**, 590 (1954).

E9. Gamma-Ray Scattering by Hydrogen.* G. S. Janes, R. Gomez, G. E. Pugh, and D. H. Frisch, *M. I. T.*—Using a liquid hydrogen target which will be described, we have observed scattered gamma rays at 50°, 90°, and 135°. The high counting rates observed by Oxley and Telegdi[1] at forward angles do not extend into our high energy channels at 50°. It is probable that they observed low-energy gamma rays of an origin similar to those described in the preceding abstract. At 90° and 135°, our low-energy data (50 to 90 Mev) is in agreement with Oxley and Telegdi, and with any reasonable theory. Our data above 90 Mev, at both 90° and 135°, suggests a somewhat lower cross section, but is not conclusive because of low counting rates.

* This work was supported in part by the joint program of the Office of Naval Research and the U. S. Atomic Energy Commission.
[1] C. L. Oxley and V. L. Telegdi, Bull. Am. Phys. Soc. **30**, No. 5, 16 (1955).

E10. Preliminary Mass Doublet Measurements with the Minnesota 16-Inch Mass Spectrometer.* T. T. Scolman, K. S. Quisenberry, and A. O. Nier, *University of Minnesota.* —The 16-inch double-focusing mass spectrometer previously described[1,2] has been modified to employ the peak matching method.[3] This method utilizes an oscilloscope presentation which facilitates focusing the spectrometer since the mass peaks are instantaneously displayed. The frequency employed is approximately 30 cps which removes the necessity of obtaining long term stability of the electric and magnetic fields. This results in a considerable simplification in the electronic circuits. Resolving powers of 30 000 to 60 000 are usually employed although values as high as 100 000 have been obtained. A series of doublets have been measured to check the consistency of the spectrometer. These doublets and their tentative values are: $CH_4-O=36.3931\pm9$; $C_2H_4-CO=36.3926\pm8$; $C_3H_8-CO_2=72.7871\pm16$; $NH_2-O=23.8164\pm5$; $NH_3-OH=23.8159\pm6$; $CH_2-N=12.5730\pm8$; $CH_3-NH=12.5845\pm13$; $CH_4-NH_2=12.5800\pm5$; $C_2H_4-N_2=25.1585\pm6$; $N_2-CO=11.2356\pm6$. From these data, in addition to the measurement of the same doublet at various masses, two mass triplet cycles can be constructed and checked for closure.

* Supported by a grant from the National Science Foundation.
[1] Collins, Scolman, and Nier, Phys. Rev. **95**, 615 (1954).
[2] Quisenberry, Scolman, and Collins, Phys. Rev. **96**, 823 (1954).
[3] Clayton F. Giese and T. L. Collins, Phys. Rev. **96**, 823 (1954).

E11. The Atomic Masses of H^1, D^2, C^{13}, and S^{33}.* K. S Quisenberry, T. T. Scolman, and A. O. Nier, *University of Minnesota.*—The Minnesota 16-inch double-focusing mass spectrometer has been used to determine the atomic masses of H^1, D^2, C^{13}, and S^{33} relative to O^{16} by the doublet method. A series of mass doublets sufficient to give the mass of C^{13} by four different cycles has been measured. The doublets used and their tentative values are: $H_2-D=1.5498\pm1$; $CH_4-O=36.3931\pm5$; $D_2O-\frac{1}{2}A^{40}=41.9390\pm13$; $C_3H_4-A^{40}=68.9344\pm13$; $C_3-A^{36}=32.4729\pm20$; $H_2O-\frac{1}{2}A^{36}=26.7937\pm6$; $C_4-SO=33.0269\pm13$; $\frac{1}{2}C_4H_8O-H_2S=25.4016\pm12$; $O_2-S=17.7599\pm9$. An average of the four cycles gives the following tentative mass values: $H^1=1.0081439\pm5$; $D^2=2.0147380\pm10$; $C^{13}=12.0038174\pm18$; $S^{33}=31.9822401\pm9$. Comparison between these values and those obtained from nuclear reaction studies will be presented with particular attention given to C^{13}.

* Supported by a grant from the National Science Foundation.

E12. Nuclear Spin and Magnetic Moment of 50-Day In^{114m}. L. S. Goodman and S. Wexler, *Argonne National Laboratory.* —The nuclear spin, magnetic moment, and the sign of the magnetic moment of 50-day In^{114m} have been determined by the atomic beam magnetic resonance method.[1,2] The values found are $I=5\hbar$ and $\mu=+4.7$ n. m. Multiple quantum transitions[3] were observed in resonances of the inactive In^{115} used for the calibration of the magnetic fields. Some properties of these transitions and the limitation in accuracy of the determination of the nuclear magnetic moment of In^{114m} introduced by their presence will be discussed.

* Work done under the auspices of the U. S. Atomic Energy Commission.
[1] J. R. Zacharias, Phys. Rev. **61**, 270 (1942).
[2] L. Goodman and S. Wexler, Phys. Rev. **99**, 192 (1955).
[3] P. Kusch, Phys. Rev. **93**, 1022 (1954).

FRIDAY AFTERNOON AT 2:15

Oriental 104

(W. H. ZINN presiding)

Apparatus and Techniques, II

Contributed Papers

G1. Monte Carlo Calculation* on Čerenkov Counters. TAKETORA YAMAGATA AND MEGUMU YOSHIMINE, *University of Illinois.*—In connection with recent developments of Čerenkov counters,[1] it was felt that they might be very suitable to measure with a fair accuracy the energy of high-energy photons and electrons. Computation on the response of such counters was performed with an electronic digital computor. Lead glass (n1.6, density 4) and $ZnBr_2$ water solution (n1.5, density 2.5) were chosen as media. A sequence of "random number," generated by the computor, determined the fate of an incident particle. All electrons and photons, produced in the medium by pairs, Compton effect and bremsstrahlung, were pursued until either they vanished, stopped or escaped. Čerenkov pulse heights were measured in units of visible quanta, and their distribution was presented for several energies (50 Mev to 1 Bev) and several counter thicknesses (2 to 40 radiation lengths). Measuring the incident energy in critical energy units and the thickness in radiation lengths, the results may be extended to other media. They may be useful to other problems like the response of scintillation counters and the efficiency of converters.

* R. R. Wilson, Phys. Rev. **86**, 261 (1952).
[1] M. H. L. Jester, UCRL 2990 (1955).

G2. Čerenkov Counter as High-Energy Photons Spectrometer. I. FILOSOFO, *University of Illinois.*—In the preparation of the equipment needed for an experiment on Compton scattering by protons at 200–300 Mev now in progress at Illinois, a large Čerenkov counter was designed and built as a detector of high-energy photons. The radiator was made of lead glass and designed following the evaluations made by Yamagata.[1] To detect the light emitted by the showers, two different kinds of phototubes were studied and compared. The counter was first tested by studying its response to cosmic rays. The pulses were recorded by a triggered oscilloscope. The counter was then tested and calibrated by using a fast electrons beam. This was obtained by deflecting through a focusing magnet the electrons emitted by a target exposed to 300-Mev rays. The distributions in the amplitude of the pulses obtained with cosmic rays and with electrons of different energies will be presented and compared with Yamagata's evaluations.

[1] See previous abstract.

G3. Microtron Injector for Electron Synchrotrons. H. F. KAISER, *Naval Research Laboratory.*—Use of the microtron as an electron injection device has been proposed by the author.[1,2] A design is described intended for a strong-focusing electron synchrotron with straight sections and which will have the specifications: (a) electron injection energies to 5 Mev, (b) on-orbit injection, and (c) no obstruction to the circulating beam. Since this injection system is more compact and less costly than available 2–5 Mev electron sources, its use is now contemplated in two instances known. The maximum possible yield which may be expected is estimated and a field cycle suitable for this method of injection is described. Large aperture at the input is achieved by a pole design which allows a wide separation of the final microtron orbit from the inner ones, with a weak magnetic field at the input. Magnetic deviation of the circulating beam is compensated in auxiliary correction fields. Preliminary experiments with available microtrons are described.

[1] H. F. Kaiser, Phys. Rev. **95**, 667(A) (1954).
[2] Kaiser, Mayes, and Willis, Phys. Rev. **98**, 1538(A) (1955).

G4. Small Model FFAG Betatron. I. General Description.* K. M. TERWILLIGER AND L. W. JONES, *University of Michigan,* F. T. COLE, *University of Iowa,* D. W. KERST, *University of Illinois,* AND R. O. HAXBY, *Purdue University and Midwestern Universities Research Association.*—The principles of FFAG accelerators[1] are being studied with a small betatron designed to accelerate electrons from 25 kev to 400 kev. The model is of the alternate field type, employing eight sectors. Each sector consists of two dc magnets producing fields equal in magnitude and opposite in direction, with the magnet giving positive curvature over twice as long as the one giving negative curvature. The radial dependence of the magnetic field is given by $H = H_0(R/R_0)^k$, where k has a constant value, 3.36, throughout the machine. In order to make equilibrium orbits of different energies geometrically similar, all pertinent magnet dimensions such as vertical aperture are scaled to be proportional to the machine radius. The proper increase in field with radius is then achieved by distributed pole face windings. The field is 40 gauss at the injection radius of 34 cm and increases to 134 gauss at the maximum radius of 49 cm, while the vertical magnet aperture increases from 4 to 6 cm over the same range. The alternating gradient focusing is designed to give 2.80 radial and 1.81 vertical betatron oscillations per revolution. A sinusoidally excited betatron core links the machine to produce a peak acceleration of 40 volts per turn.

* Supported by the National Science Foundation.
[1] K. R. Symon, Phys. Rev. **98**, 1152(A) (1955).

G5. Small Model FFAG Betatron. II. Design Calculations.* F. T. COLE, *University of Iowa,* AND D. W. KERST, *University of Illinois and Midwestern Universities Research Association.*—Analysis of orbits in the FFAG ring magnet described in the preceding abstract is complicated by the large fraction of circumference which is fringing field and by the dependence on "edge" focusing for vertical stability. We have developed approximate methods for finding the variation of field along the orbit and for discussing equilibrium orbits and small oscillations about these orbits in this field. Because orbits of different energies differ only by a scaling factor, we can write the guide field as $H(x,s) = H_0(x)F(s)$, where s is the arc length along the equilibrium orbit and x is the displacement perpendicular to that orbit. Then the orbit equations depend only on $F(s)$. We find an $F(s)$ by combining conformal mapping solutions of simpler problems. The equilibrium orbit is found by fitting together numerically orbits in different parts of the fringing field to form a closed orbit. The differential equations of oscillations about the closed orbit contain terms arising from the usual gradient focusing and terms arising from different path lengths in the field of particles of different amplitudes (edge focusing). We have solved these equations numerically and will discuss the physical interpretation of the results and final choice of magnet geometry.

* Supported by the National Science Foundation.

G6. Small Model FFAG Betatron. III. Preliminary Experimental Results.* L. W. JONES AND K. M. TERWILLIGER, *University of Michigan and Midwestern Universities Research Association.*—The wavelengths of the radial and vertical betatron oscillations in the FFAG model have been measured. The method used is to observe the position of two rays from a point electron source at similar points in successive sectors. Since an electron oscillation at similar points in successive sectors lies on a sine curve independent of its position elsewhere (by Floquet's theorem), a measurement of the spacing of two rays at similar points readily determines the wavelength The source, an injector with a pinhole, is placed at the center of a radial focusing magnet. A screen with two pinholes for each oscillation mode is put at the center of the next radial focusing magnet, defining the electron beams which are then observed on a fluorescent screen at the same point in the following sector. The measured wavelengths agree well with the calculated values. The betatron wavelengths can be tuned in this model by varying the relative strength of the positive and negative fields and by changing the field index, k. The tuning range is adequate to cross integral and half-integral resonances radially and vertically. The current status of the electron acceleration program will be discussed.

* Supported by the National Science Foundation.

G7. General Theory of Orbits in FFAG Accelerators. KEITH R. SYMON, *University of Wisconsin and Midwestern Universities Research Association.**—The magnetic field, and the character of betatron oscillations in a fixed field alternating gradient accelerator are determined if the equilibrium orbits are specified as a function of particle momentum. A suitable system of parameters for specifying a set of equilibrium orbits in a plane are introduced, and the equations for linear betatron oscillations about these orbits are derived. Two kinds of alternating gradient focusing terms appear, which may be referred to as "edge-type" and "gradient-type" focusing. Approximate formulas for betatron oscillation frequencies are derived relating them to momentum content, magnetic field flutter, and other machine parameters. The character of these relationships depends on whether the focusing is predominantly gradient-type or edge-type. An approximate treatment of nonlinear betatron oscillations can be given for machines whose equilibrium orbits are nearly circles.

* Supported by the National Science Foundation.

G8. FFAG Electron Cyclotron.* TIHIRO OHKAWA, *University of Illinois*† (introduced by D. W. Kerst).—New types of FFAG[1] accelerators having the same orbit length for all momenta are proposed. In these types electrons, injected with an energy of a few Mev, are accelerated by a fixed frequency electric field until the radiation loss becomes serious, probably at a few Bev. The necessary cavity voltage is, for example, 200 Kev with 3 Mev injection energy. Two types of guiding fields, similar to Mark I (alternate field type) and Mark V (spirally ridged type) are used. In both, the magnetic field increases exponentially in the vertical direction so that as the particle energy increases, its orbit rises vertically. The field also depends on the radius and the azimuthal angle in such a way that the focusing properties are very similar, respectively, to Mark I and to Mark V. Other types of FFAG having the orbit surface not on a median plane are also proposed.

* Reported by the present author at the meeting of the Physical Society of Japan in June, 1955.
† On leave from the University of Tokyo.
[1] Reported by the present author at the meeting of the Physical Society of Japan in October, 1953; K. R. Symon Phys. Rev. **98**, 1152(A) (1955).

Invited Papers

G9. Billion-Volt Injection into High-Energy Accelerators. L. C. TENG, *Argonne National Laboratory.* (30 min.)

G10. Cloud-Chamber Ionization Measurements and Applications. E. W. FRIESEN, *University of Indiana.* (30 min.)

FRIDAY AFTERNOON AT 2:15

Mandel Hall

(E. P. WIGNER presiding)

Invited Papers Derived from the Cosmic-Ray Congress at Guanajuato, Mexico

H1. The Primary Radiation and the Origin of Its Changes with Time. J. A. SIMPSON, *University Chicago.* (45 min.)

H2. Astrophysical Questions and the Galactic Origin of the Cosmic Rays. S. CHANDRASEKHAR, *University of Chicago.* (45 min.)

Contributed Paper

H3. Time Variation of Primary Heavy Nuclei Flux in the Cosmic Radiation.† M. KOSHIBA AND MARCEL SCHEIN, *University of Chicago.*—In view of the apparently conflicting experimental results on the subject thus far reported,[1] it is worthwhile to give the following new results. The sea-level data suggest a rather small variation, if any, of the high-energy heavy primaries.[2] However, we should note here that sea-level phenomena are appreciably affected by higher energy primaries only and that the lower energy region is where we might expect a sizeable time variation. As a consequence, the experiment should be carried out at higher geomagnetic latitudes and at the maximum possible altitude. This experi-

ment was performed at 58°N in a balloon which floated for 13 hours at an elevation of 100 000 feet. The technique of determining the time of arrival of the heavy nuclei was the same as that used by the Chicago group previously. The data thus far accumulated seem to show a similar time variation as that observed by V. H. Yngve.[3] Since the analysis is in full progress at the present time, more complete data will be presented with improved statistics.

† Supported in part by a joint program of the Office of Naval Research and the U. S. Atomic Energy Commission.
[1] T. H. Stix, Phys. Rev. **95**, 783 (1954).
[2] Lal, Peters, and Kaplon, Phys. Rev. **86**, 569 (1952).
[3] V. H. Yngve, Phys. Rev. **92**, 428 (1953).

Post-Deadline Papers, If Any

FRIDAY AFTERNOON AT 2:15

Eckhart 133

(G. BERNARDINI presiding)

Neutron Scattering and Absorption; Photoneutron Reactions

I1. Inelastic and Elastic Scattering of 1.7-Mev Neutrons.* S. D. BLOOM, G. N. GLASOE, C. O. MUEHLHAUSE, AND H. E. WEGNER, *Brookhaven National Laboratory.*—Neutrons of 1.67 Mev produced by proton bombardment of a $T-Zr$ target were scattered from various materials and the angular distriburions for both elastic and inelastic events were measured. Protons of 2.45 Mev were produced by the 18-in. BNL cyclotron in 2.5 mμsec bursts at 54 mμsec intervals. A focussed target current of 55 μamp was used for this work. The neutrons were detected with a plastic phosphor imbedded in a large LiF-Pb-CH_2 collimator. Neutron energy discrimination was achieved by the time-of-flight instrumentation described previously.[1] The ratio $R(\theta)=(d\sigma_s/d\Omega)/(d\sigma_i/d\Omega)$ was measured as a function of scattering angle for iron and is found to be strongly peaked in the forward and backward directions. For example, $R(45°, 90°, 135°)=(5.8, 2.6, 4.6)$. Preliminary data for other materials will be presented along with typical time-of-flight curves demonstrating the separation of the various neutron components.

* Work performed under the auspices of the U. S. Atomic Energy Commission.
[1] Bloom, Muehlhause, and Wegner, Phys. Rev. **99**, 654 (1955).

I2. Slow Neutron Resonance Scattering of U^{238}.* H. L. FOOTE, JR., *Brookhaven National Laboratory.*—The scattering cross section of U^{238} as a function of energy has been observed over the range 0.27 to 2 ev. A "thick-thin" target geometry[1] and a crystal spectrometer were used to make the measurements. The results obtained will be presented and discussed.

* Research performed under the auspices of the U. S. Atomic Energy Commission.
[1] H. L. Foote, Jr., and J. Moore Phys. Rev. **98**, 1161(A) (1955).

I3. Neutron Transmission Measurements on Br and Se. J. M. LEBLANC, L. M. BOLLINGER, AND R. E. COTÉ,* *Argonne National Laboratory.*—The neutron resonance structure of Br and Se have been studied with the Argonne fast chopper. The resolution used was about 0.08 μsec/m. A new Argonne chopper was also used for part of the measurements. Isotopic identification was made for some of the stronger resonances. The normal Br samples were in the form of liquid Br or liquid Br dissolved in CS_2. Neutron resonances with energies of 35.6, 54.2, 102, 134, 190, 205, 240, 295, and 317 ev were resolved in normal Br. The resonances which were identified as due to Br^{79} have energies of 35.6, 54.2, 190, 240, and 317. Those resonances assigned to Br^{81} have energies of 102 and 134. Transmission dips with energies of 553, 669, and 1540 ev were found to be characteristic of Br^{81} but because of the high level density in Br individual resonances were probably not completely resolved at energies greater than about 350 ev. The neutron transmissions of normal Se metal and enriched Se^{77} Se^{78}, and Se^{80} were measured in the energy interval up to about 10 kev. The resonances whose isotopic assignments have been made are 211 ev (77), 660 ev (77), 960 ev (77), 1830 ev (80), 4100 ev (80), and 5350 ev (80). The parameters for several resonances in Br and Se will be given.

* Work done under the auspices of the U. S. Atomic Energy Commission.

I4. The Absorption Cross Section of Gold for Slow Neutrons Measured on a Single Crystal Spectrometer.* F. T. GOULD, T. I. TAYLOR, AND W. W. HAVENS, JR., *Columbia University and Brookhaven National Laboratory.*—Columbia University's single crystal spectrometer, at the Brookhaven National Laboratory, has been adapted to work in the 4 to 8.75 A region. A mica crystal is used as monochromator and combinations of Be, BeO, and Bi are used as filtering materials. The gold cross section has been measured in the region 4.9 to 8.75 A and is in excellent agreement with results obtained by other methods.[1] A least squares fit of forty-six points to a straight line gives a slope of 54.40 b/A±0.05. The wavelength calibration based on the graphite, bismuth, beryllium, and beryllium oxide breaks is known to 0.2%. Within this accuracy, the gold cross section follows a 1/v law in the measured wavelength interval. To obtain the thermal absorption cross section, we can make an accurate correction (1.2%) for the departure from 1/v at $E=0.025$ ev, since 95% of the thermal cross section comes from the 4.9 ev level.[2] The 2200 m/sec absorption cross section is then $\sigma_{abs}=99.0\pm2.0$ barns.

* Research performed under contract with the U. S. Atomic Energy Commission.
[1] Carter, Palevsky, Myers, and Hughes, Phys. Rev. **92**, 716 (1953).
[2] Wood, Landon, and Sailor, Phys. Rev. **98**, 639 (1955).

I5. Neutron Total Cross Section of $_{92}U^{235}$ in the ev Region.* V. E. PILCHER, J. A. HARVEY, AND K. K. SETH,† *Brookhaven National Laboratory.*—The neutron total cross section of $_{92}U^{235}$ has been studied in the energy range 2 ev to 40 ev, using the Brookhaven fast chopper. The resonances in this isotope are rather small and extremely closely spaced. The average level spacing of 1.3 ev/spin state is the smallest yet reported in any isotope. This spacing is based on the number of levels up to 20 ev, since above this energy it is not always possible to separate individual resonances with the present resolution. The Breit-Wigner parameters were computed for all of the observed resonances, making use of the area method of analysis. In cases where it was not possible to obtain Γ from thick and thin sample measurements, the quantity $g\Gamma_n$ was computed from the thin sample data, making use of an average Γ of 0.1 ev. The ratio $\overline{\Gamma}_n^0/D$ is $(0.9\pm0.2)\times10^{-4}$. This is somewhat larger

than is predicted by the cloudy crystal-ball theory. The size distribution of the reduced neutron width has been determined and compared with present theories. By combining the fission data with the total cross-section data it was possible to obtain values of Γ_γ for several of the low-energy resonances. The average value for Γ_γ was found to be 30 ± 6 mv. Making use of this value of Γ_γ the quantity Γ_f was calculated for those resonances in which Γ was known.

* Work carried out under contract with U. S. Atomic Energy Commission.
† Summer student from the University of Pittsburgh Radiation Laboratory.

I6. Neutron Resonances in U^{233} and U^{235}.* V. L. SAILOR, *Brookhaven National Laboratory.*—The total cross sections of U^{233} and U^{235} have been measured with a high resolution crystal spectrometer over the range of energies from 0.1 to >10 ev. The highly complicated resonance structure has been analyzed and Breit-Wigner parameters for each resonance will be presented. Evidence has been found for interference between resonances in the fission component of the cross section. This and other special features of these cross sections will be discussed.

* Research supported by U. S. Atomic Energy Commission.

I7. Neutron Resonance Parameters and Total Cross Sections in U^{235}.* O. D. SIMPSON, R. G. FLUHARTY, F. B. SIMPSON, AND R. M. BRUGGER, *Phillips Petroleum Company.*—Total cross sections of U^{235} have been measured from 10 ev to 10 kev with a resolution of 0.05 to 0.07 μsec/meter using the Materials Testing Reactor (MTR) Fast Chopper, and resonances have been studied below 60 ev. Breit-Wigner (BW) parameters for more than 50 resonances have been obtained from transmission data. New resonances have been found at 28.8 ev, 29.4 ev, and 30.0 ev. The 25.7-ev and 35.3-ev resonances, reported by Brookhaven National Laboratories (BNL), have each been split into two components: (25.7, 26.1) and (35.0, 35.7), respectively. Other resonances reported by BNL show strong indications of being split: 13.3 ev (13.0, 13.3), 14.1 ev (13.9, 14.1), 14.6 ev (14.5, 14.7), and 15.4 ev (15.3, 15.5). Some of the resonances above 35.7 ev for which $\sigma_0\Gamma$ values will be reported are: 38.8, 40.1, 42.6, 44.2, 45.4, 47.7, 49.2, 52.3, 56.1, 57.3, 59.2, and 61.4 ev. Values of $\sigma_0\Gamma^2$ have been determined where "thick-thin" sample data were obtained. Although it is likely that many levels above 12 ev have not been resolved, BW area analyses have been made. Parameter values for some of these resonances cannot be given great weight, and higher resolution will be required at these energies before good answers can be obtained for this important reactor fuel (the level spacing is one of the smallest so far observed).

* Work performed under the auspices of the U. S. Atomic Energy Commission.

I8. Measurement of $\bar{\Gamma}_n^0/D$ Ratio by Average Cross Sections.* D. J. HUGHES AND V. E. PILCHER, *Brookhaven National Laboratory.*—The ratio of the average neutron width of slow neutron resonances to the level spacing, or "strength function," is a quantity of importance to current nuclear models. This ratio can be obtained[1] from the widths and spacings measured for individual levels but the accuracy is limited by the small number of levels that can be analyzed. However, if the average total cross section in the region 1 to 5 kev is measured with a sample so thin that no self-absorption is present, the result, after subtraction of potential scattering, gives $\bar{\Gamma}_n^0/D$ directly (in fact, at 1 kev is simply 12.9×10^4 $\bar{\Gamma}_n^0/D$ barns). This method has been tested, using the Brookhaven fast chopper, for Ag, Th, U, and Ta. The potential scattering contribution to the cross section has been eliminated by measurement of transmission for a series of sample thicknesses. The results obtained, in units of 10^{-4} are Th, 0.9 ± 0.2; U, 1.1 ± 0.2; Ag, 0.30 ± 0.06, Ta, 1.9 ± 0.2. These $\bar{\Gamma}_n^0/D$ ratios are in good agreement with the results obtained[1] from individual resonances and are of higher accuracy.

* Work carried out under contract with U. S. Atomic Energy Commission.
[1] Harvey, Hughes, Carter, and Pilcher, Phys. Rev. **99**, 10 (1955).

I9. Photoneutron Angular Distribution from Carbon. B. P. FABRICAND, B. ALLISON, AND J. HALPERN, *University of Pennsylvania.*—Previous measurements[1] of the photoproton angular distribution arising from the giant dipole resonance in the reaction $C^{13}(\gamma,p)B^{11}$ have yielded a distribution of the form $2+3\sin^2\theta$. This has been interpreted[2] as evidence for an independent particle description of the giant resonance and for the *LS* coupling scheme. In the hope of studying the process of the direct emission of photoneutrons, we have measured the angular distribution of neutrons from the giant dipole resonance in the reaction $C^{12}(\gamma,n)C^{11}$ using a zinc sulfide-paraffin-plastic scintillator as the neutron detector. In contrast to the results for photoprotons from carbon, the photoneutrons show a dip at 90° and a distribution that can be fitted by an expression of the form $a+b\cos^2\theta$. The results will be analyzed from the standpoint of distributions expected from the possible channel spins involved.

[1] Halpern, Mann, and Rothman, Phys. Rev. **87**, 164 (1952).
[2] Mann, Stephens, and Wilkinson, Phys. Rev. **97**, 1184 (1955).

I10. The Photoneutron Effect in Zr^{90} Very Near Threshold.* JOHN D. FOX AND PETER AXEL, *University of Illinois.*—The reactions $Zr^{90}(\gamma,n)Zr^{89}$ and $Zr^{90}(\gamma,n)Zr^{89m}$ have been studied in detail near threshold. The threshold for the production of Zr^{89m} is 12.37 ± 0.09 Mev. The shapes of the activation functions are interpreted by using the neutron transmissions derived from the strong absorption model, the gamma ray and reduced neutron widths as measured by neutron scattering methods.[1] and by assuming that the compound nucleus is formed in the reactions. Analysis of the data leads to an estimate of the amount of each type of process by which the incident photon is absorbed $-E2$, $E1$, or $M1$. If there is no $M1$ absorption, 60% of the absorption is of the $E1$ type; if $M1$ and $E2$ absorption occur equally, only about 10% of the absorption is $E1$. The familiar shape of photoneutron activation functions: $Y(E_\theta)\propto(E_\theta-E_{th})^2$ can be explained by assuming that large amounts of $E2$ or $M1$ absorption take place in the threshold region and that $E1$ absorption is much less important.

* Supported in part by the joint program of the Office of Naval Research and the U. S. Atomic Energy Commission.
[1] Harvey, Hughes, Carter, and Pilcher, Phys. Rev. **99**, 10 (1955).

I11. Mg(γ,n) Cross Section. PAUL F. YERGIN AND BURTON P. FABRICAND, *University of Pennsylvania.*—The published data[1,2] for natural Mg and for Mg^{25} disagree somewhat in the energy region below 11 Mev where only $Mg^{25}(\gamma,n)$ can contribute to the neutrons detected. Above the $Mg^{24}(\gamma,n)$ threshold at 11.1 Mev, however, a more serious disagreement occurs. If the measured Mg^{25} yield is subtracted from the published natural Mg yield, the resulting "$Mg^{24}(\gamma,n)$" cross section from its threshold to the $Mg^{24}(\gamma,n)$ threshold at 16.6 Mev, is extremely different from that of Mg^{25} in the same region. We have investigated this by remeasuring the natural $Mg(\gamma,n)$ cross section, using a sample of MgO. Our yields disagree with the published values in the region in question. If the Mg^{24} yield is subtracted from our measured natural Mg yield, the resulting "$Mg^{25}(\gamma,n)$" yield resembles very closely that of Mg^{25} in the same region. Spectroscopic analysis of our sample showed no significant impurities.

[1] Katz, Haslam, Goldenberg, and Taylor, Can. J. Phys. **32**, 580 (1954).
[2] R. Nathans and P. F. Yergin, Phys. Rev. **98**, 1296 (1955).

FRIDAY AFTERNOON AT 2:15

Cobb 110

(E. FEENBERG presiding)

Theoretical Physics, II

K1. A Torus Model of the Elementary Particles in which Stability May Be Achieved by Gravitational Forces Resulting from the Concentrated Electromagnetic Field.* WINSTON H. BOSTICK,† *University of California, Livermore.*—For a simple torus model of an elementary "particle" the total rest energy m_0c^2 can conceivably be equated to the sum of the electromagnetic-field energy $E_f(=e^2(\ln R/r_0)/\pi R)$ and the gravitational energy $E_g(=-Ge^4(\ln R/r_0)^2/\pi^2c^4R^2)$, where R and r_0 are the major and minor radii of the torus, and G is the gravitational constant. Entities where $|E_g|\ll|E_f|$ may be expected to be unstable. It is suggested that these entities be identified with the mesons; e.g., $\ln R/r_0\cong 180$ for the π^- meson. Entities where $|E_f|=|E_g|$, i.e., $m_0c^2=0$, may possibly correspond to photons and neutrinos. Entities where $|E_g|\cong|E_f|$ represent the possible condition of highly dynamic stability and may conceivably correspond to the electron and the proton ($\ln R/r_0\cong 5\times 10^{20}$). A truly "bound state" corresponds to $|E_g|>|E_f|$, or a negative value of m_0c^2, the interpretation of which presents difficulties. The correspondence of this model to the quantum mechanical wave function and a suggested role of the model in nuclear structure will be briefly discussed.

* Work done under the auspices of the U. S. Atomic Energy Commission.
† On leave of absence from Tufts College, Medford, Massachusetts.

K2. Bending of Light and Falling Rotators.* F. J. BELINFANTE, *Purdue University.*—Consider a linear theory of gravitation[1] yielding a bending fGM/c^2R of light passing sun mass M (with $f=4$ for Einstein). A particle traveling in the earth's field $\mathbf{g}$ then experiences an acceleration $\mathbf{a}_0=\mathbf{g}[1+(f/2-1)v^2/c^2]-f\mathbf{v}(\mathbf{v}\cdot\mathbf{g})/c^2$. Due to the v^3/c^3 terms, why do not heavy elements (with fast nucleon motion inside nucleus) fall faster than hydrogen? The acceleration of a charge in the gravitational field is $\mathbf{a}=\mathbf{a}_0+(1-v^2/c^2)^{\frac{1}{2}}(e/m_0)\{(\mathbf{E}+\mathbf{v}\times\mathbf{B}/c)[1+h(1-f-fv^2/2c^2(1-v^2/c^2))]-\mathbf{v}(\mathbf{v}\cdot\mathbf{E}/c^2)[1+h-fhv^2/2c^2(1-v^2/c^2)]\}$, where $h=GM/c^2R\approx h_0+\mathbf{g}\cdot\mathbf{x}/c^2$. Neglecting radiative effects not due to a yet undetermined gravitational acceleration $\mathbf{a}_{g1}$, the Coulomb field, from a charge e_1 at $\mathbf{x}_1$, is $\mathbf{E}\approx e_1r^{-3}\mathbf{r}[1-fh_0/2-f\mathbf{g}\cdot\mathbf{x}_1/2c^2-(f\mathbf{g}/2+\mathbf{a}_{g1})\cdot\mathbf{r}/2c^2]+e_1r^{-1}(f\mathbf{g}/2-\mathbf{a}_{g1})/2c^2$. The helical motion $\mathbf{x}_2(t_2)$ of particle e_2 in the field of e_1, and vice versa, is obtained from the unperturbed circular motion $\xi(\tau)$ by transformation $\mathbf{x}=\xi[1+(1-f/2)h]+(f/2-1)\mathbf{g}\xi^2/2c^2+\mathbf{a}_g\xi^2/2$, and $t=(1+h)\tau$, if $\mathbf{a}_{g1}=\mathbf{a}_{g2}=\mathbf{g}$, showing that such rotating dipole falls with gravitational acceleration $\mathbf{g}$ (and not $\mathbf{a}_0$) for any value of the constant f.

* Supported by National Science Foundation.
[1] F. J. Belinfante and J. C. Swihart, N.S.F. research report, Purdue University, September, 1954.

K3. Hartree-Fock Wave Functions for Mn^{+4}. W. W. PIPER AND J. S. PRENER, *General Electric Research Laboratory.*—Hartree-Fock one-electron wave functions have been obtained for the ground state (^4F) of Mn^{+4}. Hartree's interpolated wave functions[1] for Mn^{+2} were used as initial estimates for the filled shells. An approximate solution for the ($3d$) wave function was available from previous work. An IBM type 650 digital computer was utilized to carry out the computation. The differential equations were integrated by means of Numerov's difference equation[2] for second-order differential equations. Simpson's rule was used for all quadratures. A total of fifteen iterations on various individual shells were carried out. This required approximately five hours of valid machine time. The total charge belonging to any shell and included within a sphere of arbitrary radius is correct to less than 0.005 a.u. The position of the maximum in the ($3d$) wave function is 0.72 a.u. which is 0.10 A smaller than the radius reported by Hartree[1] for Mn^{+2}. Work is in progress on the lowest excited state (^4P).

[1] D. R. Hartree, Proc. Cambridge Phil. Soc. **51**, (Part 1) 126 (1955).
[2] B. Numerov, Publ. de Observ. astrophysi. central Russ. **2**, 188 (1933).

K4. A Positional Correlation Study for a System of Two Electrons.* J. S. EVANS AND R. H. TREDGOLD, *University of Maryland* (introduced by R. D. MYERS).—A system of two electrons harmonically bound to a mass much larger than their own is one of the few three-body problems which is amenable to exact solution. Such a model provides a convenient check on various approximations used to handle correlation problems whereas heretofore it has been necessary to appeal to experiment. The ground-state eigenvalue and eigenfunction have been calculated exactly and by several approximate methods. Comparison of the exact and approximate wave functions allows one to obtain a better insight into the shortcomings of the approximate methods than is obtained by the usual comparison of eigenvalues.

* Supported by the U. S. Air Force, through the Office of Scientific Research of the Air Research and Development Command.

Invited Papers

K5. Effective-Range Theory of Meson-Nucleon Scattering. FRANCIS LOW, *University of Illinois.* (30 min.)

K6. Theory of Pion Photoproduction. MARC ROSS, *Indiana University.* (30 min.)

K7. Higher-Spin Particle Formalism. D. C. PEASLEE, *Purdue University.* (30 min.)

K8. On the Relation of a Potential to the *S*-Matrix. R. G. NEWTON, *Indiana University.* (30 min.)

FRIDAY AFTERNOON AT 2:15

Kent 106

(JOHN BARDEEN presiding)

Invited Paper

N1. Energy-Band Structure of Solids with ZnS-Type Lattices. G. DRESSELHAUS, *University of California, Berkeley.* (30 min.)

Semiconductors, I

N2. Thermoelectric Power in a Semiconductor Showing High-Temperature Degeneracy. V. A. JOHNSON, *Purdue University.*—The narrowness of the forbidden energy band in intermetallic compounds makes it probable that the electron gas at room temperature and above will be sufficiently degenerate to require the use of Fermi-Dirac statistics in expressions for the electrical properties. The thermoelectric power of a semiconductor obeying Fermi-Dirac statistics, considering both holes and electrons, is

$$Q=-\frac{k}{e}\frac{\begin{array}{r}2c^{3/5}J_0(-\zeta^*-E_G^*)J_1(\zeta^*)J_1(\zeta^*)\\ -2J_1(-\zeta^*-E_G^*)J_1(-\zeta^*-E_G^*)J_0(\zeta^*)\\ \hline c^{3/5}J_0(\zeta^*)J_0(-\zeta^*-E_G^*)J_1(\zeta^*)\\ +J_0(\zeta^*)J_0(-\zeta^*-E_G^*)J_1(-\zeta^*-E_G^*)\end{array}}{}$$

$$+\frac{k}{e}\frac{c^{2/5}\zeta^*J_1(\zeta^*)+(\zeta^*+E_G^*)J_1(-\zeta^*-E_G^*)}{c^{2/5}J_1(\zeta^*)+J_1(-\zeta^*-E_G^*)}$$

if only lattice scattering by acoustical modes is present. $J_k(\zeta^*)$ is a Fermi-Dirac integral, ζ^* the reduced Fermi level, E_G^* the reduced value of the forbidden band width, and c the electron-to-hole mobility ratio. Fan and Spitzer[1] have found optical evidence for the combination of acoustical and optical modes of scattering in indium antimonide. Hence the thermoelectric power for optical mode scattering and Fermi-Dirac statistics has also been calculated and found to differ considerably from the preceding case.

[1] W. G. Spitzer and H. Y. Fan, Phys. Rev. **99**, 1893 (1955).

N3. Ionized Impurity Scattering in Semiconductors. FRANK S. HAM,* *University of Illinois.*—The Brooks-Herring analysis of the scattering of electrons or holes by ionized impurities has been generalized for ellipsoidal energy surfaces. From the effective mass approximation we find for ellipsoidal surfaces, as well as for spherical surfaces, that an electron is scattered from a state with propagation vector $\mathbf{k}$ to a state $\mathbf{k}'$ of equal energy with a probability proportional to $[(\mathbf{k}-\mathbf{k}')^2+1/\lambda^2]^{-1}$, where λ is the Debye screening length. However, for an ellipsoidal surface with an axis of symmetry the resulting relaxation times appropriate to conductivity along and perpendicular to the axis may be quite different. For a mass ratio $m_s/m_t=19$ appropriate to the conduction band of Ge, the relaxation time ratio τ_s/τ_t is about 12 if only small angle scattering is important and if lattice scattering can be neglected. The corresponding ratio for Si is 4 for $m_s/m_t=5.1$. Results for the contribution of large angle scattering will be presented, together with those for combined lattice and impurity scattering.

* NRC Fellow, 1954–1955. Now at the General Electric Research Laboratory.

N4. Infrared Properties of Selenium. R. S. CALDWELL AND H. Y. FAN, *Purdue University.**—Optical properties of liquid, amorphous, and crystalline selenium were investigated. In agreement with previous measurements, the absorption edge varies continuously throughout the liquid and solid amorphous phases by 1.4×10^{-3} ev/degree, between 140°K and 580°K. At the low absorption levels measured in the experiments, the absorption edge in the hexagonal phase is at about the same position as in the amorphous phase, and no significant difference was found by using radiation polarized parallel or perpendicular to the C-axis. The two absorption bands, at 13.5μ and 20.4μ, in amorphous selenium were observed also in the liquid phase at slightly longer wavelengths; this shift can be attributed to the temperature difference. The hexagonal phase shows a doublet band at 21.5μ. At long wavelengths, strong bands were observed around 35μ and 80μ in amorphous, and around 27μ and 70μ in crystalline samples. The reflectivity of amorphous selenium is 17.5% corresponding to the known refractive index of 2.45. The refractive indices in hexagonal selenium are $n_\perp=2.78$ and $n_\parallel=3.58$, constant in the range of measurement, 9μ to 23μ. These were measured using interference effect in thin samples.

* Supported by a Signal Corps Contract.

N5. Mechanical Properties of Si, Ge, and ZnO Whiskers. G. L. PEARSON, W. T. READ, JR., AND W. L. FELDMANN, *Bell Telephone Laboratories.*—Silicon whiskers 20μ in diameter and 2 mm long were supported at the two ends and bent by a concentrated load applied in the center through a quartz fiber hook. From 30°C to 600°C the behavior was elastic up to fracture at a maximum stress of about 2×10^{10} dynes cm^{-2}. The yield stress varied from 2×10^{10} at 600°C to 4×10^{9} at 800°C. During yielding in a hard machine, the force dropped to 0.3–0.5 times the yield force and thereafter remained constant during flow. For a given center deflection, maximum whisker curvature decreased and the length of the deformed region increased with temperature. Under constant load at 800°C yielding occurred after incubation; the creep-time curve was S-shaped, reaching a constant deflection. Pure tension and bending gave the same room temperature fracture stress. In germanium, log yield stress varied linearly with temperature with a slope of one decade per 135°C for both whiskers and bulk specimens. The fracture stress of the whiskers was 1.2×10^{10} dynes cm^{-2} and the minimum temperature for plastic deformation, 350°C. ZnO whiskers fractured at 1.5% elastic strain. The interpretation of the results will be discussed. These Si, Ge, and ZnO whiskers were furnished by J. A. Ditzenberger, H. Christensen, and D. G. Thomas, respectively.

N6. Hall Effect in Gray Tin Filaments.* E. E. KOHNKE† AND A. W. EWALD, *Northwestern University.*—To supplement a previous study of the conductivity and magnetoresistance of filamentary gray tin specimens,[1] a method for mounting the filaments to allow measurement of the Hall coefficient in the temperature range 70° to 270°K has been devised and results obtained for a number of n-type and p-type samples. It is shown that the mobility expressions $\mu_n=30.2\times10^{4}T^{-1.65}$, $\mu_p=21.8\times10^{3}T^{-2.0}$ cm^2/volt sec and the impurity concentration $N=2.5\times10^{17}$ cm^{-3} provide a very satisfactory fit to experimental data for the conductivity and Hall coefficient of a pure sample (n-type) down to 170°K. The indicated

absolute zero energy gap is 0.094 ev and an assumed energy gap temperature dependence leads to $M_e = M_h = 0.68$ M. In contradiction, p-type samples show mobility ratios greater than unity but in no specimens studied is there evidence of high mobility ratios comparable to those generally reported in InSb. A shift of the Hall crossover to higher temperatures with increasing field strengths is noted.

* Work supported by the Office of Naval Research.
† Now at Oklahoma A & M College, Stillwater, Oklahoma.
[1] A. W. Ewald and E. E. Kohnke, Phys. Rev. **97**, 607 (1955).

N7. Measurement of Magnetic Field Gradients by the Hall Effect.* R. D. REDIN AND G. C. DANIELSON, *Iowa State College.*—A magnetic field gradients measuring device, which uses the Hall effect in germanium, has been constructed. The field sensitive element is a bar of germanium 1 mm by 1 mm by 12 mm with two sets of Hall leads attached 2 mm either side of its center. One-hundred-cycle alternating current flows in the long direction of the bar. In a magnetic field two 100-cycle Hall voltages are obtained. These voltages, which are proportional to the magnetic field strength at two points of the field 4 mm apart, are subtracted to give an output directly proportional to the magnetic field gradient. The instrument will also measure field strengths and relative gradients. The instrument was tested in a calculable magnetic field produced by step pole pieces. Gradients from 5 gauss/inch to 500 gauss/inch in magnetic fields below 5000 gauss were measured. The usefulness of the instrument is still uncertain owing to errors caused by excessive field dependence of the gradient voltage.

* Work was performed in the Ames Laboratory of the U. S. Atomic Energy Commission.

FRIDAY EVENING AT 7:00

Quadrangle Club

(R. T. BIRGE presiding)

Banquet of the American Physical Society

After-dinner speakers to be announced.

SATURDAY MORNING AT 9:00

Oriental 104

(R. G. HERB presiding)

Reactions of Transmutation and Nuclear Energy Levels, I

P1. The $T(d,n)He^4$ Reaction, 1-5 Mev. C. H. JOHNSON AND A. GALONSKY, *Oak Ridge National Laboratory.*—Neutrons were produced in the $T(d,n)He^4$ reaction by bombardment of a tritium gas target with deuterons from the 5.5-Mv electrostatic generator. The monoenergetic neutron spectrum was observed in a radiator-type triple coincidence spectrometer consisting of 2 proportional counters and a NaI crystal. With both a target thickness and deuteron energy increment of 50–100 kev the 0° cross section was measured from $E_d = 1$ to 5 Mev. No sharp resonance is observed within this energy range. The 0° c.m. cross section continues to drop with increasing energy from the well-known resonance at 107 kev to 11 mb/sterad at 2.5 Mev and then rises steadily to 18 mb/sterad at 5 Mev. The total cross section decreases to 76 mb at 3.5 Mev and increases to 82 mb at 5 Mev. This increase may indicate a resonance. Angular distributions were measured from 0° to 150° at $E_d = 1.53$, 2.20, 3.05, 3.97, 4.98, and 5.79 Mev. A forward peak, which is slight at the lower energies, becomes steadily sharper with increasing energy. At 5.79 Mev the peak (0°) to valley (100°) cross-section ratio is 5:1 in the c.m. system. Beyond 100° the cross section rises by less than a factor of 2. At no energy is there symmetry about 90°.

P2. Gamma Rays from He^3 Bombardment of Deuterium. W. E. KUNZ, J. W. BUTLER, AND H. D. HOLMGREN.—Deuteron capture by He^3 [1] was confirmed by bombarding a deuterium gas target with a He^3 beam and observing the gamma-ray spectrum with a 3 in.×3 in. NaI crystal and a 20 channel pulse-height analyzer. Background gamma rays from the high-energy protons produced by the $He^3(d,p)He^4$ reaction gave peaks about 250 times that due to the deuteron capture gamma ray. With a polyethylene (CH_2) liner for the target chamber the most intense gamma ray was 4.43 Mev from protons inelastically scattered by carbon. A gold liner gave a continuous distribution of gamma rays with a maximum energy considerably higher than 4.43 Mev. For this reason a polyethylene liner was used for the remainder of the experiment. The gamma rays from deutron capture are not monoenergetic but have an energy spread of at least several Mev with a cut-off at approx 16.5 Mev. The ratio of gamma-ray yield to proton yield from the $He^3(d,p)He^4$ reaction is not a constant but increases at energies above the resonance of the proton reaction.

[1] Blair, Hintz, and Van Patter, Phys. Rev. **96**, 1023 (1954).

P3. Alpha Spectrum from $Li^7(p,\gamma)Be^{8*}(\alpha)He^4$.* E. C. LAVIER, S. S. HANNA, AND R. W. GELINAS, *Johns Hopkins University.*—States in Be^8 at 4.1, 5.3, and 5.7 Mev have been reported[1] from observations on the $Li^7(p,\gamma)Be^{8*}(\alpha)He^4$ reaction. We have observed the alpha spectrum up to $E_{\alpha x} = 11$ Mev with magnetic analysis at $E_p = 0.44$ Mev. Thin Li^7 targets were employed and the resonance reaction was monitored with the gamma radiation. Four exposures of 20–30 hours each were made to cover the spectrum. The following groups were observed: The broad structure corresponding to

the 2.9-Mev state in Be^8, the alpha and He^3 groups in the $Li^6(p,\alpha)He^3$ reaction from the small amount of Li^8 in the target, and a weak alpha group attributed to $O^{18}(p,\alpha)N^{15}$ from oxygen contamination of the target. In analyzing the alpha spectrum for possible structure which could be attributed to the existence of higher states in Be^8, it is necessary to consider the recoil motion imparted to the Be^8 nucleus by the gamma emission. We estimate that a group at $E=2.0,2.6$, or 3.7 Mev would have been observed if its intensity was greater than 1.0, 0.7, or 0.5% of the total alpha spectrum.

* Assisted by a contract with the U. S. Atomic Energy Commission.
[1] E. K. Inall and A. J. F. Boyle, Phil. Mag. 44, 1081 (1953).

P4. Search for States in Li^7 and Be^8.* R. W. GELINAS AND S. S. HANNA, *Johns Hopkins University.*—Recently evidence has been reported for the existence of a state in Li^7 at 5.5 Mev.[1] Using the $Be^9(d,\alpha)Li^7$ reaction with magnetic analysis we have searched through a region up to $E_{ex}=6.0$ Mev in Li^7. Bombarding energies were 0.50 and 0.70 Mev and the angle of observation was 70°. No particle group was observed which could not be attributed to previously well-established reactions. The Li^7 state at $E_{ex}=4.62$ Mev was resolved in several spectra. The $Be^9(d,t)Be^8$ reaction was also investigated at angles from 23° to 90° and bombarding energies from 0.47 to 1.15 Mev in order to look for a state in Be^8 at 4.0 to 4.3 Mev In this instance also a negative result was obtained.

* Assisted by a contract with the U. S. Atomic Energy Commission.
[1] Erdos, Scherrer, Stoll, Wachter, and Wataghin, Nuovo cimento 12, 639 (1954).

P5. The Reactions $Be^9(d,d')$ and $Be^9(\alpha,\alpha')$.* D. W. MILLER, V. K. RASMUSSEN, M. B. SAMPSON, AND U. C. GUPTA, *Indiana University.*—The existence of a level in Be^9 at 3.01 ± 0.1 Mev has been verified by the inelastic scattering of 21.6-Mev alpha particles and 10.8-Mev deuterons. A broad continuum of inelastic particles near 1.8-Mev excitation is found from both reactions. If one assumes that an uncorrelated three-body breakup of the compound nucleus causes the broad continuum, then the superimposed peak represents a level in Be^9 at 1.74 ± 0.1 Mev. However, within the accuracy of the present data, the observed spectrum is consistent with a three-body breakup in which a final-state potential-scattering interaction[1] between the Be^8 and the neutron occurs (scattering length about 1.3×10^{-13} cm. The existence of a state in Be^9 around 1.8 Mev is then allowed, but not required.

* Supported by the joint program of the Office of Naval Research and the U. S. Atomic Energy Commission.
[1] K. M. Watson, Phys. Rev. 88, 1163 (1952).

P6. Angular Distribution of Protons from $Be^9(He^3,p)B^{11}$ Reaction. H. D. HOLMGREN, W. E. KUNZ, AND L. BULLOCK, *Naval Research Laboratory.*—He^3 nuclei accelerated by the N.R.L. 2 Mev Van de Graaff generators have been used to investigate the angular distributions of the four highest energy proton groups from the $Be^9(He^3,p)B^{11}$ reaction.[1] These measurements were made with a multiplate reaction camera having 200 micron *C2* nuclear emulsions placed at 5° intervals over the angular region extending from 5° to 170°. All the angular distributions were observed to have an extreme in the neighborhood of 70° and exhibit a lack of symmetry about 90°.

[1] Holmgren, Bullock, and Kunz, Phys. Rev. 100, 436 (1955).

P7. Electrostatic Analysis of Nuclear Reaction Energies, IV. REN CHIBA, R. A. DOUGLAS, J. W. BROER, D. F. HERRING, AND E. A. SILVERSTEIN, *University of Wisconsin.**—Cylindrical and spherical electrostatic analyzers have been used to measure the energies of incident and outgoing charged particles as described earlier. Stable targets of deuterium and nitrogen were formed by gettering of these gases by titanium in an Evapor-ion pump. These targets (heated) were used for the $D(d,t)H^1$ and $D(d,He^3)n$ reactions; $N^{14}(d,p)N^{15*}$ and $N^{14}(d,\alpha)C^{12*}$ reactions. Also measured was the $B^{10}(\alpha,d)C^{12}$ reaction. Preliminary calculations of Q values are in agreement with earlier measurements or mass values. Further calculations and error evaluations are underway. The 9.61-Mev C^{12} level had an experimental width of ~40 kev, indicating alpha emission. Therefore J and parity are restricted to 0^+, 1^-, 2^+, 3^-. (For 4^+ the reduced width is approximately twice the Wigner limit.)

* Work supported in part by the U. S. Atomic Energy Commission and the Wisconsin Alumni Research Foundation.

P8. Analysis of $C^{13}+d$ Reactions. M. T. MCELLISTREM,* *University of Wisconsin.*†—Previously reported differential cross section for $C^{13}(d,d)C^{13}$, $C^{13}(d,p)C^{13}$ and $C^{13}(d,p)C^{14*}$, ($E_x(C^{13})=3.09$ Mev) have been analyzed to display the stripping and compound nuclear contributions. Dispersion formalism has been used to fit the elastic scattering data at two "isolated" resonances. One at $E_d=2.502$ Mev ($E_x(N^{14})=12.41$ Mev) is assigned spin and parity of 4^-. Another at $E_d=2.735$ Mev ($E_x(N^{14})=12.60$ Mev) is assigned 3^+. These assignments also agree qualtitatively with the (d,p) data. $C^{13}(d,p)$ and (d,n) cross sections have been further analyzed by the method of Bowcock,[1] which separates the data into the stripping amplitude described by Butler and all nonstripping components. The reduced widths are extracted from the stripping amplitude. The widths of C^{13} and N^{13} are found to be equal and have the value $(0.09\pm0.035)(3\hbar^2/2\mu a)$. The width of the 3.09-Mev level is found to be $(0.27)(3\hbar^2/2\mu a)$. This value is in reasonable agreement with the width of the mirror level in N^{13}.

* Now at Indiana University.
† Work supported in part by the U. S. Atomic Energy Commission and the Wisconsin Alumni Research Foundation.
[1] J. E. Bowcock, Proc. Phys. Soc. (London) 68A, 512 (1955).

P9. $C^{14}+d$ Reactions. R. A. DOUGLAS, J. W. BROER, AND REN CHIBA, *University of Wisconsin.**—Uniform thin C^{14} targets on 2500 A nickel backings were prepared in a discharge tube containing acetylene (enriched to 28.8% C^{14}). Monoergic ($\pm0.05\%$) deuterons selected by a 90° cylindrical electrostatic analyzer were used to bombard the targets. Reaction products at 135° were measured with the spherical electrostatic analyzer (0.24% resolution). For $C^{14}(d,\alpha)B^{12}$ a $Q=+0.36_4$ Mev was observed (preliminary calculation). No protons (<0.05 mb/sterad for $E_d=1.8$, 1.9, and 2.1 Mev) from $C^{14}(d,p)C^{15}$ could be found corresponding to the reported $Q=+0.12$ Mev. However, an intense proton group corresponding to a $Q=-0.96$ Mev for $C^{14}(d,p)C^{15}$ was identified. The 2.4-sec C^{15} activity was observed (NaI scintillator) to decrease sharply to near background as the deuteron energy decreased to 1.3 Mev. (For our $Q=-0.96$, $E_{th,rxn}=\sim1.1$ Mev.) No appreciable intensity of high energy (~5–10 Mev) beta activity corresponding to the ground-state transition was observable. Aluminum absorbers of 2.5 cm thickness attenuated the 2.4-sec activity only by 25% indicating the presence of high-energy gamma rays. Presumably most (if not all) of the beta transitions are to excited states of N^{15}.

* Work supported by the U. S. Atomic Energy Commission and the Wisconsin Alumni Research Foundation.

P10. Isotopic Spin-Selection Rule Violation in $O^{16}(d,\alpha)N^{14*}$.† C. P. BROWNE, *M.I.T.*—A group of alpha particles from the $O^{16}(d,\alpha)N^{14*}$ reaction, leading to the first excited state, has been observed. Previous experiments indicate that this state has $T=1$.[1] Many attempts to observe the present reaction at various energies from 2 to 19 Mev have failed[2] as they should if isotopic spin is conserved. The yields of this forbidden alpha group and of the alpha groups leading to the ground state and

second excited state have been measured as a function of bombarding energy from 5.50 to 7.5 Mev in 250-kev steps. The angle of observation was 30°. These groups have also been measured at various other angles at 7.0 Mev. A resonance is observed at about 7.0 Mev. At this energy, the intensity of the forbidden group rises somewhat, while the intensity of the two allowed groups drops sharply. The intensity ratios of the first excited-state group to the ground-state and second excited-state groups reach 14 and 48%, respectively. The M.I.T. broad-range spectrograph was used to separate the alpha groups, and nuclear plates and a scintillation counter were used to record the particles. The relative intensities with energy change are thought to be good to about 15%, while the intensity ratios of the three groups are good to 5%.

† This work has been supported in part by the joint program of the Office of Naval Research and the U. S. Atomic Energy Commission.
[1] Bockelman, Browne, Sperduto, and Buechner, Phys. Rev. **92**, 665 (1953).
[2] F. Ajzenberg and T. Lauritsen, Revs. Modern Phys. **27**, 77 (1955).

P11. Excited States of O^{16} from Proton Bombardment of N^{15}.* R. R. CARLSON AND S. BASHKIN, *State University of Iowa*.—Natural nitrogen gas targets and silver nitrate targets, with N^{15} content enriched to 61%, were bombarded with protons of energy from 0.8 Mev to 3.2 Mev. Resonances for the production of 4.4-Mev gamma rays from the $N^{15}(p,\alpha\gamma)C^{12}$ reaction were detected with a NaI(Tl) crystal. The resonance at 1660±20 kev bombarding energy[1] was found to have a width of 95±10 kev. Previously unobserved resonances were found at bombarding energies of 1990±20 kev and 3000±30 kev with widths of <30 kev and 90±20 kev, respectively. These resonances correspond to excited states in O^{16} at 13.98 Mev and 14.92 Mev, respectively. The present experiment gave no evidence of the state in O^{16} at 14.2 Mev which has been reported on the basis of the photo disintegration[2] of O^{16}.

* Supported in part by the U. S. Atomic Energy Commission.
[1] A. A. Kraus, Phys. Rev. **94**, 975 (1954).
[2] P. Stoll, Helv. Phys. Acta **27**, 395 (1954).

P12. The Inelastic Scattering of Protons from F^{19}.* B. J. TOPPEL, D. H. WILKINSON,† AND D. E. ALBURGER, *Brookhaven National Laboratory*.—The gamma radiation following inelastic proton scattering from F^{19} has been observed using 2.4- to 4.1-Mev protons from the BNL research Van de Graaff. Gamma rays of energies 1.238±0.010 Mev and 1.350±0.010 Mev are observed in the singles NaI(Tl) spectrum using 3.0-Mev protons. The angular distributions of these gamma rays show anisotropies of +29% and −29%, respectively. Three crystal pair spectrometer measurements at 3.0 Mev and 3.5 Mev indicate that a 1.449±0.010 Mev gamma ray is also present. Coincidence measurements at 3.0 Mev show that gamma rays of energies 1.233±0.010 Mev and 1.346±0.010 Mev are in prompt coincidence with 109-kev radiation while a 1.354±0.010 Mev gamma ray is in delayed coincidence with 197-kev radiation. In addition the 109-kev radiation is found to have the same energy when seen in singles or in coincidence with 1.24-Mev gamma rays. These observations imply states in F^{19} at 1.342±0.010 Mev, 1.452±0.010 Mev, and 1.551±0.010 Mev. The observed relative gamma-ray intensities show that the 1.24-Mev radiation originates mainly from the 1.34-Mev state and that the 1.34-Mev state exhibits less than an 8% branch to the $J=5/2+$ level at 197 kev. These observations together with the observed nonisotropicity of the 1.24 Mev radiation indicate an assignment $J=3/2$ for the 1.34 state.

* Work performed under the auspices of the U. S. Atomic Energy Commission.
† On leave from Cavendish Laboratory, Cambridge, England.

P13. The Pickup Reactions $F^{19}(n,d)O^{18}$.* F. L. RIBE, *Los Alamos Scientific Laboratory*.—Thin targets of Teflon were bombarded with 14.1-Mev neutrons, and reaction deuterons were detected with a proportional counter-scintillator telescope at various angles. A strong deuteron group corresponding to the ground state of O^{18} and a weak group corresponding to an excited state at 1.9±0.1 Mev were observed, and their differential cross sections were measured for laboratory angles between zero and 80 degrees. No further excited-state groups were observed for excitations up to three Mev. Above three Mev the deuteron groups were not resolved. The ground-state differential cross section is well fitted by a Butler curve with $l_p=0$, while no clear pickup structure is indicated for the 1.9-Mev excited state. Using the Butler formula to extract kinematical effects, one obtains the following values and upper limits for the dimensionless reduced-width factors θ_p^2 for the $F^{19}\rightarrow O^{18}$ transitions: Ground state—$l_p=0$: $\theta_p^2=0.036$. Relative $\theta_p^2=1.00$. 1.9-Mev level—$l_p=0$, 1, 2: $\theta_p^2\leq 0.0015$, 0.0068, 0.031. Relative $\theta_p^2\leq 0.041$, 0.19, 0.87. S-wave pickup to the excited state thus appears to be forbidden. A separate search gave no indication of ground-state protons from the reaction $F^{19}(n,p)O^{19}$.

* Work done under the auspices of the U. S. Atomic Energy Commission.

P14. A 5.3-Mev Energy Level in Mg^{24} Following the Decay of Na^{24}. F. M. TOMNOVEC AND C. S. COOK, *U. S. Naval Radiological Defense Laboratory*.—Capture gamma rays from the reaction $Na^{23}(p,\gamma)Mg^{24}$ have led to the assignment[1] of an energy level at 5.23 Mev in Mg^{24}. The spins and parities tentatively assigned to this energy level make it appear that Na^{24} should be able to decay to this level. Observation on the high-energy gamma radiations of Na^{24} using a 4 in. diameter by 4 in thick NaI(Tl) crystal scintillation spectrometer has shown radiation at 3.9 and 5.3 Mev, confirming the existence of this level in the decay of Na^{24}. The 3.9-Mev radiation,[2] according to this scheme, follows a transition from the 5.3-Mev level to the 1.38-Mev level in Mg^{24}.

[1] J. O. Newton, Phys. Rev. **96**, 241 (1954).
[2] Beghian, Bishop, and Halban, Phys. Rev. **83**, 186 (1951).

P15. Lifetimes of First Excited States of Al^{28} and B^{10}. J. C. SEVERIENS AND S. S. HANNA, *Johns Hopkins University*.—A modification of the Thirion-Telegdi recoil method,[1] incorporating coincidence counting, has been used to determine the lifetimes of states in nuclear reactions. In the reaction $Al^{27}(d,p)Al^{28*}(32\text{ kev})Al^{28}$, forward moving recoils are obtained by observing only coincidences between gamma rays and protons emitted (approximately) antiparallel to the deuteron beam. The gamma counter is at 0° to the beam, at a distance approximately $2d$, where d is the distance traveled by a recoil during its mean life. A recoil "stopper" is placed between target and counter and the coincidence yield measured as a function of stopper position. In effect, one measures the change in solid angle produced by mechanically controlling the range of the recoils. The method provides a beam of excited nuclei produced in a unique manner and with a known spatial distribution. In the reaction $Be^9(d,n)B^{10*}(\gamma)B^{10}$ the 2.86-Mev gamma was used to tag the 0.72-Mev gamma, the recoil angular distribution being obtained from the known neutron distribution. The effect of target thickness was investigated with targets of different thickness. Lifetimes of $(2.7\pm0.03)\times10^{-9}$ and $(9.5\pm2.0\times10^{-10}$ sec were obtained for Al^{28*} and B^{10*}, respectively. The method gave a negative result for the 477-kev state in Li^7.

* Assisted by a contract with the U. S. Atomic Energy Commission.
[1] J. Thirion and V. L. Telegdi, Phys. Rev. **92**, 1253 (1953).

SATURDAY MORNING AT 9:30

Mandel Hall

(R. T. BIRGE presiding)

Invited Papers on Bubble-Chamber Experiments

Q1. Hydrogen Bubble-Chamber Design and Experiments. LUIS W. ALVAREZ, *University of California, Berkeley.* (30 min.)

Q2. Pion-Proton Scattering Observed with a Liquid-Hydrogen Bubble-Chamber. D. E. NAGLE, *University of Chicago.* (30 min.)

Mesons

Q3. Meson Production in *n-p* Collisions by Cosmotron-Produced Neutrons with Energies up to 1.5 Bev.* W. A. WALLENMEYER, *Purdue University* (introduced by C. Y. CHANG).—This is a continuation at lower incident neutron energies of an experiment previously done by the Brookhaven Cloud Chamber Group.[1] 158 of about 210 three-prong events obtained from collisions between neutrons, with energies up to 1.5 Bev, and protons in a hydrogen-filled cloud chamber, have been analyzed. These events have been classified as resulting from the reactions $n+p\rightarrow p+p+\pi^-$, $\rightarrow p+p+\pi^-+\pi^0$, and $\rightarrow p+n+\pi^++\pi^-$ in the ratio 40:0:6 below 1 Bev and in the ratio 41:12:7: above 1 Bev. The observed ratio of double to single meson production is again more than 20 times higher than the ratio predicted from Fermi's statistical theory. In the center-of-mass system, in the reaction $\rightarrow p+p+\pi^-$, the protons are very strongly peaked in the forward and backward directions and have very strong tendencies toward opposite directions. In cms, in the reaction $\rightarrow p+p+\pi^++\pi^-$; p and π^+, n and π^-, and also p and n all show a very definite tendency to be emitted in opposite directions to each other. The tendency of p and π^+ to be emitted backward and n and π^- to be emitted forward which was observed in the previous experiment does not show up here.

* Performed under the auspices of the U. S. Atomic Energy Commission at Brookhaven National Laboratory and partially supported by the Purdue Research Foundation.

[1] Fowler, Shutt, Thorndike, and Whittemore, Phys. Rev. 95, 1026 (1954).

Q4. Photoproduction of π^0 Mesons in Helium.* E. L. GOLDWASSER AND L. J. KOESTER, JR., *University of Illinois.*—An experiment has been performed to compare the energy dependence, from threshold to 300 Mev, of π^0 photoproduction in helium with that in hydrogen. The neutral pions were detected by counting γ rays emitted at a laboratory angle of 84°. The photon difference method was used to show that a cross section maximum occurs in helium at a photon energy near 280 Mev. This is much lower than the 325-Mev energy of the hydrogen peak. The "elastic" process, $h\nu+\mathrm{He}^4\rightarrow\pi^0+\mathrm{He}^4$, has been shown to play an important role in the photoproduction of π^0 mesons from helium.[1,2] It seems probable that the neutral pions produced both in the elastic and inelastic processes stem basically from the strong single nucleon-pion interaction in the 3/2, 3/2 state. The observed shift in energy may be qualitatively explained under the assumption that the production process is predominantly elastic. The inelastic process, as a result of the 20-Mev He binding energy which must be supplied, should give to a shift in the opposite direction. Analysis to obtain absolute cross sections is in progress.

* Supported in part by the joint program of the Office of Naval Research and the U. S. Atomic Energy Commission.

[1] Goldwasser, Koester, and Mills Phys. Rev. 95, 1692 (1955).

[2] G. DeSaussure and L. S. Osborne, Phys. Rev. 99, 843 (1955).

Q5. Scattering of 38-Mev Positive Pions in Hydrogen.* A. M. SACHS, H. WINICK, AND B. A. WOOTEN, *Columbia University.*—Measurements have been made of the differential cross sections of 38±7 Mev positive pions scattered in hydrogen at several angles. In preliminary runs the 60-Mev external pion beam from the Nevis cyclotron, after being analyzed in a double-focusing magnet, was slowed down in LiH and defined by two scintillation counters. After scattering in a liquid hydrogen target,[1] the pions were detected by two 3 in. ×6 in. ×¼ in. counters, the second of which was 14½ in. from the target. In addition, the mass and energy of the scattered particles were identified by photographing the pulse heights in the detecting counters and a 4 in. ×7 in. liquid counter 5 inches thick, in which the pions were brought to rest. In the center-of-mass system, $d\sigma/d\Omega=0.28\pm0.20$ mb/sterad at 69 deg, $d\sigma/d\Omega=0.86\pm0.15$ mb/sterad at 100 deg, and $d\sigma/d\Omega=1.48\pm0.19$ mb/sterad at 122 deg. More recently, a magnetic channel has made available lower energy external beams of positive pions. Experiments are now in progress with better energy resolution (38±3 Mev) and improved pulse-height counters including a plastic scintillator 5½ in. ×8½ in. ×6 in. thick.

* This research was supported by the joint program of the Office of Naval Research and the U. S. Atomic Energy Commission.

[1] Bodansky, Sachs, and Steinberger, Phys. Rev. 93, 1367 (1954).

Q6. Positive Pion Scattering by Hydrogen at 260, 300, and 400 Mev.* R. S. MARGULIES, *Brookhaven National Laboratory.*—The Brookhaven six-foot diffusion chamber has been used at the Cosmotron to study elastic π^+-p scattering. With an assumed total cross section of 110 mb[1] at 260 Mev, analysis of 100 scatterings yields the least squares angular distribution $d\sigma/d\Omega=\lambda^2(0.680+0.540x+3.007x^2)$, where $x=\cos\theta$ (c.m.). This can be fitted with the phase shifts $\alpha_3=-12°$, $\alpha_{31}=-11°$, $\alpha_{33}=116°$. At 300 Mev, assuming a total cross section of 75 mb,[1] the angular distribution of 151 scatterings is $d\sigma/d\Omega=\lambda^2(0.662+0.792x+2.101x^2)$, which can be fitted with the phase shifts $\alpha_3=-17°$, $\alpha_{31}=-4°$, $\alpha_{33}=127°$. At 400 Mev, partially completed analysis, based on the 47 scattering angles so far measured, and a total cross section of 35 mb,[1] yields the angular distribution $d\sigma/d\Omega=\lambda^2(-0.03-0.60x+2.78x^2+3.07x^3)$. If it is assumed that the large forward peak is partially due to D-waves, then the distribution can be fitted by the phase shifts $\alpha_3=\alpha_{31}=-22°$, $\alpha_{33}=158°$, $\alpha(D_{3/2})=-22°$, $\alpha(D_{5/2})=0$. However, other combinations of D-wave phase shifts are possible.

* Work performed under the auspices of the U. S. Atomic Energy Commission.

[1] S. J. Lindenbaum and L. C. L. Yuan, Phys. Rev. 100, 306 (1955).

SATURDAY MORNING AT 9:15

Eckhart 133

(A. W. LAWSON presiding)

General Solid-State Physics

R1. Angular Correlation of Annihilation Radiation in Superconducting Lead. R. STUMP, *University of Kansas.*—The angular correlation of annihilation radiation from positrons stopped in a solid gives a measurement of electron momentum in the solid. A measurement of the correlation in superconducting lead was made to determine whether any change in momentum of the annihilating electrons occurs in the superconducting state. Angular correlation measurements were made on radiation from positrons stopped in lead at 300°K, 77°K, and 4°K; in each case with magnetic fields of 100 and 1200 gauss. Within the limits of accuracy of the experiment, the angular correlation is the same in each of the six cases. The electron momentum distribution is in agreement with that predicted assuming four free electrons per atom in an ideal Fermi gas at 0°K, plus a high velocity tail resulting from occasional annihilation with more tightly bound electrons. Work with other superconductors is being continued.

R2. Hall Effect and Magnetoresistance of Bi Single Crystals at He Temperatures.* R. A. CONNELL AND J. A. MARCUS, *Northwestern University.*—Measurements of the Hall coefficient and magnetoresistance have been made on single crystals grown from unpurified Cerro de Pasco bismuth. Using a modified Schubnikov technique, rods of 2 mm square cross section were obtained. Three appropriately seeded crystals of this geometry were sufficient for the examination of the six principal crystallographic oreintations. At 42°K the Hall coefficient showed pronounced de Haas-van Alphen oscillations, with periods ranging from 2.3×10^{-4} gauss^{-1} to 9.6×10^{-4} gauss^{-1}. The oscillations occurred about an approximately zero mean value, corresponding more closely to the original work of Gerritsen[1] than to the recent findings[1,2] where the oscillations were superposed on a large negative term. This difference is believed to be due to impurities, the samples having an average residual resistance ratio $\rho_{4.2°K}/\rho_{273°K} \simeq 8\times10^{-3}$. (An attempt at zone refining is being made.) The magnetoresistance was found to be roughly proportional to $H^{1.7}$, with a small oscillating term superposed. Work at lower temperatures is now in progress.

* Supported by the National Science Foundation.
[1] L. C. Brodie, Phys. Rev. **93**, 935(A) (1954).
[2] W. C. Overton and T. G. Berlincourt, Phys. Rev. **99**, 1165 (1955).

R3. Thermal Diffusivity of Uranium from Room Temperature to 1000°C.* P. H. SIDLES, *Iowa State College.*—The thermal diffusivity of uranium has been measured in the temperature range 25–1000°C. In this range uranium transforms from an orthorhombic α phase to a complex β phase at 668°C and to a cubic γ phase at 770°C. The procedure followed was to α-anneal and measure the thermal diffusivity in the α temperature range; then β-anneal and measure thermal diffusivity in the β region, transform back to the α phase, anneal and again measure the thermal diffusivity in the α region. Small segments were periodically removed from the sample for grain size determinations. The β treatment caused a large increase in grain size and a 5–10% decrease in the α region thermal diffusivity. The sample was then γ-annealed and thermal diffusivity measurements made in all three phases. The α phase grain size and thermal diffusivity after the γ treatment were not appreciably different from those after β the treatment. Thermal conductivity (K) can be calculated using the relation $K = hcd$ where h is thermal diffusivity, c is specific heat, and d is density. The thermal conductivity of uranium, obtained in this manner, will be reported.

* Work was performed in the Ames Laboratory of the U. S. Atomic Energy Commission.

R4. Electrical Conduction in Plexiglas.* RAYMOND J. MUNICK, *Argonne National Laboratory.*—The electric current from one-millimeter thick specimens of Plexiglas was studied as a function of time, temperature, and voltage. The time-dependent part, which contributes to the polarization of the dielectric, showed a slight but definite departure from the t^{-n} time decay typical of solid insulators.[1] Also, it showed a relatively small change with temperature compared to the exponential increase of the steady part, or conduction current, from 25 to 75°C. Thermal activation energies of 1.4 to 1.5 electron volts were found for the conductivity, which compare reasonably well with the value of 1.6 ev reported for unplasticized Perspex,[2] which like Plexiglas is a polymer of methyl methacrylate. The room temperature conductivities were found to be around 10^{-19} mhos per cm. The conduction currents obtained at 60 and 75°C were approximately proportional to voltage for values from 315 to 3125.

* Work performed under the auspices of the U. S. Atomic Energy Commission.
[1] M. F. Manning and M. E. Bell, Revs. Modern Phys. **12**, 215 (1940).
[2] J. F. Fowler and F. T. Farmer, Nature **175**, 516 (1955).

R5. Young's Modulus of Gold-Nickel Alloys. J. SIVERTSEN AND C. WERT, *University of Illinois.*—At high temperatures alloys of gold and nickel are solid solutions at all compositions, but at low temperatures, the stable alloy (over most of the composition range) is a mixture of a gold rich phase and a nickel rich phase. By quenching an alloy from the high-temperature region to room temperature, one can regain the solid solution characteristic of the high-temperature phase. Quenched solutions of intermediate composition decompose into a two-phase mixture when the material is annealed at slightly elevated temperatures. Changes in a number of physical properties (e.g., electrical resistance and microstructure) have been observed to accompany this phase separation. Changes in internal friction of these alloys have also been observed during this annealing, but they precede the actual phase separation as it is observed by other means. The mechanism responsible for these changes in internal friction is not known. It seemed desirable to determine whether this effect might be correlated with changes in some other physical property as well. We have measured changes in Young's modulus during the annealing of a 30% Ni alloy, and we do find an increase in the modulus occurring concurrently with changes in the internal friction.

R6. Effect of V_2O_5 on Spinel Formation.* D. M. GRIMES AND J. W. KUIPER.—Vanadium pentoxide has been found to act as a mineralizer in lowering the temperature necessary for densification and in some cases spinel formation. This has been observed for Fe_2O_3 alone and for Fe_2O_3 plus Ni^{2+}, Zn^{2+}, Li^{1+}, Cd^{2+}, Mn^{2+}, Co^{2+}, or Mg^{2+}. The necessary formation temperature is increased for Fe_2O_3 plus Cu^{2+}, Mn^{4+}, or Co^{3+}, and is nearly unaffected for Fe_2O_3 plus Ca^{2+} or Ba^{2+}. This gives resulting magnetic properties somewhat different from the usual

by eliminating the side effects of high firing temperature, such as ferrous iron.

* Grimes, Thomassen, Jefferson, and Kothary, J. Chem. Phys. (to be published).

R7. A Neutron Diffraction Study of VD_x. B. W. ROBERTS, *General Electric Research Laboratory.*—A sample of vanadium deuteride near the composition V_4D_3 has been studied by x-ray and neutron diffraction. At room temperature, x-rays disclose a swollen b.c.c. arrangement of the vanadium atoms ($a_0=3.14_8$ A) with no evidence for the deuterium locations while neutron diffraction traces yield a single diffraction peak at the 110 position. No peaks are observed at the 200, 211, or 220 positions, however, a very broad diffuse maximum is centered to a low angle of the 110 reflection. Due to the very low coherent cross section of vanadium and the favorable cross section of deuterium the neutron intensity observed in the peaks is almost entirely due to the deuterium. Neutron data taken at liquid nitrogen temperature show no evidence of a diffuse maximum. Twenty-two reflections are observed which index with a primitive cubic cell with a_0 equal 6.30 A. This cell edge is twice the edge of the b.c.c. vanadium lattice observed at liquid nitrogen temperature with x-rays and therefore requires an ordering of the deuteriums in a cell eight times the volume of the required vanadium cell. The transformation from the "ordered" to "disordered" phases occurs at 207°±10°K.

R8. On the Crystal Structure of the Solid Rare Gases.* R. U. AYRES AND R. H. TREDGOLD, *University of Maryland* (Introduced by R. D. Myers).—All the rare gases with the exception of helium are observed to solidify in the face-centered cubic structure. Previous theoretical work, however, has predicted that the close packed hexagonal structure should be energetically favorable. A semiclassical model has been developed which allows one to take account of the overlapping of the electronic charge clouds of neighboring atoms, and this has been applied to both two-body and three-body interactions In the case of pure dipole interactions the results degenerate to those previously obtained by Axilrod.[1] When the additional effect of overlap is calculated for tripole-dipole interactions a new angular dependence is derived. When the third-order terms are summed for the two lattices a significant difference in the right direction is obtained. Indeed for reasonable values of the parameters of the model the difference more than counteracts the unfavorable difference arising from the second-order terms previously obtained by other authors.

* Supported by the United States Air Force through the Office of Scientific Research of the Air Research and Development Command.
[1] B. M. Axilrod, J. Chem. Phys. 19, 719 (1951).

R9. Soft X-Ray Emission Spectrum of Germanium.* D. E. BEDO AND D. H. TOMBOULIAN, *Cornell University.*—The emission spectrum of a germanium target was investigated in the spectral region extending from 60 A to 600 A. The germanium surface was formed by evapoartion in the x-ray tube. The deposition was carried out with the target surface at room temperature and also at 400°C in an attempt to observe changes in the emission spectrum which could arise from differences existing in the structure of the target layer. No such changes were observed. Two bands whose edges lie at 102 A and 103.5 A have been detected. These are tentatively identified as transitions from the valence levels to the M_3 and M_2 states, respectively.[1] The emission lines corresponding to the $K\rightarrow M_{4,5}$ transitions have been observed previously,[2] indicating that the $M_{4,5}$ levels fall below the valence band. Thus, in the wavelength range of the present investigation, one could expect to find the $M_{4,5}\rightarrow$valence emission band. Examination of the spectrograms does not reveal the presence of this band.

* Supported by the Office of Ordnance Research, U. S. Army.
[1] J. C. Slater, Phys. Rev. 98, 1039 (1955).
[2] J. A. Bearden and C. H. Shaw, Phys. Rev. 48, 18 (1935).

R10. Brillouin Zone Studies. V. Thermoelectric Power of Dilute Magnesium Alloys. E. W. KAMMER, E. I. SALKOVITZ, AND A. I. SCHINDLER, *U. S. Naval Research Laboratory.*—At room temperature the elements Li, Al, Ag, Cd, In, Sn, Tl, and Pb form terminal substitutional solid solutions in Mg. Salkovitz and Schindler[1] have suggested that Brillouin zone overlap in these systems may be studied by observing various transport phenomena as a function of alloying additions. Such a study has now been made on the effect of these alloying additions upon the thermoelectric power. It is found that a reversal in electrical polarity occurs at low concentrations for additions of the tri- or tetra-valent additions near the region of overlap. The ratio of thermoelectric power to atomic percent impurity element is a cyclic function of atomic number. For concentrations greater than those characterized by initial overlap conditions these cycles are in phase with the valence series of the periodic table. Resistivity and Hall effect measurements[1,2] on these alloys are compared for correlations of behavior at the Brillouin zone overlap concentrations.

[1] E. I. Salkovitz and A. I. Schindler, Phys. Rev. 91, 234, 1320 (1953).
[2] Salkovitz, Pasternak, and Schindler, Phys. Rev. 98, 271 (1955).

R11. Perturbation Calculation of the Volume Exclusion Effect.* IRA JACOBS, *Bell Telephone Laboratories.*—It is desired to determine the distribution of configurations of flexible long-chain molecules considering the fact that no two parts of the chain can occupy the same position in space. Experiments[1] indicate that the mean-square chain extension increases more rapidly than the number of links in the chain N, which cannot be explained by any theory that takes account only of correlations between neighboring elements of the chain. It is shown that for $N\approx 40$ to 400, the first-order theory of James[2] predicts that the mean-square extension increases as $N^{1.20}$ in good agreement with experimental[1] and Monte Carlo[3] results. A second-order calculation gives significant corrections for large N, but there is an inherent limitation of the perturbation approach due to the fact that the relative number of allowable configurations decreases exponentially with N. Sufficient computation can extend the validity of the results to larger N, but no statements on limiting behavior can be made.

* Taken from part of a dissertation submitted to Purdue University, June, 1955.
[1] Schultz, Cantow, and Meyerhoff, J. Polymer Sci. 10, 79 (1953).
[2] H. M. James, J. Chem. Phys. 21, 1628 (1953).
[3] M. N. Rosenbluth and A. W. Rosenbluth, J. Chem. Phys. 23, 356 (1955).

R12. Time Dependence of Mechanical Breakdown Phenomena. BERNARD D. COLEMAN, *E. I. du Pont de Nemours and Company.*—A phenomenological theory of the time dependence of mechanical breakdown phenomena is presented which yields general expressions for the distribution of breaking times in ensembles of filaments which have been subjected to arbitrary loading histories. The theory is applicable to discussions of the creep failure of polymeric solids under uniaxial tensile stresses. Several articles have appeared in the literature attempting to explain observed tensile strength distributions in terms of static models which can be treated by the methods of extreme value statistics. The present treatment differs from the extreme value theories, in that its *a priori* assumptions account for the time dependence of mechanical strength measurements. This permits a calculation of the dependence of the observed tensile strength on both the sample size and the rate of loading. The distribution of lifetimes of an ensemble of fibers is discussed for three special stress histories: dead loads, loads increasing linearly with time, and sinusoidal loads. Experiments involving drawn 66 nylon monofilament yarn are cited to illustrate how the parameters which describe the average lifetime under dead load behavior of a yarn may be used to calculate its tensile strength distribution when measured with a constant rate of loading apparatus.

R13. Use of the Field Emission Microscope for Investigating Surface Conditions on an Alloy.* L. A. D'ASARO,† *Cornell University.*—An alloy of a few percent of zirconium in molybdenum is used as an emitter in a field emission microscope. When the cleaned alloy surface is heated, diffusion of zirconium from the interior onto the surface is observed. This zirconium is always found on or near the 100 plane. After flashing to 2400°K, the rate of diffusion increases. This increase is interpreted as resulting from an increased vacancy concentration produced within the alloy by the flashing. Activation energies for diffusion of zirconium from the interior onto the surface can be found. A maximum in the quantity of zirconium present on the surface as a function of heating time is interpreted on the basis of the Wagner-Johnson vacancy theory of diffusion. Under certain conditions small parallelogram shaped patterns are seen on the 100 plane. The work function of the sources of these patterns, the field at the surface of the sources, and the size of the sources are determined by a method of matching the Fowler-Nordheim equation to an experimental plot of field emission current *versus* potential.

* This research was supported by the U. S. Air Force through the Office of Scientific Research of the Air Research and Development Command.
† Now at Bell Telephone Laboratories.

SATURDAY MORNING AT 9:30

Cobb 110

(E. L. HILL presiding)

Invited Papers

S1. Recent Developments in the Theory of Atomic Spectra. FRITZ ROHRLICH, *State University of Iowa.* (30 min.)

S2. The Impact of Electronic Digital Computers on Molecular Quantum-Mechanical Calculations. C. C. J. ROOTHAAN, *University of Chicago.* (30 min.)

S3. The Measurement of Magnetic Moments of Excited Nuclear States. R. M. STEFFEN, *Purdue University.* (30 min.)

SATURDAY MORNING AT 9:15

Kent 106

(G. C. DANIELSON presiding)

Semiconductors, II

T1. Magnetoresistance and Mobility of Germanium-Silicon Alloys. M. GLICKSMAN, *RCA Laboratories.*—The magnetoresistance and Hall mobility of germanium-silicon alloys have been measured for germanium-rich and silicon-rich *n*-type single crystals. The observed variation of the magnetoresistance asymmetry as a function of alloy composition is interpreted in terms of a band structure model proposed by Herman[1] to explain the change in band gap with composition.[2] A competition between [111] and [100] ellipsoidal conduction minima occurs for alloys with 11–15% silicon content. The two sets of minima are at the same energy for crystals containing about 15% silicon. In addition, the mobility measurements combined with the magnetoresistance give information on the variation of the shape of the conduction minima with composition. For germanium-rich alloys the ratio of the longitudinal to transverse effective masses remains essentially constant for crystals containing up to 7% silicon and appears to decrease in the range 7–10% silicon. Measurements of silicon-rich alloys indicate a decrease in the effective mass ratio for alloys of only 2–3% germanium content.

[1] F. Herman, Phys. Rev. **95**, 847 (1954).
[2] E. R. Johnson and S. M. Christian, Phys. Rev. **95**, 560 (1954).

T2. Hall Effect and Magnetoresistance in *n*-Type Germanium.* W. M. BULLIS† AND W. E. KRAG, *Lincoln Laboratory.*—Measurements of the Hall and magnetoresistance coefficients of *n*-type germanium have been made on a number of single crystals with room temperature resistivities from 0.01 to 25 ohm-cm. It is shown that if the electron mobility is not strongly dependent on the temperature (or on the energy of the electron) the experimental results may be explained by calculations based on an energy independent scattering time. Although the agreement between these theoretical calculations and experiment is not exact, the symmetry properties, which are dependent on the band structure, are accurately matched. In addition, particular attention is focused on the limits of these coefficients for both high and low magnetic fields. These limits may be most easily compared with theoretical calculations based on more complicated scattering times, for example the energy dependent scattering time $\tau = l\epsilon^p$, where l is independent of the energy ϵ.

* The research in this document was supported jointly by the Army, Navy, and Air Force under contract with the Massachusetts Institute of Technology.
† On educational leave from the Diamond Ordnance Fuze Laboratories, Washington, D. C.

T3. Copper in Germanium: Recombination Center and Trapping Center. B. J. WYLUDA AND R. G. SHULMAN, *Bell Telephone Laboratories.*—The time dependent photoconductivity of copper doped *n*-type and *p*-type germanium bridges has been measured between 130°K and 293°K. Temporary hole traps[1] were found in the *n*-type samples at the lower temperatures but no traps were observed in the *p*-type. Trap concentrations agreed with the density of copper atoms to within a factor of two and were at least 100 times higher than in undoped crystals. The trapping levels are 0.2 ev above the valence band;

the capture cross section for holes, σ_p, is 10^{-16} cm^2 and independent of temperature while the capture cross section for electrons, σ_n, is temperature dependent with an activation energy greater than 0.1 ev.[3] As a result of this temperature dependence of σ_n the 0.2 ev copper level changes from a recombination center[3] at room temperature to a hole trap at lower temperatures.

[1] J. R. Haynes and J. A. Hornbeck, Phys. Rev. **90**, 152 (1953); H. Y. Fan, Phys. Rev. **92**, 1424 (1953).
[2] R. M. Baum and J. F. Battey, Phys. Rev. **98**, 923 (1955).
[3] Burton *et al.*, J. Phys. Chem., **57**, 102 (1953).

T4. Measurement of Bulk and Surface Recombination by Photoconductance. H. M. Bath and M. Cutler, *Hughes Aircraft Company.*—A refinement has been made in the theory for photoconductivity, which takes into account both surface and bulk recombination. There are two interesting cases: wavelengths that are absorbed completely at the surface, and wavelengths absorbed nearly uniformly throughout the sample. The dependence of the conductance on the two types of recombination differs in the two cases, so that one can, under proper circumstances, measure both surface recombination velocity s and bulk lifetime τ in the same sample. Experimental procedures for making these measurements have been devised and the method was proved with germanium. A further advantage for the measurement with surface absorbed light is that one can measure accurately large values of s. This cannot be done with most other standard methods except the photoelectromagnetic method, which is based on the same physical situation. The effects of sandblasting and lapping germanium surfaces were measured; the former gave s of $1\text{–}2\times10^5$ cm/sec, and the latter had values of s of $5\text{–}10\times10^5$ cm/sec. Lapped surfaces showed some evidence of healing.

T5. Recombination Radiation from Silicon. J. R. Haynes, *Bell Telephone Laboratories.*—Radiation caused by the recombination of excess electrons and holes in silicon has been reported by Haynes and Briggs.[1] Recent experiments indicate that this radiation is due to indirect transitions of electrons from the conduction band minima to the valence band with phonon cooperation (indirect intrinsic recombination radiation). Additional radiation is found at 77°K which is structure sensitive. This radiation is shown to be produced by the recombination of excess carriers with unionized donor and acceptor centers (extrinsic recombination radiation). Differences between the photon energies associated with the maximum photon emission of intrinsic and extrinsic radiation are qualitatively in accord with accepted values of ionization energies of the donor and acceptor impurities introduced in the silicon crystal growing process.

[1] J. R Haynes and H. B. Briggs, Phys. Rev. **86**, 647 (1952).

T6. The Field Effect in Silicon. S. Penman and W. L. Brown, *Bell Telephone Laboratories.*—Field effect measurements were made on silicon using large ac electric fields (peak $\sim6\times10^5$ volt/cm). The samples were first dried by heating in a desiccated nitrogen atmosphere and then the field effect studied as a function of temperature and various gaseous ambients. Oxygen tends to change the surface potential in the negative direction and nitrogen in the positive direction. Effective mobilities were found to be about an order of magnitude smaller than bulk carrier mobilities, in contrast to the results reported by Low.[1] The observation of the minimum of conductance permits the determination of the surface charge as a function of the position of the Fermi level at the surface.[2] The surface state distribution is found to be more uniform than in the germanium case with an apparent density at the center of the energy gap of about 10^{13} states/cm^2 volt. Water vapor is responsible for a substantial increase in the apparent surface state density, often to such an extent that the effective mobility is reduced below the limit of our observation (≈1 cm^2/volt sec).

[1] G. G. C. Low, Proc. Phys. Soc. (London) **B68**, 10 (1955).
[2] W. L. Brown, Phys. Rev. **98**, 1565 (1955).

T7. Thermal Defects in Silicon. C. J. Gallagher, *General Electric Research Laboratory.*—Single crystals of p-type silicon quenched from high temperatures, show marked changes in room temperature resistivity. Quenched samples are less p-type, suggesting that quenching introduces donor states in the forbidden band. Measurements of resistivity *vs* temperature give activation energies ranging from 0.35 to 0.40 ev above the valence band. Donor density (N_D), as deduced from the activation energy, acceptor density, and position of the Fermi level, varies with quench temperature according to the relation $N_D = N_0 \exp -E/kT$, where $N_0 \cong 10^{22}$ cm^{-3} and $E = 1.7$ ev. Quench temperatures ranged from 800°C to 1350°C The density of donors observed at 1350°C was about 10^{17} cm^{-3}. Quenching was done by heating in an all quartz furnace in argon, and dropping the crystal into a silicone oil bath. Small cross-section samples were used to minimize inhomogeneities. Rapid quenching is essential since annealing effects are observed at temperatures above 100°C. At 200°C, samples anneal back to their initial resistivities in two hours, with a time constant for the initial disappearance of donors of about 10 minutes.

T8. Properties of Zn-Doped Germanium. H. H. Woodbury and W. W. Tyler, *General Electric Research Laboratory.*—In addition to the 0.03 ev level observed by Dunlap,[1] Zn introduces a deeper acceptor level 0.09 ev from the valence band of Ge. The presence of two acceptor levels in equal concentrations is indicated by the temperature dependence of Hall coefficient in Zn-doped crystals containing no other impurities. The energy of the 0.09 ev level is most accurately obtained from the temperature dependence of Hall coefficient for samples in which the lower Zn levels have been compensated. No evidence for more than two Zn levels has been obtained in samples for which both the 0.03 ev and 0.09 ev levels have been compensated. Thus Zn is a double-acceptor impurity similar to other elements (Fe, Co, Ni, Mn) with a $4s^2$ configuration. The maximum Zn concentration obtained in single crystals of Ge is about 2×10^{18} cm^{-3}. Appreciable evaporation of Zn from the Ge melt during crystal growth precludes accurate determination of the distribution coefficient. However, Hall measurements on samples which crystallized immediately after Zn doping of the melt give k_0 values of $4\pm2\times10^{-4}$ for a variety of growth rates and Zn concentrations.

[1] W. C. Dunlap, Jr., Phys. Rev. **96**, 40 (1954).

T9. Scattering of Carriers from Doubly Charged Impurity Sites in Germanium. W. W. Tyler and H. H. Woodbury, *General Electric Research Laboratory.*—The effect of charged impurity sites on carrier mobility in Ge has been studied in both equilibrium and photoconductivity measurements. At 300°K the relative magnitude of hole mobility in Zn-doped and Ga-doped crystals indicates that the scattering cross section for doubly charged Zn sites is four times that for Ga sites. On cooling, Zn-doped crystals show regions of increasing mobility corresponding to the conversion of doubly to singly charged sites (0.09 ev freeze-out) and from singly charged to neutral sites (0.03 ev freeze-out). For compensated n-type samples containing double-acceptor impurity sites, intrinsic photoconductivity experiments indicate that an increase in free electron concentration is accompanied by an increase in electron mobility due to unit reduction of charge associated with hole trapping at the impurity sites. Changes in mobility are consistent with the Z^2 scattering law. In heavily doped Ge crystals (Mn,Zn), this mobility increase represents an appre-

ciable fraction of the photoconcudtivity. On saturation of hole trapping (Fe- and Mn-doped samples) the steady-state concentration of trapped holes is approximately equal to the impurity concentration. Thus hole trapping is unambiguously identified with specific double-acceptor impurities.

T10. Valence Bond Calculations of Acceptor Energies in Silicon and Germanium. R. G. SHULMAN, *Bell Telephone Laboratories.*—Recent experiments[1] have shown that boron, aluminum, gallium, and indium, acting as acceptors in silicon, have levels located at different energies in the forbidden gap. Optical measurements[2] indicate that the variation is primarily in ground state energies while energies of the excited nonpenetrating p-type states are relatively constant. These differences indicate the necessity of considering the specific contribution of the acceptor atom. Energies of tight bonding models are calculated using Morse curves to approximate interatomic potentials. The additional binding energy increases sharply from gallium to indium in qualitative accord with experiment. Silicon levels are more sensitive to the acceptor atom than germanium.[3] This can be understood by treating the additional binding energy as a perturbation in an effective mass calculation.

[1] Morin, Maita, Shulman, and Hannay, Phys. Rev. **96**, 833 (1954).
[2] Burstein, Picus, Henvis, and Lax, Phys. Rev. **98**, 1536 (1955).
[3] T. H. Geballe and F. J. Morin, Phys. Rev. **95**, 1085 (1954).

T11. Precipitation of Cu in Plastically Deformed Germanium. A. G. TWEET, *General Electric Research Laboratory.*—Bars of p-type Ge (5–15 ohm-cm)~1 mm×2.5 mm×20 mm have been twisted 30° and straightened in 90% N_2 and 10% H_2 at 500°C–525°C. These samples, together with similar undeformed specimens, were then saturated with Cu[1] at 700°C in H_2. Upon annealing at 450°C in H_2 it was observed that the Cu acceptor concentration, as determined by Hall effect measurements, is given by $N(t)=N_0e^{-t/\tau}$ for all specimens during most of the annealing process. N_0 is the initial acceptor concentration due to Cu and t is the time. For the deformed samples $\tau \cong 1$ hour, while for the undeformed samples τ is markedly greater, $\tau > 60$ hours. These data are consistent with some observations by Logan[2] upon the same system. If the precipitation is diffusion limited, which is consistent with the above rate law, and if the dislocations are copper sinks, these data indicate that the effective copper diffusion coefficient at 450°C is very much smaller than that obtained by extrapolating Fuller's data.[1] Such a reduction in diffusion coefficient would result if the Cu^+ concentration is very small.

[1] Fuller, Struthers, Ditzenberger, and Wolstirn, Phys. Rev. **93**, 1182 (1954).
[2] R. A. Logan, Phys. Rev. **99**, No. 6 (1955).

T12. Polarization of Impurities in Germanium.* F. D'ALTROY AND H. Y. FAN, *Purdue University.*—Attenuation and phase shift of 3 cm microwaves in transmission through germanium were measured at 4.2°K, at which temperature the dc resistivity of the samples used was orders of magnitude higher than at room temperature. In pure samples, the dielectric constant, ϵ, obtained is 16 ± 0.5. In samples, with a carrier concentration of the order of 10^{17} cm^{-3} in the exhaustion range, higher ϵ and conductivities higher than σ_{dc} were observed. The effect is attributed to the polarization and absorption associated with neutral impurities. This effect is superimposed on the carrier effect which is the only one responsible for the dc conductivity. The polarizability per neutral impurity atom increases with the concentration of the dominant impurity. Impurity ionization energy was estimated using the hydrogenic model. Data for samples with very low σ_{dc} and negligible carrier effect give $E_i=0.0094$ ev for antimony and $E_i=0.0076$ ev for gallium at an impurity concentration around 10^{16} cm^{-3}. At concentrations close to 10^{17} cm^{-3}, estimated E_i drops to about 0.0045 ev. From the carrier effect, it was estimated that the conductivity effective mass is over 1000 m. This is in agreement with the hypothesis that the dc conductivity is associated with carriers in an impurity band of high effective mass.

* Work supported by a Signal Corps Contract.

T13. Surface States on Silicon. H. STATZ, G. A. DEMARS, L. DAVIS, JR., AND A. ADAMS, JR., *Raytheon Manufacturing Company.*—Measurements of the conductivity of p-type inversion layers on n-type silicon have been made. The measurements correspond to experiments carried out with germanium.[1] Steady state conductance of the inversion layers as a function of bias voltage can again be interpreted by assuming such a large total density of surface states that the quasi-Fermi level at the surface cannot shift by a measurable amount with respect to the energy bands. After the bias voltage is changed, the conductance again approaches very slowly a new equilibrium value. The time constant of this transient may be of the order of one hour and thus is longer than the corresponding ones observed for germanium. The transient behavior can be explained in terms of "slow" surface states on the silicon oxide surface and "fast" states at the silicon-silicon oxide interface. Analysis of nonsteady state conductance curves gives a single energy level for the fast states with an energy of approximately 0.4 ev. below the middle of the energy gap. For the investigated specimen, the density of these states is approximately 10^{12} states/cm^2 and therefore higher than the corresponding densities found on germanium surfaces.

[1] deMars, Statz, and Davis, Phys. Rev. **98**, 539 (1955), and Statz, Davis, and deMars, Phys. Rev. **98**, 540 (1955).

SATURDAY AFTERNOON AT 1:45

Kent 106

(V. A. JOHNSON presiding)

Semiconductors, III

U1. Neutron Irradiated Silicon.* THOMAS A. LONGO AND DAVID KLEITMAN, *Purdue University.*—After fast neutron irradiation at 45°C[1] the temperature dependence of Hall coefficient and resistivity of both n-type and p-type single crystal silicon samples indicated that intrinsic behavior was approached in each sample. A 1.75μ peak in the optical absorption coefficient was observed. This peak, previously observed in polycrystalline silicon,[2] is believed to result from optical excitation rather than ionization of an introduced defect level since it is not accompanied by an increase in photoconductivity. Appreciable photoconductivity was observed beyond the fundamental region to about 1.5μ after which there is a sharp drop with a shoulder in the region between 2 and 3μ. Annealing experiments were continued on a polycrystalline

p-type silicon sample which had been previously irradiated with fast neutrons.[3] After annealing at temperatures ranging 150°C to 250°C the slopes of the Hall coefficient and resistivity *vs* $10^3/T$ decreased suggesting the rearrangement of introduced defect levels accompanying annealing. During annealing the absorption peak at 1.75μ gradually disappears and absorption extending past 30μ increases.

* Supported by a Signal Corps contract.
[1] Samples irradiated by the Oak Ridge Solid State Group.
[2] Becker, Fan, and Lark-Horovitz, Phys. Rev. 85, 730(A) (1952).
[3] R. W. Dreyfus, M.S. thesis, Purdue University, 1953.

U2. Deuteron Irradiation of Germanium at 90°K.* D. KLEITMAN AND T. A. LONGO, *Purdue University*.—Layers of germanium single crystals 100μ thick have been irradiated at 90°K with 9.6-Mev deuterons from the Purdue cyclotron. The initial rate of carrier removel with flux, $dn/d\varphi|_0$ depends upon the Fermi level (or initial carrier concentration). Rate of carrier removal decreases with irradiation. For two n-type samples with $n_0=9.9\times10^{13}$ cm^{-3} and 2.2×10^{13} cm^{-3} respectively, $dn/d\varphi|_0$ was -0.7×10^3 cm^{-1} and -3.5×10^3 cm^{-1}; the samples were converted to p-type after fluxes of 7×10^{11} deut./cm^2 and 3.5×10^{15} deut./cm^2 respectively. After warming to 300°K converted samples remained p-type. Incremental conductivity, $\Delta\sigma$, under white light illumination, increases with bombardment of n-type material, (minority carrier trapping), then falls, passing through a minimum just after conversion to p-type. After conversion, $\Delta\sigma$ again rises then finally falls off after prolonged bombardment. A shoulder to the fundamental photoconductivity near 2.3μ, and a peak at 3.5μ appear in n-type samples before conversion. After conversion a negative $\Delta\sigma$ was observed near 2.1μ, due to electron excitation from a discrete level to the conduction band and subsequent carrier recombination. The photoconductive observations are similar to those after electron bombardment.[1]

* Supported by a Signal Corps contract.
[1] Stoeckmann, Klontz, Fan, and Lark-Horovitz, Phys. Rev. 98, 1535 (1955).

U3. Thresholds for Electron Bombardment Induced Lattice Displacements in Si and Ge. PAUL RAPPAPORT AND JOSEPH J. LOFERSKI, *RCA Laboratories*.—In a recent letter[1] we presented preliminary results of experiments designed to locate the threshold energy for production of defects, probably vacancy-interstitial pairs, in Si and Ge, by high-energy electron bombardment. The method consisted of observing the properties of p-n junctions during bombardment as a function of the energy of the electrons (V_B). Because of limitations in the Van de Graaf machine, only upper limits to the thresholds were reported. However, recent improvements in the machine have made definitive experiments possible using the same technique. The significant results are that no radiation damage (at 300°K) was observed for electrons with $V_B<145$ kev in Si and $V_B<325$ kev in Ge. The maximum energy which can be imparted to an atom by an electron of threshold energy (which is interpreted as the minimum energy expended in generating a vacancy-interstitial pair, E_{Lmin}) is found to be 12.9 ev for both Si and Ge. Our results should be compared to (a) $E_{Lmin}=31$ ev deduced by Klontz from bombardment induced resistivity changes at 90°K, (b) the Wigner energy, $E_{Lmin}\approx25$ ev, (c) and the speculation by Kohn,[2] that $E_{Lmin}<15$ ev in Ge.

[1] J. J. Loferski and P. Rappaport, Phys. Rev. 98, 1861 (1955).
[2] W. Kohn, Phys. Rev. 94, 1409(A) (1954).

U4. Tracer Studies on Radiation Damaged Graphite.* G. L. MONTET, A. F. KURS, AND G. R. HENNIG, *Argonne National Laboratory*.—A study of the distribution of displaced carbon atoms in radiation damaged graphite[1] has been made using a radioactive tracer technique. Radioactive carbon (C^{11}) atoms produced by neutron or γ-ray bombardment occupy interstitial positions and act as tracers for displaced atoms. After partial annealing the distribution of the radioactive atoms was determined by controlled oxidation of the graphite and counting of carbon dioxide gas samples. The experiments indicate that appreciable motion of the displaced atoms begins at 400°C and ceases at 800°C, although complete reintegration with the lattice is achieved only by heating to 1700°C. The behavior during annealing of the displaced atoms was found to be very sensitive to the amount of damage produced in graphite. Analysis of the data on the assumption that graphite consists of perfect regions surrounded by mosaic boundaries leads to an average linear extent of the "perfect regions" of about 2600 A. A bombardment of 10^{17} neutrons-cm^{-2} introduces enough traps within the "perfect region" so that only one-fifth of the displaced atoms can reach the boundaries.

* Based on work performed under the auspices of the U. S. Atomic Energy Commission.
[1] M. Burton, J. Phys. Colloid Chem. 51, 618 (1947).

U5. Excess Noise in Plastically Deformed Germanium. JAMES J. BROPHY, *Armour Research Foundation*.—The excess noise levels of several samples of plastically deformed germanium have been examined. Single crystal, n-type germanium specimens of five ohm-centimeter resistivity were plastically deformed by bending in air at 600°C. After deformation, the samples were still n-type but the resistivity was increased by a factor of about two. These were sandblasted into 'bridges" similar to those used by Montgomery[1] to eliminate effects due to noisy electrodes. The excess noise level is increased three or four orders of magnitude by deformation and may be represented by $\langle\Delta v^2\rangle=KI^{4.5}f^{-1.0}$ volts^2/cycle, where $\langle\Delta v^2\rangle$ is the mean square excess noise voltage, I is the sample current in milliamperes, f is the frequency, and K is a constant of the order of 10^{-13}. The usual inverse frequency spectrum characteirstic of excess noise is observed, but the current dependence differs from the usual square law variation expected for a conductivity modulation phenomena.

[1] H. C. Montgomery, Bell System Tech. J. 31, 950 (1952).

U6. Electrical Properties of Mg_2Sn at Low Temperatures. W. R. HOSLER AND H. P. R. FREDERIKSE, *National Bureau of Standards*.—Conductivity and Hall coefficient of several n- and p-type single crystals were measured in the range from 2 to 300°K. In most specimens both acceptors and donors are present. The number of carriers at exhaustion lies between 10^{16} and 10^{17} cm^{-3}. Maxima in the Hall coefficient were observed in all samples at low temperatures, while the slope of the conductivity becomes very small in this region. The position of the Hall maxima varies between 6 and 66°K; impurity activation energies (as calculated from the slope of $RT^{\frac{3}{2}}$ *vs* $1/T$) range from 0.003 to 0.03 ev. Similar effects have been observed in Ge and InSb; this behavior has been attributed to impurity band conduction.[1] The Mg_2Sn compound shows an additional feature: all samples approach about the same Hall coefficient (4500–6500 cm^3/coulomb) in the helium range independent of the value at exhaustion. The product $R\sigma$ of different samples lies between 15 and 30 cm^2/volt-sec at very low temperatures.

[1] Hung and Gliessmann (1950); Hrostowski (1955); Fritzsche, Phys. Rev. 99, 400, 406 (1955).

U7. Electrical Properties of the Semiconductors Mg_2Si and Mg_2Ge.* C. R. WHITSETT AND G. C. DANIELSON, *Iowa State College*.—The electrical resistivities and Hall coefficients of single crystals of Mg_2Si and Mg_2Ge have been measured in the temperature range 60°K to 1000°K. Since the Hall coefficients were always negative, electron conduction always predominated over hole conduction in these particular samples. At 300°K the densities of electrons from impurity levels were 10^{17} to 10^{18} per cm^3 and the Hall mobilities were about 200

cm²/volt-sec. Above 300°K the temperature dependence of the mobility in Mg_2Si was given by $9(10^8)T^{-1}$ cm²/volt-sec, but in Mg_2Ge the temperature dependence was more complicated. In the intrinsic conduction region ($T>500$°K) the resistivities were found to be given by $\rho=A\exp(\Delta E/2kT)$ with $A=0.00032$ ohm-cm and $\Delta E=0.48$ ev for Mg_2Si and $A=0.00012$ ohm-cm and $\Delta E=0.64$ ev for Mg_2Ge. It was estimated that for Mg_2Si $\mu_n/\mu_p\sim1.3$ and for Mg_2Ge $\mu_n/\mu_p>2.5$. The effective masses of electrons and holes in Mg_2Si were estimated to be respectively 1.8 and 2.0 times the free electron mass.

* Work was performed in the Ames Laboratory of the U. S. Atomic Energy Commission.

U8. Reduction of Charge Carrier Concentration in InSb at 4.2°K by a Strong Magnetic Field. R. W. KEYES AND R. J. SLADEK, *Westinghouse Research Laboratories.*—Hall measurements on *n*-type InSb indicate that the concentration of mobile charge carriers is not drastically reduced by cooling from 77°K to 4.2°K. Adams[1] has pointed out that at magnetic fields of about 10 000 gauss the cyclotron radius becomes equal to the Bohr radius in *n*-type InSb and consequently an appreciable lowering of the impurity energy level is to be expected at higher fields. To check these ideas the electrical resistivity and Hall effect of two *n*-type InSb samples[2] having donor concentrations of $\sim10^{14}$ and $\sim10^{16}$ cc^{-1} were measured at 4.2°K in a (transverse) magnetic field of intensities up to 82 500 gauss using the high magnetic field facilities of the Cryogenics Branch at the Naval Research Laboratory. The Hall measurements indicate that a large reduction of the charge carrier concentration occurred in the $\sim10^{14}$ sample but not in the $\sim10^{16}$ sample. In addition the Hall mobility was strongly field dependent in both samples. The temperature dependence of the Hall coefficient showed no anomalies of the type usually attributed to impurity band formation.

[1] E. N. Adams (private communication).
[2] Obtained from Dr. S. Kurnick, Chicago Midway Laboratories.

U9. Electrical Breakdown in InSb at Low Temperature. RALPH BRAY, *Purdue University.*—Reversible electrical breakdown in *p*-type InSb has been observed at 4.2°K under pulse conditions. It is characterized by a vertical rise in current, followed by a negative resistance region, and results in increase in conductivity by a factor $\gtrsim10^6$. The effect resembles low temperature breakdown in Ge,[1] which has been attributed[2] to free carrier multiplication by impact ionization of neutral impurities. Breakdown occurred at 43 volt/cm in samples having $\sim4\times10^{13}$ holes/cm³ at exhaustion, and Hall mobility ~4000 cm²/volt sec at 77°K. At low voltage, at 4.2°K, the samples exhibited the Hung anomaly[3] in Hall effect and resistivity, and gave, in transverse magnetic field (3000 gauss), the anomalous *negative* magnetoresistive ratio,[3] $[(\Delta\rho/\rho u)\sim-2\%]$. At higher voltage, in the prebreakdown region of slowly rising conductivity, a *reversal to positive* magnetoresistive ratio was obtained. The magnetic field increased the critical breakdown electric field. It seems therefore that the negative magnetoresistive effect is associated solely with the conduction in the impurity band.

[1] F. J. Darnell and S. A. Friedberg, Phys. Rev. **98**, 1860 (1955). This latest reference contains the previous references.
[2] Sclar, Burstein, Turner, and Davisson, Phys. Rev. **91**, 215(A) (1953).
[3] H. Fritzsche and K. Lark-Horovitz, Phys. Rev. **99**, 400 (1955).

U10. Plasma Resonance in Semiconductor Crystals. G. DRESSELHAUS, A. F. KIP, AND C. KITTEL, *University of California, Berkeley.*—Observations are reported of an electron plasma resonance absorption line in a magnetic field in an *n*-type crystal of InSb at 9000 and 24 000 Mc and at 4° and 77°K. The magnitude of the plasma frequency and its dependence on rf frequency and on the orientation of the figure axis of the specimen relative to the static magnetic field are in approximate agreement with the elementary theory of the plasma resonance developed previously by the authors. For a spherical sample and an isotropic effective mass m^*, the resonance occurs at a magnetic field such that $\lambda_c=\omega-\omega_p^2\omega^{-1}$, where $\omega_c=eH/m^*c$, ω is the applied microwave angular velocity,

$$\omega_p^2=\frac{4\pi Ne^2}{3m^*}\left(1+\frac{4\pi}{3}\chi\right)^{-1},$$

N is the carrier concentration, and χ is the dielectric susceptibility. The line shape for experiments carried out under conditions of carrier modulation are "derivative like" due to the dependence of the resonance frequency on carrier concentration. The effect can be used to determine experimentally the value of the charge density. The experimental measurements of carrier density in InSb thus far have been only approximate because of the difficulty of obtaining good geometry at the small dimensions required to stay within the skin depth limitation.

U11. Preparation and Electrical Properties of Bi_2Te_3.* T. C. HARMAN, S. E. MILLER, AND H. L. GOERING, *Battelle Memorial Institute.*—Bi_2Te_3 has been prepared by a number of techniques from zone-melted Bi, and Te which has been purified by multiple distillation. For thermoelectric device applications, it was found that the best technique for preparing both *n*-type and *p*-type Bi_2Te_3 is quenching the compound from above its melting point and annealing for long periods of time near its melting point. For the preparation of single crystals for fundamental studies, the best technique was found to be zone melting in a tellurium atmosphere. Bi_2Te_3 dissociates to some extent at the melting point and the elements, Bi and Te, have segregation coefficients near unity. Iodine and excess Te are *n*-type impurities in Bi_2Te_3, while Pb and excess Bi are *p*-type. The resistivity and thermoelectric power have been measured as functions of temperature from 200°K to 700°K for *n*-type and *p*-type specimens with varying impurity concentrations. A *p*-type specimen had a thermoelectric crossover at 450°K. An *n*-type specimen had a thermoelectric power of -180 $\mu v/°C$ at 300°K. The intrinsic resistivity slope indicates a small energy gap.

* This work is supported by a contract with the Tellurium Development Committee.

SATURDAY AFTERNOON AT 1:30

Mandel Hall

(L. W. ALVAREZ presiding)

Invited Paper

V1. Properties of Heavy Mesons Produced at the Bevatron. GERSON GOLDHABER, *University of California, Berkeley.* (30 min.)

Heavy Mesons and Hyperons

V2. Production of Hyperons and *K*-Mesons in the High Energy* π^- Beam of the Berkeley Bevatron. MARCEL SCHEIN AND D. M. HASKIN, *University of Chicago.*—Stacks of Ilford G-5 pellicles have been exposed to the 4.8 Bev and 3.0 Bev negative pion beams of the Berkeley Bevatron. A number of heavy unstable particles have been found and have been traced back to the star in which they originate. Of particular interest are cases of K^- production, since it can be assumed that they originate according to the reaction

$$\pi^- + P \rightarrow K^+ + K^- + N.$$

The observed K^+/K^--ratio is roughly one in the π^- beam in contrast to 100 in the proton beam, which supports this hypothesis. In addition, one event has been located in which a π meson undergoes a nuclear collision resulting in a track of minimum ionization and a K^+-meson. No other fragments are visible in the collision. This fact together with the approximate validity of conservation laws in the elementary interaction supports the above suggested interpretation.

* Supported in part by a joint program of the Office of Naval Research and the U. S. Atomic Energy Commission.

V3. Hyperfragments in Light Elements Produced by the Berkeley Bevatron.* DANIEL LEENOV, D. M. HASKIN, AND MARCEL SCHEIN, *University of Chicago.*—A number of hyperfragments have been observed in exposures to the 3.0-Bev and 4.8-Bev π^- and the slow K^- beams of the Berkeley Bevatron, including cases of H_1^{3*} and H_1^{4*}, in which one neutron is replaced by a Λ^0 hyperon. A H_1^4 was produced by the nuclear capture of a Σ^- hyperon which was in turn produced by the interaction of a 3.0 Bev negative pion. It is proposed that the production of the Λ^0 results from the reaction $\Sigma^- + P \rightarrow \Lambda^0 + N$. In the case in question, a 255 μ long track with charge one stops and undergoes a colinear decay into a negative pion and a He_2^4 recoil. The pion was followed to the end of its range and the total energy release in the decay was found to be 50.8 Mev, giving a binding energy for the Λ^0 in H_1^{4*} of 7 ± 2 Mev. Cases of tritium hyperfragments giving events with two protons and a π meson will be discussed. The binding energy of the Λ^0 hyperon in tritium was found to be 5 ± 2 Mev.

* Supported in part by a joint program of the Office of Naval Research and the U. S. Atomic Energy Commission.

V4. Analysis of Capture Stars of K^--Mesons from the Berkeley Bevatron.* D. M. HASKIN, D. B. WILLIAMS, E. GOODMAN, AND MARCEL SCHEIN, *University of Chicago.*—K^--stars produced by 6.2 Bev protons have been found in a magnetically analyzed channel of the Berkeley Bevatron. All of the observed events are consistent with the scheme of Gell-Mann and Pais. The following reactions are possible: $K^- + (P,N,P,N) \rightarrow (\Lambda^0,\Sigma^+,\Sigma^0,\Sigma^-) + \pi^0$; $K^- + (P,N,P) \rightarrow (\Sigma^+,\Lambda^0,\Sigma^0) + \pi^-$; and $K^- + P \rightarrow \Sigma^- + \pi^+$. The average prong number for the K^--stars is 3.3 indicating that Λ^0 hyperons must frequently escape from the absorbing nucleus. Two K^--stars have been found with the unusually large number of 10 visible prongs. The energies of the emitted π mesons fall into at least two distinct groups: (a) 50–80 Mev; (b) 100–140 Mev. This is in good agreement with the abovementioned reactions. Pions in group (b) are much less frequent than those in (a), indicating a higher recapture probability of the π^- at higher energy. Several cases of positive and negative hyperons and hyperfragments have been found and a few individual cases will be discussed. In one case, the capture of the K^- leads to the emission of two π mesons, one of them carrying an energy of 140 Mev and the other one much lower. The event can possibly be interpreted as: $K^- + N \rightarrow \Lambda^0 + \pi^-$ assuming the Λ^0 decays from an orbit inside the nucleus.

* Supported in part by a joint program of the Office of Naval Research and the U. S. Atomic Energy Commission.

V5. Nuclear Collisions of 5.7 Bev Protons and 3.0 Bev π^- Mesons.* R. E. CAVANAUGH, D. M. HASKIN, AND MARCEL SCHEIN, *University of Chicago.*—Stars produced by 5.7-Bev protons and 3.0-Bev π^- mesons from the Berkeley Bevatron have been found by the method of following along tracks in Ilford G-5 emulsion. The average prong number for the proton stars is 10.7 and for the pion stars 9.3. The maximum prong numbers observed are 30 and 20, respectively. The average number of visible shower tracks is 2.1 for the proton initiated stars, and 0.9 for the π^- initiated stars. The maximum number of shower tracks found amounted to 6 and 4 respectively. Among the proton events there are 3 cases where a pion is ejected into the backward hemisphere. No case of a similar kind has been found in the pion beam. From 50 events in each beam, the mean free path is found to be 37.6 ± 5.3 cm. and 35.5 ± 5.0 cm. This should be compared with the geometrical mean free path for nuclear collisions in the emulsion, which is 25 cm. The relatively large difference has interesting theoretical implications.

* Supported in part by a joint program of the Office of Naval Research and the U. S. Atomic Energy Commission.

V6. Disintegration of Hyperfragments. J. SCHNEPS, M. S. SWAMI, AND W. F. FRY, *University of Wisconsin.**—A systematic search for hyperfragments has been made in nuclear emulsion exposed to 6 Bev protons and 3 Bev π mesons from the Bevatron; to 3 Bev protons from the Cosmotron; and to cosmic rays. A total of eighty hyperfragments have been observed. The average Z of these hyperfragments is about 5. In most cases the kinetic energy of the hyperfragments is low, i.e., less than 15 Mev. It was possible to measure the binding energy of the Λ^0 particle in 3 cases of ${}_\Lambda H^3$, ${}_\Lambda H^4$, 2 cases of ${}_\Lambda He^4$, ${}_\Lambda He^5$, ${}_\Lambda Be^7$, ${}_\Lambda Be^8$ (or ${}_\Lambda Be^9$), ${}_\Lambda Be^{10}$ (or ${}_\Lambda Be^{11}$), and ${}_\Lambda C^{11}$. In general for $Z<3$ mesonic decay of hyperfragments is predominant while for $Z>3$ the nonmesonic decay is predominant. However an example of the nonmesonic decay of helium and of the mesonic decay of carbon have been observed. An estimate of the momentum of the bound Λ^0 hyperon can be obtained for the light nuclei.

* Supported in part by the Atomic Energy Commission and by the Graduate School.

V7. Proton Nucleus Collisions at 6 Bev.* U. HABER-SCHAIM, *University of Illinois.*—An analysis of stars produced by the proton beam of the Bevatron will be presented. The frequency distributions of heavy and light tracks and the angular distribution of light tracks will be discussed in relation to the mechanism of the proton nucleus collision.

* This work is supported by the Joint program of the Office of Naval Research and the U. S. Atomic Energy Commission.

V8. The Spin of the τ^+ Meson.* D. M. RITSON, A. ODIAN, B. T. FELD, AND A. WATTENBERG, *M. I. T.*—Measurements of the angular correlation and energy distribution of the π^- from 54 τ^+ mesons have been studied in a large emulsion stack irradiated in the Berkeley K^+-meson beam. An analysis based on the suggestions of Dalitz shows the π^- energy distribution of these 54 events to be asymmetric and favors a τ meson with spin 1 and even parity.

* This work has been supported in part by the Joint program of the Office of Naval Research and the U. S. Atomic Energy Commission.

V9. Effects of Angular Momentum on τ-Decay Schemes.* BERNARD T. FELD, *M. I. T.*—The angular correlation and energy distribution in the decay $\tau^+ \rightarrow \pi^+ + \pi^+ + \pi^-$ can be described, according to the method of Dalitz, in terms of the angular momenta l and L of the odd- and the *di-pi*, respectively

For l or $L>0$, angular momentum barrier penetration effects influence the energy distributions. Since the barrier penetration factors depend on the range of the forces between the decay particles, different assumptions as to this range lead to different results for the expected energy distribution of the odd π. Typical results will be shown to illustrate this effect. Another barrier effect is in the relative probability of the different possible decay modes, especially in cases in which there are two of comparable probability (e.g., a τ of spin 2 and negative parity can decay by $l=0$, $L=2$ and $l=2$, $L=0$). Angular distributions will be shown, under various assumptions concerning the force range, for these ambiguous decay schemes. Some of these effects have been discussed by Fabri at the Pisa Conference on Elementary Particles.

* This work has been supported in part by the joint program of the Office of Naval Research and the U. S. Atomic Energy Commission.

V10. π^--P Collisions at 1.0 Bev.* W. D. Walker and W. D. Shephard, *University of Wisconsin*.—Interactions of 1.0 Bev. π^- mesons with protons have been observed using the Brookhaven hydrogen diffusion Chamber. The present tabulation includes about 160 interactions. The cross sections observed are

Reaction products	σ in mb
$\pi^-+P(\theta_\pi<40°)$	20
$\pi^-+P(\theta_\pi>40°)$	6
$\pi^++\pi^-+N$	11.5
$\pi^-+\pi^0+P$	6.5
3π's+nucleon	~3
Associated pairs	~1

The diffraction cross section seems to be nearly equal to the inelastic cross section. This would indicate that for the $I=\frac{1}{2}$ state of the π^-P system that waves of $l=0,1,2k$ are almost completely absorbed. This corresponds to a range of interaction of about 8×10^{-14} cm. The inelastic processes are rather different from those observed at 1.5 Bev as far as the angular and momentum distributions. The angular distribution of the nucleons is nearly isotropic which is in contrast to the results at 1.5 Bev.

* This work has been supported by the U. S. Atomic Energy Commission and the Wisconsin Alumni Research Foundation.

V11. Production of Heavy Unstable Particles in π^-P Collisions at 1.0 Bev.* W. D. Shephard and W. D. Walker, *University of Wisconsin*.—In the course of the experiment on π^-P collisions at 1.0 Bev 5 examples of associated production in the gas have been found. There are three cases of $\Lambda^0-\theta^0$, one of "Ξ^0"$-\theta^0$,[1,2] and one of Σ^--K^+. The total cross section for the production of associated pairs at this energy seems to be about 1 mb. The hyperons, as observed by the Brookhaven group,[2] seem to decay preferentially in the plane of production. The angles observed between the plane of production and plane of decay of the hyperon are $20°\pm5°$, $40°\pm10°$, $36°\pm8°$, $10°\pm5°$, $10°\pm5°$. The observed angles of production of the hyperons in the π^-P center of mass seem consistent with an isotropic distribution. This result seems to hold for the Λ^0's emerging from the walls of the chamber also. These results are to be compared with the Brookhaven group's results at 1.4 Bev in which the hyperons seem to go preferentially in the backward hemisphere.[1]

* This work has been supported by the U. S. Atomic Energy Commission and the Wisconsin Alumni Research Foundation.
[1] Fowler, Shutt, Thorndike, and Whittemore, Phys. Rev. **98**, 121 (1955).
[2] W. D. Walker, Phys. Rev. **98**, 1407 (1955).

V12. Double-Plate Cloud-Chamber Study of V^0-Particles. I. Classification. I. C. Gupta, W. Y. Chang, and A. Snyder, *Purdue University*.—During the past year, our two rectangular cloud chambers[1] have been used separately for the study of V^0-particles, each containing one 2-inch Pb plate and two thinner ones ($\frac{1}{4}$ and $\frac{1}{8}$ inch). Up to now 138 V-events have been obtained from about 60% of the films taken. 66 events show clear association with the nuclear interactions in the first or second plate and have been analyzed according to the $\alpha-\epsilon$ projection procedure.[2] $\alpha-\epsilon$ plots were prepared beforehand respectively for the θ^0 and Λ^0 particles of different momenta. For each event, α and ϵ values were found from the measured angles of the two decay products relative to the V^0-particle. With the help of the $\alpha-\epsilon$ plots, two alternative sets of ionizations of the decay products were obtained and compared with their measured ionizations. In this way, 31 events have been classified as θ^0 particles, 30 as Λ^0 particles, and 5 as neither. Coplanarity and isotropy of emission in the rest system are being investigated respectively from the distribution of the angle between the plane of the V-event and direction of the V^0-particle and that of the $\alpha-\epsilon$ points in the $\alpha-\epsilon$ plots.

[1] G. del Castillo, Ph.D. Thesis, Purdue University, 1954; Phys. Rev. **98**, 1163 (1955).
[2] J. Podolanski and R. Armenteros, Phil. Mag. **45**, 13 (1954); D. B. Gatyher, Phil. Mag. **45**, 570 (1954).

V13. Double-Plate Cloud-Chamber Study of V^0-Particles. II. Mean Decay Times of θ^0 and Λ^0 Particles. A. Snyder, W. Y. Chang, and I. C. Gupta, *Purdue University*.—The mean decay times of the 31 θ^0 particles and 30 Λ^0 particles (see other abstract) have been calculated according to the statistical procedure of Bartlett.[1] For each event, the decay length, the "total potential" decay length, and the "plate-potential" decay lengths were measured from the same point 0.2 cm below the plate surface concerned. The terminal point of the "total potential" decay length was taken as one at which the shortest prong would have 3 cm from the illumination edge or the last plate. Since the V-events in the last gas space were ignored, the terminal point was not extended to this gas space. The velocity of the V^0-particle was calculated from the two distances of its $\alpha-\epsilon$ point to the foci of the $\alpha-\epsilon$ plot. Hence, the different decay lengths were converted into decay times. According to the statistical procedure for T/τ being small, the mean decay time for the 31 θ^0 particles is found to be $\left(1.83^{+0.35}_{-0.25}\right)\times10^{-10}$ sec, and for the 30 Λ^0 particle $\left(3.47^{+0.70}_{-0.49}\right)\times10^{-10}$ sec. Methods of measurements have been examined and will be discussed.

[1] M. S. Bartlett, Phil. Mag. **44**, 249, 1407 (1953).

V14. K-Meson Lifetimes.* Luis W. Alvarez, Frank S. Crawford, Jr., Myron L. Good, and M. Lynn Stevenson, *University of California, Berkeley*.—Since the various species of K-mesons produced at the Bevatron have masses equal within the rather small experimental error,[1] it becomes a critical matter to see if the lifetimes of the separate species are the same, or different. A counter experiment to investigate this point is being carried out. K^+-mesons, momentum-analyzed in the magnet arrangement of Kerth and Stork, are detected by a scintillation counter telescope and brought to rest in one of the scintillators. A side counter telescope of four counters detects the decay fragments, distinguishing between $K_{\tau2}$, $K_{\mu2}$, and τ decays. In one experiment in which 127 $K_{\mu2}$'s and 72 $K_{\tau2}$'s were observed to decay, preliminary results give equal lifetimes for the $K_{\mu2}$ and $K_{\tau2}$, approximately 1.3×10^{-8} sec. Results for the τ are not yet clear-cut.

* This work was performed under the auspices of the U. S. Atomic Energy Commission.
[1] R. W. Birge *et al.*, Phys. Rev. **99**, 329 (1955).

SATURDAY AFTERNOON AT 1:30

Eckhart 133

(M. B. SAMPSON presiding)

Reactions of Transmutation, II; Coulomb Excitation, Fission

W1. (p,α) Reactions in Cl and K. E. ALMQVIST, R. L. CLARKE, AND E. B. PAUL, *Chalk River Laboratories.*—The reactions $Cl^{35}(p,\alpha)S^{32}$, $Cl^{37}(p,\alpha)S^{34}$, $K^{39}(p,\alpha)A^{36}$, and $K^{41}(p,\alpha)A^{38}$ have been observed using a magnetic spectrometer, and their excitation functions and Q-values measured. Targets that measured about 1 kev thick for 1.9-Mev protons were used. The energy scale of the Van de Graaff generator was established by observing the $Li^7(p,n)Be^7$ threshold. The magnetic analyzer was calibrated using groups of α particles from reactions of precisely known Q-values. All measurements were made at 90° to the beam. The Q-values are

$Cl^{35}(p,\alpha)S^{32}$	$Q=1.865\pm0.015$ Mev
$Cl^{37}(p,\alpha)S^{34}$	$Q=3.015\pm0.015$ Mev
$K^{39}(p,\alpha)A^{36}$	$Q=1.267\pm0.020$ Mev
$K^{41}(p,\alpha)A^{38}$	$Q=4.002\pm0.015$ Mev.

Eighteen well-defined resonances corresponding to levels in A^{36} were observed in the $Cl^{35}(p,\alpha)$ reaction between 1.30- and 2.51-Mev proton energy. Twenty-two resonances corresponding to levels in A^{38} were observed in the $Cl^{37}(p,\alpha)$ reaction between 1.0- and 2.5-Mev proton energy. There is published data[1] up to 1.8 Mev which agrees with the present results.

[1] Brostrom, Madsen, and Madsen, Phys. Rev. **83**, 1265 (1951).

W2. Excitation Functions for Alpha-Induced Reactions on Lead.* WALTER JOHN,† *University of California.*—The excitation functions for alpha-induced reactions on several lead isotopes have been measured. A procedure has been developed for preparing enriched lead isotope targets by evaporation. Stacked foils were bombarded by the alpha-beam of the 60-inch cyclotron. The induced polonium alpha activities were separated by alpha pulse-height analysis. The measured excitation functions for $Pb^{206}+\alpha$ were compared to the excitation functions for $Bi+p$. Since the compound nucleus formed is the same, the comparison gives a test of the predictions of Bohr's compound nucleus theory. The ratios of corresponding cross sections are in agreement with the compound nucleus theory. However, the excitation functions are displaced in energy by an amount not predicted by the theory. The discrepancy, 0.8 Mev is slightly outside of the errors. The comparison of $Ni^{60}+\alpha$ and $Cu^{63}+p$ made by Ghoshal[1] has been checked with more recent mass values and a discrepancy of 3.2 Mev is found. These discrepancies will be discussed.

* This research was performed under the auspices of the U. S. Atomic Energy Commission.
† Present address: Department of Physics, University of Illinois.
[1] S. N. Ghoshal, Phys. Rev. **80**, 939 (1950).

W3. The Photodisintegration of Lithium and Helium near 200 Mev.* J. H. SMITH AND M. Q. BARTON, *University of Illinois.*—We have made additional measurements of correlated protons and neutrons ejected from lithium and helium by 285-Mev bremsstrahlung using previously reported techniques.[1] Protons of several energies from 55 Mev to 130 Mev were observed at 75° to the x-ray beam, and the angular distributions of their correlated neutrons were measured. In general the results are consistent with a deutron-like interaction between nucleons in the complex nucleus modified by a reasonable ground-state momentum wave function. However, deviations from this model will be discussed.

* This work was supported in part by the joint program of the Office of Naval Research and the U. S. Atomic Energy Commission.
[1] M. Q. Barton and J. H. Smith, Phys. Rev. **95**, 573 (1954).

W4. High-Energy Photoproton Emission at 175°.* C. A. TATRO AND T. R. PALFREY, JR., *Purdue University.*—The Z dependence of the cross section for emission of 50- to 75-Mev photoprotons at 175° in the laboratory has been measured. Targets of Be, C, Al, Cu, Cd, and Pb were bombarded by a 280-Mev gamma-ray bremsstrahlung spectrum from the Purdue electron synchrotron. A three-counter telescope placed behind a deflection magnet detected the emitted protons, which were identified by pulse-height analysis of photographs of the three counter pulses. Absolute cross sections have been obtained for two energy intervals, and Z dependences for three energy groups. Contrary to the results of previous experiments at more forward angles, where the cross section was found to be proportional to Z, the ratio σ/Z at 175° increases by a factor of about 1.7 between Be and Pb, rising most rapidly between Be and Al.

* Supported in part by the U. S. Atomic Energy Commission.

W5. Coulomb Excitation of Energy Levels in Br and Re. E. A. WOLICKI, L. W. FAGG, AND E. H. GEER, *Naval Research Laboratory.*—Isotopically enriched targets of KBr and metallic Re have been bombarded with protons and alpha particles. The following gamma rays have been observed as a result of Coulomb excitation: Br^{79} 219 kev; Br^{81} 278 kev; Re^{185} 126, 160, 286 kev; and Re^{187} 135, 168, 303 kev. Coincidences have been observed between the 126 and 160 and between the 135 and 168 kev gamma rays. Reduced transition probabilities have been measured. In the case of the Re isotopes, cascade to crossover ratios have been obtained. Measurements on the Re nuclei are in agreement with the results of other workers.[1,2]

[1] McClelland, Mark, and Goodman, Phys. Rev. **97**, 1191 (1955).
[2] H. Mark and G. Paulissen, Phys. Rev. **99**, 1654(A) (1955).

W6. Coulomb Excitation of In^{115m} by Alpha Particles.* R. R. MCLEOD, *Purdue University.*—The thick-target activation curve for production of the isomer In^{115m} (4.5 hours) by alpha particles in the energy range from 7 to 20 Mev has been measured. The cyclotron was utilized as the source of alpha particles. The absolute isomeric yield was determined at each alpha-particle energy from measurements of the intensity of the 335-kev gamma radiation of In^{115m}, using a well-type scintillation counter and a twenty-channel analyzer. The energy dependence of the cross section obtained from the thick-target yield is consistent with the excitation of one quadrupole level of approximately 1.5-Mev energy, from which the isomeric state is reached by spontaneous decay processes. The contribution from direct excitation of the isomeric state is negligible.

* Supported in part by the U. S. Atomic Energy Commission.

W7. Coulomb Excitation of Samarium.* B. E. SIMMONS,† K. F. FAMULARO, AND G. D. FREIER, *University of Minnesota.*—Equipment previously described[1] was used to detect gamma rays produced by proton bombardment of isotopically enriched samarium (thick oxide) targets. Results below are gamma-ray energy; isotopic origin; excitation function agreement with Coulomb excitation theory[2] for E-2 and for E-1 interactions; and, at proton energy E_p, angular distribution coefficients $a_i)_t$ in $1+0.3571a_2)_tP_2(\cos\theta)+1.143a_4)_tP_4(\cos\theta)$. The $a_i)_t$ agree with empirical E-2 results of McGowan and

Stelson[3] but not with E-2 theory.[3] Nuclear transition probabilities are being calculated.

E_γ-kev	Origin	E-2 e.f.	E-1 e.f.	$a_2/_1$	$a_4/_1$	E_p-Mev
85±3	Sm^{154}	yes	no	0.281±0.072	−0.021±0.029	2.07
124±2	Sm^{152}	yes	no	0.346±0.033	+0.016±0.015	2.28
337±3	Sm^{150}	yes	yes	0.815±0.095	−0.069±0.039	2.61
562±8	Sm^{148}	(weak)	...	...	...	...

* This work supported in part by the Office of Naval Research and the U. S. Atomic Energy Commission.
† Now at the Knolls Atomic Power Laboratory.
[1] Simmons, Van Patter, Famularo, and Stuart, Phys. Rev. 97, 89 (1955).
[2] K. Alder and A. Winther, Phys. Rev. 96, 237 (1954), and private communication, 1954.
[3] F. K. McGowan and P. H. Stelson, Phys. Rev. 99, 127 (1955).

W8. Coulomb Excitation of Re, In, and Hg by Protons. ROBERT H. DAVIS, AJAY S. DIVATIA, R. D. MOFFAT, AND D. A. LIND, *University of Wisconsin.**—Thick targets of natural and isotopically enriched rhenium, iridium, and mercury in the form of metallic and oxide powders have been bombarded with protons of energies up to 3.2 Mev. To analyze the composite spectra, the resolution, variation of Compton shape with gamma energy, and the efficiency of the scintillation spectrometer were determined by means of absolutely calibrated gamma-ray sources. The agreement between the observed dependence of gamma-ray yield on proton energy and that predicted by Coulomb excitation theory for $E2$ transitions identified the following gamma rays (in kev) as decay radiations from Coulomb excited energy levels: Re^{185}, 125, 158, 280; Re^{187}, 135, 163, 300; Ir^{191}, 115, 133, 216, 356; Ir^{193}, 143, 230, 368; Hg^{199}, 159, 209; Hg^{200}, 375. An additional line from Hg at 424 kev was observed. The deformation parameters evaluated from the cross sections have been compared with those determined from the excitation energy; the deformation seems to fit the systematic trend already established in this mass region. The presence of the 115-kev line belonging to In^{191} implies the existence of a level at this energy in addition to the known levels at 133 and 356 kev. The error in the energy assignments depends on the complexity of the particular composite peak and varies from 1 to 3%.

* Work supported by the U. S. Atomic Energy Commission and the Wisconsin Alumni Research Foundation.

W9. Coulomb Excitation of In^{115}, I^{127}, Ta^{181}, Th^{232}, and U^{238}. AJAY S. DIVATIA, ROBERT H. DAVIS, R. D. MOFFAT, AND D. A. LIND, *University of Wisconsin.**—Gamma rays resulting from proton or alpha-particle bombardment of In^{115}, I^{127}, Ta^{181}, Th^{232}, and U^{238} were studied using a NaI(Tl) scintillation spectrometer. Gamma-ray yields were measured as a function of the incident particle energy and compared with the theory of electric excitation. Reduced transition probabilities for excitations have been obtained from absolute cross-section measurements and compared with their values based on single particle estimates. The gamma rays observed under proton bombardment are, In^{115}: 512±12 kev; I^{127}: 208±7, 392±8, 438±10, 631±10, 751±25, 941±50 kev; and Ta^{181}: 137±3, 165±4, 302±4 kev. Those observed under alpha-particle bombardment are, I^{127}: 60±2, 201±4 kev; Th^{232}: 50±5 kev; and U^{238}: 45±3 kev. The yields for the gamma rays of Ta^{181} have been compared with those obtained by Stelson and McGowan.[1] The excitation curve for the 512-kev gamma ray of In^{115} differs markedly from the theoretical $E2$ excitation curve; the gamma ray probably arises from a nuclear reaction. The excitation curves for the 392-kev and 941-kev gamma rays of I^{127} differ from the theoretical $E2$ curves to some extent; all the other gamma rays follow an $E2$ excitation function.

* Work supported by the U. S. Atomic Energy Commission and the Wisconsin Alumni Research Foundation.
[1] P. H. Stelson and F. K. McGowan, Phys. Rev. 99, 112 (1955).

W10. Measurement of Energy Variation of the Neutron Multiplication, η, for U^{233}, U^{235}, and Cu^{239} in the Thermal Region.* H. PALEVSKY, R. L. ZIMMERMAN, R. M. EISBERG, AND D. J. HUGHES, *Brookhaven National Laboratory.*—A new method has been developed that gives directly the variation of η, the number of neutrons produced per neutron absorbed, with energy in the thermal region in a direct and unambiguous way. A beam of thermal neutrons passes through a "thin" (1/v) counter and then falls on a thick foil of the material being investigated. The fission neutrons from the foil are detected by a scintillation counter. As essentially all the neutrons are absorbed by the thick foil the thin counter gives the absorption rate, whereas the emission rate of fission neutrons is given by the scintillation counter. In this way the ratio of the counting rates of the scintillator to the thin counter is directly proportional to η. The energy of the incident neutrons is determined by time of flight method using the Brookhaven slow chopper. The results are normalized to the known thermal value of η with no attempt at absolute calibration of the counters. Measurements have been made by this method for U^{235}, U^{233}, and Pu^{239}. The measurements made with U^{235} and U^{233} indicate that in the region from 0.01 to 0.10 ev η is constant within experimental error (±1%). In Pu^{239}, η decreases by about 15% from 0.01 to 0.1 ev.

* Work carried out under contract with U. S. Atomic Energy Commission.

W11. Energy Dependence of η for U^{235} in the Region 0.04–1.0 ev.* J. R. SMITH AND E. H. MAGLEBY, *Phillips Petroleum Company.*—Measurements have been made of the energy dependence of η, the number of fission neutrons emitted per neutron absorbed, for U^{235} in the energy region 0.04–1.0 ev. Two 5-in. Hornyak buttons on DuMont 6364 photomultiplier tubes count fission neutrons from a target of U^{235} placed between them in the Bragg beam of the MTR crystal spectrometer. A sample changer moves the target into and out of the beam, enabling a single thin BF_3 counter behind the target to serve as both flux monitor and transmission detector. The data are normalized to the Brookhaven slow chopper results, which were normalized to the thermal value of $\eta = 2.08$. Below 0.1 ev η is essentially flat. Above 0.1 ev it falls to a value of 1.9 for the 0.3-ev resonance, then rises to a peak of about 2.2 between 0.5 and 0.7 ev. In the neighborhood of 1 ev η decreases as the 1.12-ev resonance is approached.

* Work performed under the auspices of the U. S. Atomic Energy Commission.

W12. The β^- Energy Distribution from Thermal Fission of U^{235}.* C. O. MUEHLHAUSE AND S. OLEKSA, *Brookhaven National Laboratory.*—The energy spectrum of β^- rays from thermal fission of U^{235} has been measured from 0.67 Mev to 6.7 Mev and found to be in good agreement with that predicted by E. Wigner and K. Way.[1] The spectrum and its absolute intensity was used to infer the neutrino spectrum emitted by a thermal reactor, and to compare relative rates of such reactions as $p(\nu,n)\beta^+$, $d(\nu,2n)\beta^+$, and $Cl^{37}(\nu_0,e^-)A^{37}$.

* Work performed under contract with the U. S. Atomic Energy Commission.
[1] E. Wigner and K. Way, Phys. Rev. 73, 1318 (1948).

SATURDAY AFTERNOON AT 1:45

Cobb 110

(R. A. SAWYER presiding)

General Physics

X1. Reduction of Optical Reflectivity of Glass by Positive Ion Bombardment. R. L. HINES, *Ford Motor Company.*—Bombardment of glass by krypton positive ions with an energy of 60 kev and a current density of 20 microamperes per cm² is known to reduce the optical reflectivity of glass.[1] The finite penetration of the positive ions produces a radiation damaged region whose index of refraction is intermediate between that of glass and air. The reflection coefficient will be a minimum, for a given wavelength of light, when the depth of the radiation damaged region is one quarter of a wavelength. To investigate this phenomena, a polished plate glass (composition by weight 72% SiO_2, 14% Na_2O, 12% CaO) is bombarded by an argon positive ion beam. The reflection coefficient for tungsten light fo the bombarded glass surface is measured as a function of bombardment time, ion beam current density, and ion energy. For a 33-kev argon ion beam and a current density of 100 microamperes per cm², the reflectivity decreases rapidly as a function of bombardment time and reaches a limiting value in approximately one minute. The limiting value of reflectivity is independent of current density from 50 to 460 microamperes per cm². The reflectivity decreases with increasing ion energy and passes through a minimum of 0.16 times the reflectivity of an untreated glass surface for bombardment by 42-kev argon ions.

[1] J. Koch, Nature **164**, 19 (1949).

X2. The Auger Effect in Iron, Nickel, Copper, Zinc.* CHARLES E. ROOS, *University of California, Riverside.*—The *K* fluorescence yields were measured by a scintillation counter method,[1] which utilizes the isotropic emission of fluorescent x-rays. Collimated primary x-rays passed through a sample foil and were detected by a scintillation counter. By moving the foil one could vary the solid angle subtended by the counter from 1.97π to 0.02π. This enabled one, effectively, to turn the fluorescent radiation "on" and "off." The difference between these two readings is primarily due to fluorescence. From a ratio of this difference and the direct primary beam, the *K* fluorescence yield of the sample can be determined. The following preliminary values were obtained: Fe – (0.29); Ni – (0.35); Cu – (0.39); and Zn – (0.43). The probable error is approximately 3%. Corrections were made for counter efficiency, phosphorescence of the NaI-Tl crystal and the effects of scattering, and absorption. These new values are uniformly 10% lower than the average of the earlier measurements, which all used the ionization chamber method. The new results give better agreement with theory.

* Experimental measurements were made at the Johns Hopkins University.
[1] C. E. Roos, Phys. Rev. **93**, 401 (1954).

X3. Normal Coordinate Treatments and Thermodynamic Properties of PF Cl_2 and POF Cl_2. EDWARD A. PIOTROWSKI AND JOSEPH S. ZIOMEK, *De Paul University.*—The Raman spectral data for PF Cl_2 and POF Cl_2 were collected and examined for the best available values of the wave numbers ($\Delta\sigma$), intensities (I) and depolarization factors (ρ). The values adopted for ($\Delta\sigma$,ρ) are as follows: for PF Cl_2: 200*P*, 327*P*, 524*P*, 827*P*, 496*D* and 271*D*; for POF Cl_2: 207(0.55), 300(0.6), 386(0.3), 547(0.05), 894(0.45), 1331*P*, 620(6/7), 372(6/7), and 254(6/7) in kaysers. No infrared data for these two substances were available. Next normal coordinate treatments (*FG* matrix method) on the basis of the most probable model (C_s) were conducted for PF Cl_2 and POF Cl_2. Here the *F* matrix elements were estimated in such a manner that the potential constants for PF Cl_2 had nearly the same values as the corresponding constants in PF_3 and P Cl_3 and for POF Cl_2 the potential constants had nearly the same values as the corresponding ones in PO Cl_3, POF_3, and PF Cl_3. Finally the above spectral data were used to calculate the values of the thermodynamic properties for these substances up to a rigid rotator harmonic oscillator approximation for temperatures from 200°K to 1000°K.

X4. Normal Coordinate Treatment for the Out-of-Plane Vibrations of Ethylene Type Molecules.* J. M. DOWLING, *Illinois Institute of Technology.*—Using the Wilson[1] *FG* matrix method the wave numbers corresponding to the out-of-plane fundamental frequencies for a number of ethylene type molecules were calculated. The *g* (inverse kinetic energy) matrix elements were calculated from the **s** vectors derived explicitly in the papers of Malhiot and Ferigle.[2] All possible second-degree terms were included in the *F* matrix describing the potential energy function. Numerical calculations were carried out for C_2H_4, asymmetric $C_2H_2F_2$, asymmetric $C_2H_2Br_2$, the *cis*- and *trans*-isomers of $C_2H_2Cl_2$, and all of their deuterated analogs. The 57 out-of-plane fundamentals were calculated for the above 19 molecules. Of these 57 fundamentals, 50 have been reported in the literature and are reproduced with an average deviation of 2.2K (cm^{-1}).

* This investigation was supported in part by grants from the Research Corporation and the National Science Foundation.
[1] E. B. Wilson, Jr., J. Chem. Phys. **7**, 1047 (1939); **9**, 76 (1941).
[2] R. J. Malhiot and S. M. Ferigle, J. Chem. Phys. **22**, 717 (1954); **23**, 30 (1955).

X5. Potential Constants for the CHDClBr, CH_2F_2, CD_2F_2, and $CHDF_2$ Molecules.* A. G. MEISTER, J. M. DOWLING, A. N. TAKATA, AND A. J. BIELECKI, *Illinois Institute of Technology.*—The potential constants for the most general quadratic potential function were calculated for these molecules using the Wilson *FG* matrix method. For CHDClBr, the potential constants were found to be the same as those used for CH_2ClBr and CD_2ClBr in previous investigations in this laboratory.[1] The agreement between the observed and calculated wave numbers of the fundamentals of CHDClBr was to within 2.5%. For CH_2F_2 the agreement was to within 1%. No comparison could be made for CD_2F_2 and $CHDF_2$ because no observed wave numbers of the fundamentals could be found in the literature.

* This investigation was supported in part by grants from the Research Corporation and the National Science Foundation.
[1] Weber, Meister, and Cleveland, J. Chem. Phys. **21**, 930 (1953).

X6. Frequencies and Relative Intensities of R_1 and R_2 Bands in KCl.* ROBERT HERMAN,† *University of Maryland,* AND M. C. WALLIS AND R. F. WALLIS, *Applied Physics Laboratory, The Johns Hopkins University.*—Measurements have been made of the intensities of the R_1 and R_2 bands in KCl as a function of duration of *F*-light irradiation. Both x-rayed and additively colored crystals were used. The x-raying and the *F*-light irradiation were done at room temperature. The optical absorption measurements were made at liquid nitrogen temperature. In both the x-rayed and additively colored samples the ratio of the R_2 and R_1

band intensities varied by less than a factor 1.5 when the individual intensities varied by a factor 6 or greater. No other pair of bands showed such a small variation in their intensity ratio. Theoretical frequencies and oscillator strengths were obtained for the $1s\sigma-2p\sigma$ and $1s\sigma-2p\pi$ transitions of H_2^+ immersed in a dielectric medium. Using the high-frequency dielectric constant of KCl, the calculated frequencies correspond to 1900 and 490 $m\mu$, respectively; the oscillator strengths are 0.25 and 0.47. Frequencies were obtained for the $^1\Sigma_g^+-{}^1\Sigma_u^+$ and $^1\Sigma_g^+-{}^1\Pi_u$ transitions of H_2 immersed in a dielectric medium. For KCl the calculations yield 765 and 620 $m\mu$. It appears possible that the observed R_1 and R_2 bands may arise from two transitions of the system of two electrons trapped at a pair of negative ion vacancies.

* This work supported by the Bureau of Ordnance, Department of the Navy.

† On leave from Applied Physics Laboratory, The Johns Hopkins University.

X7. Electron Loss Cross Section for Fast Helium Atoms. C. F. BARNETT AND P. M. STIER, *Oak Ridge National Laboratory*.—The cross section for electron loss has been determined for fast helium atoms passing through gases. The energy range studied was from 30 to 200 kev and the stopping gases investigated were hydrogen, helium, nitrogen, oxygen, neon, and argon. Helium ions from the Cockcroft-Walton accelerator were converted to fast helium atoms by charge exchange. This atomic beam entered a differentially pumped gas cell within which a transverse electrostatic field could be applied. The cross section was determined by observing the attenuation as a function of gas pressure. It will be shown that as the fast neutral atoms are formed by electron capture, it appears that an appreciable number are left in the metastable state. Subsequent collisions produce an equilibrium distribution between the ion, metastable state atom and ground-state atom components. The electron loss cross sections to be reported are for the neutral component of such an equilibrium beam. Curves will be presented showing the rapid increase in these cross sections as the velocity of the helium atom is increased. The cross sections at 200 kev are 6.0, 10.0, 19.8, 23.0, 23.0, 37.2×10^{-17} cm²/atom for H_2, He, Ne, N_2, O_2, and A, respectively.

X8. Measurement of Electron Mobilities in Gases. JOSEPH C. BOWE, *Argonne National Laboratory*.—The drift velocity of electrons moving in collision equilibrium with a gas under the action of a uniform electric field is determined by measuring the time required for them to cross the gap of a parallel plate condenser. A flash tube capable of delivering intense, short duration bursts of ultraviolet light is used to release photoelectrons from the cathode. The number of photoelectrons released with each burst of light is large enough to permit the use of a transient amplifier for the amplification of the signal. The time of drift is obtained by displaying the signal on an oscilloscope. The parallel plate condenser is mounted in a metal chamber 8 inches in diameter by 4 inches and is part of a helium tight all metal system free from soldering fluxes and organic materials which might contaminate the gas. Some difficulties encountered in securing a tight, all metal system will be discussed. Data obtained in the gases studied will also be presented.

X9. Electroluminescence in Zinc Sulfide. W. A. THORNTON, *General Electric Research Laboratory*.—A simple theory, based upon a single-level trapping and field-release process, predicts detailed dependences of electro-luminescence light output wave form and integrated light output on voltage, frequency, and temperature. Extensive data, obtained with the use of zinc sulfide phosphor powder layers, are in qualitative or quantitative agreement with the theory. Negligible frequency dependence of integrated light output at low fields and low temperatures is predicted and experimentally confirmed. Small temperature dependence, over a wide range of temperatures, at high fields and low frequencies and strong temperature dependence at low fields and high frequencies is predicted and observed; this latter effect is an explanation for both strong and weak temperature dependences being reported in the literature. A proposed sequence of processes throughout the voltage cycle is based upon the theory plus supplemental data involving glow curves, photoluminescence, and spectral content of the electroluminescence emission.

SATURDAY AFTERNOON AT 1:45

Oriental 104

(R. H. CRANE presiding)

The Brookhaven Electron Analog

Y1. The Electron Analog.* G. K. GREEN, E. D. COURANT, L. J. HAWORTH, AND H. S. SNYDER, *Brookhaven National Laboratory*.—An electron accelerator has been constructed to test in detail the particle orbits of a strong-focusing, or alternating-gradient, synchrotron. This electron accelerator is not a model of any specific large synchrotron, but is rather an analog of the general alternating-gradient focusing system. The orbit of this machine is 45 feet in diameter and the aperture 0.8 inch square. Electrons are injected from a small Van de Graaff at 1 Mev and can be accelerated by a single rf cavity to a maximum energy of 10 Mev. Guide and focusing fields are electrostatic. 160 hyperbolic lenses make up the basic alternating-gradient field which can be modified linearly by electrostatic quadrupoles, and nonlinearly by sextupoles and octupoles. The machine is designed to explore all classes of resonances over at least one full diamond of the stability diagram, and to pass through the phase transition at about the geometric mean of its energy range.

* Work carried out under contract with U. S. Atomic Energy Commission.

Y2. Electron Analog—Construction.* D. D. JACOBUS, C. L. GOULD, J. J. GRISOLI, AND I. J. POLK, *Brookhaven National Laboratory*.—The lenses of the electron analog are fabricated of Type 303 stainless steel. Hyperbolic surfaces were machined with formed milling cutters. The electrodes were spaced in aluminum frames with accurately ground ceramic insulators. Five sets of paired bending lenses, one quadrupole lens, one sextupole lens, one octupole lens, and one set of pickup electrodes are pinned in true relative positions to an aluminum box girder. Sixteen of these box girder assemblies were placed on a true circle by the use of a radius bar and micrometer gauge, with concrete piers as supports. The surrounding

vacuum chamber is farbicated of ferritic stainless steel, and is independently supported through expansion joints. The radial and vertical positions of the aperture, and all other critical dimensions, were calibrated on each assembled bending lens. The average deviation was of the order of ± 0.002 in. Sixteen ten inch mercury diffusion pumps, each with cold wall type of liquid nitrogen trap and freon baffle, produce a pressure of 5 to 6×10^{-7} mm of Hg in the system. Convaseal is used as the gasket material. Refrigerated baffles prevent oil migration from a Kinney forepump to the mercury pumps. The entire system uses about 20 liters per hour of liquid nitrogen.

* Work carried out under contract with U. S. Atomic Energy Commission.

Y3. Electron Analog—Electrical System.* J. G. Cottingham, N. C. Christofilos, M. Plotkin, E. C. Raka, and R. H. Rhéaume, *Brookhaven National Laboratory.*—Electrical equipment for the electron analog required the solution of several unusual circuit problems. The 20 kv inflector potential must be removed precisely within a fraction of the revolution period (140 millimicroseconds) to allow the passage of the beam through the inflector on the second and successive revolutions. The potential difference on the guide field electrodes is increased linearly to 60 kv in 5 milliseconds, balanced with respect to ground. The system of electrostatic field-correction lenses can be energized either with linearly rising potentials, or with numerous combinations of steady potentials. Beam position, intensity, and revolution frequency are sensed by pickup electrodes and their associated amplifiers. Frequency information from the pickup electrodes is processed through an electronic phase correction circuit and feeds a power amplifier which applies the rf potential to the accelerating gap of the ferrite-loaded cavity. Electronic means for crossing the phase transition have been designed.

* Work carried out under contract with U. S. Atomic Energy Commission.

Y4. Electron Analog—Initial Setup.* J. Spiro, J. G. Cottingham, E. E. Courant, and R. R. Kassner, *Brookhaven National Laboratory.*—To prevent the accumulation of tolerances in the stacking of lenses, and the resultant perturbation on the electron beam, a specified arrangement was devised. The gauge measurements of individual lens assemblies were reduced to equivalent horizontal and vertical displacements of the electrical field. The lenses were then sequenced so that low order azimuthal harmonics of the horizontal deviation were minimized. The corresponding vertical deviations were then in random order. Computations indicate that the resulting equilibrium orbit excursion is 0.03 inch radially, ($\frac{1}{2}$ the extreme variation between lenses), and 0.07 inch vertically (twice the extreme between lenses). Measurements taken around the electron orbit after preliminary degaussing showed a residual magnetic field varying up to one gauss. Some of the techniques used to reduce these fields to 20 milligauss will be presented. Focusing, steering, and observation of the injected beam are accomplished along the pipe connecting the Van de Graaff to the inflector tank. The timing system of the electron analog is synchronized with the 60-cycle line frequency. Stray magnetic fields from an unsynchronized alternator near the Van de Graaff electron source produced an undesirable beat in the injected beam. A synchronizer reduced the beat, and careful adjustment of the injection system reduced the jitter.

* Work done under contract with U. S. Atomic Energy Commission.

Y5. Electron Analog—Performance and Interpretation. I.* *E. C. Raka, E. D. Courant, R. R. Kassner, L. J. Laslett,† H. S. Snyder, and J. Spiro, *Brookhaven National Laboratory.*—The injected beam is allowed to circulate in a static guide field permitting an investigation of the nature of the equilibrium orbit. Various configurations of correction fields are applied and their effects on the betatron oscillations, usable aperture, and resonance bands are studied. Observation of the beam is accomplished both by visual and electrical methods. From oscilloscope patterns it is possible to identify the class of resonance excited, although not the order. Application of the rf accelerating voltage has been carried out successfully, and preliminary results under dynamic operating conditions will be described.

* Work carried out under contract with U. S. Atomic Energy Commission.
† On summer leave from Iowa State College.

Y6. Electron Analog—Performance and Interpretation. II.* E. D. Courant, R. R. Kassner, E. C. Raka, Lloyd Smith,† and J. Spiro, *Brookhaven National Laboratory.*—The quadrupole correcting lenses in the electron analog can be adjusted so as to change the frequencies ν_x and ν_y of the horizontal and vertical betatron oscillation. According to the linear theory resonances should make the beam unstable if ν_x or ν_y are integral or half-integral, or if $\nu_x+\nu_y$ is integral. The integral resonances always lead to complete loss of the beam over a range of about 100 volts of quadrupole voltage. This range can be narrowed by appropriate settings of "kicker" electrodes. The half-integral and sum resonances sometimes lead to complete loss of beam in narrow bands; sometimes the beam survives. If the quadratic component of the focusing field contains azimuthal Fourier harmonics of the order 3ν (produced with kickers or sextupoles) there is also loss when ν is $\frac{1}{3}$ integral or if $2\nu_x+\nu_y$ is integral. Partial losses at $\nu=\frac{1}{4}$ integer can be induced by azimuthal variations in the cubic field. These nonlinear resonances can also be explained by theory. When the quadrupole voltages are varied with time so as to run through resonances, the beam is generally lost if and only if the corresponding resonance causes loss under static conditions.

* Work carried out under contract with U. S. Atomic Energy Commission.
† On leave from University of California.

SUPPLEMENTARY PROGRAMME

SP1. $Sr^{86,87,88}$, Y^{89}, Zr^{92} (γ,n) Cross Sections. Paul F. Yergin and Burton P. Fabricand, *University of Pennsylvania.**—We have measured these cross sections from threshold to 23 Mev. All show the usual giant resonance, at about 16 Mev. The width of the resonances show systematic variation not attributable to $(\gamma,2n)$ or (γ,pn) contributions. They provide further evidence of the effect of the magic neutron number, 50, on the giant resonance width. The lesser widths are not associated with greater heights; instead the integrated cross section decreases substantially when the peak becomes narrower. We also observe that the rise of the cross section into the peak, from 12.5 to 15.5 Mev, is almost exactly the same in shape and magnitude for all 5 isotopes, as well as for the previously measured[1] Zr^{90} and Zr^{91}. In agreement with the conjecture of Wapstra[2] we find the $Sr^{88}(\gamma,n)$ threshold to be at about 11.5 Mev, not at 9.5 Mev as previously reported.

* To be given at the end of Session I if the chairman rules that tim permits.
[1] R. Nathans and P. F. Yergin, Phys. Rev. **98**, 1296 (1955).
[2] A. H. Wapstra, Physica **21**, 385 (1955).

Author Index to Papers Presented at the 1955 Chicago Meeting

Alexeff, Igor and Edward C. Peterson—B5
Almqvist, E., R. L. Clarke, and E. B. Paul—W1
Alvarez, Luis W.—Q1
——, Frank S. Crawford, Jr., Myron L. Good, and M. Lynn Stevenson—V14
Artman, J. O.—D5
Ayres, R. U. and R. H. Tredgold—R8
Barnett, C. F. and P. M. Stier—X7
Barschall, H. H. and S. E. Darden—C10
Bath, H. M. and M. Cutler—T4
Baumann, N. P., F. W. Prosser, Jr., and R. W. Krone—E1
Bedo, D. E. and D. H. Tomboulian—R9
Belinfante, F. J.—K2
Bloom, S. D., G. N. Glasoe, C. O. Muehlhause, and H. E. Wegner—I1
Bollinger, L. M., R. E. Coté, and J. M. LeBlanc—B10
Bostick, Winston H.—K1
Bowe, Joseph C.—X8
Bray, Ralph—U9
Brockhouse, B. N. and H. P. Myers—D3
Brophy, James J.—U5
Browne, C. P.—P10
Bullis, W. M. and W. E. Krag—T2
Caldwell, R. S. and H. Y. Fan—N4
Carlson, R. R. and S. Bashkin—P11
Cavanaugh, R. E., D. M. Haskin, and Marcel Schein—V5
Chandrasekhar, S.—H2
Chiba, Ren, R. A. Douglas, J. W. Broer, D. F. Herring, and E. A. Silverstein—P7
Church, E. L. and J. Weneser—C9
Cole, F. T. and D. W. Kerst—G5
Coleman, Bernard D.—R12
Connell, R. A. and J. A. Marcus—R2
Connors, D. R., W. C. Miller, and B. Waldman—A9
Cork, J. M., M. K. Brice, D. W. Martin, L. C. Schmid, and R. G. Helmer—A7
Cottingham, J. G., N. C. Christofilos, M. Plotkin, E. C. Raka, and R. H. Rhéaume—Y3
Courant, E. D., R. R. Kassner, E. C. Raka, Lloyd Smith, and J. Spiro—Y6
D'Altroy, F. and H. Y. Fan—T12
D'Asaro, L. A.—R13
Davis, Robert H., Ajay S. Divatia, R. D. Moffat, and D. A. Lind—W8
Dempsey, D. F., W. C. Miller, and B. Waldman—B11
Divatia, Ajay S., Robert H. Davis, R. D. Moffat, and D. A. Lind—W9
Douglas, R. A., J. W. Broer, and Ren Chiba—P9
Dowling, J. M.—X4
Dresselhaus, G.—N1
——, A. F. Kip, and C. Kittel—U10
Duffield, R. B., M. E. Bunker, J. P. Mize, and J. W. Starner—A6
Edwards, Palmer L.—D2
Evans, J. S. and R. H. Tredgold—K4
Fabricand, B. P., B. Allison, and J. Halpern—I9
Feld, Bernard T.—V9
Ferguson, G. A., C. W. Peters, and F. E. Jablonski—B8
Filosofo, I.—G2
Foote, H. L., Jr.—I2
Fox, John D. and Peter Axel—I10
Franzen, W., P. Huber, and L. Schellenberg—B9
Friesen, E. W.—G10
Gallagher, C. J.—T7
Gelinas, R. W. and S. S. Hanna—P4
Geller, Z. and W. Low—B12
Gilbert, T. L.—D6
Glicksman, M.—T1
Goldhaber, Gerson—V1
Goldwasser, E. L. and L. J. Koester, Jr.—Q4
Gomez, R., G. E. Pugh, D. H. Frisch, and G. S. Janes—E8
Goodman, L. S. and S. Wexler—E12
Gould, F. T., T. I. Taylor, and W. W. Havens, Jr.—I4
Gove, Norwood, Fred A. Smith, and R. A. Becker—A3
Graves, William E. and Allan C. G. Mitchell—A4
Green, G. K., E. D. Courant, L. J. Haworth, and H. S. Snyder—Y1
Grimes, D. M. and J. W. Kuiper—R6
Grodzins, Lee and Henry Motz—A5
Gupta, I. C., W. Y. Chang, and A. Snyder—V12
Haber-Schaim, U.—V7
Ham, Frank S.—N3
Harman, T. C., S. E. Miller, and H. L. Goering—U11
Haskin, D. M., D. B. Williams, E. Goodman, and Marcel Schein—V4
Haynes, J. R.—T5
Herman, Robert, M. C. Wallis, and R. F. Wallis—X6
Herring, D. F., R. A. Douglas, E. A. Silverstein, and Ren Chiba—B7
Hines, R. L.—X1
Hollander, J. M., W. G. Smith, and J. W. Mihelich—A12
Holliday, J. E. and E. J. Sternglass—B3
Holm, Dale M. and H. V. Argo—E3
Holmgren, H. D., W. E. Kunz, and L. Bullock—P6
Hosler, W. R. and H. P. R. Frederikse—U6
Hughes, D. J. and V. E. Pilcher—I8
Igo, G., H. E. Wegner, and R. M. Eisberg—E4
Jacobs, Ira—R11
Jacobus, D. D., C. L. Gould, J. J. Grisoli, and I. J. Polk—Y2
Janes, G. S., R. Gomez, G. E. Pugh, and D. H. Frisch—E9
John, Walter—W2
Johnson, C. H. and A. Galonsky—P1
Johnson, V. A.—N2
Jones, L. W. and K. M. Terwilliger—G6
Joseph, J.—C6
Kaiser, H. F.—G3
Kammer, E. W., E. I. Salkowitz, and A. I. Schindler—R10
Keyes, R. W. and R. J. Sladek—U8
Kikuchi, Chihiro—D8
King, R. W.—C3
Kisslinger, L. S.—C2
Kleitman, D. and T. A. Longo—U2
Kohnke, E. E. and A. W. Ewald—N6
Koshiba, M. and Marcel Schein—H3
Kottwitz, David A.—D4
Kunz, W. E., J. W. Butler, and H. D. Holmgren—P2
LaVier, E. C., S. S. Hanna, and R. W. Gelinas—P3
LeBlanc, J. M., L. M. Bollinger, and R. E. Coté—I3
Leenov, Daniel, D. M. Haskin, and Marcel Schein—V3
Loebner, E. E.—B4
Longo, Thomas A. and David Kleitman—U1
Low, Francis—K5
Lowe, I. J., L. O. Bowen, and R. E. Norberg—D9
Magnusson, L. B., D. W. Engelkemeir, M. S. Freedman, F. T. Porter, and F. Wagner, Jr.—A11
Margulies, R. S.—Q6
Martin, David W., S. Bradley Burson, and James M. Cork—A1
Matarrese, Lawrence M. and Chihiro Kikuchi—D7
McEllistrem, M. T.—P8
McLeod, R. R.—W6
Meister, A. G., J. M. Dowling, A. N. Takata, and A. J. Bielecki—X5
Miller, D. W., V. K. Rasmussen, M. B. Sampson, and U. C. Gupta—P5
Mobley, R. C., C. H. Blakewood, and D. C. Ralph—D1

Montet, G. L., A. F. Kurs, and G. R. Hennig—U4
Morinaga, H. and E. Bleuler—A2
Muehlhause, C. O. and S. Oleksa—W12
Munick, Raymond J.—R4
Nagle, D. E.—Q2
Newton, R. G.—K8
Odian, Allen, Bernard Feld, William Rankin, Peter Stein, Albert Wattenberg, and Roy Weinstein—C8
Ohkawa, Tihiro—G8
Ohnuma, Shoroku and David Feldman—C5
Palevsky, H., R. L. Zimmerman, R. M. Eisberg, and D. J. Hughes—W10
Pearson, G. L., W. T. Read, Jr., and W. L. Feldmann—N5
Peaslee, D. C.—K7
Penman, S. and W. L. Brown—T6
Pilcher, V. E., J. A. Harvey, and K. K. Seth—I5
Piotrowski, Edward A. and Joseph S. Ziomek—X3
Piper, W. W. and J. S. Prener—K3
Pruett, Charles H. and Roger G. Wilkinson—A8
Pugh, G. E., R. Gomez, D. H. Frisch, and G. S. Janes—E7
Quisenberry, K. S., T. T. Scolman, and A. O. Nier—E11
Raka, E. C., E. D. Courant, R. R. Kassner, L. J. Laslett, H. S. Snyder, and J. Spiro—Y5
Rappaport, Paul and Joseph J. Loferski—U3
Rarita, William—C4
Redin, R. D., and G. C. Danielson—N7
Ribe, F. L.—P13
Ritson, D. M., A. Odian, B. T. Feld, and A. Wattenberg—V8
Roberts, B. W.—R7
Rohrlich, Fritz—S1
—— and J. Joseph—C7
Roos, Charles E.—X2
Roothaan, C. C. J.—S2
Ross, Marc—K6
Sachs, A. M., H. Winick, and B. A. Wooten—Q5
Sailor, V. L.—I6
Schein, Marcel and D. M. Haskin—V2
Schneps, J., M. S. Swami, and W. F. Fry—V6
Scolman, T. T., K. S. Quisenberry, and A. O. Nier—E10
Scott, Mary Jean and Ralph E. Segel—E2
Severiens, J. C. and S. S. Hanna—P15
Shephard, W. D. and W. D. Walker—V11
Shulman, R. G.—T10
Sidles, P. H.—R3
Simmons, B. E., K. F. Famularo, and G. D. Freier—W7
Simpson, O. D., R. G. Fluharty, F. B. Simpson, and R. M. Brugger—I7
Simpson, J. A.—H1
Sivertsen, J. and C. Wert—R5
Slepian, Joseph—B1
Smith, J. H. and M. Q. Barton—W3
Smith, J. R. and E. H. Magleby—W11
Snyder, A., W. Y. Chang, and I. C. Gupta—V13
Spiegel, V., Jr., B. Waldman, and W. C. Miller—E5
Spiro, J., J. G. Cottingham, E. D. Courant, and R. R. Kassner —Y4
Statz, H., G. A. deMars, L. Davis, Jr., and A. Adams, Jr.—T13
Steffen, R. M.—S3
Sternglass, E. J. and M. M. Wachtel—B2
Stump, R.—R1
Symon, Keith R.—G7
Tatro, C. A. and T. R. Palfrey, Jr.—W4
Tauber, G. E. and T. Y. Wu—C1
Teng, L. C.—G9
Terwilliger, K. M., L. W. Jones, F. T. Cole, D. W. Kerst, and R. O. Haxby—G4
Thornton, W. A.—X9
Tomnovec, F. M. and C. S. Cook—P14
Toppel, B. J., D. H. Wilkinson, and D. E. Alburger—P12
Tweet, A. G.—T11
Tyler, W. W. and H. H. Woodbury—T9
Vegors, Stanley, H., Jr., and Peter Axel—A13
Waldman, B., V. Spiegel, Jr., and W. C. Miller—E6
Walker, W. D. and W. D. Shephard—V10
Wallenmeyer, W. A.—Q3
Weinman, J. A., J. R. Cameron, and R. G. Herb—B6
Whitsett, C. R. and G. C. Danielson—U7
Wolicki, E. A., L. W. Fagg, and E. G. Geer—W5
Wood, G. T. and P. S. Jastram—A10
Woodbury, H. H. and W. W. Tyler—T8
Wyluda, B. J. and R. G. Shulman—T3
Yamagata, Taketora and Megumu Yoshimine—G1
Yergin, Paul F. and Burton P. Fabricand—I11, SP1